Physical and numerical investigations of the dynamic interaction of granulates and fluid

Vom Promotionsausschuss der
Technischen Universität Hamburg

zur Erlangung des akademischen Grades

Doktor-Ingenieur (Dr.-Ing.)

genehmigte Dissertation

von
Désirée D. Plenker

aus
Wuppertal

2020

1. Gutachter: Prof. Dr.-Ing. Jürgen Grabe
2. Gutachter: Prof. Dr.-Ing. Holger Schüttrumpf

Tag der mündlichen Prüfung: 27.11.2020

Physical and numerical investigations of the dynamic interaction of granulates and fluid

von

Désirée D. Plenker

Herausgegeben von

J. Grabe

Technische Universität Hamburg
Institut für Geotechnik und Baubetrieb

Veröffentlichungen des Instituts für Geotechnik und Baubetrieb

46

Herausgeber:

Univ.-Prof. Dr.-Ing. Jürgen Grabe
Technische Universität Hamburg
Institut für Geotechnik und Baubetrieb
Harburger Schloßstraße 20
D – 21079 Hamburg
e-mail: *grabe@tuhh.de*

ISBN: 978-3-936310-48-1 (Erstausgabe)

Druckerei

Druckzentrum Neumünster GmbH
Rungestraße 4
24537 Neumünster

In derselben Reihe erschienen:

1. J. Grabe (Hrsg.), 2000: Verbrennungsrückstände. Tagungsband, ISBN 3-936310-00-9
2. J. Grabe (Hrsg.), 2001: Schaden- und Risikomanagement im Tiefbau. Tagungsband, ISBN 3-936310-01-7
3. J. Grabe, 2003. Bodenmechanik und Grundbau. ISBN 3-936310-03-3
4. J. Grabe (Hrsg.), 2003: Euronormen in der Geotechnik – Was ändert sich? Tagungsband, ISBN 3-936310-04-1
5. J. Grabe (Hrsg.), 2003: Bodenverdichtung, Experimente - Modellierung - Geräteentwicklung - Baustellenberichte - F+E-Bedarf. Tagungsband, ISBN 3-936310-05-X
6. M. Kelm, 2004: Numerische Simulation der Verdichtung rolliger Böden mittels Vibrationswalzen. Promotion, ISBN 3-936310-06-8
7. J. Grabe (Hrsg.), 2004: Kaimauern - Messungen und Numerik. Tagungsband, ISBN 3-936310-07-6
8. J. Stein, 2005. Experimentelle und numerische Untersuchungen zum Düsenstrahlverfahren. Promotion, ISBN 3-936310-09-2
9. J. Grabe (Hrsg.), 2005: Grenzschicht Wasser und Boden - Phänomene und Ansätze. Tagungsband, ISBN 3-936310-10-6
10. J. Grabe (Hrsg.), 2005: FEM in der Geotechnik - Qualität, Prüfung, Fallbeispiele - Tagungsband, ISBN 3-936310-11-4
11. B. Mardfeldt, 2006: Zum Tragverhalten von Kaikonstruktionen im Gebrauchszustand. Promotion, ISBN 3-936310-12-2
12. J. Grabe (Hrsg.), 2006: Optimierung in der Geotechnik - Strategien und Fallbeispiele. Tagungsband, ISBN-13: 978-3-936310-13-9
13. T. Bierer, 2007: Bodenschwingungen aus Straßenverkehr auf unebener Fahrbahn im Zeitbereich - experimentelle und theoretische Untersuchungen. Promotion, ISBN-13: 978-3-936310-14-6
14. J. Grabe (Hrsg.), 2007: Bemessen mit Finite-Elemente-Methoden. Tagungsband, ISBN-13: 978-3-936310-15-3
15. K.-P. Mahutka, 2008: Zur Verdichtung von rolligen Böden infolge dynamischer Pfahleinbringung und durch Oberflächenrüttler. Promotion, ISBN-13: 978-3-936310-16-0
16. J. Grabe (Hrsg.), 2008: Seehäfen für Containerschiffe zukünftiger Generationen. Tagungsband, ISBN-13: 978-3-936310-17-7
17. F. König, 2008: Zur zeitlichen Traglastentwicklung von Pfählen und der nachträglichen Erweiterung bestehender Pfahlgründungen. Promotion, ISBN-13: 978-3-936310-18-4
18. S. Henke, 2008: Herstellungseinflüsse aus Pfahlrammung im Kaimauerbau. Promotion, ISBN-13: 978-3-936310-19-1

19. J. Grabe (Hrsg.), 2009: Spundwände – Profile, Tragverhalten, Bemessung, Einbringung und Wiedergewinnung. Tagungsband, ISBN-13: 978-3-936310-20-7
20. J. Dührkop, 2009: Zum Einfluss von Aufweitungen und zyklischen Lasten auf das Verformungsverhalten lateral beanspruchter Pfähle in Sand. Promotion, ISBN-13: 978-3-936310-21-4
21. O. Möller, 2009: Zum Langzeit-Kompressionsverhalten weicher organischer Sedimente. Promotion, ISBN-13: 978-3-936310-22-1
22. J. Grabe (Hrsg.), 2011: Ports of container ships of future generations. Tagungsband, ISBN-13: 978-3-936310-23-8
23. S. Kinzler, 2011: Zur Parameteridentifikation, Entwurfs- und Strukturoptimierung in der Geotechnik mittels numerischer Verfahren. Promotion, ISBN-13: 978-3-936310-24-5
24. G. Qiu, 2012: Coupled Eulerian Lagrangian Simulations of Selected Soil-Structure Problems. Promotion, ISBN-13: 978-3-936310-25-2
25. X. Ma, 2013: Nutzung der oberflächennahen Geothermie mittels Energiepfählen und Erdwärmesonden. Promotion, ISBN-13: 978-3-936310-26-9
26. J. Grabe (Hrsg.), 2013: Proceedings of the Conference on Maritime Energy COME 2013. Tagungsband, ISBN-13: 978-3-936310-28-3
27. J. Grabe (Hrsg.), 2013: Bemessen mit numerischen Methoden. Tagungsband, ISBN-13: 978-3-936310-29-0
28. T. Pucker, 2013: Stoffmodell zur Modellierung von stetigen Materialübergängen im Rahmen der Optimierung geotechnischer Strukturen. Promotion, ISBN-13: 978-3-936310-30-6
29. S. Henke, 2013: Untersuchungen zur Pfropfenbildung infolge der Installation offener Profile in granularen Böden. Habilitation, ISBN-13: 978-3-936310-31-3
30. J. Grabe (Hrsg.), 2014: Ports for Container Ships of Future Generations. Tagungsband, ISBN-13: 978-3-936310-32-0
31. J. Grabe (Hrsg.), 2014: Offshore Basishäfen, Tagungsband, ISBN-13: 978-3-936310-33-7
32. C. Rudolph, 2015. Untersuchungen zur Drift von Pfählen unter zyklischer, lateraler Last aus veränderlicher Richtung, Promotion, ISBN-13: 978-3-936310-34-4
33. J. Grabe (Hrsg.), 2015: Morphodynamics 2015, Tagungsband, ISBN-13: 978-3-936310-35-1
34. T. Hamann, 2015: Zur Modellierung wassergesättigter Böden unter dynamischer Belastung und großen Bodenverformungen am Beispiel der Pfahleinbringung, Promotion, ISBN-13: 978-3-936310-36-8
35. B. Schümann, 2015: Beitrag zum dynamischen Dreiphasenmodell für Boden auf Basis der Finite-Elemente-Methode, Promotion, ISBN-13: 978-3-936310-37-5

36. M. Milatz, 2015: Untersuchungen zum Einfluss der Kapillarität auf das hydraulisch-mechanische Verhalten von granularer Tragschichten für Verkehrswege, Promotion, ISBN-13: 978-3-936310-38-2
37. H. Kaya, 2016: Bodenverschleppung und Spaltbildung infolge der Einbringung von Profilen in Dichtungsschichten aus Ton, Promotion, ISBN-13: 978-3-936310-39-9
38. J. Grabe (Hrsg.), 2017: Proceedings of the Conference on Maritime Energy COME 2017. Tagungsband, ISBN-13: 978-3-936310-40-5
39. B. Kocak, 2017: Zur numerischen Modellierung von hydraulisch-mechanisch gekoppelten Prozessen in gesättigten granularen Böden mittels Smoothed Particle Hydrodynamics, Promotion, ISBN-13: 978-3-936310-41-2
40. K. Siegl, 2017: Zur Pfahldynamik von gerammten Großrohrpfählen und der daraus resultierenden Wellenausbreitung in Wasser und im Meeresboden, Promotion, ISBN-13: 978-3-936310-42-9
41. J. Grabe (Hrsg.), 2017: Numerical Methods in Geotechnics, Tagungsband, ISBN-13: 978-3-936310-43-6
42. J. Grabe (Hrsg.), 2018: Digitale Infrastruktur und Geotechnik (DIG 2018), Tagungsband, ISBN-13: 978-3-936310-44-3
43. D. Osthoff, 2018: Zur Ursache von Schlosssprengungen und zu einbringbedingten Lageabweichungen von Spundwänden, Promotion, ISBN-13: 978-3-936310-45-0
44. E. Heins, 2018: Numerical based identification of the pile-soil interaction in terms of the axial pile bearing capacity, Promotion, ISBN-13: 978-3-936310-46-7
45. K. Seitz, 2020: Zur Topologieoptimierung von geotechnischen Strukturen und zur Tragfähigkeitssteigerung des Baugrunds durch Scherfugenverfestigung, Promotion, ISBN-13: 978-3-936310-47-4

Editor's Preface

Die Betrachtung von Boden als Partikel-Fluid-System ermöglicht neue Einblicke in die hydro-mechanischen Prozesse beispielsweise beim Überströmen von Wasser über einen Sandboden. Hierbei interagiert das strömende Wasser mit dem Porenwasser. Die Auftriebs- und Schleppkräfte führen zum Herauslösen einzelner Partikel und damit zur Erosion des Sandes. Gleichzeitig ändert sich die turbulente Grenzströmung durch das Herauslösen der Partikel. Diese mikromechanischen Vorgänge sind nicht linear und nur unzureichend abzubilden. Bisher gibt es hierzu daher lediglich empirische oder zumindest halb-empirische Modelle. Hier einen Schritt weiter zu kommen, hätte große Relevanz für das Verständnis, die Modellierung und die zutreffendere Prognose von Erosionsvorgängen beispielsweise an Sohlen, an Uferböschungen, an im strömenden Wasser gegründeten Strukturen wie bei Brückenfundamenten, Ufereinfassungen und bei Gründungen von Windenergieanlagen offshore.

Frau Plenker führt hierzu experimentelle und numerische Untersuchungen durch. Sie betreibt Versuche in einem selbst konstruierten Versuchskasten und in einer Rinne des Wasserbauinstituts der TUHH. Für die numerischen Untersuchungen wendet sie die Methode der gekoppelten Diskreten Elemente und der Fluiddynamik (CFD-DEM) an. Sie verwendet das Programm CFDEM®, DCS Computing, Linz. Aufgrund der Größe der gewählten Randwertprobleme wählt sie eine im Porenraum nicht aufgelöste (unresolved) Diskretisierung. Sie befasst sich zunächst mit dem Absinken eines Partikels im Wasser. Hier kann sie die numerischen Ergebnisse gut mit analytischen Lösungen vergleichen. Danach untersucht sie das Kollabieren einer Bodensäule in Luft und unter Wasser und vergleicht ihre Versuchsergebnisse mit den Simulationsergebnissen. Dies ist ein bereits vielfach untersuchter Benchmark für verschiedenste numerische Ansätze wie beispielsweise die Material Point Method (MPM) oder die Smooth Particle Hydrodynamics (SPH). Als drittes befasst sie sich mit der eingangsgenannten Zielsetzung, den Bewegungsbeginn einzelner Partikel bei der Überströmung mit Wasser zu modellieren.

Zielsetzung der Arbeit von Frau Plenker ist die Beantwortung einer ganzen Reihe von Forschungsfragen, siehe Kapitel 3, die sich zusammenfassen lassen in:

1. Gelingt es das Absinken einer Kugel im Wasser mit Hilfe des verwendeten Programms CFDEM basierend auf der unresolved CFD-DEM Methode zutreffend zu modellieren? 2. Wie beeinflusst das Fluid das Kollabieren einer Sandsäule? 3. Was kennzeichnet den Bewegungsbeginn eines überströmten Partikels auf einem Partikelbett?

Zur Bearbeitung der ersten Zielsetzung führt sie numerische Simulationen durch und variiert dabei die Lage des Startpunktes des Partikels relativ zum Gebiet. Die zweite Zielsetzung untersucht sie experimentell in einem selbst konstruierten Versuchsstand in Luft und unter Wasser. Sie wertet die Partikelbewegungen mit der Particle Image Velocimetry (PIV) aus und vergleicht diese mit den numerischen Ergebnissen. Als drittes führt sie Versuche in einer Rinne am überströmten Einzelpartikel aus und interpretiert die Ergebnisse mit Hilfe der numerischen CFD-DEM Simulation.

In Kapitel 1 führt sie in die Thematik und Motivation ihrer Arbeit ein.

Der Stand der Wissenschaft zur Interaktion von Partikeln mit Flüssigkeiten auf mikromechanischer Skala wird in Kapitel 2 von ihr in aller Kürze beschrieben und in Bezug auf ihre

Zielsetzung diskutiert.

In Kapitel 4 beschreibt sie die Grundlagen der von ihr verwendeten numerischen Methode. Zunächst geht sie auf die Diskrete-Elemente-Methode (DEM) und dann auf die Kopplung der DEM mit der Computational Fluid Dynamic (CFD) ein.

Das Absinken einer Kugel im Wasser wird in Kapitel 5 behandelt. Das numerische Modell wird in Abschnitt 5.2 aufgestellt. Die verwendete Diskretisierung zeigt Abb. 5.4. Die Partikeleigenschaften werden am Institut für Partikeltechnologie der TUHH bestimmt. Zunächst behandelt sie das Absinken einer Einzelkugel. Abb. 5.6 zeigt, an welcher Stelle das Partikel zugefügt wird, in einem Netzknoten oder im Zentrum der Zelle. Abb. 5.7 zeigt, dass die Positionierung mit zunehmendem Verhältnis von Zellvolumen zum Partikelvolumen weniger Einfluss auf die Absinkgeschwindigkeit hat. Die Abb. 5.16 zeigt die Abhängigkeit der Sinkgeschwindigkeit vom Partikeldurchmesser unter Ansatz verschiedener „Drag-force“ Modelle im Vergleich zur Gleichung nach Stokes (1851) und anderen wie Zanke (1982), Gibbs (1971), Soulsby (1997) und Dietrich (1982) auf. Am besten passen die numerischen Ergebnisse zu den Ansätzen von Dietrich (1982), wobei die „Drag-force“ Modelle von DiFelice und Koch-Hill die größten Übereinstimmungen ergeben. Naheliegend wäre nun die CFD-DEM Methode auch zur Untersuchung des Absinkens mehrerer Partikel oder von Partikelklumpen zu verwenden. Solche Untersuchungen hat Frau Plenker durchgeführt, aber nicht in ihre Arbeit aufgenommen, da die Simulationsergebnisse nicht verifiziert oder validiert wurden. Das wäre aber durchaus eine interessante Untersuchung für nachfolgende Wissenschaftler. Allerdings ist fraglich, ob die „Drag-force“ Modelle für mehrere, beim Absinken sich berührende oder kollidierende Partikel gelten.

In Kapitel 6 behandelt sie das Kollabieren einer Sandsäule in Luft und in Wasser. In Abschnitt 6.2 erläutert sie ihren Versuchsstand, siehe Abb. 6.3. Sie unterscheidet ein langsames und ein schnelles Herausziehen der Stützwand. Die Ergebnisse an Luft sind in den Abb. 6.8 und 6.11 dargestellt. Deutlich sind die dynamischen Effekte zu erkennen. Die Abb. 6.19 und 6.35 zeigen den Vergleich der gemessenen mit den numerisch simulierten Böschungen als Funktion der Zeit. Es ergibt sich eine gute Übereinstimmung. Anschließend untersucht sie das Kollabieren der Böschung unter Wasser. Sie untersucht das schnelle Herausziehen der Stützwand. Abb. 6.49 zeigt die experimentellen Ergebnisse und die Abb. 6.53 sowie 6.54 zeigen die korrespondierenden numerischen Ergebnisse zu verschiedenen Zeitpunkten. Abb. 6.55 stellt die Position des Böschungsauslaufs über die Zeit zum Vergleich dar. Es zeigen sich Abweichungen in der zeitlichen Entwicklung. In der Simulation wird die Endstellung schneller erreicht. Die Variation des „Drag-force“-Modells hat keinen großen Einfluss, siehe Abb. 6.59.

Die Initialisierung des Sedimenttransports wird in Kapitel 7 untersucht. Zunächst stellt sie die Grundlagen von Grenzschichtströmungen (Abschnitt 7.1) und der Initialisierung der Partikelbewegung (Abschnitt 7.2) dar. In Abschnitt 7.3 geht sie dann in die von ihr in einer Rinne durchgeführten Versuche ein. Sie untersucht die Strömungsverhältnisse an einem auf einem Partikelbett liegenden Einzelpartikel. Abb. 7.21 zeigt die gemessenen Geschwindigkeitsfelder. Deutlich wird die Abnahme der Geschwindigkeit im Bereich der Grenzströmung zum Partikelbett und die reduzierte Geschwindigkeit im Bereich des Einzelpartikels, was mit einer Schleppkraft einhergeht. Diese lässt sich messtechnisch allerdings nicht erfassen. Die Abb. 7.24 zeigt das gemessene, gemittelte Geschwindigkeit-

sprofil. Daraus lässt sich nach Gl. 7.39 die Schubspannung ableiten, deren Ergebnis in Abb. 7.25 dargestellt ist. Abb. 7.26 zeigt das Shields-Diagramm, in das die ermittelten Werte eingetragen sind. Hier zeigt sich ein erheblicher Unterschied. Die numerische Simulation des Bewegungsbeginns wird in Abschnitt 7.4 behandelt. Sie modelliert zunächst die Überströmung einer rauen Oberfläche mit OpenFOAM und vergleicht die berechneten Geschwindigkeitsprofile mit den Messungen, siehe Abb. 7.29. Als nächstes verwendet sie die gekoppelte CFD-DEM Methode unter Verwendung periodischer inlet-outlet Bedingungen. Die Ergebnisse sind in Abb. 7.33 dargestellt. Die Übereinstimmung mit den Messdaten insbesondere in der Grenzschicht ist geringer als bei den vorherigen OpenFoam Simulationen. Abschnitt 7.4.3 behandelt die Modellierung des Erosionsprozesses, siehe Abb. 7.35. Da die Grenzschicht nur bedingt abgebildet wird, sind auch Zweifel an der numerischen Abbildung des Erosionsprozesses angebracht. Hier besteht offensichtlich noch Forschungsbedarf, die Prozesse in der Grenzschicht numerisch zutreffender zu erfassen. Vermutlich werden hierfür numerische Ansätze benötigt, die die Strömungsprozesse im Porenraum ausreichend schnell mitabbilden können. Aufgelöste CFD-DEM Simulationen sind hierfür noch nicht ausreichend schnell. Vielleicht ist hier der Ansatz der Latice-Boltzmann Methode zielführender. Abschnitt 7.5 schließt die Untersuchung mit einer Diskussion ab.

Frau Plenker hat aus meiner Sicht in Teilen eine äußerst komplexe Fragestellung bearbeitet. So sind die Untersuchungen zum Absinken eines Partikels im Wasser und zur Untersuchung des Kollabierens einer Sandsäule in Luft und im Wasser leistbar. Sie untersucht beide Randwertprobleme mit großer Sorgfalt und zieht die richtigen Schlüsse. Wirklich komplex ist dagegen die numerische Simulation des Erosionsbeginns eines Partikels auf einem Partikelbett. Die Interaktion der turbulenten Grenzströmung mit einem beweglichen Rand ist eine wirklich „harte Nuss“. Sie hat dazu wertvolle Untersuchungen durchgeführt, aber das Problem an sich ist nicht gelöst und bedarf weiterer Forschungsarbeiten. Ein möglicher Ansatz bietet die gut parallelisierbare Latice-Boltzmann Methode, welche mit der Diskreten Elemente Methode gekoppelt wird (LBM-DEM). Hieran wird aktuell an mehreren Forschungseinrichtungen beispielsweise in Erlangen und Austin, Texas, geforscht.

Frau Plenker hat mit ihren experimentellen und numerischen Untersuchungen einen wesentlichen wissenschaftlichen Beitrag zum Stand der Wissenschaft an der Schnittstelle von Wasserbau und Geotechnik geleistet.

Frau Plenker lebt inzwischen in Delft, Niederlande, und arbeitet für Deltares. Für ihren weiteren Lebensweg wünsche ich ihr alles Liebe. Es war mir eine Freude sie zu betreuen und ich hoffe, wir bleiben weiterhin in Kontakt.

Hamburg, 15.01.2021

Univ.-Prof. Dr.-Ing. Jürgen Grabe

Author's Preface

Die vorliegende Dissertation enthält Untersuchungen zur Interaktion von granularen Partikeln und Fluid an geotechnischen Phänomenen, mit denen ich mich während meiner Tätigkeit als wissenschaftliche Mitarbeiterin am Institut für Geotechnik und Baubetrieb der Technischen Universität Hamburg beschäftigt habe. Meine Arbeit befasst sich mit der detaillierten Fluid-Partikel Interaktion zwischen granularen Partikeln, dem Porenfluid und freiem Fluid in der Wassersäule anhand von drei markanten geotechnischen/ hydrodynamischen Phänomenen: dem Absinken eines Partikels, dem Versagen einer Partikelsäule und dem individuellen Bewegungsbeginn an einem Partikelbett. Die Untersuchungen werden basierend auf einem hybriden Modellierungsansatz durchgeführt, der physikalische Modellversuche mit visuellen und nicht-intrusiven Messmethoden sowie numerischen Modellierungen mit der gekoppelten CFD-DEM Methode umfasst. Dabei wird die Fluid-Partikel Interaktion auf der Partikelebene und die Auswirkungen der individuellen Interaktion auf das Verhalten einer Partikelmasse analysiert.

Mein besonderer Dank gilt Herrn Prof. Dr.-Ing. Jürgen Grabe für die Betreuung und die Unterstützung während meiner Forschungstätigkeit an seinem Institut und die Möglichkeit, meine Forschungen mit meiner Promotion abschließen zu können. Die Arbeit am Institut für Geotechnik und Baubetrieb hat mir die Möglichkeit gegeben, meinen Horizont auf vielfältige Weise zu erweitern. Weiterhin danke ich Herrn Prof. Dr.-Ing. Holger Schüttrumpf für anregende Gespräche, sein Interesse an meiner Arbeit und die Begutachtung meiner vorliegenden Dissertation. Bei Herrn Prof. Dr.-Ing. Peter Fröhle möchte ich mich ganz herzlichen für die erfolgreiche Kooperation mit seinem Institut bedanken sowie für die Übernahme des Prüfungsvorsitzes.

Diese Arbeit erforderte für verschiedenste Ansätze themenübergreifende Expertise. Daher möchte ich mich für die Unterstützung der Mitarbeiter am Institut für Wasserbau der Technischen Universität Hamburg bedanken, die mich während der zahlreichen Modellversuche in der Strömungsrinne unterstützt haben. Weiterhin möchte ich mich bei Mitarbeitern des Instituts für Partikeltechnologie (SPE) und Fluid Dynamik und Schifftheorie (FDS) der technischen Universität Hamburg für hilfreiche Grundsatz-Diskussionen bedanken. Für zahlreiche offene Diskussionen und Unterstützung möchte ich mich zudem bei den Entwicklern von CFDEMcoupling Dr.-Ing. Christoph Goniva und Dr.-Ing. Alice Hager bedanken.

Für die niemals endende Unterstützung bedanke ich mich herzlich bei meinen ehemaligen Kollegen am Institut für Geotechnik. Die zahlreichen Diskussionen, kritisches Hinterfragen, motivierenden Worte und nette Gespräche haben meine Zeit am Institut für Geotechnik und Baubetrieb bereichert und diese Arbeit möglich gemacht. Auch meinen Kollegen der Stichting Deltares möchte ich danken für ihr offenes Ohr und Unterstützung in den letzten Zügen der Dissertation.

Bei der Durchführung der physikalischen Modellversuche habe ich tatkräftige Unterstützung von einzelnen Studenten der TUHH erhalten. Ich möchte mich daher herzlich bei Deniz Kacmacz, Zeineb Kassem und Gerian Ölscher bedanken.

Am Ende gilt mein besonderer Dank meiner Familie und meinen Freunden. Dank ihrer großartigen Unterstützung und Liebe während aller Höhen und Tiefen meiner Arbeit an

der Dissertation habe ich es soweit bringen können. Ihre Ermutigung und Motivation waren mir eine große Stütze, für die ich ihnen immer dankbar sein werde. Insbesondere möchte ich auch meinen Eltern danken, die mich gelehrt haben, neugierig auf die Welt zu sein und die mich immer ermutigt haben, groß zu träumen. Danke auch an meinen Freund Karel für seine liebevolle Unterstützung und Ermutigung egal zu welcher Tageszeit.

Delft, den 02.02.2021

Désirée Plenker

Keywords:

fluid-particle-interaction, particle mechanics, interaction forces, particle drag force, discrete-element-method (DEM), computational fluid dynamics (CFD), coupled CFD-DEM, unresolved, CFD-DEM, granular flow, particle-image-velocimetry (PIV), sedimentation, motion threshold, erosion, boundary layer

Schlagwörter:

Fluid-Partikel-Interaktion, Partikelmechanik, Interaktionskräfte, Partikelwiderstandskraft, Diskrete-Elemente-Methode (DEM), Computational Fluid Dynamics (CFD), gekoppelte CFD-DEM, unresolved CFD-DEM, Granulares Fließen, Particle-Image-Velocimetry (PIV), Sedimentation, Bewegungsbeginn, Erosion, Grenzschicht

Contents

1 Introduction

The characterisation of granular soil takes mostly place on a macroscopic level. Thereby, the soil is commonly treated as a continuum substance, which complex behaviour requires sophisticated material models. However, already on a structural level granular soil can be identified as a compound of granular particles and fluid or gas inside the pore voids. These components are interacting and constitute to the complex behaviour of granular soil. In partially or fully saturated soil, the presence of fluid has a significant effect on the behaviour of the material.

In geotechnical engineering the stress-strain behaviour of soil as well as the change of pore-water pressure due to deformation, can be modelled sufficiently by constitutive models, assuming soil as a continuum. This approximation by a continuum covering the effects due to interaction between fluid and granular media, is sufficient for most engineering applications. However, in specific phenomena this approximation is not valid and the detailed interaction processes need to be taken into account. This is especially the case for phenomena, that take place at the interface between granular soil and fluid at submerged conditions.

To discuss this phenomena and the corresponding processes, it is necessary to understand the character of granular soil besides the continuum approach. As already mentioned, granular soil is neither an uniform nor heterogeneous material but rather a multi-component medium. It consists at fully saturated conditions of disperse mineral grains and pore fluid within the voids. The individual grains interact with each other and build a solid grain skeleton. This structure carries the inner stresses of the material at drained conditions. Besides the grain to grain interaction, an interaction between the grains and the pore fluid takes place as well. At the soil-fluid interface, this interaction is extended due to the presence of the free fluid of the water column. Thus, the free fluid interacts with the grains in the transition zone of the boundary. Additionally, the porous character of soil allows an interaction between the interstitial pore fluid and the free fluid, which is accompanied by an exchange of mass and momentum between the internal and the external flow field.

Due to the complexity of these superimposing processes, little is known about the exact fluid-particle interaction on a grain scale and its influence on phenomena which take place in fluid-soil interaction. Whilst this factor is often negligible in engineering applications, in some specific phenomena the multi-component characteristic of soil and the influences due to the fluid-particle interaction need to be taken into account. These are scenarios including e. g. transition from static to a dynamic state or general highly dynamic scenarios like slope failures, granular flows and debris flows at submerged conditions, deposition of soil material in water, fluidisation effects or influence of pore water pressure and exchange between the internal and external flow field on sediment transport processes. In these

scenarios the investigation of the detailed processes on a grain scale is difficult due to its dynamic character, the great deformations arising from it and the small scale on which those interaction processes occur. These facts prohibit the application of regular physical tests with classical geotechnical or hydraulic engineering measurement techniques, since they are often intrusive and would effect the phenomena itself or the surrounding flow situation.

With innovative measurement techniques and new numerical methods for geotechnical applications it becomes possible to investigate these phenomena closer and to gain new insights into the corresponding fluid-particle interaction. On the side of physical tests, high speed recordings and the Particle Image Velocimetry (PIV) enables a non intrusive way to analyse the trajectories of highly dynamic particle packings. Further, coupling the CFD and DEM method provides an opportunity to investigate the exact behaviour inside a submerged particle packing, the particle contacts and the fluid-particle interaction in numerical simulations.

In this thesis, a hybrid modelling approach consisting of physical tests and numerical simulations with the coupled CFD-DEM is applied to investigate the interaction between granular material and fluid on phenomena of fluid-soil interaction. To apply a homogeneous and well-defined granular material, spherical glass particles are used as a substitute of the granular soil phase. This approach gives the opportunity to neglect influences arising from the angularity of natural grains and to focus on the detailed interaction process. The interaction between the granular particles, the pore-fluid and the free-fluid is investigated by behalf of three prominent scenarios. In a first benchmark test, the numerical method is applied on the scenario of a sinking fully exposed particle to verify the numerical results on basis of this analytically well known example. Following, the scenario of a submerged collapsing particle column is extensively analysed by means of physical tests and corresponding numerical simulations. Thereby, several variations of the slumping procedure give new insights into the collapse mechanism, the transition between the static and dynamic state and the behaviour as well as interaction of particle and fluid phases during the collapse process. Furthermore, the motion threshold at a particle bed is investigated. Therefore, physical tests are conducted in a flume with a rough boundary. Additional numerical simulations give new insights into the detailed processes and influences on a particle of a permeable boundary.

2 State of the Art on the Interaction between Granular Media and Fluid

This thesis focusses on the interaction processes between the granular and the fluid phase in fluid-soil interaction processes, which arise from the multicomponent characteristic of granular soil. Thereby, the investigations concentrate on specific natural phenomena which can be reproduced only with respect of the soil multi-component characteristics. Thus, the representation of the granular soil as a disperse multi-component material is essential for the investigations. By means of this chapter, the representation of the interaction between the granular phase and fluid by numerical approaches is presented and discussed. Therefore, numerical approaches are presented and discussed in Section 2.1 with respect to the spatial representation of the fluid and granular soil media, the representation of fluid-soil interaction and further the interaction between granular material, void and free fluid. Section 2.2 presents the analytical and empirical solutions to describe the detailed fluid-particle interaction on an exposed single particle or within a particle group. Based on the corresponding discussion in this chapter, the objectives of this thesis and the procedure are identified.

2.1 Numerical Simulation of Fluids and Granular Material

In this section, the representation of fluid and granular material and their interaction is presented and discussed for different numerical approaches. Since it is essential to understand the specific characteristics of each medium, the physical composition of the two phases are introduced in a more detailed way, to assess the simplifications and assumptions of the different numerical methods.

In the most cases the medium water is assumed as incompressible, since its compressibility is negligible small for Mach numbers $\mathrm{Ma} < 0.3$. Further, it is classified as a Newtonian fluid, in which the fluid flow is characterised by a linear relation between viscous stresses and the local strain rate. Thereby, the viscosity is an isotropic constant value independent of the stresses or flow velocity. While water is a homogeneous medium, fully granular soil is characterised as a heterogeneous mixture. It consists of a deformable and porous skeleton of disperse mineral particles of different sizes and shapes and the pore fluids water and gas, which fill the pore space. Assuming fully saturated conditions, the pore space is filled by water only. The mechanical and hydro-mechanical properties of granular soil, depends on the properties of the individual components and the interaction between them.

Considering the representation of the two media, the numerical methods can be differentiated by different length scales to macroscopic, mesoscopic, microscopic and hybrid

approaches (Stanford, 2018). Following, relevant approaches for the simulation of fluids and soils are presented on the base of length scale differentiation. There is no claim for completeness of possible numerical simulation techniques.

2.1.1 Macroscopic or continuum approach

In the macroscopic approach or continuum approach, a material is modelled by a continuum as a representative volume. Thereby, the mechanical behaviour of the continuum is defined by continuum mechanics and, thus, rather by macroscopic properties.

A branch of the continuum mechanics is the fluid mechanics, which describe the static and dynamic behaviour of fluids. Fluids like water can likely be represented by a continuum, since the non-continuousness is just noticeable on a molecular level. Most natural flows and physical problems can be modelled by a continuum approach, since a macroscopic physical length scale is more representative than the microscopic length scale of the molecular mean free path. By means of fluid mechanics, the behaviour of a fluid continuum can be expressed by conservation equations of a closed system. This includes the conservation of mass, momentum and energy. As long as the concerning physical problem is not of a thermodynamical kind, the equation system reduces to the conservation of mass and momentum. The motion of a viscous fluid is described by the Navier-Stokes equations, which combine the conservation equations of mass and momentum to a system of partial differential equations. The Navier-Stokes equation system describes the fluid flow exactly, but is of such complex manner, that it can not be solved analytically. Hence, several simplifications exist for specific fluid mechanical problems e. g. ideal fluid or laminar flow (Musall, 2011). If a simplification is not possible, infinitesimal calculus is required to solve the Navier-Stokes equations.

In contrast to fluids, the non-continuous character of granular soil cannot be identified just on a molecular level, but already visually by the naked eye. This complicates the classification of the continuum approach by length scale. Defining the microscopic approach corresponding to those of fluids, it is represented on an atomic or molecular level. Similar to fluid mechanical problems, this length scale is not relevant for the most engineering soil mechanical problems. However, the heterogeneous characteristic of soil on a more structural level, can indeed mean an important role in the representation of the soil behaviour. The structural components are above molecular size and contain already material properties like density, viscosity, friction or elasticity. As a result, the continuum approach defines not just the continuous representation of the structural components, but the approximation of the material on a more phenomenological level (Klausner, 1991). This means, the soil is considered as an entity, in which the material behaviour is described by phenomenological laws rather than by the behaviour and interaction of its structural components.

As result of the heterogeneity of soil, the fundamentals of soil mechanics are not a classical branch of continuum mechanics. The above presented approach of conservation balances of continua is not expedient, since most geotechnical phenomena are statically indeterminate and dissipative (Kolymbas, 2011). As a result, additional equations in form of

constitutive equations are necessary to describe the soil behaviour. An ideal constitutive model describes the stress-strain behaviour of a soil for all conditions and influences. However, since the soil behaviour is extremely complex, constitutive equations are just an approximation for specific limited conditions. In constitutive equations, strain and stress fields are considered respecting the theory of Terzaghi, who enabled the calculation of normal and shear stresses for the individual phases. For porous media, the behaviour of soil, treated as a continuum, can be handled by two different theories. The first theory is the approach of volume ratios, in which the single phases can be treated individual by the theory of continuum mechanics. A famous example is the theory of Biot (1941, 1956a,b). In contrast to the second theory, which is based on the approach of mixing theory. Thereby an average value of the solid and fluid fractions in a region is generated and further treated as an average mixture continuum (Ehlers, 1996). Both theories result in a complex constitutive equations system, in which the strain and stress fields of the continuum need to be treated by infinitesimal calculus.

In numerics, several methods exists to solve the complex partial differential equation system. The methods can the differentiated into spatial and temporal discretisation schemes. Following, the common spatial discretisation methods shall be highlighted.

The most common discretisation schemes are mesh based Eulerian approaches like the Finite Difference Method (FDM), the Finite Volume Method (FVM) or the Finite Element Method (FEM). Thereby, a mesh divides the investigation area into a number of finite discrete nodes. The division enables the solution of the governing equation system by infinitesimal calculus. The FDM provides a simple implementation by replacing the equation derivatives by finite difference quotients between neighbouring nodes. However, it is also strongly limited to very simple mesh geometries. The FVM is based on the balance of fluxes over the faces of a control volume. Thereby, more complex meshes are possible, although block structured meshes are required. The FVM is by definition conservative and, thus, a very common discretisation scheme in Computational Fluid Dynamics (CFD). The FEM is the most flexible method in mesh generation. Opposed to the FDM and FVM, the derivatives of the governing equation system are not replaced by difference quotients. Rather, the investigation area is divided into finite elements, whereby the element nodes are equipped with specific weighting functions. This weighting functions describe the transformation of an information from one node to the neighbouring nodes and, though, replace the derivatives in the equation system (Musall, 2011). Because of the unlimited flexibility of the FEM, which enables the refinement of local areas, this method is popular in simulations of geotechnical engineering. In combination with a Coupled Eulerian-Lagrangian (CEL) approach, the FEM enables even mesh deformations. Further informations on the formulation and the advantages of the presented differential discretisation schemes can be found in Ferziger et al. (2008), Forkel (2004), and Musall (2011).

However, several investigations in geotechnical engineering deal with large deformations. In this case, mesh based methods like the FEM or CEL are limited, since highly skew elements give less accurate results. A solution are mesh free methods like the Smoothed Particle Hydrodynamics (SPH). In SPH the continuum is approximated by a cloud of material points. Thereby, a particle represents a specific mass or volume and, thus, is still

a continuum mechanical approach. The interaction between the particles is modelled via a kernel function, which affects all neighbouring particles within a specific radius. Further, conservation equations give the method conservative features. However, since the SPH method is very new for engineering purposes, there are still problems with the definition of boundary conditions. Since, the SPH method can be easily extended to different fields, it is equally appropriate for the representation of fluid as well as solid. Further information of the modelling of saturated soil as a two-phase medium are presented in Kocak (2017).

Another promising approach is the Material Point Method (MPM). It is based on a Eulerian as well as a Lagrangian approach. Similar to SPH a specific mass of the continuum is represented by discrete Lagrangian material points. Since the amount of mass represented by a material point, does not change over the simulation, the method is mass conservative by definition. In contrast to SPH, an additional Eulerian mesh is applied in MPM, to solve the balance of momentum (Nguyen, 2014). Although a mesh is applied in this approach, it is assigned to the mesh-free methods. Similar to SPH, the MPM is appropriate for the simulation of fluids as well as soil. More informations about the method and its application are given in Ceccato et al. (2017), Chmelnizkij et al. (2017), and X. Zhang et al. (2016).

2.1.2 Mesoscopic Boltzmann approach

On a microscopic level, the behaviour of fluids can be described by a quantity of molecules and their interaction. The molecular interaction of gases are simple to characterise, since the particle collisions are limited. In the case of dilute gases, the molecular particles are spread over a wide area and the inter-particle collisions can be assumed as one-on-one events. In liquids like water, the molecular particles interact continuously, since they are kept close to each other by intermolecular attracting forces (Viggen, 2014). In contrast to a pure microscopic approach, which tracks the particles on a molecular level, a mesoscopic approach attempts a description of a quantity of particles. This is assumed by the concept of kinetic theory. The kinetic theory gives macroscopic quantities like density, pressure, viscosity or temperature by the statistically characterisation of particle distributions. The statistical behaviour of a particle system is given by the Boltzmann equation (Boltzmann, 1872). The Boltzmann equation considers a probability distribution of a typical particle and describes the evolution of this distribution in space and time. Therefore, microscopic quantities like the microscopic velocity as well as the inter-particle collisions are considered. The original equation is limited for dilute gases with a long molecular free mean path and, thus, a small number of particles inside a given volume. However, a derivation of the Boltzmann equation, the continuous Boltzmann equations, contain classical conservation laws of mass and momentum and, thus, can be transferred to the Navier-Stokes equation (Hadjiconstantinou, 2006). The Boltzmann equation can capture even complex physics of fluid mechanics at low Mach numbers, while the formulation as well as the solution of the governing equations are much simpler than classical CFD approaches based on the complex Navier-Stokes equation system. The continuous Boltzmann equation is solved by infinitesimal calculus in the so called Lattice-Boltzmann Method (LBM). Thereby, the discretisation in time and space is achieved via a mesh (or lattice) with a finite number of

nodes. It is important to remember, that a particle in the LBM represents a quantity of molecular particles.

More details on the discretisation schemes as well as the underlying algorithm are given in S. Chen et al. (1998), He et al. (1998), Maquignon (2017), and Viggen (2014). A huge benefit of the LBM is the allowance of a massive parallelisation of the code. This is due to the confinement of the steps of the algorithm, to a local node and the ultimate neighbouring nodes. In the past years, the LBM became an approved method for the numerical representation of fluids. Since, soils consists already of a heterogeneous mixture on a structural level, the LBM is inappropriate to simulate the behaviour of soils on a mesoscale. However, to describe the fluid flow in porous media, the LBM is indeed popular. Thereby, the particle skeleton of the soil is represented by a static structure, given as solid boundaries to the discretised fluid domain. Hence, it is not possible to simulate a deformation of the particle structure due to interaction.

2.1.3 Discontinuum approach

Concerning the numerical representation of water and soil together on a discontinuum level, the term "microscopic" is applied in many investigation (e. g. Bartzke (2012) and Luding (2008)). However, the definition of microscopic for the individual materials need to be discussed. Following the trend of the previous sections, the representation of water on a microscale would imply the representation on a molecular level. In this case the term "micro" is irritating, since the molecular characterisation happens on a nanoscale. However, for most engineering purposes of geotechnical or hydraulic engineering, the nanoscale is not representative.

As already discussed previously, the definition of a microscopic level in soil mechanics is not clear. An interpretation, corresponding to the microscale definition of water, would imply a molecular characterisation. However, the representation of soil on a molecular level is not characterising the material behaviour, since it consists of different components, which are clearly separated on a nanoscale. Rather, the more representative scale is the structural level, in which the material components can be identified individually by the naked eye. On the structural level, the scale ranges according to the size distribution of the mineral particles. This includes fractions of the micrometre range, up to the centimetres range. On this scale the remaining soil components water and air are sufficient represented by a macroscopic continuum approach.

It is evident that the term "microscopic" is insufficient for the collective characterisation of the different materials as discussed previously. However, the representation of the materials on the different levels of observation are connected by discontinuum consideration. The molecular representation of water as well as the structural representation of the soil solid fraction are based on discontinuous disperse elements. Thus, the discontinuum approach is a more sufficient term to describe this level of observation, which is applied following.

According to Cundall et al. (1992), a discontinuous material can be distinguished by a continuous one "(...) by the existence of contacts or interfaces between the discrete bodies that comprise the system". The behaviour of this individual discrete particles can

be mainly characterised by the particle movement and particle interaction. Therefore, an explicit scheme is applied (Cundall et al., 1979). The unknown informations of the next timestep at one particle are calculated from the already known informations in that particle as well as the immediate neighbouring particles. Thus, the underlying governing equations can be solved locally for each timestep and each particle. The independence of the governing equations is guaranteed by the size of the chosen timestep. In every physical system exists a maximum speed in which an information is able to travel e. g. a compressional wave speed in a elastic solid (Hart, 1988). Thus, the computational timestep is chosen so sufficiently small that an information cannot exceed further than from one to the immediate neighbouring particle in contact. By this restriction it is ensured, that the governing equations for every individual particle can be solved independently.

In discontinuum simulation, two different approaches exist, to model the particle interaction and the resulting movement. They are differentiated by the interaction mechanism of the particle contact into either a hard-sphere or a soft-sphere approach:

- The hard-sphere approach is based on an event driven formulation. During a collision event, the involved particles interact via a momentum exchange. Subsequently, the new particle trajectories are calculated on the basis of momentum conservation. Thus, the hard-sphere approach is limited to pairwise interaction of fully rigid particles. Further, the event driven scheme, assumes a small interaction time compared to the time of a free movement. As a consequence, the hard-sphere approach is suitable to dilute systems only.
- The soft-sphere approach considers the exchange of forces during a collision event. Thereby, particles interact via short- or long range contact forces. The resulting individual trajectories are determined by Newton's law of motion. In the soft-sphere approach, the particles are assumed to be deformable. The deformation is represented by an overlapping of the particles. The contact forces arise at a first contact and are subsequently determined from the deformation history by a force-displacement law. In contrast to the hard-sphere approach, it is necessary to define material constants for the particles, since the applied stiffness in the force-displacement law is based on the particle elasticity. By the contact force formulation, the representation of multiple contacts is enabled. Thus, the soft-sphere approach is appropriate for dense particle systems.

The numerical simulation of water and soil on a discontinuum base is related to the discontinuum length scale of the material. Water is considered discontinuous on the nano scale. Thus, Molecular Dynamics (MD) is applied for the representation of atomic or molecular movements and interaction. In MD the particles describe mass points without a specific size. In the application of dilute gases, the hard-sphere model is applied, since the calculation scheme is faster than the soft sphere approach. However, for more dense materials like fluids, the soft-sphere approach is applied as well. Thereby, molecular mechanic models define the force-displacement laws.

The numerical representation of granular soil particles is enabled by the Discrete Element Method (DEM). The approach of the DEM is very similar to those of the MD, since the DEM constitutes an advanced branch of MD. The DEM is the only method, which deals actually with real particles of a defined mass, volume and discrete properties like

density, friction or elasticity. As a consequence, additional forces like tangential contact forces or rotational degrees of freedom need to be considered in the contact force and trajectory determination. In the most applications, the soft-sphere approach is used for the DEM method. Especially, in geotechnical engineering the physical problems concern dense particle systems, which are governed by multiple particle interaction. Thus, the soft-sphere approach is the only possibility for a sufficient simulation. However, the discontinuous representation of soil particles is extremely computational expensive. Even for a small volume, millions of particles of different sizes need to be modelled. As a consequence, the discontinuum approach is limited to a relative small volume of soil, if the soil grains are modelled on the real scale.

More details on discontinuous numerical approaches are given in Cundall et al. (1979), Cundall et al. (1992), Hart (1988), and van der Hoef et al. (2006).

2.1.4 Hybrid approaches

Hybrid approaches combine two or more of the previously presented numerical methods. Thereby, hybrid approaches are differentiated by the combination or coupling of the approaches into three main categories:

- The Multi-domain coupling approach models separate areas of a simulation domain by different numerical approaches. This allows to simulate the interaction of rigid or highly ductile materials with highly deformable materials. In geotechnical engineering the coupling of the FEM and DEM method are an appropriate approach to simulate the interaction of rigidly bodies with a granular assembly (see e. g. Dratt et al., 2017; Michael et al., 2015).
- The Multi-scale modelling combines two approaches at different spatial and temporal scales to describe a material system. This approach is appropriate for applications, where continuum approaches are not accurate enough to simulate a specific behaviour. The representation of soil as a multicomponent medium with a coupling of CFD and DEM is highly interesting for fundamental research in geotechnical engineering.
- The hierarchical Multi-scale modelling applies continuum mechanical and particle based approaches to solve a boundary value problem by taking the non-linear material behaviour into account. A prominent example are the investigations of Guo et al. (2014, 2016) to model the mechanical behaviour of soil. Thereby, the FEM is employed to solve the boundary value problem. The DEM derives the required non-linear material respond at each FEM Gauss integration point.

Following, this section focuses on the Multi-scale modelling, which is the only relevant method of the previous presented hybrid approaches for the simulation of fluid-soil interaction. Multi-scale models enable the individual representation of soil as a mixture of its components. On a structural level, the soil skeleton is characterised by a discontinuous representation, while the pore fluid is still characterised by a continuum. For the representation of the pore fluid, every continuous CFD is appropriate such as methods

based on macroscopic Navier-Stokes equations (FVM, FEM, SPH, MPM) as well as mesoscopic Lattice-Boltzmann equations (LBM). The disperse soil particles are represented by discontinuous DEM. This method is known as coupled CFD-DEM. Following, the well established approach of FVM-DEM is further described on behalf of the Multi-scale CFD-DEM coupling.

For the representation of fluid by a mesh-based continuous approach, two different kinds of CFD-DEM methods need to be distinguished (Goniva et al., 2012). The methods differentiate corresponding to the ratio between the particle and the fluid cell size. The first method is the resolved CFD-DEM. Thereby, a particle is resolved by hundreds of CFD cells. A combination with the Immersed-Boundary-Method enables the simulation of detailed flow processes at the boundary of a particle. Due to the high degree of detailedness in the resolved CFD-DEM method, the simulation of the fluid turbulences on the CFD side are often fully resolved by Direct Numerical Simulations (DNS). This combination allows a high detailed simulation of the flow processes and interaction in porous media. However, the resolved approach requires a highly fine meshing of the fluid domain. This results into high computational costs for the simulation. Thus, the resolved CFD-DEM is limited to the simulation of the flow field around a few particles. The more common method is the unresolved CFD-DEM, where the fluid cells represent larger volumes than the DEM particles. To capture the impact of the particles on to the fluid phase and vice versa, a void-fraction field is introduced into the CFD calculations. The computational costs are lower than those of the resolved CFD-DEM. However, since the solid soil fraction is modelled by a disperse DEM approach, the computational costs are still high. The unresolved CFD-DEM guarantees a wider field of applications in geotechnical and hydraulic engineering like fluidisation effects, dilatancy or erosion. Hence, the coupling procedure of unresolved CFD-DEM is presented in a more detailed way hereafter. The interaction between the phases is established by a coupling of the governing equations. Therefore, fluid-particle force-models are required, which calculate the individual interaction forces like buoyancy, drag or pressure gradient force (Crowe et al., 2012). On the side of the DEM, the additional interaction forces are considered in the sum of forces in Newton's law of motion. On the side of the CFD code, the conservation equations of mass and momentum are expanded by a void-fraction factor to the volume-averaged Navier-Stokes (VANS) equations (Zhao et al., 2013). This void-fraction represents the percentage of fluid within a control volume. Furthermore, the momentum exchange due to interaction forces is considered by an additional term in the conservation of momentum.

The CFD-DEM represents a powerful tool with specific interest for the simulation of water and soil interaction, since the interaction forces can neither be measured nor derived from the boundaries in physical tests. Although, the application is limited to small spatial dimension so far, a better understanding of the detailed interaction mechanics on a microscopic scale can gain new knowledge on the macroscopic behaviour.

2.1.5 Discussion

All previously presented numerical methods are powerful tools in engineering practice to model various applications. However, with respect to the aim of investigating the influence

of fluid-particle interaction based on the multi-component characteristic of soil, most of the methods are not applicable. This is very true for all continuum methods based on the Eulerian approach. However, although Lagrangian methods like the SPH method are able to represent the mixture of different phases and great deformations it is still a continuum method and, thus, not applicable to represent the multi-component character of soil and the corresponding interaction processes at the fluid-soil interface. Thus, discontinuum methods are required to represent the soil components. The coupled CFD-DEM is able to represent soil on a structural level as granular particles and surrounding fluid. Further, it is able to capture the interaction of fluid and particles by interaction modelling. With the coupled CFD-DEM it becomes possible to investigate the detailed processes within a particle packing and to generate information of the internal behaviour, which cannot be captured by physical tests. A critical point of the CFD-DEM is its computational expensiveness. Even for a few ten-thousand particles huge computational resources are required. This limits the size of the investigated particle volume. As a consequence, the unresolved CFD-DEM is applied in this thesis. It reduces the computational costs significantly without resigning the multi-component characteristics and the detailed fluid-particle interaction. The unresolved CFD-DEM has the disadvantage, that the fluid flow around the particles is rather approximated and not as detailed as in the resolved CFD-DEM. However, the scenarios which are investigated in this thesis require a higher amount of particles. This disqualifies the resolved CFD-DEM for the investigations.

2.2 Interaction between Fluid and Granular Particles

The interaction between fluid and granular particles is a phenomenon which can be found in various common problems of process engineering, hydraulic engineering or geotechnical engineering. Examples for multiphase applications are bubble flows, spray granulation or blast furnace convection in industry, sediment transport and scour development in hydraulic engineering or cohesion, fluidisation, suffusion and pore water pressure effects in geotechnical engineering. These examples can be differentiated into dilute and dense multiphase problems. In dilute mixtures, the flow of granular particles is mainly affected by the interaction between the fluid and the particles. In contrast, dense flow is governed by inter particle contact. Following, interaction forces between fluid and a single granular particle and between fluid and a particle group are presented and discussed.

2.2.1 Forces on a single particle in fluid flow

The fluid-particle interaction forces are identified at a fully exposed particle in a infinite flow field (see Figure 2.1). Fluid-particle interaction forces can be differentiated in particle body forces such as particle weight F_G or buoyancy F_B, drag force F_D, pressure gradient forces F_{Pr}, acceleration induced forces like virtual mass force F_{VM} or Basset force F_{Ba} and lift forces F_L. In this chapter, approaches for the determination of the individual interaction forces are presented. Thereby, almost all of these approaches need to be adopted to physical influences such as particle shape, particle surface roughness or influences of

solid walls. However, in this thesis spherical shaped glass particles are applied, to focus on the interaction between particle ans fluid and to neglect influences resulting from shape effects. Therefore, effects which result from a non-spherical shape are not part of this section. More information on further influences on e. g. the drag force calculation can be found in Sommerfeld (2000), Crowe et al. (2012) or Michaelides et al. (2016). The effect of walls or fixed particle systems on to the particle fluid interaction is discussed in Section 7.2.1.

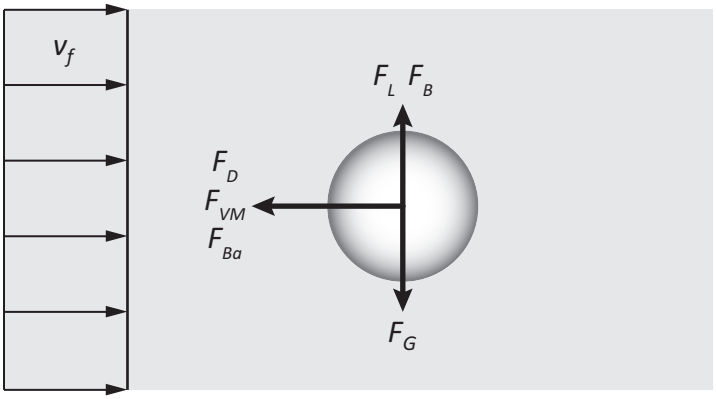

Figure 2.1: Interaction forces at a fully exposed sphere in a infinite flow field

Body forces

The particle weight F_G represents the body force due to gravitation, which is opposed to the hydrostatic buoyancy F_B. In some formulations, both forces are combined to the submerged weight $F_{G'}$.

$$F_G = \frac{\pi}{6}\rho_p d_p^3 g \qquad \text{and} \qquad F_B = \frac{\pi}{6}\rho_f d_p^3 g \tag{2.1}$$

In Equation 2.1, ρ_p or ρ_f represents the particle or fluid density, d_p the particle diameter and g the gravitational acceleration. Other fluid-particle body forces are e. g. the Coulomb force or thermophoretic force (Sommerfeld, 2000). The Coulomb force occurs for particle movement in an electric field, while the thermophoretic force results from particle movement in a flow with high temperature gradients. However, for the considered problems of geotechnical and hydraulic engineering those forces are not of interest.

Pressure gradient force

The pressure gradient force F_p is induced by a local pressure gradient around the particle. Thereby, the force acts towards the decreasing direction of the gradient. The formulation of the total pressure force can be derived from the Navier-Stokes equation. Thereby, the pressure gradient is defined by the summation of terms representing the fluid acceleration, the viscous shear stresses and the gravitational acceleration. With the assumption of a constant pressure gradient over the particle diameter, the total pressure gradient force is defined by the particle mass m_p as

$$F_{Pr} = m_p d_p^3 \frac{\rho_f}{\rho_p}\left(\frac{dv_f}{dt} - g\right) \qquad . \tag{2.2}$$

Depending on the representation of the pressure gradient force in numerical codes, the two terms of Equation 2.2 are treated together or separately as pressure gradient and buoyancy force. In the case of a separate consideration, the buoyancy is usually combined with the particle weight to the submerged weight. Further details can be found in Z. Y. Zhou et al. (2010).

Drag force

The drag force F_D is the predominant fluid-particle interaction force and the main cause for fluidisation effects in granular packings (Zhu et al., 2007). Drag results from the resistance of a particle against the flow (see Figure 2.1). The resistance is caused by voidial forces due to dynamic pressure as well as viscous forces. Thereby, the total drag force depends mainly on the particle shape as well as the particle Reynolds number, which is defined as

$$\mathrm{Re}_p = \frac{d_p(v_f - v_p)}{\nu_f} \quad . \tag{2.3}$$

The first analytically solution for F_D was given by Stokes (1851), for the estimation of viscous drag on a spherical particle in a viscous, infinite fluid (Richardson et al., 1954). This analytical approach is valid as long as the total drag force is dominated by viscous forces. However, this only holds true for very small Reynolds numbers. Newton developed a method to calculate the drag resistance at higher Reynolds numbers, where the drag resistance is mainly caused by dynamic pressure forces (see Equation 2.4). In this approach, a dimensionless empirical drag coefficient c_D is introduced. The value of c_D depends on the flow characteristic around the particle and needs to be defined by experiments. Numerous researchers supplemented the approach of Newton and created the so called drag curves, which give the drag coefficient as a function of the particle Reynolds number for a specific shape (Schlichting et al., 2017).

$$F_D = \frac{\pi}{8} c_D \varrho_f d_p^2 (v_f - v_p)|v_f - v_p| \tag{2.4}$$

In the case of a spherical particle, the drag curve could be differentiated into four main regions (see Figure 2.2). In the first region at $\mathrm{Re}_p \leq 1$, the Stokes region, the total drag is dominated by viscous forces. Thus, c_D can be defined by Stokes law, which gives a linear correlation between c_D and Re_p by $c_D = 24/\mathrm{Re}_p$ (see Figure 2.2 graph ①) (Zanke, 1982).

With increasing Re_p, the pressure distribution over the particle surface changes due to evolving vortexes and, thus, the drag forces increases. In this transition zone, the relation between c_D and Re_p is non-linear and can be approximated by the correlation of Schiller et al. (1933), (see Equation 2.5).

$$c_D = \frac{24}{\mathrm{Re}_p}\left(1 + 0.15\ \mathrm{Re}_p^{0.687}\right) \qquad \text{for} \qquad 1 < \mathrm{Re}_p < 10^3 \tag{2.5}$$

Within the Newton regime at $\mathrm{Re}_p > 1000$, the drag coefficient remains almost constant at $c_D = 0.445$ ($\pm 13\%$) (Decker, 2005). This can be explained by an almost consistent wake size and structure behind the particle. In the Newton regime, the viscous forces are minimal compared to the voidial forces and can be neglected (Sommerfeld, 2000). A

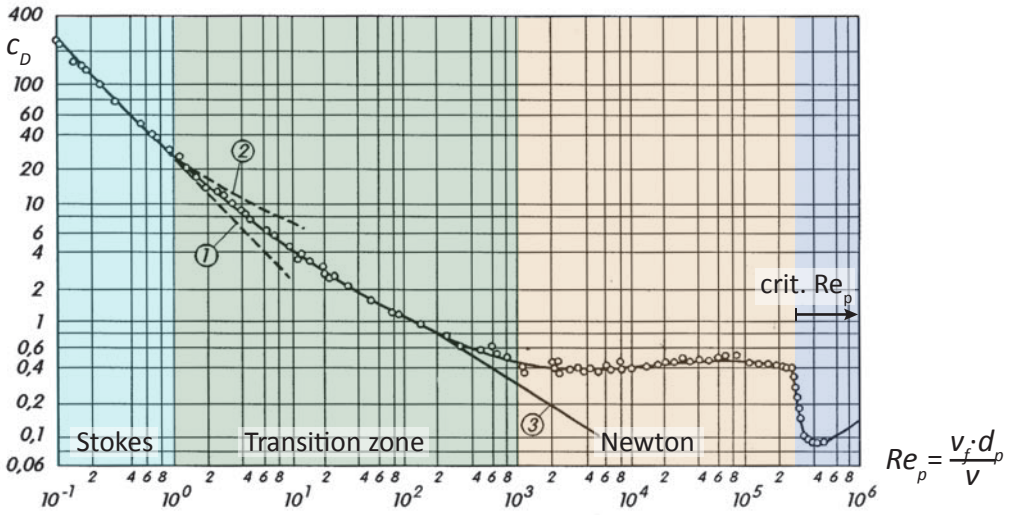

Figure 2.2: Drag coefficient c_D for spheres as a function of Re_p (adapted according to Schlichting et al., 2017)

critical Re_p is reached at $3.5 \cdot 10^5$. After this critical state the drag coefficient decreases abruptly because of a transition from a laminar to a turbulent boundary layer around the particle and a reduced wake area. However, in applications like sediment transport or fluidisation, this region is not of interest, since Reynolds numbers are usually smaller.

Virtual mass force and Basset force

The virtual mass force F_{VM} and the Basset force F_{Ba} belong to the acceleration induced forces which act opposed to the flow. The virtual mass force represents an additional viscous force against a change in acceleration. Besides the mass of the particle, the attached surrounded fluid needs to undergo the same changes in acceleration, which is equivalent to adding a virtual mass to the particle. The Basset force is based on the delayed transformation of the boundary layer around the particle after a change in relative velocity. Hence, it is often referred to as the history force.

The first estimations of the acceleration induced forces F_{VM} and F_{Ba} are based on the approaches of Boussinesq (1885), Basset (1888) and Oseen (1927). Based on their investigations, the first equation of motion for small particles in a viscous fluid has been developed, which is well known as the BBO-equation. Besides the viscous drag, the BBO-equation takes also the virtual mass as well as the Basset force into account. The following analytical equations for the virtual mass force and the Basset force are based on the BBO-equation:

$$F_{VM} = \frac{1}{6}\pi d_p^3 \rho_f \left(\frac{d(v_f - v_p)}{dt} \right) \tag{2.6}$$

$$F_{Ba} = \frac{1}{4} d_p^2 \sqrt{\pi \rho_f \mu} \int_0^t \frac{\frac{d}{dt}(v_f - v_p)}{\sqrt{t - t'}}\, dt' \quad . \tag{2.7}$$

This analytical solution is appropriate for small Re_p with creeping flow conditions of the

Stokes regime ($\mathrm{Re}_p \ll 1$) only. An estimation at higher Re_p is only possible by empirical models (Sommerfeld, 2000). The first approach for higher Re_p was developed by Odar et al. (1964). For the extended approach, the empirical coefficients c_{VM} and c_{Ba} are introduced to a correct of the BBO-equation for higher Reynolds numbers.

The estimation of the virtual mass force was corrected further by Auton et al. (1988). In Auton's (1988) approach, the fluid velocity derivative is replaced by the substantial derivative (see Equation 2.8). Furthermore, Michaelides et al. (2011) presented a new interpretation of the approach of Odar et al. (1964) and the estimation of c_{VM} and c_{Ba}. According to Michaelides et al. (2011), c_{VM} is not a function but rather a constant with $c_{VM} = 0.5$ for $0 < \mathrm{Re}_p < 500$. This assumption is supported by several analytical studies and experiments. As a consequence, c_{Ba} is redefined to a new correlation, depending on the particle Reynolds number and the Strouhal number Sl. For the case of turbulent flows or an initial flow velocity, the approach of Reeks et al. (1984) should be taken into account. Thereby, the modified approach of Odar et al. (1964) is expanded by an additional term defined in Equation 2.9, which includes the initial velocity difference $(v_f - v_p)_0$.

$$F_{VM} = \frac{1}{6} c_{VM} \pi d_p^3 \rho_f \left(\frac{Dv_f}{Dt} - \frac{dv_p}{dt} \right) \tag{2.8}$$

$$F_{Ba} = \frac{1}{4} c_{Ba} d_p^2 \sqrt{\pi \rho_f \mu} \left[\int_{t_0}^{t} \frac{\frac{d}{dt'}(v_f - v_p)}{\sqrt{t - t'}} \, dt' + \frac{(v_f - v_p)_0}{\sqrt{t}} \right] \tag{2.9}$$

$$\text{with} \quad c_{VM} = 0.5$$

$$c_{Ba} = 6.0 - 3.16 \left[1 - \exp\left(-0.14 \mathrm{Re}_p Sl^{0.82} \right)^{2.5} \right]$$

Nevertheless, the Basset force is neglected in most simulations, since the computation is very time consuming. Numerical studies of Sommerfeld (1996) have shown that the consideration of the Basset force leads to an increase of the computational costs by a factor 10. Thus, (Sommerfeld, 2000) recommends a consideration of the Basset force only for applications with a significant influence like oscillatory flows. Hjelmfelt et al. (1966) proofed the negligence of the Basset force for multiphase mixtures with a high density ratio and very small particles. Unfortunately, these conditions are not fulfilled for the application with sand/glass particles and water. According to Paladino et al. (2004), the virtual mass force is just significant, if the density of the particle is much smaller than the density of the surrounding fluid. In that case, the accelerated added mass of the continuous phase around the accelerated particle is big compared to the particle mass itself. For the simulation of solid disperse particles in fluid, the virtual mass force is mostly neglected.

Lift force

For a fully exposed particle in fluid, a divergence in the axis-symmetric flow field around the particle indicates a transverse force, orthogonal to the flow direction. This so called lift force does not necessarily lead to a lift of the particle, but could rather lead to a sink as well. Two different forces, the Saffman and the Magnus force, are distinguished in literature as the cause of the lift. The Saffman force $F_{L,Sa}$ is generated by shear flow. The non-uniform velocity distribution results in the non-uniform pressure distribution at the particle surface. The resulting force acts towards the lower pressure equivalent to the

higher fluid velocity at the particle. According to the Saffman force, the lift of the Magnus force $F_{L,Ma}$ is induced by a non-uniform velocity distribution at the particle surface and the resulting pressure differential. Though, the velocity differential of the Magnus force is caused by particle rotation ω_p.

The analytical approach for the shear induced lift $F_{L,Sa}$ is based on Saffman (1965, 1968), who conducted physical tests on a cylinder in a shear flow at low Re_p. In the original formulation, the Saffman force was not clearly separated from the Magnus force since both phenomena were considered. However, the common formulation for the Saffman force represents the special case of $\omega_p \to 0$ (Michaelides et al., 2016). More details can be found in Bagchi et al. (2002) or Michaelides et al. (2016). Equation 2.10 defines the extended expression of Saffman's approach for three dimensional flow according to Sommerfeld (2000).

$$F_{L,Sa} = 1.615\ d_p^2 \sqrt{\rho_f \mu_f} \left(\frac{1}{\sqrt{|G|}} \right)^{0,5} ((v_f - v_p) \times G) \tag{2.10}$$

Thereby, G represents the shear rate, which could be replaced by $G = \omega_f = \nabla \times v_f$ according to the approach of Auton (1987). Saffman's analytical formulation is strictly limited to low Reynolds numbers $\mathrm{Re}_p \ll 1$, low shear Reynolds numbers $\mathrm{Re}_G \ll 1$ and assumes a large shear rate in relation to the relative velocity between particle centre and corresponding fluid velocity at that point v_r: $\varepsilon_G \ll 1$ (see Equation 2.11).

$$\mathrm{Re}_G = \frac{G d_p^2}{\nu_f} \quad ; \quad \mathrm{Re}_r = \frac{v_r d_p^2}{\nu_f} \quad ; \quad \varepsilon_G = \frac{\mathrm{Re}_G^{1/2}}{\mathrm{Re}_r} \tag{2.11}$$

McLaughlin (1991) extended the assumption of Saffman for high shear rates ε_G. The corresponding experiments on the lift at unbound shear flow showed, that the lift force decreases if ε_G decreases. Based on McLaughlin's (1991) approach and the numerical investigation of Dandy et al. (1990) at $0.1 < \mathrm{Re}_p < 100$, Mei (1992) developed his empirical solution for finite ε_G and higher Re_p to:

$$J(\varepsilon_G) = \frac{F_L}{F_{L,Sa}} = \begin{cases} (1 - 0{,}3314\ \xi^{0,5}) \exp\left(-\frac{\mathrm{Re}_p}{10}\right) + 0{,}3314\ \xi^{0,5} & (\mathrm{Re}_p \leq 40) \\ 0{,}0524(\xi \mathrm{Re}_p)^{0,5} & (\mathrm{Re}_p \geq 40) \end{cases} \tag{2.12}$$

$$\text{with} \quad \xi = 0{,}5 \frac{\mathrm{Re}_p}{\mathrm{Re}_G} \quad \text{and} \quad (0.005 < \xi < 0.4)$$

With Mei's (1992) approach, the Saffman force can be considered by Equation 2.13, whereby $c_{L,Sa}$ is the correction $J(\varepsilon_G)$ in Equation 2.12.

$$F_{L,Sa} = 1.61 d_p^2 c_{L,Sa} \sqrt{\rho_f \mu_f} \left(\frac{1}{\sqrt{|\omega_f|}} \right)^{0,5} ((v_f - v_p) \times (\nabla \times v_f)) \tag{2.13}$$

In contrast to the studies mentioned before, numerical investigations at even higher Reynolds numbers have shown, that the Saffman force changes signs. Kurose et al. (1999) simulated a fixed fully exposed particle in a homogeneous shear flow at Reynolds numbers of

$1 \ll Re_p \ll 500$. The results of the simulations showed a change of direction at $\mathrm{Re}_p \approx 60$, which is cased by pressure and viscous forces in terms of flow separation. However, in the case of a fixed rotating sphere in a homogeneous shear flow, the total lift force does not change signs, but tends to a constant value at $\mathrm{Re}_p \geq 200$ (Kurose et al., 1999).

An analytical solution for the Magnus force was first derived by Rubinow et al. (1961) as

$$F_{L,Ma} = \frac{\pi}{8} d_p^2 \rho_f \left[\omega_r \times (v_f - v_p)\right] \tag{2.14}$$

with the relative rotation velocity ω_r given as

$$\omega_r = \frac{1}{2} \nabla \times v_f - \omega_p \quad . \tag{2.15}$$

Since this approach is limited to small Reynolds numbers, a lift coefficient $c_{L,Ma}$ is introduced as a correction function for higher Reynolds numbers. Crowe et al. (2012) defines this formulation as

$$F_{L,Ma} = \frac{\pi}{8} \rho_f d_p^2 c_{L,Ma} \frac{|v_f - v_p|}{|\omega_r|} [(v_f - v_p) \times (\omega_r)] \tag{2.16}$$

For low Reynolds numbers, $c_{L,Ma}$ can be defined by the approach of Rubinow et al. (1961). Oesterlé et al. (1998) developed an empirical correlation for moderate Reynolds numbers based on experiments. Both approaches are given by Equation 2.17.

$$c_{L,Ma} = \begin{cases} 2\Omega_* & (\mathrm{Re}_p \leq 1) \\ 0.45 + (2\Omega_* - 0.45) \exp(-0.075\ \Omega_*^{0.4}\ \mathrm{Re}_\omega^{0.7}) & (10 \leq \mathrm{Re}_p \leq 140) \end{cases} \tag{2.17}$$

with

$$\mathrm{Re}_\omega = \frac{d_p^2 |\omega_r|}{\nu_f} \quad \text{and} \quad \Omega_* = \frac{d_p \omega_r}{2|v_f - v_p|} \tag{2.18}$$

Similar to the Saffman force, the Magnus force changes signs at different flow characteristics. The reason for this behaviour is yet not fully clear. More details are discussed in Section 7.2.1 or in Crowe et al. (2012) and Tanaka et al. (1990).

According to Bagchi et al. (2002) and L. Zeng et al. (2005), the Magnus force is significant smaller than the Saffman force. Especially for low and high Reynolds numbers, the lift due to rotation becomes negligible. However, also at moderate Reynolds numbers the influence of the rotation induced lift is so small that it barely affects the particle trajectories (Bagchi et al., 2002).

2.2.2 Particle-fluid interaction at a particle group

The beforehand presented approaches are based on the assumption of an isolated particle in an infinite flow field. For granular flows or flow through granular packings the fluid-particle interaction becomes more complicated.

The estimation of the lift force in a particle group is barely presented in literature. The lift of a single particle in a group of other particles is discussed mainly for particle groups at a boundary layer. For this specific application, Zanke (2003) remarks that a particle needs to be fully exposed to experience a significant influence of the classical dynamic lift due to shear flow or particle rotation. Thus, the classical lift in a particle bed is of minor importance. In contrast, the turbulent lift due to turbulence induced pressure differences represent a relevant influence on the fluid-particle interaction at a particle bed (see further information in Section 7.2.1). Thus, in this section the effect due to the presence of other particles is discussed for the most significant fluid-particle interaction force: the drag force (O'Sullivan, 2011).

The main impact on the drag force estimation by the presence of other particles, is caused by the reduced volume for the fluid flow. This results in a high fluid velocity gradient and leads to a higher shear stress on to the particles. To capture this effect, the particle packing or the void fraction α_f of a particle system is introduced to the fluid-particle interaction force formulation.

So far, there is no analytical solution for the drag force estimation in a particle packing. However, several empirical correlations exist, which according to J. Li et al. (2003) can be differentiated into three different types of drag correlations:

- (semi-) empirical drag correlations by use of pressure drop data,
- (semi-) empirical drag correlations by use of bed expansion experiments,
- drag correlations by direct numerical simulations.

The first class is based on investigations of the pressure drop caused by fluid flow through a porous media. In geotechnical engineering, the most simple estimation of a loss of pressure in porous media, is the famous approach of Darcy. According to Darcy's law, the pressure loss is linearly proportional to the filter velocity v_{filter}. Hence, the pressure loss over the distance x in flow direction of v_f is defined to

$$-\frac{dp}{dx} = \frac{\mu_f v_f}{k_f} \quad . \tag{2.19}$$

Thereby, k_f is defined as the intrinsic macroscopic permeability of the porous media and the fluid velocity v_f represents the filter velocity v_{filter}. The law of Darcy holds true for small flow velocities in which the viscose forces dominate the flow characteristic. With an increase in velocity, the viscous forces start to stand back behind inertial forces and turbulent influences. To consider those turbulent effects, Darcy's law was extended by Forchheimer (1901). Forchheimer's (1901) solution for a pressure drop in porous media consists of two terms (see Equation 2.20). The first one equals the approach of Darcy and gives a proportional relation between the fluid velocity and the viscous pressure loss by a factor a. The second term represents the turbulent inertial effects with a quadratic relation between factor b and the fluid velocity. With increasing fluid velocity, the inertial term gets more and more dominant, since v_f is included as a second order formulation.

$$-\nabla p = a v_f + b|v_f|v_f \tag{2.20}$$

The determination of the factors a and b has been the basis of many investigations. A compilation can be found in Wittmann (1980) or van Gent (1993).

Ergun (1952) developed an empirical solution for the Forchheimer (1901) approach, which is still very common for the estimation of pressure loss in porous media. Ergun's (1952) investigations lead to the following drag model with the interphase momentum exchange coefficient of the drag correlation ξ, the particle volume V_p and the void fraction α_f:

$$\begin{aligned} F_D = &\quad \frac{V_p \xi}{1-\alpha_f}(v_f - v_p) \\ \text{with} \quad \xi = &\quad 150\frac{(1-\alpha_f)^2}{\alpha_f^2}\frac{\mu_f}{d_p^2} + 1.75\frac{(1-\alpha_f)}{\alpha_f}\frac{\rho_f}{d_p}|v_f - v_p| \end{aligned} \tag{2.21}$$

For this empirical approach, Ergun (1952) conducted experiments with homogeneous, spherical particles. Thus, the solution is appropriate for monodisperse particle packings of process engineering, but less for realistic grain distributions of soil (Kocak, 2017). Since Ergun's (1952) investigations were based on dense particle packings ($\alpha_f \approx 0.4$), the approach seems weak for more dilute fluid particle mixtures. Opposed to dense mixtures, the particle movement in dilute mixtures is only weakly affected by other particles and the drag is approximated by a drag correlation of a single particle. The boundary between a dense and a dilute mixture regime is often adopted at a void fraction of $\alpha_f \cong 0.8$. Gidaspow (1994) took those transition into account and combined the drag correlations of Ergun (1952) and Wen et al. (1966). As long as the void fraction is smaller than 0.8 the approach of Ergun (1952) is adopted, while at $\alpha_f > 0.8$ the approach of Wen and Yu (1966) is employed (see Equation 2.22). The Reynolds number of a particle packing Re_{p,α_f} is based on the superficial relative velocity between particle and fluid and includes the local void fraction α_f.

$$\begin{aligned} \text{for } \alpha_f \leq 0.8 \quad \xi = &\quad 150\frac{(1-\alpha_f)^2}{\alpha_f^2}\frac{\mu_f}{d_p^2} + 1.75\frac{(1-\alpha_f)}{\alpha_f}\frac{\rho_f}{d_p}|v_f - v_p| \qquad \text{(Ergun)} \\ \text{for } \alpha_f > 0.8 \quad \xi = &\quad \frac{3}{4}c_D\frac{|v_f - v_p|\rho_f(1-\alpha_f)}{d_p}\alpha_f^{-2.7} \qquad \text{(Wen \& Yu)} \\ \text{and} \quad c_D = &\quad \frac{24}{\mathrm{Re}_{p,\alpha_f}}(1 + 0.15\mathrm{Re}_{p,\alpha_f}^{0.687}) \qquad (\mathrm{Re}_{p,\alpha_f} \leq 1000) \\ c_D = &\quad 0.44 \qquad (\mathrm{Re}_{p,\alpha_f} > 1000) \\ \text{with} \quad \mathrm{Re}_{p,\alpha_f} = &\quad \frac{d_p \alpha_f \rho_f |v_f - v_p|}{\mu_f} \end{aligned} \tag{2.22}$$

According to Koch et al. (2001), the approach of Ergun (1952) leads to an over prediction of the drag force for less dense packings at $\alpha_f > 0.5$. Furthermore, the instantaneous split between the two approaches results in an instantaneous increase or decrease of the drag force. Kafui et al. (2002) recommends the approach of Di Felice (1994), which provides a more smooth transition between a dilute and a dense packing, since it is a single-function correlation.

The approach of Di Felice (1994) belongs to the second class of drag force correlations, which is based on the correlation between the superficial velocity and the bed expansion

by Richardson et al. (1954). In this correlation, the effect of other particles is considered in local void fraction and an exponent which is related to the flow regimes or particle Reynolds number. Di Felice (1994) extended the general drag force equation for single spheres (see Equation 2.4) by a voidage function $\alpha_f^{1-\chi}$ which corrects the single sphere formulation for the presence of other particles (see Equation 2.23). For the calculation of the drag coefficient c_D, Di Felice (1994) employed the approach of DallaValle (1948).

$$\begin{aligned} F_D &= \frac{\pi}{8} c_D \rho_f d_p^2 (v_f - v_p)|v_f - v_p| \alpha_f^{1-\chi} \\ \text{with} \quad \chi &= 3.7 - 0.65 exp\left[-\frac{(1.5 - \lg \mathrm{Re}_{p,\alpha_f})^2}{2}\right] \\ \text{and} \quad c_D &= \left(0.63 + \frac{4.8}{\sqrt{\mathrm{Re}_{p,\alpha_f}}}\right)^2 \end{aligned} \tag{2.23}$$

The third class of drag correlations is based on micro scale simulations with a e. g. direct numerical or Lattice-Boltzmann approach (Choi et al., 2001; J. Zhang et al., 1999). This advancement is rather new, compared to the other drag correlations, since micro scale simulations need high computational effort. The most common approach was developed by Koch and Hill (2001), which can be found in Equation 2.24.

$$\begin{aligned} F_D &= \frac{V_p \xi}{1 - \alpha_f}(v_f - v_p) \\ \text{for } \mathrm{Re}_{p,\alpha_f} < 40 \quad \xi &= \frac{18 \nu_f \alpha_f (1 - \alpha_f)}{d_p^2}\left(F_0(\alpha_p) + \frac{1}{4} F_1(\alpha_p) \mathrm{Re}_{p,\alpha_f}^2\right) \\ \text{for } \mathrm{Re}_{p,\alpha_f} > 40 \quad \xi &= \frac{18 \nu_f \alpha_f (1 - \alpha_f)}{d_p^2}\left(F_0(\alpha_p) + \frac{1}{2} F_3(\alpha_p) \mathrm{Re}_{p,\alpha_f}\right) \\ (\alpha_p < 0.4) \quad F_0(\alpha_p) &= \frac{1 + 3(\alpha_p/2)^{1/2} + (135/64)\alpha_p \ln(\alpha_p) + 17.14\alpha_p}{1 + 0.681\alpha_p - 8.48\alpha_p^2 + 8.16\alpha_p^3} \\ (\alpha_p > 0.4) \quad F_0(\alpha_p) &= \frac{10\alpha_p}{(1 - \alpha_p)^3} \\ F_1(\alpha_p) &= 0.110 + 5.10 \cdot 10^{-4} e^{11.6\alpha_p} \\ F_3(\alpha_p) &= 0.0673 + 0.212\alpha_p + \frac{0.0232}{(1 - \alpha_p)^5} \end{aligned} \tag{2.24}$$

Thereby, α_p describes the particle volume fraction. Koch and Hill (2001) conducted Lattice-Boltzmann simulations on fluidised and fixed particle-gas-systems. According to Bokkers et al. (2004), the Koch and Hill (2001) model predicts significantly higher values for low Reynolds numbers and significantly lower values for high Reynolds numbers than the Gidaspow (1994) approach. For the simulation of gas injections in a fluidised monodisperse particle bed, the authors acknowledge that the model of Koch and Hill (2001) yield better results than the Gidaspow (1994) model. Additionally, J. Li et al. (2003) recommend the Koch and Hill (2001) drag model and identify a good predictive capability for this approach for fluidised bed simulations.

2.2.3 Discussion

On an analytical base, the different fluid-particle interaction forces can be clearly distinguished (see Section 2.2.1). However, this approaches are only valid for a fully exposed particle in an infinite flow field, where the influences evoking this forces can be clearly distinguished. This is applicable only for very dilute fluid-particle mixtures and for particles which are not positioned in a boundary layer field. However, for phenomena taking place at a fluid-soil boundary none of this restriction are fulfilled. First, the fluid-particle mixtures are dense with dominating particle-particle contacts and, second, the presence of a boundary affects the local flow situation, which results in different effects than in an infinite flow field. In a dense packing, the reduced pore volume leads to high velocity gradients and an increased shear stress on the particle surface. Nevertheless, empirical models exist to describe the proportionally greatest fluid-particle interaction force - the drag force - within a particle packing (see Section 2.2.2). But also those can get to their limit if it comes to highly dynamic behaviour of the dense packing, such as investigated in (J. Li et al., 2003). Since, the pore volume changes continuously in a dynamic mixture and, thus, the local boundaries for each individual particle, the drag force becomes significantly non-linear or anisotropic. Further, the particle-particle interaction within a dynamic dense mixture influence the flow field of the fluid phase. Thus, dissipative particle interactions have a significant influence on the development of heterogeneous flow structures, which affect the particle transport massively. According to J. Li et al. (2003), the model of Koch and Hill (2001) gives the best results for highly dynamic dense fluid-particle mixtures. The complexity of dense fluid-particle mixtures is even increased for the presence of a boundary. This applies both for particles near a boundary as well as particle positioned at the surface of a boundary (more details on this later in Section 7.2.1). For this reason, the fluid-particle interaction forces near a boundary are often simplified to two components: the drag force component, for the forces in flow direction, and the lift force, representing the force component orthogonal to the flow direction. The high velocity gradient at the boundary and the great turbulences make the flow field highly anisotropic, which makes it difficult to find analytical solutions to describe the forces acting on a particle positioned near a boundary. This is also valid for a particle positioned at the surface of a boundary, but further the presence of the other particles need to be taken into account. The complexity is illustrated by the fact, that the so far conducted investigations are not even agreeing, if the lift force on a particle near a boundary is trending into the direction of the boundary or vice versa (see Section 7.2.1). Thus, it is little known about the exact and detailed interaction between fluid and particles near or at a boundary. However, to investigate phenomena on the interaction of fluid and particle and to determine those influences on the macroscopic behaviour at fluid-soil interaction it is crucial, to get a better understanding on the forces which are acting between the fluid and the particle and to identify the relevant forces.

3 Research Objectives and Methodology

The interaction between granular soil and fluid is characterized by several superimposed small scale interaction processes, motivated by the multi-component characteristics of granular soil. On a structural level, it consists of granular disperse grains, which are interacting with each other in the form of particle-particle contact, and interstitial void fluid, which interacts further with the granular material. Due to the presence of a free fluid at the fluid-soil boundary, the surface-near granular material interacts further with the external flow field of the free water. Additionally, the interstitial void fluid interacts with the free fluid by means of an exchange of mass and momentum between the internal and the external flow field.

On a structural level, the interaction between granular particles as well as their interaction with the surrounding fluid, is described by forces. The determination of fluid-particle interaction forces in a dense mixture environment is rather complex. The small scale interaction processes are superimposing, which prevents a clear segregation of the various influences of the surrounding flow field on to the individual particle. This prohibits an analytical solution as it is defined for an exposed single particle in a infinite flow field (see Section 2.2). For the dominating fluid-particle interaction force - the drag force - several empirical force models exist for the application in dense mixtures. However, it is unknown how well those models are applicable for specific geotechnical applications, like the transition from static to dynamic state and vice versa or the presence of a sharp interface of the granular phase at the soil-fluid boundary. Further, it is unclear whether besides the drag force also other fluid-particle interaction forces need to be taken into account, such as e. g. lift forces near the boundary.

The small scale interaction processes in between the granular particles and the interaction of the granular particles with the surrounding fluid and their influence on the macroscopic mechanisms cannot be easily investigated with physical tests. In contrast, numerical simulations give the opportunity to investigate non-intrusively the internal processes on a small scale and further link this behaviour to the overall macroscopic mechanism. To capture the described processes it is crucial to represent the dispersity of the granular media as well as the interaction with the fluid. According to Section 2.1, the multi-scale approach represents the only numerical approach, that is capable of this representation. Thereby, the coupled CFD-DEM represents a common numerical approach in process engineering to model the behaviour of mixtures consisting of a granular and a fluid phase. However, its application in geotechnical engineering is just very recently and, thus, less investigated.

In this thesis, geotechnical phenomena of fluid-soil interaction shall be investigated with respect to the multi-component characteristic of granular soil and the interaction processes that arise from this. However, to focus on the detailed complex interaction processes between granular particles, internal and external fluid the presentation of the granular phase is simplified. Therefore, the granular material in the investigations of this thesis is represented by spherical granular particles. Furthermore monodisperse particle packings are assumed. This approach neglects influences arising from the grain size distribution and the angular shape of the granular particles in natural soil.

For the investigation of the detailed interaction processes between the granular particles, the internal and external fluid a hybrid modelling approach is applied in this thesis. The hybrid modelling approach includes physical tests with corresponding numerical simulations based on the unresolved CFD-DEM method. The physical tests give an insight into the investigated processes and build the basis for validation of the numerical method for the specific applications. The material behaviour during the physical tests is analysed by non-intruding measures including high-speed recordings and a PIV analysis. Thereby, the PIV analysis is conducted either for the movement of the granular phase or for the flow field of the fluid phase. Corresponding to the physical tests, numerical models are established to investigate the mechanisms further and in specific the internal interaction processes.

In the physical tests, monodisperse glass particles are applied as granular material. Glass particles offer the advantage of well-defined material characteristics and a similar particle density to natural soil grains. In the numerical simulations, perfectly spherical particles with the characteristics of the glass particles are applied. On the numerical side, this simplified approach offers significant benefits as well. The application of monodisperse particles renders the complex establishment of particle packings with a certain size distribution and porosity unnecessary. Furthermore, the application of a particle distribution requires higher number of particles for the same volume than a monodisperse packing, which result in higher computational costs per simulations. The assumption of fully spherical particles in the physical and numerical investigations reduces the computational costs further, since the DEM code applies multi-particle clumps to represent angular particles.

By means of the above described approach, the interaction between granular particles, internal and external fluid is investigated for three applications: the sinking procedure of a single particle in fluid, the collapse procedure of a submerged particle packing and the erosion at a particle bed. The investigation on the sinking procedure of a single particle serves as a benchmark, to investigate the limits and and the sensitivity to model-effects of the unresolved CFD-DEM method. Thereby, the sedimentation of a single sphere represents an analytically well investigated scenario and gives the opportunity to validate the results by numerous analytical approaches. The collapse of a particle column is characterised by the transformation from a static to a highly dynamic state. Thereby, the submerged conditions have a significant influence on the collapse mechanism in comparison to dry conditions. Furthermore, the initiation of motion at a particle layer shall be investigated, with taking the disperse characteristic and the permeability of the granular phase into account. A successful reproduction of erosion processes on a structural level by means of a numerical method, would enable the investigation of several influences on sediment trans-

port, such as pore-water pressure fluctuations. A better understanding of the small scale processes could further improve existing empirical models. Based on this paraphrased motivation and the literature studies in Chapter 2 the following research questions are formulated:

- The unresolved CFD-DEM method is well known for the simulation of dynamic mixtures. How does the method perform on applications which represent a limit case such as the behaviour of a single particles or the interaction at a clear boundary?
- The empiric models on fluid-particle interaction, applied in the CFD-DEM method, are based on the interaction between fluid within a particle packing. Do the interaction models also hold for the limiting case of an individual particle?
- Which influence do model characteristics such as the spatial discretisation of the fluid domain have on the modelling of fluid-particle interaction? Do other model effects occur at the investigation of single particle behaviour?
- How do the individual particle properties affect the behaviour of the overall particle mass in the numerical simulations? Which effect does the particle-particle interaction have on the transition between a static and dynamic case at the collapse procedure?
- How does the presence of fluid effect the collapse mechanism? Which effect has the presence of fluid on the particle-particle interaction? Which fluid-particle interaction occurs at the fluid-particle packing boundary or the particles within the particle mass? Which influence has the fluid-particle interaction on the transition between a static to a dynamic state at the column collapse?
- What is the motion threshold for individual spherical particles on a particle layer? Can (half-)empirical motion threshold models be applied for the force equilibrium on particle scale?
- Which effect has the resistance emerging from the particle positioning on the motion threshold?
- Can the unresolved CFD-DEM method reproduce the flow characteristics along a boundary?
- Can the unresolved CFD-DEM method reproduce the motion threshold along a particle layer for individual particles? Which force models need to be included and perform well?
- Can an unresolved CFD-DEM model reproduce erosion or transport processes along a particle layer? Which interaction occurs between the internal and external flow field during the erosion or transport process along a particle layer?

These research questions are going to be answered within this thesis.

The structure of this thesis is inspired by the previously presented research objectives. In Chapter 4 the chosen numerical method is presented in a more detailed way. Subsequently, the numerical method is applied on the benchmark investigation in Chapter 5. For the benchmark, the scenario of a free settling particle in fluid is investigated. By means of the benchmark, the limits and specifications of the unresolved CFD-DEM method are tested. Thereby, the influence of the particle and fluid-cell volume ratio, the initial position of the

particle in the mesh and the different fluid-particle interaction forces are investigated in a sensitivity study.

Afterwards, in Chapter 6 the submerged granular flows are investigated by the scenario of a collapsing particle column. Thereby, the fundamentals on granular slumping on macroscopic scale are presented shortly. The investigation of the collapse procedure is divided into two main differentiations. First, the dry collapse mechanism is investigated, before the submerged case is further analysed. Further, the collapse scenario is differentiated into a slow and a fast collapse procedure, defined by the extraction speed of the movable wall. Thereby, different mechanisms of the macroscopic behaviour shall be addressed, to investigate the effect of the particle behaviour. For all differentiations, physical tests as well as numerical simulations are conducted. Thereby, the particle-particle contact is extensively investigated by means of the dry collapse scenario, to link the particle contact formulation and the particle properties to the macroscopic collapse behaviour. The investigations of the submerged collapse procedure focus on the influence of fluid-particle interaction inside the particle packing as well as the on the deposit surface and their effect on the macroscopic behaviour.

The defined particle properties from Chapter 6 are applied in the investigations of erosion at a particle bed. Thereby, physical tests are conducted to define a motion threshold along a rough particle boundary, to gain detailed information on the motion threshold, the resistance of the particle due to its position and the detailed flow processes at incipient motion. The results of the physical tests are compared to common half-empirical models on the motion threshold. Further, the incipient motion threshold is modelled by numerical simulations. To compare the flow situation in the tests with those in the numerical simulations, the test scenario is modelled by the coupled CFD-DEM method. Finally, the verified numerical model shall be applied for the scenario of erosion at a permeable particle layer.

All applied abbreviations or notations are presented in Appendix A of this thesis.

4 Numerical Fundamentals of the Coupled CFD-DEM Method

The coupled CFD-DEM approach is rather new in the field of geotechnical engineering. Thus, the governing equations and models of the numerical approach are briefly presented in this chapter. In the first section, the DEM approach for the numerical modelling of disperse granular material is presented. Afterwards, the governing equation and models of the coupled CFD-DEM are introduced. For more detailed information on the presented content, literature recommendations are given at the corresponding passages.

4.1 Discrete Element Method - Disperse Phase

The Discrete-Element-Method (DEM) has been developed by Cundall (1971) for the simulation of three-dimensional body-collisions in rock-mechanical problems. The method allows the simulation of large numbers of disperse particles in a Lagrangian formulation. Thereby, the particle represent discrete bodies with a defined diameter and mass, which are interacting and influencing each other. The DEM approach enables the simulation of a high number of particles (based on computational powers up to $\approx 10^6$) and highly dynamical processes.

The DEM approach can be distinguished by the approach of contact modelling into the so called hard-sphere and the soft-sphere approach. The hard-sphere-model assumes the particle as rigid non-deformable bodies. The contact between particle interaction is modelled by conservation of momentum. Therefore, the particle trajectories before and after a collision are determined by momentum exchange. However, this procedure is limited by a pair-wise contact. Multiple contacts are not possible. Hence, the hard-sphere-model is limited to rather dilute particle systems and is often applied for molecular dynamic simulations (Cundall et al., 1992; Lu et al., 2015). The soft-sphere model presumes the particles to be deformable. The algorithm of the approach is based on the assumption that the deformation of individual particles due to particle-particle or particle-wall interaction is infinitesimal small in comparison to the deformation of the overall dense particle packing (Cundall & Strack, 1979). Thus, the deformation of particles due to interaction is not modelled but approximated by an overlapping of inter-penetrating particles. The particle overlap is applied to determine particle contact forces by a force-deformation scheme (van der Hoef et al., 2006). By means of the particle contact forces, the particle trajectories of the following timestep during an interaction are determined. The soft-sphere-model enables the simultaneous contact of multiple particles and is suitable for the reproduction of dense particle systems. Nonetheless, it is also more complex and computational expensive

in comparison to the hard-sphere-model (Lu et al., 2015). However, the soft-sphere-model is of higher interest for geotechnical applications, where usually dense particles systems are applied. Thus, the soft-sphere-model is applied in the numerical simulations of this thesis. The governing equations and models of the soft-sphere DEM are presented following.

4.1.1 Governing Equations

In the soft-sphere DEM (hereinafter DEM), the movement of the individual particles and the corresponding trajectories are determined by taking the forces on the particle into account. The resulting translational and rotational particle velocities of the next timestep can be determined by Newton's second law (Cundall et al., 1979) to

$$m_p \frac{d}{dt}\mathbf{v}_p = \sum \mathbf{F}_i \quad \text{and} \quad I_p \frac{d}{dt}\boldsymbol{\omega_p} = \sum \mathbf{T}_i \qquad . \tag{4.1}$$

Thereby, m_p represents the particle mass, $\mathbf{v}_p$ the translational particle velocity, $\mathbf{F}_i$ the sum of forces, I_p the moment of inertia, $\boldsymbol{\omega_p}$ the particle angular velocity and $\mathbf{T}_i$ the sum of torques on the particle.

To determine the particle trajectories of the next timestep, the particle forces at the current timestep need to be known. The sum of particle forces can be distinguished into the total contact forces as the sum of individual contact forces exerted by all neighbouring particles in contact, the total external forces like gravitation and the sum of remaining particle-particle forces (van der Hoef et al., 2006). Examples for forces of the latter type are e. g. adhesive forces like cohesion, the Van-der-Waals-force or electrostatic repulsion forces. Since none of those are applied in this thesis, see Johnson (1987) and Zhu et al. (2007) for further information.

The particle contact forces are defined as interaction forces, which are exerted between two particles in contact. As described earlier, the interaction between two particles is approximated due to an overlapping of the interacting particles. Via a force-displacement law, a correlation between the overlapping (displacement) and the corresponding exerted force is defined. Several force-displacement laws exist, which are based on rheological models defining different material behaviour. The most common force-displacement models are based on a visco-elastic material behaviour, which takes besides the elastic contribution of the contact also the dissipation due to plastic deformation into account. The rheological components of a visco-elastic force-displacement law are illustrated in Figure 4.1 for the example of two interacting particles. The contact force can than be determined by Equation 4.2. For the determination of contact forces, a normal and a tangential component need to be distinguished.

$$\mathbf{F}_{p,n} = k_n\,\boldsymbol{\delta}_n - c_n\,\Delta\mathbf{v}_{p,n} \quad \text{and} \quad \mathbf{F}_{p,t} = k_t\,\boldsymbol{\delta}_t - c_t\,\Delta\mathbf{v}_{p,t} \tag{4.2}$$

Thereby, k_n and k_t represent the elastic spring stiffness and c_n and c_t the damping coefficient in normal and tangential direction respectively. Further, $\boldsymbol{\delta}_n$ and $\boldsymbol{\delta}_t$ describes the particle overlap distance, while $\Delta\mathbf{v}_{p,n}$ and $\Delta\mathbf{v}_{p,t}$ represent the relative particle velocity between the two interacting particles.

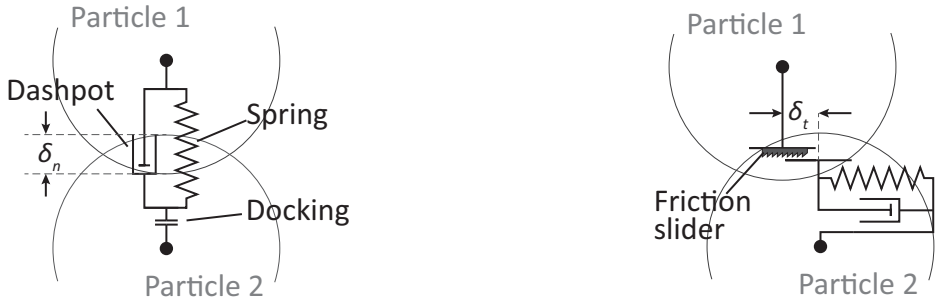

(a) Normal contact force (b) Tangential contact force

Figure 4.1: Scheme of rheological components of a visco-elastic force-displacement law during contact between two particles

In the conducted DEM simulations the Hertz-Mindlin & Deresiewicz model is applied to determine the rheological coefficients of Equation 4.2. Thereby, the normal spring stiffness k_n in Equation 4.3 is determined by Hertz's contact theory (Hertz, 1881), while the tangential spring stiffness k_t in Equation 4.4 is calculated on basis of Mindlin & Deresiewicz (1953). For the calculation of the damping coefficients c_n and c_t a non-linear damping term of Tsuji et al. (1992) is applied (Hu et al., 2011).

$$k_n = \frac{4}{3} E^* \sqrt{r_p^* \delta_n} \quad \text{and} \quad c_n = -2\sqrt{\frac{5}{6}} e^* \sqrt{2E^* \sqrt{r_p^* \delta_n} m^*} \tag{4.3}$$

$$k_t = 8G^* \sqrt{r_p^* \delta_t} \quad \text{and} \quad c_t = -2\sqrt{\frac{5}{6}} e^* \sqrt{8G^* \sqrt{r_p^* \delta_n} m^*} \tag{4.4}$$

with $$e^* = \frac{\ln(e)}{\sqrt{\ln^2(e)+\pi^2}}, \qquad \frac{1}{r_p^*} = \frac{1}{r_{p,1}} + \frac{1}{r_{p,2}}, \qquad \frac{1}{m^*} = \frac{1}{m_1} + \frac{1}{m_2},$$
$$\frac{1}{E^*} = \frac{(1-\nu_{p,1}^2)}{E_1} + \frac{(1-\nu_{p,2}^2)}{E_2}, \qquad \frac{1}{G^*} = \frac{2(2-\nu_{p,1})(1+\nu_{p,1})}{E_1} + \frac{2(2-\nu_{p,2})(1+\nu_{p,2})}{E_2}$$

Thereby, E represents the Young's modulus, r_p the particle radius, e the coefficient of restitution, ν_p the Poisson number and m the particle mass. The indices 1 and 2 distinguish the parameters for the two interacting particles. The marking * describes the effective parameter. More details on the applied model can be found in Antonyuk (2006), Balevičius et al. (2004), Nosewicz et al. (2017), and Zhu et al. (2007).

Besides the spring and the dashpot component the tangential contact model in Figure 4.1b includes a friction slider. This ideal-plastic friction slider represents the effect of sliding after the tangential contact forces overcome a certain limit of static friction (Goniva et al., 2012; Silbert et al., 2001). Thereby, the static friction is equivalent to the characteristics of Coulomb friction. To take the effect of sliding into account, the determination of the tangential contact force in Equation 4.2 needs to be expanded to

$$\mathbf{F}_{p,t} = \min\left[\left|k_t\, \boldsymbol{\delta}_t - c_t\, \Delta \mathbf{v}_{p,t}\right|,\ \mu_s \cdot \mathbf{F}_{p,n}\right] \qquad . \tag{4.5}$$

Besides the previously described contact modelling, additional contact models can be added to the equations in Equation 4.1. A well-established addition is the supplementation of a rolling friction model. The rolling resistance or rolling friction μ_r is often applied to take non-spherical particle shapes or inter-particle bonds into account (Ai et al., 2011). Thus, the rolling friction provides an effective model mechanism to control the translational and rotational motions as well as the energy dissipation at particle contact (H. Zhou et al., 2016). According to Iwashita et al. (2000), Y. C. Zhou et al. (1999), and Zhu et al. (2007), the rolling friction is of importance for applications in which the torque plays a significant role, such as the transition between static and dynamical states, the formation of shear bands or heaps. In the conducted numerical simulations the elastic-plastic spring dashpot (EPSD) model from Ai et al. (2011) is applied as rolling friction model. For the implementation in the contact modelling procedure see Kloss (2016).

All previously presented governing equations of the DEM algorithm can be resolved locally. This requirement is controlled by the chosen DEM timestep length Δt. In the DEM, the independence of the equations is based on such a sufficiently small timestep, that an information cannot propagate further than from one particle to its immediate neighbour during one timestep (Cundall et al., 1979; Hart, 1988). To achieve a sufficient modelling of particle interaction, it is further required to resolve the particle contact event in several timesteps to reproduce the phase of deformation and repulsion during a collision. According to van der Hoef et al. (2006), the timestep should resolve the contact event in at least 5 timesteps, whereby better results are obtained by a resolution of 15-20 timesteps per contact event. The required timestep resolution can be estimated by means of the Rayleigh time (see Equation 4.6), Hertz time (see Equation 4.7) or Cundall Time (see Equation 4.8) (Jensen et al., 2014). According to Jensen et al. (2014), the applied DEM timestep width should be 20% of the minimum value.

$$\Delta t_{\text{Raleigh}} = \frac{\pi \cdot r_p}{0.1631(\nu + 0.8766)} \sqrt{\frac{\rho_p}{E/[2(1+\nu_p)]}} \tag{4.6}$$

$$\Delta t_{\text{Hertz}} = 2.87 \left[\frac{(\rho_p 4/3\pi r_p^3)^2}{r_p E^2 v_{p,\max}} \right]^{0.2} \tag{4.7}$$

$$\Delta t_{\text{Cundall}} = 0.2\pi \sqrt{\frac{\rho_p 4/3\pi r_p^3}{E/[3(1+2\nu_p)]\text{NORMK}}} \tag{4.8}$$

Thereby, NORMK is a stiffness parameter, which is typically assumed to 0.1 to 0.001.

The algorithm of DEM alternates between Newton's second law to determine the particle trajectories and the force-displacement law to estimate the particle forces. The computational sequence of DEM algorithm according to Cundall & Strack (1979) is vividly illustrated in Stein et al. (2004).

4.1.2 Contact detection

An essential part of the DEM algorithm is the contact detection. Thereby, the adjacent neighbouring particles are identified, which might lead to particle-particle contact. How-

ever, the comparison of each particle position with every other particle position would lead to immense computational costs. For that reason, the DEM algorithm includes a step to generate neighbouring lists. The neighbouring lists contain for each particle all particles, which might result in a contact within the next timestep. Thus, all particles pairs are excluded that are too far away from each other to be in contact (Kloss et al., 2012). This exclusion is determined by a certain distance from the examined particle. This so called cut-off distance needs to be chosen to a sufficiently great value that all relevant particles are included in the neighbour list. A too big cut-off distance will greatly reduce the computational efficiency (van der Hoef et al., 2006). Besides the chosen cut-off distance, the computational costs can be further adapted by the frequency of neighbour-list generation to every n timesteps. However, in dense particle packings the neighbouring list should be updated for each new timestep. More details on the contact detection are given in Kloss et al. (2012).

4.2 Coupled CFD-DEM - Fluid-Particle Interaction

The term of Computational Fluid Dynamics (CFD) comprises a high number of different approaches and models for the reproduction of fluid behaviour such as the transport of liquid or gaseous fluids. Thereby, Eulerian as well as Lagrange approaches are present. In this thesis, the term CFD is applied for an Eulerian approach based on the Finite-Volume-method. Thus, the CFD domain is discretised into cells. As already described in Section 2.1.4, the coupled CFD-DEM needs to be distinguished into two different approaches regarding the ratio between DEM-particle and CFD-cell size. In this chapter the unresolved CFD-DEM is introduced, which is further applied in this thesis. For further information on the resolved CFD-DEM or the difference between the approaches see Hager (2014). Following, the governing equations of the unresolved CFD-DEM are presented. Further, relevant sub-models of the method are introduced.

4.2.1 Governing Equations

In the coupled CFD-DEM the fluid phase is assumed as an incompressible fluid. The characteristic behaviour of an incompressible viscous fluid can be described by the partial differential equation system of Navier-Stokes. However, the derivative volume-averaged Navier-Stokes equations are applied in the coupled CFD-DEM, to take the presence of the granular particle phase into account. The volume-averaged Navier-Stokes equations are based on the research on Two-fluid-modelling of Anderson & Jackson (1967). Thereby, the volume fraction of DEM particles inside a CFD cell is taken into account in the conservation equations of mass and momentum (see Equation 4.9 and Equation 4.10).

$$\frac{\partial \alpha_f}{\partial t} + \boldsymbol{\nabla} \cdot (\alpha_f \mathbf{v}) = 0 \tag{4.9}$$

$$\frac{\partial}{\partial t}(\alpha_f \mathbf{v}) + \boldsymbol{\nabla} \cdot (\alpha_f \mathbf{v}\mathbf{v}) = -\frac{1}{\rho_f}\alpha_f \boldsymbol{\nabla} p + \boldsymbol{\nabla} \cdot (\alpha_f \boldsymbol{\tau}_f) + \boldsymbol{R}_{pf} \tag{4.10}$$

Thereby, α_f represents the volume fraction occupied by fluid within a CFD cell, $\mathbf{v}$ the averaged velocity of the fluid within one CFD cell, ρ_f the fluid density and $\boldsymbol{\tau}_f$ represents the fluid stress tensor. The additional term R_{pf} represents the momentum exchange between the particle phase and the fluid medium. The definition of the momentum exchange term R_{pf} is based on the relative velocity between fluid and particle phase and the momentum exchange coefficient K_{pf} (see Equation 4.11). The momentum exchange coefficient is based on the interaction forces between the particle and the fluid phase (see Section 4.2.1).

$$\boldsymbol{R}_{pf} = K_{pf} \cdot (\mathbf{v} - \mathbf{v}_p) \tag{4.11}$$

The previously presented governing equations for the coupled CFD-DEM represent just one possible approach denoted a Model A. In this case, the pressure drop $\boldsymbol{\nabla} p$ is assumed to be shared by the fluid as well as the particle phase (van Wachem, 2000; Zhu et al., 2007). Thus, the fluid as well as the particle phase pressure are included in the conservation equation of momentum (Hager, 2014). In the second approach of Model B, the pressure drop is applied in the fluid phase solely. More details on the different formulations can be found in Bouillard et al. (1989), Gidaspow (1994), Kafui et al. (2002), and Z. Y. Zhou et al. (2010).

In the explanations of Equation 4.9 and Equation 4.10, the velocity was determined as v to make clear that it represents the fluid velocity with the presence of the granular particles. However, the pure fluid velocity would be equivalent to the effective velocity around the particles. Since, this quantity is not defined in the unresolved CFD-DEM, the average velocity is following denoted as the fluid velocity v_f.

4.2.2 Momentum exchange model and coupling algorithm

The coupling of the CFD-DEM is considered by the interaction between the particle and the fluid phase. This is represented by the volume fraction as well as the momentum exchange coefficient. To determine the required quantities, the relevant information need to be communicated between the CFD and the DEM algorithm. In the CFD-DEM this is implemented by a so called Co-simulation. In a Co-simulation two numerical time integration algorithms are coupled. This is established by independent dynamic subsystems (CFDEM and LIGGGHTS), which are separately simulated (Schmoll, 2015). The transfer of input/output quantities is established by a synchronisation of the subsystem timestep. The applied software of CFDEM applies therefore as explicit or alternating approach, which is denoted as Gauß-Seidel-communication pattern. In this coupling algorithm the subsystems are coupled serial. In a first step, the positions and velocities of the particles are determined on DEM side. This informations of the exchange fields are transferred to the CFD subsystem. By behalf of a voidfraction model, the corresponding CFD-cells to the particle positions are computed and the resulting volume fractions determined. In the case of several particles in one cell, an average particle velocity is established. By means of the relative velocities between the particles and the fluid phase, the fluid-particle interaction forces are computed. This information is transferred to the DEM solver and is taken into account in the sum of external forces at the determination of particle trajectories for the next timestep. On side of the CFD, the interaction forces are applied in

the momentum-exchange term. Subsequently, the CFD algorithm solves the conservation equations of mass and momentum to determine the fluid velocities. Thenceforward, the coupling routine starts over with the determination of the particle positions and velocities (Kloss et al., 2012).

4.2.3 Interaction forces

By the application of the DEM for a coupled CFD-DEM simulation, the sum of external forces need to be extended by the fluid-particle interaction forces. Those have been sufficiently discussed in Section 2.2. The considered forces in the momentum exchange coefficient K_{pf} are based on the implemented force models in the simulation. As described in Section 2.2, the drag force F_D represents the proportionally largest interaction force. Numerous model exist for the determination of drag forces. The selection of a specific model is amongst others based on the fluid-particle mixture density. Since dense mixtures are applied in this thesis, drag models based on (semi-) empirical correlations are applied in the numerical simulations (see Section 2.2.2). Further, the coupled CFD-DEM code includes force models on virtual mass or lift.

For the determination of the fluid-particle interaction forces, the resulting values can be interpolated at the exchange between the CFD information and the DEM algorithm. Thereby, the information of a CFD-cell is interpolated to the position of the individual particle. Without the interpolation, the value at the cell centre is applied. However, the application of this interpolation is limited to the cell, which contains also the particle centre. Thus, in the case the particle volume is located in more than one cell, the interpolation is applied in the cell which contains the particle centre only.

4.2.4 Voidfraction estimation

As stated in Section 4.2.1, the conservation equations of mass and momentum are weighted by the fluid volume fraction α_f. To estimate the volume fraction of particles within a CFD cell α_p, several voidfraction-models are established in the coupled CFD-DEM. The most easy approach is to assign all the particles and the corresponding volume to the cell, where their centre is positioned. Apparently, this approach is going to overestimate the volume fraction for some cells, while for other cells the volume fraction is underestimated. This approach leads to erroneous results due to a inhomogeneous volume fraction field if the particle size approaches cell size (Kloss et al., 2012). An improved approach is the divided voidfraction model. Thereby, the particle volume is equally divided by 29 distributed marker points representing a certain volume. Thus, the particle volume can be divided more evenly over the cells, in which it is enclosed. This model is likely applicable for a particle size in the range of a CFD cell. However, this approach has the drawback of inapplicability over processor boundaries. The presence of the particle is going to be registered only in the cell in which the particle centre is present. This might lead to erroneous results near processor boundaries. Another alternative approach is a trilinear voidfraction model. Thereby, the particle volume is distributed over 8 neighbouring cell centres using trilinear interpolation, which results to a very smooth particle volume distribution. However, this

approach can be applied for structured meshes with cubic cells only. Thus, it is very limited in its application. In the conducted numerical simulations, the divided voidfraction model is applied, since it has been sufficiently tested for simulations in which the particle size is in range of a CFD cell.

4.2.5 Smoothing

The mapping of the exchange fields from the DEM domain on to the CFD domain needs to be handled with care. At cell sizes approximately in the size of a DEM particle, just a few cells consider the mapping of the exchange fields. This leads to peaks and holes in the solution of the CFD domain. According to Vangoe et al. (2017), already small irregularities in the voidfraction field might lead to pressure fluctuations on side of the CFD. To prevent irregularities and improve the stability of the numerical solution, a smoothing approach can be applied.

By smoothing, the exchange fields are smeared out over the CFD domain. Thereby, the smeared exchange fields affect the fluid over a specific smoothing distance l_{smooth}. Radl et al. (2014) and Vangoe et al. (2017) recommend to set the smoothing length to three times the particle diameter. The smoothing of an exchange field Θ is applied by a diffusion equation, which is given to

$$\frac{\partial \Theta}{\partial t} = D_{smooth} \nabla^2 \Theta \quad . \tag{4.12}$$

Thereby, D_{smooth} represents the diffusion coefficient, which is defined to $D_{smooth} = l^2_{\text{smooth}}/\Delta t$. This laplacian diffusion equation ensures conservation of the exchange fields. Thereby, the mean particle velocity field remains fixed in cells where the particles are present and smoothing effect is applied only to neighbour cells (Radl et al., 2014).

For large ratio of cell size to particle diameter, this smoothing is of minor affect. The smoothing affect, which is inherent to the mapping algorithm itself, ensures already good results (Radl et al., 2014). More details on the smoothing process is given in Pirker et al. (2011) and Radl et al. (2014).

4.2.6 Turbulence modelling

For the simulation of fluid turbulences, turbulence models need to be applied in the CFD simulation. Thereby, the turbulence models are purely based on the CFD side. The presence of the granular particle phase is not considered in the turbulence modelling of unresolved CFD-DEM.

Turbulent flows can be simulated by different approaches. The direct numerical simulations (DNS) solves all turbulences directly. Thus, also the smallest dissipative turbulences need to be resolved numerically. This requires an extremely fine meshing of the CFD regime and huge computational costs. For that reason the DNS is not suitable for applied problems. The Large-eddy-simulation (LES) represents a combination of the very precise DNS and empirical models. Thereby, greater and energy intense turbulence structures

are resolved by the DNS. In contrast, the small-scale turbulences are approximated by empirical turbulence models (Ferziger et al., 2008). However, also the LES requires a very fine meshing of the numerical CFD domain and is computational costly. Thus, its application is mostly limited to applications, where empirical models cannot achieve sufficient accuracy in turbulence modelling.

The most common approach of turbulence modelling in engineering applications is based on statistical turbulence models which are applied with Reynolds-averaged Navier-Stokes (RANS) equations. Thereby, the fluid velocity is represented by an averaged value $\overline{v}_f$ and a turbulent fluctuation component v_f'. The integration of this approach in the Navier-Stokes equation leads to additional turbulent stresses, the Reynolds stresses of the turbulent fluctuation. The additional stress terms need to be solved by introducing additional equations to the equation system. This additional equations are based on empirical turbulence models. Two different model approaches need to be distinguished into Reynolds stress models and turbulent viscosity models. Thereby, Reynolds stress models assume anisotropic turbulences and, thus, independent Reynolds-stress tensor components. In contrast, turbulent viscosity models assume isotropic turbulences, which are proportional to the gradient of the average flow velocity according to the approach of Boussinesq (1885). Thereby, the turbulent viscosity ν_t represents the proportionality factor, which describes the flow characteristics.

The determination of the turbulent viscosity ν_t can be established by numerous models. The approaches are distinguished by the number of differential equations, which needed to be solved besides the Navier-Stokes equations. This differential equations represent the transport of turbulent quantities. In CFD modelling, the methodology of two-equations models is applied in widespread applications. Thereby, different turbulent quantities, such as the turbulent kinetic energy k, the dissipation rate ϵ or the specific dissipation rate ω, are applied. More detailed information on the different turbulence models, their benefits and drawback are presented in Davidsson (2006), Ferziger et al. (2008), Menter (1994), Menter et al. (2003), N. D. Pope et al. (2006), Rumsey (2015), and Wilcox (1991).

Following, some specification on wall-near turbulence modelling are presented for common two-equation turbulence models:

- k-ω model: The k-ω model is based on an approach of Saffman, which has been further developed by Wilcox (1988). The k-ω model belongs to the low-Re turbulence models and enables the possibility to resolve the wall-near turbulence parameters without additional damping formulations like wall-functions (Wilcox, 1991). With a sufficient resolution of the wall-near area, the viscous as well as the logarithmic overlap layer can be resolved.
- k-ϵ model: The k-ϵ model represents the most applied turbulence model in engineering applications (S. B. Pope, 2000). It belongs to the approaches for higher Reynolds numbers (high-Re turbulence model). At high Reynolds numbers, the viscous boundary layer becomes very flat and a discretisation with very flat cells would be required. To prevent this, the high-Re model applies wall-functions, which replace the otherwise required damping characteristics near the wall. The wall-functions approximate the local wall-near velocity-gradient and, thus, the wall-near values of the turbulence parameters. By means of this approach, the discretisation with a more

coarser mesh becomes applicable. However, to model the velocity gradient near the wall sufficiently, the nearest grid point need to be positioned in the logarithmic wall region of the overlap layer (more details in Section 7.1).

- k-ω-SST model: The k-ω-SST (Shear Stress Transport) model of Menter (1992) combines the benefits of the k-ω and the k-ϵ model (Laurien et al., 2013). By means of so-called blending functions, the turbulence modelling approach switches from the k-ω model in the wall-near modelling areas to the k-ϵ model in the region of the outer flow region (Menter, 1994). Thus, the sensibility on the outer flow region of the k-ω model is avoided without renouncing the detailed resolution of the turbulence parameters in the wall-near area (Menter et al., 2003). The k-ω-SST is available for a low-Re as well as a high-Re formulation with wall functions.

5 Sedimentation of Spheres

The sedimentation of a single sphere is an analytically well investigated scenario, due to its simplicity and clear boundaries. Thus, analytical approaches exist to describe the settling procedure, the exact settling velocity as well as the fluid-force interaction. Further, investigations based on physical tests or numerical simulations gave detailed insights into the microscopic fluid-particle interaction and the detachment of the fluid flow from the sphere under different Reynolds number regimes.

The sedimentation process of a single particle represents an ideal scenario to validate the fluid-particle force estimation in the CFD-DEM method. Due to the exclusivity of a single particle, the simulation focusses on the fluid-particle interaction. The effect of different force models or other boundaries of the coupling procedure can be investigated in detail. In this chapter, sensitivity studies are conducted to investigate model effects of the coupled CFD-DEM method on the representation of the sedimentation process. Therefore, parameters of the sedimentation procedure, like the acceleration distance or the final settling velocity, are applied for comparison purpose. The final numerical model is validated with common analytical models in literature.

5.1 Fundamentals of Sedimentation

The sedimentation of a particle in fluid is a representative example of the interaction between fluid and particles. Although, its seems to be a simple process with limited influencing quantities, the interaction between fluid and particle is by no means simple. During the settling process, a free falling particle accelerates due to gravity. Opposed to gravity, the viscous fluid exerts a resisting drag force on the particle. This drag force increases with increasing settling velocity. The total drag force consists of two parts. The first part is a resistance due to viscous friction forces, which depend on the particle surface roughness. The second part is based on inertial pressure resistance, which result from the lee sided wake of the particle. The wake form depends on the flow separation around the particle (see Figure 5.1). More details on the flow separation and the wake shape is given in Schlichting et al. (2017) and Zanke (1982). With increasing settling velocity, the resistant pressure force increases with the wake size and the viscous friction force becomes negligible small. As already presented in Section 2.2, there are more fluid-particle forces than the drag force. Hence, the drag force is the dominating interaction force, the other interaction forces are neglected in this study.

A free falling particle reaches a constant velocity as soon as the drag force equals the accelerating gravitational force. This constant velocity is denoted as terminal velocity or

settling velocity. This settling velocity is the cause for numerous investigations in the past decades. Today, a large number of analytical and empirical models exist for the estimation of the settling velocity.

Reynolds number regime	Flow regime	Flow form	Flow characteristic
$Re < 1$	Creeping flow		Steady, no wake
$3-4 < Re < 30-40$	Vortex pairs in wake		Steady, symmetric separation
$\begin{matrix}30\\40\end{matrix} < Re < \begin{matrix}80\\90\end{matrix}$	Onset of Karman vortex street	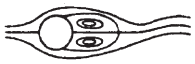	Laminar, unstable wake
$\begin{matrix}80\\90\end{matrix} < Re < \begin{matrix}150\\300\end{matrix}$	Pure Karman vortex street		Karman vortex street
$\begin{matrix}150\\300\end{matrix} < Re < \begin{matrix}10^5\\1.3\cdot10^5\end{matrix}$	Subcritical regime		Laminar, with vortex street instabilities
$\begin{matrix}10^5\\1.3\cdot10^5\end{matrix} < Re < 3.5\cdot10^6$	Critical regime	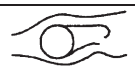	Laminar separation Turbulent reattachment Turbulent separation Turbulent wake
$3.5\cdot10^6 < Re$	Supercritical regime (transcritical)		Turbulent separation

Figure 5.1: Flow regimes around a cylinder at different Re_p-regimes (adopted after Schlichting et al., 2006)

The settling velocity of a single particle is determined mainly by the particle diameter, the fluid and particle density as well as the fluid viscosity. For natural sediments, further the effect of irregular shapes or sharp edges need to be taken into account. To reach the final settling velocity, a particle needs a specific time or distance. According to Meng (2004), this acceleration time t_s and acceleration distance l_s can be estimated by Equation 5.1 and Equation 5.2.

$$t_s = \frac{\operatorname{arccosh}\left(1/\sqrt{0.05}\right)}{\sqrt{\frac{c_D \rho_f A_c g(\rho_p - \rho_f)}{2 V_p \rho_p^2}}} \tag{5.1}$$

$$l_s = \frac{2 V_p \rho_p}{c_D \rho_f A_c} \ln\cosh\left(\sqrt{\frac{c_D \rho_f A_c g(\rho_p - \rho_f)}{2 V_p \rho_p^2}}\, t_s\right) \tag{5.2}$$

The required acceleration distance for different particle diameters, according to Equation 5.2 is shown in Figure 5.2. Thereby, the settling velocity approach of Zanke (1977) is

applied, which is going to be presented amongst others in the following. It can be seen, that till a particle diameter of 2.79 mm the acceleration distance increases exponentially, while at higher particle diameters the acceleration distance increases linearly. This is due to the influence of the drag coefficient c_D. At a particle diameter of 2.79 mm the particle Reynolds number exceeds a value of 1000 and, thus, reaches the Newton region in Figure 2.2. In this region, the drag coefficient no longer increases, but remains as a constant value.

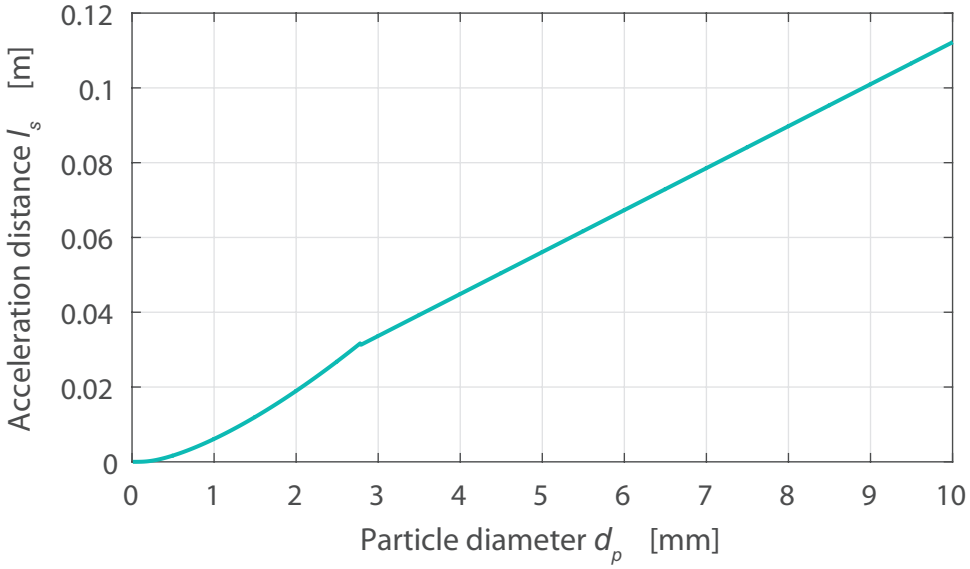

Figure 5.2: Acceleration distance l_s of a settling sphere, before the constant settling velocity v_s is reached

The determination of the settling velocity for a free falling particle can be derived from the equation of Basset–Boussinesq–Oseen (BBO-equation). A particle, which has reached its settling velocity, is falling under stationary conditions: $\frac{\partial v_p}{\partial t} = \frac{\partial v_f}{\partial t} = 0$. This condition reduces the BBO equation significantly and the settling velocity can be derived to

$$v_s = \left(\frac{4}{3} \frac{\rho_p - \rho_f}{\rho_f} \frac{g d_p}{c_D} \right)^{0.5} \quad . \tag{5.3}$$

In this equation, the drag coefficient remains as the only unknown parameter. However, the drag coefficient is based amongst others on the particle Reynolds number and can be estimated by experiments. Other solutions for different Reynolds number regimes are presented following.

The first analytical investigation on the estimation of the settling velocity has been done by Stokes (1851). Stokes (1851) analysed the Navier-Stokes equation for laminar flow conditions with $\mathrm{Re}_p < 1$. At this range, the inertia terms of the Navier-Stokes equation can be neglected. Stokes (1851) derived the drag coefficient in this region to $c_D = {}^{24}/_{\mathrm{Re}_p}$.

Consequently, the settling velocity of a sphere at low particle Reynolds numbers is defined to

$$v_s = \frac{g}{18\nu_f}\frac{\rho_p - \rho_f}{\rho_f} d_p^2 \quad . \tag{5.4}$$

Several investigations exceeded this approach to higher particle Reynolds numbers (see Dey, 2014; Malcherek, 2007b). For the settling velocity of a sphere, Gibbs et al. (1971) gives Equation 5.5 as a universal solution for finite particle Reynolds numbers.

$$v_s = \frac{\left(9\nu_f^2 + g d_p^2 \frac{\rho_p - \rho_f}{\rho_f}(3.869 \cdot 10^{-3} + 0.024801 d_p)\right)^{0.5} - 3\nu_f}{0.011607 + 0.074405 d_p} \tag{5.5}$$

A mathematically simpler universal solution for the settling velocity of spheres for lower and higher Reynolds numbers is given by Zanke (1977) to

$$v_s = \frac{30\nu_f}{d_p}\left(\sqrt{1 + (0.155 D^*)^3} - 1\right) \quad . \tag{5.6}$$

Whereby, D^* represents the dimensionless particle diameter. Figure 5.3 presents different approaches for the settling velocity in comparison. The approaches of Stokes (1851), Gibbs et al. (1971) and Zanke (1977) are very similar for low particle diameters. At higher particle diameters, the approach of Stokes (1851) gives too high results for the settling velocity, since it is based on the viscous resistance only and neglects the effect of inertia. The approach of Gibbs et al. (1971) lies in between the solutions of Stokes (1851) and Zanke (1977) for higher particle diameters.

As already mentioned before, the estimation of the settling velocity for natural sediments is more complex. According to Dey, 2014, an accurate estimation for sediment particles is rather far from being resolved. However, Soulsby (1997) provided an approach for the settling velocity of natural sand particles to

$$v_s = \frac{\nu_f}{d_p}\left[(10.36^2 + 1.049 D^{*3})^{0.5} - 10.36\right] \quad . \tag{5.7}$$

A more complex formulation for the settling velocity of natural sediment is given by Dietrich (1982) in Equation 5.8. Thereby, Dietrich (1982) introduces additional parameters to include the effects of irregular particle shapes. The parameter R_1 describes the influence of the particle diameter as well as the particle density. The parameter R_2 includes the effect of a shape irregularity. Therefore, the Corey shape factor (CSF) is respected in the formulation. The factor describes the ratio between the length of the shortest axis a and the longest axis b of the particle with the axis of a medium length c to $CSF = {}^{c}/\sqrt{ab}$. For a perfectly spherical particle, the Corey shape factor and, thus, the factor R_2 becomes $CSF = R_2 = 1$. Besides an irregular shape, a natural sediment particle is characterised by its angularity. This influence is respected in parameter R_3. Thereby, the parameter P describes the angularity according to Powers (1953), which is defined for spheres with a

value of 6 and with lower values for more angular shapes.

$$
\begin{aligned}
v_s &= \left(\frac{\rho_p - \rho_f}{\rho_f} g \nu_f R_2 R_3 10^{R_1}\right)^{1/3} \qquad (5.8)\\
\text{with} \quad R_1 &= -3.76715 + 5.78832 \lg D^* - 0.88335 (\lg D^*)^2 - 0.15525 (\lg D^*)^3 \\
&\quad +0.04536 (\lg D^*)^4 \\
R_2 &= 1 - \frac{1 - CSF}{0.85} \\
R_3 &= \left[0.65 - \left(\frac{CSF}{2.83} \tanh(3 \lg D^* - 4.6)\right)\right]^{1+(3.5-P)/2.5}
\end{aligned}
$$

Figure 5.3 shows all the previously presented approaches for the settling velocity. The geometrical parameters for the approach Dietrich (1982) for natural sediments have been adopted to the characteristics of a sphere. It can be seen, that at low particle diameters all approaches give identical values for the settling velocity. At a particle diameter of approximately 0.1 mm the graphs representing the approaches of Zanke (1977), Soulsby (1997) and Dietrich (1982) show a flatter course and, thus, a reduced gradient. Thereby, the results are very similar. As discussed previously, the approach of Stokes (1851) and Gibbs et al. (1971) overestimate the settling velocity in this region.

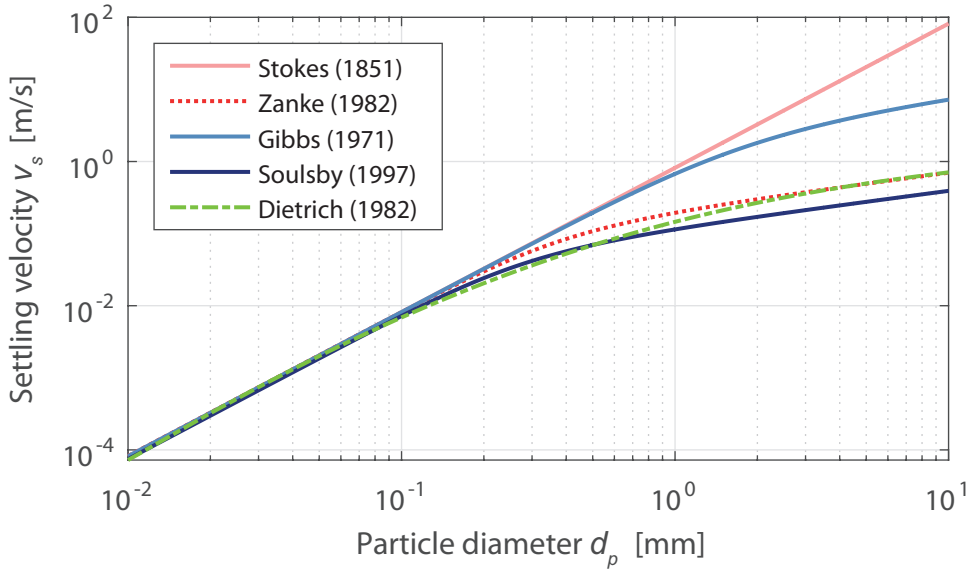

Figure 5.3: Final settling velocity for different particle diameter for various theoretical approaches

5.2 Development of numerical model

The numerical model for the simulation of sedimentation consists of a cylindrical fluid domain which is build with the CFD code. The domain is completely filled with fluid.

Single particles of different diameters are placed in the upper region of the fluid domain, to generate the initial condition of the later simulation.

5.2.1 Spatial discretisation

The sedimentation process of the particles take place along the rotational axis of the cylinder. To ensure a regularly structured meshing in this region of interest (ROI), the cylinder consists of an inner block-structured mesh, which provides perfectly cubic cells. An outer region is attached to the inner block, which is build by four skewed arcs. In this regions, the cubic cells deform to a curved shape and close in the circular cross section of the cylinder (see Figure 5.4). The system of coordinates in the numerical model is defined due to the z-axis, which is positioned along the rotational axis of the cylinder, while the plane of the x- and y-axis are positioned at the bottom of the cylinder. Thus, the x- and y-axis build the circular base area. The gravitational acceleration is defined into negative z-direction.

The spatial dimensions of the block-structured inner and curved outer mesh of the cylinder are coupled to the size of the investigated particle. The inner block-structured mesh has a length and width of 20 times the particle diameter. The total cylinder radius is given to 30 times the particle diameter.

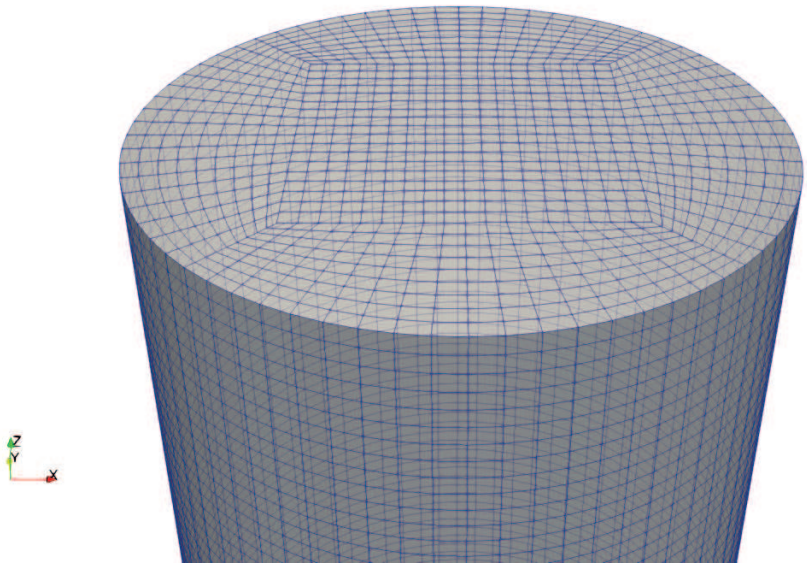

Figure 5.4: Top of the cylindrical mesh representing the fluid domain for the fine mesh configuration with $V_{cell}/V_p = 3$

In the simulation, the ratio between the particle diameter and the cell size of the inner block is varied to investigate the influence of mesh refinement. This is done by the ratio between the particle and the cell volume, which is applied to $V_{cell}/V_p = 3$, 15 and 30. With the assumption of a cubical cell shape, the cell length and the corresponding discretisation

of the inner block is derived. The properties of the final mesh are given in Table 5.1, based on a particle diameter of 3 mm.

Table 5.1: Mesh specification at different volume ratio configurations for the 3 mm particle diameter

Diameter d_p	Volume ratio ROI V_{cell}/V_p	Cell length ROI l_{cell}	Cells per side inner block	Total cells model
3 mm	3	3.49 mm	18	138996
3 mm	15	5.96 mm	10	24900
3 mm	30	7.51 mm	8	12672

5.2.2 Parametrisation fluid phase

The fluid phase is represented by water. Therefore, the viscous shear behaviour is characterised by a Newtonian approach with a fluid viscosity of $1.0 \cdot 10^{-6}$ m^2/s. The fluid density if given to 1000 kg/m^3 (see Table 5.2).

Table 5.2: Fluid properties

Property	Unit	Value
Density ρ_f	kg/m^3	1000
Viscosity ν_f	m^2/s	$1.0 \cdot 10^{-6}$

The boundaries of the fluid phase are differentiated into three regions: the cylinder lid, the cylinder bottom and the curved cylinder walls. While the latter two are assumed to be impermeable, the fluid can enter and exit via the cylinder lid. The boundary conditions for the fluid velocity v_f are defined to a no-slip condition at the walls, while the boundary faces at the cylinder lid are defined by the cell-centre value. The dynamic pressure p is defined by a total pressure condition of $p = 0$ at the cylinder lid. Thus, the whole fluid domain has a dynamic pressure of $p = 0$ at initial state.

Since, the sedimentation process is simulated with the unresolved CFD-DEM, the resolution of the spatial discretisation is not fine enough to resolve the wake turbulences. However, a turbulence model is not able to capture the detailed turbulences. Thus, the turbulence is not modelled in the simulation. A dummy turbulence model is applied, which sets the turbulent viscosity to zero at the RANS equations. The comparison of simulations without turbulence modelling and with turbulence modelling based on a k-ϵ model resulted in almost identical sinking velocities.

5.2.3 Parametrisation particle phase

In the DEM simulation, the Hertz-model is chosen as particle contact model. The basic Hertz-model is extended by models respecting tangential damping forces and rolling resistance. For all these three models, a parameter set of material properties is required. The particles consist of a soda-lime glass, which density ρ_p is given to 2500 N/mm^2 by the manufacturer. Further, laboratory tests are conducted at the Department of Geotechnical Engineering and Construction management (GBT) and the Institute of Solids Process Engineering and Particle Technology (SPE) of Hamburg University of Technology to provide the remaining required properties. The tests, which have been conducted at the SPE, were part of the research project „Multiskalenmodellierung physikalischer Prozesse an der Grenzfläche Wasser/Boden“ founded by the German research founding organisation (DFG) (see Kanitz et al., 2018). In the laboratory tests, particles with a diameter of 3 mm and 1-1.3 mm are tested.

The Young's modulus E of the particles were determined by a texture analyser at SPE. At a test, a single particle is placed between two steel plates and loaded until failure. Thereby, the particle strain and the corresponding stress are measured. By the analysis of the resulting stress-strain curve, the stress and breaking behaviour of the particle can be characterised. According to Antonyuk (2006), the stress-strain behaviour of a granular particle can be differentiated into four regions. In the first region, the first contact between the steel plates and the particle leads to a instant increase of strain due to micro-plastic creeping. This region is followed by a region, which is dominated by elastic deformation. In the third region, the stress behaviour is characterised by a irreversible plastic deformation due to creeping. The results of the texture analyser show in this region a perfectly plastic deformation for the glass particles, which is given by linear course of the strain-stress curve. In this region, the Youngs modulus is determined to $E = 2149.4$ N/mm^2 for the 3 mm particles and $E = 2319.7$ N/mm^2 for the 1-1.3 mm particles.

Further, the coefficient of restitution e was determined at the SPE. Therefore, drop tests are conducted by a collision tester. During a test, solid particles are impacting on a dry surface under different angles. Since, the coefficient of restitution is characterised by the loss of kinetic energy in consequence of the impact, it can be determined by the ratio of the relative velocities before and after the impact. Therefore, the particle velocities are measured during the laboratory tests. The glass particles show a very elastic behaviour in the tests. Thus, the coefficient of restitution was determined to $e = 0.98$ for the 3 mm particles and to $e = 0.84$ for the 1-1.3 mm particles.

The coefficient of friction μ_s of the glass particles has been determined in geotechnical triaxial shear tests. Therefore, a monodiperse sample was tested under drained condition in a CD test (see Figure 5.5). For the 3 mm particles an effective friction angle of $\varphi' = 25.5°$ was determined, while the effective friction angle for the 1-1.3 mm particles was defined to $\varphi' = 22.7°$. With the assumption of $\mu_s = \tan\varphi'$, the coefficient of friction can be calculated to $\mu_s = 0.48$ for the 3 mm particles and $\mu_s = 0.42$ for the 1-1.3 mm particles.

Besides the laboratory test, the coefficient of rolling resistance and the Poisson number are based on assumptions and experiences. It is known, that a sphere moving on a horizontal plate with an initial translational velocity will gradually loss its kinetic energy and finally

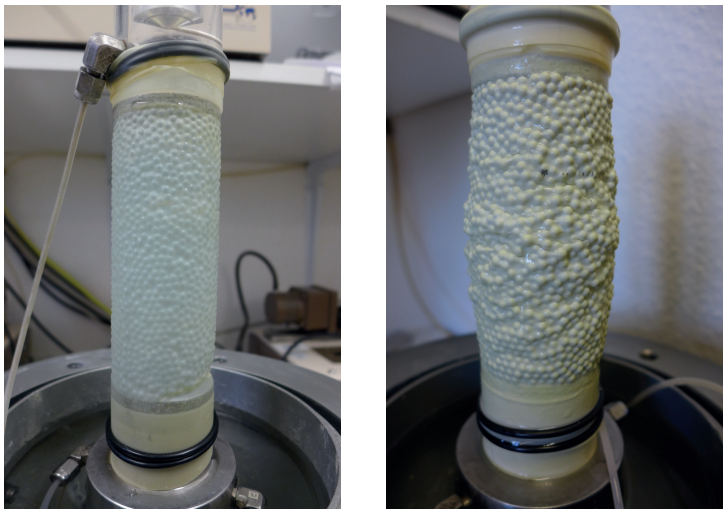

Figure 5.5: Monodisperse material sample with 3 mm particles in the triaxial shear test - Initial condition and final condition after failure

stop after travelling a certain distance because of the resistance from its interaction with the plate. According to Ai et al. (2011), the coefficient of rolling resistance can be estimated based on this principle by an angle of rolling resistance to $\mu_r = \tan \varphi_r$. Thereby, φ_r is defined as the angle of a slope on which the rolling resistance torque on a particle is equal to the driving force of gravity. The glass particles have a sphericity of 0.98, which represents a very round particle shape. Thus, the angle of rolling resistance is assumed to be very small. For the simulation, the coefficient of rolling resistance is assumed to 0.005, which represents a corresponding angle of $\varphi_r = 0.29°$. Further, the Poisson number ν_p is assumed to a value of 0.3. This value is applied in Zhao et al. (2013) and Z. Y. Zhou et al. (2011) for the simulation of sand particles.

A summary of the particle properties are provided in Table 5.3. More details on the experimental determination of granular particle properties are given in Antonyuk (2006) and Crowe et al. (2012).

Table 5.3: Particle properties for the 3 mm and 1-1.3 mm glass particles

Property	Unit	3 mm	1-1.3 mm
Density ρ_p	kg/m^3	2500	2500
Youngs modulus E	N/mm^2	2149.4	2319.7
Coeff. restitution e	-	0.98	0.84
Poisson number ν_p	-	0.3	0.3
Coeff. friction μ_s	-	0.48	0.42
Coeff. rolling friction μ_r	-	0.005	0.005

The boundaries for the particle phase are assumed as rigid walls corresponding to the surface shell of the fluid domain in Section 5.2.1.

5.2.4 Coupling properties

The DEM timestep of the simulations is given to 10^{-5} s. The coupling interval between the fluid and the particle phase is established to every 50 DEM timesteps. Thus, the CFD timestep is defined to $5 \cdot 10^{-4}$ s.

The divided voidfraction model is applied in the simulation. Thus, the particle volume is divided into equally regions and the particle volume in a cell is determined by the fractional volumes centroids. The averaging model of the single sphere simulations is defined by the dilute condition. Thus, the particle velocity inside a CFD-cell is evaluated from a single particle. The fluid-particle interaction forces are limited to the drag force. Thereby, different drag models are investigated, such as the approach of Di Felice (1994), Gidaspow (1994) and Koch and Hill (2001).

5.3 Numerical Simulation of the Sedimentation of a Single Particle

The numerical simulation of the sedimentation process of a single sphere should give an insight into the modelling of the fluid-particle interaction by the numerical approach of coupled CFD-DEM. Therefore, different drag force models are applied and their effect on the settling procedure or rather the fluid-particle interaction is investigated. Beforehand, a sensitivity study on the numerical approach is conducted, to investigate the sensitivity of the results regarding the spatial discretisation and the ratio of cell size to particle diameter, the initial positioning of the particle and the application of smoothing models. A validation of the numerical model is enabled by the analytical approaches presented in Section 5.1.

5.3.1 Sensitivity study

In the sensitivity study, model effects are investigated. To analyse the effect of the spatial discretisations, different ratios of cell to particle volume are applied in the model. Further, the initial position (IP) of the free particle relative to the mesh cells is varied in two variations. In the first variation, the particle is positioned directly in the origin of the x and y axis at the cylinder top at $z = 0.45$ cm. Thereby, the particle volume is equally divided over four cells (see Figure 5.6 left). In the second variation, the particle is placed in the centre of a cell and, thus, fully enclosed by the cell (see Figure 5.6 right). The distribution of the particle-volume over one or more cells has direct influence on the calculation of the voidfraction and, thus, on the calculation of the interaction-force exchange field. Especially, in the case of a similar volume of the cell and the particle, the IP is expected to have a huge significant impact on the simulation results. For this reason, the effect of a

smoothing model is investigated for variations of the V_{cell}/V_p ratios as wells as the initial particle position. Thereby, the effect of smoothing for bigger V_{cell}/V_p ratios is expected to be minimal.

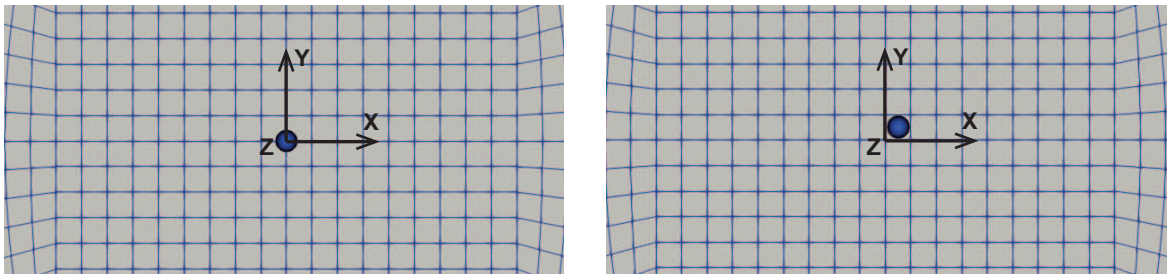

Figure 5.6: Top view on xy-plane with the different initial positions at the origin (left) and centre (right) of the settling particle for the mesh configuration $V_{\text{cell}}/V_p = 3$

In the sensitivity study, particle diameters of 1 mm and 3 mm are applied. For all simulations of the sensitivity study, the Koch and Hill (2001) drag model is applied. Further, all simulations are parallelised by 10 processors. Thereby, the simulation domain is subdivided over the z-axis into 10 equally sized regions.

The simulations of the sensitivity study show identical sequences. From the start of the simulation, the particle accelerates into negative z-direction. During the simulation, the particle accelerates due to gravitational forces. The drag force acts opposed to this acceleration. The drag resistance increases with increasing particle velocity, till the settling velocity is reached. During the settling process, the particle does not deviate significantly from its position in x and y. Neither significant rotational particle velocities develop during the settling process. However, the interaction between the fluid at rest and the particle lead to an acceleration of the fluid. Thereby, the settling of the particle results in a trace of accelerated fluid along the particle path. With increasing distance from the particle, the fluid velocity in the trace decreases. Besides the fluid velocity, the dynamic pressure of the fluid is affected in the immediate vicinity of the particle. In accordance to the theory (see Section 5.1), the dynamics pressure is increased on the luv-side of the particle, while the lee-sided region of the wake shows a decrease of the fluid pressure. After a few centimetres of falling distance, the particle reaches its settling velocity. At this point, the velocity as well as the drag force remains constant. However, some simulations show deviations in the results for the settling velocity consistency.

A compilation of the resulting sinking velocities in the sensitivity study are presented in Table 5.4. In the following paragraphs, the individual influences of the conducted variations are discussed in detail.

Effect of positioning

The results in Table 5.4 show a clear effect of the initial position of the particle. This is especially significant for the mesh with a low volume ratio. Independent from the particle diameter, the simulations show a huge deviation between the sinking velocity for the IP at the origin and the IP at the cell centre. At the small V_{cell}/V_p ratio, the simulation results

Table 5.4: Results of sensitivity study

V_{cell}/V_p	Position	Smoothing	v_s [m/s] for $d_p = 1$ mm	v_s [m/s] for $d_p = 3$ mm
3	origin	no	0.1626	0.3041
3	centre	no	0.1808	0.3493
3	origin	yes	0.1623	0.2977
3	centre	yes	0.1623	0.2984
15	origin	no	0.1627	0.2994
15	centre	no	0.1668	0.3100
15	origin	yes	0.1626	0.2975
15	centre	yes	0.1627	0.2984
30	origin	no	0.1627	0.2985
30	centre	no	0.1652	0.3050
30	origin	yes	0.1626	0.2974
30	centre	yes	0.1628	0.2983

for the particle diameter $d_p = 1$ mm in a sinking velocity of 0.1626 m/s for the IP at the origin, while for the IP at the cell centre a sinking velocity of 0.1808 m/s is reached. For the particle diameter $d_p = 3$ mm, the deviation is even greater with a sinking velocity of 0.3041 m/s for the IP at the origin and 0.3493 m/s at the IP at the cell centre.

Figure 5.7 shows the z-component of the particle velocity $v_{p,z}$ as a function of the height z for the different refined meshes. It can be seen, that the sinking velocities are higher for the IP at the cell centre. Thereby, the deviations between the different IP are higher for the mesh with lower volume ratio, while at higher V_{cell}/V_p the effect becomes less significant. Further, the stability of the solution varies with the IP. While the simulations with an IP at the origin lead to a constant sinking velocity, the simulation with the IP at the cell centre show a fluctuation of the sinking velocity. Once again, this effect is greater for meshes with lower volume ratio. The numerical solution seems to be less stable for the IP at the cell centre.

The simulations with a particle diameter $d_p = 3$ mm show several inconsistencies in the calculation of the sinking velocity for the IP at the cell centre. Thereby, it is peculiarly that for all meshes some inconsistencies relate to a regular pattern which is arranged in 5 cm sections. This can be explained, by the parallelisation of the simulation runs in which the model volume is divided in z-direction. Every 5 cm the particle needs to cross the boundary of two processors. The applied voidfraction model based on divided volumes, is not defined over processor boundaries. Thus, the voidfraction of the cell in the previous processor region decreases, till the particle moves over the boundary. This decrease in

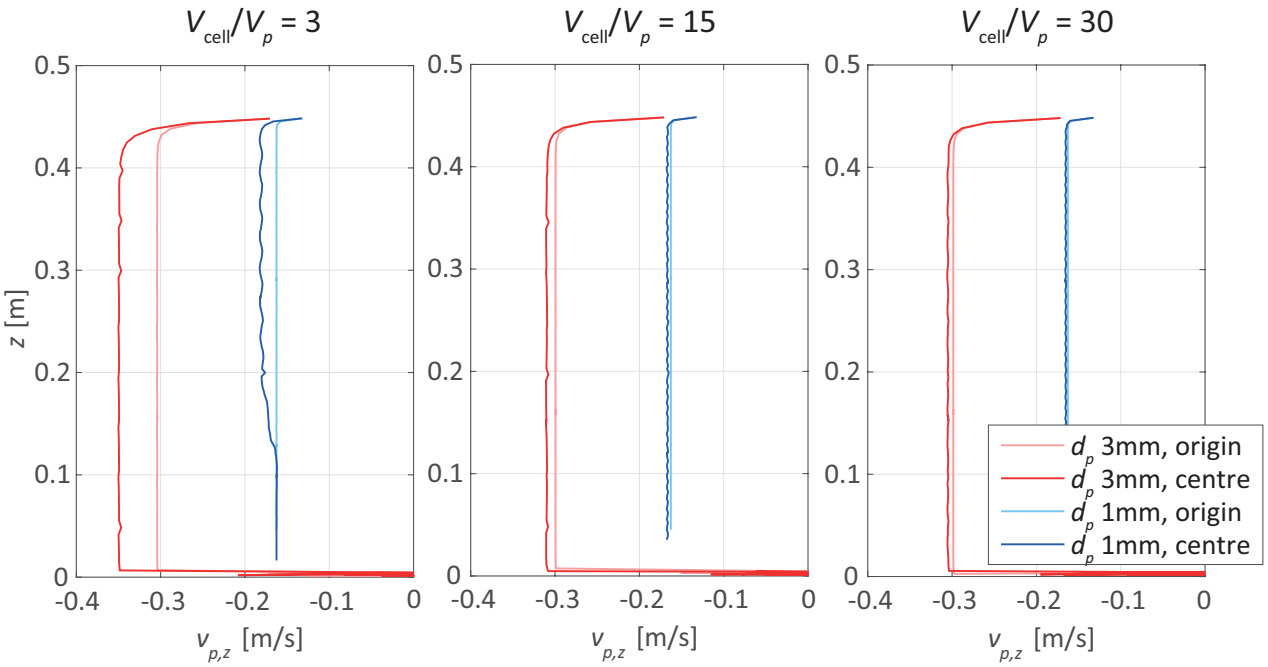

Figure 5.7: Results for the variation of the initial particle position for $d_p = 1$ mm and $d_p = 3$ mm at different mesh configurations

voidfraction induces a momentary decrease in the sinking velocity. With ongoing particle movement, the solution stabilises again as soon as the particle volume is fully positioned in the new processor region. In the case of the already divided IP at the origin this effect is minimal and not recognisable in the results. Opposed to this behaviour, the inconsistencies for the simulation with a particle diameter of $d_p = 1$ mm show a fluctuation of the solution. The curve fluctuates constant around an average value. Thereby, the fluctuations cannot be associated with influences from the processor boundaries. It seems the whole numerical solution is in-stable in this simulations. Again, the fluctuations are greater for the mesh with a small volume ratio, while this effect is damped for higher volume ratios.

Besides the deviation of the sinking velocity, the trace of accelerated fluid behind the particle shows clearly different shapes for the individual initial positions. Figure 5.8 presents the y-normal cross section of the cylinder for the mesh with the volume ratio $V_{\text{cell}}/V_p = 3$. For better presentation the cylinder cross section is turned clockwise by 90°. The trace of accelerated fluid behind the particle with the IP at the cell centre shows an uniform shape and development. Thereby, the maximum fluid velocities are concentrated in the cells the particle passed. Further, the maximum fluid velocity is not in the ultimate vicinity of the particle, but approximately 1 cm behind. In contrast, the trace of the particle with the IP at the origin shows less concentrated fluid velocities. The trace behind the particle is not of an uniform shape, but rather shows a lurching detachment of the fluid. Further investigations showed, that this pattern is related to the drag force calculation. In the drag force model, an interpolation scheme is activated. Thereby, the data from the CFD domain is interpolated to obtain the fluid velocity at the position of the particle centre be-

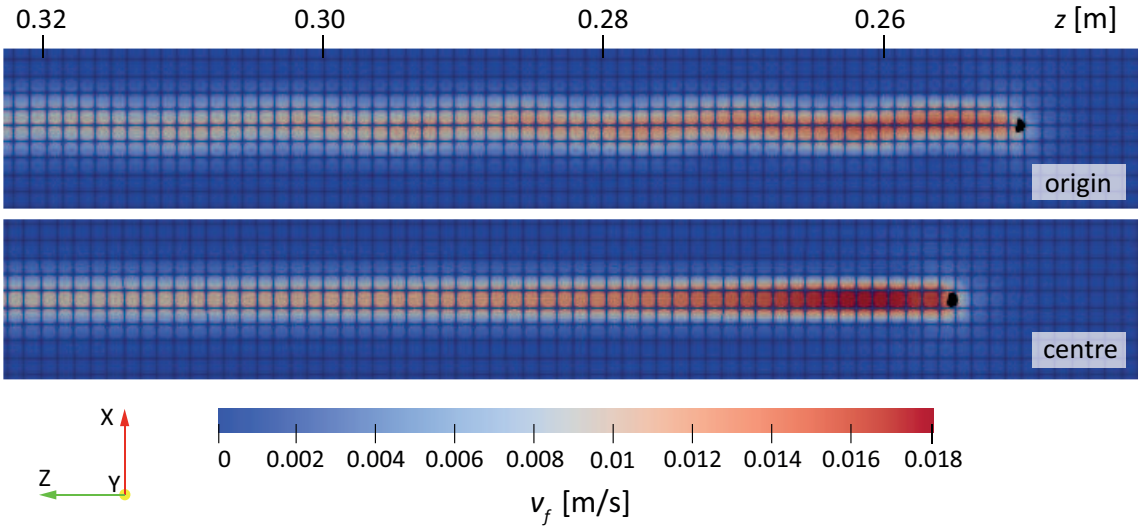

Figure 5.8: Representation of the settling process by the fluid velocity paths at different initial positions for a particle with $d_p = 1$ mm at a mesh with $V_{\text{cell}}/V_p = 3$ (orientation is rotated by 90° counter-clockwise)

fore it is passed to the CFDEM interaction force calculation. Without this interpolation, the transferred CFD data is based on the informations of the CFD-cell centre. However, due to its definition the interpolation scheme is applied only in the cell which contains the particle centre. Due to numerical purposes, the particle centre is besides the IP not exactly located in the xy-origin. Rather, the particle centre circles with minimal displacements over the four cells positioned around the origin. As a consequence, the interpolation scheme is applied in varying cells. Due to the interpolation, the exchanged fluid velocity between the CFD and the force model algorithm, is higher than the non-interpolated data at the cell centre. Thus, the particle receives an asymmetric force distribution in the x- or y- direction. However, the asymmetric drag forces in the xy-plane lead to an asymmetric detachment of the fluid along the particle sedimentation path. As a consequence, the fluid trace experiences this oscillating pattern. This effect is not eliminated by different volume ratios. The development of an oscillating pattern occurs for all levels of mesh refinement. The simulations for the IP at the cell centre show no comparable phenomena.

A cause for the instabilities of the simulation results with an IP at the cell centre can be found in the calculation of the drag force. Figure 5.9 presents the z-component of the drag force $F_{D,z}$ as a function of the particle height z at different volume ratios V_{cell}/V_p for $d_p = 1$ mm. The drag force is calculated identically to $1.284{\cdot}10^{-5}$ N for the simulations with the IP at the origin, independent of the volume ratio. This value stays constant, after the particle reached its sinking velocity. This proves a high stability of the numerical solution over the different volume ratios. In contrast, the results of the drag force for the IP at the cell centre. For all volume ratios, the function shows an oscillation of the drag force. Thereby, the peak amplitude of the oscillation is lower for the meshes with higher volume ratio. The oscillation of the drag force leads to a fluctuation of the sinking velocity (see Figure 5.7). This fluctuation in the sinking velocity, explains the displacement of the

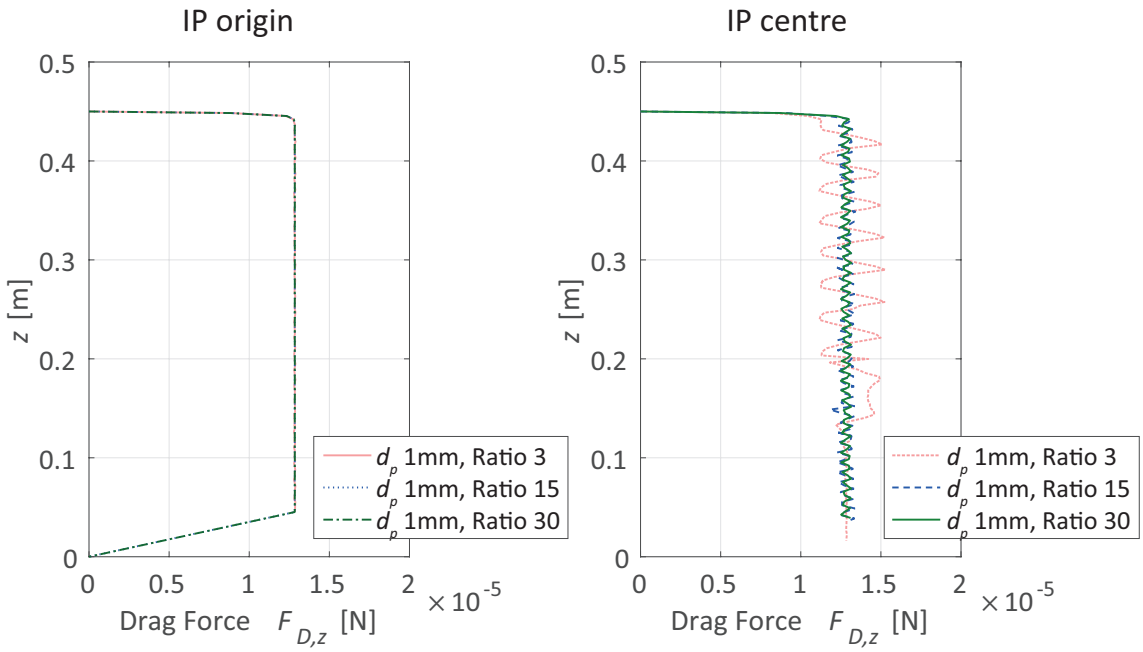

Figure 5.9: Drag force as a function of the particle height z for the IP at the origin (left) and the cell centre (right) for different V_{cell}/V_p with $d_p = 1$ mm

maximum fluid velocity field in the particle trace shown in Figure 5.8. In the presented position, the particle is in a phase of increasing drag force and, thus, its sinking velocity decelerates. However, the significant fluctuation is limited to the simulation with a particle diameter of $d_p = 1$ mm. The simulations of $d_p = 3$ mm do not show any oscillation, but indeed deviations in the solution of the sinking velocity. In all cases, the sinking velocities for the IP at the cell centre are higher in comparison to the simulation results with the IP at the origin.

The IP at the cell centre lead to less stable numerical results. This fact is related to the fully enclosement of the particle within one cell. This position effectuates huge voidfraction gradients and, thus, all exchange fields between neighbouring cells. The irregularities are caused by the method itself. The code of the resolved CFD-DEM in CFDEM is optimised for the simulation of large numbers of particles. The application on a more dilute problem seems to cause numerical instabilities due to high gradients. However, it is important to have the knowledge about this inconsistencies, but as it could be seen, it is possible to prevent these effects.

Effect of ratio between cell size and particle diameter

The investigations on the particle initial position prove, that the volume ratio is not the main factor for accurate results. However, the spatial discretisation and so the volume ratio between particle and cell volume has indeed an effect on the stability of the simulation. In the simulations with the IP at the cell centre, the application of a higher volume ratio reduces the deviations of the results. A higher volume ratio of a coarser mesh leads to a higher voidfraction whereby the exchange fields have a reduced effect on the

numerical results in the corresponding cell. This effect is equal to a damping of numerical instabilities, by reducing the influence of the particle velocities within a cell. In contrast, the simulations with the IP at the origin show minor effects of the applied refinement of the spatial discretisation on the results (see Figure 5.9), since the distribution of the particle volume over several cells leads to a more stable simulation already.

In general, the spatial discretisation of the fluid domain in CFD-DEM simulations is subjected to certain conditions regarding the convergence of the results. In pure CFD simulations, the solution should converge against the exact value with increasing refinement of the spatial discretisation. However, in coupled CFD-DEM the discretisation of the fluid domain is limited in its refinement by the ratio between the cell size and the particle diameter. Thus, a high mesh resolution with a supposed accurate discretisation can lead to numerical instabilities in the calculation of the exchange fields, if the cell size is chosen too small. As a result, the spatial discretisation of the fluid phase needs to balanced the desired accuracy of the CFD field with the required accuracy for the correct determination of the exchange fields.

Figure 5.10 presents the fluid pressure distribution around the particle during the settling process at different volume ratios. As already discussed, the particle induces a region of higher pressure at the particle luv-side and a region of lower pressure on the lee-side of the particle. The limits of the coloured representation differ for every individual figure at different V_{cell}/V_p. This is due to illustrative purposes, since the limits differ too much for a consistent representation. In all figures, the pressure field in the cells containing the particle as well as the neighbouring cells are affected by the presence of the particle. According to Figure 5.10, the coarser mesh results in a greater radius of affected fluid cells in comparison to the finer meshes. Nonetheless, the fluid pressure in the coarse mesh is significantly smaller than those of the fine mesh. A look on the drag force in the left diagram of Figure 5.9 shows, that all cases give the same interaction force. Hence, the results of the CFD-DEM simulation is consistent for all different meshes although different spatial discretisation are applied. This fact proves the stability of the CFD-DEM method and its results for the IP at the origin.

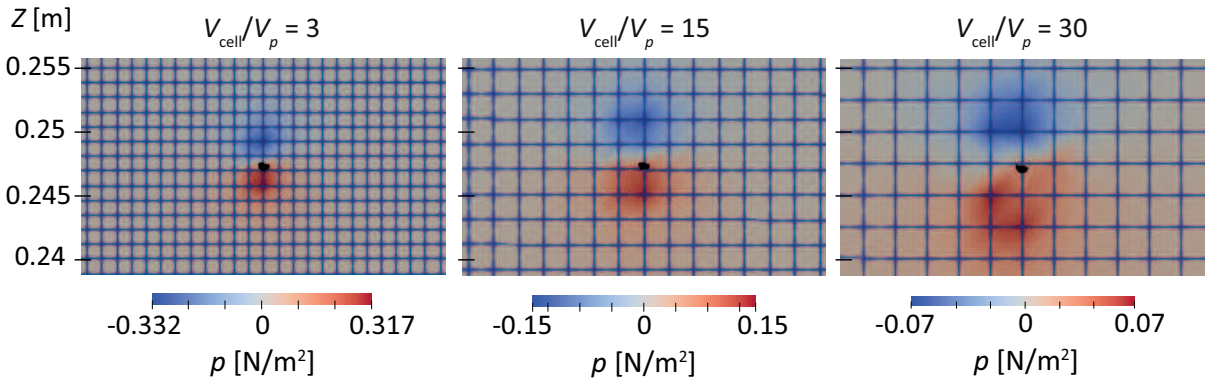

Figure 5.10: Pressure distribution around the sinking particle at different V_{cell}/V_p

Effect of smoothing

To exclude the possibility of significant numerical instabilities, as seen for the initial position at the cell centre, it is possible to include a smoothing model into the coupling routine. This smoothing model is recommended for simulations where the particle size is similar to the cell size and, thus, have a small volume ratio between cell and particle. As described in Section 4.2.5, the smoothing model affects the calculation of the exchange fields. The exchange fields are smeared over a specific distance, the smoothing length. In the simulations of the sensitivity study, the smoothing length is chosen to be three times the particle diameter, as recommended in Radl et al. (2014). The application of a smoothing model should prevent instabilities in the results such as those appeared due to the IP at the cell centre. Since, the position of the particle cannot be controlled for every application of the software, it is important to find a solution to eliminate model instabilities.

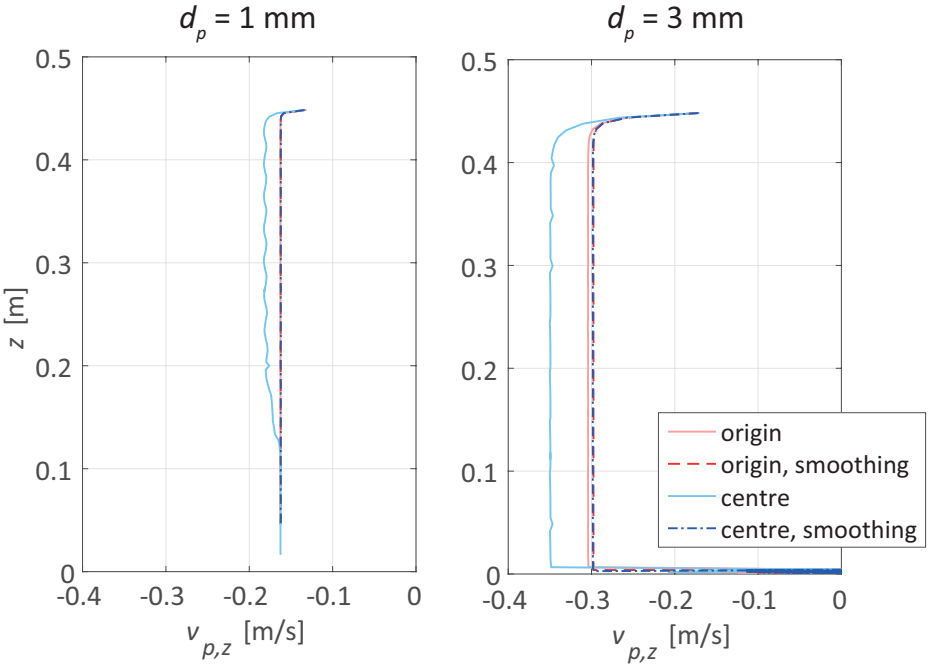

Figure 5.11: Particle velocity $v_{p,z}$ for different initial positions at mesh configuration $V_{\text{cell}}/V_p = 3$ with or without smoothing

Figure 5.11 presents the z-component of the particle velocity as a function of the particle position on the z-axis. The data includes the simulation results for the small volume ratio of $V_{\text{cell}}/V_p = 3$ for both particle diameters and both IP for a variation with and without smoothing. For the IP at the origin, the simulations result in the same sinking velocity for applied smoothing and without smoothing. A minimal deviation can be recognized for the particle diameter of 3 mm with a sinking velocity of 0.304 m/s without smoothing and 0.298 m/s with smoothing (see Section 5.1). However, this difference is so minimal that its in the range of mm per second. Further, a visual analysis of the simulations shows that the same oscillating trace of the sinking particle is present for the case with smoothing and also without smoothing.

In contrast, the results for the IP at the cell centre show greater deviations between the smoothing and the non-smoothing simulations. The simulations including smoothing show a steady sedimentation procedure which results in a constant sinking velocity. Thereby, the sedimentation procedure is identical to the results of the IP at the origin with smoothing. The smoothing model seems to ensure the convergence of the results. The simulations without smoothing give clearly deviating results with higher sinking velocities and show an oscillation of the sinking velocity. The effect of the smoothing on the different IP can be explained by the division of the particle volume. While the IP at the origin guarantees per definition the division of the particle volume over several cells, the IP at the cell centre requires a smoothing model to have a similar effect on the calculation of the exchange fields. The division of the exchange fields over cells and neighbouring cells seems to be an important factor for the accuracy of the simulation.

However, a problem with the momentum exchange coefficient K_{pf} becomes apparent for the simulations including smoothing. Although all other fields on the fluid and the particle side look correct, the K_{pf} field shows an abnormal distribution in the visual treatment of Paraview (see Figure 5.12). Although the smoothing length is chosen to be three times the particle diameter, the by the particle affected cells seem to be arranged in a circle in way greater distance to the particle rather than at the particle and the adjacent neighbouring cells. Also for smaller smoothing lengths the effect is apparent. The reason for this behaviour could not be identified yet. Since this behaviour is not accurate, the smoothing model is excluded in further simulations, to prevent eventual effects on the results.

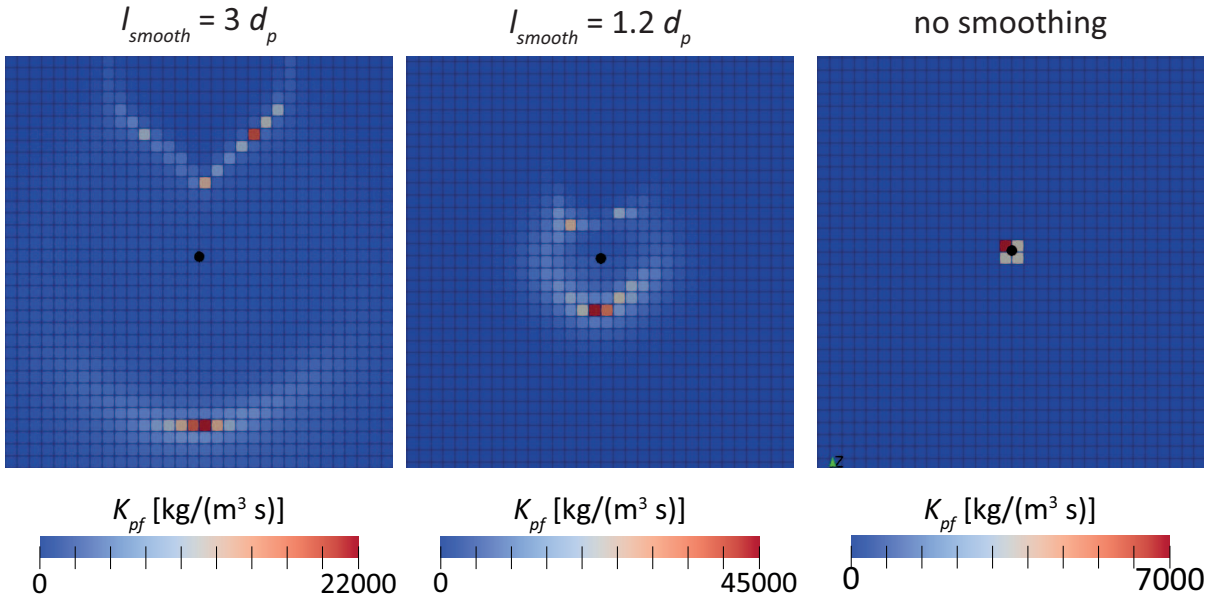

Figure 5.12: Exchange field of momentum exchange K_{pf} around a settling particle for a smoothing length of $l_{\text{smooth}} = 3d_p$ (left), $l_{\text{smooth}} = 1.2d_p$ (middle) and without smoothing (right)

The sensitivity study showed the particular influences due to the particle IP as well as the spatial discretisation with different cell-particle volume ratios. The method showed

irregularities depending on the position of the particle. The code of resolved CFDEM seems to be not stable for very dilute applications, where detailed informations are investigated. The application of a smoothing model, can help to prevent irregularities. However, the application of smoothing results in an abnormal representation of the K_{pf} field. Thus, the application of a smoothing model is not recommended before the cause and eventually effects on the results are identified. The application of a higher volume ratio between the particle and the mesh cells can damp eventual effects which result from the positioning of the particle.

5.3.2 Results of the sedimentation process

The new insights of the sensitivity study are applied for the simulations of sedimentation for different particle diameters. Thus, the particle is positioned initially at the origin of the cylindrical simulation domain. The volume ratio between the particle and the CFD cells is chosen to be $V_{\text{cell}}/V_p = 3$. Further, no smoothing model is applied. The height of the cylinder mesh is adapted for the small particle diameters, since the small particles reach their settling velocity already after a short distance. Thereby, the number of cells is significantly reduced and the calculation speed of the simulation is increased. For $d_p = 0.1$ mm the cylinder height is reduced to 20 cm and for $d_p = 0.5$ mm to 25 cm. The drag model in the simulations are varied, to specify the different effects on the sedimentation process and to validate the results with common analytical approaches from literature. The applied drag force models are based on the approaches of Di Felice (1994), Gidaspow (1994) and Koch & Hill (2001) (see Section 2.2.2).

The results of the simulations are presented in Table 5.5. Therefore, the final sinking velocity and the corresponding drag force are determined. The drag force as well as the sinking velocity are increasing with increasing particle diameter. The variation of the drag force model for constant particle diameter yields very similar results for the drag force. This proves the accessibility of all different drag force models, since they all result in the same final equilibrium at the particle between the drag resistance and the driving force due to gravity. In contrast, the sinking velocities defers for the different drag force models. Thereby, the deviation of the sinking velocity for different force models increases with increasing particle diameter. For the smaller particle diameters of $d_p = 0.1$ mm and $d_p = 0.5$ mm, the Di Felice model results in the smallest sinking velocities, followed by the Koch & Hill model and finally the Gidaspow model with the highest values. This succession changes at $d_p = 1$ mm and stays constant for the higher particle diameters. Thenceforward, the Koch & Hill model gives the lowest sinking velocity, while the Di Felice model results in higher values. However, the greatest values are still given by the Gidaspow drag force model.

Besides the total values for the sinking velocity and the corresponding drag force, the progression of those quantities over the settling process are analysed. The progress of the drag force over the particle position on the z-axis is presented for selected examples in Figure 5.13. As indicated in Table 5.5, the final drag forces corresponding to the settling velocity are very similar for all different drag force models. From the particle diameter $d_p = 1$ mm on, an acceleration phase in the early stages of the settling process are evident.

Table 5.5: Simulation results for different force models and particle diameters

Particle diameter d_p [mm]	Drag model	Dragforce $F_{D,z}$ [N]	Sinking velocity v_s [m/s]	Re_p [-]
0.1	Di Felice	1.2840E-08	0.0118	1.18
0.1	Gidaspow	1.2841E-08	0.0123	1.29
0.1	Koch & Hill	1.2841E-08	0.0123	1.29
0.5	Di Felice	1.6055E-06	0.097	49
0.5	Gidaspow	1.6050E-06	0.104	52
0.5	Koch & Hill	1.6052E-06	0.101	51
1	Di Felice	1.2844E-05	0.184	184
1	Gidaspow	1.2841E-05	0.202	202
1	Koch & Hill	1.2841E-05	0.162	162
2	Di Felice	1.0276E-04	0.310	621
2	Gidaspow	1.0273E-04	0.365	729
2	Koch & Hill	1.0273E-04	0.240	481
3	Di Felice	3.4673E-04	0.407	1222
3	Gidaspow	3.4672E-04	0.508	1523
3	Koch & Hill	3.4671E-04	0.298	893
4	Di Felice	8.2131E-04	0.489	1954
4	Gidaspow	8.2184E-04	0.640	2559
4	Koch & Hill	8.2186E-04	0.345	1381
5	Di Felice	1.6051E-03	0.560	2798
5	Gidaspow	1.6054E-03	0.764	3821
5	Koch & Hill	1.6052E-03	0.387	1935
6	Di Felice	2.7722E-03	0.624	3742
6	Gidaspow	2.7143E-03	0.883	5296
6	Koch & Hill	2.7737E-03	0.425	2548

For smaller particle diameters, the acceleration phase is so short that it is not apparent in the presentation of the analysis in Figure 5.13. The comparison of the drag force process shows, that the final drag force is reached after different settling distances of the particle. The differences are minor for $d_p = 1$ mm, but evident for the higher particle diameters.

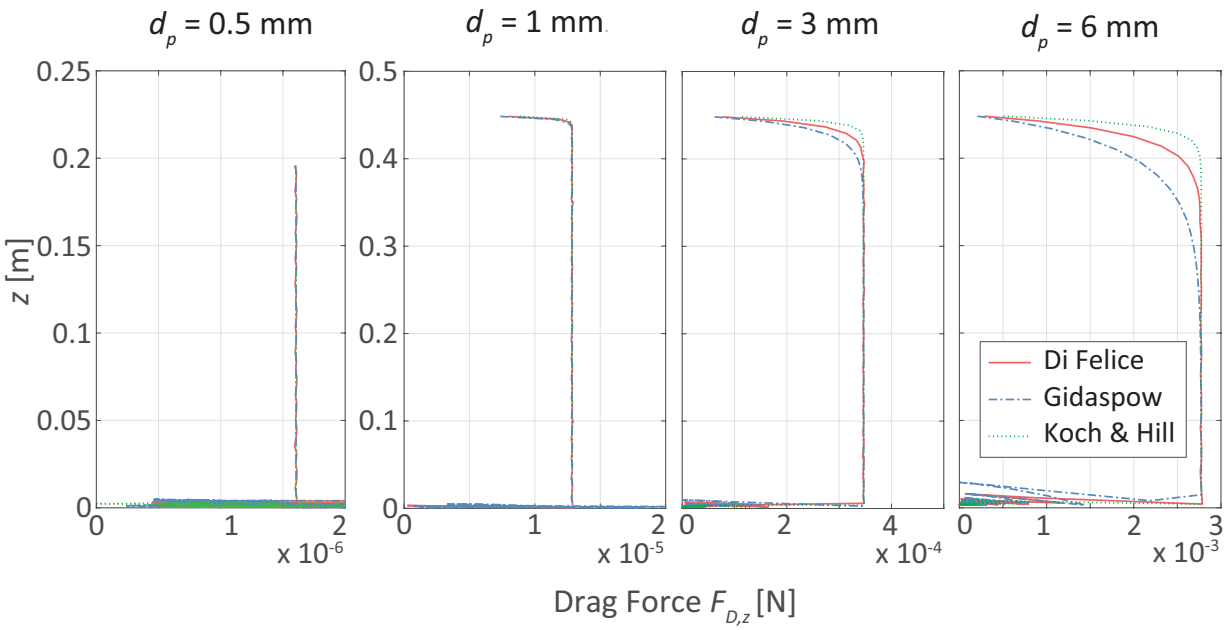

Figure 5.13: Vertical drag force $F_{D,z}$ over the height z for $d_p = 0.5$ mm, $d_p = 1$ mm, $d_p = 3$ mm and $d_p = 6$ mm

The differences in distance are increasing with the particle diameter. Thereby, the simulations with the Koch & Hill model result in the shortest distance, followed by Di Felice and Gidaspow. This behaviour proves, that the acceleration of the particle is calculated differently for the individual drag force models. This behaviour becomes more apparent in the process of the particle velocity over the settling process. Figure 5.14 presents the process of the particle velocity $v_{p,z}$ over the height z of the particle. Thereby, the selected examples correspond to the examples in Figure 5.13. Since, the z-axis is defined against the direction of the gravitational acceleration, the velocity values have a negative sign. The graphs in Figure 5.14 show the same acceleration phase of the particle in the beginning of the settling process. Similar to the progression of the drag force, the particle velocity acceleration takes place over a different distance for the individual drag force models. This becomes especially evident for the highest particle diameter of $d_p = 6$ mm. The Koch & Hill model results in the shortest acceleration distance and, thus, reaches its settling velocity very fast. The Di Felice model results in a greater acceleration distance, while the greatest acceleration distance is present for the Gidaspow model. To compare the simulation results with analytical approaches, the acceleration distance for a spherical particle according to the theory of Meng (2004) (see Equation 5.2) is implemented as a light red background-area in Figure 5.14. The comparison between the analytical approach and the simulation results show, that the Gidaspow model overestimates the acceleration distance significantly. The Di Felice as well as the Koch & Hill model give better results, whereby Di Felice gives a slightly longer acceleration distance and Koch & Hill a slightly smaller acceleration distance.

The acceleration distance and, thus, the particle velocity is related to the calculation of

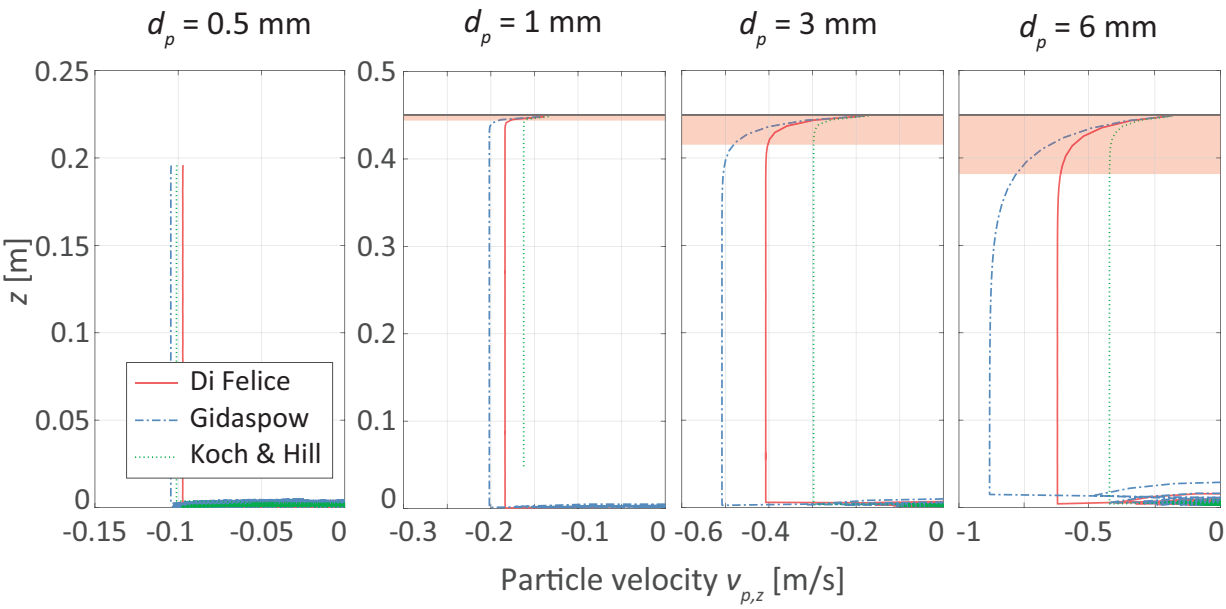

Figure 5.14: Particle velocity $v_{p,z}$ over the particle height z for $d_p = 0.5$ mm, $d_p = 1$ mm, $d_p = 3$ mm and $d_p = 6$ mm

the drag force by the individual drag force models. It is plausible, that a shorter distance to reach the final drag force, results in a higher resistance already at a greater height of the z-axis and thus reduces the acceleration distance of the particle (see Figure 5.13 and Figure 5.14 for $d_p = 6$ mm and the Koch & Hill drag force model). However, although the final drag force is equal for the drag force models, the final settling velocity differs. This behaviour is clarified by the presentation of Figure 5.15. Figure 5.15 shows the progress of the drag force over the corresponding particle velocity for the particle diameter $d_p = 6$ mm. The graphs illustrate, that the development of the particle velocity is very different for the different drag models. The incremental drag force and the particle velocity mutually influence each other and differ for each model. However, for the same particle drag force, the drag force models result in different particle velocities.

For further validation, the final settling velocities are compared to common analytical approaches presented beforehand in Section 5.1. Therefore, the simulation results as well as the analytical approaches are implemented in Figure 5.16. In this graphs, the differences between the sinking velocities for the different drag force models seems less significant. All simulation results are near the course of the analytical approaches for higher Reynolds-numbers of Zanke (1982), Soulsby (1997) and Dietrich (1982). However, the sinking velocity for the smallest particle diameter of $d_p = 0.1$ mm is clearly overestimated in all the numerical simulations. The sinking velocity of the simulations indicate a Reynolds-number around $\mathrm{Re}_p \approx 1$. It seems, all drag force models result in an overestimation of the sinking velocities at the low Reynolds-number regime. For higher particle diameters, the simulations give a better accordance to the analytical approaches. Thereby, the Gidaspow model seems to give slightly too high sinking velocities. This is congruent to the analysis of the acceleration distance. Also regarding the final sinking velocities, the Di Felice as

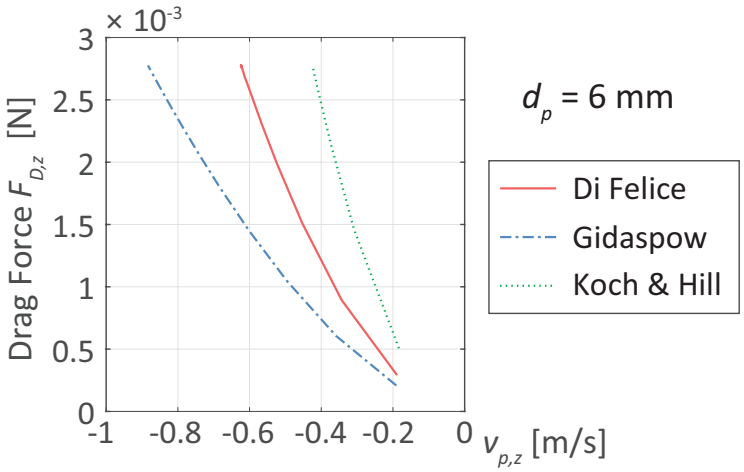

Figure 5.15: Drag force $F_{D,z}$ against the particle velocity $v_{p,z}$ during the sinking process for $d_p = 6$ mm

well as the Koch & Hill model give better results. Thereby, the graphs of Di Felice and Koch & Hill have the highest accordance with the analytical approach of Zanke (1982).

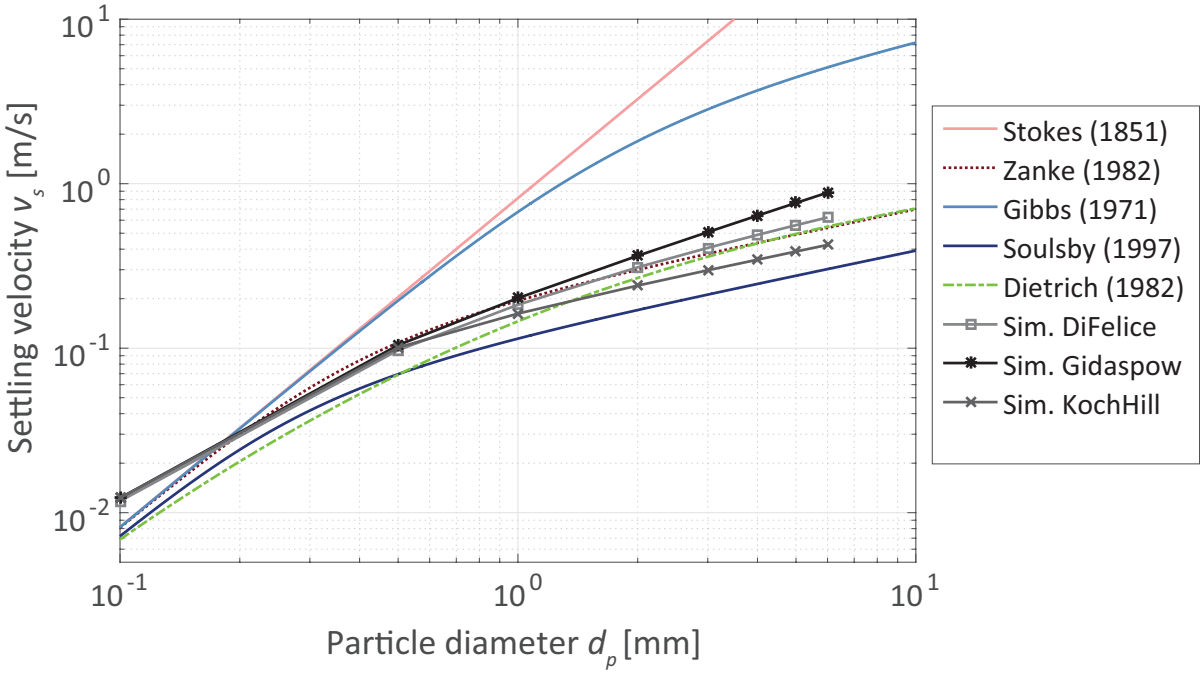

Figure 5.16: Comparison of analytical approaches, simulation and test results for the final settling velocity

5.4 Conclusion

The sedimentation process of a single particle has been successfully reproduced in the numerical simulations with the unresolved CFD-DEM method. Thereby, the final settling velocity as well as the settling process match the results of common analytical approaches. The positive results prove a good reproduction of the fluid-particle interaction by the coupling algorithm and the different drag force models. The best results have been achieved with the drag force models based on the approaches of Di Felice (1994) or Koch & Hill (2001).

However, the sensitivity study shows a high significance of the applied initial conditions and setup of the numerical simulations. Thus, the initial position of the particle represents a major factor for the accuracy of the numerical results. Since the unresolved CFD-DEM coupling is optimized for the simulation of a high number of particles within a CFD cell, the detailed investigation of a single particle represents an extremely limiting case for this method. The investigations on the initial position showed a positive effect on the stability due to the division of the particle volume over several fluid cells. However, the method is able to successfully model the behaviour of a single particle in fluid, but the influence of the initial setup needs to be investigated closely. Besides the initial position of the particle, the spatial discretisation and, thus, the volume ratio between fluid cell and particle represent a significant influence on the simulation results. Thereby, a small ratio give more accurate results but increases the vulnerability of the simulation to numerical errors. Thus, a sensitivity study needs to be conducted before a simulation to identify the optimal fluid cell to particle volume ratio. After the conducted simulations, a volume ratio greater or equal $V_{\text{cell}}/V_p = 3$ is recommended.

With the successful reproduction of the sedimentation process of a single particle with the unresolved CFD-DEM, the method is of interest to investigate sedimentation processes further. The sedimentation process of single particles is of interest for e. g. the dumping of geotextile containers for scour protection measures (see Heins et al., 2015; Plenker et al., 2016b). Further, the detailed sedimentation and fluid-particle interaction process of particle groups can be investigated. The sedimentation of particle groups deviates from the analytical laws for the settling of individual particles. The settling process for a particle group in clear fluid leads to higher settling velocities than obtained for a single particle. This is due to secondary mixing processes between the particles, which reduce the drag resistance against the particle group (Zanke, 1982). This effect has been investigated in several studies (e. g. Meng, 2004, Liang et al., 1996). However, the coupled CFD-DEM gives the opportunity to investigate the detailed mixing processes between groups of different packing density and particle sizes in a non-intrusive way. The fundamental process of settling particle groups is of interest for various applications such as submerged deposition processes, backfilling, sedimentation in flow-reduced areas or oil sand tailing ponds.

6 Investigations of Granular Flows: Collapse of a Particle Column

Granular flow is a phenomenon significant for a large number of natural processes and industrial applications such as debris flows, landslides or transport of granular media. Most of these applications are characterised by a multiphase problem. Within these applications, the solid granular material interacts with the interstitial water. In the case of underwater landslides or littoral sediment transport, the multiphase problem is extended by the interaction between granular material, interstitial as well as surrounding water. These complex interaction and their effects on the granular flow behaviour are not fully understood yet. Although, continuum mechanical approaches are able to capture the overall characteristics of this events, the specific effects at the grain scale are not taken into account. However, to describe the macro-mechanical behaviour of granular flows correctly, it is necessary to understand those micro-mechanical interactions and their effect on the macroscopic characteristics of granular flow events. A better understanding of mechanisms on a grain scale like the slumping process and material transport in the presence of fluid, could lead to better predictions of flow patterns, slumping velocity or deposit thickness of e. g. natural hazards. The CFD-DEM method gives the opportunity, to investigate the fluid-particle and particle-particle interaction, which cannot be obtained easily by experimental evaluations due to highly dynamic processes and the necessity of contactless measurements.

This chapter examines granular flows by the scenario of a collapsing particle column. Thereby, the collapse is investigated under dry as well as submerged conditions. The dry collapse investigation focus on the dry collapse mechanisms, the detailed particle-particle as well as wall-particle interaction and their relation to the specific collapse mechanism of the granular mass. Therefore, physical tests as well as numerical simulations with the pure DEM approach are conducted. The investigations under dry conditions allows the detailed analysis of the particle contact formulation of the DEM model and its influence on the simulation of granular flows. In this context sensitivity studies are conducted to investigate the material parametrisation (see Section 5.2.3) and its influence on the contact formulation as well as the granular flow mechanism. Furthermore, the investigations of dry particle collapse are differentiated into a slow and a fast collapse scenario, which are dominated by different mechanisms. In the slow collapse scenario, the granular flow is based on a high number of fractional slumping events. In contrast, the fast collapse scenario consists of one instantaneous big slumping event of the granular material. The fast collapse is dominated by a highly dynamic behaviour, while the slow collapse is dominated by small shear failure events. With this differentiation, different components of the DEM contact modelling are addressed. The gained knowledge on the dry collapse mechanism

are applied for the investigations on the granular flows under submerged conditions. Thus, the detailed influence due to the presence of a viscous fluid are identified. Similar to the investigations on dry collapse, physical tests as well as numerical simulations are applied for the investigation of the submerged collapse. The numerical simulations of the submerged case are implemented in the coupled CFD-DEM method. This numerical simulations focus on the detailed fluid-particle interaction and its influence on the collapse mechanism of the granular material.

Before the results of the physical tests and numerical simulations are presented and discussed, the following section gives introduces into the theory of dry granular slumping. Therefore, current investigations of other authors on the specific field of granular slumping are presented.

6.1 Fundamentals of Granular Slumping

This section presents the physical complexity of the problem granular slumping. Thereby, actual physical as well as numerical investigations on the problem are presented. While in the previous Chapter 5 the interaction between a single particle with the surrounding fluid was investigated, the behaviour of a particle quantity is discussed in this chapter. Further, the characteristic behaviour and interaction of this particle quantity in fluid is investigated.

The phenomenon of multiphase granular flows appears in numerous disciplines like hydraulic and ocean engineering, geotechnical engineering and process engineering. As a result, granular flow problems are presented in a wide field of research applications. Nevertheless, due to the complex interaction and highly dynamic processes the numerical simulation of multiphase granular flow represents a challenging problem. Thus, a simplified scenario of a multiphase granular flow is assumed. The applied scenario is very well-known as the two dimensional dam break problem (see Figure 6.1). In the classical dam break scenario, the interaction between a liquid and a gas is investigated. This problem has been well studied (Sun et al., 2015). The recommended works of Crosta et al. (2009), Kerswell (2005), Lajeunesse et al. (2005), Lube et al. (2005, 2004), and Rondon et al. (2011) deal with granular material within the dam break problem. However, the numerical investigations of the dam break problem are mostly limited to continuum mechanical representations of the applied materials. The representation of granular material by particles is less applied so far. In recent investigations of X. Li et al. (2016) and Park et al. (2018) a particle-fluid mixture is used for the dam break problem. However, thereby the particle-fluid mixture represents the slumping material in air. As a consequence, research is legging behind in numerical simulations of multiphase granular flows. Hence, basic research and the development of a numerical modelling technique regarding this topic are necessary.

Figure 6.1 shows the initial setup of the considered dam break problem. The material column is inserted on the left side of a basin. Thereby, the material has an initial height h_0 and an initial width of l_0. The characteristics of the slumping progress depend strongly on the initial aspect ratio a ($a = h_0/l_0$) of the installed material sample. According to

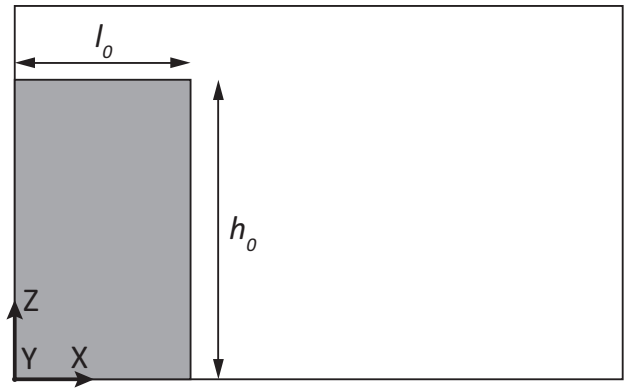

Figure 6.1: Scheme of material sample with given aspect ratio $a = h_0/l_0$ in the dam break scenario

Lajeunesse et al. (2005) and Lube et al. (2005, 2004) the spreading velocity, the final extent of the deposit and the energy dissipation during the slumping can be scaled without an influence of the material properties. However, these quantities depend on the initial aspect ratio a. This assumption is based on numerous experiments, which have been conducted by Lajeunesse et al. (2005) and Lube et al. (2004) under consideration of different granular materials like glass beads, rice, sand, salt, couscous and sugar. However, according to the results of Balmforth et al. (2005) the material friction is indeed a factor for the estimation of the precise final shape of the deposit. This fact is further investigated in the investigations of this thesis.

The characteristic of the material collapse is distinguished into two main types by Lajeunesse et al. (2005). For small aspect ratios, the granular material propagates trough avalanching of the flanks. The final deposit describes a truncated conical shape for aspect ratios $a < 0.74$, while for a fully conical shape develops for $a > 0.74$ (see Figure 6.2). At even higher aspect ratios, the material propagation changes: the upper part of the column collapses but conserves its shape, while the material at the columns foot propagates into positive x-direction. The final deposit is separated into a steep slope at the left wall and a large almost flat region in positive x-direction (see Figure 6.1 and Figure 6.2).

Figure 6.2: Final deposit slopes for different aspect ratios in the physical tests of Lajeunesse et al. (2005)

Further, the results of Lajeunesse et al. (2005) shows a clear sequence in temporal evolution of the collapse independent from the aspect ratio, if the propagation of the material is

scaled by the free fall time $t_c = \sqrt{h_0/g}$. The propagation evolution can be differentiated into three sections. In the first section ($t < 0.8t_c$) the deposit propagation accelerates and, thus, the spreading of the deposit tip in positive x-direction. Subsequent, the foot of the material propagates at nearly constant velocity for about $2t_c$. In the last sequence, the material propagation decelerates until it reaches the final deposit position after approximately $0.6t_c$. Lajeunesse et al. (2005) as well as Lube et al. (2004) define approximately $3t_c$ as a guide value for the total duration of the collapse.

The final deposit height h_∞ and run-out distance of the front l_∞ of the resulting slope are part of the investigations of Balmforth et al. (2005), Lajeunesse et al. (2005), and Lube et al. (2005, 2004). In all investigations the authors determine a dependency of the final deposit on the initial aspect ratio. Hence, simple power laws on the basis of a are developed and are presented in Table 6.1. Thereby, Δl represents the difference between the final run-out distance l_∞ and the initial material width l_0.

Table 6.1: Power laws for the estimation of the final deposit run-out distance and height

Approach	Scaled run-out distance	Scaled final height
Lajeunesse (2005)	$\frac{\Delta l}{l_0} = \begin{cases} a & a \lesssim 3 \\ a^{2/3} & a \gtrsim 3 \end{cases}$	$\frac{h_\infty}{l_0} = \begin{cases} a & a \lesssim 0.7 \\ a^{1/3} & a \gtrsim 0.7 \end{cases}$
Lube (2005)	$\frac{\Delta l}{l_0} = \begin{cases} c_1 a & a < 1.8 \\ 1.9a^{2/3} & a > 2.8 \end{cases}$	$\frac{h_\infty}{l_0} = \begin{cases} a & a \leq 1.15 \\ c_2 a^{2/5} & a > 1.15 \end{cases}$
Balmforth (2005)	$\frac{\Delta l}{l_0} = c_3 a^{0.9 \pm 0.1}$	$\frac{h_\infty}{l_0} = c_3 a^{0.6} \quad a > 2$

According to Lube et al. (2005), the coefficient c_1 (see Table 6.1) for the estimation of the run-out length needs to be determined experimentally. In the conducted tests of Lube et al. (2005), a good agreement with the experimental results is achieved for different granular materials by applying $c_1 = 1.2$. Also Balmforth et al. (2005) apply a coefficient c_3 for the run-out distance. Thereby, c_3 is a function of the material properties. Contrary to Lube et al. (2005), Balmforth et al. (2005) recognise a dependency of c_3 on the material internal friction φ and the friction at the bottom. The coefficient c_2 for the estimation of the final deposit height shows only small variations within the different tests of Lube et al. (2005) and can be defined to $1.0 - 1.1$.

6.2 Physical Tests on the Column Collapse under Dry Conditions

The investigations of a particles column collapse under dry conditions is differentiated into two cases. In the first case, the particle column collapses under a controlled and slow manner, by a slow lifting of a movable wall. Thereby, the collapse mechanism is dominated by small and short slumping events, which take place in intervals. In contrast the second case, which is conform to the classical dam break problem. Thereby, the whole particle column collapses in one fast dynamical slumping by a fast extraction of a movable wall. In this case, the damping behaviour in the whole particle system is a predominant factor. By means of this differentiation, the focus is directed to different elements of the contact modelling in the DEM simulations.

The slow as well as the fast collapse are investigated in small scale physical tests at the laboratory of the Institute of Geotechnical Engineering and Construction Management of the Hamburg University of Technology. The evaluation of the physical results is conducted by PIV analysis. Before the physical test setup as well as the tests results are presented, the PIV method is introduced to give an insight into this complex technique.

6.2.1 Fundamentals about the PIV analysis

The analysis of the physical test results is performed using the non-intrusive Digital Particle Image Velocimetry (DPIV). The DPIV analysis technique enables the quantitative and qualitative flow visualisation. To achieve this, high frequency series of pictures are recorded to capture the displacement of particle groups. By application of the DPIV the particle displacement is calculated for particle groups by cross-correlations between two interrogation areas. Further, the velocities of the particles can be derived from the time interval Δt between the pictures and the displacement of the particle in this time interval. The classical application of the PIV method is the visualisation of fluid flow. Therefore, tracer particles are added to the fluid. This tracer particles are highly reflecting and have neutral density regarding the fluid. Thereby, an equal buoyancy and inertia behaviour of the particles in the fluid is achieved. In the physical tests, a thin sheet within the fluid mass is illuminated. The beforehand added tracer particles reflect the light, which is captured by an image sensor (camera), positioned parallel to the illuminated sheet. Since the material is intransparent, the application of the DPIV technique for the visualisation of granular flows is limited to the visible border areas in a physical test. According to D. J. White et al. (2001) the PIV analysis assesses the texture of individual grains as well as the light and shadows which is formed between adjacent grains. For an increase of texture D. J. White et al. (2001) recommends the application of coloured material. The distance between the camera and the region of interest depends on the size of the recorded area. However, there are some restrictions for the application of granular material, since a particle should be dissolved into at least 3 pixels for optimal conditions (Thielicke, 2014).

In the physical tests of this thesis, the MATLAB® based open source software PIVlab© is applied. Following, the procedure of a DPIV analysis in PIVlab is presented. The proce-

dure of a DPIV analysis is differentiated into three steps of pre-processing, image evaluation and post-processing. More detailed information on the individual steps and implemented tools can be found in Raffel et al. (2017), Thielicke (2014), and D. J. White et al. (2001).

6.2.2 Test setup and evaluation for slow collapse tests

The setup consists of a small plexiglas tank with an inner length of 25 cm, a depth of 10.2 cm and a height of 40 cm. In a distance of 9.3 cm from the left wall a rack is installed from the middle to the top of the front and back wall (see Figure 6.3). This mechanism

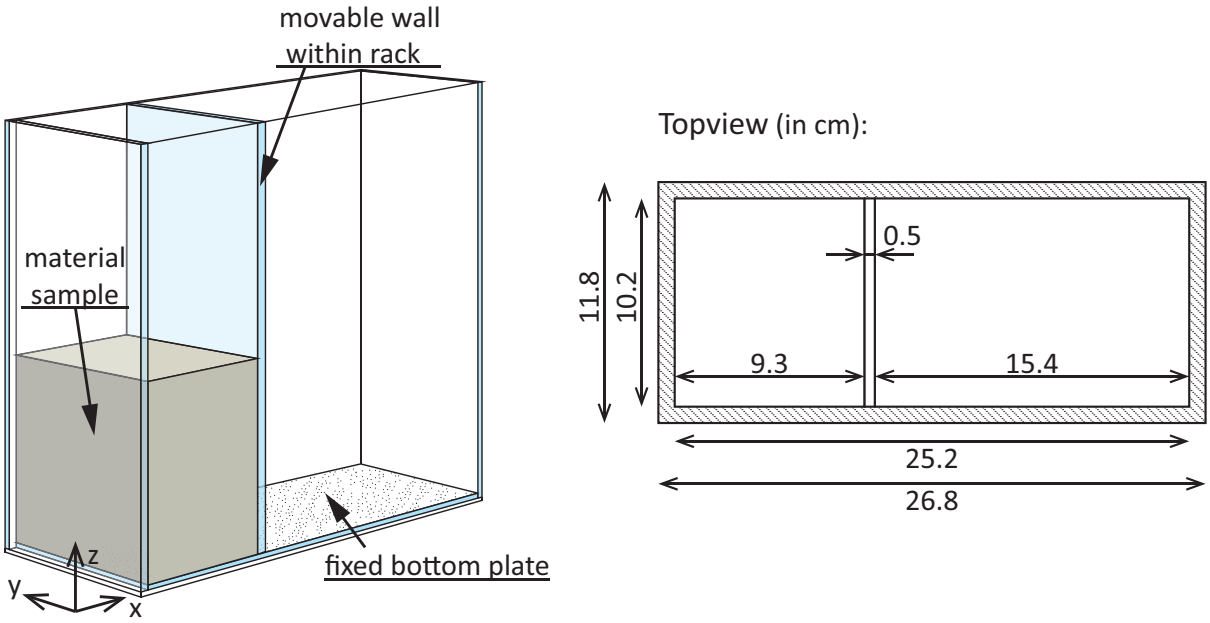

Figure 6.3: Scheme of the physical test setup: Plexiglas tank with material sample behind the movable wall (left) and top-view on the test setup with corresponding measures (right)

guides a movable wall which is attached to the grooves of the rack. The movable wall is reinforced by an additional plexiglas beam to prevent bending caused by the horizontal pressure of the investigated material. To close the gap between the tank and the movable wall while ensuring an easy pull-out of the movable wall, a polyester felt is glued to the front and back wall. On the bottom of the tank, a plexiglas plate with an attached layer of particles is positioned. Thereby, the particle size corresponds to the investigated test material (see Figure 6.4). The material applied in the physical tests of slow and fast collapse are glass particles with a diameter of 3 mm and 1.15 mm. The glass particles of the smaller diameter are not as monodiperse as the 3 mm particles. Rather, the material diameter is distributed between 1 and 1.3 mm. Following the particles with the 1-1.3 mm diameter are described by its mean of 1.15 mm.

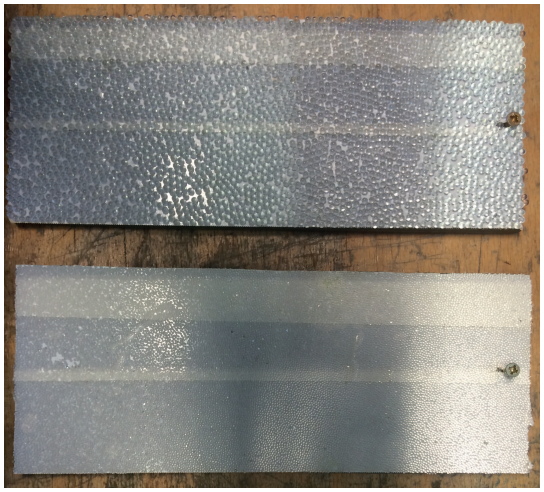

Figure 6.4: Bottom plates with attached glass particles of 3 mm (top) and 1-1.3 mm (bottom)

The test setup starts by filling the testing material into the space on the left side of the movable wall up to a specified height. Thereby, the glass particles are poured layer wise into the tank. The surface of the material sample is smoothed out to an even level. In total five tests per material are conducted. Thereby, the mass of the first test is reused for the subsequent tests of a test series. As a consequence, the height of the testing volume varies slightly by a maximum of ± 0.75 mm. An aspect ratio of $a = 1.7$ is applied in all tests. With a given initial width of the material volume of l_0 =9.3 cm, the test volume height is provided to h_0 =15.8 cm. This includes the height of the attached particle layer at the bottom. At the beginning of each test the movable wall is lifted slowly by a hydraulic press. Thereby, the constant press lifting velocity was reduced to the slowest velocity of 0.7 mm/s to initiate the slowest possible slumping procedure. However, the test results showed, that the movable wall was not lifted in a consistent manner. The analysis of the resulting images showed a variance between 0.69 and 0.72 mm/s. As a result of bending of the wall due to the horizontal particle load, this variation is induced by canting of the wall during lifting.

The test were recorded via a Full-HD (1920x1070 px) video recording with 24 fps, which is sufficient for the considered investigation due to the the approximated duration of the collapse process of $\approx$ 90 s. A reflex camera of type Nikon D700 was positioned in 50 cm distance to the tank front. Further camera adjustments are given in Table 6.2. The illumination of the plexiglas tank was established by LED spotlights. However, to reduce the influence of flickering due to the alternating voltage the spotlights were attached to a rectifier, which transform the alternating current to a direct current.

The video recordings of the tests, were converted to an image series and further evaluated with the DPIV analysis. The images are pre-processed with the CLAHE filter (tile size 10 px), a high-pass filter (filter size 15 px) and the intensity capping filter to improve the validity of the image information. The images are evaluated with a DFT approach in combination with window-deformation correlation. Therefore, the first pass of the cross

Table 6.2: Camera properties for Nikon D700 at slow collapse tests

Property	Value
Frame rate	24 fps
Shutter speed	1/100 s
ISO light-sensitivity	100

correlation is of a size of 50 px with an overlapping of 50%. Further, a second pass with a side length of 30 px and a third pass with a side length of 20 px are applied for a more detailed evaluation. The window deformation is interpolated via a spline approach, which is more precise according to Thielicke et al. (2014). The peak finding technique is based on a $2 \cdot 3$ Gaussian point fit.

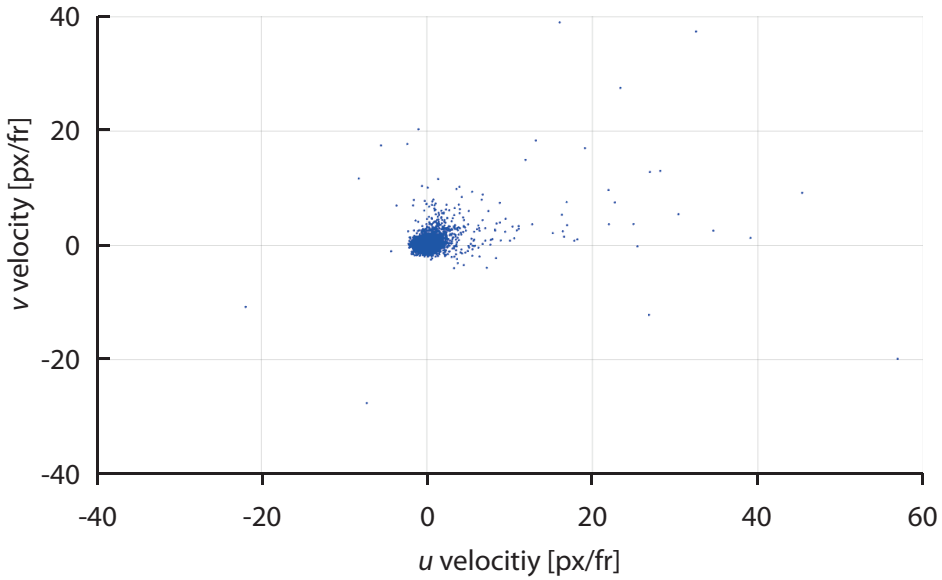

Figure 6.5: Schematic representation of the summarized velocities in different direction over time after image evaluation with PIVlab (representation of not calibrated data in pixel per frame frequency)

After the image evaluation, the results are post-processed via vector validation. Therefore, all vectors of the image series are represented in a vector plot, which differentiates between horizontal (u velocity) and vertical (v velocity) velocity vectors. The resulting vector plot is given in Figure 6.5. The velocity vectors concentrate very much at low velocity values. With slightly increasing velocities, the concentration reduces. However, the plot represents a very good image evaluation, since the outlier can be clearly identified. The vector limits are chosen for -0.004 m/s till 0.016 m/s for the v velocity and -0.004 m/s till 0.020 m/s for the u velocity. All outliers are deleted from the image evaluation. The outliers concentrate at the immediate slope surface, where higher particle velocities are

reached. It seems, the temporal resolution of 24 fps is not sufficient for the representation of this fast movement at the slope. The lack of information seems to lead to a high amount of outliers. To fill the remaining gaps after the vector limiting, new values are interpolated from the surrounding valid vectors. Exemplary, Figure 6.6 shows a segment of a particle slope before and after applying the vector limits. The interpolated values are marked by an orange colour. The outliers at the immediate top of the slope are deleted from the solution. The subsequent vector interpolation results in a smoothed vector field. However, the interpolated information needs to be handled with care, especially for a high amount of interpolated data.

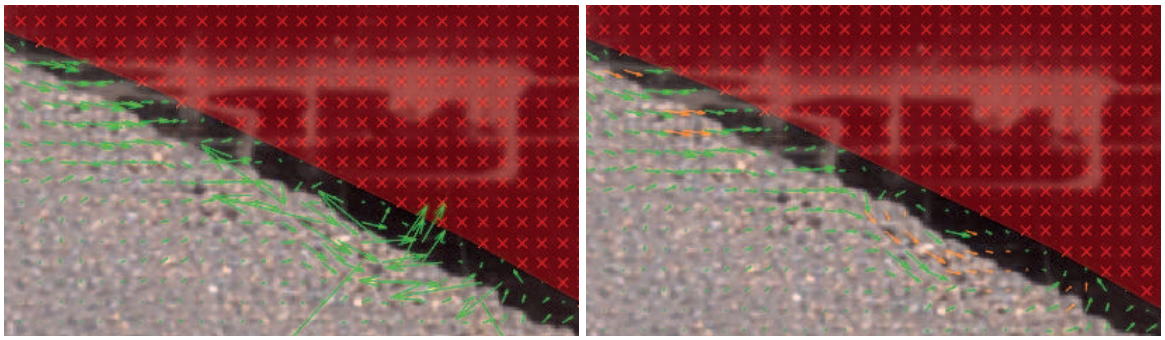

Figure 6.6: Velocity vectors near the deposit surface before (left) and after (right) vector validation

The analysis of the test showed some irregularities in the test procedure, which might lead to minimal different behaviour in the physical tests in comparison to the simulations. Although the movable wall had a reinforcement, the wall is bending over the particle column height. Due to the bending, the foot of the movable wall is positioned about 1.5 mm more into the positive x-direction than the top part. This bending also affects the consistency of the movable wall lift. The videos show, that the movable wall cannot move freely at the beginning of the tests, but rather cants at a few points due to the load from the side. This intensifies the interval behaviour between the particles at rest and the avalanches. Further, the total duration of the tests might be slightly effected. However, all these irregularities might have a minimal effect on the test procedure, but the final state should not be affected.

6.2.3 Test results of slow collapse

The slow collapse tests show good accordance within the individual tests series. The slumping mechanisms as well as the final position of the material are conform in all tests for the glass particles with a diameter $d = 3$ mm as well as $d = 1.15$ mm. Before the final position and slumping progress are discussed, the slumping mechanism of the slow collapse is presented following. Since the total duration of each test varies, the normalised

test time t^* is introduced. Thereby, t^* is defined as the dimensionless quotient of the considered time t during testing and the total test duration T (see Equation 6.1) to

$$t^* = t/T \quad . \tag{6.1}$$

At the beginning of the test the movable wall is lifted constantly and a gap rises between the fixed particles of the bottom plate and the foot of the movable wall. This gap needs to enlarge, before the first particles start to move within the particle column. The 1.15 mm particles start to move immediately as the gap has a height equal to the particle diameter. In contrast the 3 mm particles start to move at a gap height of approximately 4 mm due to tilting. The first particles at the column foot move through the gap and in positive x-direction. Thereby, a slope develops with proceeding lift of the wall (see 6.7b at $t^* = 0.32$). After the development of the slope, the slumping mechanism of the slow collapse proceeds in consistent manner by alternating stationary and discharge/slumping intervals (see Figure 6.7a). When the gap between the upper slope surface and the foot of the movable wall becomes to approximately the size of the applied particles, the adjacent particles in the column leave their position and exit through the gap. Thereby, also the particles which are positioned beneath the movable wall foot at the top of the slope are entrained into the discharge. The particles of the discharge avalanche over the slope surface and entrain the particles of the slope surface, till they reach the fixed particles of the bottom plate. Due to the high friction of the fixed particle bed, the lower avalanching particles stop moving and arrange in a stable position. As an effect of this stabilised new slope foot, the avalanching particles are stopped by the already stabilized particles at the lower slope surface and the deposit surface becomes static. The discharge of particles through the gap ends, when the top of the former avalanche becomes stationary and blocks the gap.

The particle discharge is accompanied by slumping inside the particle column. Thereby, the slumping particles fill the space of the discharge. The slumping mechanism is similar to ground shear failure. The classical ground shear failure mechanism is characterised by a vertical and horizontal movement due to vertical loads. Thereby, the ground material moves along a slip joint in which the shear resistance of the material is exceeded. In this slip joint the natural interlocking of the particles, the friction forces as well as the weight forces of the moved material body do not provide enough resistance against shear failure. In soil mechanics the curved slip joints are often approximated by a composed system of straight lines, which are connected via a so called logarithmic spiral (Kolymbas, 2011). A similar mechanism is present in the considered physical tests. Around the foot of the movable wall a curved slip joint is visible, which converts to the avalanching discharge in the area of the deposit slope. In negative x-direction this curved slip joint seems to transform from a curved form to a straight scheme. This straight part of the slip joint is slightly inclined counter-clockwise and proceeds to the surface of the particle column (see Figure 6.7d). Along this slip joint the particles slump downwards and against the movable wall. After the end of the discharge process the slumping particles arrange in a stable position and the whole slumping mechanism comes to a rest. The particles stay in this arrangement until this procedure repeats.

Figure 6.7 indicates the particle magnitude velocity at different t^* for a test with 3 mm particles. The tests with 1.15 mm particles lead to similar results and are presented in the

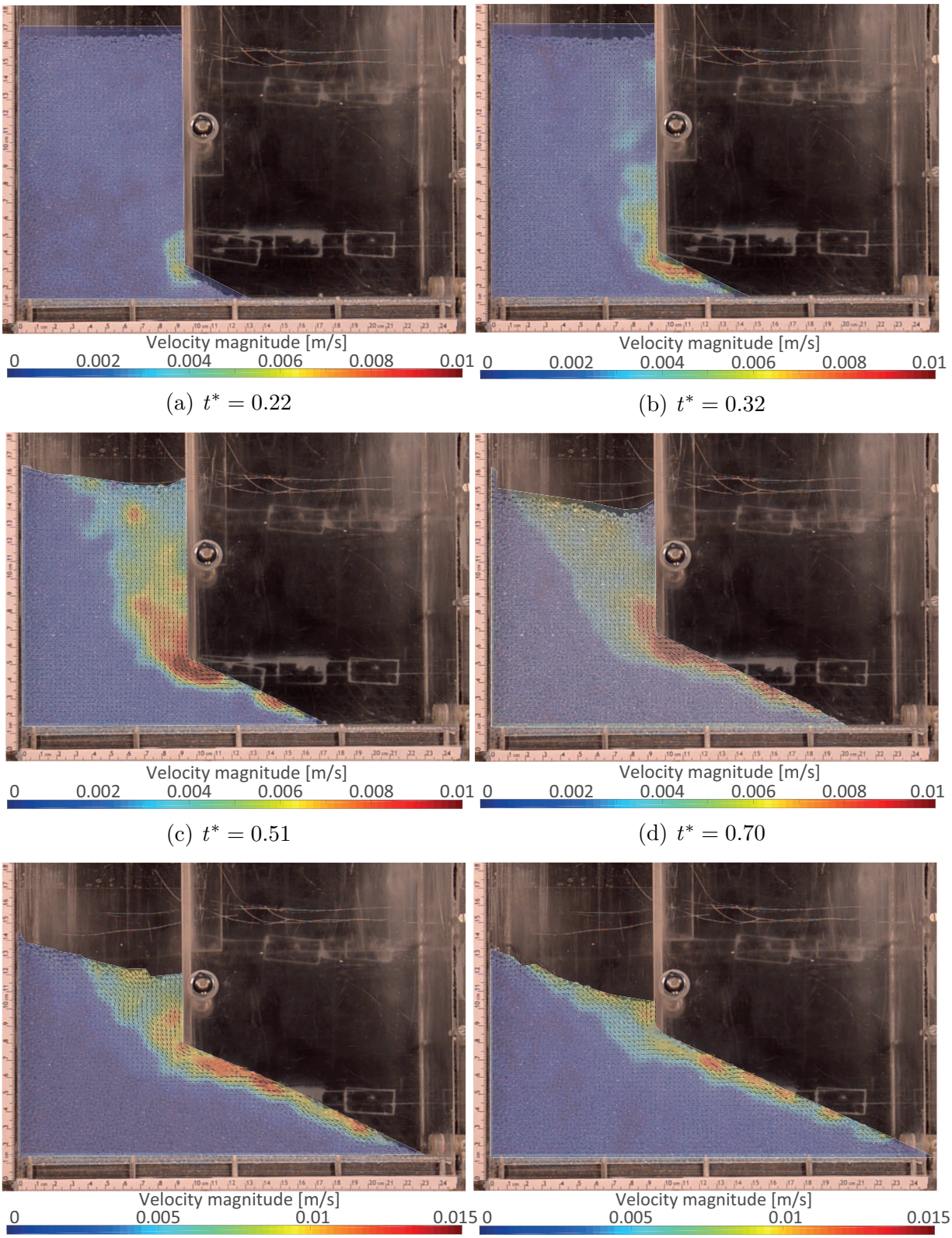

(a) $t^* = 0.22$ (b) $t^* = 0.32$

(c) $t^* = 0.51$ (d) $t^* = 0.70$

(e) $t^* = 0.83$ (f) $t^* = 0.90$

Figure 6.7: Slow collapse of particle column with 3 mm glass particles - Characteristic slumping mechanisms over time represented by the velocity magnitude of the particle phase from the PIV analysis

Appendix in Figure B.1. The diverse time interval between the images results from the not fluently proceeding slumping mechanism. To illustrate the affected slumping area at different stages of the test, images are selected, which show the peak of a slumping event. At the early stage of the test, a clear particle movement is visible for the particles which leave their position through the gap only. Since the slumping distance is minimal and very limited in the area around the proceeding gap (see Figure 6.7a), slumping inside the particle column is barely analysable by the PIV. With ongoing lift of the movable wall the area of slumping particles increases with the discharge mass. The particle displacement in the adjacent region on the left side of the movable wall is clearly visible in Figure 6.7b. Furthermore, the avalanche of particles at the slope surface is illustrated. The maximum particle velocity can be found around the foot of the movable wall. The particles move around that foot and exit through the gap. As described previously, this movement results in a curved sliding joint. The particles beneath this joint stay unaffected by slumping. Similar to the ground shear failure, the curved form of the slip joint proceeds upwards into a straight joint. This sliding joint is inclined into negative x-direction. Particles positioned on the left side of this sliding joint are not affected by slumping and stay stationary. In comparison to Figure 6.7a, Figure 6.7b shows an enlarged slumping area, which comprises the particles positioned near the movable wall over its full height. However, the displacement of the particles at the upper part of the particle column is still too minimal to be apparent in the PIV images. Nevertheless, the effect of slumping can be seen at the upper column surface. At this stage of the test a funnel-shaped recess develops at the column surface, which results from the discharge of particles, the corresponding slumping of the upper particles as well as the extraction of the movable wall. While the particle discharge leads to a deepening of the surface towards the wall, the extraction of the wall results in an entrainment of the adjacent particles due to friction forces. Thus, the funnel shows an amount of particles which are lifted next to the movable wall. This effect is greater for the 1.15 mm particles.

With increasing extraction of the movable wall, the affected area of the slumping mechanism increases. Since the deposit slope is getting higher and wider, the slope surface increases with progressing test time. Thus, a discharge and avalanche event comprises more mass than before. As a result, the time intervals between characteristic changes in the test view become shorter (see Figures 6.7d and 6.7e). Further, the duration of the particle discharge and the corresponding slumping inside the particle column increase. With an increase of the particle discharge, the displacements of the particles and the particle velocity increases as well. While the 3 mm particles reach maximum velocities around 0.012 m/s for a discharge event at $t^* = 0.22$, the maximum increases to 0.015 m/s at $t^* = 0.51$ and finally 0.019 m/s at $t^* = 0.90$. The 1.15 mm particles reach smaller velocities. The maximum particle velocities during an discharge event measured as approximately 0.003 m/s at $t^* = 0.22$ and increase to 0.008 m/s at $t^* = 0.56$ and finally 0.014 m/s at $t^* = 0.98$. However, even if a clear increase of particle velocities can be observed, the absolute values need to be handled with care, since PIVlab bears no possibilities to judge the accuracy of the PIV analysis.

The presentation of the slumping mechanism in Figure 6.7 shows a development of the appearance of the sliding joint. All figures show a curved joint around the foot of the

movable wall. As described previously, this curve merges to a straight sliding joint, which leads upwards into negative x-direction. The angle of the straight part of the sliding joint ϑ decreases over the ongoing slumping process. This is related to the reduced vertical loads by overlying particles as the slope height increases. The Figure 6.7a and Figure 6.7b show almost no inclination of the sliding joint. The sliding joints of the remaining figures show angles of approximately 68.7° in 6.7c, 62.4° in 6.7d, 57.9° in 6.7e and 53.4° in 6.7f. However, these angles represent an instantaneous value. ϑ varies slightly over the process of one discharge event.

According to the earth pressure theory of Coulomb (1776), the active slip surface angle of a sliding mass against a wall ϑ_{ag} can be determined by the friction angle φ of the soil material, the active wall friction angle δ_a, the angle of wall inclination α as well as the slope angle of the surface of the sliding mass β (see Equation 6.2). Due to the performed triaxial tests described in Section 5.2.3, the friction angle φ of the material is known. φ is given as 25.5° for the 3 mm particles and 22.7° for the 1.15 mm particles. Assessment values for the wall friction angle are defined in DIN 4085:2017-08 Table A.1. The norm recommends $\delta_a = 0$ for smooth wall surfaces. Since the wall is slightly bended by 1.5 mm over the column height, the wall angle is determined to $\alpha = 0.54°$.

$$\vartheta_{ag} = \varphi + \operatorname{atan}\left(\frac{\cos(\varphi-\alpha)}{\sin(\varphi-\alpha)+\sqrt{\frac{\sin(\varphi+\delta_a)\cdot\cos(\alpha-\beta)}{\sin(\varphi-\beta)\cdot\cos(\alpha+\delta_a)}}}\right) \quad . \tag{6.2}$$

According to Equation 6.2, ϑ_{ag} can be determined to 57.8° for the 3 mm particles and to 56.4° for the 1.15 mm particles under the assumption of $\beta = 0$. Thereby, ϑ_{ag} decreases with increasing values for β. This result is clearly smaller than the measured joint angles at the beginning of the tests. However, Equation 6.2 represents an approximation of the sliding joint angle for sliding masses which move against a wall. Thereby, the earth pressure against the wall depends strongly on the interaction between the wall and the soil (DIN 4085:2017-08, Appendix C). Thus, a rotational movement of the wall around the wall head results in different earth pressure profiles than the classical mechanism of a rotation around the wall foot. In the slow collapse tests, the fracture mechanism is not affected by the material pressure against the wall only, but also by vertical particle movement and, thus, the mechanism of the performed tests is not directly comparable to the earth pressure theory. Due to the vertical downward movement and the development of a slumping mechanism alike to ground shear failure, the initial angles of the sliding joints are higher than the assumed slip surface angle ϑ_{ag} of earth pressure theory. However, the decrease of the slip joint angle with reduced height and, thus, reduced load, corresponds to the theory. Further it needs to be considered, that the slow slumping mechanism results in small discharge events, which imply smaller particle displacement than a single slumping event. Thus, the smaller outer particles displacement which is located at the border of the actual sliding joint might not be recognized by the PIV analysis. However, a PIV analysis with 8 fps and, thus, longer time intervals between the images, resulted in approximately the same angles than presented previously. Hence, the small particle displacements are also less significant over a longer duration of an slumping event.

As soon as the foot of the movable wall is not in contact with the particle column any

more, the remaining particles on the left side avalanche over the particle slope. In the case of the 1.15 mm particles, the material spreads very smooth over the whole deposit slope. As a result, the final slope surface has a very even shape with a consistent angle over the whole height. The behaviour of the 3 mm particles differs. Similar to the 1.15 mm particles, the remaining 3 mm particles at the left side avalanche over the deposit slope. However, the mass of particles moving at this final avalanche is clearly less than for the 1.15 mm particles, since the particles stop moving after a few centimetres in a stabilized position already. The major amount of particles at the upper slope remain at this upper area. As a result, the final deposit slope has a slightly less steep upper part, which coincides approximately with the former position of the movable wall. This difference for the 3 mm and 1.15 mm particles is visualised by the silhouette of the final slope shape (see Figure 6.8). The cause for this behaviour is the higher angle of internal friction of the coarse material.

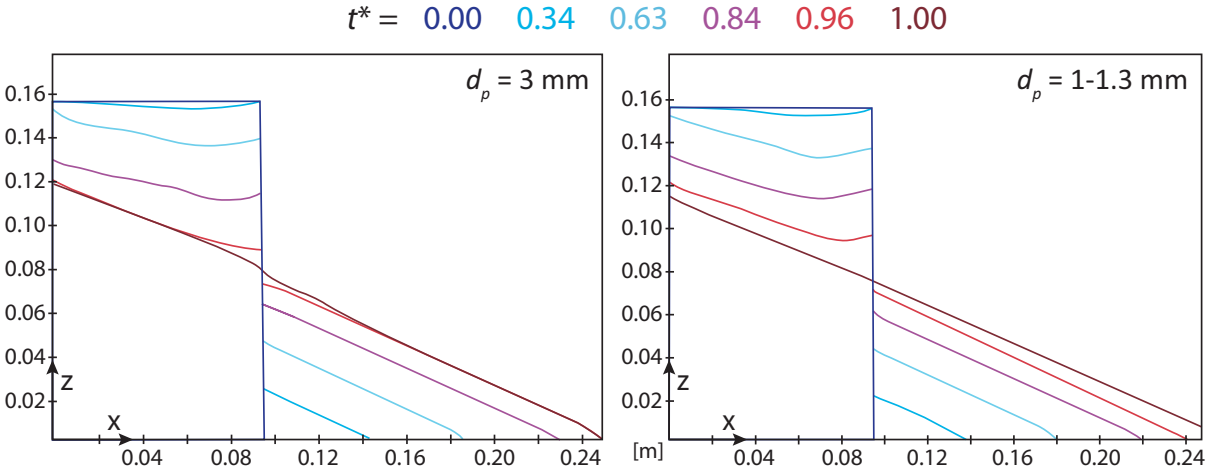

Figure 6.8: Sketch of the outer silhouette of the 3 mm (left) and 1.15 mm (right) glass particles during the slow collapse tests. The colour of the silouhette corresponds to the normalised test time t^*

Figure 6.8 shows the outer silhouettes of the 3 mm and the 1.15 mm particles during a slow collapse test. Thereby, the colours from blue to red represent the characteristic silhouette at different moments in normalised time t^*. In all tests the angle of the developing slope is consistent. Thus, the silhouettes are parallel. Just the foot of the 3 mm particles has a steeper angle. This is due to the fixed layer of particles at the bottom of the test reservoir. Since the particles are fixed, they provide higher shear resistance to the overlying particles. As described previously, the outer silhouette shows the development of a funnel shaped surface due to particle discharge and the slumping of the particles near the wall. Thereby, the major part of the funnel consists of a downward inclined slope which ranges from the outer left wall to approximately three-quarter of the distance to the movable wall. From that point, the surface merges to an upwards inclined slope until it reaches the movable wall. After the development of the funnel, the slope angles stay parallel for the downwards as well as the upwards inclined slope (see Figure 6.8 at times $t^* = 0.63$ and $t^* = 0.84$). Thereby, the angle of the left slope is slightly smaller than the angle of the deposit slope on

the right side of the movable wall. This is conform for the tests with 3 mm and 1.15 mm particles, whereby the deviation between the slope angles is less for the 1.15 mm particles. It seems that the upward directed forces induced by the lift of the movable wall prevent the slope from reaching the angle of the deposit slope. In contrast to the 1.15 mm particles, the upwards inclined slope of the funnel for the 3 mm particles is more uneven. This is due to the coarser characteristic of the material and the higher ratio between the particle diameter to the width of the particle column. The higher ratio supports an intermeshing of the coarser material and tilting during slumping. The particles show a less smooth and fluent behaviour. Assuming the same ratio between the particle diameter to width of the column as for the 1.15 mm particles tests, the 3 mm particles are expected to show a smoother behaviour. However, the 1.15 mm particles show a higher attraction to the plexiglas walls. In the tests a few surface particles of the column stick to the plexiglas walls due to electrostatic attraction. As a result, the upwards inclined slope next to the movable wall is more pronounced in the silhouettes of the 1.15 mm particles. Due to the electrostatic attraction and the smaller mass of the 1.15 mm particles are the 1.15 mm particles more affected by the lift of the movable wall.

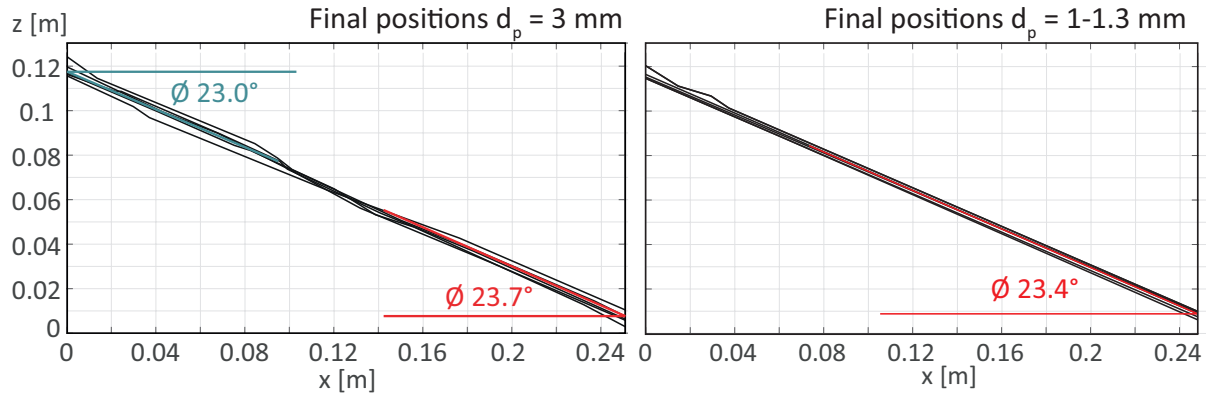

Figure 6.9: Resulting final deposit shape for five slow collapse tests with glass particles of 3 mm (left) and 1.15 mm (right) diameter

The final slope shapes of all tests are presented in Figure 6.9. The characteristic of the slope can be described by its angle, which is defined as the angle of repose ϕ. Because of the previously described behaviour of the 3 mm particles after the extraction of the wall, two slope angles are distinguished: the angle at the foot and the top part of the slope. In contrast, the tests of the 1.15 mm particles result in an even and smooth slope with a consistent inclination. Thus, the slope characteristic is defined by a single angle of repose. The resulting slope angles of the individual tests as well as the resulting average values and standard deviation are given in Table 6.3. Since the number of tests are too small to represent a population, the standard deviation is calculated on the basis of a sample approach (see Equation 6.3). The average slope angles, differ just slightly for the different sized materials. The tests with the 3 mm particles result in an average slope foot angle of 23.9°, while the slope top angle was slightly smaller with 22.9°. The angle of repose in the 1.15 mm particle tests resulted in an average angle of 23.4°. This result is conform

to the observations of Lajeunesse et al. (2005) and Lube et al. (2005, 2004). According to the investigations of Lajeunesse et al. (2005) and Lube et al. (2005, 2004), the final shape of the deposit depends mainly on the initial aspect ratio of the material column. The material properties such as the material diameter and, thus, the internal friction has less effect. Further, the standard deviation of the final angles is small for both the 3 mm as well as 1.15 mm particles. However, the standard deviation of the final foot angle is smaller compared to the top angle.

$$\sigma_s = \sqrt{\frac{\sum(x_i - \bar{x})^2}{n-1}} \tag{6.3}$$

Besides the final slope angles, Table 6.3 presents the duration of the physical test until a final deposit state is reached. Thereby, the duration differ more widely than the final slope characteristics. For the 3 mm particles the total test duration varies between 97.3 s and 100.5 s, while the average duration is 99.4 s. The 1.15 mm particle tests take longer and vary between 100.0 s and 104.4 s with an average of 102.2 s. Test number 5 is excluded of this evaluation, since the recording started later than the test itself. The longer duration of the 1.15 mm particles is induced by the final slumping mechanism after the movable wall is fully extracted. As described above, a small number of 3 mm particles moves down the slope in an avalanche. The most particles stay in place and build the shallower top of the slope. In contrast the 1.15 mm particles, which move over the full slope length in a big avalanche until the slope reaches a consistent slope angle. This process takes more time to reach a final state than the mechanism of the 3 mm particles. The bigger differences in the duration of the individual tests of the same material is induced by different final movements of the particles. In some tests, single particles still move downwards the slope while in other tests the particles are stationary immediately after the extraction of the wall and the final avalanche.

Table 6.3: Results of the slow collapse tests for glass particles with 3 mm and 1.15 mm diameter

Test	Glass 3 mm			Glass 1.15 mm	
	Slope angle top	Slope angle foot	Duration [s]	Slope angle	Duration [s]
1	23.8°	24.3°	100.5	23.4°	103.7
2	22.5°	23.8°	101.2	23.4°	100.6
3	22.8°	24.1°	99.5	23.7°	100.0
4	22.5°	23.9°	98.6	23.5°	104.4
5	23.1°	23.5°	97.3	23.1°	98.0
∅	22.9° ±0.54°	23.9° ±0.30°	99.4 ±1.54	23.4° ±0.22°	102.2 ±2.2

6.2.4 Test setup and evaluation for fast collapse tests

The fast collapse tests take place in the same plexiglas tank described in Section 6.2.2. Further, the identical testing materials of 3 mm and 1.15 mm glass particles are applied in the fast collapse tests. However, the mechanism of movable wall extraction is adapted to the requirements of the fast tests. Thus, the movable wall is attached to a lever arm, whose distant end is connected to a falling weight (see Figure 6.10). Further, the plexiglas tank is fixed to a massive steel structure, to prevent a displacement of the tank due to the impulse of the movable wall extraction. However, it becomes evident in first test trials, that the tank dimension are too small for a smoothly fast collapse with a material sample of the initial size corresponding to the slow collapse tests. The material spreads into positive x-direction (see Figure 6.3) and hits against the opposite wall. Thus, the collapse mechanism as well as the final deposit are mainly affected by the impact with the static wall. To prevent this behaviour, the size of the material sample was reduced to an initial width of $X_0 = 6.2$ cm and an initial height of $Z_0 \approx 10.54$ cm, while the aspect ratio kept constant at $a = 1.7$. Thereby, the applied material sample is no longer mass consistent, but rather replaced for every new test. As a result, the height of the samples varies slightly. However, the aspect ratio deviates just minimal with 1.69 and 1.74 for the 3 mm tests and 1.68 and 1.77 for the 1.15 mm tests. This less significant deviations are not affecting the slumping or deposition characteristics in a significant manner. The packing density of the particle packings is in average $\varrho_d = 1480$ kg/m^3 for the 3 mm particles and $\varrho_d = 1620$ kg/m^3 for the 1.15 mm particles. This is equivalent to a porosity of $n = 0.408$ for the 3 mm particles and $n = 0.352$ for the 1.15 mm particles.

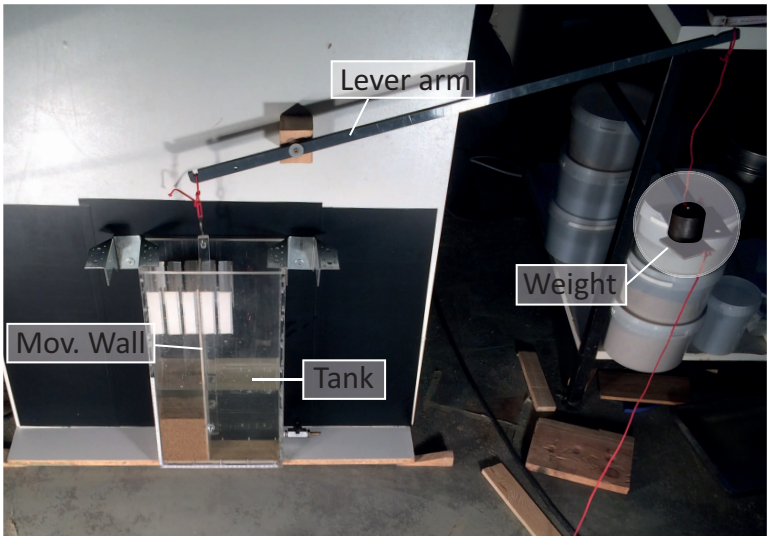

Figure 6.10: Setup of fast collapse tests - A lever arm with an attached weight is connected to the movable wall

In contrast to the slow collapse tests, the fast collapse tests take place over a fractional amount of time. Thus, the visual documentation requires a high speed camera system. The applied camera system in the fast tests consists of the FASTCAM Mini UX50, which

provides a 1.3 MPx resolution (1280x 1024 pixels) to a frame rate up to 2000 fps. At this resolution, the 3 mm particles are resolved by ≈ 15 px and the 1.15 mm particles by ≈ 6 px if the image covers the full basin length. Thus, the resolution provides optimal conditions for the PIV analysis. In the tests, a frame rate of 500 fps is applied. To provide a sufficient illumination of the testing region, a LED pulsing system is installed. This system consists of two LED heads which provide an intensive green light. Besides an consistent illumination, the LED system enables a pulsed mode, which can be synchronized with the recording frequency of the high speed camera. Anyway, in the fast collapse tests the illumination takes place in a consistent manner.

The recorded images are further evaluated by the DPIV analysis. Therefore, the images are preprocessed with the the CLAHE filter (tile size 15 px), a high-pass filter (filter size 20 px) and a wiener de-noise filter to improve the contrast and increase the validity of the calculated vector informations. Equal to the previous collapse tests, the images are evaluated with a FFT approach in combination with window-deformation correlation (see Thielicke, 2014). Therefore, three passes with 50% overlap are applied for the cross correlation. The passes have a size of 80 px, 54 px and 34 px for the 3 mm tests and 50 px, 32 px and 20 px for the 1.15 mm tests. The window deformation is interpolated via a spline approach and the peak finding technique is based on a $2 \cdot 3$ Gaussian point fit. Further, the correlation is repeated 5 times to increase the accuracy of the calculated vectors. Although this repetition increases massively the calculation time, the amount of invalid vectors is decreased significantly.

6.2.5 Test results of fast collapse

After the generation of an initial state, the movable wall is extracted in a fast manner due to the falling weight. Since the particle column reacts slightly time delayed to the wall extraction, the collapse can be distinguished into three phases: an acceleration phase, a phase of consistent movement and a deceleration phase. Thereby, the greatest displacements take place in the first 0.5 s, in which the sample material spreads in positive x-direction. After this major displacements, the deposit is not fully stationary. Rather, the topmost particles of the deposit surface are still moving. However, the displacements in this stage are less significant compared to the previous ones. Following, the slumping mechanism and the behaviour of the deposit is presented in detail. Afterwards, the final deposit shape and the deposits evolution in time of the collapse is discussed.

As presented previously, the fast tests begin with the extraction of the movable wall. Thereby, the extracted wall undergoes an acceleration phase before it is lifted with approximately consistent velocity. This acceleration phase takes about 0.06 s. The movable wall is fully extracted after approximately 0.15 s. The adjacent particles are accelerated with the wall into positive z-direction, due to frictional contact forces. However, since the movable wall is extracted with a high velocity, the contact between the wall and the particles in the lower column half is very short timed. As result, these particles show almost no distinct velocities in positive z-direction, but are rather affected mainly by gravitation after they loose contact to the wall. In contrast, the adjacent particles in the upper column third have wall contact over a longer time period, while they experience no load

from particles positioned above. As a result, they show greater vertical velocities in the direction of the extraction and the particles are slightly lifted. Thus, the column surface is displaced above the initial height of the particle column. This lift can be observed in the outer silhouette at $t = 0.1$ s presented in Figure 6.11 for the 3 mm (a) as well as the 1.15 mm (b) particles. At this stage of the test, the majority of the particle column is still in the shape of the initial state. However, the internal slumping mechanism is already fully developed (see Figure 6.12b). The particles are moving gravity driven along a clear defined slip joint with an angle of approximately 60°. The particles underneath this slip joint are not displaced. The particles in the lower area of the sliding mass are deviated horizontally into positive x-direction due to the course of the slip joint and the deflection of the static particle cone. In contrast, the upper particles are moving mainly vertical due to gravity into negative z-direction. In the further evolution of the tests, the upper particles move downwards and the particles on the left side of the column are entrained into the slumping movement. This is simultaneous to the full extraction of the movable wall. Corresponding to the movement of the upper particles, the initial particle displacements are mainly vertical. This vertical movement is deviated as soon as the particle reach the vicinity of the slip joint. Due to the mobilisation of the left sided particle mass, the course of the slip joint has rearranged. The slip joint is now inclined under an angle of approximately 50°. The slip joint inclination flattens further, since the lower end proceeds into positive x-direction with the deposit. At $t = 0.2$ s, the dominating vertical velocity of the upper particles has fully transformed to a vertical and horizontal movement due to influence of the slip joint (see Figure 6.12c). Further, the particle column looses its initial shape and merges to the shape of a wedge (see Figure 6.11).

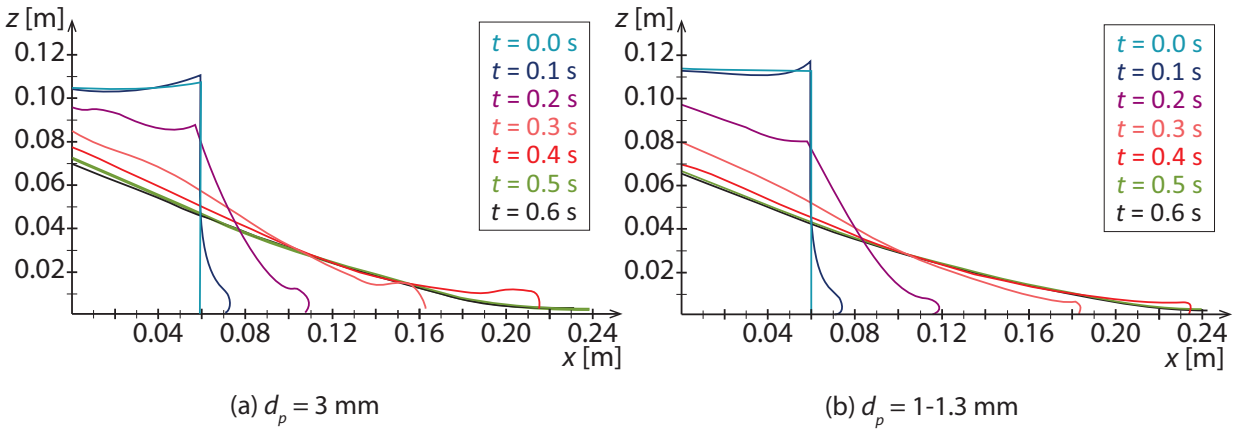

Figure 6.11: Sketch of the outer silhouette of the 3 mm (left) and 1.15 mm (right) glass particles during the fast collapse tests. The colour of the silhouette corresponds to the test time t

At $t = 0.3$ s the deposit has fully lost its initial shape. At this stage, the shape of the outer silhouette modifies just slightly compared to the high deformations at the previous stage. Rather, the deposit tip moves forward into positive x-direction, while the height of the deposit top is decreasing (see Figure 6.12d). The subjacent particles are unaffected from

displacements and stay stationary, while the deposit surface moves over a stationary core of the deposit. At the tip of the deposit wedge, individual particles part from the deposit mass and move ahead of the particle majority. This behaviour occurs in particular for the 3 mm particles. This effect is initiated by irregularities and high roughness of the fixed particle layer. Due to the roughness, the individual front particles are deviated from their course when they impact with the fixed particles. Further, the high particle elasticity intensifies the irregular dynamics and lead to a jumping movement. The proceeding particles collide with the right basin wall, before the deposit mass has reached its final length (see Figure 6.12e and Figure 6.11 at $t = 0.4$ s). As a result, the particles are reflected and move against the direction of the deposit mass or settle down in the vicinity. This process is dominated by chaotic movements of the individual particles. Simultaneously, the deposit mass decelerates and come to a rest $t \approx 0.5$ s. However, it is not fully clear, if the abrupt stop of the deposit mass is influenced by the chaotic movements of the individual particles. Thus, it is questionable, if the final deposit length is equal to those of a particle collapse in a longer basin.

After the deposit reached its final length, the number of moving particles is reduced significantly. Just at the immediate surface, the particles are still moving along the deposit top (see Figure 6.12f). This superficial particle movement generates minimal deformations of the deposit slope, before it reaches its final shape at $t \approx 0.6$ s. It needs to be considered, that not all particles have become stationary yet at this time. Single particles are still rolling over small distances along the slope surface into positive x-direction. However, the final shape of the deposit is not changing significant any more.

Figure 6.13 presents the compilation of the final state for all physical tests with 3 mm and 1.15 mm particles. The final shapes are very much conform for both materials. Further, the final shape of the 3 mm and the 1.15 mm particles are very much alike. The deposit forms a slope, which is flattening in x-direction. Thereby, the 3 mm particles result in a slope top angle of 21.4° with a standard deviation of 0.85°, while the 1.15 mm particles result in an average angle of 21.5° with a standard deviation of just 0.31°. The smaller standard deviation for the 1.15 mm particles are congruent to the behaviour during the fast collapse tests. The whole material behaves very smoothly like a quantity or a viscous fluid. Thus, the deviations of the results are smaller of those for the 3 mm particles, which have a less smooth behaviour due to the coarser material. The similar final shapes are conform with the theories of Lajeunesse et al. (2005). According to Lajeunesse et al. (2005), the final shape is more depending on the initial aspect ratio of the material than on the material properties like the particle size.

As discussed previously, the collapse can be distinguished into an acceleration phase, a phase of consistent velocity as well as a deceleration phase. To investigate this behaviour, the movement of the deposit tip is observed over time. Therefore, the data of the PIV analysis is applied. The position of the deposit tip could be identified by the prompt increase of velocities. Thus, the PIV velocity x-components are analysed over a line parallel to the x-axis, in the height of approximately one particle above the surface of the fixed particle layer. An algorithm of the MATLAB toolbox, identifies the exceed of the velocity component v_x over a certain limit and extracts the corresponding position for every image of the PIV analysis. The established limit was reduced for the acceleration phase, to take

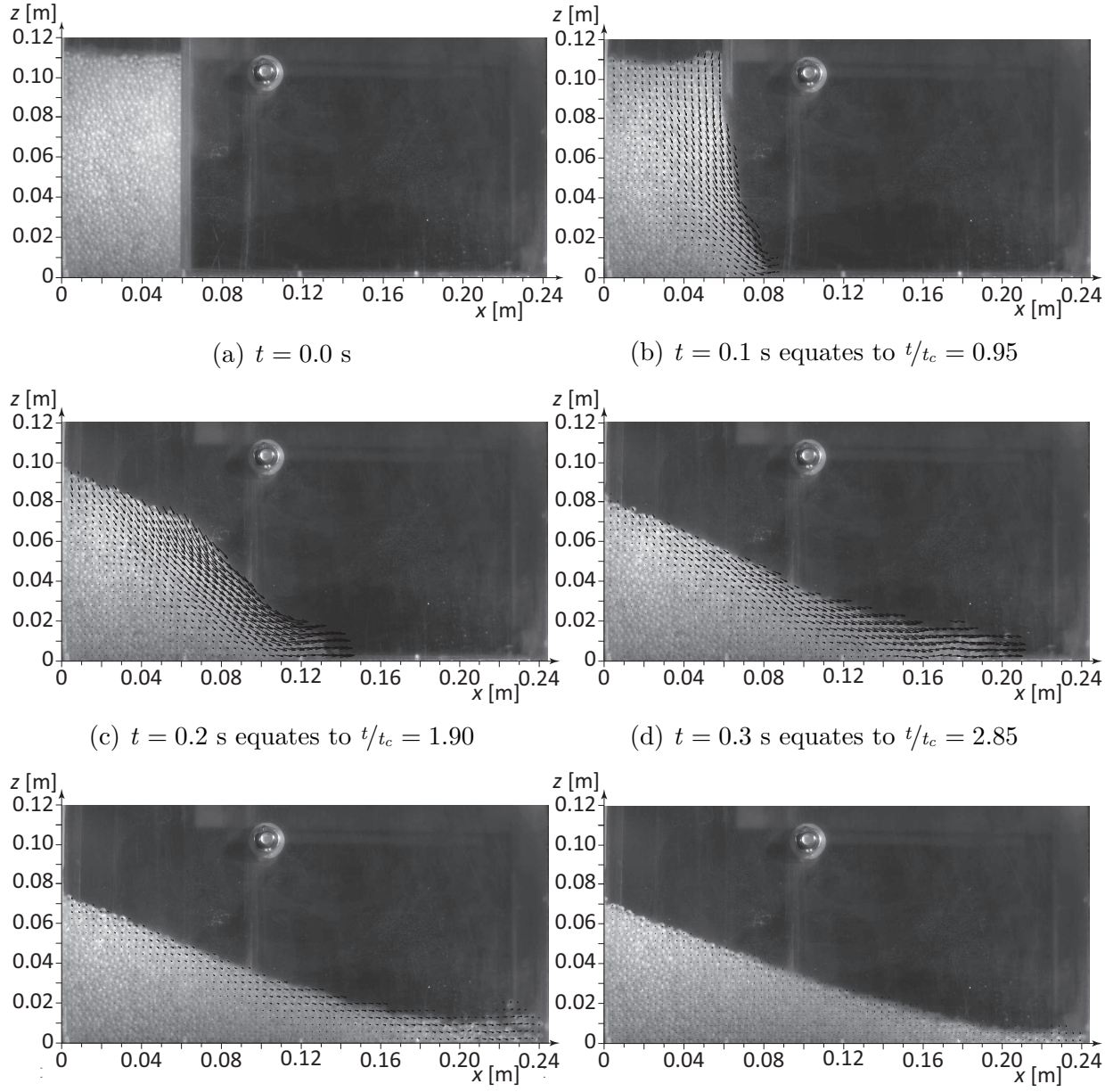

(a) $t = 0.0$ s

(b) $t = 0.1$ s equates to $^{t}/_{t_c} = 0.95$

(c) $t = 0.2$ s equates to $^{t}/_{t_c} = 1.90$

(d) $t = 0.3$ s equates to $^{t}/_{t_c} = 2.85$

(e) $t = 0.4$ s equates to $^{t}/_{t_c} = 3.80$

(f) $t = 0.5$ s equates to $^{t}/_{t_c} = 4.74$

Figure 6.12: Fast collapse of the particle column with 3 mm glass particles - Characteristic slumping mechanisms over time represented by the velocity magnitude of the particle phase from the PIV analysis

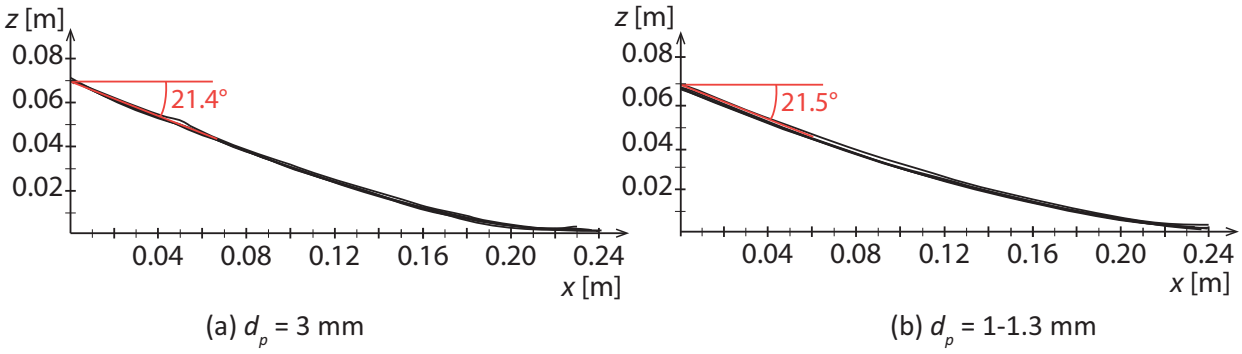

Figure 6.13: Compilation of the final deposit shape of the 3 mm (left) and 1.15 mm (right) glass particles for the fast collapse test

care of smaller velocities at this stage of the test. Unfortunately, the single particles ahead of the deposit tip are a reason for inaccuracies in the results. However, those effects are very limited and can be clearly identified, since the results give a sufficient idea of the curve progression. Figure 6.14 presents the spread of the deposit over time for selected tests of 3 mm and 1.15 mm particles. The results of the remaining tests are presented in Figure B.5 and Figure B.6. Thereby, the position of the deposit tip is defined by the scaled run-out distance x^+ and the characteristic time scale t^+. The scaled run-out distance x^+ represents the normalised distance the deposit foot travelled (see Equation 6.4), while t^+ represents the time scaled by the free fall time $t_c = \sqrt{X_0/g}$ (see Equation 6.5). These dimensionless parameters are adopted from the investigations of Lajeunesse et al. (2005), who identified those as the characteristic quantities.

$$x^+ = \frac{x - X_0}{X_0} \tag{6.4}$$

$$t^+ = t/t_c \tag{6.5}$$

Based on this parameters, Lajeunesse et al. (2005) identified the time evolution of the deposit length to an acceleration phase of $T = 0.8t_c$, a phase of constant velocity for $T = 2t_c$ and a deceleration time of $T = 0.6t_c$. These limits are also included into Figure 6.14 as vertical lines. Thereby, the limits regard to the lower time axis, where the zero coordinate is set equal to the first movements of the particles. Since the particles react time delayed, this zero point is not corresponding to the start point of the tests at $t = 0$. According to Figure 6.14, the defined limits of Lajeunesse et al. (2005) match very well the results of the conducted physical tests for the 3 mm as well as the 1.15 mm cases. The acceleration phase matches perfectly to the temporal evolution till $0.8t_c$. The subsequent phase of constant movement seems to exceed the duration of $2t_c$ slightly. However, the tests do not show a clear deceleration phase. Although the end of the tests seems to match with the overall limits, the deceleration is not as distinct than the acceleration phase. Rather, the constant movement stops and the maximum run-out distance is reached. This might result from the limited dimension of the plexiglas tank. Although the material seems to

stop before the wall is fully reached, the individual particles ahead of the deposit, might influence the deposit after the impact with the wall. As a result, the deposit shows no deceleration but a more prompt stop. Thus, the reached run-out distance is not the characteristic run-out distance for this aspect ratio. However, the temporal evolution of the deposit, can be described very well by the limits of Lajeunesse et al. (2005).

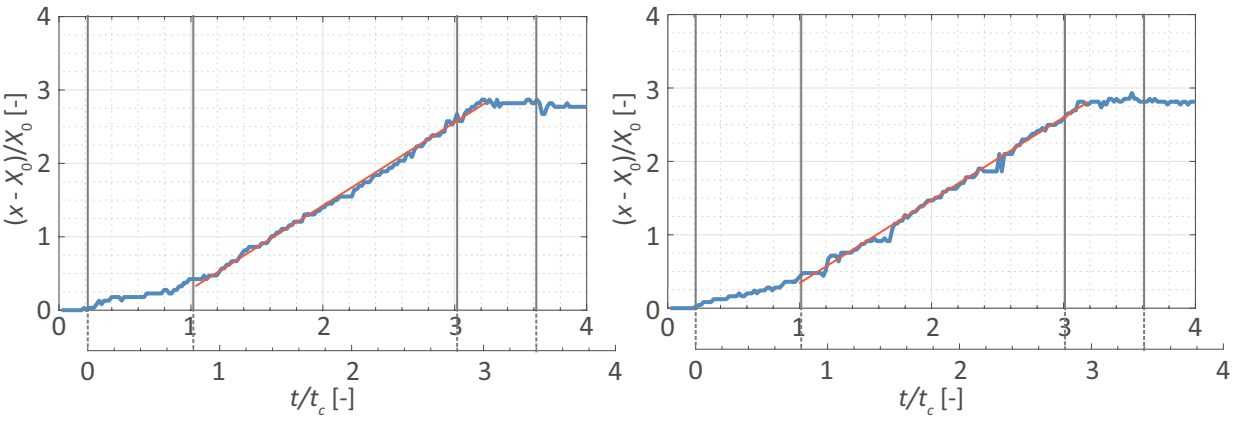

(a) Test 4 with $d_p = 3$ mm

(b) Test 1 with $d_p = 1.15$ mm

Figure 6.14: Evolution of the deposit tip position during the slumping process for 3mm and 1mm

The evolution of the deposit tip results in a long section of constant spreading. Based on the inclination of the graph in Figure 6.14, a constant deposit tip velocity can be estimated. For the 3 mm particles this constant velocity is in average 0.60 m/s, while the 1.15 mm particles result in an average constant velocity of 0.66 m/s. The resulting velocities defer significantly for the different materials. This differences might be motivated by the different dry density of the particle packings. The packing of the 1.15 mm particles has a higher dry density and, thus, contains a higher mass than the 3 mm packing at the same volume. Thus, 1.08 kg in average are employed for the 3 mm particle packing and 1.18 kg for the 1.15 mm particles. The higher mass for the 1.15 mm packing result in a higher load and motivate the faster slumping movement and the higher velocity of the deposit tip. Thereby, the standard deviation for the average velocity for the 3 mm particles of 0.032 is significant higher than for the 1.15 mm particles with 0.011. Thus, the constant velocity of the 3 mm particles varies more. This diffusion might be motivated by the analysis of the PIV data. While the 1.15 mm particles show a very smooth behaviour and, thus a clear recognisability, the identification of the 3 mm particle deposit tip is less clearly. This effect lead to higher fluctuations in the evaluation of the deposit tip evolution in 6.14a. Thus, the estimated average velocity for the 3 mm particles need to be handled with care.

The end of the tests is defined at the point, when all particles groups have become static and just single particles are still under movement. For the 3 mm as well as the 1.15 mm particles, this characteristics are reached after approximately 0.61 s. Thereby, the tests show good accordance. The standard deviation for the total duration of the tests is 0.006 for the 3 mm particles and 0.192 for the 1.15 mm particles.

6.3 Numerical Simulation of the Column Collapse under Dry Conditions

The numerical simulation of submerged particle slumping is highly sensitive to the chosen contact formulation, the applied particle properties and the fluid-particle interaction. The great number of influencing parameters complicates the assignment of modelled slumping behaviour characteristics to a specific influence or parameter. Hence, in a first step the contact formulation as well as the properties of the numerical simulation are investigated under dry conditions. The limitation to dry conditions allows to focus on the particle contact formulation in the DEM model and its detailed influences on the simulation of granular slumping.

Corresponding to the physical tests in Section 6.2, two different interpretations of the dam break problem are differentiated in the simulation: a slow collapse and the classical fast collapse. This differentiation is motivated by the definition of the applied visco-elastic Hertz contact model (Kloss et al., 2011). As described in Section 4.1.1, the Hertzian model is based on a normal and a tangential contact force between two particles. Further, every individual contact force is differentiated into rheological elements with a elastic share (spring force) and a viscous share (dashpot). While the elastic spring force increases proportional with the virtual overlap of the two particles, the damping of the dashpot share increases proportional with the relative velocity between the two particles in contact. By the differentiation of a slow and a fast collapse, the two components of the contact force are addressed differently. During the slow collapse, the incremental slumping mechanism leads to small particle velocities and the particle contacts consist over longer durations. Thus, the influence of damping in the particle system should be reduced for this case. In contrast, the frictional forces dominates the granular flow behaviour. In the fast collapse case, the whole particle system collapses at once in a highly dynamic avalanche. Contrary to the slow collapse the contacts are short and the damping behaviour at impact is a predominant factor in the whole particle system. By means of both investigations of the dry particle slumping, the material properties are investigated and validated for further investigations on granular slumping in fluid. Since different particle properties are assigned to the individual contact force components, an assignment to a specific slumping character is possible. However, it is unclear how significant property variations affect the contact behaviour and the whole slumping mechanism. Sensitivity studies should give an idea about the influence of individual properties in the contact model of the numerical simulation. As an initial parameter set, the particle parametrisation in Section 5.2.3 are applied.

6.3.1 Development of a numerical model for slow collapse

For the numerical simulation the same material as in the physical tests is considered. Thereby, the glass material is represented by monodiperse particle packings. However, the coarse 3 mm particles have a manufacturing tolerance of ± 0.3 mm. Further, the fine glass material is based on a distribution between 1-1.3 mm diameter. In the numerical tests this

distribution is simplified by an average particle diameter of 1.15 mm. As a consequence, the particle diameter can deviate between the physical tests and the numerical simulation up to 10% of its diameter for the 3 mm particles and 13% of its diameter for the 1.15 mm. Thus, also the packing density will deviate slightly between the physical tests and the numerical simulations. The exact effective occurrence of this deviation cannot be determined, since the deviations are too small to be determined by sieves. However, as described in Section 6.2.2 a visual evaluation of the particle distribution attests a homogeneous distribution. The minimal and maximal diameter of 1 mm or 1.3 mm is rare in the distribution. This variance between simulation and physical tests might lead to small differences in the results. However, the effort to create realistic packings with particle distributions is disproportional to the improvement by respecting diameter tolerances (for more informations on the generation of polydisperse particle packings see Winkler et al., 2014, 2015). Besides a variance in diameter, the monodisperse particles in the simulations differ from the real glass beads by a perfect sphericity. According to the product specification of Sigmund Lindner GmbH, the sphericity of the 3 mm particles is $\geq$0.98, while the 1.15 mm particles have a sphericity of $\geq$0.95. This deviation in the particle shape is even smaller than the deviation in diameter. As a result, the effect on the slumping behaviour is expected to be reflective.

The particle contact is modelled by the Hertz contact model with enabled tangential damping (see Section 4.1.1). Further, the alternative elastic-plastic spring-dashpot model (EPSD2) is applied to model the rolling friction. Therefore, a coefficient of rolling friction μ_r needed to be defined. The parametrisation for the coefficient of rolling friction as well as the remaining particle properties have been presented in Section 5.2.3. The corresponding particle properties for the 3 mm as well as 1.15 mm particles are presented in Table 5.3. Contrary to the previous simulations in Chapter 5, the simulation of particle slumping requires the implementation of two different materials, which represent on one hand the glass particles and on the other hand the plexiglas walls. However, a study of the interaction between the particles and plexiglas material lead to similar results compared to the interaction between glass particles. Thus, the inter-particle properties are also used for the interaction of the particles with the plexiglas walls. Thus, the behaviour at a particle-wall contact is equal to a particle-particle contact.

The numerical model considers the same dimensions as the plexiglas tank used in the physical tests. The model includes two solid walls normal to the x-direction as well as the z-direction. Thereby, the position of the x-normal and the bottom z-normal walls are equal to the plexiglas walls in the physical tests. The origin of the coordinate system is positioned in the lower left corner at the front wall (see Figure 6.1). The simulation domain ends in z-direction 25 cm above the bottom plate, to ensure enough space for the test procedure. In the y-direction the domain is characterised by periodic boundary conditions. Thus, the particles which leave the domain over a y-normal boundary border, entrain the domain again from the other y-normal boundary. As a result, the particles are supported by other particles. This has the same effect as an infinite particle mass. This effect allows to shrink the simulation domain in the y-direction and, thus, reduce the computational costs. While the plexiglas tank has a depth of 10.2 cm, the simulation domain is reduced to 4.5 cm for the 3 mm particles and to 0.8 cm for the 1.15 mm particles.

The motivation for these dimensions is the German norm DIN 18130-1:1998. This norm describes the standard laboratory test for the evaluation of the permeability of soil. The permeability test is conducted at a cylindrical soil sample. The diameter of this sample is recommended to ten times the diameter of the maximum grain size in the case of very uniform material to guarantee a representable result of the test. Thus, this dimension is further applied as a value for the depth of the simulation domain. The recommendation results in an initial depth of the simulation domain of 3 cm for the 3 mm particles and of 1.15 cm for the 1.15 mm particles. However, the depth for the 3 mm case was later extended to 4.5 cm, since the tests showed a high amount of tilting. The extension of the domain was unproblematic regarding computational costs, since the 3 mm case required less particles per volume. With a domain depth of 4.5 cm an appropriate simulation time was obtained. In contrast, the 1.15 mm case requires higher numbers of particles per volume. Additionally, the available uniform parallelisation approach of the simulation domain is inconvenient for the slumping simulation, since the particle mass is highly unevenly distributed over the domain. As a result, even a high rate of parallelisation did not improve the calculation time. Thus, the simulation domain was adapted from 1.15 cm to 0.8 cm to reduce the extremely high simulation time for a depth of 1.15 cm. This resulted in a reduction of ≈ 22000 particles. A comparison of the slumping mechanism and final deposit for both y-depths showed no increase of tilting for the smaller y-dimension. Hence, the smaller depth of 0.8 cm is adopted for the simulations.

The initial state for the collapse tests is generated by using a previous initiation simulation. As a first step, a small amount of particles is generated over the whole simulation domain. After settling of the particles under influence of gravity, all redundant particles are deleted to obtain a boundary layer of approximately one particle diameter size. The remaining particles are allocated to a specific particle group, which is later excluded from the DEM algorithm. As a result, the particles stay fixed at their initial position, while an interaction with free moving particles is enabled. As a next step, the movable wall is activated in the simulation. The plexiglas wall of the physical tests is represented by a two-dimensional stereo-lithography CAD (stl) mesh. Since the contact between the particle mass and the wall is clearly limited to just one side of the wall, a two dimensional representation is sufficient. The movable wall is positioned in x-normal direction at $x = 9.3$ cm. The mesh bottom is one particle diameter above the ground, to take the particle boundary layer inserted previously into account. Afterwards, the initial state of the particle packing is generated. Therefore, a random distribution of particles is generated on the left side of the movable wall. Following, the particles settle under gravity to form a stable packing. This step is repeated once to reach an appropriate column height. The final height as well as an even upper surface are reached by deletion of the redundant particles over the specific height of 15.8 cm.

The particle generation command includes a random number, which controls the insertion algorithm. The variation of this random number allows the generation of different particle packings. Five initial particle packings are created for the 3 mm particle simulations to investigate the effect of different particle packing on the simulation results. For the 1.15 mm particles, the number of initial particle packings is reduced to three cases, since the simulations including particles with a diameter of 1.15 mm give more consistent simulation

results. Further, the computational costs for the 1.15 mm particles are very high. Table 6.4 presents the characteristics of the individual initial packings and the corresponding particle numbers as well as the reached packing porosity.

Table 6.4: Initial state packings for 3 mm and 1.15 mm particles

	3 mm			**1.15 mm**		
Test case	y [cm]	Number Particles	Porosity n	y [cm]	Number Particles	Porosity n
C	4.5	28304	0.402	0.8	88156	0.404
1	4.5	28248	0.404	0.8	88309	0.403
2	4.5	28287	0.403	0.8	88297	0.402
3	4.5	28645	0.395	0.8	88044	0.402
4	4.5	28694	0.394			
5	4.5	28671	0.395			

Besides the previously described varied initial packing, an additional particle packing (C) is created for each particle diameter. This particle packing should identify the inner rearrangements of the particles by marking individual layers at initial state. Therefore, 2 cm thick layers are implemented into the particle packing, whereby the particles of the individual layers differ by minimal different diameters. The particle diameter of the inserted particles alternates from one to the other sequence. In the odd-numbered layers, the original diameter is applied. In the even-numbered layers, the original particle diameter is extended by $2 \cdot 10^{-4}$ mm. The minimal deviation of the particle diameter can be used to associates particles to a certain layer at initial state. The final result and initial state of the particle packing C is presented in Figure 6.15.

After the generation of the initial state, the movable wall is lifted with 0.7 m/s. In contrast to the physical tests, the lifting velocity is truly constant (see Section 6.2.2). The simulation shows a simulation time of 120 s for the slumping process and, thus, exceeds the duration of the physical tests with a average duration of 99.4 s. However, since the lifting velocity of the movable wall is not constant, the numerical tests is allowed to result in different numerical simulation time.

6.3.2 Results of numerical simulation of slow collapse

The numerical simulations of the slow particle collapse show good accordance for the test series. The slumping characteristics as well as the final state show similar results for the different inital particle packings. Those are later presented in more detail to present the slumping characteristics. However, the effect of different initial particle packings on the results is indisputable for the numerical simulations in comparison to the physical tests as discussed later. For the investigation of the slumping behaviour, the simulations are

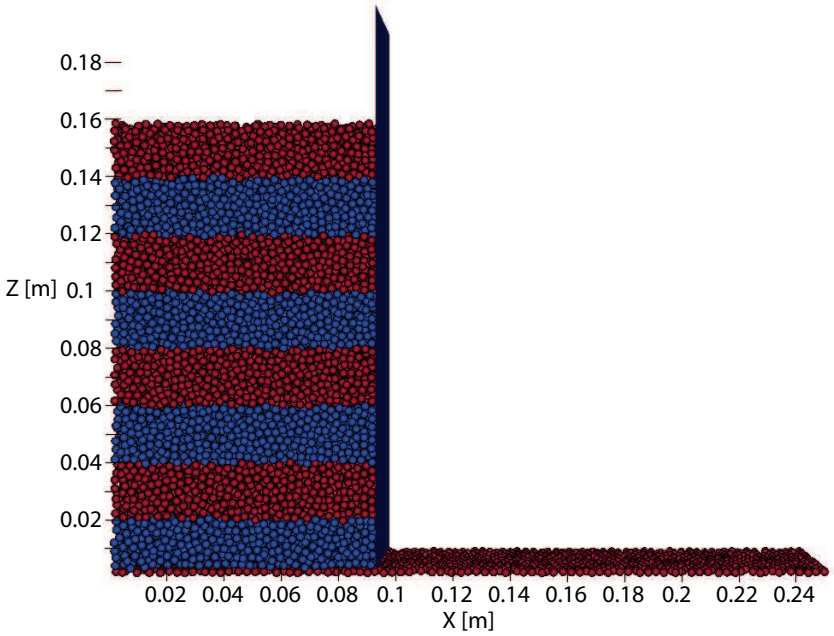

Figure 6.15: Initial state of slow collapse simulations under dry conditions with coloured identification layers

analysed using the particle velocities and particle paths during slumping as well as the particle positions at a final state. Before the final state and the validation with the physical tests are presented, the slumping mechanism and its deviation from the physical tests are discussed.

Since the simulation time of 120 s is comparatively high for a DEM simulation, the calculation time is very long with approximately 105 h for each 3 mm particle simulations and 460 h for each 1.15 mm particle simulation. This calculation time belong to simulations, which are parallelised with 48 processors on the high performance compute cluster of the TUHH.

To analyse the slumping mechanism of the slow collapse simulation, the particle velocity v_p of the particle packing with 3 mm particles is illustrated in Figure 6.16. Thereby, the normalised time t^* corresponds to the selected relative times in the physical tests illustrated in Figure 6.7. A direct comparison between the slumping mechanism of the physical tests and the simulation is given in Figure B.2 and Figure B.3. The slumping mechanisms in the simulations are very pronounced, since the individual particle velocity is presented in contrast to the velocity of a particle assembly in the PIV analysis. Thus, even the slowest movements are recognized by the data analysis of the simulation. The slumping behaviour of the simulation is very similar to the slumping behaviour observed during the physical tests. The characteristic behaviour of particle discharge, the resulting avalanche over the deposit slope and the simultaneous slumping inside the particle column are identical to the physical tests. However, the slumping area of affected particles during the slumping is greater in the simulations compared to the physical tests. In the beginning of the tests, this greater slumping area is mainly characterised by a wider area of a slumping body

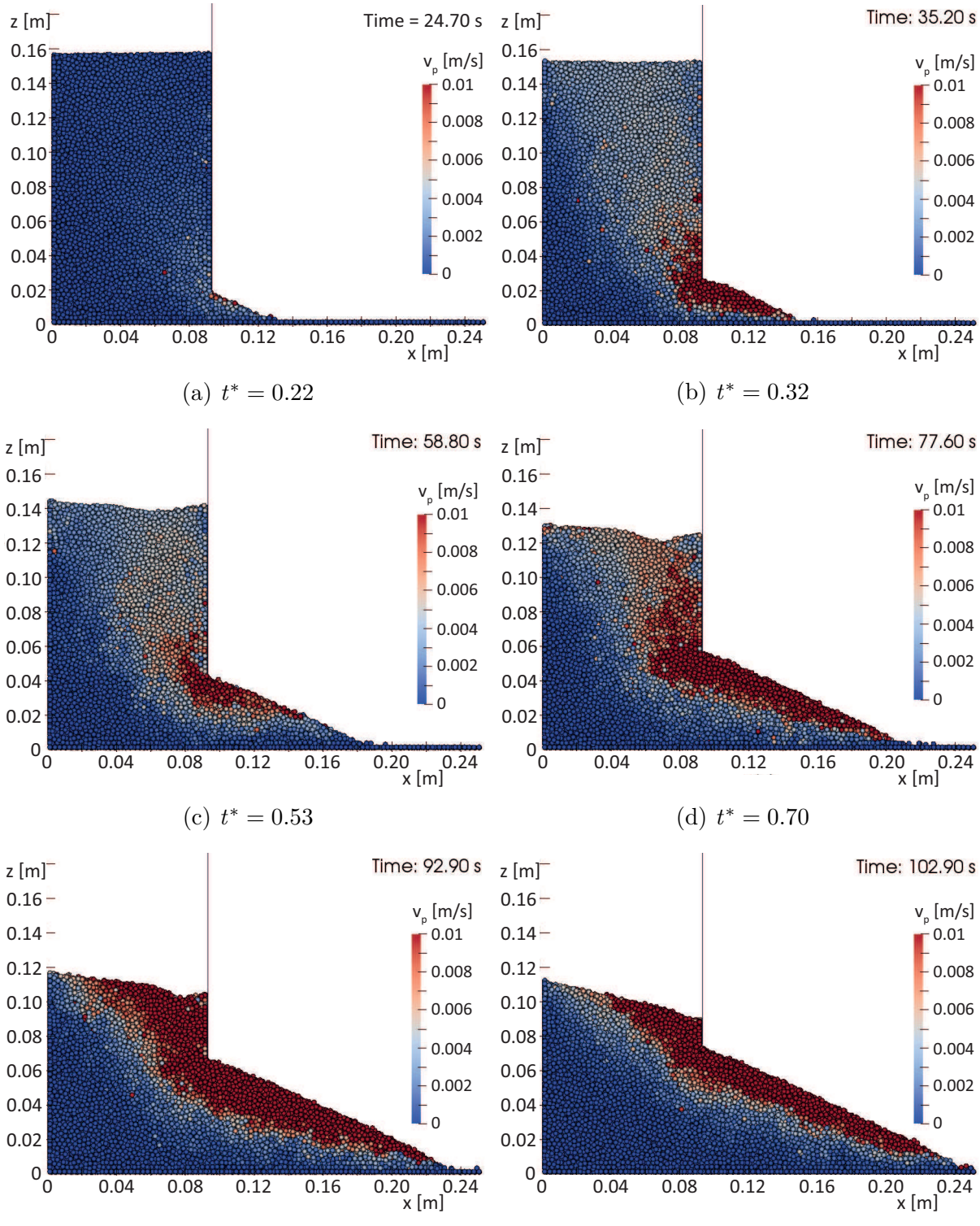

(a) $t^* = 0.22$ (b) $t^* = 0.32$

(c) $t^* = 0.53$ (d) $t^* = 0.70$

(e) $t^* = 0.84$ (f) $t^* = 0.93$

Figure 6.16: Simulation of slow collapse of particle column with 3 mm glass particles - Characteristic slumping mechanisms at different time represented by the particle velocity v_p

(see Figures 6.16a and 6.16b). Further, the curved sliding joint at the lower area of the slumping mass lies deeper than in the physical tests. Thus, a greater amount of mass seems to be displaced in horizontal direction.

This behaviour is confirmed by the particle displacement illustrated in Figure 6.17. The particle displacements over different time intervals are presented. The moving particle mass and the corresponding slip joint can be clearly identified by the particle paths. As already presented in Figure 6.16, the bottom of the curved slip joint is positioned deeper than in the physical tests. After half of the simulation, the slip joint reaches the fixed bottom plate. Thus, the whole shear failure mechanism is affected by this fixed boundary edge. Just in later stages (see Figure 6.17c), the slip joint is positioned above the fixed plate. However, Figure 6.17 proofs that the slumping mechanism includes a greater area and, thus, more material than in the physical tests. This difference might be motivated by particle friction. The effect of the particle friction coefficient on the moving volume above the slip joint is further investigated in the later sensitivity study.

By illustrating the particle displacements, the whole extent of the slumping volume becomes more clearly. This is especially true for the upper part of the slumping volume. As discussed in Section 6.2.3, the slip joint of the material is divided by a curved lower part and a straight part in the upper section of the particle column. However, at the immediate visible surface of the particle column, the slip joint of the slumping mechanism merges into a flatter joint of the surface discharge. In this surface discharge the particles of the column surface move slowly into the direction of the movable wall, towards the hollow of the funnel. As a consequence, the estimation of the angle for the straight slip joint is precarious. Figure 6.17 presents further an estimation for the slip joint angles. These angles vary up to 4° for the different initial packings. In average, the slip joint angles are 67.1° at $t^* \approx 0.36$, 69.1° at $t^* \approx 0.53$, 63.1° at $t^* \approx 0.71$ and 55.0° at $t^* \approx 0.89$. The simulations of the 1.15 mm particles result in slightly smaller angles, which is reasonable due to the reduced particle size and, thus, friction angle of the material. All initial packings for the 3 mm and the 1.15 mm particles have in common that the angle becomes steeper between $t^* \approx 0.36$ and $t^* \approx 0.53$. This increase of steepness results from a widening of the curved part in the lower slumping body (see Figure 6.17b). This widening is based in the development of the slumping mechanism in the early stages of the collapse. In 6.17a the area affected by slumping reaches the fixed plate. This fact is congruent with the perception in Figure 6.16b of a deeper lying curved sliding joint at the lower area of the slumping mass than in the physical tests. As a result, the slumping mechanism cannot fully develop, since an expansion to lower areas is not possible. However, with processing extraction of the movable wall, the wall tip relocates in positive z-direction. Since the wall tip is also the centre of the lower ground shear failure mechanism, the higher position promotes the full development of the curved slip joint. This effect might be even intensified by the decrease of the load due to the remaining particle column with proceeding collapse. This effect is not present in the physical tests, since the curved part of the slumping mechanism is not as deep as in the simulations. As a result, the curved slip joint is already fully developed at earlier stages than in the physical tests. Thus, the angles of the straight slip joint decrease from the beginning of the formation of the slumping mechanism. In the simulations, this decrease is congruent to the later stages after the full development of the

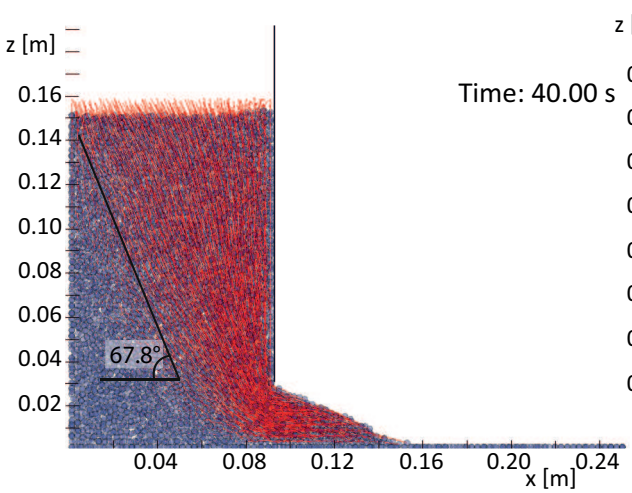

(a) Particle displacement till $t^* = 0.36$

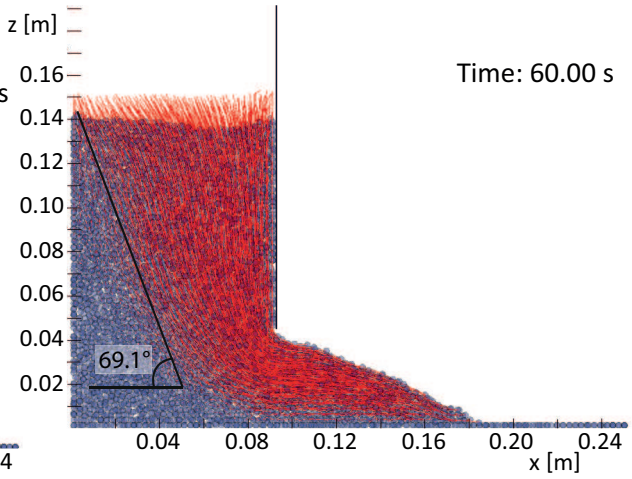

(b) Particle displacement from $t^* = 0.36$ till $t^* = 0.53$

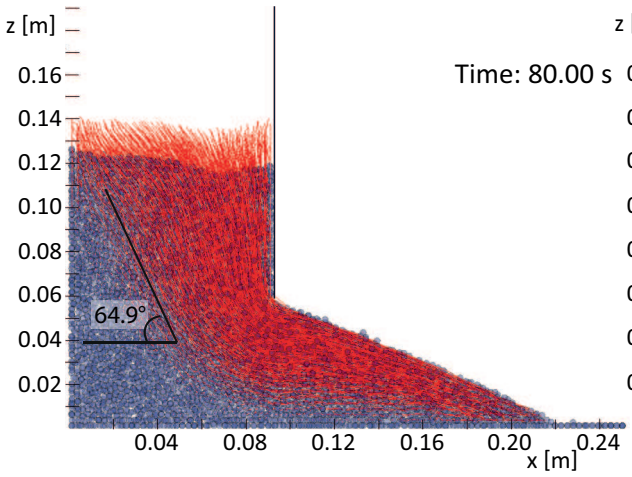

(c) Particle displacement from $t^* = 0.53$ till $t^* = 0.71$

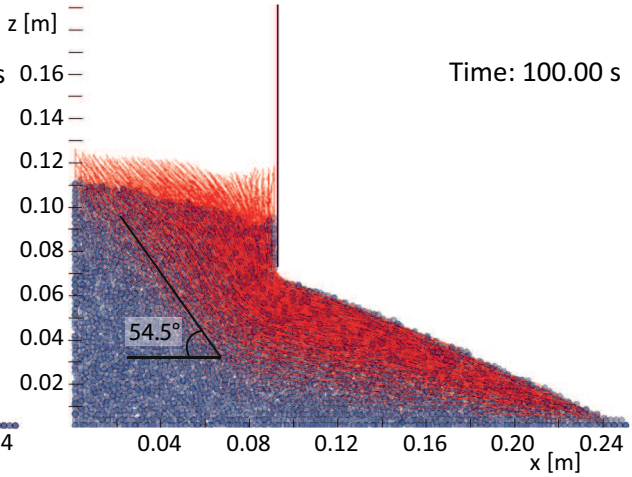

(d) Particle displacement from $t^* = 0.71$ till $t^* = 0.89$

Figure 6.17: Slow collapse of particle column under dry conditions - particle displacements over the slumping process

slumping mechanism.

The simulation enables a closer study of the slumping behaviour within the particle column. The layered initial particle packing allows the observation of the long-term internal displacements during the slow collapse. The particle displacements of the individual layers at different stages of the simulation are presented in Figure 6.18. At the early stage of the simulation, the particles pour through the growing gap beneath the movable wall. Thereby, the discharge of particles consists of particles of the layer, in which the movable wall foot is embedded (see Figure 6.18a). As a consequence, the deposit slope comprises the layered structure of the particle column. However, the layered structure of the particle column is clearly affected by slumping already at this early stage. The lower particle layers slope down and merge into the layers of the discharge slope. Due to this particle movement, all

the layers positioned above slope down as well, but show a less steep inclination than the layers below. Further, the layers are clearly affected by the extraction of the movable wall. All adjacent particles next to the movable wall are lifted during the extraction process. In Figure 6.18a this is most pronounced for the third and forth layer from the bottom of the particle column. While the lower particle layers show a clear sink next to the wall, the higher layers are characterised by a small but more even lowering. This is due to the slumping mechanism and the run of the sliding joint. The areas to the left side beneath the sliding joint of the lower particle layers are not affected by the slumping, while above the joint the displacements due to slumping increase with increasing vicinity of the movable wall (see Figure 6.16b). Contrary to the lower particle layers, the higher layers are affected equally by the slumping over the whole column width. This results from a more uniform distribution of the particle displacements in a greater distance to the particle outlet at the foot of the movable wall, due to the widening of the affected slumping mass with increasing height. However, this uniform displacement of the upper layers is valid for the early stages of the collapse only. With proceeding discharge and slumping, the increasing skewness of the lower layers result in a likewise increasing skewness of the upper layers (see Figure 6.18b). Thereby, especially the upper three layers show an intense sink approximately 2 cm left of the wall. This sink can be explained by the slumping mechanism illustrated in Figure 6.16d. At the therein presented slumping event, the highest particle velocities and, thus, greatest displacements occur approximately 2 cm left of the movable wall for the higher particles layers. The particles nearer to the movable wall are influenced by the frictional forces and the lift of the movable wall.

At this stage of the simulation another phenomenon becomes clearer. The layers inside the deposit slope become evident in Figure 6.18b. However, the layers are neither parallel to the deposit slope angle nor to the sliding joint angle inside the particle column. While Figure 6.18a shows layers which are almost parallel to the deposit slope angle, Figure 6.18b illustrate a rather flat layers in the deposit slope. This flatting can be explained by the particle discharge and the following avalanche. As discussed previously, the area of the slumping mass is of greater extent for the simulations compared to the physical tests. This is especially true for the lower area of the slumping mass along the curved sliding joint, which results from the load of the overlying particles. While in the physical tests the joint was positioned approximately 1.5 cm beneath the foot of the movable wall, in the simulations the lower curved sliding joint is positioned approximately 2.5 cm beneath the embedded wall foot. As a result, the horizontal discharge in the simulations is greater than in the physical tests. A comparison of a video sequence of the physical tests and the simulations proofs this assumption. Especially at later stages of the collapse, the horizontal particle discharge in the simulation is significant larger and comprises deeper areas than in the physical tests. This horizontal discharge is responsible for the flattening of the layers in positive x-direction in the simulations. The discharge of the particles seems to be less shallow than seen in the physical tests. Further, the avalanche seems to entrain more particles than expected. As a result, the layered structure flattens near the foot of the deposit slope and the particles from different layers mingle.

Since the development of the inner slumping mechanism differs slightly between the physical test and the simulation, the outer silhouette differs slightly as well. The outer silhouette

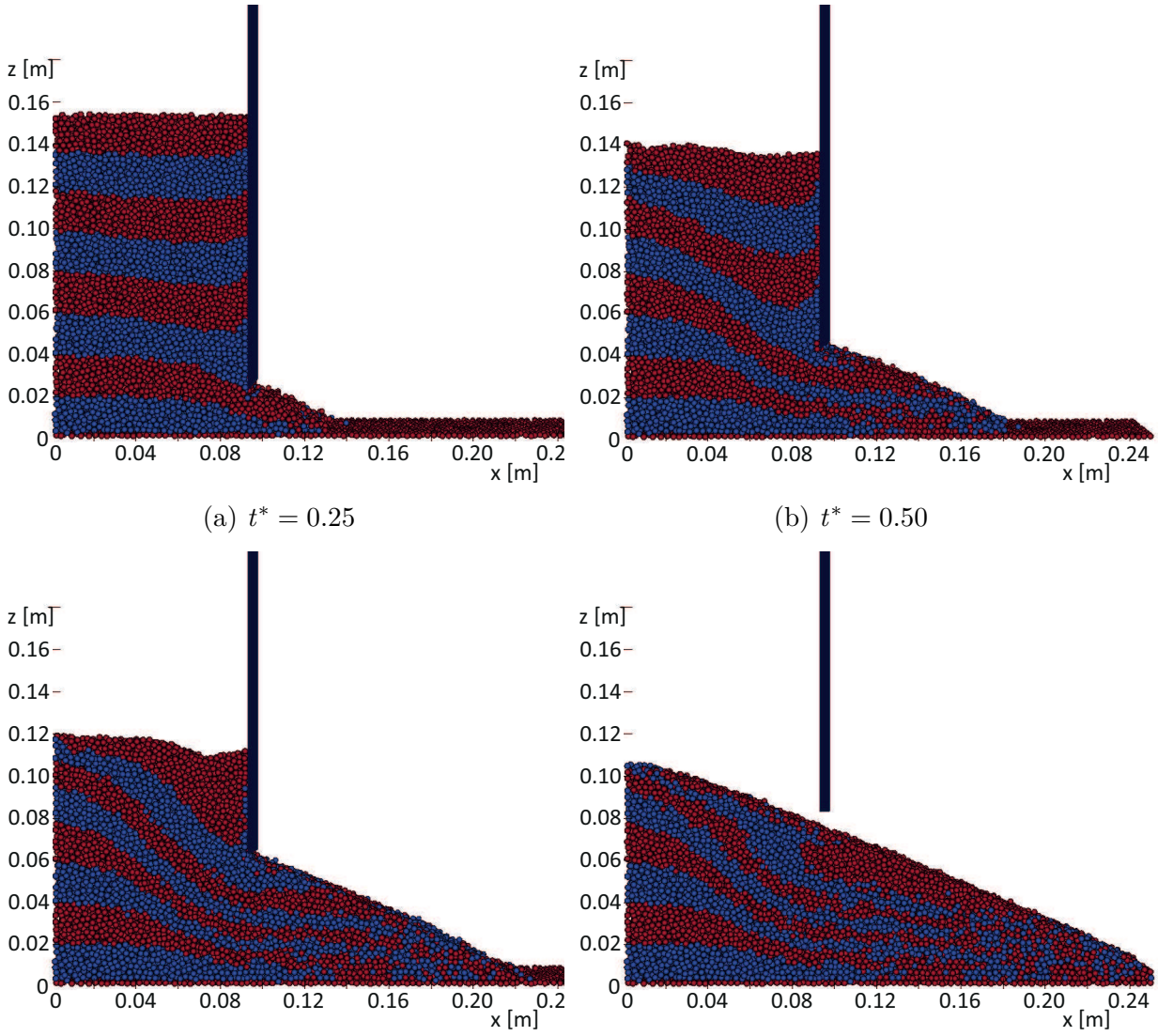

(a) $t^* = 0.25$ (b) $t^* = 0.50$

(c) $t^* = 0.75$ (d) $t^* = 1.00$

Figure 6.18: Simulation of slow collapse with particles of 3 mm diameter - Particle slumping and mixing illustrated by evolution of coloured particle layers during slumping process

during the collapse process of the simulation as well as the physical tests is presented for the 3 mm particle case in Figure 6.19. The comparison of the physical tests and the simulation at $t^* = 0.63$ shows differences for the shape of the surface of the particle column. While the surface in the physical tests is slightly inclined downwards, the surface in the simulations is flatter. Although the surface in the simulations inclines downwards as well, the surface angle is smaller than in the physical test. This might be caused by the wider slumping area of the simulations. However, the analysis of the video sequences of the physical tests and the simulations identifies another influencing factor. In the physical tests, the evolving drawdown in the surface is compensated by a surface discharge from the left side only. The simulations show a compensation from the left as well as the right

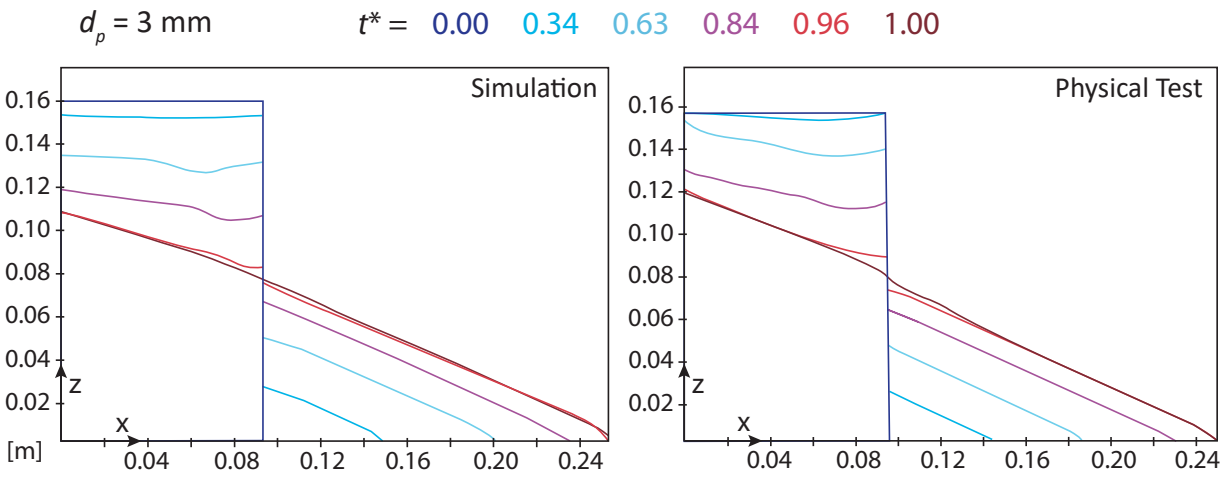

Figure 6.19: Evolution of outer silhouette of the deposit during a slow collapse simulation (left) and physical test (right) for 3 mm glass particles

side near the movable wall. Thus, the generation of a steeper slope on the left side if prevented. This effect is illustrated in Figure 6.18c. In Figure 6.18c the examination of the most upper red layer shows the entrainment of a few blue particles from the layer underneath in adjacent vicinity of the movable wall. This implies an upwards facing particle movement near the movable wall, which results in an additional surface discharge from the right side into the drawdown of the column surface.

The differences in the slumping mechanism are most likely caused by the particle contact formulation in the simulation. The greater slumping areas might result from incorrect calculations of the normal or tangential forces of the particle-particle contact, caused by e. g. a wrong property set. Thus, the influence of the individual properties on the contact modelling is investigated in the sensitivity study described in see Section 6.3.3. Further, the previously discussed upward particle movement near the movable wall is caused by the particle-wall contact model formulation. The effect of the extraction of the movable wall onto the adjacent particles seems to be overestimated in the simulations. The tangential movement of the adjacent particles due to the contact with the movable wall is overestimated. Thus, the tangential interaction forces between particles and wall seems to be too high or the sliding criteria for the tangential forces (presented in Section 4.1.1) is too high, which is equivalent to a too high particle-wall friction. The most probable responsible properties of the contact modelling are the coefficient of Coulomb's friction μ_s and rolling friction μ_r for the particle-wall contact. The reduction of the Coulomb's friction would reduce the maximum force before the particle slides along the wall surface and, thus, would reduce the lifting of particles due to the wall.

The less inclined surface slope of the particle column in the simulations is consistent during the whole collapse process. Figure 6.19 illustrates that the slope angle stays flatter than in the physical tests also for the normalised times at $t^* = 0.84$ and $t^* = 0.96$. However, the development of the deposit slope shows better accordance. The angle of the deposit slope is consistent in the simulations. Thus, the outer silhouettes of the deposit slope remain

parallel to each other during the collapse. This is in accordance with the physical tests. In contrast, the comparison of the development of the deposit slope foot shows differences at individual points in time. The major difference occurs at $t^* = 0.63$. At this time, the foot is positioned at $x \approx 0.200$ m in the simulation, while it is positioned at $x \approx 0.186$ m in the physical tests. However, this phenomenon can be explained by the slumping mechanism which proceeds in intervals. Thus, a discharge and the resulting avalanche might occur slightly later in the simulation than in the physical tests. As a result, the process for the slow collapse seems to differ slightly. Especially with progressing time, the effect of a single discharge event becomes more significant on the position of the slope foot since the amount of mobilised mass is greater than in early stages of the collapse. However, the foot position of the deposit slope is in good accordance for the other points in time in Figure 6.19.

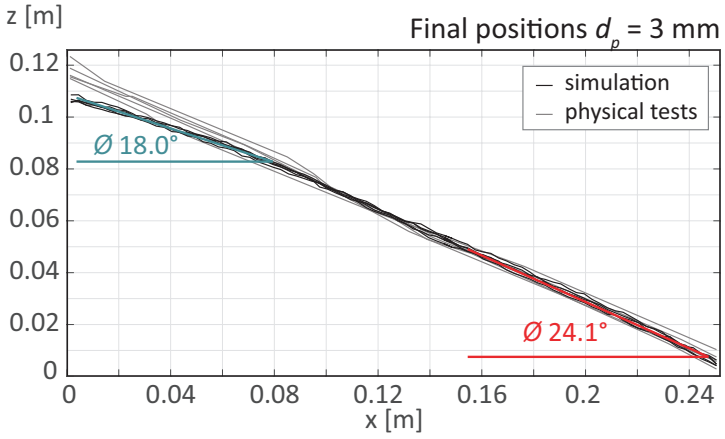

Figure 6.20: Resulting final deposit shape for slow collapse simulation with 3 mm particles (left) and 1.15 mm particles (right) diameter

As a result of the deviation between the simulation and the physical test in the outer silhouette during the slow collapse, the final shape of the deposit differs as well. While the angle of the deposit slope (slope foot) seems to agree with the physical tests, the upper part of the slope (slope top) shows clearly deviations. Figure 6.20 presents the final positions of all simulations (black lines) and physical tests (grey lines) for the 3 mm case. Further, the corresponding final angles of the slope are summarised in Table 6.5. The deposit slope seems to be in good agreement with the tests. The average slope angle at the slope foot in the simulations is with 24.1°±0.36° just slightly steeper than in the physical tests with an average of 23.9°±0.30°. However, the angle of the slope top differs significantly between the simulation and the physical test. While the simulations result in an average top angle of 18.0°±0.70°, the physical tests result in an average angle of 22.9°±0.54°. Thus, the ratio between the foot and the top angle of the final slope is with an average of 1.33 even greater in the simulations than in the physical tests (see Table 6.5). This behaviour is similar for the 1.15 mm particles. While the slope was constantly inclined in the physical tests, the slope has a bend in the position of the movable wall. Thereby, the angle is in average 21.5°±0.32° for the slope foot and 18.3°±0.67° for the slope top, which results in an angle

ratio of 1.2°±0.06°. The significant difference in the average top and foot angle for the tests and the simulation result from the previously discussed evolution of the surface of the particle column in the simulation. Since, the angle of the left slope is already smaller during the slow collapse compared to the physical tests, the angle of the final state is smaller too. However, the standard deviation of the physical tests and the simulation are equally small. Thus, the simulations model the scenario realistically.

Although the slumping mechanism inside the particle column differs slightly between simulation and physical test, the deposit of the avalanching particles seems to be modelled correctly. The deposit slope of a granular material is defined by the angle of repose ϕ. For loose, cohesionless, dry material the angle of repose can be determined by the angle of internal friction φ and the corresponding coefficient of Coulomb's friction μ_s (Kolymbas, 2011). A steeper deposit angle would imply a higher coefficient of Coulomb's friction. However, this correlation is not necessarily true for the numerical simulation. First, the angle of internal friction defines directly the coefficient of Coulomb's friction in the physical tests. In the numerical simulations, the angle of internal friction is influenced by the coefficient of Coulomb's friction as well as by the coefficient of rolling friction of the contact formulation. Thus, a direct transfer of φ to μ_s might not be possible. Second, although the frictional coefficients of μ_s and μ_r have a high impact on the calculations of the tangential contact forces the difference of the internal slumping behaviour might be caused by other properties of the contact formulation or from an incorrect contact modelling in general. To investigate the influence of the individual properties and to improve the numerical results further, a sensitivity study is conducted.

Table 6.5: Results of the slow collapse simulations for glass particles with a diameter of 3 mm and 1.15 mm

Sim	Glass 3 mm				Glass 1.15 mm	
	Slope angle top	Slope angle foot	Ratio foot/top	Duration [s]	Slope angle	Duration [s]
1	17.5°	23.7°	1.35	111.0	23.4°	103.7
2	17.5°	24.7°	1.41	109.9	23.4°	100.6
3	17.4°	24.0°	1.29	110.4	23.7°	100.0
4	18.7°	24.2°	1.28	112.4	-	-
5	18.8°	24.1°	1.28	110.4	-	-
∅ Sim	18.0° ±0.70°	24.1° ±0.36°	1.33	110.8 ±0.97°	21.5° ±0.32°	-
∅ Tests	22.9° ±0.54°	23.9° ±0.30°	1.04	99.4 ±1.54	23.4° ±0.22°	102.2 ±2.2

Besides the final state angles, Table 6.5 presents the duration of the simulation. The duration of the numerical simulation is identified via the analysis of global kinetic Energy.

Therefore, the global kinetic energy E_{kin} and the global rotational kinetic energy $E_{\text{kin,rot}}$ are an output during the simulation. The kinetic energy and the rotational kinetic energy are defined by

$$E_{\text{kin}} = \frac{1}{2} m_p v_p^2 \quad \text{and} \tag{6.6}$$

$$E_{\text{kin,rot}} = \frac{1}{2} m_p \omega_p^2 \quad . \tag{6.7}$$

The global value of these parameters represents the sum of kinetic energy of all particles in the DEM algorithm. Figure 6.21 presents the development of kinetic energy during a slow collapse test for a 3 mm particle simulation. The kinetic energy varies between approximately 10^{-4} J at discharge/slumping events and 10^{-9} J during the resting phase between those events. The end of the simulation is defined as the point in time the final kinetic energy drops beneath a value of 10^{-11} J. At this point, no movement of the particles is visible any more. After the slope stabilised, further slumping events of few particles are recognized by a global kinetic energy above the threshold value. Additionally, the discharge/slumping events during the slow collapse can be identified by the kinetic energy. In Figure 6.21 each peak represents an interval of particle movement due to deposit avalanches or slumping. Thereby, the height of the kinetic energy peaks tends to increase with proceeding simulation. This results from the amount of mobilised particles during a slumping/avalanche event as well as the higher particle velocities at later stages of the slow collapse.

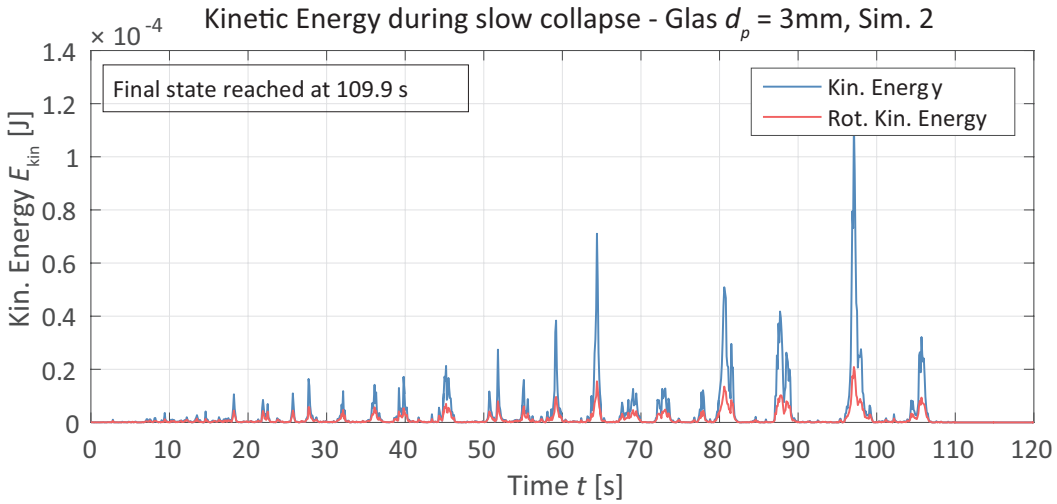

Figure 6.21: Kinetic energy E_{kin} and rotational kinetic energy $E_{\text{kin,roll}}$ during a slow collapse test with 3 mm particles

The analysis of the kinetic energy results in an average simulation duration of 110.8 s for the slow collapse of the 3 mm particles. This is significantly more than the duration of the physical tests with a duration of 99.4 s duration. In contrast, the standard deviation of the collapse duration in the simulations (±0.97 s) is smaller than in the physical tests (±1.54 s). The comparison of the position of the deposit slope foot of the simulations and

the physical tests during the slow collapse showed that the physical tests elapse slightly faster than the simulations. At the early stage of the collapse, the temporal shift is not recognisable. At 60 s the temporal shift appears to be $\approx$ 1 s. At 80 s the temporal shift increased dramatically to $\approx$ 6 s. At the end of the collapse, this temporal shift has increased to $\approx$ 10 s. The reason for this behaviour is unclear. Since the case of the slow collapse was investigated to analyse the simulation behaviour of a less dynamical case, the system dynamics were expected to have less impact on collapse process. However, it might be that the dynamic part of the contact formulation has a higher impact than expected. Another influence is of course the influence of the statical part of the contact formulation or the chosen properties for the contact formulation model. Further, the extraction velocity of the movable wall in the simulations might differ slightly from the reality since some problems in the consistency occurred. Since the time shift between the physical tests and the simulations is significant, the effect of the contact modelling onto the simulation duration is investigated in the sensitivity study.

6.3.3 Sensitivity study on slow collapse

The sensitivity study of the numerical model considering the slow collapse is performed to answer the questions raised in Section 6.3.2. Therefore, single properties of the contact formulation are varied and their influence onto the slumping mechanism and final state is analysed:

- Young's modulus
- Poisson's ratio
- coefficient of restitution
- coefficient of Coulomb's friction for particle-particle contact
- coefficient of Coulomb's friction for particle-wall contact
- coefficient of rolling friction

The initial particle packings of Section 6.3.2 are used within the sensitivity study. Since the stationary condition at the initial state of the individual particle packings is based on the previously applied property setting in Section 6.3.2, an additional step needs to be implemented in the simulations of the sensitivity study to reach the stationary conditions after adoption of the properties. Therefore, the simulation is extended by an additional initial step of 2 s, before the movable wall is lifted. Afterwards, the simulation proceeds identical to the previous simulations.

As already presented in Section 6.3.2 the calculation time for the numerical simulations is excessive. Thus, the calculation time of the simulations is decreased by a reduced simulation time for the sensitivity study. This is achieved by an increased extraction velocity of the movable wall. Instead of 0.7 mm/s the wall is lifted with 1.15 mm/s. The increase of 1.4 times the original lifting velocity is not expected to have a huge impact on the slumping mechanism. To verify the similarities of the slumping mechanism for an increased extraction velocity and the slow extraction velocity, the simulations of Section 6.3.2 are repeated considering the faster extraction velocity. The results are presented in Table 6.6.

The total duration of the collapse decreases to an average of 77.6 s. The average results of the final slope shapes for different wall extraction velocities show minimal deviations. Thus, the final top and foot angle are 18.5° and 23.6° for the faster extraction and 18.0° and 24.1° for the original case. However, the standard deviation of the results increases significantly for the foot angle from ±0.36° to ±0.67°. In contrast the standard deviation for the top angle reduces from ±0.70° to ±0.54°. However, all standard deviations are still very small for geotechnical purposes. Due to the small number of comparative simulations, the standard deviation might even increase for a representative population. Nonetheless, standard deviations are sufficiently small to consider the results of the simulations with increased extraction velocity as satisfying.

Table 6.6: Results of the slow collapse simulations for glass particles with 3 mm and 1.15 mm diameter

Sim	Glass 3 mm				Glass 1.15 mm	
	Slope angle top	Slope angle foot	Ratio foot/top	Duration [s]	Slope angle	Duration [s]
1	19.0°	24.4°	1.17	77.8	23.4°	103.7
2	18.5°	23.3°	1.17	77.9	23.4°	100.6
3	17.6°	22.6°	1.20	77.3	23.7°	100.0
4	18.0°	23.8°	1.21	77.4	-	-
5	18.4°	23.7°	1.22	77.8	-	-
∅ Sim ($1^{mm}/_{s}$)	18.5° ±0.54°	23.6° ±0.67°	1.28	77.6 ±0.27	23.4° ±0.70°	102.2 ±0.70°
∅ Sim	18.0° ±0.70°	24.1° ±0.36°	1.33	110.8 ±0.97°	23.4° ±0.97°	102.2±0.97°
∅ Tests	22.9° ±0.54°	23.9° ±0.30°	1.04	99.4 ±1.54	23.4° ±0.22°	102.2 ±2.2

The first variations of the sensitivity study are conducted for the Young's modulus, the Poisson ratio as well as the coefficient of restitution. The Young's modulus as well as the Poisson ratio are included within the spring and the dashpot component of the contact force calculation. The coefficient of restitution is taken into account for the dashpot component only. Hence, all properties influence the damping behaviour in the collapsing particle system. This influence is of interest for the development of the collapse in the simulations. As far as the properties have a significant impact on the particle behaviour in the simulations, the overall duration of the simulations might be affected as well. This might be an explanation for the longer duration of the simulations in comparison to the physical tests. However, the sensitivity analysis of the Young's modulus, the Poisson ratio as well as the coefficient of restitution show no significant influence on the slow collapse

characteristics. Thus, the results are presented in the Appendix **??**. Nonetheless, the results of this studies are discussed with the results of the other studies in Section 6.3.4.

The slow collapse case is part of the investigation of the submerged dam break problem to analyse the collapse behaviour considering reduced damping influence and, thus, to analyse the effect of frictional forces on the final results as well as the slumping behaviour. As a consequence, damping is not expected to change significantly through the variation of its characteristic values. In contrast to the previously discussed variations, the variation of the friction coefficients are expected to have a higher influence on the collapse characteristic. In the sensitivity study the Coulomb's friction coefficient and the coefficient of rolling friction for the particle-particle contact are varied. Further, the Coulomb's friction coefficient for the particle-wall contact is varied to investigate the impact of lift forces on the slumping mechanism. The sensitivity study is conducted for the 3 mm particle case.

Influence of coefficient of Coulomb's friction for particle-particle contact μ_s

The coefficient of Coulomb's friction μ_s represents a key parameter for the calculation of tangential contact forces. As presented in Section 4.1.1, the coefficient of Coulomb's friction defines the upper limit, which the tangential spring forces can reach considering the Coulomb's criterion. Therein, the upper limit $F_{p,t,\max}$ is defined by the product of the coefficient of Coulomb's friction and the total normal contact force as $F_{p,t,\max} = \mu_s \cdot F_{p,n}$. If the tangential force is smaller than $F_{p,t,\max}$, the tangential contact force can be determined by the Hertz contact model. If the tangential force would exceed the upper limit, the particles begin to slide and $F_{p,t}$ is equated to the Coulomb's criterion $F_{p,t,\max}$. Thus, the coefficient of Coulomb's friction defines the point where two particles in contact begin to slide. As a consequence, the resistance against sliding is increased for a higher coefficient of Coulomb's friction. In the slow collapse test, this should affect the angle of the deposit slope as well as the slumping mechanism. As described in Section 5.2.3, the chosen value for the coefficient of Coulomb's friction $\mu_s = 0.48$ is based on the friction angle φ', which has been determined by triaxial tests. For dry non-cohesive soils, the friction angle is often set equivalent to the angle of repose ϕ for a loose soil sample. Thus, the friction angle can be compared to the angle of the deposit slope in the physical tests or the simulations. The triaxial tests determined an angle of friction of $\varphi' = 25.5°$ for the 3 mm material. This is similar but slightly higher with 1.8° than in the results for the final deposit slope in the physical tests. However, the column collapse is accompanied by an internal slumping mechanism and, thus, horizontal internal movements. As a result, the tests are not fully comparable to the classical pouring tests, in which the angle of friction can be distinguished by tests. However, the deposit slope angle should increase significantly with an increasing coefficient of Coulomb's friction. In the variation of the sensitivity study, the coefficient of Coulomb's friction is chosen as 0.48, 0.51, 0.55, 0.60, 0.70 and 0.80.

Figure 6.22 presents the top and foot angle of the slope for its final state. The results of all initial packings and the average values are also included within the figure. Further, a linear trendline is approximated for the average values of the slope angles. The results for the angle of the deposit slope foot clearly increases with an increasing coefficient of Coulomb's friction. Thereby, the linear trendline matches the average values very well. The average values deviate just slightly from the trendline. The average values and their standard deviation are summarised in Table 6.7. The deposit slope angle increases from

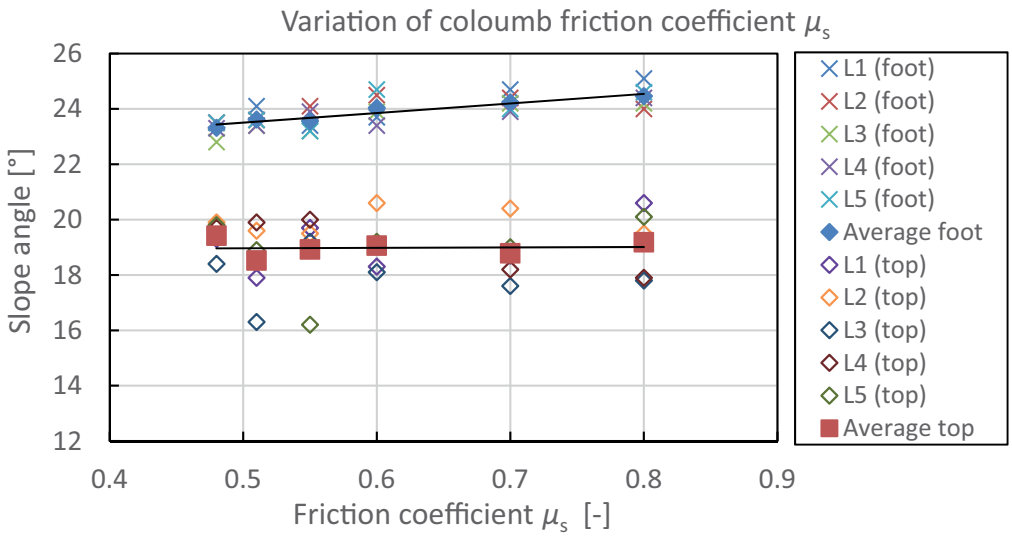

Figure 6.22: Final top and foot angles at the final deposit shape for the variation of the coefficient of Coulomb's friction with 3 mm glass particles

an average value of 23.3° in average for the initial friction coefficient of 0.48, to an average of 24.5° in average, for the maximum friction coefficient of 0.80. Thereby, the standard deviation of all variations is small, with a maximum deviation of ±0.55° for $\mu_s = 0.60$. The corresponding friction angle for $\mu_s = 0.80$ is $\varphi' = 38.7°$. Thus, the simulation defines a significant smaller angle of repose than the equivalent friction angle corresponding to the defined coefficient of Coulomb's friction. This discrepancy increases with increasing coefficient of Coulomb's friction. Thus, the assignment of the friction angle based on the coefficient of Coulomb's friction is not appropriate for the angle of repose of the final deposit slope. A relevant factor within this result might be that two friction parameters (coefficient of Coulomb's friction and rolling resistance) are handled within the contact formulation. Thus, the direct comparison of one of these parameter with the angle of repose might be inappropriate.

Further, the final top slope angles are presented in Figure 6.22. The trendline of the average results represents a consistent average angle of approximately 19.0° for all variations of the coefficient of Coulomb's friction. The individual results of the different initial packings show significant differences. The standard deviation is significantly higher than the variation of the results of the deposit foot angle. The maximum deviation is ±1.55° for the variation considering $\mu_s = 0.55$. The significant differences over identical parameters independent of the variation of μ_s imply, that the top angle depends less on the friction parameter than the particle arrangement at the end of the test. Very low angles of 18.0° or less represent the final state with a clear plateau in the area of the former particle column. However, the development of a specific final arrangement seems not to be related to the coefficient of Coulomb's friction since e. g. the plateaus develop for all variations. However, to identify a possible relationship between the coefficient of Coulomb's friction and the slumping mechanism, the column collapse and the internal deformations are investigated.

Table 6.7: Average results of the variation of the coefficient of Coulomb's friction for the slow collapse with glass particles of 3 mm diameter

coefficient of Coulomb's friction [-]	Slope angle top	Slope angle foot	Ratio foot/top	Duration [s]
0.48	19.4° ±0.61°	23.3° ±0.30°	1.20	78.5 ±1.22
0.51	18.5° ±1.46°	23.6° ±0.29°	1.28	77.1 ±0.83
0.55	18.9° ±1.55°	23.6° ±0.42°	1.25	79.1 ±1.07
0.60	19.1° ±0.99°	24.0° ±0.55°	1.26	77.5 ±1.30
0.70	18.8° ±1.05°	24.2° ±0.32°	1.29	78.2 ±0.61
0.80	19.2° ±1.28°	24.5° ±0.42°	1.28	79.4 ±1.25
∅ Sim	18.5° ±0.54°	23.6° ±0.67°	1.28	77.6 ±0.27
∅ Tests	22.9° ±0.54°	23.9° ±0.30°	1.04	99.4 ±1.54

A comparison of the particle displacements of the variations reveal a time delay of the collapse development in time for the simulation with the higher friction coefficients. This relation becomes also apparent by reviewing the average simulation duration in Table 6.7. Although, for $\mu_s = 0.48$ and $\mu_s = 0.55$ a slight deviation from the described trend in terms of the duration exists. However, the total duration of the column collapse is affected mainly by two aspects: First, the total development during the collapse and, second, the final discharge event. The final discharge event influences the total collapse duration. Thereby, the point of the final state is reached after a single big avalanche, which results in slope ratios between 1.1 and 1.3, or a smaller avalanche in combination with the development of a plateau corresponding to slope ratios of approximately 1.3 and greater. However, in some cases, the final state is not reached after the final avalanche when the movable wall is fully lifted. Rather, a second smaller avalanche event occurs subsequently to the first one, which involves a smaller amount of particles or even single particles only. This event increases the total duration of the column collapse, although the collapse itself has no delay. However, an explicit relationship between the final avalanche mechanism and its duration cannot be identified for the variation of the friction coefficient. Thus, the collapse process development is considered for the analysis of influences from the friction coefficient variation.

As described previously, the collapse process seems to be delayed for the higher values of the friction coefficient. This becomes evident for the height of the column surface, as well as the particle displacements (see Figure 6.23). For the simulations involving $\mu_s = 0.80$, the surface height is clearly higher than for the cases with lower friction coefficients. Further, the particle displacements are smaller for reduced coefficients of Coulomb's friction. This phenomenon can be explained by the shape of the tip for the deposit slope. Figure 6.23

presents a detail of the deposit slope and the particle displacements after 20 s for $\mu_s = 0.48$ and $\mu_s = 0.80$. At this early stage of the collapse, the deposit slope angle for $\mu_s = 0.80$ is clearly greater. The steeper angle reduces the amount of discharged material, before the gap between the movable wall and the deposit slope is closed again. As a result the reduced amount of discharge material causes a delay in the collapse process and, thus, reduced particle displacements.

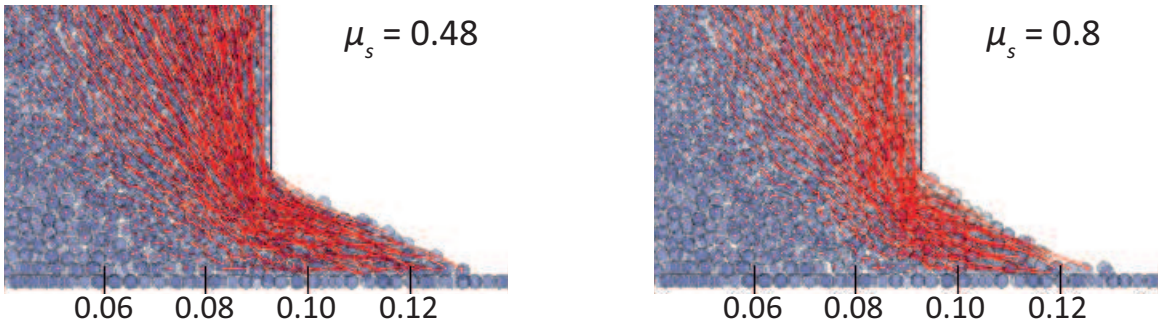

Figure 6.23: Detailed illustration of the particle displacements at the deposit slope after 20 s of simulation time for $\mu_s = 0.48$ (left) and $\mu_s = 0.80$ (right)

The inner slumping mechanism is of high interest for the variation of the friction coefficient. However, the differences in the variations are less intense than expected. Besides the previously mentioned differences due to the steeper deposit slope and a resulting delay in the collapse process, the slumping deviates only slightly. Figure 6.24 presents the particle displacements at $t^* \approx 0.51$ for different μ_s. The angles of the straight part of the slip joint are plotted for the individual variation. Thereby, the angles decrease with increasing μ_s. Though, this trend is not as obvious for all initial packings. However, the increase of the straight slip joint angle in approximately the first half of the collapse, which has been observed in Section 6.3.2, occurs also in the simulations of the μ_s variation. Thereby, the increase of the straight slip joint angle seems to be unaffected from the value of μ_s. Nevertheless, the shape of the slip joint seems to be slightly different in the variations. For the original value of $\mu_s = 0.48$ the lower part of the slip joint is curved to a greater extent at the transition from the straight to the curved part of the joint than for the higher μ_s. As a result, the width in x-dimension of the slumping volume in the height of the joint transition decreases with increasing μ_s. This effect is valid for all simulations. The increased friction affects the development of the logarithmic spiral. Due to the wider width for simulations involving $\mu_s = 0.48$, the logarithmic spiral seems more curved than for the other cases. As a result, also the depth of the logarithmic spiral seems to be affected. For $\mu_s = 0.8$ the displacements occurs at a small distance above the fixed particle layer, while for $\mu_s = 0.48$ and $\mu_s = 0.60$ the displacements are present adjacent to the fixed particle layer.

The small differences in the form of the logarithmic spiral result from the increased resistance against sliding for particle contact. Due to the higher resistance, more particles resist the slumping movement. This resistance does not affect the slip joint angle of the slumping mechanism in the variations. However, the development of the logarithmic spiral

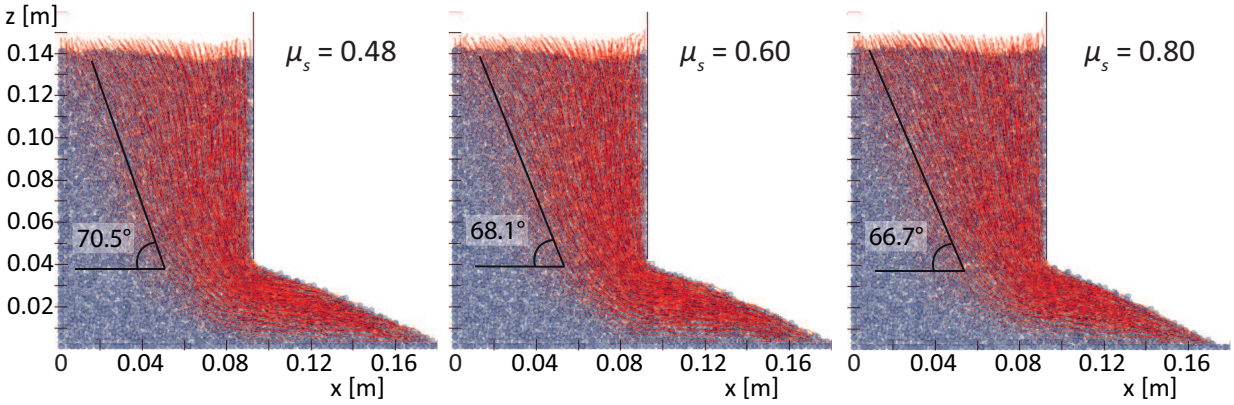

Figure 6.24: Particle displacements of initial packing 1 after $t^* \approx 0.51$ for $\mu_s = 0.48$ (left), $\mu_s = 0.60$ (middle) and $\mu_s = 0.80$ (right)

is affected. Especially at the transition from a vertical to a horizontal movement of the particles, the higher resistance results in a shift of the slip joint into the direction of the deposit slope. All variations of μ_s show less significant influences of μ_s on the slumping mechanism than expected. In contrast, the development of the deposit slope shows an obvious impact of μ_s.

Influence of the coefficient of Coulomb's friction for particle-wall contact $\mu_{s,w}$

In addition to the coefficient of Coulomb's friction for the inter particle contacts, the coefficient of Coulomb's friction for the particle-wall contact $\mu_{s,w}$ represents an important property for the correct modelling of the slumping mechanism. As presented in Section 6.3.2, the simulations show a high entrainment of single particles by the movable wall. Those particles are lifted over the height of a particle layers as shown in Figure 6.18. Further, this entrainment results in opposite directed forces on the adjacent particles. This effect can influence the development of the surface angle of the particle column. In the simulations this angle is clearly less steep than in the physical tests. Thus, the assumption of equal values for the coefficient of Coulomb's friction for particle-particle and particle-wall contacts might not be sufficient. To investigate the effect of particle-wall friction on the angle of the column surface, the final top slope angle and the entrainment of adjacent particles to the movable wall, $\mu_{s,w}$ is varied to 0.1, 0.2, 0.3, 0.4 and 0.6. Since the entrainment of the adjacent particles by the movable wall seems to be overestimated, the focus is placed on lower values than the original value of $\mu_{s,w} = \mu_s = 0.48$. Thereby, it needs to be considered that the particle-wall contact is not limited to the movable wall but rather to all plexiglas walls of the physical tests.

Figure 6.25 illustrates the angles at the top and the foot of the final slope. The average values and their standard deviation are listed in Table 6.8. The final slope foot angles vary only slightly for the variations. This was expected since this angle is based on the particle deposit, which is unaffected by wall influences. In contrast, the particle mass of the column is affected by two plexiglas walls in x-direction. Thus, the column slumping mechanism is influenced by the particle-wall contact. However, the results in

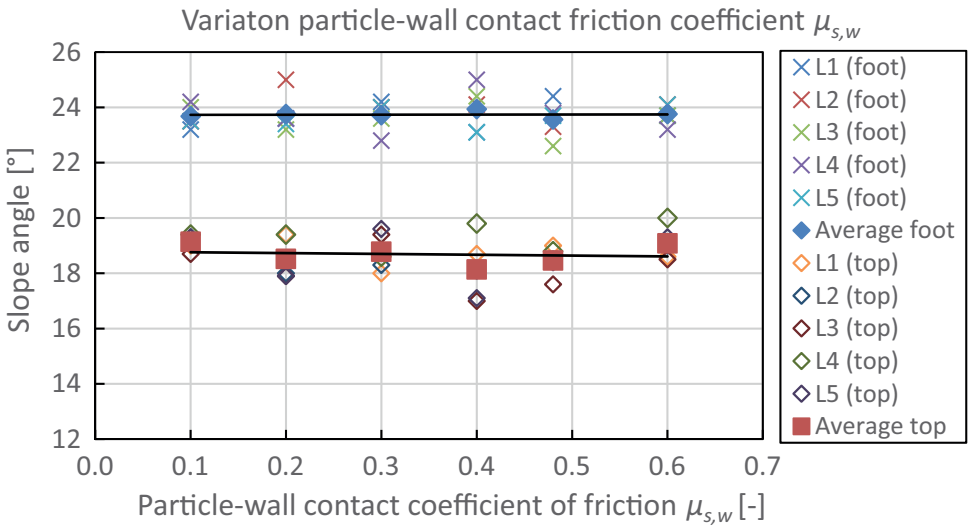

Figure 6.25: Final top and foot angles of the final deposit shape for the variation of the coefficient of Coulomb's friction at particle-wall contact with 3 mm glass particles

Figure 6.25 show no clear trend for the final slope top angle. The average values are barely different and vary between 18.1°±1.7° for $\mu_{s,w} = 0.4$ to 19.1°±0.4° for $\mu_{s,w} = 0.1$ and $\mu_{s,w} = 0.6$. Thus, the highest top angle values are obtained for the lowest and the highest value in the variation of $\mu_{s,w}$. However, the deviation of the average values in this variation is smaller than the standard deviation within each individual variation. Thus, a clear improvement for the representation of the final top angle cannot be achieved by the performed variations. Similar to the previous investigations about the coefficient of Coulomb's friction, the influence of the particle-wall contact is not significant for the development of the slumping mechanism and the development of the slope at the column surface. However, the influence of the wall might be overestimated in the beginning of the simulations as well. The variation of $\mu_{s,w}$ is always valid for both walls, which limit the particle column in x-direction. As a result, the particle column is evenly affected by the variation. This could explain, the consistency of the top slope angle. However, due to the extraction the influence of the movable wall was expected to be more significant than the static wall on the left side. This assumption was based on the strong particle entrainment near to the movable wall. However, this effect cannot be proven by the results of the performed variation.

Figure 6.26 illustrates the upper part of the particle column after 43.3 s for different $\mu_{s,w}$. The representation of initial particle layers enables the investigation of the particle displacements and the mechanism of the particle slumping. The variation of $\mu_{s,w}$ shows a significant impact on the slumping mechanism at the immediate vicinity of the walls. At the static wall on the left side, the former completely horizontal layers are inclined by different angles at the wall for different $\mu_{s,w}$. With decreasing $\mu_{s,w}$ this wall angle decreases. Since the development of this angle is based on particle displacements, the impact is greater for the upper layers e. g. the second red layer from above (see Figure 6.26).

Table 6.8: Average results of the variation of the coefficient of Coulomb's friction for the slow collapse with glass particles of 3 mm diameter

coefficient of Coulomb's friction [-]	Slope angle top	Slope angle foot	Ratio foot/top	Duration [s]
0.10	19.1° ±0.29°	23.7° ±0.41°	1.24	77.2 ±0.97
0.20	18.5° ±0.80°	23.8° ±0.71°	1.29	77.2 ±0.79
0.30	18.8° ±0.69°	23.7° ±0.56°	1.26	77.7 ±1.59
0.40	18.1° ±1.17°	23.9° ±0.83°	1.32	78.2 ±1.37
0.48	18.5° ±0.54°	23.6° ±0.67°	1.28	77.6 ±0.27
0.60	19.1° ±0.61°	23.8° ±0.37°	1.22	79.3 ±1.43
∅ Sim	18.5° ±0.54°	23.6° ±0.67°	1.28	77.6 ±0.27
∅ Tests	22.9° ±0.54°	23.9° ±0.30°	1.04	99.4 ±1.54

This region is affected by particle slumping in early stages of the collapse (see Figure 6.16). At $\mu_{s,w} = 0.1$ this angle decreases even to approximately zero. Thus, the layers are almost perfectly horizontal (see Figure 6.26 right).

As described previously, the impact of the $\mu_{s,w}$ variation is distinctive for regions with high particle displacements. Thus, the effect is significant for the vicinity of the movable wall on the right side of the particle column. The extraction of the movable wall is opposed to the movement of the particles and, thus, intensifies the effect of the wall-particle interaction. The first phenomenon of the variation of $\mu_{s,w}$ is the particle entrainment. For higher $\mu_{s,w}$ the particles in immediate vicinity of the wall are entrained by the wall. For $\mu_{s,w} = 0.6$ the particles are displaced by a distance of a layer height. As a result, blue coloured particles are entrained significantly into red coloured areas and vice versa. However, this entrainment includes only particles, which are in direct contact with the movable wall. The particles in contact with this entrained particles cannot follow this movement completely. As a result, a funnel develops, which has a minimum extend of 2.0 cm on the left sight of the movable wall. The entrainment of particles is clearly reduced for $\mu_{s,w} = 0.3$. Nevertheless, the layers are significantly deformed by the wall-particle interaction and a funnel develops, which has similar dimensions compared to $\mu_{s,w} = 0.6$. However, at $\mu_{s,w} = 0.3$ the deepest point of the funnel is positioned nearer to the movable wall, with approximately 1.5 cm distance. The development of a funnel is abrogated for $\mu_{s,w} = 0.1$. In this simulation the friction between particles and wall is reduced. Hence, no particle entrainment occurs. Further, the inclination of the adjacent particle layers is reduced to zero. This has already been observed for the static wall on the left side. As a result of the reduced particle-wall friction and, thus, resistance against the vertical movement, the development of a funnel shape is prevented.

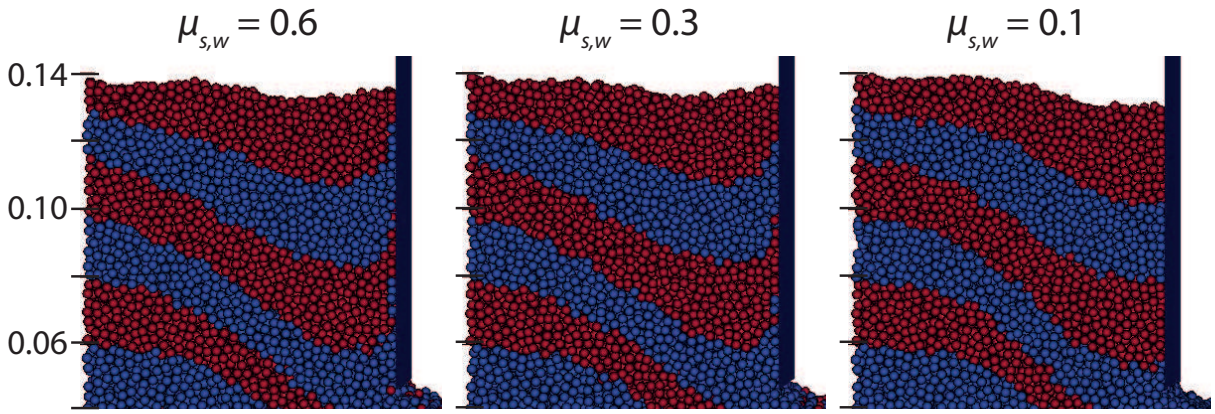

Figure 6.26: Detailed illustration of the particle paths and mixing in the particle column characterised by coloured layers after 43.3 s for different $\mu_{s,w}$

This effect can also be observed by studying the slumping mechanism. Figure 6.27 illustrates the particle velocities during one slumping event at $t^* = 0.40$ for $\mu_{s,w} = 0.6$ and $\mu_{s,w} = 0.1$. While the area of the logarithmic slumping mechanism is the same for both variations, the upper slumping mechanisms differ. For the variation with higher $\mu_{s,w}$ shown in Figure 6.27a, the affected slumping area is significantly wider than for the variation with lower $\mu_{s,w}$ in Figure 6.27b. Due to the higher particle-wall friction and resistance against vertical movement, the particles near the movable wall are decelerated. As a result, the significant particle movements into vertical direction take place a few centimetres left of the movable wall. This area of higher particle velocities corresponds to the minimum of the skewed particle layers in Figure 6.26 (left). In contrast, the highest particle velocities in the variation with $\mu_{s,w} = 0.1$ take place directly next to the movable wall. Due to the small particle-wall friction, the resistance is too low to decelerate the vertical particle movement significantly. This corresponds to the particle layer minimum directly at the movable wall in Figure 6.26 (right). Since the maximum particle displacements take place directly at the wall, the area of moving particles during slumping in the simulations considering $\mu_{s,w} = 0.1$ seems to be reduced in its width compared to the variation with higher $\mu_{s,w}$.

Although the internal particle displacements are clearly affected by the variation of the particle-wall friction, the effect on the surface of the particle column is less significant. As already discussed previously, the top angle of the final slope shows no clear trend for the variation of $\mu_{s,w}$. In Figure 6.25, the average top angles differ up by 1° only. To investigate the development of the columns top surface, the outer silhouette of the surface for different $\mu_{s,w}$ is illustrated in Figure 6.28. Thereby, the silhouettes at $t = 60$ s and $t = 74$ s are compared as an example. At $t = 60$ s, the collapse is well proceeded and the left end of the column surface has a height of 0.12 cm while the foot of the movable wall is positioned at approximately 0.62 cm from the top of the bottom plexiglas plate. At $t = 74$ s the collapse is almost finished. At this time, the column is about one centimetre high and the foot of the movable wall is positioned at approximately 0.75 cm. To enable a good comparison of the individual silhouettes, the left end of the silhouette is positioned at the

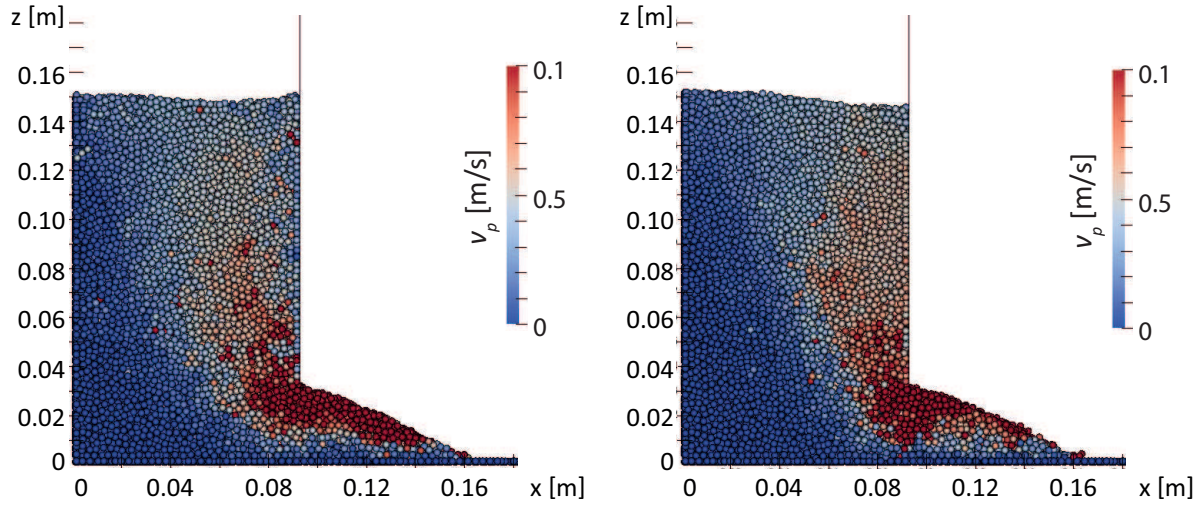

(a) $\mu_{s,w} = 0.6$ (b) $\mu_{s,w} = 0.1$

Figure 6.27: Variation of wall friction coefficient $\mu_{s,w}$ - Slumping mechanism visualised by the particle velocities v_p at $t^* = 0.40$ for $\mu_{s,w} = 0.6$ and $\mu_{s,w} = 0.1$

same starting point independent of its original height. This simplifies the comparison of the surface angles.

The silhouettes in Figure 6.28 at $t = 60$ s show minor differences in the surface angle. The angles of $\mu_{s,w} = 0.1$ and $\mu_{s,w} = 0.6$ differ by approximately 2° only. However, a tendency for steeper angles with decreasing $\mu_{s,w}$ can be observed. Thus, the silhouette for $\mu_{s,w} = 0.6$ results in the shallowest surface. The silhouettes for $\mu_{s,w} = 0.3$ and $\mu_{s,w} = 0.2$ are almost identical but a little bit steeper and the silhouette for $\mu_{s,w} = 0.1$ results in the highest inclination. However, the silhouette for $\mu_{s,w} = 0.48$ differs from that trend and has an inclination comparable to $\mu_{s,w} = 0.1$. But in contrast to the other silhouettes, for $\mu_{s,w} = 0.48$ a short distance on the left side shows a steeper slope. The subsequent part is inclined less, which seems to meet the discussed trend. Thus, the whole curve seems to be moved downwards in comparison to the other silhouettes. However, the general trend of slightly smaller surface angles for higher $\mu_{s,w}$ can be observed for other initial packings as well. Since the whole simulation process and the final result depends strongly on the initial packing, the marginal characteristics of this trend might be easily overlain by individual processes resulting from the initial packing. In the vicinity of the movable wall, most silhouettes describe the already described funnel. In contrast, the curve for $\mu_{s,w} = 0.1$ shows no increase close to the movable wall. As already observed in Figure 6.26, the silhouette ends in a steeper slope to the movable wall.

At $t = 74$ s the characteristic funnel or slope shape has vanished. Hence, all silhouettes show an evenly inclined slope defined by a greater angle than for $t = 60$ s. The highest slope angle occurs for the surface of $\mu_{s,w} = 0.6$ with 16°, while the smallest angle occurs for the surface of $\mu_{s,w} = 0.2$ with 13°. Thus, the slope angles differ by 3° only. At this point, the trend observed at $t = 60$ s seems to be inverted. The variations with higher $\mu_{s,w}$ are inclined under a bigger angle than the variations with smaller $\mu_{s,w}$. This inversion of the trend might be explained by the current slumping mechanism. The development of a

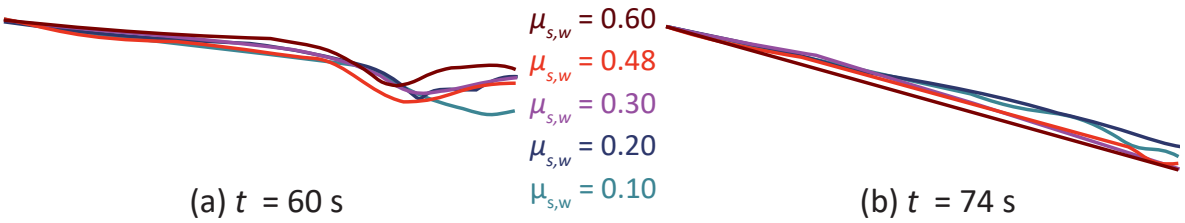

Figure 6.28: Packing surfaces on left side of the movable wall at $t = 60$ s and $t = 74$ s at initial packing 5 for different $\mu_{s,w}$

funnel is characteristic for the slumping mechanism of ground shear failure. This slumping mechanism occurs at early stages of the simulation, where the column has a certain height and, thus, a cloading is applied to the particles with a megnitude defined by the height of the occurring gap. As discussed previously, the funnel is caused by the interaction between the wall and the adjacent particles. The higher the particle-wall friction, the higher the resistance against the vertical movement of the particles. As a result, the development of a steeper slope as seen in the physical tests is prevented and the simulations with higher resistance result in shallower surfaces than those with smaller particle-wall friction. At later stages within the simulations, the load of the higher particles in the column on the lower positioned particles is so reduced significantly causing the slumping mechanism of ground shear failure to merge into a more superficial particle movement (see Figure 6.16f). With proceeding transition of this mechanism, the influence of the particle-wall resistance from the movable wall on the slumping mechanism decreases. As a result, the funnel shaped surface transforms into a smoother slope. It seems, that at this stage higher particle-wall friction supports the development of steeper slopes. However, this effect is sufficiently small to make a noticeable difference for the slope top angle of the final state.

In general the impact of the particle-wall friction on the slope top angle of the final state has been overestimated beforehand. The differences between the final angles are negligible. Hence, that possible effects or trends are less important than to the influence of the initial packing and the individual collapse mechanism. In contrast, the particle-wall friction has a high impact on the development of the internal slumping mechanism. The width of the slumping mechanism and the particle entrainment next to the movable wall is reduced for lower $\mu_{s,w}$. Since the slumping volume occurs wider in the simulations than in the physical tests (see Figure 6.7c), the particle-wall friction should be reduced for the simulations. Based on the intensity of the particle entrainment, particle-wall friction coefficients between 0.2 and 0.3 lead to better results.

Influence of coefficient of rolling friction μ_r

Before the results of the sensitivity study for the investigations of the coefficient of rolling frition μ_r is presented, the difference between the friction coefficients is discussed shortly. As suggested previously, the coefficient of Coulomb's friction μ_s represents an important factor on the column collapse simulation. The slumping mechanism as well as the development of the deposit slope are affected by the variation of the particle-particle and the particle-wall friction. While the coefficient of Coulomb's friction μ_s based on Coulomb's

friction law represents the resistance against a tangential translational sliding of a particle, the coefficient of rolling friction μ_r represents the resistance against rotational rolling of a particle. Similar to the normal and tangential contact model of Hertz the applied elastic-plastic rolling friction model described the momentum using springs and dashpots (see Section 4.1.1). Thereby, the spring momentum has a mobilisation limit, which is defined by the coefficient of rolling friction. Since μ_r represents an additional resistance against rolling a significant impact on the collapse simulation results is expected for the development of the deposit slope as well as the characteristics of the particle avalanches. Further, the transformation from a ground shear failure mechanism to a superficial particle displacement might lead to significant changes in the slumping mechanism with varied μ_r. In the variation μ_r the initial value of $\mu_r = 0.005$ is varied to 0.0001, 0.01, 0.015 and 0.02. These values of μ_r correspond to rolling friction angles φ_r of 0.06°, 0.57°, 0.86° and 1.15°.

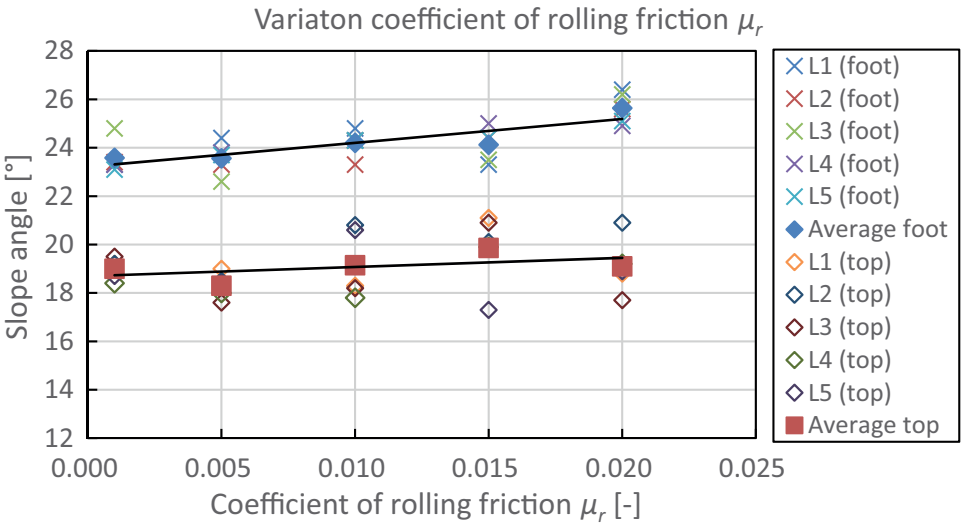

Figure 6.29: Final top and foot angles at the final deposit shape for the variation of the coefficient of rolling friction with 3 mm glass particles

The individual slope angles of the final state and the corresponding average results of the simulations are presented in Figure 6.29, which includes a linear trendline based on the average results. The average values and their standard deviation are listed in Table 6.9. According to Figure 6.29, the foot angles of the final state slope increase significantly with increasing rolling friction. Thereby, the foot angle increases by an average value of 2.0° from 23.6° for $\mu_r = 0.001$ to 25.6° for $\mu_r = 0.02$. Though, the average angles for $\mu_r = 0.001$ and $\mu_r = 0.005$ as well as $\mu_r = 0.01$ and $\mu_r = 0.015$ are in compliance. However, since the simulations show a strong dependency of the final state on the initial packing with a maximum standard deviation of ±0.70°, this accordance might converge more likely with the trendline for a higher number of simulations. Nevertheless, a clear trend can be observed for the entity of results. The individual result for the angle of the slope foot cause higher standard deviations for μ_r than the variation of μ_s, with an aberration of maximum ±0.7° at $\mu_r = 0.015$. An asymmetric or edged shape of particles results in higher particle inertias and in a higher friction angle for the material. The contact modelling extended by

an additional momentum resistance due to rolling friction, seems to reproduce this effect sufficiently.

Table 6.9: Average results of the coefficient of rolling friction variation for the slow collapse with glass particles of 3 mm diameter

coefficient of Coulomb's friction [-]	Slope angle top	Slope angle foot	Ratio foot/top	Duration [s]
0.001	19.0° ±0.44°	23.6° ±0.69°	1.24	77.5 ±0.65
0.005	18.3° ±0.54°	23.6° ±0.67°	1.28	77.6 ±0.27
0.010	19.1° ±1.44°	24.2° ±0.55°	1.27	78.0 ±0.58
0.015	19.9° ±1.52°	24.1° ±0.70°	1.22	78.8 ±1.94
0.020	19.1° ±1.16°	25.6° ±0.66°	1.34	79.2 ±1.95
∅ Sim	18.5° ±0.54°	23.6° ±0.67°	1.28	77.6 ±0.27
∅ Tests	22.9° ±0.54°	23.9° ±0.30°	1.04	99.4 ±1.54

In contrast to the foot angle, the results for the slope top angle of the final state illustrated in Figure 6.29 show no clear trend. The linear trendline describes a minimal increase with increasing μ_r. However, since the individual simulation results vary significantly, especially for the higher values of μ_r with a maximum standard deviation of 1.52° for $\mu_r = 0.015$, this trend needs to be treated carefully. To prove the validity of this trend, additional initial packings need to be investigated. However, as already observed beforehand the final top angle shows a stronger dependency on the development of the characteristic final slope. Two major mechanisms define the development of a shallow plateau with a width of the former particle column and steeper angles which result from a greater final avalanche after the extraction of the movable wall. However, the simulations show no clear trend for the final characteristics as a function of μ_r. Though, the chosen higher values for μ_r cause a greater standard deviation of the individual results.

The investigation of the slumping mechanism shows a delay for the simulations with higher μ_r. Equally to the variations of μ_s, the higher resistance against rolling results in higher angles of the deposit slope during the collapse. As a result of the higher deposit angles, the amount of material discharge is reduced. This leads to smaller delays in the collapse process compared to the simulations with lower μ_r values. This phenomenon displays in longer durations for the whole collapse process (see Table 6.9). Thus, the duration of the collapse increases with increasing μ_r. Another phenomenon is the characteristic of the individual slumping events and their frequencies. The simulations with smaller μ_r cause higher frequencies of the occurring slumping events. Thereby, especially for an early stage of the collapse, smaller slumping events with few discharges alternate with bigger slumping events with a high discharge. In contrast, for the simulations with higher μ_r the

number and frequency of slumping events is significantly decreased. Though, the slumping events for higher μ_r include bigger discharge masses for every single slumping event. This behaviour can also be observed in the output of the kinetic energy during the collapse process. Figure 6.30 presents the kinetic energy development exemplary for variations with $\mu_r = 0.001$ and $\mu_r = 0.02$ for initial packing 4. Therein, the observations from the collapse characteristics are included. While the kinetic energy in Figure 6.30a results in a higher number of peaks, the kinetic energy in 6.30b results in less but more distinct peaks. This confirms the assumption of less but bigger slumping events for higher rolling friction. This phenomenon has not been observed for the variation of μ_s. It seems, that the rolling friction coefficient has a higher impact on the slumping processes than the coefficient of Coulomb's friction.

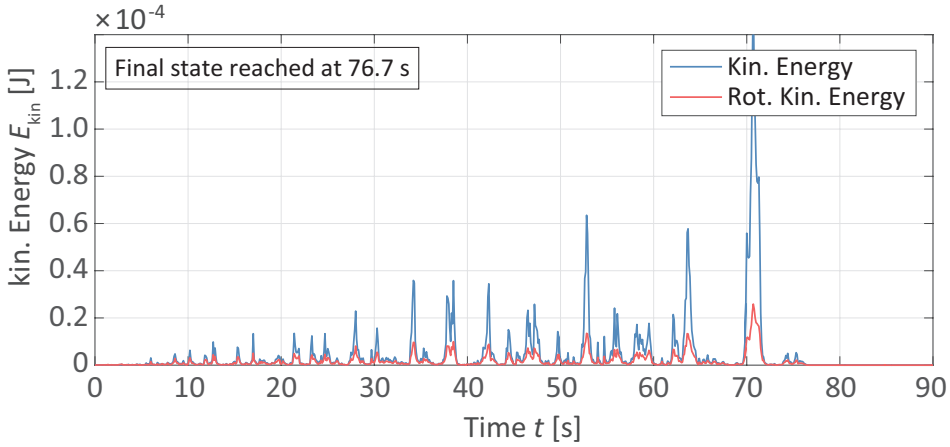

(a) $\mu_r = 0.001$

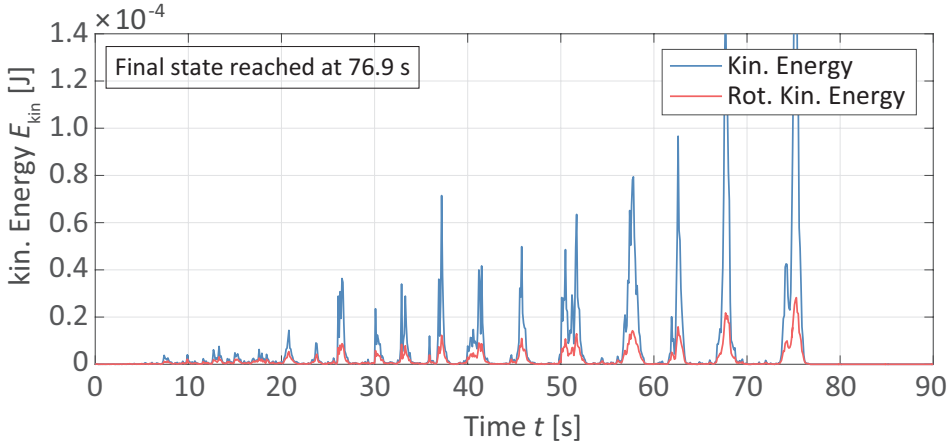

(b) $\mu_r = 0.02$

Figure 6.30: Comparison of kinetic energy evolution over time for initial packing 4 with $\mu_r = 0.001$ and $\mu_r = 0.02$

The comparison of the slumping characteristics for the different variations and initial packings shows a clear trend for the slumping mechanism. Thus, the slip joint is shifted into positive x-direction with increasing μ_r. Further, the straight slip joint is inclined under

a steeper angle. As a result, the active slumping area is slimmer for the simulations with higher μ_r. Thereby, not just the upper part of the slumping area is affected but rather the logarithmic part of the ground shear failure mechanism as well. Figure 6.31 describes the slumping mechanism by the particle velocity v_p for the variations $\mu_r = 0.001$ at $t^* = 0.43$ and $\mu_{s,w} = 0.02$ at $t^* = 0.45$. It can be seen, that the slip joint is significantly shifted into positive x-direction for the higher value of μ_r. Further, the logarithmic part of the shear failure slip joint is smaller than for the variations with lower μ_r. For the simulations with lower μ_r, the logarithmic spiral reaches the fixed particle plate. In contrast, the logarithmic spiral is limited by its slip joint above the fixed particle plate in the simulations including $\mu_r = 0.02$. This trend of the simulations is conform with geotechnical theory. A higher friction between the particles causes higher friction angles. As a result, the resistance against shearing is higher and more particles resist the slumping movement and remain stationary.

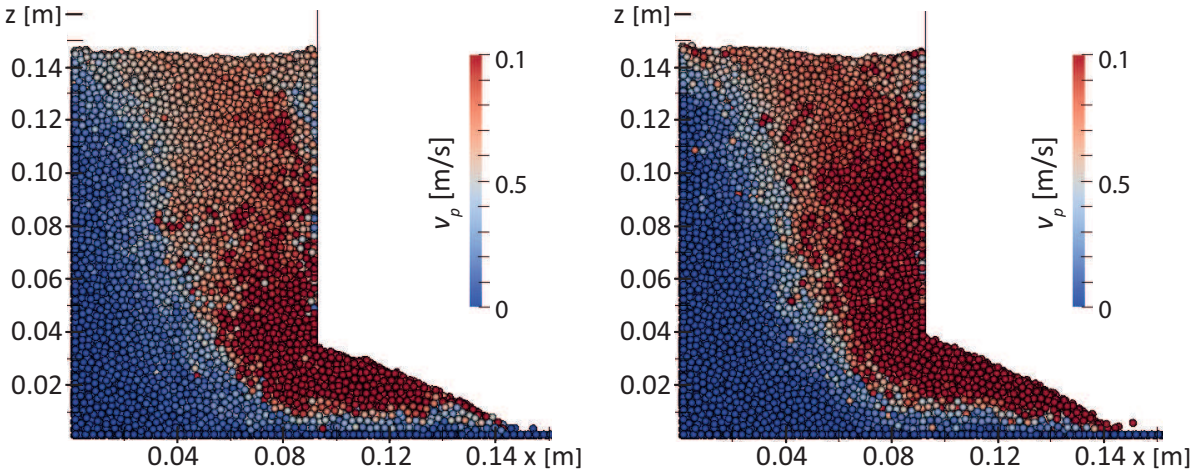

(a) $\mu_r = 0.001$ (b) $\mu_r = 0.02$

Figure 6.31: Variation of rolling friction - slumping mechanism illustrated by the particle velocity v_p for $\mu_r = 0.001$ at $t^* = 0.43$ and $\mu_r = 0.02$ at $t^* = 0.45$ (initial packing 2)

The outer silhouette of the column surface seems to be unaffected by the variation of μ_r. There is no clear trend for the development of the column surface during the collapse. However, since the investigation of $\mu_{s,w}$ showed a high impact of the friction between the particles and the movable wall on the development of the column surface, the influence of μ_r might be overlain by the influences of a high $\mu_{s,w}$.

6.3.4 Conclusion for slow collapse simulation

The sensitivity study of the slow collapse simulations provides a good insight into the contact modelling and the influences of the individual properties on the slumping mechanism. The magnitude of the influence of the individual properties varies. Thus, the Young's

modulus, the Poisson's number as well as the coefficient of restitution have a less significant impact on the mechanism of the slow column collapse. However, since the particles do not experience loads besides the columns dead weight and the collapse happens slowly, the properties were expected to have less significant influences. Thus, the simulations show a realistic description of these properties within the slow collapse mechanisms. In contrast, the variations of the coefficient of Coulomb's friction for the particle-particle as well as particle-wall contact and coefficient of rolling friction caused significant changes in the slumping mechanism as well as the generation of the deposit slope.

A major impact on the whole mechanism has been proven by the particle-wall interaction defined by $\mu_{s,w}$. Thereby, the entrainment of particle by the movable wall for the initial value of $\mu_{s,w} = 0.48$ seems to be over estimated in the simulation. In the physical tests, the surface of the column showed less influences by the movable wall than in the simulations. Thus, the value of $\mu_{s,w}$ should be reduced for further simulations. The impact of $\mu_{r,w}$ is expected to be less significant than $\mu_{s,w}$, since the particle movement adjacent to the wall is dominated by translational movements rather than rotational movements.

The variation of the coefficient of Coulomb's friction μ_s and the coefficient of rolling friction μ_r show a high impact on the slumping mechanism as well as the deposit slope. The angle of the deposit slope is significantly affected by an increase of rolling friction. For a high value in rolling friction considering $\mu_r = 0.02$ an average deposit slope angle of 25.6° developed. This high rolling friction resulted further in a reduced size of slumping area. Thus, the resulting mechanism in the simulations at high rolling friction is more likewise the mechanism in the physical tests. However, since the deposit slope angle is clearly overestimated for this high rolling friction value, the rolling friction can only be increased to a limit. Since, the variation of μ_s has a smaller impact on the slumping mechanism and the deposit slope, a suitable solution might be the general reduction of μ_s and the increase of μ_r. This in combination with a reduction of $\mu_{s,w}$ can improve the dimensions of the slumping mechanism for the slow collapse in comparison to the physical tests. Hence, this variation of the friction parameters is going to be applied in the fast collapse tests in Section 6.3.5.

In general, the simulation results of the slow collapse gave realistic results. The mechanisms of the collapse are in accordance with those of the physical tests. This includes the characteristic collapse intervals, the avalanching and development of the deposit slope as well as the internal slumping mechanism and its transformation during the collapse. Thereby, the original simulations as well as all variations of the sensitivity study lead to reliable results with good standard deviations. Although the number of conducted simulations per variation is small, the trends of the average results correspond well to geomechanical theory. In most cases the standard deviations for the final results were equal or even less than the deviations of the physical tests. However, the simulations showed a high impact of the initial packing on the final results.

To improve the material property set of the slow collapse simulations, additional variations are conducted. The parameter sets are based on the conclusions of the sensitivity study presented previously. Thus, the wall-particle friction coefficient is reduced to $\mu_{s,w} = 0.2$. Further, the coefficient of rolling friction is increased to $\mu_r = 0.007$ or $\mu_r = 0.01$, which gave better results in the sensitivity study without an overprediction of the deposit slope

inclination. The best results were achieved for the variation of $\mu_{s,w} = 0.2$ and $\mu_r = 0.007$. The average final deposit slope foot angle resulted in 23.7°. Further, the final top angle is slightly increased to an average of 20.0°. Thus, the ratio between foot and top angle is reduced. The slumping mechanism in the physical tests is better represented for the variation of the particle-wall contact considering $\mu_{s,w} = 0.2$in Section 6.3.3. A reduction of the coefficient of particle-particle Coulomb's friction resulted in no further improvement. In the end, the use of $\mu_{s,w} = 0.2$ and $\mu_r = 0.007$ is very promising to obtain realistic results for the simulation of a slow collapse of a particle column.

6.3.5 Development of numerical model for fast collapse

The numerical simulation of the fast column collapse corresponds to the conducted physical test. The dimensions of the test basin are adopted for the simulations and are equal to those in the slow collapse simulations. Further, the dimensions of the material sample in the physical tests is applied. Thus, the initial particle packings have a height of $H_0 = 10.54$ cm and a length of $X_0 = 6.2$ cm, which results in an aspect ratio of 1.7. Thereby, the height of the fixed particle layer is not included in H_0. The depth of the simulation domain was adopted from the slow collapse simulations. Thus, the boundaries in y-direction have periodic conditions and a depth of 4.5 cm for the 3 mm particles and 1 cm for the 1.15 mm particles. The x-normal as well as the lower z-normal wall has a fixed position and its properties are equal to a solid plexiglas wall (material type 2). In contrast, the simulation domain is not limited by a upper z-normal wall. As in the simulations of the slow collapse, 5 different particle packings are investigated for the 3 mm particles and 3 particle packings for the 1.15 mm particles to analyse the effect of different particle packings on the simulation results. These packings are generated by two steps of particle insertion and a gravity based settlement afterwards. The final height is reached by the elimination of the redundant particles. Further, one particle packing is generated by alternating insertion of particles of different types. Therefore, a third material type 3 if defined, which has the same properties as the remaining particles. Due to allocation of different types, the particle layers can be distinguished without a modification of the particle diameter. The number of particles and corresponding porosity for the different packings is presented in Table 6.10.

The sensitivity study of the slow collapse showed the necessity to improve the initially adopted material properties for the particles (material type 1) (see Section 6.3.4). As a result, the coefficient of Coulomb's friction μ_s is differentiated for a particle-particle (P-P) $\mu_{s,p} = 0.48$ and particle-wall (P-W) contact $\mu_{s,w} = 0.48$. Since all applied walls are of the same material type 2, the particle-wall contact properties are equal for every wall. Further, the coefficient of rolling friction μ_r of the particle-particle contact is increased to $\mu_r = 0.007$, since the characteristics of the slumping mechanism are improved.

To reproduce the physical tests, the extraction velocity of the movable wall needs to be known. Therefore, the position of the moveable wall foot is analysed during the extraction of the wall every 10 images or 0.02 s. Since, the movable wall canted during its extraction in the slow 3 mm particle tests, the fast 1.15 mm test results are adopted for the evaluation of the wall extraction velocity. In Figure 6.32 the foot height is plotted against time for

Table 6.10: Initial state packings for 3 mm and 1.15 mm particles

	3 mm			1.15 mm		
Test case	y [cm]	Number Particles	Porosity n	y [cm]	Number Particles	Porosity n
C	4.5	12505	0.399	1	49401	0.382
1	4.5	12435	0.402	1	49447	0.397
2	4.5	12434	0.402	1	49450	0.397
3	4.5	12435	0.402	1	49409	0.398
4	4.5	12456	0.401			
5	4.5	12444	0.402			

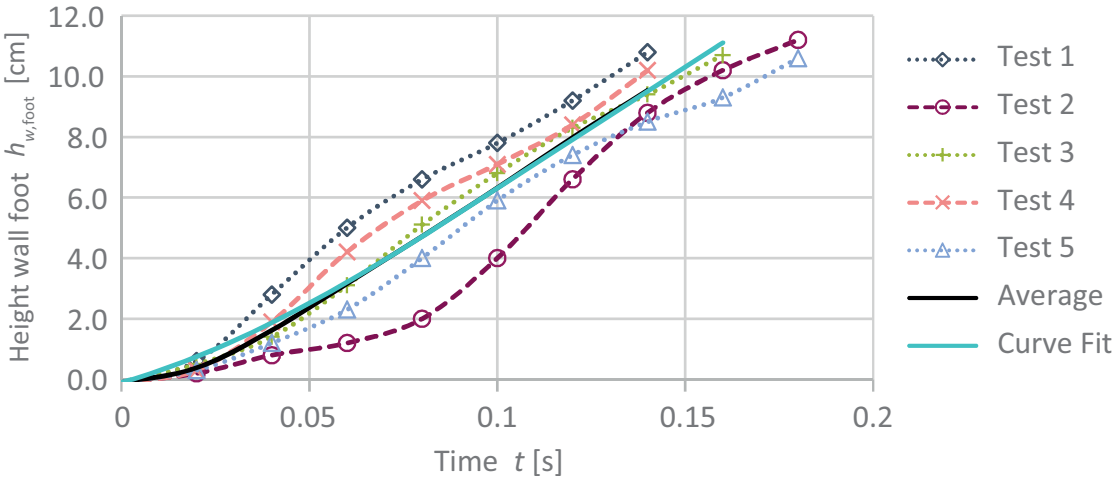

Figure 6.32: Extraction of movable wall over time in physical tests with 1.15 mm particles

every physical test. It becomes evident, that the extraction of the wall can be differentiated into an acceleration phase and a phase of constant velocity. This behaviour becomes even clearer for the averaged lifting process over all tests (see black graph in Figure 6.32). The progression of the average graph is adopted for a curve fit. The average graph can be reproduced by a polynomial function of third order to

$$z_{w,\text{foot}} = -10.9 \cdot t^3 + 4.054 \cdot t^2 + 0.3443 \cdot t \quad . \tag{6.8}$$

This curve fit is also illustrated in Figure 6.32. To reproduce the extraction velocity, the derivative of the function $z_{w,\text{foot}}$ needs to be determined. According to the average graph, the wall is moving at constant velocity after 0.87 s. Thus, the function of the wall extraction velocity was differentiated into an acceleration phase ($t < 0.87$ s) and a

constant phase ($t \geq 0.87$ s) (see Equation 6.9).

$$v_{z,\text{wall}} = \begin{cases} -32.7 \cdot t^2 + 8.108 \cdot t + 0.3443 & (t < 0.87 \text{ s}) \\ 0.8 & (t \geq 0.87 \text{ s}) \end{cases} \tag{6.9}$$

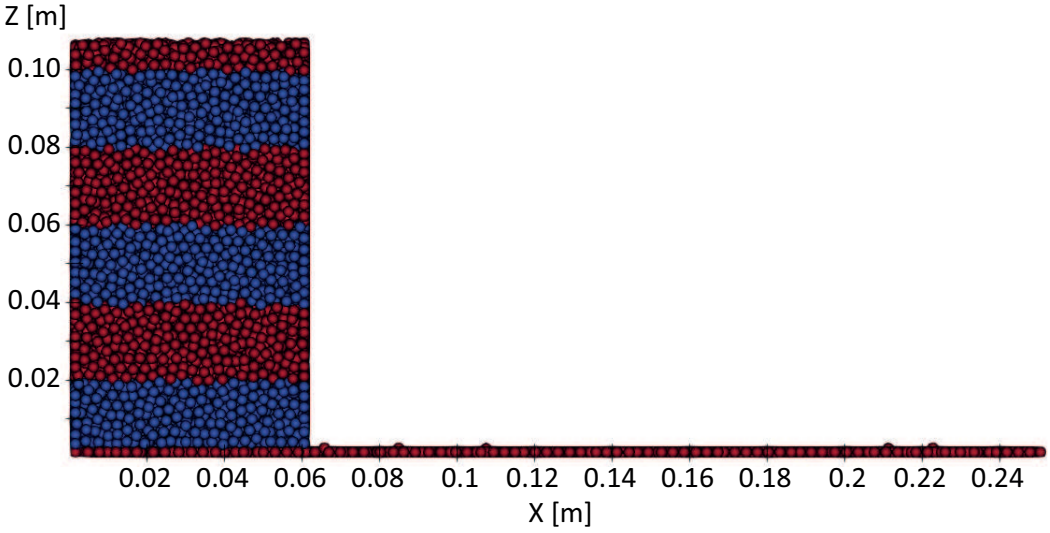

Figure 6.33: Initial state of fast collapse simulations under dry conditions with coloured identification layers for $d_p = 3mm$

6.3.6 Numerical simulation of fast collapse

The simulation of the fast particle column collapse show a good representation of the physical tests. The process of particle slumping, characterised by an acceleration phase, a phase of constant spreading are reproduced. Further, the variation of the initial packings give individual but similar results for the applied property setting. Following, the slumping mechanism and the process of the collapse is presented in detail. Therefore, the outer silhouette during the collapse are presented in Figure 6.34 as well as the internal slumping mechanism for the 3 mm particles in Figure 6.37. For further information, the internal slumping mechanism for the 1.15 mm particles is presented in the appendix in Figure B.7.

Corresponding to the physical tests, the simulation starts with the extraction of the movable wall. As a result, the material starts to exit through the growing gap at the lower right side of the column. Simultaneously, the particles which are adjacent to the movable wall are lifted by the extraction. As a result, the particles at the upper column surface near to the wall are lifted above their initial position for the 3 mm as well as the 1.15 mm material (see Figure 6.34). The lifting of upper particles adjacent to the wall occurs also in the physical tests. In contrast, the subsequent initiation of the collapse occurs differently for the test and the simulation. While in the simulation the column starts to collapse almost directly after the development of a small gap due to the extraction of the movable wall, the particles in the physical tests keep their position longer. This becomes apparent by

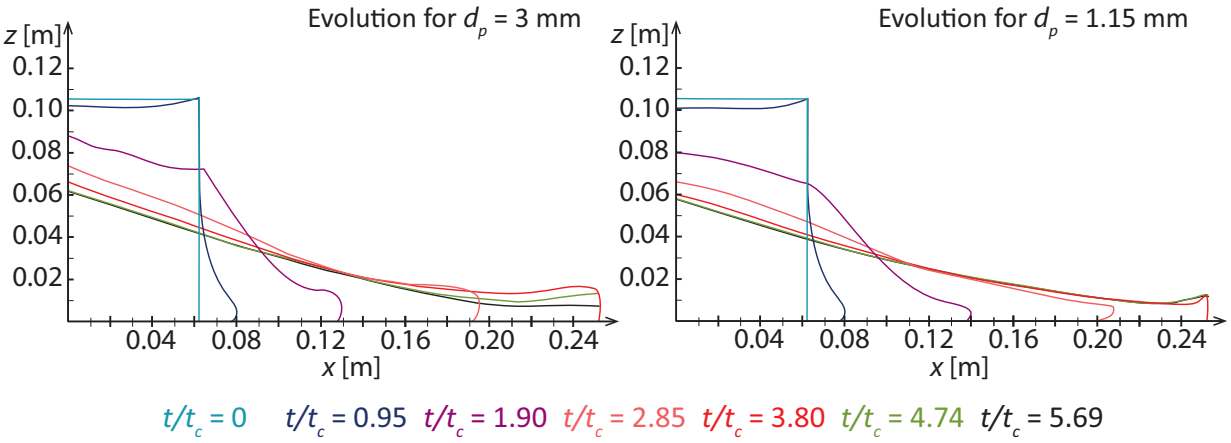

Figure 6.34: Scheme of the outer deposit silhouette over time with the 3 mm (left) and 1.15 mm (right) glass particles during the fast collapse simulation. The colour of the silhouette corresponds to the test time t

the analysis of the first displacements of the particles in the upper section of the column. As described previously, the particles near to the movable wall are lifted slightly. In contrast, the particles in greater distance to the movable wall remain in their initial position during the first moments of movable wall extraction. In the case of the physical tests, the particles remain non-displaced till a gap height of approximately 6 cm. In contrast, in the simulations occurs a subsidence of the upper particles already at a gap height of approximately 4 cm in the simulation. As a result, the whole collapse of the column is initiated earlier in the simulations for the 3 mm as well as the 1.15 mm particles. This effect becomes even clearer in the comparison of the outer silhouettes of the physical tests and the simulations for the same ratio of t/t_c during the collapse process for the 3 mm particles in Figure 6.35. At $t = 1.90\ t_c$ and the subsequent timesteps, the outer silhouette of the physical tests is delayed in comparison to the simulation. This delay in the simulation might result from less support of the column from side of the movable wall. The reduction of the particle-wall contact friction, motivated by the slow collapse simulations, might not be sufficient for the fast collapse. A higher friction between particle column and movable wall might stabilise the column for a longer time and, thus, reduce the temporal differences of the early collapse between physical tests and simulation. This influence is going to be investigated in the sensitivity study in Section 6.3.7.

When all upper particles are entrained into the collapse, the internal slumping mechanism becomes apparent. Similar to the physical tests, the movement of the upper particle mass is dominated by a vertical movement in the first instance. After the vertical displacement, the particles are deflected into a horizontal movement due to a deflection along the slip joint. This behaviour is illustrated by the path-lines of the slumping mechanism for the 3 mm particles represented in Figure 6.36. The path-lines at $t = 1.35\ t_c$ in Figure 6.36a can be clearly differentiated in a vertical dominated movement for the upper particles of the column. The illustrated slumping mechanism in the simulations are in good agreement

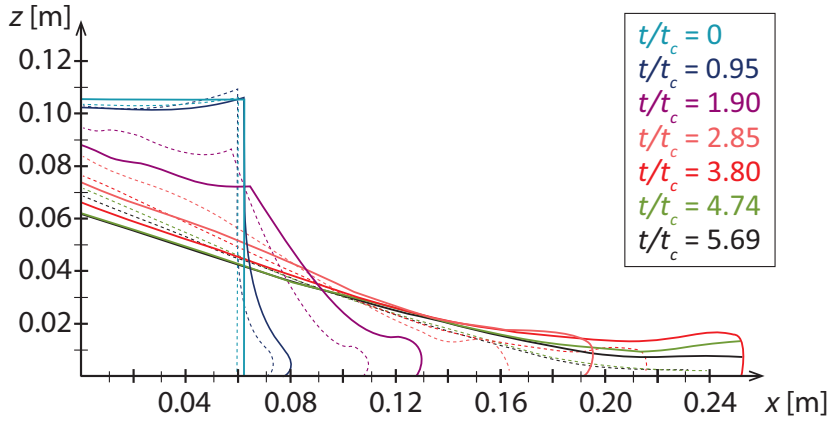

Figure 6.35: Evolution of the column slumping during collapse in the physical tests (dashed line) and the simulation (continuous line) represented by the outer deposit silhouette with the 3 mm glass particles. The colour of the silhouette corresponds to equal time ratios t/t_c

with the physical tests. The slumping mass moves along a slightly curved slip joint, similar to the slip joints occurred in the early stages of the slow collapse tests. The particles underneath this slip joint stay stationary. The upper part of the slip joint runs straight and has an inclination of approximately 45.4° in average. Thus, the resulting slip joint at this stage is significantly smaller in the simulations than in the physical tests with approximately 60°.

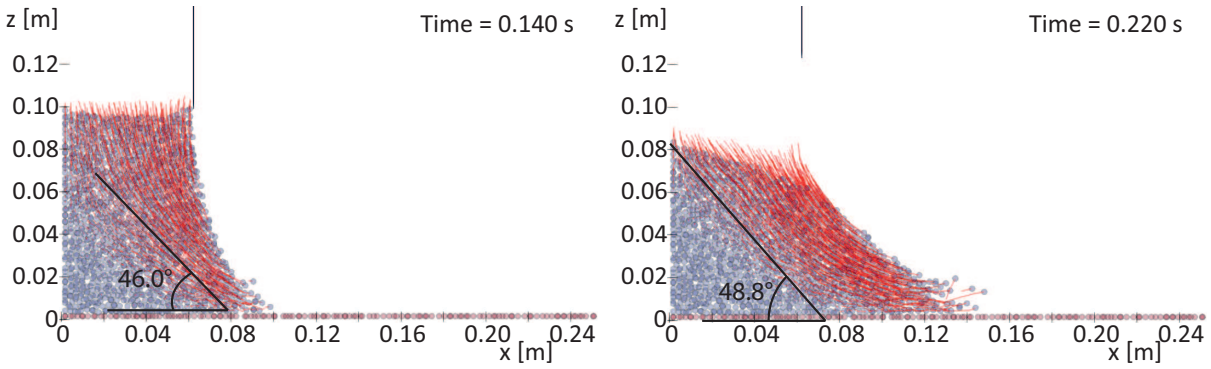

(a) $t/t_c = 1.35$ (b) $t/t_c = 2.12$

Figure 6.36: Simulation of fast collapse of particle column with 3 mm glass particles - Particle paths of particle packing 4 for $t/t_c = 1.35$ and $t/t_c = 2.12$

Figure 6.36b illustrates the path-lines at a slightly later point in the simulations at $t = 2.12\ t_c$. At this point, the vertical dominated movement has fully merged into a horizontal movement along the slip joint. This development leads to an adjustment of the slip joint. The very upper slip joint is now inclined under an angle of in average 49.2°. This is in good accordance with the physical tests, which had a inclination of approximately 50° at the same stage of the test. This slip joint can be also recognised in Figure 6.37b. In

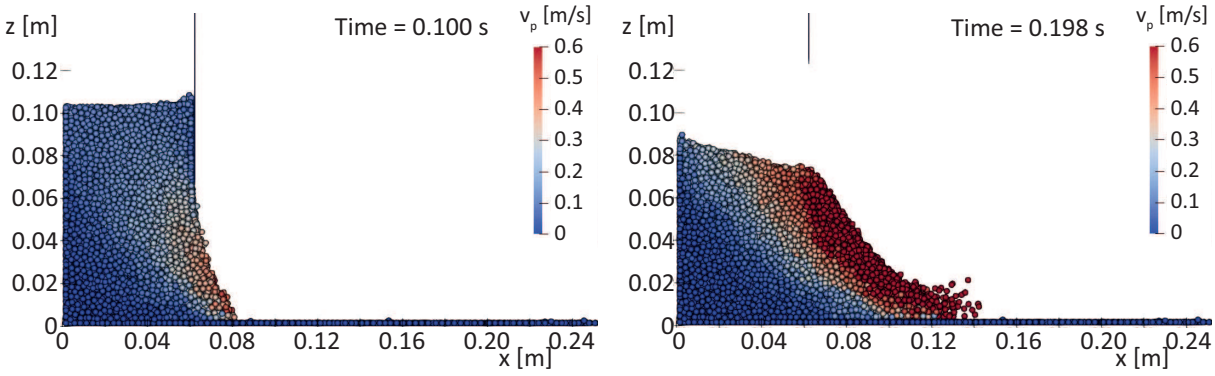

(a) $t = 0.95\ t_c$

(b) $t = 1.90\ t_c$

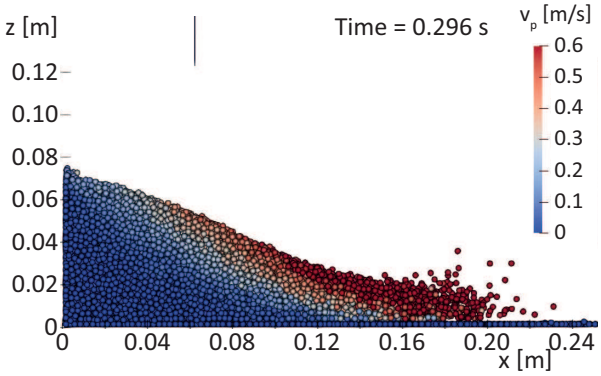

(c) $t = 2.85\ t_c$

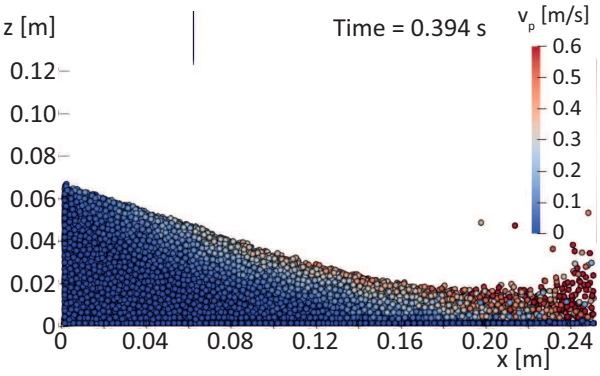

(d) $t = 3.80\ t_c$

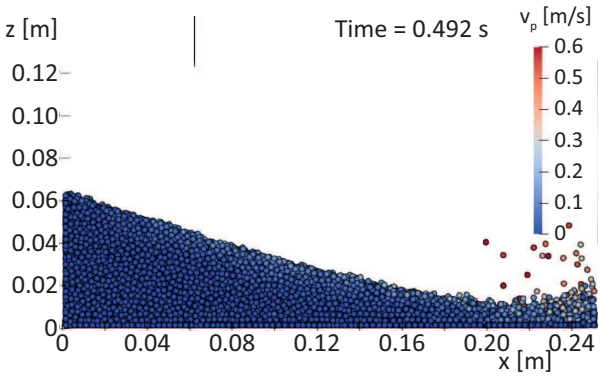

(e) $t = 4.71\ t_c$

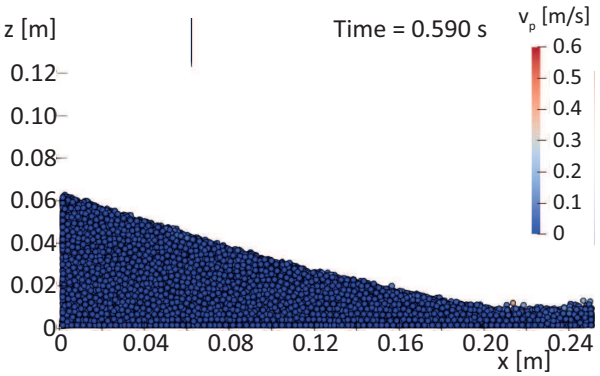

(f) $t = 5.96\ t_c$

Figure 6.37: Simulation of fast collapse with 3 mm glass particles - Characteristic slumping mechanisms at different time represented by the particle velocity v_p

accordance with the physical tests, the deposit tip as well as the particles along the slope of the former right side of the column undergo the greatest displacements and, thus, have the highest velocities, which are increased in comparison to Figure 6.37a.

At approximately 0.23 s, which is equal to $t = 2.2\ t_c$, the deposit has fully lost the markers of the initial state. At this point, the slumping mechanism of the 3 mm and 1.15 mm particles has merged to a fully horizontal dominated movement. Thus, the material expands

into positive x-direction. The velocity of the particles in the moving material decreases with increasing distance to the deposit tip as well as with increasing distance to the deposit surface (see Figure 6.37c). At the tip of the moving material, individual particles are distracted from the main material mass (see Figure 6.37c). The resulting jumping movement of these individual particles is more significant in the simulations than in the physical tests. While, in the physical tests just a few particles disengage and move slightly faster than the majority of the particles, a bigger group of individual particles is triggered in the simulations. Further, the particles jump higher in the simulations and cause a chaotic behaviour in front of the deposit tip. This behaviour is related to the elasticity of the particles. A perfect elastic behaviour is equal to a full energy conservation during an impact. The overestimated jumping characterises too much preservation of kinetic energy after an impact. This behaviour can be adjusted by a decrease of the coefficient of restitution, which is the dominating parameter in the calculation of the damping at particle contact. The influence on the slumping process is further investigated in the sensitivity study in Section 6.3.7.

With the spreading of the material, the particles at the deposit are decelerated. This is due to the influence of the interaction with the fixed particle layer and the already deposited stationary particles. However, the deposit tip remains at its high velocity and collides with the wall on the right. As a result, individual particles are reflected into negative x-direction, whilst others jump chaotic near to the static wall. This behaviour is less significant in the physical tests. First, the individual particles in the physical tests show less elastic behaviour during the impact and remain near the static wall instead of being reflected into negative x-direction after the impact. Second, the deposit tip in the physical tests is significantly more decelerated at the last stages of the spreading. As a result, the majority of the deposit tip does not reach the static wall in the tests, but is decelerated and stops before the impact with the wall. This discrepancies between physical tests and simulations become apparent in Figure 6.35. The spreading deposit slope is significantly thicker in the simulations at $t = 3.80\ t_c$, whereas the highest point of the deposit slope is significant lower than in the physical tests. Thus, the material spreading is overestimated in the simulations.

After the impact with the wall, a further spreading of the deposit is prevented. However, the particles at the immediate deposit surface continue with their movement down the slope (see 6.37e). Thereby, the number of moving particles decreases with time until single particles are moving only. In contrast to the physical tests, supplementary individual particle movement is initiated by single particles which have been previously reflected by impact with the static wall. Thus, small particle groups avalanche after collision of the jumping particles with the deposit. The final shape is reached at approximately 0.58 s for the 3 mm particles and 0.57 s for the 1.15 mm particles and, thus, at a similar time than in the physical tests with approximately 0.61 s for the 3 mm as well as 1.15 mm particles. However, similar to the physical tests, the deposit it not fully stationary at $t = 5.96\ t_c$ in Figure 6.37f. Single particles still roll over a small distance at the deposit slope. The final slope at a stationary state is presented in Figure 6.38. Thereby, the final deposit silhouettes of the simulations as well as the physical tests are illustrated. It is apparent, that the simulations result in a deposit slope under a smaller angle than in the physical

tests. While the physical tests result in an average angle of 21.4° for the 3 mm and 21.5° for the 1.15 mm case, the simulations result in an average angle of 17.4° for the 3 mm and 16.6° for the 1.15 mm case.

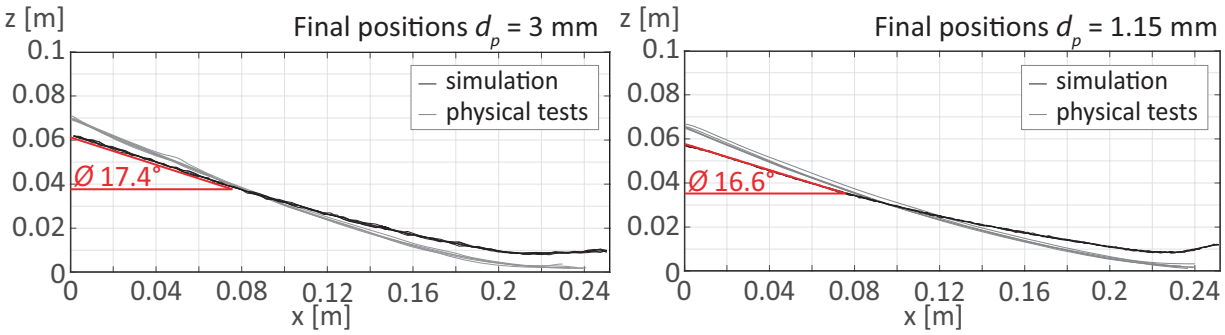

Figure 6.38: Resulting final deposit shape for fast collapse simulation with 3 mm particles (left) and 1.15 mm particles diameter (right)

The overall displacements of the particles can be obtained from the collapse of the initial packing with coloured layers for the 3 mm particles (see Figure 6.39). In contrast to the slow collapse tests, the deposit slope is not generated from superficial avalanches, but by a single entire collapse of the column and simultaneous spreading into positive x-direction. Due to the fast extraction of the movable wall, the particles in the different particle layers are engaged in the slumping mechanism almost simultaneously. A small delay between lower and the upper layers is initiated by the longer supporting effect of the movable wall for the upper layers. As a result of this abrupt collapse initiation, the internal layers are just slightly skewed between Figure 6.39a and Figure 6.39b. Due to the spreading of the deposit, the initial layers are stretched and become thinner and longer. Thereby, the particles in the lowest layers are decelerated due to the interaction with the fixed particle bottom layer and their spreading is decelerated till they become stationary. As a result, the upper particle layers spread over this stationary particles and build the final deposit which is presented in Figure 6.39d. Just the particles on the most right are arranged in a chaotic way due to the impact with the wall and the corresponding mixing.

The evolution of the deposit tip over time was analysed by extracting the position of the lowest particles. An Matlab algorithm identified the particle positions with the maximum x-component. To exclude the individual particles, which jump ahead of the deposit tip from the detection algorithm, an additional condition is implemented to extract the position of the 5 furthest (for 3 mm particles) or rather 10 furthest (for the 1.15 mm particles) particles, which are in a maximum distance of one particle diameter. Since the individual particles are more isolated from other particles, this assumption should exclude the majority of the single particles jumping ahead. Although the condition can be also fulfilled by the jumping particles, this occurrence should be in a lower frequency and could be easily identified as an outlier. The development of the deposit tip for the 3 mm and the 1.15 mm particles are presented for an exemplary simulation in Figure 6.40. For comparison purpose, the deposit evolution of the physical tests are illustrated also. It needs to be taken into account, that the origins of $t = 0t_c$ were matched for the comparison of

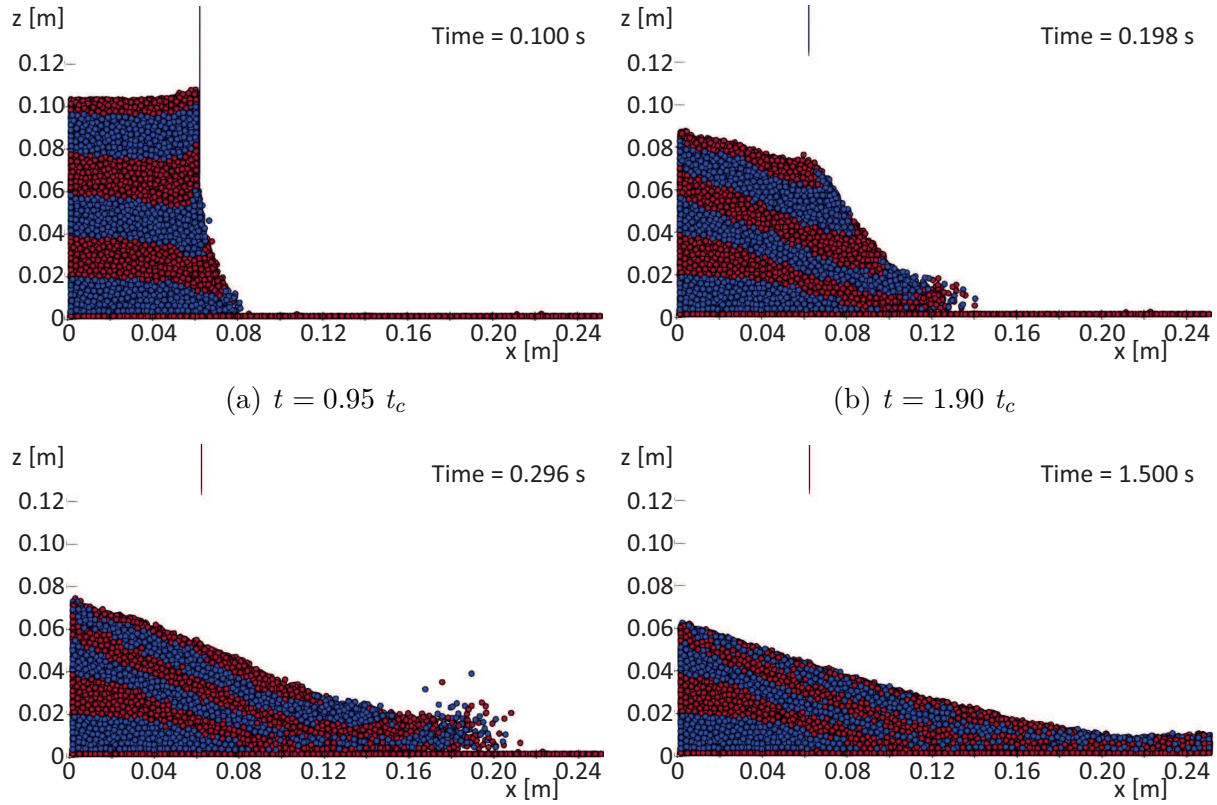

(a) $t = 0.95\ t_c$

(b) $t = 1.90\ t_c$

(c) $t = 2.85\ t_c$

(d) $t/t_c = 14.46$

Figure 6.39: Simulation of fast collapse with 3 mm glass particles - Characteristic displacements and mixing represented by coloured layers

the simulations and the physical tests. This point in time does not represent the begin of the test/simulation but rather the point of initial slumping movement. The comparison of the absolute time would show that the initialisation of the slumping is starting earlier in the simulations than in the physical tests. The results of the remaining simulations are presented in the appendix in Figure B.8 and Figure B.9.

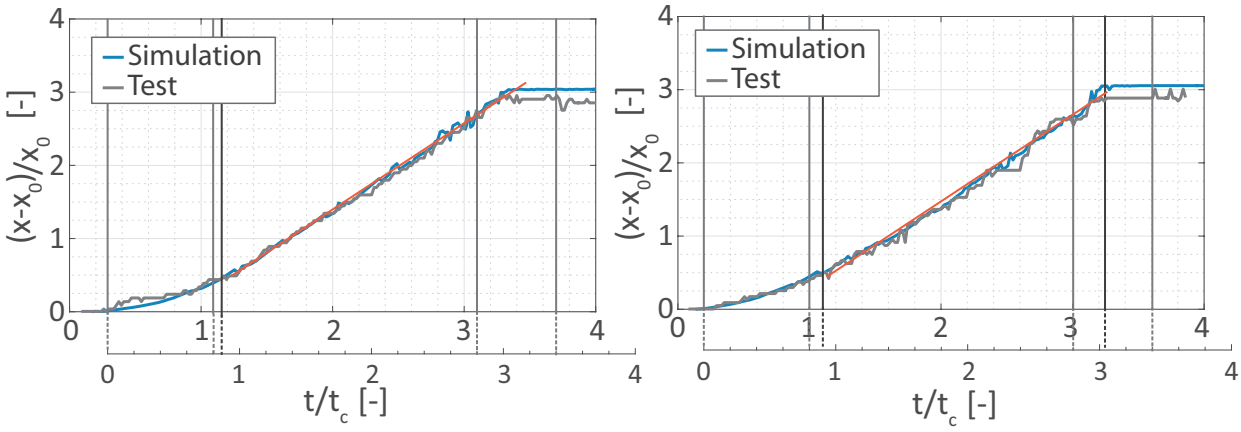

(a) $d_p = 3$ mm (b) $d_p = 1.15$ mm

Figure 6.40: Time evolution of the deposit tip spreading during the fast collapse tests for 3 mm and 1.15 mm glass particles in comparison to the physical tests; light grey lines correspond to the limits of Lajeunesse et al. (2005) whereby the black lines correspond to the limits arisen from the simulation

The partition of the collapse evolution into an acceleration part and a part of constant deposit spreading can be adopted on the simulations. The evolution shows good accordance between the simulations and the physical tests. The acceleration phase as well as the phase of constant spreading is clearly visible in all graphs (see Figure 6.40). This confirms that also the development in time of the slumping mechanisms is reproduced in the simulations. However, the limitation of this phases given by Lajeunesse et al. (2005) (light grey lines) are less applicable for the evolution in time for the simulations than for the physical tests, since the transition between the phases is slightly shifted (see black lines). The acceleration takes in average approximately $t = 0.9\ t_c$ for the 3 mm particles and in average $t = 1.0\ t_c$ for the 1.15 mm particles instead of $t = 0.8\ t_c$. Thus, the acceleration phase takes longer in the simulations than in the physical tests. Further, the transition between acceleration and consistent phase are less clear to identify. The subsequent phase of consistent spreading is also slightly longer than in the physical tests. In contrast to the physical tests, no deceleration phase can be recognised in the deposit tip evolution over time. As already mentioned before, the impact of the material with the right wall is of higher velocity in the simulations than in the physical tests. In the physical tests the particle mass spreads less wide and the begin of a deceleration phase is recognizable. In the phase of constant spreading, the deposit tip moves with a velocity of 0.72 m/s for the 3 mm particles and 0.73 m/s for the 1.15 mm particles. This is faster than in the physical tests with a constant tip velocity of in average approximately 0.61 m/s for the 3 mm and

0.66 m/s for the 1.15 mm particles. This increase of velocity corresponds to the longer acceleration phase in the simulations.

In contrast to the physical tests, the simulation can provide more information on the particle behaviour such as the evolution of the particle mass kinetic energy. Therefore, the kinetic energy and the rotational kinetic energy are distinguished (see Section 6.3.2). In contrast to the slow collapse, which consisted of several smaller slumping events, the fast collapse is characterized by a single big slumping event. This collapse characteristic is graphically represented by the kinetic as well as rotational kinetic energy for the 3 mm and the 1.15 mm particles in Figure 6.41. The graphs are very similar for the different particle diameters. The curve of kinetic energy rises to a maximum at 1.90 t_c. Afterwards the kinetic energy decreases till approximately $t = 6.00\ t_c$. The peak of kinetic energy is equal to the point, till which the rotational kinetic energy increases. Afterwards, the rotational kinetic energy remains approximately constant over 1.00 t_c before its drops again and reaches 0 at approximately $t = 6.00\ t_c$. The peak of kinetic energy is consistent for all simulations and is positioned for the 3 mm particles at in average $t = 1.92\ t_c \pm 0.002$ and for the 1.15 mm particles at in average $t = 1.88\ t_c \pm 0.024$. This peak is conform to the point, where all particles dominated by vertical movements are deviated into a horizontal movement along the slip joint. This behaviour is conform to the assumption in the physical tests of Lajeunesse et al. (2005). At this point, the movement of the particles, which were vertically falling, is merging also into a rolling motion and the rotational kinetic energy becomes maximal since the maximum number of particles is in a rolling motion. This high amount of rotational kinetic energy stays constant (see plateau in plateau in Figure 6.41) till the first particles are stopped due to the contact with the right wall. This is the reason, the rotational kinetic energy starts to drop at approximately 3.00 t_c. With ongoing evolution more particles are decelerated and the rotational energy decreases even further.

All in all, the fast collapse is good reproduced by the simulations for the 3 mm as well as the 1.15 mm particles. The characteristic mechanisms as well as the different spreading phases are also present in the simulations. However, the material in the simulations is spreading further than in the physical tests. Additionally, the particles show a very elastic behaviour at the impact with other particles or walls. An adaptation of the particle coefficient of restitution as well as the particle-particle contact friction might improve the results. It seems, the gained knowledge of the slow collapse sensitivity study in Section 6.3.3 is not fully adaptable on the fast collapse simulation. While the adoption of the coefficient of rolling friction to a higher value gives good results, a reduction of the particle-wall contact friction seems not fully suitable for the fast collapse. The faster collapse initiation in the simulation might result from too low friction between particles and wall. These aspects are part of the sensitivity study for the fast collapse simulation in the following section.

6.3.7 Sensitivity study on fast collapse

The sensitivity study of the fast collapse simulation shows the dependency of the collapse mechanisms from the material properties. As in Section 6.3.3, single properties are varied at the 3 mm particles to investigate their influence onto the slumping mechanism as well

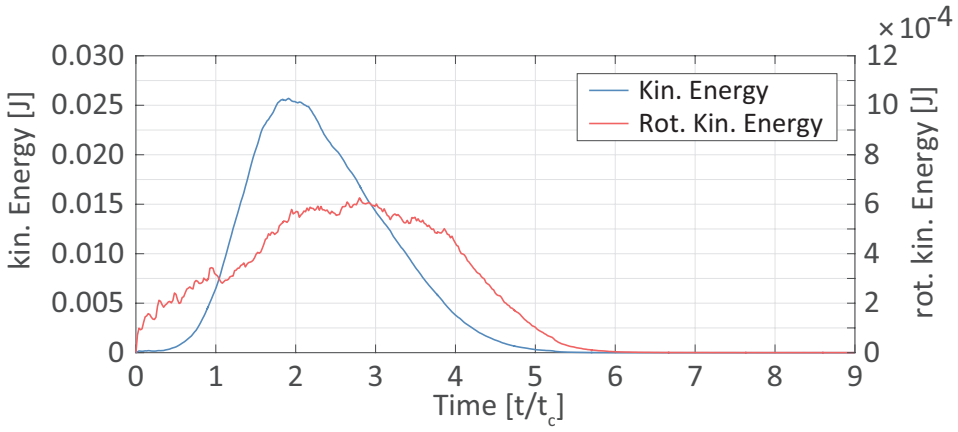

(a) $d_p = 3$ mm

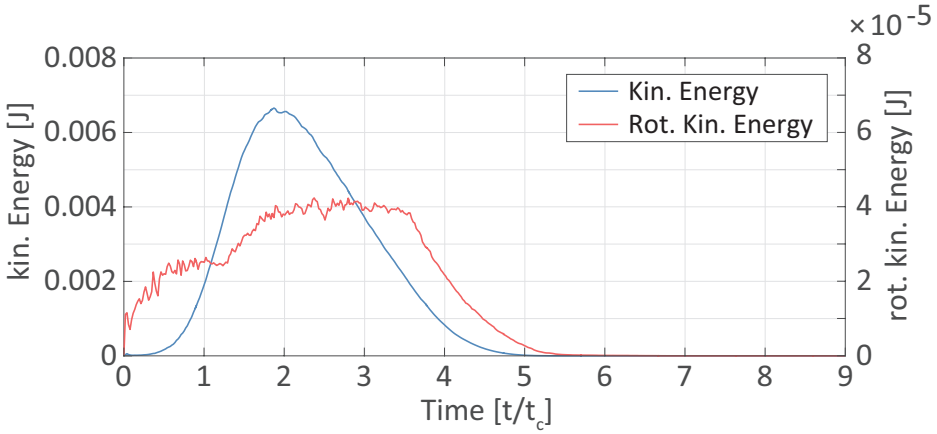

(b) $d_p = 1.15$ mm

Figure 6.41: Kinetic energy and rotational kinetic energy of the global particle system over time for the fast collapse simulation

as the final state. In contrast to the previous sensitivity study of the slow collapse, the damping effects should have a higher impact on the very dynamic simulation than before. Following properties are investigated:

- coefficient of restitution
- coefficient of Coulomb's friction for particle-particle contact
- coefficient of Coulomb's friction for particle-wall contact
- coefficient of rolling friction

In the simulations of the sensitivity study, the initial particle packings of Section 6.3.6 are applied. Previous to the collapse simulation, an additional simulation step of 2 s is executed, to adapt the changes in the contact modelling properties on the initial particle packing. The simulation starts with the extraction of the movable wall.

Influence of coefficient of restitution e

The coefficient of restitution e has a high impact on the damping characteristics of the individual particle contact and, thus, a high impact on the whole particle system. While

in the slow collapse the variation of e resulted in no significant influences on the slumping characteristics, the highly dynamic fast collapse should be affected in a more significant way by a variation of e. In the previous presented simulations of the fast collapse, individual particles engage at the deposit tip from the slumping material and jump ahead. The number of these individual particles is greater in the simulations than in the physical tests. Additionally, the impact of the particle mass with the right wall results in a greater number of chaotic jumping particles. This behaviour might result from an overestimation of e in the simulations, which results in a high extent of energy conversation during an impact. However, the particles have a higher velocity at wall contact, which also results in greater kinetic energy after the impact and a greater deflection.

In the sensitivity study the initial values of 0.98 coefficient of restitution is varied to 0.8 and 0.9. In a first impression of the slumping behaviour, the variation of $e = 0.8$ gives the best results considering the jumping of particles at contact with the right wall. The number of individual particles ahead of the tip is significant less and the particles jump less high (see Figure 6.42). Since less particles are involved, the amount of particles on the right side of the basin is reduced for the simulations with $e = 0.9$ and especially for $e = 0.8$. Further, the particle velocity before the impact with the wall is clearly reduced for the $e = 0.8$ and $e = 0.9$ variations. Figure 6.42 presents the moment after the first individual particles collided with the right wall. The number of the impacting particles as well as their velocities are reduced for the lower coefficient of restitution. Thus, the reduction of the dynamic behaviour of the particles is not only based on the reduced damping, but also based on the reduced particle velocities in the whole system.

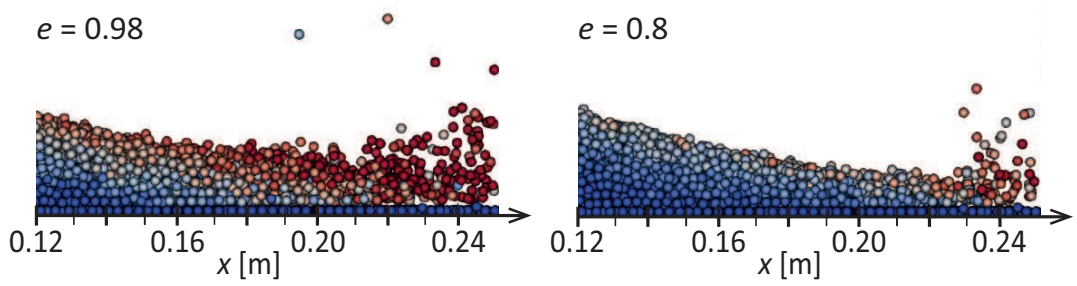

Figure 6.42: Tip of the spreading deposit after the first particle impacts with the right wall for $e = 0.98$ (left) and $e = 0.8$ (right)

The slumping mechanism itself shows no significant differences to the simulations in Section 6.3.6. Also, the final shape of the deposit varies barely from the original simulations. Thus, the final height of the deposit on the left side remains on 6.4 cm over the variation and the corresponding slope top angle decreases just slightly from in average 17.4° at $e = 0.98$, to 17.3° at $e = 0.9$ and 17.1° at $e = 0.8$ (see Table 6.11).

In contrast to the characteristic slumping mechanisms, the evolution of the collapse over time differs significantly for the variation of e. The duration of the collapse process increases significantly with decreasing coefficient of restitution. Thus, the duration in which the deposit mass reaches the right wall increases from in average $t = 3.06\ t_c$ at

$e = 0.98$, to $t = 3.26\ t_c$ at $e = 0.9$ and to $t = 3.43\ t_c$ at $e = 0.8$ (see Table 6.11). The reduction of e is equal to a greater amount of damping at an impact between two particles. Besides the damping of the individual particle contact, the reduction of e results further in a damping of the movement for the whole particle system.

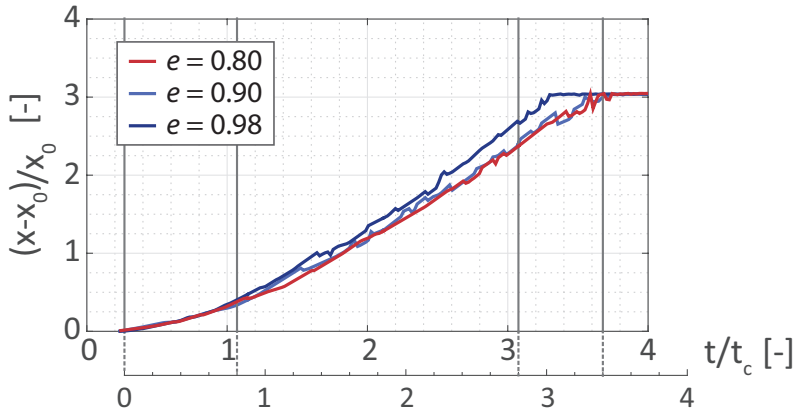

Figure 6.43: Evolution in time of the deposit tip spreading during the fast collapse tests for the variation of the coefficient of restitution e

Figure 6.43 presents a representative example of the deposit tip spreading over time. The results for the remaining initial packings are presented in Figure B.10 and Figure B.11. Corresponding to the previous presentations of the deposit tip evolution, the limits of the characteristic phases are included. Besides the limits according to Lajeunesse et al. (2005) (bright grey lines), the limits arise from the resulting graphs are added (black lines). Corresponding to the increase in total duration of the material spreading, also the duration of the acceleration phase increases with decreasing e. The acceleration phase lasts for $t = 0.90\ t_c$ for the original simulation with $e = 0.98$ and the variation $e = 0.9$, but increases to $t = 0.94\ t_c$ for the variation of $e = 0.8$. However, the increase of the acceleration phase is marginal compared to the total delay for the whole collapse. Thus, the majority of the delay must result from the phase of consistent velocity spreading. According to Figure 6.43, the duration of the phase of consistent velocity is increasing with decreasing e. This implies a lower spreading velocity of the deposit for the variations with lower e. The spreading velocity can be identified by the gradient of the graphs in Figure 6.43. Thus, the spreading velocity can be defined to in average 0.67 m/s for the variation $e = 0.9$ and 0.66 m/s for the variation $e = 0.8$, in contrast to original velocity of 0.72 m/s for $e = 0.98$. The smaller spreading velocities of the deposit tip correspond to the smaller particle velocities at the impact with the static wall, observed in Figure 6.42. However, although the particle velocities are clearly smaller for the variation with lower e, no deceleration phase can be observed in Figure 6.43.

In contrast to the slumping mechanism and the subsequent spreading, the peak of kinetic energy is not delayed in the variation. The position of the peak is equivalent to in average $t = 0.200\ t_c$ for $e = 0.9$ and $t = 0.194\ t_c$ for $e = 0.8$. This varies just slightly from the original position at $t = 0.199\ t_c$ in average for $e = 0.98$ (see Table 6.11).

Table 6.11: Average results for the coefficient of restitution variation for the fast collapse with glass particles of 3 mm diameter

e [-]	Slope angle top	Final height [cm]	Spreading velocity [m/s]	Duration till wall impact [t_c]
0.98	17.4° ±0.13°	6.4 ±0.04	0.72 ±0.02	3.05 ±0.08
0.9	17.3° ±0.34°	6.4 ±0.07	0.67 ±0.01	3.26 ±0.02
0.8	17.1° ±0.19°	6.4 ±0.04	0.66 ±0.05	3.43 ±0.07
∅ Test	21.4° ±0.85°	7.00 ±0.00	0.60 ±0.02	≈ 3.0

The variation of e showed, that with a higher damping due to a lower coefficient of restitution not just the individual particle contact is damped but rather the whole behaviour of the particle system. This causes a significant divergence to the characteristic behaviour and their evolution in time. The original value of $e = 0.98$ results in the best representation of the slumping evolution over time. The correct representation fo the slumping process over time is treated more relevant than the deflection at the wall impact.

Influence of coefficient of Coulomb's friction for particle-wall contact $\mu_{s,w}$

The sensitivity study of the slow particle collapse (see Section 6.3.3) showed a sensibility of the slumping mechanism from Coulomb's friction coefficient for particle-wall contact $\mu_{s,w}$. Thereby, a reduction of $\mu_{s,w}$ resulted in a better representation of the internal slumping characteristics as in the physical tests. However, the reduction of $\mu_{s,w} = 0.4$ suggests a contrary trend for the fast collapse simulations. The entrainment of adjacent particles by the movable wall extraction seems to be an important factor to simulate the collapse initiation of the particle column correctly. In the physical tests the particles remain in their initial position for a longer time before the first particles participate in the slumping movement. In contrast, the slumping movement in the simulations is initiated faster (see Figure 6.35). Thus, the effect of the particle-wall friction needs to be investigated regarding its effect on the collapse evolution in the simulation.

The investigations of $\mu_{s,w}$ include the variation of $\mu_{s,w} = 0.5$ and $\mu_{s,w} = 0.6$ besides the initial value of $\mu_{s,w} = 0.4$. A compilation of the average results is presented in Table 6.12. The analysis shows a marginal influence on the slumping mechanism by the variation of $\mu_{s,w}$. Thus, the final deposit shape remains unaffected from the variations. The final slope angle of the deposit varies just slightly with 17.4° for $\mu_{s,w} = 0.4$ and $\mu_{s,w} = 0.6$ and 17.8° for $\mu_{s,w} = 0.5$. Also the final height of the deposit varies just slightly.

The shape of the collapse mechanism itself is slightly affected by the $\mu_{s,w}$ variation. Thus, the outer silhouette at the early stage of the collapse is affected. Figure 6.44 shows the upper particles of the column during the extraction of the movable wall for different values of $\mu_{s,w}$. At this point, the wall is almost fully extracted and the wall foot is positioned at a height of 0.09 cm. The particles adjacent to the wall are lifted slightly higher for greater $\mu_{s,w}$ values. However, the effect is marginal and has a small effect on the collapse evolution only. Figure 6.45 shows the outer silhouette during the collapse for $\mu_{s,w} = 0.4$

Table 6.12: Average results for the variation of particle-wall friction for the fast collapse with glass particles of 3 mm diameter

$\mu_{s,w}$ [-]	Slope angle top	Final height [cm]	Spreading velocity [m/s]	Duration till wall impact [t_c]
0.4	17.4° ±0.13°	6.40 ±0.04	0.72 ±0.023	3.05 ±0.080
0.5	17.8° ±0.64°	6.39 ±0.09	0.71 ±0.012	3.09 ±0.074
0.6	17.4° ±0.54°	6.34 ±0.06	0.71 ±0.040	3.14 ±0.233
∅ Test	21.4° ±0.85°	7.00 ±0.00	0.60 ±0.02	≈ 3.0

and $\mu_{s,w} = 0.6$. The outer shape of the slumping material is slightly affected by the variation of $\mu_{s,w}$ only. Neither, the evolution of the slumping material at the early stage of the collapse, nor the subsequent evolution of the deposit tip is significantly affected. Just at $t = 0.95\ t_c$, the silhouette shows an influence of the more considerable lift of the movable wall adjacent particles. Thus, the slip joint angles defer marginal from the original simulations. For the variation of $\mu_{s,w} = 0.5$ the angle o the slip joints are 46.3° in average for $t = 1.35\ t_c$ and 49.7° in average for $t = 2.12\ t_c$, while the corresponding angles for $\mu_{s,w} = 0.4$ resulted in 45.4° and 49.2° in average.

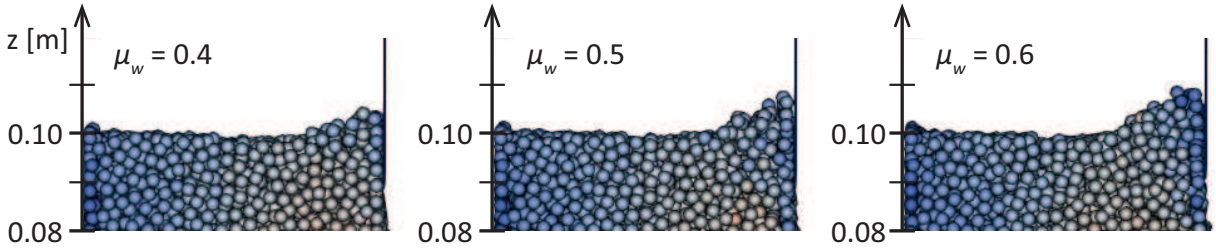

Figure 6.44: Lift of surface particles due to contact with the movable wall during extraction for $\mu_{s,w} = 0.4$ (left), $\mu_{s,w} = 0.5$ (middle) and $\mu_{s,w} = 0.6$ (right)

Also the evolution of the deposit tip, shows no significant influence of the variation of wall friction. The duration of the acceleration phase does increases marginal over the variation. Thus, also the total duration of the collapse increases to a very small amount. While the original simulations lead to a total duration of $t = 3.05\ t_c$, the variations resulted in $t = 3.09\ t_c$ for $\mu_{s,w} = 0.5$ and in $t = 3.14\ t_c$ for $\mu_{s,w} = 0.6$. The spreading velocity of the deposit tip at the continuous phase is not significantly affected (see Table 6.12). However, a significant improvement of the collapse evolution cannot be achieved by the adaptation of $\mu_{s,w}$.

Influence of coefficient of Coulomb's friction for particle-particle contact μ_s

The simulation of the fast collapse reproduces the characteristic mechanisms of the observed behaviour in the physical tests. However, the final deposit shape diverts from the

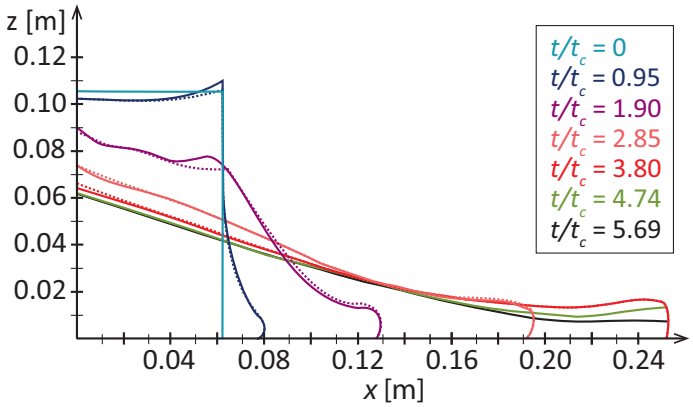

Figure 6.45: Resulting final deposit shape for fast collapse simulation with $\mu_{s,w} = 0.4$ (continuous line) and $\mu_{s,w} = 0.6$ (dotted line)

geometry in the physical tests. Thus, the deposit has a smaller height and a smaller inclination of its slope. The sensitivity study of the slow collapse in Section 6.3.3 showed that the coefficient of Coulomb's friction for particle-particle contact μ_s has a significant influence on of the deposit slope angle and the deposit height. A higher μ_s resulted in steeper slope angle. To investigate the influence of μ_s on the fast collapse slumping mechanism and the final deposit shape, μ_s is varied to $\mu_s = 0.55$ and $\mu_s = 0.6$ besides the initial value of $\mu_s = 0.48$. Thereby, the knowledge of the previous variation has been established and the particle-wall friction coefficient was applied to $\mu_{s,w} = 0.5$.

The characteristic results of the variations are presented in Table 6.13. It is evident, that the characteristic parameters of the final deposit shape show just minimal deviations. The average final top angle of the deposit slope is with 17.8° equal for all variations. The average final deposit height varies barely with 6.39 cm at $\mu_s = 0.48$, 6.45 cm at $\mu_s = 0.55$ and 6.44 cm at $\mu_s = 0.60$. The average results of this parameters as well as the individual simulation results are further illustrated in Figure 6.46. Besides single outliers the results vary just slightly and cause low standard deviations (see Table 6.13). The applied trendline in the presentation of the deposit heights in Figure 6.46 (right) implies a minimal trend to greater deposit heights with increasing friction coefficients. However, this effect is not significant.

In contrast to the sensitivity study of the slow collapse, the variation of μ_s for the fast collapse simulation results in no significant influence neither in the final deposit shape nor in the slumping mechanism itself. The final deposit geometry is very similar for all variations. Further, the analysis of the outer silhouette during the collapse yield just minimal deviations between the variations of μ_s.

Since the outer silhouettes showed no significant differences for the slumping process over the variations of μ_s, the development in time of the deposit tip shows neither significant deviations. Table 6.13 presents the spreading velocity of the deposit tip as well as the duration till the deposit tip reaches the opposed right wall. The spreading velocity varies

Table 6.13: Average results for the variation of Coulomb's friction for the fast collapse with glass particles of 3 mm diameter

μ_s [-]	Slope angle top	Final height [cm]	Spreading velocity [m/s]	Duration till wall impact [t_c]
0.48	17.8° ±0.64°	6.39 ±0.09	0.71 ±0.012	3.09 ±0.074
0.55	17.8° ±0.21°	6.45 ±0.06	0.69 ±0.009	3.07 ±0.057
0.60	17.8° ±0.46°	6.44 ±0.03	0.70 ±0.005	3.15 ±0.100
∅ Test	21.4° ±0.85°	7.00 ±0.00	0.60 ±0.02	≈ 3.0

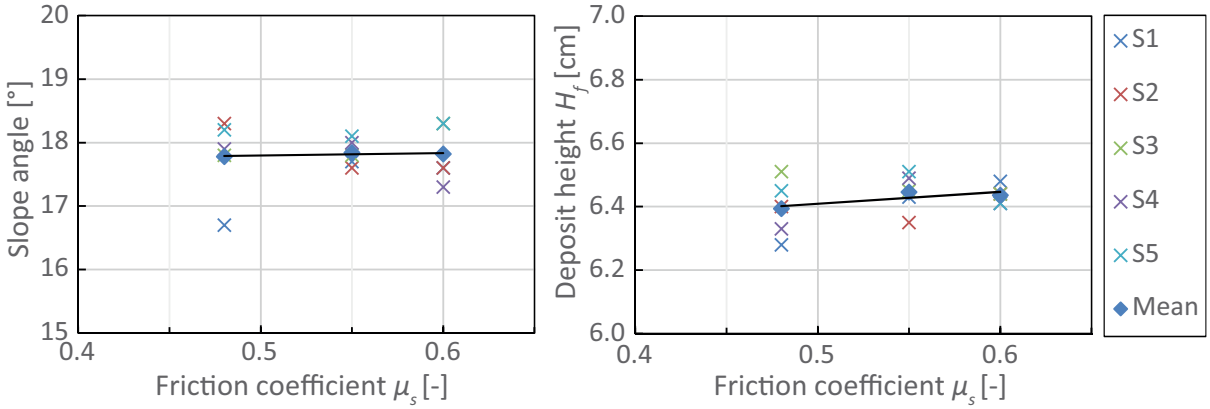

Figure 6.46: Resulting final slope angles and final deposit height for the variation of particle friction μ_s

just slightly to 0.71 m/s at $\mu_s = 0.48$, 0.69 m/s at $\mu_s = 0.55$ and 0.70 m/s at $\mu_s = 0.60$. The duration till the wall impact varies also minimal with $t = 3.09\ t_c$ at $\mu_s = 0.48$, $t = 3.07\ t_c$ at $\mu_s = 0.55$ and $t = 3.15\ t_c$ at $\mu_s = 0.60$. This minimal deviations can also be caused by the analysis of the results. For further informations, the outer silhouettes during failure, the final deposit shapes as well as the evolution in time of the deposit tip are presented in Figure B.14 and following.

The previous results showed no significant influence of the coefficient of Coulomb's friction μ_s on the slumping mechanism of the fast failure. However, so far just parameters of exterior characteristics are investigated. To investigate the characteristics inside the particle packing during slumping, the internal slip joint angles are analysed. Therefore, the slip joint angles at $t = 2.12\ t_c$ are determined. At this point, the initial vertical movement of the particles has transformed to a horizontal dominated movement and the particle mass slides along a clear joint. Thereby, the slip joint runs straight at the upper part of the particle mass and merges to a curved course near to the fixed particle layer. The determined angles describe the course of the straight upper part of the slip joint. The average slip joint angles at $t = 2.12\ t_c$ are 49.7° ±1.203° at $\mu_s = 0.48$, 50.7° ±0.604° at $\mu_s = 0.55$

and 52.5° ±1.224° at $\mu_s = 0.60$. Thus, the inner slip joint angle increases marginal with increasing μ_s. However, this trend is not valid for all individual simulations with different particle packings. The resulting slip joint angles of three out of five particle packings are increasing with increasing μ_s.The marginal trend occurs for the average values only.

The previous results have shown no significant influence of the friction coefficient the fast collapse process. In contrast to the slow collapse, almost no differences for the variations can be detected. The reduced influence of the coefficient of Coulomb's friction for the fast collapse needs to be explained in the highly dynamic behaviour of the particles. After the extraction of the movable wall, the particle column collapses and the particle packing dissolves. Thereby, the material shows a fluid-like behaviour during the fast collapse. This characteristics occur also in fluidisation processes, where the grains of a (partially) saturated material loose contact due to e. g. excess pore water pressure which exceeds the forces between the grains. As a result, the former solid soil looses its ability to transfer shear stresses over the grain skeleton and the effective shear stresses become zero $\sigma_{\text{eff}} = 0$. Thus, the soil behaves fluid like under applied stress. In the fast collapse, the particle skeleton dissolves due to the great and highly dynamic deformation, which results in a reduction of particle contacts and a fluid-like behaviour. While at $t = 0$, the particle packing 3 consisted of 679943 contacts for in total 13359 particles, the number of particles contacts is reduced to e. g. 264676 at $t = 2.12\ t_c$ for the variation $\mu_s = 0.48$. Figure 6.47 presents the contact forces between particles at $t = 2.12\ t_c$ for the variations $\mu_s = 0.48$ and $\mu_s = 0.60$. Thereby, the particle contacts are visualised by tubes connecting the centres of two particles in contact. The colour of the tube corresponds to the amount of the contact force. The particles, which are positioned underneath the slip joint can be clearly identified, by the high amount of particles contacts in this region. In this region, the particle skeleton stays intact and, thus, concentrates a high number of particle contacts. In contrast, the number of particle contacts for the slumping particle mass is reduced. Thereby, the contacts are characterised by short particle impacts. The contact during an impacts persists a split second only, before the particle separate and new contacts are generated. This is contrary to the slow collapse, where the slumping movement was dominated by long-lasting contacts and an intact particle skeleton for the transmission of friction forces. In the fast collapse process, the particles are decelerated due to contact with already static particles or the fixed particle layer (see Section 6.3.6). With decreasing particle velocity and, thus, increasing duration of particle contact, the friction forces gain influence again. The decelerated particles of the deposit build a new soil skeleton and a new force chain system is formed.

The presentation of force chains illustrates that the behaviour of the slumping particle mass is no longer dominated by long particle contacts in the fast collapse simulations and no particle skeleton is present in the slumping particle mass. Since the influence of μ_s relies on particle contact for the transfer of shear stresses, the dissolving of the particle mass as well as the reduced duration of contact cause a cut down of the influence of frictional forces. The dominating forces at this stage are the gravitational acceleration and the damping at particle impact.

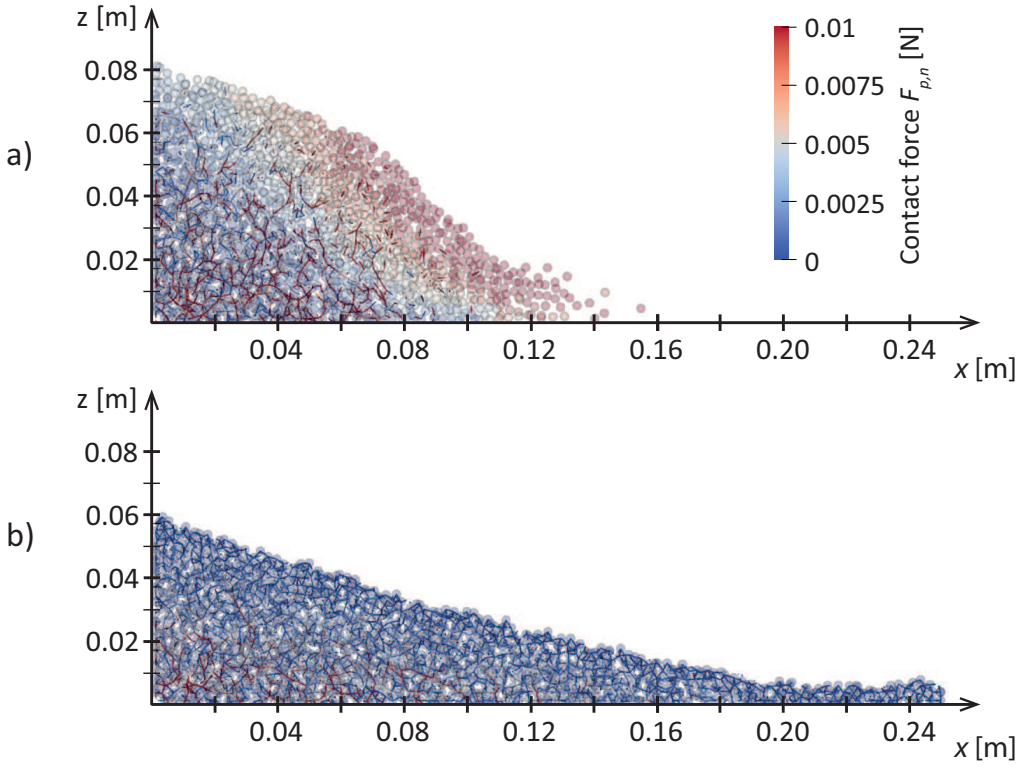

Figure 6.47: Illustration of force chains at $t = 2.12\ t_c$ (a) and $t = t_f$ for $\mu_s = 0.48$ for an 1 cm thin slice in y-direction (force chain colour corresponds to the normal contact force $F_{p,n}$)

Influence of the coefficient of rolling friction μ_r

In the previous variation, the minimal influence of particle friction μ_s on the slumping behaviour has been discussed. The cause for this reduced influence has been found in the dissolving of the particle mass and the reduced contacts. Thus, the influence of the rolling friction coefficient μ_r on the slumping mechanism should be small as well. However, the decelerated particle movements are dominated by rolling. Thus, the rolling friction might have a higher influence at a later stage of the slumping process.

In this sensitivity study, the initial value of $\mu_r = 0.007$ is varied to 0.008, 0.009 and 0.010. The resulting deposit slope angles, the deposit heights for the individual simulations as well as the corresponding average values of the variations are presented in Figure 6.48. The average results of the deposit slope angles and the final deposit heights show no significant deviations. The average results of the variations and their standard deviations are further presented in Table 6.14. Similar to the variation of μ_s, the characteristic parameters of the final deposit shape show no significant deviations over the variation μ_r. Thus, the average values of the deposit slope angle are 17.8° for the variations $\mu_r = 0.007$ and $\mu_r = 0.008$, 17.5° for the variations $\mu_r = 0.009$ and 18.1° for the variations $\mu_r = 0.010$. The applied linear trendline of the deposit slope angle convey a trend of increasing angles with increasing values of μ_r (see Figure 6.48). However, the decrease of the slope angle value for $\mu_r = 0.008$ implies, that negligible small deviations also result from the random

applied particle packings.

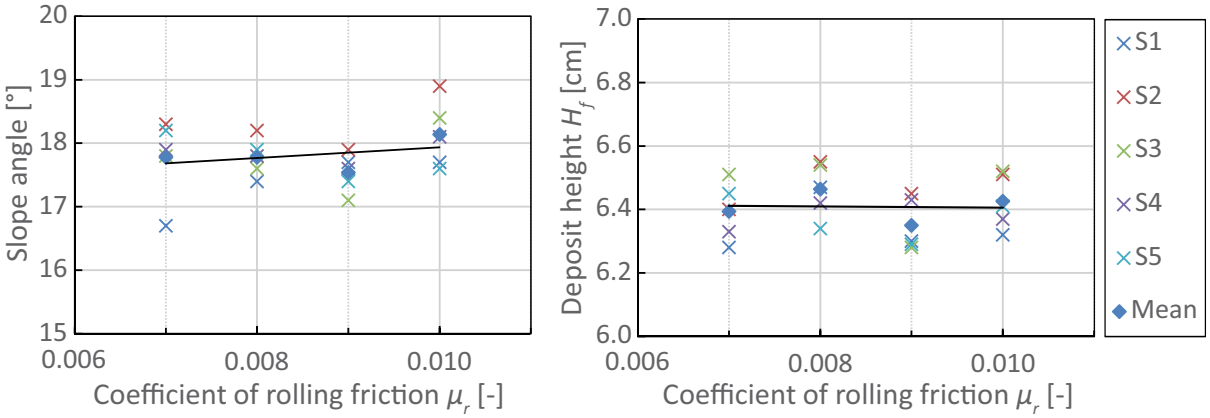

Figure 6.48: Resulting final slope angles and final deposit height for the variation of rolling friction μ_r

Table 6.14: Average results for the variation of rolling friction for the fast collapse with glass particles of 3 mm diameter

$\mu_{s,w}$ [-]	Slope angle top	Final height [cm]	Spreading velocity [m/s]	Duration till wall impact [t_c]
0.007	17.8° ±0.64°	6.39 ±0.09	0.71 ±0.012	3.09 ±0.074
0.008	17.8° ±0.30°	6.46 ±0.09	0.71 ±0.006	3.09 ±0.022
0.009	17.5° ±0.31°	6.35 ±0.08	0.70 ±0.013	3.09 ±0.074
0.010	18.1° ±0.53°	6.43 ±0.09	0.70 ±0.008	3.10 ±0.061
∅ Test	21.4° ±0.85°	7.00 ±0.00	0.60 ±0.02	≈ 3.0

Similar to the variation of μ_s, the variations of μ_r result in no significant visible changes neither in the final deposit shape nor in the slumping mechanism itself. The final deposit geometry is almost identical for all variations. This is equivalent for the analysis of the outer silhouette during the collapse, which yields just minimal deviations for different μ_r. The evolution of the deposit tip during the slumping process show neither significant deviations. Table 6.14 presents the average spreading velocity of the deposit tip as well as the average duration till the deposit tip reaches the opposed right wall. The spreading velocity varies minimal with 0.71 m/s for $\mu_r = 0.007$ as well as $\mu_r = 0.008$ and 0.70 m/s for $\mu_s = 0.0.009$ as well as $\mu_s = 0.010$. Thus, the deviations are even less than in the variations of μ_s. The average total duration is almost identical for the variations with $t = 3.09$ t_c for $\mu_r = 0.007$, $\mu_r = 0.008$ and $\mu_r = 0.009$ and $t = 3.10$ t_c for $\mu_s = 0.010$. For further informations, the outer silhouettes during failure, the final deposit shapes as well as the evolution in time of the deposit tip are presented in Figure B.18 and following.

Further, the internal slip joint angles at $t = 2.12\ t_c$ are analysed to detect possible deviations of the material slumping characteristics for the variation of μ_r. The form of the slip joint merges from a upper straight part to a curved course near to the fixed particle layer. The determined angles describe the course of the straight upper part of the slip joint. The average slip joint angles at $t = 2.12\ t_c$ result to 49.7° ±1.203° at $\mu_r = 0.007$, 51.5° ±0.999° for $\mu_r = 0.008$, 51.8° ±0.084° for $\mu_r = 0.009$ and 51.6° ±0.576° for $\mu_r = 0.010$. In contrast to the variation of μ_s, the inner slip joint angle is not clearly increasing with increasing μ_r. Rather, the higher variations of μ_r show almost no difference in their slip joint angle. Thus, a trend of the slip joint angles for different μ_r is not significant compared to the influence of the random particle packings.

6.3.8 Conclusion for fast collapse simulation

The fast collapse simulations reproduce successful the mechanisms of the particle slumping from the physical tests. The simulations show the same characteristics of the slumping process, containing the transition from a vertical to a horizontal dominated movement, the slumping along a slip joint and the transformation of the slip joint course during the collapse. Further, the slumping process over time is likely reproduced. The analysis of the deposit tip position over time enables indicates a phase of acceleration and the transition to a phase of constant movement of the particle mass. However, the deceleration phase observed in the physical tests is not part of the simulation, since the particles are less decelerated in the simulation than in the physical tests and the particles collide with the right wall before a deceleration occurs. Thus, the particles have a higher velocity at the impact with the right wall. As a consequence, the final shape of the simulation deposit is slightly flatter and lower compared to the physical tests.

The simulation of the fast collapse test visualise the internal process in the slumping mass as well as the later deposit. Thus, the particle mass dissolves during the slumping process. The transition of the granular particle skeleton to a highly dynamic dissolved state reduces the particle contacts to approximately 30% of the number of contacts at the initial state. At the highly dynamic state, the particle interaction is dominated by short particle impacts. The dissolved particle mass is not able to transfer stresses and the effective stresses become zero.

The sensitivity study of the fast collapse simulation has given an insight into the property depended behaviour of the fast slumping mechanisms. Thereby, a significant difference of the property dependencies in contrast to the slow collapse simulations has been proven. The highest influence on the slow collapse mechanism is based on frictional forces by means of particle-particle or particle-wall Coulomb's friction and rolling friction. However, the fast collapse test simulations show no significant influence of frictional forces by means of the coefficients of Coulomb's friction and rolling friction. In contrast, properties defining the damping behaviour at particle contact become relevant. Thus, the coefficient of restitution has a significant impact on the evolution in time of the highly dynamic slumping process. The simulations have shown, that the particle mass dissolves during the slumping process and is henceforth dominated by short timed particle impacts. The reduction of the number of particle contacts and the short impact time cause the reduced influence

of frictional forces. For the transfer of stresses and, thus, frictional forces a intact grain skeleton is required. In contrast, the dissolving of the particle mass eliminated the transfer of forces and the effective stresses become zero. Since, the majority of the particle skeleton and, thus, the particle contacts stay intact at the slow collapse simulation, the influence of friction defining properties is significant. The coefficient of restitution affects the damping characteristics during a particle impact and affects the energy conservation in the granular particle system. Thus, a variation of the damping properties has a significant influence on the highly dynamic slumping behaviour of the fast collapse simulations, which are dominated by short timed particle impacts rather than stress transfer.

Besides the reverse correction of the particle-wall friction coefficient to $\mu_w = 0.5$, the sensitivity study of material properties has confirmed the applied property setting from the final slow collapse simulations. Thus, the initial particle properties of Section 6.3.1 in combination with $\mu_w = 0.5$ will be applied for the study of the fluid-particle interaction at the fast particle column collapse under submerged conditions.

6.4 Physical Tests on the Submerged Column Collapse

The investigations of granular slumping of a particle column under dry conditions gave a comprehensive insight into the leading mechanisms and their representation with the DEM method. Extensive sensitivity studies identified the influences of the material properties on the contact modelling and the corresponding influences on the particle mass behaviour. The influence of the particle properties on the slumping characteristics are different for the slow or the fast collapse scenario. Thus, the differentiation into two collapse scenarios was necessary to understand the diversity in dominating mechanisms and their representation by for the contact modelling in the DEM.

In this chapter the granular slumping of a submerged particle column is investigated. Thereby, the analysis focuses on the interaction between the granular material and the fluid and the effects on the slumping mechanisms. Therefore, physical tests are conducted to investigate the leading mechanisms and to identify the effects due to the particle-fluid interaction (see Section 6.4). The analysis of the physical tests under dry conditions help to identify the influences of this interaction on the collapse process. To analyse the complex micro-mechanical interactions between the particles and the free water as well as the pore water, a numerical CFD-DEM based model is generated. The numerical investigations are presented in Section 6.5. The results of the physical tests are applied for the validation of the numerical simulations.

The differentiation into a slow and a fast collapse scenario was important for the investigation of the contact modelling under dry conditions. However, the physical tests demonstrate that this differentiation is not reasonable for the investigations under submerged conditions. The slow tests under submerged conditions show the same mechanisms as in the investigation under dry conditions. Besides the slumping mechanisms, also the final deposit shape results in almost identical shapes (see Table 6.15). This outcome is reasonable, since the slow collapse test is characterised by a slow failure consisting of short slumping events as well as persistent contact between slumping particles. This prevents the particles to reach higher velocities even at dry conditions. The interaction between the fluid and the particle mass is dominated by two effects: the reduction of weight due to buoyancy and the damping of the particle mass movement due to the fluid viscosity. On the particle scale this damping is mainly caused by the drag force. Other fluid-particle interaction forces are expected to be negligible in this context. However, this damping effect seems to be minimal in the slow collapse tests, since no high particle velocities are reached independent of the applied particle diameter. Thus, the investigation of the slow collapse case under submerged conditions is not a relevant case of fluid-particle interaction and relevant for the investigation of particle-particle contact implementation of the DEM formulation only.

A CFD-DEM simulation has higher computational costs, than a pure DEM simulation. Thus, the author recommends to investigate slow collapse scenarios with a pure DEM approach. The effect of buoyancy can be reproduced by adoption of the particle density or the gravitational acceleration.

According to the results of the slow collapse tests, only the fast collapse tests are investigated further.

Table 6.15: Results of the slow collapse tests for glass particles with 3 mm and 1.15 mm diameter under dry and submerged conditions

Test	Glass 3 mm		Glass 1.15 mm
	Slope angle top	Slope angle foot	Slope angle
∅ Tests water	22.6° ±0.22°	24.7° ±0.26°	23.1° ±0.08°
∅ Tests dry	22.9° ±0.54°	23.9° ±0.30°	23.4° ±0.22°

6.4.1 Test setup and evaluation for fast collapse tests

The physical tests of the submerged fast collapse take place in the beforehand applied plexiglas tank illustrated in Figure 6.3 (see Section 6.2). Further, the same testing material of 3 mm and 1.15 mm glass particles are used. The material sample corresponds to the tests under dry conditions and has an aspect ratio of 1.7 with an initial width of $X_0 = 6.1$ cm and an initial height of $Z_0 \approx 10.4$ cm. The extraction of the movable wall is accomplished again with the falling-weight mechanism described in Section 6.2.4. After the insertion of the required material mass, the plexiglas tank is filled with water very slowly till a height of approximately 25 cm. To reduce the amount of enclosed air in between the particles, the granular material is stirred till no bubbles get out any more. Afterwards, the material surface is smoothed out again.

The adjustments of the high-speed camera as well as the illumination corresponds to the dry column tests. Further, the PIV analysis calibrations are adopted.

6.4.2 Test results of fast collapse under submerged conditions

The physical tests of the fast collapse under submerged conditions show significant differences in the collapse process to the characteristics under dry conditions. The slumping process is considerable slower, since the fluid viscosity adds an additional resistance against the particle movement. Although, the whole collapse process proceeds in a delayed manner, the characteristic mechanisms of the previously investigated dry slumping can be recognized. Thus, the collapse process can be differentiated into three characteristic phases: an acceleration phase, a phase of constant movement as well as a deceleration phase. However, due to the interaction of the movable wall and the particle mass with the free fluid, fluid flow and vortexes are provoked in the fluid, which affects the collapse process. Following the differences in the collapse process are presented in detail and the influence of the fluid-particle interaction is discussed.

As the physical tests under dry conditions, the submerged tests begin with the extraction of the movable wall. The extraction itself is consistent to the process under dry conditions. However, the effect of the extraction on the submerged particle column is significantly different. In the dry case, the particle column collapse is initiated with the discharge of the particles at the column foot, while the movable wall is still supporting the upper part of the column. For the submerged column, this initial movement is initiated delayed.

Prior to this, the extraction of the movable wall is accompanied by an entrainment of the particles adjacent to the movable wall out of the column into the free fluid. Thereby, the majority of the particle column stays intact. Figure 6.49a presents this early state at $t = 1.0\ t_c$. The adherent free fluid next to the column as well as the fluid in the column voids is accelerated due to the wall extraction. Since the pore-fluid movement is impeded by the presence of the above and lefter particles, the accelerated pore-fluid is entrained into the free fluid. As a consequence, the adjacent particles are entrained by the accelerated fluid into positive x- and z-direction and build dissolved clouds. This phenomenon is illustrated in Figure 6.49a. With greater distance to the movable wall tip, the particles in the dissolved particle clouds start to sink down (see lower regions in Figure 6.49a). This particle movement is significantly slower than by the previous entrainment. The particles positioned at the column surface are entrained to a greater extent by the extraction of the movable wall, since the movement of the particles is not hindered by the load of overlying particles. Thus, the particle-wall contact as well as the fluid flow induced by the wall extraction lead to greater particle entrainment. The particle movements of the entrained particles in Figure 6.49a - 6.49c illustrate that the particles move upwards before they start to sink down. Thereby, the particle move in a counter-clockwise elliptical path. This movement could be induced by a counter-clockwise vortex, which developed due to the wall extraction in the free fluid area above the particle column.

After the extraction of the wall, the column collapse starts with the dissolving of the particles at the column foot (see Figure 6.49b). In contrast to the tests under dry conditions, the particle movements is characterised by dissolving and less by a clear slumping movement. The whole process is significantly delayed due to the resistance of the water. The dissolved particle clouds affiliate to the particle mass during the collapse process. However, the characteristics of the dissolved mechanism show similarities to the mechanism under dry conditions. The particle mass moves along a slip joint of stationary particles and undergoes a transition from a vertical to a horizontal movement. Due to the dissolving of the particle column the vertical movement is deviated at a significantly greater height into a horizontal movement than under dry conditions. The whole fluid-like behaviour of the dissolved particle mass is significantly more viscous than in the dry collapse tests. In contrast to the dry tests, the 3 mm particle mass is so much decelerated by the water that the final deposit is not reaching towards the right wall (see 6.49f). The 1.15 mm particles are clearly decelerated as well, but still impact with the opposite wall.

As described in the dry tests, after generation of a slope shape the slumping mechanism is characterised by a movement of the particles at the surface over the deposited particle mass. This behaviour occurs also for the submerged slumping process. However, at approximately $t = 5.7\ t_c$ this superficial movement of the 3 mm particles is affected by the fluid. At this time a small ripple begins to form (see Figure 6.49e at $x \approx 13$ cm). Thereby, a certain area of particles seems to undergo a higher resistance due to the fluid than the rest, what results in a local piling-up of particles. Subsequently, this first ripple is further transported with the spreading superficial particles. In the following, two more ripples begin to form near the slope foot. As a result, the final shape of the deposit in Figure 6.50a is characterised by three slight bumps at the lower section of the deposit. This shape is consistent for all five tests with 3 mm particles.

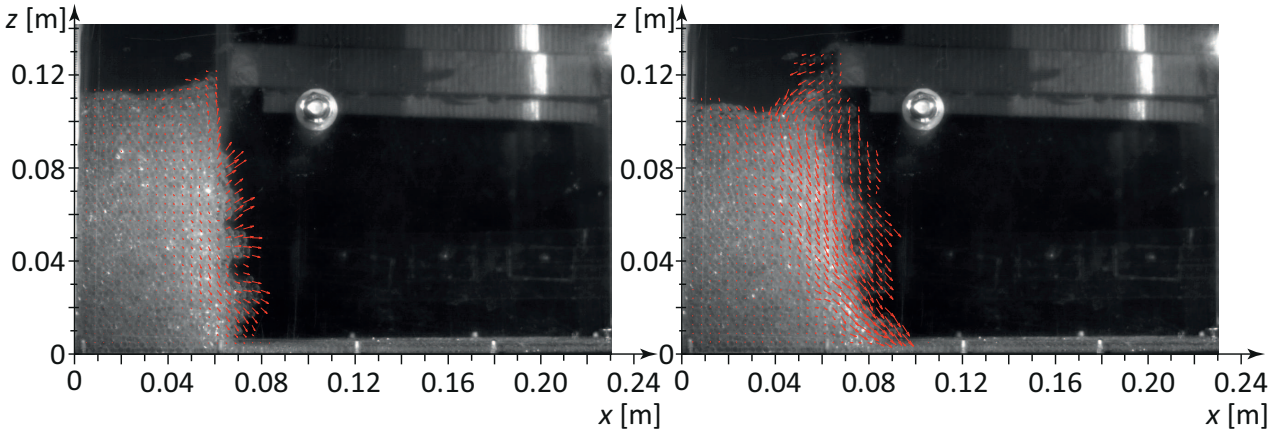

(a) $t = 1.0\ t_c$

(b) $t = 2.0\ t_c$

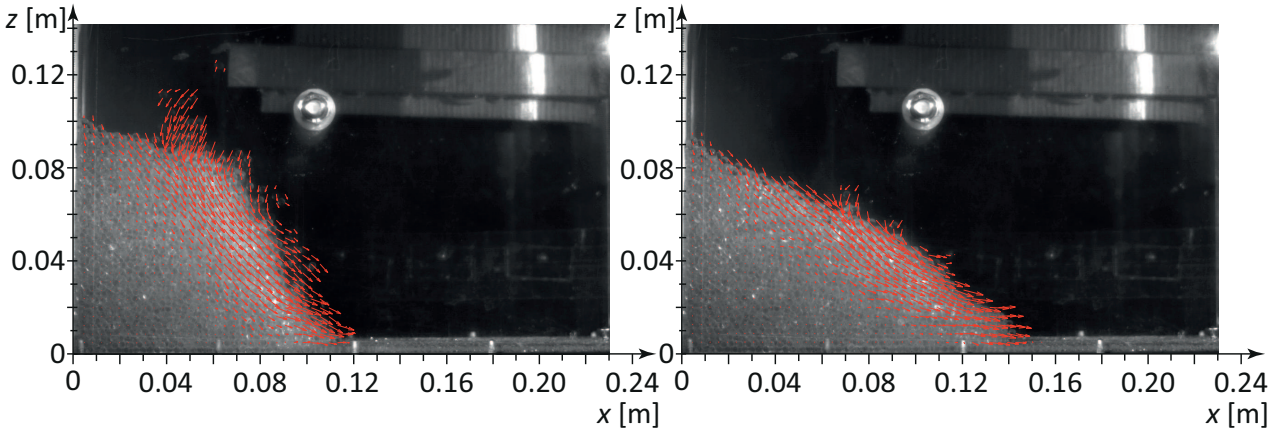

(c) $t = 3.0\ t_c$

(d) $t = 4.0\ t_c$

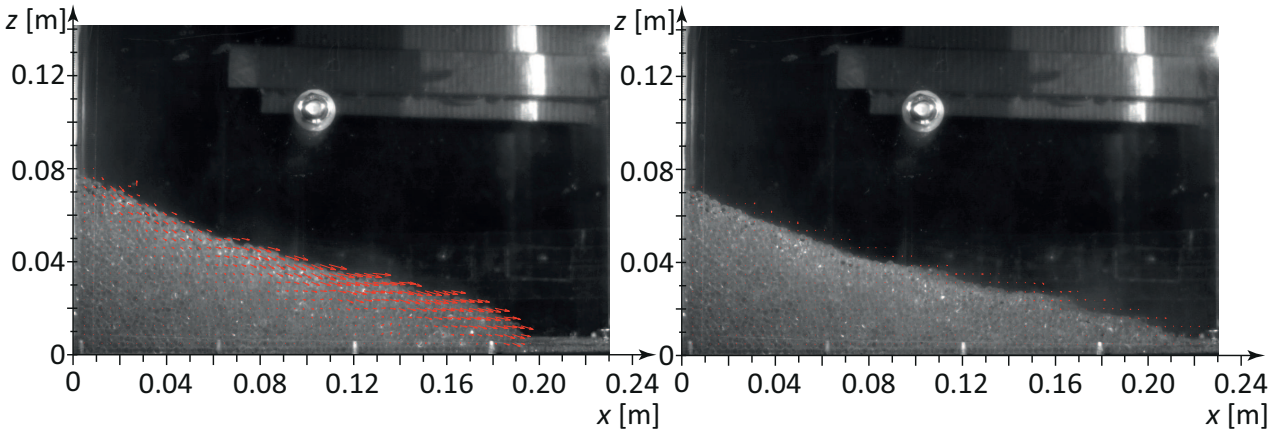

(e) $t = 6.0\ t_c$

(f) $t = 10.0\ t_c$

Figure 6.49: Fast collapse of a submerged particle column with 3 mm glass particles - Characteristic slumping mechanisms over time represented by the particle velocity magnitude of the PIV analysis

The generation of ripples is even clearer for the 1.15 mm particles tests in Figure 6.50b. In the tests with $d_p = 1.15$ mm, the first ripples form already at an earlier stage at

approximately $t = 4.8\ t_c$. However, the whole slumping process is faster for the smaller particles. For more information about the slumping mechanism of the 1.15 mm particles see Figure B.27.

The piling-up of particles needs to be caused by free fluid flow, initiated by the wall extraction and extrusion due to the particle mass collapse. While the extraction of the wall results in a counter-clockwise vortex on the former left section of the movable wall, a clockwise vortex might be initiated on the right side. The flow direction is opposed to the movement of the slumping particles and causes the locally increased resistance. However, it is unclear how the slumping of the particle column itself affects the initiated fluid flow and the resulting vortex, since the pile up effect is restricted to a local phenomenon. The numerical simulations should reveal more details on this.

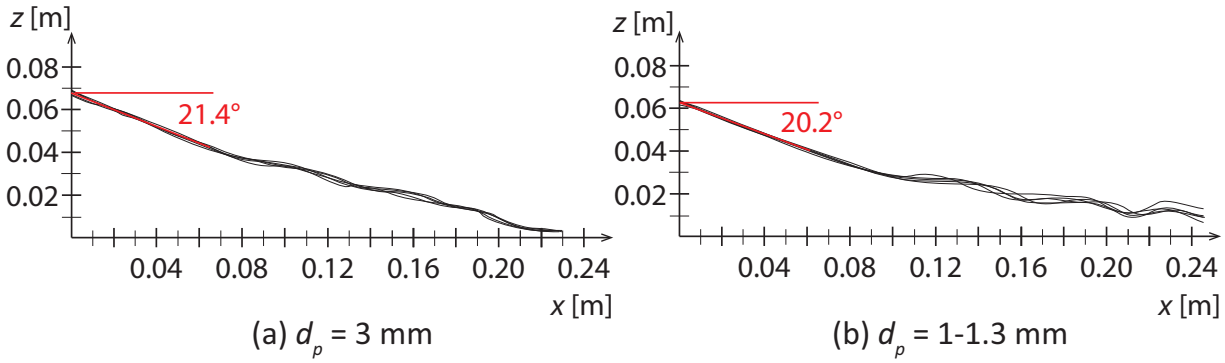

Figure 6.50: Sketch of the final deposit shape of the 3 mm (left) and 1.15 mm (right) glass particles for the submerged fast slumping tests

The final deposit silhouette of the submerged slumping tests result in a slope under an angle of in average 21.4° for the 3 mm particles and 20.2° for the 1.15 mm particles. In comparison to the results of the dry cases, the angle of the 3 mm particles remains unchanged while the angle is reduced by in average 1.3° for the 1.15 mm particles (see Table 6.16). The comparison of the final deposit silhouette in Figure 6.49f and Figure 6.50a presents an important difference between the dry and the submerged column tests. While the final silhouette in the dry tests resulted in a constant shape over the basin depth in y-direction, the final silhouette of the submerged tests is slightly irregular over the depth. The silhouettes in Figure 6.50 are strictly limited to the constitution directly at the plexiglas wall. The new inhomogeneity in depth must result from the fluid-particle interaction. Thus, the induced currents in the fluid are not consistent over the basin depth.

The analysis of the deposit tip evolution for the submerged tests occur more precarious than for the dry tests. As before, the position of the deposit tip is detected by the position of high velocities along a line above the fixed particle layer by a Matlab algorithm. Since, the deposit tip moves with the highest velocity compared to the remaining deposit, the position can be identified. However, the generation of particle clouds due to the wall extraction prevent the distinct identification of the deposit tip at the early stage of the tests. Although, the deposit tip can be identified by the naked eye, the algorithm cannot

distinguish between the velocity vectors of the dissolved particles in the cloud and those of the deposit tip. As a result, the acceleration phase of the collapse is not as clear as in the dry tests, especially for the 1.15 mm particles. However, the subsequent movement of the deposit phase can be analysed more accurate and shows again a phase of constant spreading and a phase of deceleration (see Figure 6.51). Figure 6.51a presents the tip movement over time for the 3 mm particles and Figure 6.51b the tip movement over time for the 1.15 mm particles at test 1. All results for the deposit tip development in time are presented in the Appendix in Figure B.28 and Figure B.29. The total duration till the deposit reaches its final length increases significant in the submerged slumping tests. While, the tests under dry conditions resulted in a duration of $T = 3.2\ t_c$ for the 3 mm and $T = 3.1\ t_c$ for the 1.15 mm particles, the submerged tests result to a duration of $T = 6.8\ t_c$ for the 3 mm and $T = 7.8\ t_c$ for the 1.15 mm particles. However, this number are not fully comparable, since the materials do not reach the true final length in the dry slumping scenarios due to the limitation of the basin. In both cases, an acceleration phase can be observed, which lasts till in average $t = 1.58\ t_c$ for the 3 mm particles and $t = 1.99\ t_c$ for the 1.15 mm particles. However, especially for the 1.15 mm case the identification of the collapse initiation might be inaccurate, since the movement of the dissolved particle cloud superimpose with the early spreading of the material. Thus, the given duration of the acceleration phase should be handled with care. The subsequent phase of constant spreading is more explicit and lasts for in average $t = 4.40\ t_c$ for the 3 mm particles and $t = 4.63\ t_c$ for the 1.15 mm particles. Thereby, the tip reaches a constant velocity of in average 0.245 m/s for the 3 mm particles and 0.286 m/s for the 1.15 mm particles (see Table 6.16). The very low standard deviation of the determined tip velocity for both cases substantiates the results of the individual tests. The deceleration phase differs for the different applied material. While, the deposit tip for the 3 mm particles fully decelerates already before the maximum length of the basin is reached, the 1.15 mm particles decelerate but impact with the opposed x-normal wall. The duration of deceleration takes $t = 0.84\ t_c$ for the 3 mm particles and $t = 1.21\ t_c$ for the 1.15 mm particles.

Following, the differences between the tip development in time for the different materials as well as the test conditions are discussed in more detail. Therefore, Table 6.16 summarises the results of the submerged tests and the results of the tests under dry conditions. The comparison of the dry and submerged conditions show a significant reduction of the tip velocity for the submerged cases. Thus, the velocity is reduced to 40.6% of the value of the dry tests for the 3 mm particles and to 43.1% for the 1.15 mm particles. The velocity reduction results from the additional viscous resistance of the fluid against the movement of the particle material movement. Further, it can be seen, that the 1.15 mm particles reach a higher constant spreading velocity than the 3 mm particle for the dry case and the submerged case. For the dry case the finer particles are 1.10 times faster than the 3 mm particles, while for the submerged case the finer particles are 1.17 times faster. The smaller spreading velocity of the 3 mm particles than the 1.15 mm particles can be caused by a sum of several influences. On one hand, the greater diameter of the coarser particles results in greater drag forces and, thus, a greater resistance by the viscous fluid against particle movement. On the other hand, the collapsing particle material represents a particle group and, thus, group effects need to be taken into account. This effects

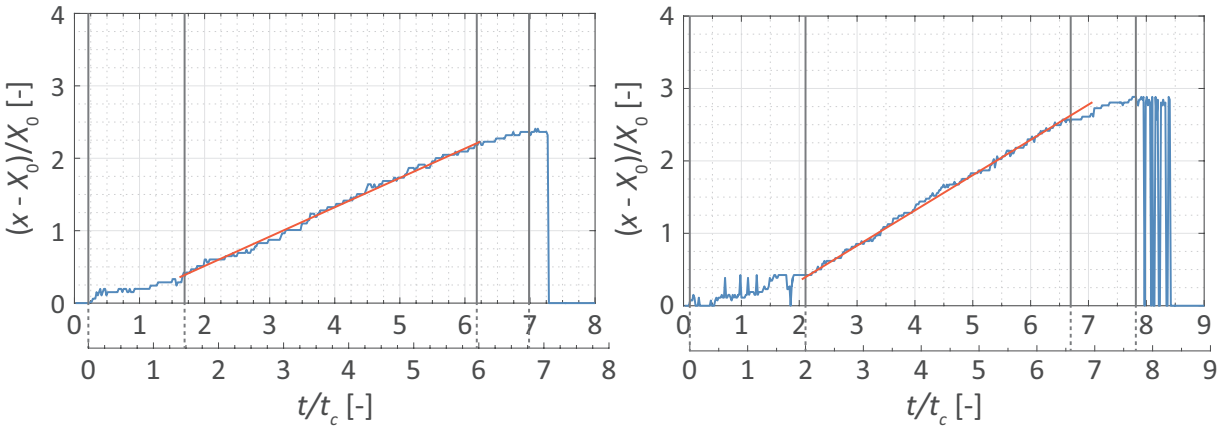

(a) Test 1 with $d_p = 3$ mm (b) Test 1 with $d_p = 1.15$ mm

Figure 6.51: Movement of the deposit tip over time for the submerged slumping tests with $d_p = 3$ mm and $d_p = 1.15$ mm

can be illustrated by an example of a settling particle group. Thus, free falling particles groups reach higher settling velocities than a single particle of the same diameter. In a particle group the front particles accelerate the surrounding water. As a result, the relative velocity between the already accelerated fluid and particle in the wake of the first particle is reduced. This reduction in relative velocity results in a lower drag for the following particles and the total particle group is settling at a faster velocity, whereby the particle positions in the group are changing. A similar effect occurs for the particle material in the submerged slumping tests. The particles react as a group against the viscous water resistance. Whereby the coarser material experiences a higher resistance as a group than the group consisting of finer particle diameters. A possible explanation lies in the acceleration of the surrounding fluid and in specific the pore-fluid by the particles, which are in turn accelerated by gravitation. In case of the 1.15 mm particles, the dissolved particle group is less permeable and the particles and the surrounding pore-water form a compound against the free fluid drag resistance. This affect occurs also for the 3 mm particles, but due to the higher permeability the free fluid can penetrate into the slumping mass and result into a higher drag resistance as a group.

Due to the reduced collapse velocity, the duration of the total collapse is significantly increased for the submerged slumping case. Thus, the duration increases by a factor 2.1 for the 3 mm particles and by a factor 2.6 for the 1.15 mm particles. Thereby, the different final lengths for the 3 mm case under dry and submerged conditions need to be taken into account. This increase in total duration is caused by the additional viscous resistance of the fluid, which also decreased the spreading velocity. Thereby, the duration of the different phases of the collapse process in time is longer for the 1.15 mm particles than for the coarser 3 mm material.

The presented tests give a good idea about the processes and the interaction between the particles and the surrounding fluid. However, the phenomenon of the grouping effect needs to be proven. Further, the effect of the induced free fluid flow on the collapse process is unclear such as the reverse influence of the moving particle material on the fluid. To get a

Table 6.16: Average results for the submerged fast collapse tests in comparison to the tests under dry conditions

Tests	Glass 3 mm			Glass 1.15 mm		
	Slope angle	Duration final width $[t_c]$	Tip velocity [m/s]	Slope angle	Duration final width $[t_c]$	Tip velocity [m/s]
∅ Submerged	21.4° ±0.54°	6.8 ±0.08	0.245 ±0.004	20.2° ±0.24°	7.8 ±0.14	0.286 ±0.005
∅ Dry	21.4° ±0.85°	3.2 ±0.30	0.603 ±0.019	21.5° ±0.31°	3.0 ±0.07	0.663 ±0.011

better idea of this point, the behaviour of the water needs to be in investigated additional to the particle collapse process. The numerical simulation of the submerged fast collapse gives the possibility to investigate this interaction in detail.

6.5 Numerical Simulation of the Submerged Column Collapse

The physical tests showed the collapse characteristics for the submerged fast collapse tests. The influence of the fluid-particle interaction became apparent in a damping of the collapse process. The submerged collapse in the physical tests is investigated further by numerical simulations with the CFD-DEM approach. Thus, the complex micro-mechanical interactions between the individual particles and the free water as well as the pore water shall be identified. Further, the behaviour of the individual phases can be investigated separately. The results of the physical tests are later applied for the validation of the numerical simulations.

The numerical simulation of the submerged particle collapse is based on the findings of the investigations under dry conditions. Thus, the simulation domain, properties and chronology of the fast collapse under dry conditions in Section 6.3.6 are applied for the DEM side of the coupled CFD-DEM simulation. The CFD domain is based on the DEM simulation. A decidedly description of the coupled CFD-DEM simulation setup is given following. Afterwards, the results of the simulations are presented and the effect of different drag-force models are investigated.

6.5.1 Development of numerical model

The simulation domain of the submerged collapse simulations are based on the plexiglas basin and the applied fluid volume in the physical tests. Thus, the simulation domain has a height of 25 cm equal to the fluid height and a width of 25.2 cm equal to the

basin length. The depth of the simulation domain is based on the specifications in the slumping simulations under dry conditions. Thereby, the depth is differentiated regarding the applied slumping material. The 3 mm particle simulations have a depth of 4.5 cm, while the 1.15 mm simulations have a depth of 1 cm. To test the influence of the reduced domain depth on the 1.15 mm particles, an identical simulation with 2 cm depth has been investigated. The differences between the simulations regarding the collapse characteristic as well as the final deposit shape were marginal. Thus, the depth of the simulation domain is adopted to the smaller dimension, since a greater depth would increase the number of required particles and the computational costs. However, depth varying results as seen in the physical tests are neglected by this assumption.

The chosen boundary conditions (BC) for the simulation are differentiated between the DEM and the CFD domain. The BC for the DEM simulations are equal to those of the simulations under dry conditions (see Section 6.3.5). The x-normal as well as the lower z-normal wall are defined as rigid walls with a property setting of the plexiglas wall (material type 2). The domain is open in its upper z-normal boundary. The y-normal walls have periodic BC. In the CFD domain, the BC are specialised individually for every simulation parameter except for the y-normal boundaries, which have symmetric BC. In OpenFOAM the symmetric boundary condition sets the face-normal components of a parameter to zero as well as the face-normal components derivatives. The cell values are than adopted to the boundary face. The BC of the x-normal boundaries and the lower z-normal boundary are defined as impermeable walls. The fluid velocity v_f has a no-slip condition at this boundaries. For the remaining parameters the cell-centre value is adopted to the boundary face with exception of the turbulence related parameters. The BC for the turbulence parameters are explained in the following paragraph by means of the applied turbulence model. The upper z-normal boundary is defined as atmosphere and gives the opportunity for fluid inflow/outlet. At this boundary, the dynamic pressure p is defined by a Dirichlet-condition which is given to $p = 0$. For the fluid velocity v_f, a combined BC for inflow and outflow is defined. In the case of outflow, the cell-centre value is adopted to the boundary face, while for inflow the value is obtained from the boundary normal component of the cell-centre value. All other parameters adopt the cell-centre value to the atmosphere boundary face.

Before the BC for the turbulence parameters are presented, the chosen turbulence model need to be discussed. The high amount of particles in the slumping mass limits the coupled simulation to an unresolved simulation. Thus, the CFD cells need to be bigger than the DEM particles. This requirements substantiate the choice of a statistical turbulent viscosity models in combination with RANS. As described in Section 4.2.6, the most established two-equation transport models are the k-ω and the k-ϵ model. Regarding the resolution of the wall-near turbulences, the models can be further differentiated into high-Re and low-Re models. While the low-Re models use a refined mesh in the wall-near region to estimate the turbulences based on the viscous sublayer, the high-Re models uses a coarser mesh to estimate the wall near turbulences based on the logarithmic law with the help of wall-functions. Independent of the resolution, every approach is bound to specific requirements regarding the wall-near meshing, which is based on the wall-near velocity profile. Higher velocities require a finer resolution in wall normal direction to

estimate the turbulences. Since, the simulations of a collapsing particle column start at a motionless state and higher velocities are induced due to the wall extraction and the collapse, the changes in the wall-near region are too great to chose a pure low-Re or a pure high-Re approach. Either the wall-near velocity at lower values or greater values would be calculated wrong or the required meshing would conflict with the requirements for an unresolved simulation. To find a solution, a combination of the k-ω and the k-ϵ model is applied: the k-ω-SST model. Thereby, the model blends between the k-ω and the k-ϵ formulation dependent on a blending function, which respects the distance of the present cell from the wall. In combination with specific wall functions in OpenFOAM, also the turbulence calculation in the wall-near cells merges between the characteristic representation of the wall-near velocity for the low-Re approach of the k-ω model and the high-Re approach of k-ϵ model. Nonetheless, this approach of merging wall functions is not very accurate for boundary layer flow problems. However, a highly accurate modelling of the ultimate wall-near velocity and turbulence is not as relevant than the simulation of the velocities and turbulences within the simulated domain.

With the merged wall function approach for the BC of the turbulence parameters, an evenly ordered spatial discretisation is applied in the simulation. Thereby, the meshing of the CFD domain is based on a block-structured mesh with constant cell widths. Thus, the cells have a cubic shape. Thereby, the cell sides have a length of three times the particle diameter. This mesh resolution give sufficient results. The resolution of the mesh has a big impact on the calculation of the drag force. Thus, the final length of the deposit is related to the mesh resolution. For coarser meshes, the final deposit length is smaller than for finer meshes. This is due to the CFD-DEM averaging of the particle velocities and, thus, the interaction forces in a CFD cell. The particle velocities are averaged for the particles positioned in the corresponding cell to determine the interaction force. After the collapse of the particle column the deposit spreads in positive x-direction, whereby just the upper layers of particles are moving. In the case of a coarse mesh the average particle velocity within a cell is calculated from moving particles as well as stationary particles. This reduces the averaged particles velocity significantly. As a result, the relative velocity between fluid and particles is overestimated and, thus, the drag force. The overestimation of the drag force leads to a higher deceleration of the slumping mechanism.

As in Section 6.3.5, the extraction velocity of the movable is investigated in the physical tests. Thereby it becomes evident, that the extraction of the movable wall for the submerged simulations need to be adapted. The extraction velocity is higher than in the dry cases (see Figure 6.52). Therefore, the lifting of the wall foot is analysed and a curve fit is generated. This curve fit is applied to calculate the wall extraction velocity, which is provided to the equation in Equation 6.10.

$$v_{z,\text{wall}} = \begin{cases} -147.87 \cdot t^2 + 26.66 \cdot t + 0.1786 & (t < 0.09 \text{ s}) \\ 1.38 & (t \geq 0.09 \text{ s}) \end{cases} \tag{6.10}$$

In the DEM simulations, the movable wall is represented by a 2D mesh. This mesh is not recognized on the side of the CFD simulation. However, the simulation of the interaction between the wall and the free fluid and the reproduction of the induced flows is essential for a successful simulation of the submerged column collapse. Thus, a movable wall is

required for the CFD simulation. Though, the representation of a solid wall requires a solid boundary in CFD simulation. This in turn would require a dynamic mesh approach in the CFD solver, which is not yet implemented in CFDEM. Thus, the movable wall is approximated by a dense wall of particles. Thereby, the diameter of the applied particles is 0.5 cm and, thus, equal to the width of the movable wall in the physical tests. The particles are arranged over the full height of the simulation domain in an evenly arrangement of rows over each other. Thereby, the particles are packed so close, that they are just touching each other. The particles are assumed as a separate group of particles, which are moving as a unity with the velocity presented in Equation 6.10. The group of particles has no time contact with the remaining particles of the column and are not included in the DEM algorithm. Thus, the slumping particles are just in contact with the 2D mesh rather than the particles representing the movable wall. In contrast, the particles interact with the fluid and the fluid flows due to the wall extraction can be captured in the simulation. However, the resulting fluid motion might differ from the physical tests, since no absolutely impermeable boundary is created.

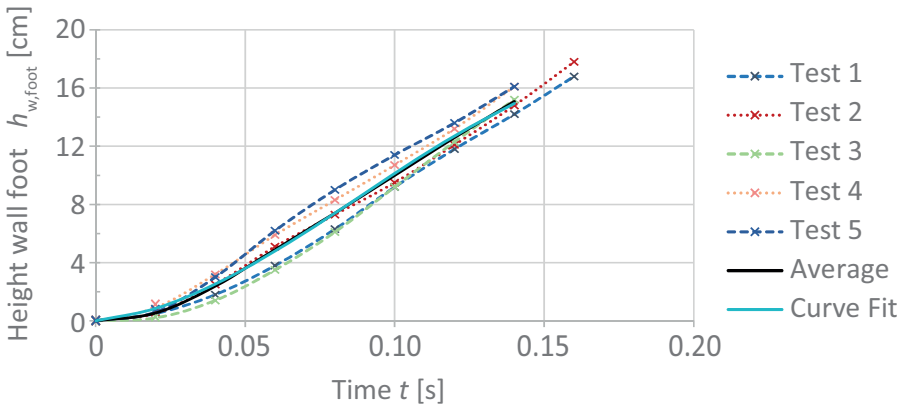

Figure 6.52: Extraction of movable wall in physical slumping tests under submerged conditions

The material properties for the movable wall as well as the other rigid walls are assumed as identical and equivalent to those applied in the fast dry column tests. The properties of the granular material are assumed equally to those applied in Section 6.3.7. The water is represented as Newtonian fluid with a kinematic viscosity of $\nu_f = 1.0 \cdot 10^{-6}$ m^2/s and a density of $\varrho_f = 1000$ kg/m^3. The interaction between the fluid and the particle phase is limited to the drag force as the most significant interaction force. In the simulation the Koch & Hill (2001) drag model is applied. However, to investigate the fluid-particle interaction for different drag models, two further drag force models are applied: The Di Felice (1994) model and the Gidaspow (1994) model.

6.5.2 Results of fast collapse simulation under submerged conditions

As in the physical tests, the collapse process in the simulations is clearly decelerated due to the presence of the fluid in comparison to the dry test. The acceleration and deceleration

phase as well as the phase of constant spreading is significantly extended. Thus, the interaction between the fluid and the particle phase in form of an additional resistance due to the drag force is captured in the simulations. The CFD-DEM simulation enables the detailed investigation of each individual phase. In the following the detailed collapse mechanism in the simulation is presented. Further, the collapse dynamics for each phase are discussed by analysing the spreading of the material tip over time.

Figure 6.53 and Figure 6.54 present the submerged particle collapse over time for particles with $d_p = 1.15$ mm and initial packing 4. Thereby, the left sided figures illustrate the fluid phase presented by the fluid velocity v_f, while the right sided figures illustrates the disperse particle phase presented by the particle velocities v_p. The figures present a cutout of the simulation domain till a height of 16 cm due to presentation purpose. The characteristics of the particle collapse are illustrated by the 1.15 mm particles, since the particle and the fluid velocities are higher than for the bigger 3 mm particles. The collapse of the 3 mm particles is presented in the appendix at Figure B.30 and Figure B.31. The collapse process is similar disregarding small divergences in the final shape and the dynamical evolution.

Figure 6.53a illustrates the state at $t \approx 1.0\ t_c$. At this state, the movable wall is fully extracted from the particle column height. In contrast to the dry simulations, the position of the particles is still very similar to the initial state although the whole movable wall is already extracted. However, the collapse process is slightly advanced in comparison to the physical tests. While in the physical tests, the collapse is delayed due to the fluid interaction, the delay in the simulations is less significant. Thus, the whole particles column in Figure 6.53a moved already downwards to a height of approximately 10 cm, while in the physical tests the column has still the initial height of approximately 10.6 cm (see Figure 6.49a). This delay in the physical tests is most likely an effect of dilatancy. Dilatancy describes the change in volume of a granular packing due to shear deformations. In the case of a medium to dense packing, the volume of the packing increases under shear deformations. The increase of volume is based on greater void volume due to the rearrangement of particles. Under submerged conditions, the free fluid needs to entrain into the pore system to fill the voids. However, the fluid cannot enter the porous voids easily due to the restricted flow cross section in the porous media and, thus, is limited to enter the porous media with a filter velocity. In the case of the collapsing column, this limitation of inflow into the voids results into a small pore water under-pressure which slows down the (shear) deformation due to the collapse. This effect is not captured in the simulations, since the flow around the particles is not resolved.

The phenomenon of dissolved particle cloud development as a result of the wall extraction does not occur in the simulations. The extraction of the movable wall accelerates the free water. Thereby, a trail of fluid with a higher velocity is positioned on the lee side of the movable wall. This trail of accelerated fluid entrains adjacent particles near the column top but does not entrain surface particles out of the column side as seen in the physical tests. The entrainment is further affected by the friction between the particles and the moving wall. The fluid within the particle column is accelerated with the collapse particles and moves downwards with the particle phase. This fluid represents the pore-fluid inside the particle skeleton. However, since the unresolved CFD-DEM does not resolve the flow around the particles this pore-fluid is further appointed as averaged pore-fluid.

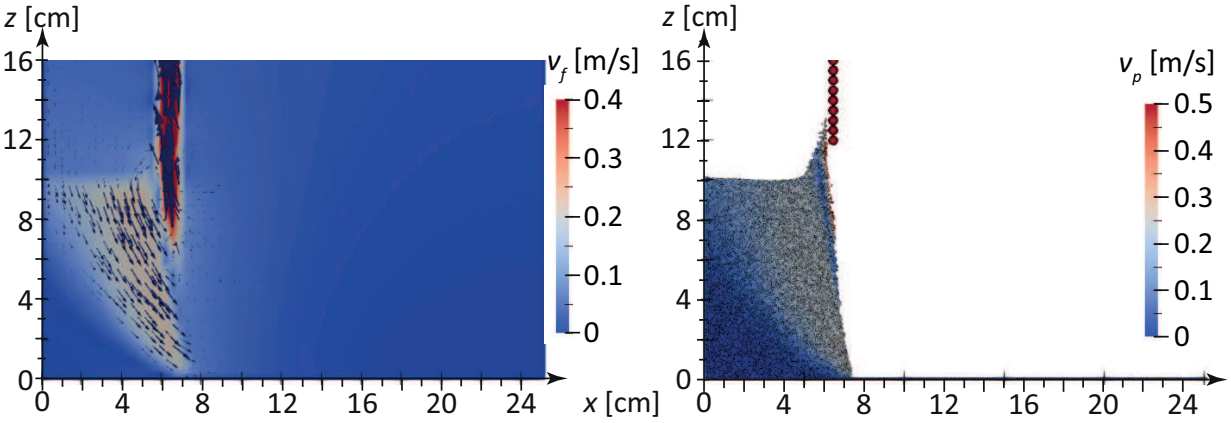

(a) $t \approx 1.0\ t_c$

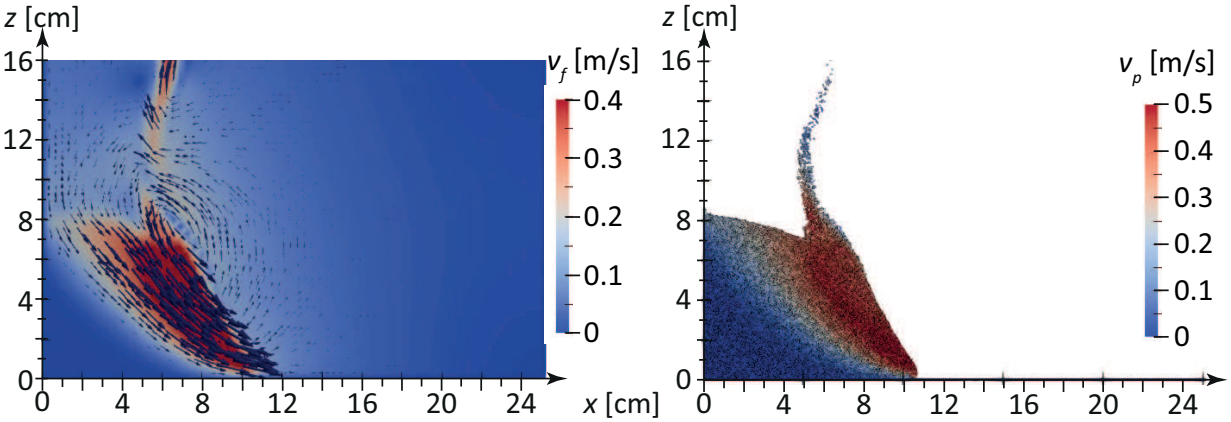

(b) $t \approx 2.0\ t_c$

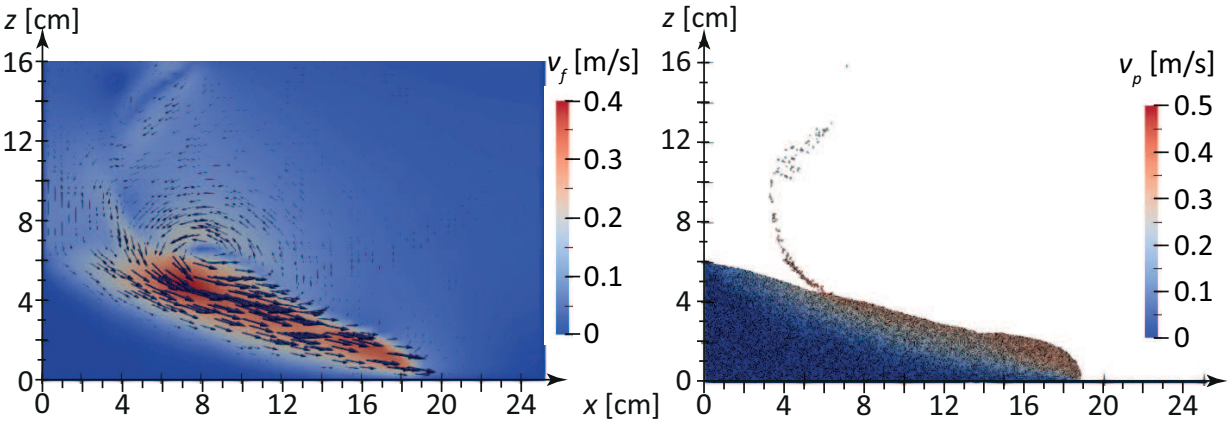

(c) $t \approx 4.0\ t_c$

Figure 6.53: Fast collapse of a submerged particle column with 1.15 mm glass particles - Collapse characteristics at selected points in time for the fluid phase (colouring based on fluid velocity v_f) (left) and the particle phase (colouring based on particle velocity v_p) (right)

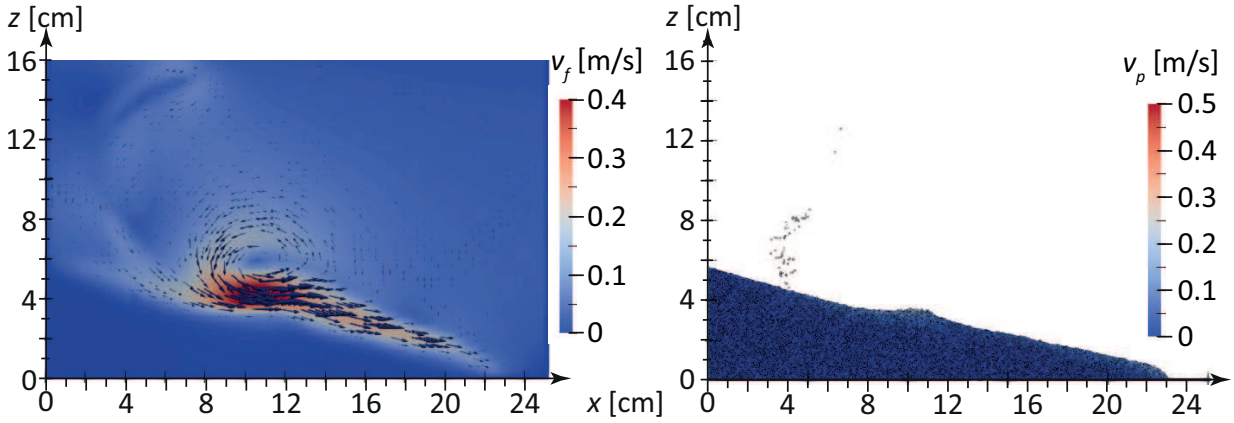

(a) $t \approx 6.0\ t_c$

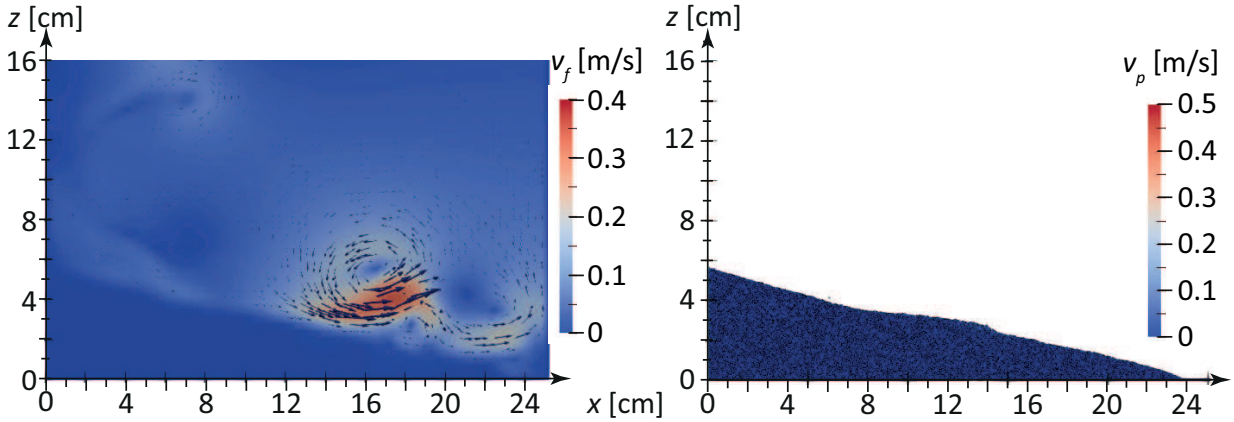

(b) $t \approx 10.0\ t_c$

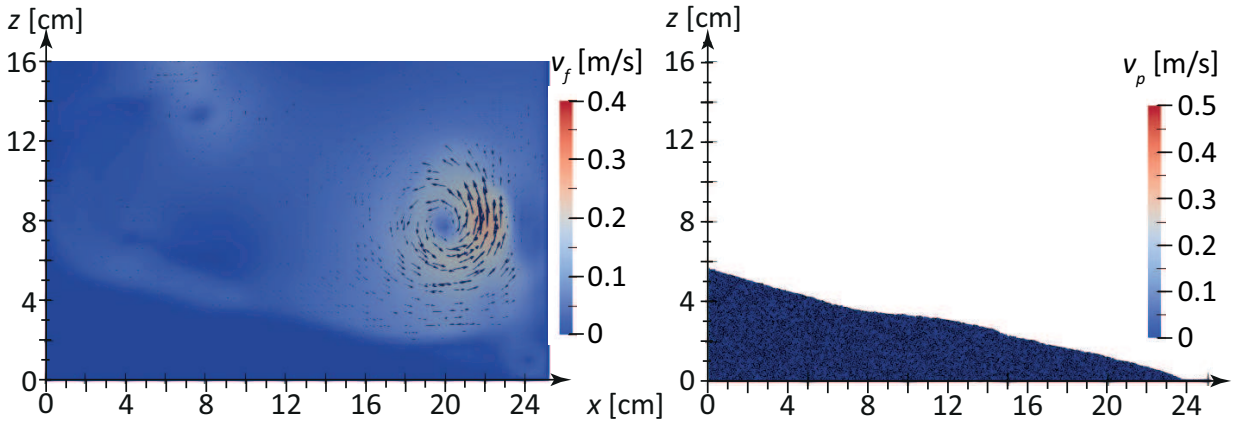

(c) $t \approx 17.0\ t_c$

Figure 6.54: Fast collapse of a submerged particle column with 1.15 mm glass particles - Collapse characteristics at selected points in time for the fluid phase (colouring based on fluid velocity v_f) (left) and the particle phase (colouring based on particle velocity v_p) (right)

At Figure 6.53b the collapse is fully developed and the initial shape of the particle column significantly deformed. The particles move along a slip-joint over a wedge of stationary particles. Although the internal mechanism is similar to the dry case, the lower area of the deposit tip is more blunt than in the dry simulations due to the additional resistance of the fluid. This characteristic is equal to the behaviour in the physical tests. However, the significant dissolving of the particles during the collapse as seen in the physical tests is not captured in the simulations. Although, the fluid-particle interaction effects the collapse in the simulations significantly, the collapse characteristics are still more similar to the dry slumping process. In Figure 6.53b, the influence of particle entrainment by the movable wall becomes apparent. The upper particles adjacent to the movable wall are lifted high up with the accelerated fluid below the movable wall foot. This behaviour is overestimated in comparison to the physical tests. However, while in the physical tests the entrained particles build dissolved particle clouds, the particles in the simulations are not dissolving but rather build a trail. This effect is less significant for the 3 mm particles. The averaged pore-fluid is further accelerated with the moving particles. Thereby, the collapse process in combination with the flow generated by the wall extraction, induces the development of a big vortex approximately at the former upper right corner of the particle columns. This vortex is becomes more clear in Figure 6.53c. At this stage, the lower layers of the particle mass is already decelerating, while the particle movement at the surface of the deposit and the deposit tip itself is still moving. The highest fluid velocities are no longer limited to the averaged pore-fluid but rather in the free fluid above the deposit surface below the vortex. Due to the column collapse, the averaged pore-fluid as well as the free fluid is accelerated. Thereby, the acceleration takes place due to the interaction of the free fluid with the averaged pore-fluid as well as the interaction between the free fluid and the surface particles. The averaging of the fluid phase in the CFD-DEM simulation approximates this behaviour. However, while the averaged pore-fluid is equally accelerated and decelerated with the particles, the free fluid is less significant influenced by the particle deceleration after the development of the deposit slope. As a result, the accelerated free fluid remains at higher velocities while the particles and the averaged pore water are significantly decelerated in Figure 6.53c. This behaviour is even more significant in Figure 6.54a. At this stage, the majority of the particles become stationary, while the free fluid velocities above the deposit surface are still high. Thus, the vortex moves into positive x-direction although the particles are stationary. The velocities of the free fluid are that high, that the deposit surface is subsequently affected by the vortex and the material is pushed into positive x-direction and builds a small ripple. This development of ripples occurs also in the physical tests. However, the ripples in the physical tests are positioned at the deposit foot and are generated during and slightly afterwards the final spreading of the material. In the simulations, the particles are already static when the ripple develops. In the simulation of the 3 mm particles, the phenomenon of ripples does not occur since the bigger particles have a higher resistance and the free fluid velocities are even smaller than in the 1.15 mm simulation. In Figure 6.54b the free fluid vortex is positioned more downwards the deposit slope and lost intensity in velocity due to the interaction with the deposit surface. Due to the slower fluid velocities, the particles are less affected by the free fluid flow. Due to the vortex movement, the developed ripple is flattened and compose a flatter section in the deposit slope between approximately

x =8 cm and x =12 cm. At this stage, the particle deposit reaches its final position. It is evident, that the final deposit shape for the 1.15 mm particles defers from the physical tests. While the particles in the tests reach the opposed x-normal wall, the particles in the simulations decelerate before the deposit reaches this wall. For the 3 mm particles, this difference is less significant. Subsequently, the DEM particles stay stationary and the vortex moves further into x-direction and than upwards as it comes closer to the x-normal wall (see Figure 6.54c). The final deposit packing is slightly more loose than the initial packing. Thus, the initial packing of the 3 mm particles had in average a fluid volume fraction of 0.4004, while the final deposit has a fluid volume fraction of 0.4117. For the 1.15 mm particles, the initial packing had a fluid volume fraction of 0.3962 in average, while the final deposit has a fluid volume fraction of 0.4086.

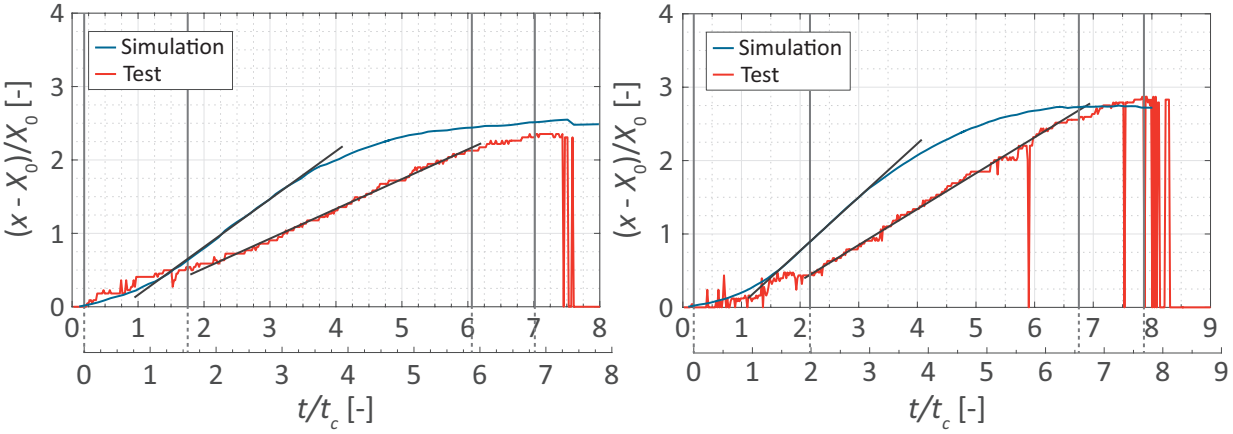

(a) $d_p = 3$ mm (b) $d_p = 1.15$ mm

Figure 6.55: Evolution of the deposit tip position over time at the submerged fast collapse with 3 mm and 1.15 mm glass particles: Comparison of simulations and physical tests

The CFD-DEM simulations show, that the generation of ripples is not an effect of the flow induced by the wall extraction, but by the free fluid velocities which result from the column collapse. However, the chronology of the collapse process and the interaction is different for the physical tests and the simulation. Thus, the consequences of this interaction is different as well. Figure 6.55 presents the evolution in time of the deposit tip for the physical tests and the simulations in contrast. The duration till the deposit tip reaches its final state is similar. However, the progression of the three characteristic phases is different. The acceleration phase for the slumping lasts clearly longer for the physical tests than in the simulations with in average $t = 1.58\ t_c$ for the 3 mm particles and $t = 1.99\ t_c$ for the 1.15 mm particles. In the simulations, the acceleration phase lasts in average approximately $t = 1.30\ t_c$ for the 3 mm particles and $t = 1.40\ t_c$ for the 1.15 mm particles. Thereby, it is important to keep in mind, that not just the acceleration of the deposit tip is different, but the whole initiation of the collapse. The particle column in the physical tests keeps the initial position over a slightly longer time before it dissolves, while the particle mass is already moving in the simulations. However, the collapse simulations under dry conditions resulted in an acceleration phase duration of in average

$T = 0.9t_c$ for the 3 mm particles and $T = 1.0t_c$ for the 1.15 mm particles. Thus, also the simulations reproduce the support of the initial particle column due to the viscous fluid and the resulting delay. However, the dissolving of the particle packing in the physical tests represents a crucial effect, which is not captured in the simulations. Since a drag resistance is included and, thus, a damping effect on the particle movement is present in the simulations, this dissolving needs to be based on other phenomena. A possible effect might be again dilatancy. After the first shear deformations of the particle column in the physical tests, additional pore fluid fills the voids. However, with ongoing deformations and, thus further change in void volume, the pore fluid cannot flow outside easily and damps the movement of the particles within the collapsing particle mass. The particles mass assumes dissolved. Thus, the interaction between the particles is even more reduced than in the dry slumping tests. This effect can be increased by the lubrication force. The lubrication force represents a hydrodynamic viscous force arising from radial pressure in the interstitial fluid being squeezed from the space between two close solid surfaces (W. Zhang et al., 2005). This additional resistance against particle contact, might increase the dilatancy effect.

The acceleration phase merges to a phase of spreading at constant velocity. Thereby, the constant spreading phase is shorter in the simulations than in the physical tests. The comparison of the physical tests under submerged and under dry conditions shows, that the constant spreading velocity is significantly reduced by an factor of approximately 2.5 for the 3 mm particles and 2.3 for the 1.15 mm particles (see Table 6.17). The constant spreading velocity in the simulation is higher than in the physical tests. The constant velocity in the simulations is 1.6 times as high for the 3 mm particles and 1.5 times as high for the 1.15 mm particles as in the physical tests (see Table 6.17). As a result, the position of the deposit tip in the simulations is ahead of the position in the physical tests. The spreading velocity of the simulations under dry conditions is also higher than those in the physical tests. The reduction of the spreading velocity from the dry to the submerged conditions in the simulations is a factor of 1.8 for the 3 mm particles and 1.7 for the 1.15 mm particles. Thus, the velocity reduction is less significant than in the physical tests.

Subsequently to the shorter phase of constant spreading, the simulations show a long deceleration phase. Since the deceleration phase is very long, the overall slumping duration in the simulations is similar to those in the physical tests with a shorter deceleration phase. In contrast to the 3 mm particles, the length of the deposit is smaller for the 1.15 mm particles in the simulations than in the physical tests. As a result, it takes a longer duration till the deposit reaches its final width in the physical tests. The final deposit length in the simulations is 21.88 $\pm$0.16 cm for the 3 mm particles and 23.66 $\pm$0.08 cm for the 1.15 mm particles. In the physical tests, the 3 mm particle deposit reached a length of 21.93 $\pm$0.34 cm, while the 1.15 mm particles filled the whole width of 25.2 cm of the basin. Thus, the length of the 3 mm particles is very similar in the simulations and the physical tests. However, the results for the 1.15 mm particles show that the final width in the simulations is under-predicted. It is possible, that the total length is not varying too much in the simulations. To get a better estimation on that, different materials at different axes ratios need to be investigated in a bigger domain.

Table 6.17: Average results for the submerged fast collapse simulations in comparison to the physical tests under submerged and dry conditions

	Glass 3 mm			Glass 1.15 mm		
	Top slope angle	Duration final width [t_c]	Tip velocity [m/s]	Top slope angle	Duration final width [t_c]	Tip velocity [m/s]
∅ Sub. sim	17.1°	6.39 ±0.05	0.397 ±0.004	16.7°	5.67 ±0.02	0.436 ±0.0059
∅ Sub. tests	21.4° ±0.54°	6.8 ±0.08	0.245 ±0.004	20.2° ±0.24°	7.8 ±0.14	0.286 ±0.005
∅ Dry sim	17.8° ±0.30°	3.09 ±0.02	0.71 ±0.006	16.6 ±0.32°	3.08 ±0.04	0.729 ±0.004
∅ Dry tests	21.4° ±0.85°	3.2 ±0.30	0.603 ±0.019	21.5° ±0.31°	3.0 ±0.07	0.663 ±0.011

The faster collapse process in the simulation has an impact on the interaction between the free fluid phase and the particle mass. As described above, the collapse induced vortex in the simulations creates ripples in the middle of the deposit surface after the final state is reached, while in the physical tests the phenomenon of ripples takes place in the deceleration phase at the lower deposit slope. This differences is caused by the deviating chronology of the collapse process. Assuming that the same flow patterns are induced by the collapse for the simulations and the physical tests and also the induced flow velocities are similar, the faster spreading process of the particle mass in the simulations leads to the completion of the collapse process before the interaction between the vortex and the deposit surface occurs. The slower spreading in the physical tests results in an interaction of the vortex with the particle mass before the collapse process is completed. However, it is uncertain if the induced flow in the simulations are equal to those of the physical tests, since the fluid velocities are not measured in the physical tests. But the development of ripples in the physical tests as an result of the interaction between fluid and particles prove, that the accountable flow pattern is induced at the early stage of the collapse. The early vertical movement and deflection into a horizontal spreading at the early collapse process induces the clockwise vortex pattern. The vortex follows the movement of the deposit and moves along the deposit surface. However, the flow pattern might deviate in the physical tests and further lead to different results. Ti investigate this point further, it is necessary to find a possibility to measure the free fluid velocities in the physical tests independent from the granular material. A possibility might be the application of a florescent tracer and a corresponding filter for the high-speed camera to investigate the fluid flow only.

The interaction between the fluid and the particle phase during the collapse process is presented by means of the drag force in Figure 6.56 for all individual particle packing simulations. Therefore, the global drag force F_D is normalized by the global particle weight F_G. The global value of a certain parameter denotes the summation of the particle

values over the global domain. Thereby, neither the particles of the bottom layer nor the particles representing the movable wall are included. For both particle diameters, the global normalized drag force $F_D^* = F_D/F_G$ increases after the begin of the simulation (see Figure 6.56). The normalised drag force reaches a maximum after $t \approx 0.8\ t_c$ for the 3 mm particles and at approximately $t \approx 0.6 - 0.7\ t_c$ for the 1.15 mm particles. Thereby, the maximum value is $F_D^* \approx 3$ for the 3 mm particles and $F_D^* \approx 4.8$ for the 1.15 mm particles. The higher normalised drag force values for the 1.15 mm particles cannot be caused by different averaging due to the voidfraction model, since the spatial discretisation is based on the particle diameter and, thus, have for both particle diameters the same relation between the particle and the cell volume. However, the magnitude of the drag force is determined by means of the relative velocity between fluid and particle phase (see Section 2.2.2). Since the 1.15 mm particles reach higher velocities in the simulations, the relative velocity is also higher and causes greater drag forces. The high drag forces directly after the collapse initiation are caused by two influences: First, the acceleration of all particles due to gravity accompanied by a vertical particle movement; Second, the extraction of the movable wall. Due to the interaction between the wall and particles during the extraction, the particles adjacent to the movable wall are accelerated with the movable wall. This acceleration induces locally high relative velocities between fluid and particles and, thus, high drag forces (see Figure 6.57a). However, the number of adjacent accelerated particles is decreasing with ongoing extraction of the wall. As a result, the peak is positioned beforehand of the total extraction of the wall at $t \approx 1.05\ t_c$. After the peak value, the normalised drag force declines significantly till $t \approx 1.5\ t_c$. This point in time is equivalent to the end of the acceleration phase of the deposit tip spreading and the transition from a vertical movement to a horizontal spreading of the particles (see 6.55b). After this moment in time, the development of the drag force deviates for the 3 mm and the 1.15 mm particles. While for the 3 mm particles the drag force decreases slowly, the normalised drag force for the 1.15 mm particles increases till approximately $t \approx 2.5\ t_c$ before it starts to decrease. This phenomenon results from the extraction of the movable wall and the accompanied particle entrainment. For the 1.15 mm particles, a higher number of particles is lifted more significantly with the movable wall than in the 3 mm particle simulations (see Figure 6.57b). Around $t \approx 1.5\ t_c$ the majority of the entrained particles reach the zenith of their path, which is accompanied by a deceleration and a acceleration afterwards. This new acceleration induces the re-increase of the drag forces subsequent to $t \approx 1.5\ t_c$. As the lowest entrained particles merge with the collapsing particle mass, the global drag force is decreasing again.

After the collapse characteristics merge to a horizontal spreading, the particles with maximum drag force are positioned at the right surface of the deposit mass and especially at the deposit tip (see Figure 6.57b). Thereby, the flatter the deposit becomes, the more the maximum drag forces are concentrated at the deposit tip. Thereby, the surfaces orthogonal to the spreading direction show the highest drag forces. In the case of the 1.15 mm particles, the thickness of the area with higher drag forces is approximately two particles diameters from the surface. This proves the behaviour of the particle mass as a continuum, since the free fluid is not intruding into the voids in-between the particles. Although, the glass material is coarse in the range of sand or fine gravel, the water is not significantly flowing through the particle system at the fast collapse. However, to investigate how deep

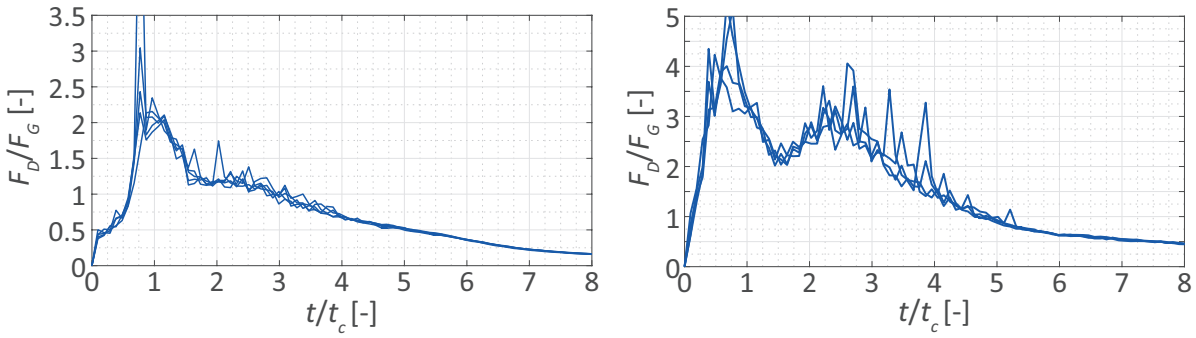

(a) $d_p = 3$ mm (b) $d_p = 1.15$ mm

Figure 6.56: Simulation of submerged fast collapse with 3 mm and 1.15 mm glass particles - Evolution of global drag force over time normalized with the global particle weight

the free water intrudes into the particle skeleton for different sized materials, a resolved CFD-DEM simulation should give more detailed insights.

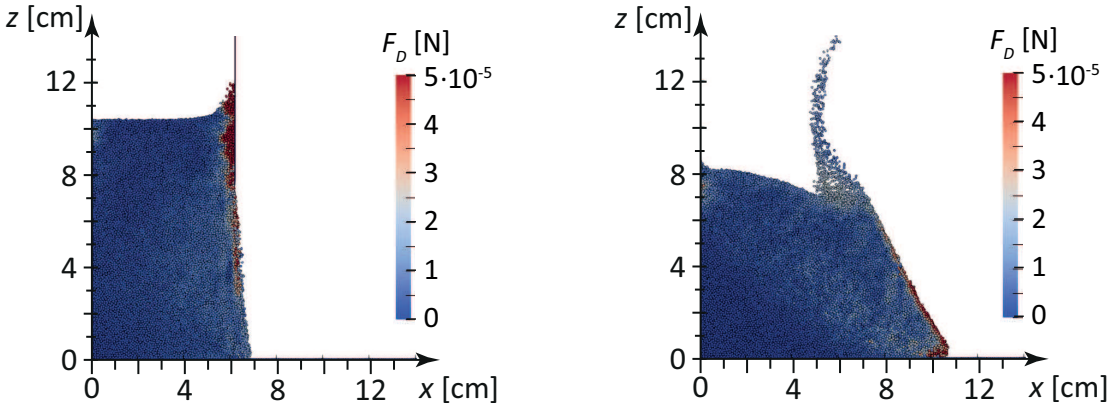

(a) $t/t_c \approx 0.75$ (b) $t/t_c \approx 2$

Figure 6.57: Particle drag force F_D at the submerged collapse simulation with $d_p = 1.15$ mm

6.5.3 Variation of drag force model

To investigate the influence of different drag force models, simulations with the Di Felice and Gidaspow drag model have been conducted additionally to the previously presented Koch & Hill simulations. The specification of the individual models is discussed in Section 2.2.2. For the collapse process, the deviations between the individual drag models are very small. However, by the analysis of the final deposit shape, the deposit tip evolution and the normalised drag forces, small deviations become apparent. Those are presented in the following paragraphs.

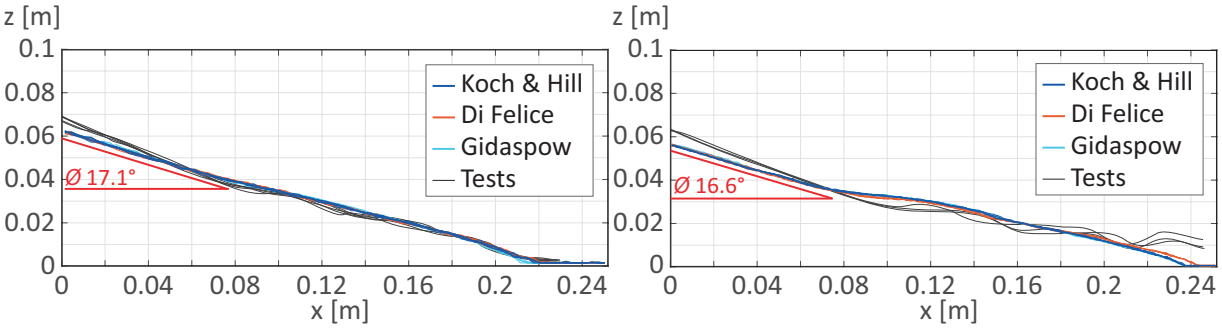

(a) $d_p = 3$ mm (b) $d_p = 1.15$ mm

Figure 6.58: Final deposit shape of the submerged fast collapse simulations for different drag models with 3 mm and 1.15 mm glass particles in comparison to the final shapes of the physical tests

Figure 6.58 presents the final shape of the deposit for the simulations with 3 mm and 1.15 mm particles for different drag models. Further, the results of the physical tests are included. The final shape is barely affected by the variation of the drag models. The outer silhouette is highly similar for all simulations. Minimal deviations can be observed for the length of the deposit (see Table 6.18). Thereby, the order of the drag models regarding the final length is the same for the 3 mm as well as the 1.15 mm particles. The smallest deposit length is for both cases obtained by the Gidaspow (1994) model with in average 21.29 cm for the 3 mm and 23.62 cm for the 1.15 mm particles. Thereafter, the Koch & Hill (2001) model results to a deposit length of in average 21.88 cm for the 3 mm and 23.66 cm for the 1.15 mm particles. The greatest length for the final deposit is caused by the Di Felice (1994) model with in average 22.21 cm for the 3 mm and 24.33 cm for the 1.15 mm particles. However, the deviations are still small with a maximum difference between the models of 0.92 cm for the 3 mm particles and 0.71 cm for the 1.15 mm particles.

Table 6.18: Average results for the submerged fast collapse simulations in comparison to the physical tests under submerged and dry conditions

	Glass 3 mm		Glass 1.15 mm	
	Final length [cm]	Tip velocity [m/s]	Final length [cm]	Tip velocity [m/s]
∅ Koch & Hill	21.88 ±0.16	0.397 ±0.004	23.66 ±0.08	0.436 ±0.0059
∅ Di Felice	22.21 ±0.28	0.395 ±0.009	24.33 ±0.08	0.457 ±0.005
∅ Gidaspow	21.29 ±0.14	0.383 ±0.003	23.62 ±0.06	0.435 ±0.006
∅ Tests	21.93 ±0.34	0.245 ±0.004	25.2 ±0	0.286 ±0.005

The different final lengths for the different drag models become also apparent in the analysis of the deposit development over time, presented in Figure 6.59. The above obtained

order of the drag models regarding the final deposit length can be also recognised in the deposit spreading over time. For each point in time, the deposit propagation for the Gidaspow (1994) model is always smaller than those of the other models. In contrast, the Di Felice (1994) model results in the furthest deposit propagations over the collapse process. However, the differences in deposit propagation over the deposit development over time are minimal and, thus, the transition between the phases of the spreading.

For each particle diameter, two models result in almost the same deposit propagation development, while one model is slightly deviating (see Figure 6.59). Although the order of the models regarding the deposit propagation over time is the same for both particle diameters, the divergent model is different. Thus, for the 3 mm particles the Koch & Hill (2001) model gives very similar results as the Di Felice (1994) model, while for the 1.15 mm particles the Koch & Hill and the Gidaspow (1994) model give similar results. This needs to be related to the model definitions. The Koch & Hill (2001) model as well as the Gidaspow (1994) model have switches to change the equation at a certain volume fraction limit. For the Koch & Hill (2001) model, a switch is defined by the fluid volume fraction $\alpha_f = 0.6$, while for the Gidaspow (1994) model a switch is given at $\alpha_f = 0.8$. However, the fluid volume fraction in the cells within the region of slumping particles is in both simulations below the limits of the switches. Just for the cells at the surface of the particle mass, this high amount of fluid volume fraction is reached. Further, the Koch & Hill (2001) model and the Gidaspow (1994) model have a switch based on the particle packing Reynolds number Re_{p,α_f}. This one is defined to $\mathrm{Re}_{p,\alpha_f} = 40$ for the Koch & Hill (2001) model and to $\mathrm{Re}_{p,\alpha_f} = 1000$ for the Gidaspow (1994) model. However, under the assumption of maximal fluid volume fraction of $\alpha_f = 0.4$ inside the particle mass and a maximum relative velocity of 0.5 m/s according to the simulation results, the switch of the Gidaspow (1994) model is not exceeded. Contrary, the switch of the Koch & Hill (2001) model is reached easily in the simulations of both materials. Thus, the exceedance of a certain limit of a switch is not the reason for the changes in accordance between the models, but needs to be caused in the formulation itself.

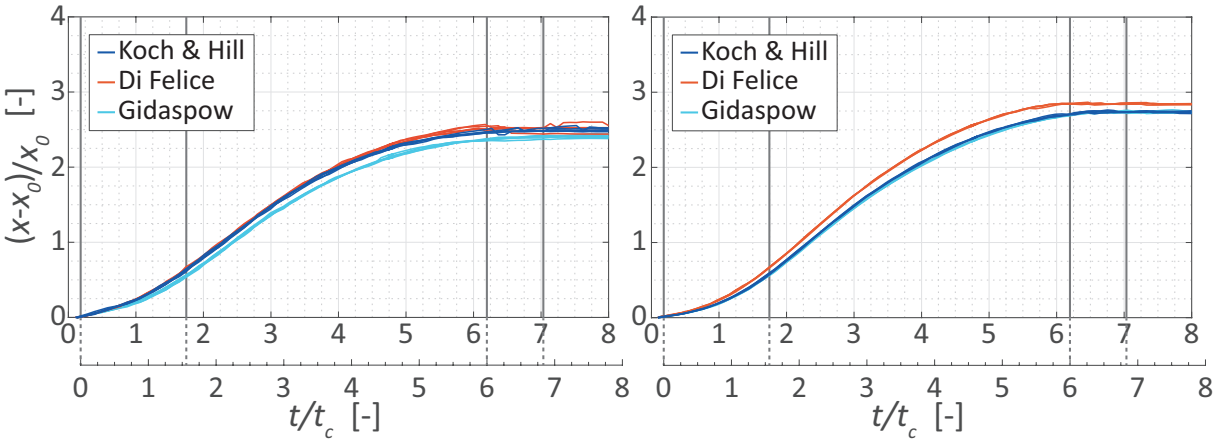

(a) $d_p = 3$ mm (b) $d_p = 1.15$ mm

Figure 6.59: Evolution of the deposit tip position over time for submerged fast collapse simulation for different drag models with 3 mm and 1.15 mm glass particles

Figure 6.60 presents the drag force evolution for the 3 mm and the 1.15 mm particles for the individual drag force models. As in the deposit propagation over time, the course of the normalised drag force is similar for all drag models. For all models, the drag force increases significantly in the first moments of the simulation. For the 3 mm particles, the normalised drag force reaches its peak at about $t \approx 0.8\ t_c$. Thereby, the global drag force of the Gidaspow (1994) model increases faster and reaches its peak earlier, followed by the Koch & Hill (2001) model and the Di Felice (1994) model. The differences are negligible for the simulations with 1.15 mm particles. For both particle diameters, the normalised drag force reduces till $t \approx 1.5\ t_c$ for all drag models. This phenomenon as well as the following decrease of the global drag force has already been discussed above. It is apparent, that for both cases the Di Felice (1994) model results in a smoother course with less peaks.

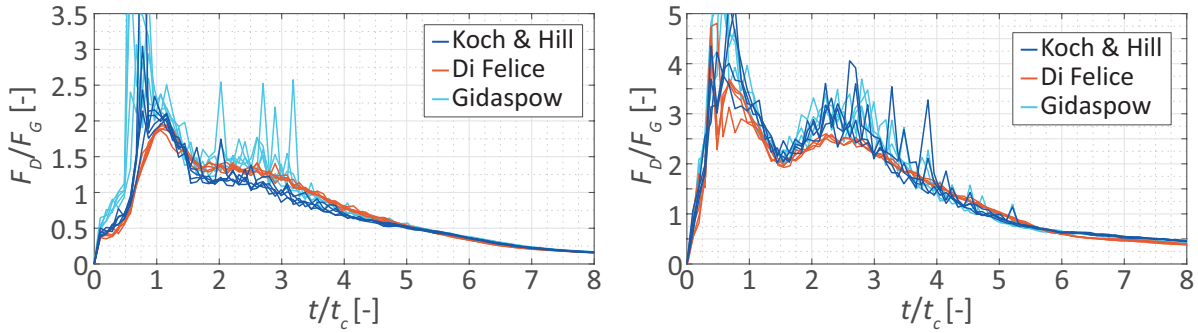

(a) $d_p = 3$ mm (b) $d_p = 1.15$ mm

Figure 6.60: Evolution of global drag force normalized with the global particle weight over time for the submerged fast collapse simulation at different drag force models

6.6 Conclusion

The examination of the collapse of a granular particle columns under submerged conditions have been distinguished into an investigation with dry boundary conditions and an investigation with submerged conditions. The analysis of the slumping behaviour under dry conditions gave an insight into the granular slumping mechanisms and their representation in the DEM simulations by a rheological viscous-elastic modelling of the particle-particle and particle wall contact. To investigate all aspects of the representation of granular slumping, the dry investigation has been distinguished into a controlled slow collapse and a dynamically fast collapse. For each collapse, other components of the contact modelling are predominantly addressed and, thus, other material properties, which correspond to the particular contact component. This differentiation into divergent collapse scenarios is not reasonable for the submerged investigations. The physical tests of the submerged slow collapse showed, that the slumping is almost identical to those under dry conditions. Thus, the influence of the interaction with the viscous fluid on the slumping process is negligible small. Hence, the investigation of slow granular movements in fluid can be sufficient reproduced by tests or simulations assuming dry conditions. In contrast, the investigations

on the fast collapse scenarios show significant impact of fluid-particle interaction on the collapse characteristics.

All investigations under dry and submerged conditions based on a hybrid modelling approach, consisting of physical tests and numerical simulations. The physical tests gave a first insight into the collapse characteristics and build the basis for validation of the corresponding numerical simulations. The numerical simulations with the discrete modelling of the granular media offered the possibility to investigate the detailed material behaviour on particle level. The numerical simulation of the submerged collapse by the with CFD-DEM enabled the investigation of fluid-particle interaction as well as the analysis of the behaviour of every phase individually.

The investigation of the slow collapse under dry conditions reveal the slumping characteristics of a strictly controlled granular slumping in small segments. Thus, periods of stagnation and small slumping events alternate. The mechanism of the individual slumping events is similar to the fracture mechanism of ground shear failure with a combined vertical and and sideways displacement of the particle mass due to vertical loads. The sliding joint consists of a upper linear section and a logarithmic spiral around the gap between the deposit and the tip of the movable wall, whereby the sliding mass merges into avalanching discharge. The inclination of the sliding joint changes over the collapse process. Thus, the inclination becomes flatter with decreasing load due to the collapse process. With every slumping event, material exits from the column formation and avalanche over a growing deposit wedge. The angle of the wedge slope is constant over the collapse progress. Thereby, the angle of repose, with 23.9° for the 3 mm particles and 23.4° for the 1.15 mm particles, is smaller compared to the angle of repose corresponding to the chosen friction coefficient.

The corresponding simulations give further insights into the slow collapse slumping mechanism. Thereby, the simulation reproduces the characteristics of the physical tests. The slumping mechanism as well as the final state are very similar to the physical tests. However, in the simulations the upper section of the final deposit shape differs slightly from those in the physical tests. Thus, the upper section is inclined under an smaller angle than the lower deposit section of the slope, which developed from particle discharge. The bend of the slope is positioned near the location of the movable wall. The reason for this deviation from the physical tests is based on the development of a funnel at the surface of the collapsing column. In the simulations, the slopes of the funnel are less inclined than in the physical tests. The development of a funnel was investigated further in the sensitivity study.

By the representation of force chains in the physical test, it could be proven, that the particle contacts for a comprehensive particle skeleton is restored after every slumping event. This behaviour is also reassured by the progression of kinetic energy. The process of kinetic energy is dominated by small peaks in energy, alternating with phases where the energy is zero. The peak of energy per slumping event increases with the collapse process, since the number of particle particles increases, which are involved within a individual slumping event.

The sensitivity study of the slow collapse simulations revealed a high dependency of the slumping mechanism from the coefficient of Coulomb's friction for particle-particle and

particle-wall contact as well as the rolling friction coefficient. The high significance of this properties is motivated by the small slumping events, in which the a small amount of particles loose contacts and participate in the slumping mass. As a result, the transitional contact forces base on Coulomb's friction have a high impact the particle movements. Variations of the properties such as the Young's modulus, the Poisson's ratio or the coefficient of restitution have no significant effect on the slumping mechanism or the final deposit shape. The Coulomb's friction for particle-particle contact μ_s affects primary the development of the deposit. Thus, the deposit slope angle of repose increases with increasing μ_s, while the angle of the final slope top is unaffected. The influence of μ_s on the angle of repose is present from the early development of the deposit slope onwards. In contrast, the coefficient of Coulomb s friction for particle-wall contact $\mu_{s,w}$ has no effect on the generation of the deposit slope or the final deposit shape. Hence, the internal slumping characteristics are affected. The entrainment of particles by the movable wall is increased for higher $\mu_{s,w}$. Further, the development of the surface funnel is affected. For smaller $\mu_{s,w}$, the entrainment of particles by the movable wall is reduced and the the slope next to the movable wall becomes shallower. The near wall particle entrainment affects further the formation of the sliding joint. For lower $\mu_{s,w}$ values, the sliding joint is positioned more right, since the otherwise entrained particles are part of the slumping mass. The highest impact on the slow slumping mechanism represents the coefficient of rolling friction μ_r. With increasing μ_r, the final deposit slope angle increases significantly, while the final slope top angle increases slightly. The higher rolling resistance reduces the number of slumping events and simultaneously increases the amount of particles per event. This development is proven by the progression of kinetic energy, which gives higher peak values and a the reduced number of slumping events. Further, the internal slumping mechanism is affected due to the higher rolling resistance. With higher rolling resistance, the straight slip joint part is inclined under a steeper angle.

The characteristics of the fast collapse under dry conditions differ significantly from the mechanisms in the slow collapse scenarios. The granular column collapses in one highly dynamic slumping event. While in the slow collapse scenario, the most particle contacts stay intact during a slumping event, the initial particle compound of a sustainable particle skeleton dissolves and the particle contacts are reduced to approximately 30% of the contacts at the initial state accounting to the results of the numerical simulations. Further, the duration of the particle contacts is reduced and the manner of contact changes. While the contacts in the segmented slumping of the slow collapse are lasting longer due to a sliding/rolling relative movement, the contacts in the dissolved slumping particle mass of the fast collapse are reduced to a fractional amount of time and limited to short impact events. Thus, in the DEM simulations different components of the contact modelling are addressed.

The physical tests of the fast collapse under dry conditions bridge the new investigations with the previous investigations of other authors (e. g. Lajeunesse et al., 2005). Thereby, the theory of three different phases for the spreading of the granular material could be confirmed. Thus, the spreading deposit of the collapse is first accelerating, moves than under a constant velocity and finally decelerates again. The numerical DEM based simulations reproduce this characteristics of the physical tests successfully. The slumping

mechanism during the collapse is accurate. Further, the development of the deposit over time is reproduced. The chronological development over time is almost identical between the physical tests and the simulations. However, the initiation of the deposit spreading in the simulations is slightly ahead of the physical tests, with an offset time of approximately $T = 0.1\ t_c$.

The simulations reveal more detailed characteristics about the internal slumping mechanism and the behaviour on particle scale. As presented previously, the representation of particle force chains show the significant dissolve of the particle skeleton during the fast slumping process. Further, the transition between an initially vertical to a horizontal movement at the early stages of the slumping at $t \approx 1.9\ t_c$ could be confirmed by the progression of kinetic energy. Thus, the kinetic energy in the global systems increases after the collapse initiation since the particles are accelerated into negative z-direction due to gravitational acceleration. At $t \approx 1.9\ t_c$ the global kinetic energy reaches its peak value. At this point, the first particles are deviated when they reach the slip joint of the slumping mass. This deviation transforms the vertical falling movement into a horizontal spreading. This transition characterises the point of highest kinetic energy during the slumping process.

The validation of the numerical simulation showed, that the adoptions on the property setting motivated by the slow collapse sensitivity study is not fully sufficient for the fast collapse simulations. While a decrease of the particle-wall coefficient of Coulomb's friction resulted in a better reproduction of the particle-wall interaction during the slumping process in the slow collapse scenario, this adoption resulted in less accurate results in the fast slumping simulations. The sensitivity study of the fast collapse simulation revealed the necessity to investigate the properties for each new applications to validate the contact modelling and the effect on the particle mass behaviour. In the sensitivity study of the fast collapse simulations, the coefficient of restitution e had the highest impact on the slumping process. Thereby, the slumping mechanism itself or the final deposit shape was merely affected but rather the development of the clumping process over time. Lower values of e resulted in a higher damping and, thus, dissipation of energy during a particle impact. This damping on particle scale resulted further to a damping of the global slumping process of the particle mass. The spreading velocity of the deposit tip was significantly reduced for lower values of e and the whole slumping process proceeds over a longer duration in time. In contrast, the properties regarding Coulomb's friction or rolling friction had less significance in the simulation. The coefficient of Coulomb's friction μ_s had no significant effect on the slumping mechanism. Also the particle rolling friction μ_r had no significant effect on the slumping process and resulted to a minimally steeper arrangement at the deposit slope only. In contrast, the coefficient of wall friction $\mu_{s,w}$ had some effect on the slumping initiation. Due to higher $\mu_{s,w}$, more wall adjacent particles are entrained by the movable wall extraction and the lifting due to the entrainment of the particles becomes higher. As a result, the initiation of the slumping is affected, since a greater entrainment constitutes an opposed particle movement to the downwards collapse and, thus, delays slightly the slumping initiation. However, this effect in minor and is not appropriate to improve the faster collapse initiation in the simulation in comparison to the physical tests since the wall entrainment is significantly overestimated at too high values.

Other properties like the Poisson ratio or the Young's modulus had no effect on the fast slumping simulation.

In total, the two scenarios of the slow and fast slumping scenario constitute a good possibility to validate the contact modelling in the DEM simulations for granular flow scenarios. According to Lajeunesse et al. (2005), the slumping is almost equal for each granular media, if the initial aspect ratio of the probe is identical. This phenomenon is proven by the conducted physical tests and also covered in the numerical simulations. The differences between the 3 mm and the 1.15 mm or rather 1.15 mm particles is minor regarding the slumping mechanisms. It might be appropriate to investigate the influence of the Young's modulus and the Poisson ratio again for scenarios with additional load, since those properties are expected to have an impact on the contact modelling under higher loadings. However, the sensitivity studies revealed the suitability of the laboratory tests to define the property setting. The determined particle Young's modulus, the Coulomb friction as well as the coefficient of restitution could be adopted for the numerical simulations. The assumption for the coefficient of rolling friction was not appropriate and needed to be adapted to a factor 7. Thus, the significance on the theoretical background of the coefficient of rolling friction need to be handled with care and possible assumptions need to be investigated and validated. All in all, the validated numerical models of the dry collapse can be likely applied for investigations on granular slumping or granular flow problems. By means of the validated models, different axis ratios, particle diameters or properties can be investigated to gain detailed insights into the slumping characteristics, the particle-particle interaction, the particle-wall interaction as well as the development of the slumping over time.

With the gained knowledge from the dry slumping scenarios, the investigations on the submerged collapse scenario concentrate on the fluid-particle interaction. Since, this interaction is not a relevant or dominant factor in the slow collapse simulations, the investigations concentrate on the fast collapse scenario. The most significant impact between the dry and the submerged collapse investigations is the relevance of the applied particle diameter. While in the dry scenarios the slumping mechanism as well as the final deposit shape was barely affected by the particle diameter, the collapse characteristics differ in the submerged collapse scenario for the different particle sizes according to the physical tests. For both particle diameters, the whole collapse is significantly decelerated due to the presence of viscous fluid. The viscous fluid adds an additional resistance against the particle movement. On particle scale, the drag force acts opposed to the direction of the particle trajectory and increases the resistance with increasing relative velocities between fluid and particle. Further, the physical tests show that the particle packing dissolves completely. Thereby, dilatancy leads to an increased volume of the particle-fluid mixture and increases the dissolved separation of the particles in the mixture.

The deposit spreading in the physical tests undergoes still three phases of acceleration, constant spreading and deceleration. But the duration of the phases increases such as the total duration. Due to the limitation of the basin, the comparison between the dry and the submerged temporal evolution is limited to the acceleration phase. Thereby, the acceleration phase extends from $T = 0.9\ t_c$ for the 3 mm and the 1.15 mm particles to $T = 1.6\ t_c$ for the 3 mm and $T = 2.0\ t_c$ for the 1.15 mm particles. While under

dry conditions, the collapse development over time is similar for the different particle diameters, the diameter has a significant impact in the submerged case. It is evident, that the acceleration phase extends significantly for the 1.15 mm particles than the 3 mm particles due to the interaction with the fluid. This behaviour is directly related to the particle diameter or rather the permeability of the material. To investigate this relation further, more different particle diameters need to be investigated. The interaction between the granular material and fluid leads further to an initiation of free fluid flow in the physical tests. Thus, the extraction of the wall and the collapsing material accelerated the averaging pore fluid as well as the free fluid and leads to flow which interacts with the particles vice versa. Thus, on the left side of the movable wall above the initial column surface, a counter-clockwise vortex is initiated. This vortex effects the trajectories of the particles, which have been entrained and lifted by the movable wall extraction. Also on the right side of the basin flow is initiated, which leads to the generation of small ripples at the lower part of the deposit slope. However, since the fluid flow is not captured by the PIV analysis, the exact fluid flow pattern cannot be extracted from the physical tests. A more detailed investigation of the fluid flow in the physical tests could be established by the application of fluorescent tracer and a filter for the high speed camera, to distinguish between the particle and the fluid phase.

The simulation of the submerged collapse reproduces the decelerated behaviour of the tests very well. Similar to the physical tests, the duration of the collapse process is significantly extended. In comparison to the simulations of the dry slumping, the acceleration duration extends from $T = 0.9\ t_c$ to approximately $T = 1.5\ t_c$ for both particle diameters. Thus, the difference in the collapse process over time between the diameters is not covered in the simulations. The collapsing particles reach higher spreading velocities in the simulations than in the physical tests. Further, the phase of constant spreading is significantly shortened in the simulation and merges to a significantly extended deceleration phase. Thus, the collapse development over time is less accurately reproduced in the simulations. Also the significant dissolving on the physical tests is not captured in the simulations. Thus, the effect of dilatancy is not reproduced in the unresolved CFD-DEM. However, the dilatancy effect has a high impact on the collapse process over time and the collapse characteristics and, therefore, required for an improved accuracy in the simulation.

The analysis of the individual phases in the simulations reveal new insights into the collapse process. Thus, the fluid-particle interaction is investigated by the analysis of the drag forces. The simulations reveal, that particles with higher drag force are positioned just at the surface of the slumping particle mass and especially at the deposit tip. Thus, the free fluid is not significantly intruding into the voids and the particle mass and the accelerated averaged pore fluid acts with the particles like a continuous mass. Although, the particle mass is rather permeable, the collapse occurs to be too fast to allow a flow through the particles. The individual phase representation of the simulation showed further details on the initiation of the fluid flow. It proves the development of a counter-clockwise vortex on the left side of the basin due to the wall extraction. In contrast, the free fluid flow on the right side of the basin is not initiated by the movable wall extraction only but rather from the collapsing particle mass. The collapse of the column and the transition from a vertical to a horizontal particle movement induces a clockwise vortex which moves

along the deposit surface into positive x-direction. The flow velocity in this vortex is high enough to move the particles at the immediate surface of the deposit and generates the ripples. However, due to the faster collapse process in the simulations, the ripples occur in the middle of the deposit than rather at the slope end as in the physical tests.

The delay between the physical tests and the numerical simulation in the submerged collapse investigations is the major cause for deviations in the collapse characteristics. The variation of the drag force model lead to no clear preference for the simulation of the fluid-particle interaction, since the results were very similar. Just at the collapse behaviour over time small differences occur. The dissolving of the particle mass in the physical tests is a crucial factor in the accurate reproduction of the submerged collapse in the simulations. Thus, this phenomenon needs to be adopted in the simulations to improve the collapse characteristics and especially the development of the collapse over time. Since dilatancy cannot be captured without resolving the flow around the particles, a fluid-particle interaction model needs to be developed to cover the phenomenon of dilatancy in the resolved CFD-DEM simulations. Also the inclusion of the lubrication force should lead to an improvement of accuracy (see also Hager et al., 2017).

Another improvement of the tests concerns the size of the applied basin. The dimension in x-direction is too small to achieve the full deposit length. This impedes the analysis of the whole collapse process, how it is done in the investigations of Lajeunesse et al. (2005). The full final deposit length, the corresponding total duration of the collapse as well as the analysis of the deceleration phase would give valuable asset to the investigations and possibilities for further comparison with the existing theory.

7 Investigations on the Initiation of Sediment Transport

The interaction between soil and fluid at a bed is ubiquitous but still not fully understood. The interaction leads to complex flow structures in the so called boundary layer and might lead to a permanent transformation of the bed structure and form by erosion, transport and sedimentation. The boundary layer flow is characterised by boundary layer flow theory, which is presented in Section 7.1 of this chapter. Thereby, the common approaches are able to describe the character of a boundary layer flow successfully. These approaches neglect the interaction between the internal as well as the external flow field and the character of the boundary as an transition region. However, a more accurate representation of this transition area would enable the characterisation of the interaction processes of the internal and external flow field as well as the interaction between the (void-) fluid and the disperse granular material of the bed. A representation of the boundary as a transition area would also affect the understanding of sediment transport.

The majority of the commonly applied approaches to describe sediment transport are based on empirical considerations, which give just limited awareness over the detailed processes on a grain level as well as the character of the soil material. Thus, there is very limited knowledge on the exact interaction forces between fluid and a granular particle which is positioned at a boundary. The investigation of the small scale processes at the boundary or inside the transition area are prevented by its complexity and small scale as well as its sensitivity to external influences, which inhibit physical tests with common measurement technique. However, visual based investigation methods like the PIV method allow the investigation of the local flow field without interference. Further, the coupled CFD-DEM gives the possibility to get more detailed information over the interaction processes taking place between fluid and a granular material. The combination of non-intruding measurements techniques with coupled CFD-DEM simulations might be able to gain new knowledge over the small scale processes taking place at the boundary and during sediment transport processes. Therefore, the point of incipient motion of the erosion process shall be investigated nearer in this chapter by means of a hybrid approach of physical tests and numerical simulations. To allow a direct comparison between physical tests and numerical simulation it of highest importance to create a testing scenario, in which all boundaries are highly defined and reproducible. For this reason an innovative physical tests setup is applied, in which the incipient motion of an individual particle is investigated Section 7.3. This setup is later adopted in the numerical simulations (see Section 7.4). The knowledge from the previous investigations of Chapter 5 and Chapter 6 are integrated in the simulation setup.

7.1 Fundamentals on Boundary Layer Flow

Wall-near flow or flow around bodies is characterised by the interaction between the solid and the fluid. At a solid surface, the fluid adheres to the boundary. As a result, the fluid flow experiences shear forces. Real fluids like water show a resistance against deformation or shearing which is based on inner friction processes on a molecule scale: the viscosity. Due to this inner resistance, the region of the wall-near flow is affected by a no-slip condition at the surface and is denominated as boundary layer flow. The following section gives an overview of the boundary layer flow theory on smooth and rough walls. Furthermore, the particular characteristics of boundary layer flow at permeable beds and particle beds are discussed with respect to the micro-scale fluid-particle interaction at a particle bed.

7.1.1 Boundary layer flow at a smooth surface

The boundary layer flow was first defined by Prandtl (1905) as the transition zone between the boundary affected flow and the undisturbed freestream area. The bulk of the flow region is represented by the freestream. In this region the viscosity can be neglected, while in the thin boundary layer near the wall the viscosity needs to be taken into account. The height of the boundary layer is denominated as the boundary layer thickness δ. Since, the transition between the boundary layer and the freestream is continuous, the boundary layer thickness is defined as the point, where the velocity reaches a percentage of 99% of the freestream velocity (Schlichting et al., 2017).

The influence of the viscosity on the flow is considered by a frictional law, which describes the ratio of the gradient of the wall parallel velocity $\partial v_{f,x}/\partial z$ and the resulting viscous shear stresses τ_v. In the case of Newtonian fluids like water, this ratio is characterised by a proportional relation defined by the kinematic viscosity ν_f or the dynamic viscosity η_f (see Equation 7.1). Regarding static temperature and pressure conditions the viscosity as well as this relation remains constant.

$$\tau_v = \eta_f \frac{\partial v_{f,x}}{\partial z} \tag{7.1}$$

A special case of this friction is the so called wall shear stress τ_0, which describes the complete shear stress due to frictional resistance of the solid boundary on to the fluid (Schlichting et al., 2017):

$$\tau_0 = \eta_f \left(\frac{\partial v_{f,x}}{\partial z} \right)_0 \tag{7.2}$$

The flow characteristics in the boundary layer are related to the pressure distribution of the freeflow, the wall roughness, the level of disturbance of the freeflow and, especially, the Reynolds number Re. For very small Reynolds numbers Re ≈ 1 the boundary layer stays laminar and the micro-scale exchange of mass or momentum takes place only between adjacent layers. At this stage, the flow is dominated by viscous forces. At higher Reynolds numbers the boundary layer becomes turbulent and is dominated by turbulent mixing over

several layers. The exchange of mass and momentum in the turbulent regions takes place in larger scale. Although the turbulent processes are based on momentum exchange, it leads to the same effect as an additional shear stress on the flow. These apparent stresses are defined as Reynolds stresses.

Before these turbulent Reynolds stresses are discussed further, dimensionless wall units are introduced. By means of dimensionless wall units, the wall-near boundary flow can be described analytically and a comparison of different flow situations is enabled. The velocity distribution and the shear stress estimation in the boundary layer is characterised by the dimensionless velocity v_f^+ and the dimensionless wall distance z^+ given as

$$v_f^+ = \frac{v_{f,x}}{v_f^*} \qquad \text{and} \qquad z^+ = \frac{z\, v_f^*}{\nu_f} \qquad . \tag{7.3}$$

Thereby, the friction velocity v_f^* represents the given wall shear stress in units of velocity (Soulsby, 1997) to

$$v_f^* \;=\; \sqrt{\frac{\tau_0}{\rho_f}} \qquad . \tag{7.4}$$

By means of the dimensionless units, the velocity distribution of the wall-near boundary layer is given as a function f of $v_f^+ = f(z^+)$. To find analytical formulations for this function, further characteristic regions of the boundary layer are distinguished. Therefore, a multitude of references discuss the characterisation of turbulent boundary layer flow, such as Schlichting et al. (2017), S. B. Pope (2000), Malcherek (2007a), Dittrich (1998) or Wilcox (1994). Thereby, the spatial separation of the regions differs slightly. However, the transition between the characteristic regions is of fluent manner. A clear apportionment is of artificial kind, since it depends mainly on the Reynolds number of the freestream, but provides a helpful orientation for the boundary layer specification. In the following, the well-known approaches of Schlichting et al. (2017) and S. B. Pope (2000) are presented.

Figure 7.1 provides an overview of the characteristic regions in the boundary layer. In close proximity to the boundary surface at $z^+ < 5$ a thin sublayer is located. In this so called viscous sublayer the viscous forces dominate over the turbulence influences. As a consequence, Equation 7.1 holds true since the turbulent apparent stresses, or Reynolds stresses, are negligible compared to the viscous stresses. In this region the velocity distribution is given as a linear relation of Equation 7.5 which is visualised in Figure 7.2.

$$v_f^+ \;=\; z^+ \tag{7.5}$$

With increasing distance from the wall, the viscous forces lose influence while turbulent effects increase. While the viscous forces represent 100% of the shear stresses at the direct boundary surface, the percentage decreases quickly to a content of 50% at $z^+ \approx 12$ (see Figure 7.3). At this point the turbulent forces are higher than the viscous forces. At $z^+ \approx 50$ the viscous wall region or inner layer ends and the viscous contribution is not significant to the shear stresses any more (see Figure 7.1).

The transition between the viscous-dominated inner and the turbulent-dominated outer flow layer is performed in the so called overlap layer or, more common, the logarithmic

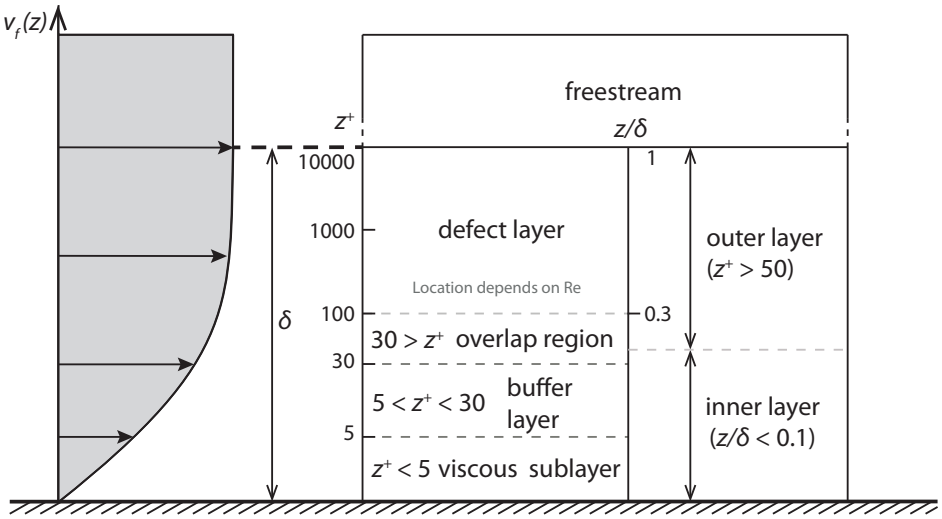

Figure 7.1: Characteristic regions of a turbulent boundary layer at a smooth wall in logarithmic scale based on S. B. Pope (2000) and Wilcox (1994)

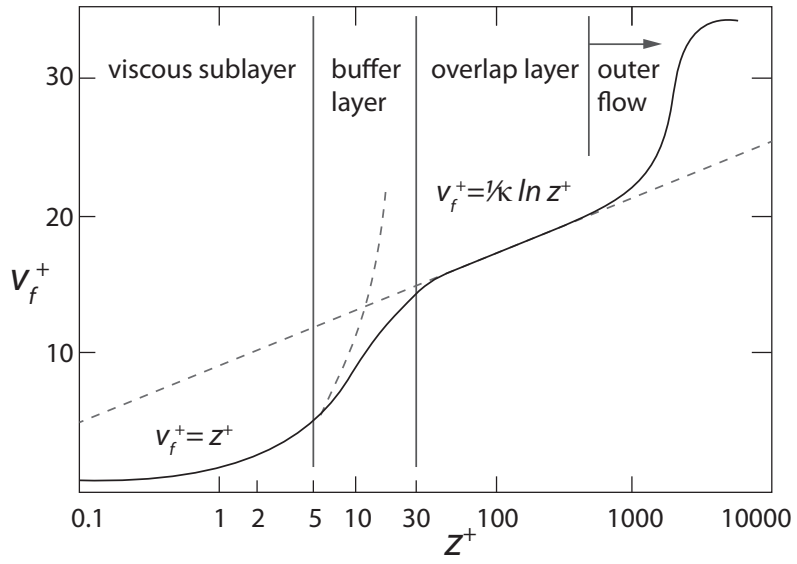

Figure 7.2: Characteristic layers of the boundary layer and the corresponding formulas of the velocity profile sections (adopted after Liu, 2016)

wall region at $z^+ > 30$ (see Figure 7.1). In this region, the turbulent induced Reynolds stresses need to be taken into account for the shear stress estimation. Therefore, the velocity needs to be differentiated into a mean value $\overline{v_f}$ and a velocity fluctuation part v_f'. Since the turbulent fluctuations are the reason for the increase of shear stresses, the Reynolds stresses can be written as

$$\tau_{ij}' = -\rho_f \overline{v_{f,i}' v_{f,j}'} \quad . \tag{7.6}$$

Thereby, $v_{f,i}'$ and $v_{f,j}'$ represent different spatial components of the fluctuation. Based on

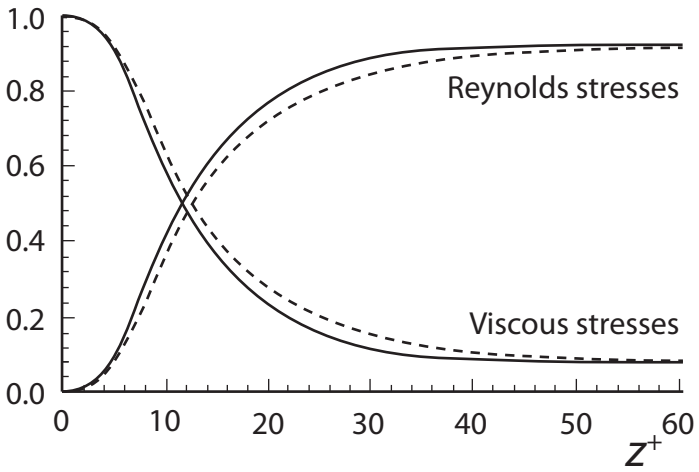

Figure 7.3: Viscous and Reynolds shear stresses in turbulent channel flow (S. B. Pope, 2000) (based on data from Direct Numerical Simulations of Kim et al. (1987) at Re = 5600 (dashed line) and Re = 13750 (solid line))

this expression, Prandtl (1905) developed the mixing length theory. The theory defines a solution to estimate the Reynolds stresses with the mean velocity by introducing a mixing length l_m, which represents the distance a small fluid mass travels. Thus, the turbulent shear stresses in a wall-near region can be estimated by the following solution:

$$\tau'_{ij} = \tau_t = \rho_f (\kappa z)^2 \left| \frac{\partial \overline{v'_{f,i}}}{\partial x_j} \right| \frac{\partial \overline{v'_{f,i}}}{\partial x_j} \tag{7.7}$$

Thereby, the mixing length l_m is replaced by κz, according to the assumption that the mixing length is proportional to the distance to the wall. κ represents the von Kármán constant, which is given as 0.41 for the turbulent boundary region.

The approach of Prandtl (1905) gave a solution for the estimation of the turbulent induced stresses. Through derivation of Equation 7.7, the velocity distribution in the overlap region is given in Equation 7.8 which is also visualized in Figure 7.2. This expression is well known as the logarithmic law of the wall.

$$v_f^+ = \frac{1}{\kappa} \ln\left(z^+\right) + C \tag{7.8}$$

This formulation is a universal law, since it is valid for all turbulent boundary layers independent of the Reynolds number (Schlichting et al., 2017). It is valid till a height of approximately $z/\delta < 0.3$ or $z/H < 0.2$ (X. Chen et al., 2004; S. B. Pope, 2000; Schlichting et al., 2017). Whereby H represents the water height. The constant C is based on experiments and depends mainly on the wall roughness (see Section 7.1.2). The value of C for hydraulic smooth walls has been determined from numerous experiments. The original measurements of Nikuradse (1933) result in a value of 5.5, while Schlichting et al. (2017) and Wilcox (1994) indicate a value of 5.0. S. B. Pope (2000) concludes, that most of the given values for C are within a range of 5% of 5.2.

The region between the viscous sublayer and the overlap layer is appointed as the buffer layer. It represents the transition between the validity of the viscous function (see Equation 7.5) and the function of the overlap region (see Equation 7.8).

Above the overlap region at $z^+ \geq 100$ the outer layer continues. In this region the large scale turbulent eddy shear dominates and the characteristic is independent from the wall distance and the Reynolds number (Schlichting et al., 2017). Furthermore, the mean flow velocity v_f converts to the free stream velocity V_f. In this area the logarithmic law of the wall becomes inadequate. Rather, a defect law is initiated to describe the velocity with an perturbation approach. Thus, the region is denoted as defect layer. Von Kármán developed a formulation for the velocity estimation in the defect region to

$$\frac{V_f - v_f}{v_f^*} = f\left(\frac{z}{\delta}\right) \qquad . \tag{7.9}$$

Based on this approach, Coles (1956) introduced a formulation for the function f at turbulent boundary layer flows. Coles's (1956) solution is usually denoted as the wake function, since the approach takes the effect of wakes in the outer layer into account. The wake function $f\,(z/\delta)$ depends no longer on the length scales of the inner boundary region, but on the length scales of the outer flow. Coles (1956) noted in his research that the deviation above the log layer is comparable to a wake like shape relative to the freestream. Based on his study, he developed Cole's log-wake law, which is given to

$$v_f^+ = \frac{1}{\kappa} \ln\left(\frac{z}{z_0}\right) + \frac{2\Pi}{\kappa} \sin^2\left(\frac{\pi}{2}\tilde{z}\right) \tag{7.10}$$

Thereby, Π is denoted as Coles wake parameter which represents the deviation from the logarithmic law of the overlap layer and $\tilde{z} = z/H$. For further details, see the work of Coles (1956), García (2008), and F. M. White (1974).

7.1.2 Boundary layer flow over rough walls

The previous section gave an insight into boundary layer flow theory at smooth surfaces. However, García (2008) specifies, that the assumption of hydraulic smooth surfaces in nature is valid for muddy bottoms or beds of silt and fine sand only. For beds consisting of coarse sand or gravel, the viscous sublayer vanishes and the characteristic structure of the boundary layer presented in Section 7.1.1 is affected.

The analytical characterisation of flow over rough walls, goes back to the experiments of Nikuradse (1933), wherein the resulting friction over sand particles in sand roughened pipes is investigated. Nikuradse (1933) introduced the sand roughness k_s to describe the roughness element height, which corresponds to the diameter of the sand grains. According to the conducted experiments, three different flow regimes over rough surfaces can be identified. Those can be distinguished by the roughness characteristic number k_s^+, which uses Nikuradse's sand roughness k_s as characteristic length:

$$k_s^+ \quad = \quad \frac{v_f^* k_s}{\nu_f} \tag{7.11}$$

(a) *Hydraulically smooth flow* ($k_s^+ \leq 5$): For a hydraulic smooth flow regime, the roughness height k_s needs to be much smaller than the height of the viscous sublayer δ_v which can be approximated as

$$\delta_v = \frac{11.6\nu_f}{v_f^*} \tag{7.12}$$

Since the roughness elements are fully submerged in the viscous sublayer, the boundary regions above are not affected by the roughness (see Figure 7.4 (a)). Therefore, the velocity distribution still corresponds to the formulation given in Section 7.1.1. According to Bartzke (2012), the roughness height needs to be less than one third of the sublayer thickness to maintain a smooth flow regime.

(b) *Transitional flow* ($5 < k_s^+ < 70$): In the transitional flow regime the height of the roughness elements corresponds approximately to the size of the viscous sublayer height (see Figure 7.4 (b)). Hence, the region above the viscous sublayer is no longer unaffected by the roughness. The roughness elements cause small vortices which result in an additional loss of energy due to Reynolds shear stresses (Nikuradse, 1933). At this point, viscous and turbulent Reynolds stresses have an influence on the surface-near velocity distribution. With an increase of the roughness element height k_s and concurrent the Reynolds number Re, the percentage of the roughness influence due to turbulent shear stresses increases as well.

(c) *Fully rough flow* ($k_s^+ \geq 70$): At this flow regime the roughness height is much higher than the viscous sublayer. Bartzke (2012) indicates a roughness height seven times larger than the viscous sublayer thickness to reach a fully turbulent flow characteristic. At the fully rough regime, the roughness indicated vortices annihilate a viscous sublayer (Dey, 2014). The turbulence acts in between the roughness elements as well. As a result the roughness elements are fully exposed to the turbulent boundary flow region (see Figure 7.4 (c)). At this point, the velocity distribution and the shear stresses are mainly affected by the turbulence and the drag on to the roughness elements, while the viscous shear of the fluid can be neglected.

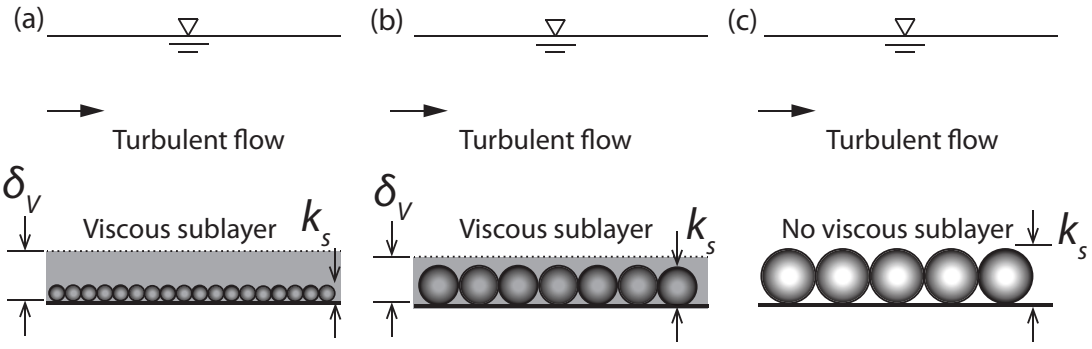

Figure 7.4: Influence of roughness elements at impermeable walls for different flow regimes (adopted according to Dey, 2014).

The above given limits for the rough flow regimes correspond to the original values of Nikuradse (1933). Schlichting et al. (2006), Dittrich (1998) and Zanke (1982) accept the

same limits. In contrast, F. M. White (1974) assumes the limits to $k_s^+ \leq 4$ for hydraulic smooth flow and $k_s^+ \geq 60$ for the fully rough regime. It needs to be taken into account, that the distinction between different flow regimes over rough surfaces takes place in the inner boundary layer only (see Figure 7.1). The outer flow is unaffected by the rough influence.

Based on Nikuradse's (1933) experiments, a universal law has been developed, which has been presented for smooth flow in Section 7.1.1. The universal formulation of Nikuradse's (1933) approach, to describe the surface-near velocity profile for smooth as well as rough surfaces, will be presented below. Although, the experiments of Nikuradse have been performed in pipe flow, they also can be established for open channel flow (Dey, 2014). The universal formulation of Equation 7.8 is adapted by adjusting the integrational constant C, which goes back to the flow characteristics right at the surface. By means of a new interpretation of C, the universal formulation is merged to the velocity distribution at the viscous sublayer or rather the velocity distribution at the immediate surface region. Therefore, the assumption $v_f = 0$ in a very small distance from the surface z_0 needs to be established. Thus, the reinterpreted universal law yields to the formulation, defined in Equation 7.13. It needs to be considered, that the value of κ remains unchanged at 0.41, since it is an universal constant of turbulent flow and therefore independent of the surface roughness (García, 2008).

$$v_f^+ = \frac{1}{\kappa}\left(\ln(z) - \ln(z_0)\right) = \frac{1}{\kappa}\ln\left(\frac{z}{z_0}\right) \tag{7.13}$$

At a smooth surface the distance z_0 correspond to the height of the viscous sublayer δ_v (see Equation 7.12). At rough walls, z_0 represents the virtual origin displacement of the velocity profile and is dependent on the surface roughness. Therefore, z_0, also denoted as bed roughness length, can be determined in a proportional relation to the sand roughness k_s. This assumption leads to the formulation of the universal law as

$$v_f^+ = \frac{1}{\kappa}\ln\left(\frac{z}{k_s}\right) + C^*(k_s^+) \tag{7.14}$$

Thereby, $C^*(k_s^+)$ is an empirical function of the roughness characteristic number k_s^+ and needs to be defined by experiments. The experiments of Nikuradse (1933) lead to a representative curve of $C^*(k_s^+)$, given in Figure 7.5. Those can be transferred to the empirical formula, given in Equation 7.15. García (2008) adds an empirical fit for the transition area between $5 > k_s^+ < 70$:

$$C^*(k_s^+) = \begin{cases} \frac{1}{\kappa}\ln(k_s^+) + 5.5 & k_s^+ \leq 5 \\ 8.5 + \left[\frac{1}{\kappa}\ln(k_s^+) - 3\right] exp\left(-0.121\left[\ln(k_s^+)\right]^{2.42}\right) & 5 < k_s^+ < 70 \\ 8.5 & k_s^+ \geq 70 \end{cases} \tag{7.15}$$

An alternative solution for the vertical velocity profile in an open channel flow is given by Swamee (1993). This approach covers the range from hydraulic smooth, transition area to the fully rough regime by a continuous function. García (2008) gives the formulation as

$$v_f^+ = \left(\left(\frac{\nu_f}{v_f^* z}\right)^{10/3} + \left[\frac{1}{\kappa}\ln\left(1 + \frac{9\left(v_f^* z/\nu_f\right)}{1 + 0.3\left(v_f^* k_s/\nu_f\right)}\right)\right]^{10/3}\right)^{-0.3} \tag{7.16}$$

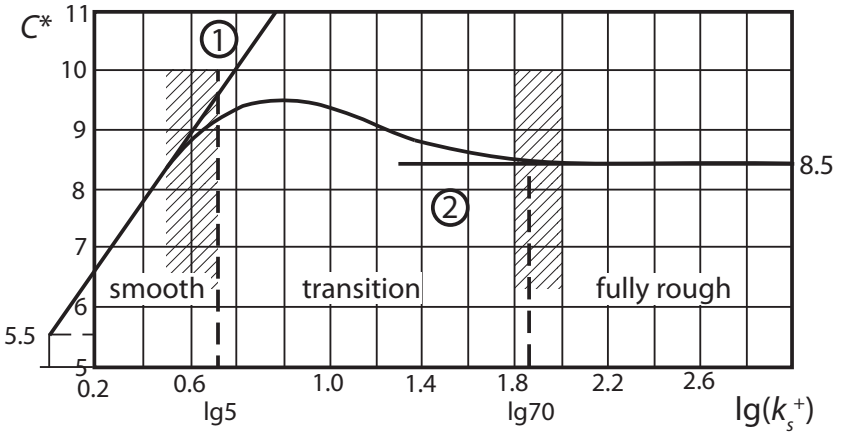

Figure 7.5: Function C^* in relation of roughness characteristic number k_s^+. (adapted after Dittrich, 1998)

The influence of surface roughness on the velocity distribution in the inner boundary layer is illustrated in Figure 7.6. Therein, the mean velocity profile for different characteristic roughness numbers k_s^+ is presented. With an increasing height of the roughness elements, the linear distribution immediately at the surface vanishes. This is due to increasing turbulences, which annihilate a viscous sublayer.

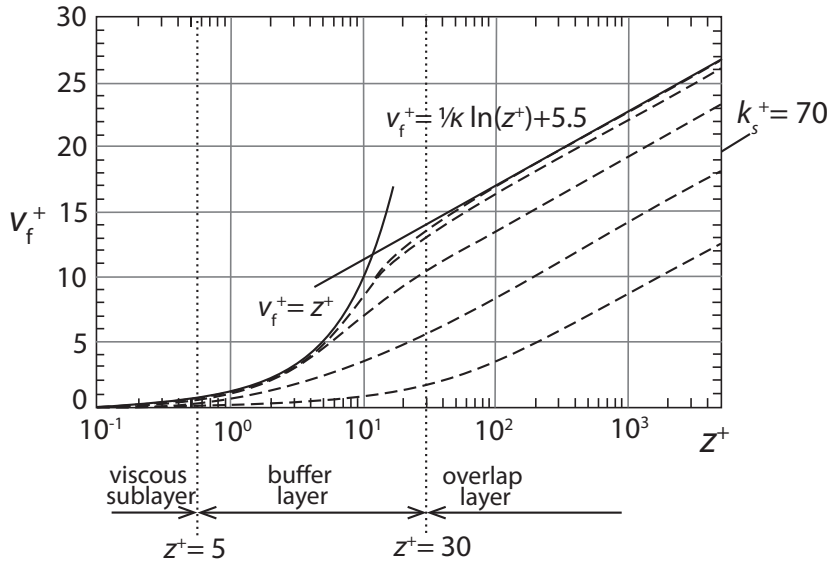

Figure 7.6: Influence of characteristic roughness on the mean velocity distribution in the inner boundary layer (adopted according to Lee et al., 2012 and Blocken et al., 2007)

An alternative solution to describe the velocity profile over rough boundaries is given by the so-called outer form of the overlap law. Instead of the inner attributes of the

rough surface outer attributes of the flow are introduced into the formulation. Thereby, a characteristic length scale is no longer given by the roughness height k_s but by the flow depth H. More details of this approach can be found in Dittrich (1998), García (2008), and Schlichting et al. (2017). However, the inner as well as the outer formulation are valid for a restricted area of $z/H < 0.2$ only. To apply the overlap law outside of this region, a correction function is needed which takes the effect of wakes into account. Therefore, Coles (1956) wake function (see Section 7.1.1) is added to the overlap law leading to following formulation by Nakagawa et al. (1993)

$$v_f^+ = \frac{1}{\kappa} \ln\left(\frac{z}{H}\right) + 5.5 + f\left(\frac{z}{H}\right) \quad . \tag{7.17}$$

The above presented formulation of the universal law with the integrational constant $C^*(k_s^+)$ is based on the correlation between virtual origin displacement z_0 and the roughness height k_s. An alternative approach is based on the direct estimation of the displacement height z_0. The results of Nikuradse's (1933) experiments can be given as a simplified formulation for z_0 by the fit of Colebrook et al. (1937) by

$$z_0 = \begin{cases} \nu_f/9v_f^* & (k_s^+ \leq 5) \\ \nu_f/9v_f^* + k_s/30 & (5 < k_s^+ < 70) \\ k_s/30 & (k_s^+ \geq 70) \end{cases} \tag{7.18}$$

or the continuous fit of Christoffersen et al. (1985) by

$$z_0 = \frac{k_s}{30}\left[1 - \exp\left(\frac{-v_f^* k_s}{27\nu_f}\right)\right] + \frac{\nu}{9v_f^*} \quad . \tag{7.19}$$

Thereby, it needs to be considered that the assumption of $v_f(z_0) = 0$ holds true for rough surfaces only and applies to impermeable beds. Several investigations of flow over a permeable bed have shown, that the flow velocity is not zero right at the bed surface but at a distance below the surface within the bed (X. Chen et al., 2004). The consequences of a rough permeable bed are discussed in greater detail in Section 7.1.3.

7.1.3 Boundary layer flow over permeable particle systems

Natural granular beds consist of a porous structure which allows a complex interaction between the inner flow field through the porous bed and the external flow field above. Thus, a mass, momentum and energy transfer across the interface of a free fluid and particle system is enabled. As a result, the no-slip condition at the boundary surface no longer holds true, but needs to be replaced by a continuous transition between external and internal flow field. The detailed interaction between the internal and external flow field and the interaction with the permeable bed is not completely understood yet. Following, the occurring phenomenons at a flow over a rough permeable bed are discussed. Further, first approaches to describe the mean velocity profile over a permeable bed are presented.

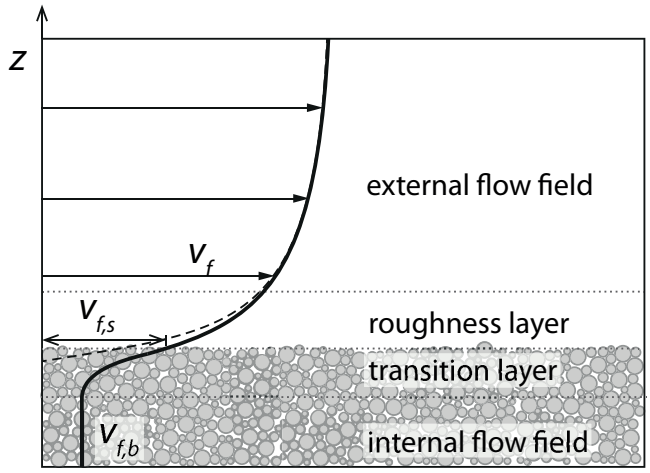

Figure 7.7: Profile of mean velocity over permeable bed (dashed line represents the velocity distribution according to theory presented in Section 7.1.2 while the solid line represents the realistic velocity distribution at a permeable bed) - not to scale (adopted according to Manes et al., 2009)

Zagni et al. (1976) investigated the flow over a particle bed consisting of lead or steel. The results imply, that the resistance of a permeable surface shows a higher resistance to the external flow than the impermeable one at equal roughness. Further, Zippe et al. (1983) showed, that in contrast to impermeable surfaces, the friction of a permeable bed still increases after it reached a fully rough flow state. Thus, the resistance remains not constant after that stage, but rather increases with increasing Reynolds numbers. This phenomenon was further investigated by Nakagawa et al. (1988). The authors performed physical tests on the flow field over glass particles. Nakagawa et al. (1988) found out, that above the bed surface the mean velocities were higher than estimated by the classical logarithmic law of the wall over rough impermeable surfaces. The reason of this effect is given by a strong momentum exchange due to eddy-shedding from individual roughness elements. This momentum exchange increases with the bed height as well as the porosity of the bed material, since the momentum exchange becomes more active. The region, where the momentum exchange takes place, is denoted as the roughness layer (see Figure 7.7). The roughness layer is defined as the region between the bed surface and the height z in which the velocity profile deviates from the classical logarithmic law for rough boundaries. Newer investigations based on highly detailed numerical simulations, proof the existence of this roughness layer (see e. g. Breugem et al., 2006 and Stoesser et al., 2007). Experiments of Manes et al. (2009) showed, that turbulences which have been induced in the external flow field are penetrating into the porous media and affect the momentum exchange field. Thereby, the turbulences dissipate exponentially but still reach lower bed levels.

Besides the roughness layer, the slip velocity $v_{f,s}$ on top of the bed surface presents a characteristic quantity for the velocity (Nakagawa et al., 1988). The presence of a slip velocity implies that for an permeable bed, the no-slip condition at the boundary no longer holds true. Rather, a transition area exists in which the mean velocity of the external flow

field reduces to the velocity of the internal flow field $v_{f,b}$ (see Figure 7.7). Beavers et al. (1967) were the first to examine this approach. At this time, the idea of a slip velocity was not completely new, but so far not established. The authors developed a semi-empirical expression to describe the slip velocity as well as the mean velocity in the transition region around the slip velocity at laminar flow. Later, Beavers et al. (1970) verified the assumption of a continuous transition between external and internal flow field by a wide range of experimental tests. According to Nield (2009), the Beaver-Joseph equation is defined as

$$\left.\frac{\partial v_f}{\partial z}\right|_{z\approxeq 0} = \frac{\alpha_s}{\sqrt{k_f}} \left(v_f|_{z\approxeq 0} - v_{f,b} \right) \qquad . \tag{7.20}$$

Thereby, α_s is a dimensionless slip coefficient depending on parameters of the porous media and has been investigated by several researchers Breugem et al. (2005), Neale et al. (1974), Nield et al. (2017), Ochoa-Tapia et al. (1995), and Salinger et al. (1994). Most of them used very high porosities and laminar conditions, which is inapplicable for the application of a granular sediment bed with lower porosities (Nair et al., 2015). The velocity inside the porous media $v_{f,b}$ can be approximated by Darcy's law or other approaches described in Section 2.2.2. v_f as well as the partial derivative $\frac{\partial \mathbf{v}_f}{\partial z}$ are estimated near $z = 0$, while $v_{f,b}$ is evaluated at a small distance above $z = 0$. Thus, a thin layer inside the porous medium is defined in which the transition takes place (Nield et al., 2017).

Nair et al. (2015) conducted 2D-experiments to formulate a universal expression for the slip velocity. The most investigations on this topic are restricted to highly porous material and low Reynolds numbers (e. g. Breugem et al., 2006, Ochoa-Tapia et al., 1995 and Q. Zhang et al., 2009), which is far from realistic conditions at natural beds. Contrary, Nair et al. (2015) applied porous material with a high porosity of $n = 0.8$ as well as moderate porosity of $n = 0.65$. Based on the results, Nair et al. (2015) derived a relation between the mean velocity of the free flow and the slip velocity. For the higher porosity, the slip velocity is represented by $v_{f,s} = 0.4\,V_f$, while at the lower porosity the slip velocity reduces to $v_{f,s} = 0.133\,V_f$. Further, the results showed that the slip velocity depends only marginal on the Reynolds number of the flow. These results are consistent with the research of Nakagawa et al. (1988). The authors determined an increase of the slip velocity and the roughness layer height with increasing porosities or height of the porous material caused by a more active momentum exchange.

As described above, the momentum exchange between the internal and the external flow field affects the flow characteristics of the roughness layer above the particle bed, but also the transition layer inside the porous bed (see Figure 7.7). The thickness of the transition layer $\delta_{b,tr}$ has been investigated by Goharzadeh et al. (2005). The authors conducted experiments on the flow over a monodispersed granular particle bed. The velocity distribution of the external and internal flow field has been measured by PIV techniques. According to the results of Goharzadeh et al. (2005), the thickness of the transition layer is in the range of a particle diameter $\delta_{b,tr} \approx d$. Thus, the thickness was proven to be bigger than assumed in previous literature, where the thickness is commonly given as $\delta_{b,tr} \approx \sqrt{k_f}$ for the Brinkmann equation (Ochoa-Tapia et al., 1995; Vafai et al., 1990). Morad et al. (2009) extended the results of Goharzadeh et al. (2005) with further

experiments involving polydisperse particle beds. In the case of a polydisperse particle bed, the authors found a proportional relation between the transition layer thickness and a characteristic particle diameter given as

$$\delta_{b,tr} \approx d_{21} = \frac{\sum {}^{x_i}/_{d_i}}{\sum {}^{x_1}/_{d_i^2}} \quad . \tag{7.21}$$

In Figure 7.8 the phenomena of fluid flow over a permeable porous particle packing is summed up to a detailed velocity profile at the bed near region. Its is shown, that the external boundary-near flow field can still be represented by the traditional logarithmic law of the wall (see Section 7.1.2). Just in the ultimate vicinity of the boundary, the velocity profile deviates from the theory. At this point, the interaction between internal and external flow field becomes evident. As already described above, in this region the velocity is higher than estimated by the classical logarithmic law. Furthermore, the origin of the logarithmic velocity profile is positioned below the bed surface at the virtual bed level z_0. At this point the logarithmic velocity profile reduces to zero. However, experiments negotiate the assumption of a no-slip condition at porous beds. Rather, a transition zone with high gradient is located at the most upper part of the porous medium. With increasing depth, the velocity reduces to the pressure gradient seepage velocity $v_{f,b}$.

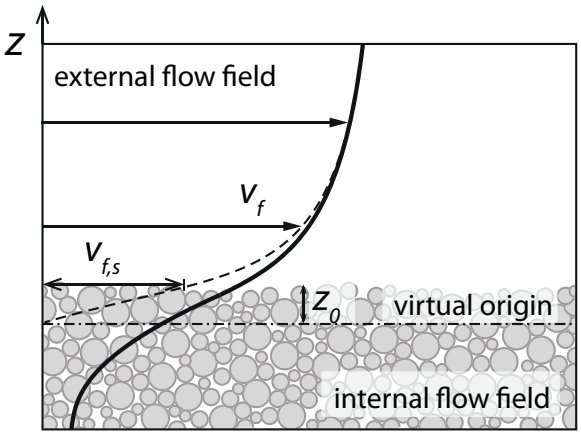

Figure 7.8: Detail of the mean velocity profile immediate at the permeable bed (see Figure 7.7)

By means of Figure 7.8 it becomes clear, that a realistic representation of the transition zone at a permeable surface requires a continuous definition of the pressure, stress and velocity distribution (Mendoza et al., 1992). However, all these characteristic phenomena of permeable beds are mostly neglected in engineering practice. Besides the continuous definitions of Brinkman (1949) or Beavers et al. (1967, 1970) in numerical Two-Fluid Modelling, modified forms of the classical logarithmic law are applied in engineering practice (e. g. Hokenson, 1985; Zippe et al., 1983 and Mendoza et al., 1992). By this, the resistance of a rough permeable boundary is assumed as equal to a rough impermeable boundary (Gupta et al., 1985). As represented in Figure 7.7, this assumption holds true sufficiently

for the region above the roughness layer. Hence, depending on the application purpose, this simplification is appropriate.

Table 7.1 provides a selection of different investigations of the velocity profile over a permeable bed. Compared to the original logarithmic law for impermeable rough walls (see Equation 7.14), the formulations show a modification of κ and C^* at fully rough flow. Furthermore, the specification of the virtual origin z_0 in the denominator of the logarithmic term is defined differently. In the original equation the virtual origin was replaced by the roughness height k_s. The material parameter d_{50} represents the particle diameter corresponding to 50% mass fraction of a grain distribution.

Table 7.1: Selection of different logarithmic laws for the velocity distribution over a permeable bed

Source	Material	Bed height	z_0	Velocity law
Mendoza et al. (1992) and Nezu (1977)	-	-	z_0	$v_f^+ = \frac{1}{\kappa} \ln\left(\frac{z}{z_0}\right) + \frac{v_{f,s}}{v_f^*}$
Gupta et al. (1985)	$d_{50} = 9.8$ mm	5.5 cm	d_{50}	$v_f^+ = \frac{1}{0.28} \ln\left(\frac{z}{d_{50}}\right) + 8.21$
Cheng et al. (1998a)	$d_{50} =$ 1.95/5.83 mm	7.8 cm - 15.4 cm	$2d_{50}$	$v_f^+ = \frac{1}{\kappa} \ln\left(\frac{z}{2d_{50}}\right) + 8.5$
X. Chen et al. (2004)	$d_{50} = 2.47$ mm	20 cm	$2d_{50}$	$v_f^+ = \frac{1}{\kappa} \ln\left(\frac{z}{2d_{50}}\right) + 8.4$

The theoretical analysis and experiments of Mendoza et al. (1992) and Nezu (1977) resulted in a modified law for permeable beds. Thereby, the constant C^* is replaced by a term considering the slip velocity $v_{f,s}$ and the friction velocity v_f^*. Some estimations of the slip velocity have been presented above. However, so far there exists no method to calculate the slip velocity and the virtual origin directly (X. Chen et al., 2004).

The approaches of X. Chen et al. (2004), Cheng et al. (1998b), and Gupta et al. (1985) are based on experiments. The experimentally determined velocity distributions are fitted to formulations of the universal logarithmic law of the overlap layer. Gupta et al. (1985) examined the mean velocity profile over impermeable and permeable beds at equal roughness. Therefore, the authors investigated the flow over a 5.5 cm high gravel bed. Thereby, it is not fully clear, if a uniform material with a grain diameter of 9.8 mm is used or if the value represents a medium grain diameter of d_{50}. In contrast, X. Chen et al. (2004) and Cheng et al. (1998b) investigated experimentally the effect of upward or downward seepage over permeable beds on to the velocity distribution. The authors applied a bed material with a d_{50} equal to 1.95 mm, 5.83 mm or 2.47 mm. Cheng et al. (1998b) also vary the bed height. While the latter two approaches use $2d_{50}$ as a representation for the virtual origin, Gupta et al. (1985) use a value of d_{50}. According to the authors, this approximation is recommended for shallow flow applications. Further estimations of the virtual origin for realistic sediment beds can be found in Table 3.1 of Dey (2014).

In comparison to the original formulation for impermeable walls, the approaches of Gupta et al. (1985) and X. Chen et al. (2004) show a slight variation of the intergenerational constant C^*. However, the clearly reduced value of the von Kármán constant κ for the formulation of Gupta et al. (1985) seems more significant. The authors interpret the reduced value by a change of dissipation of the mean flow energy. This assumption if verified by the Committee on Hydromechanics of the Hydraulics Division (1963) and the research of Nezu (1977). The authors confirm a decrease of κ with an increase of the velocity gradient and thus increasing porosity. In contrast, Dittrich (1998) and Zippe et al. (1983) approve that the value of κ stays constant, if the virtual origin and the logarithmic law of the overlap layer are applied properly. However, numerical tests conducted by Breugem et al. (2006) imply that a reduction of κ is just appropriate at very high porosities of the bed material. For porosities equal or less 60% the von Kármán constant stays unchanged at the well known value of 0.4.

7.2 Fundamentals on Incipient Motion of Particle Transport

Section 7.1 introduced the complex interaction between a particle bed and an internal as well as an external flow field in the boundary layer region. Thereby, the particle bed was assumed to be static. In case of a free disperse particle system, the mutual interference reaches its maximum at the state of erosion and sediment transport. Particle entrainment and sediment transport are of considerable interest for research since it increases the complexity of flow characteristics in a way which can not be fully captured so far. Thereby, the resulting consequences are volatile and affect the concurrence of water and human life immensely, since the natural dynamic sediment transport phenomena is contrary to a static long-term dimensioning of near-water constructions, infrastructure or flood protection systems.

This work focuses on the process of erosion and specifically on the moment of incipient motion at a granular bed. Till today there is no universal analytical solution to describe the complex processes and interactions at the boundary layer of a particle bed. The numerous influences on side of the transport medium (flow conditions, turbulence, flow height, inclination, salinity, etc.), the transported medium on particle level (size, shape, roughness, particle density, adhesion, etc.) and on packing level (packing density, porosity, grain size distribution, angle of repose, bed roughness, permeability, etc.) as well as ecological influences (vegetation, conglutination, etc.) prohibit an analytical solution. However, in engineering practice and research exist a large number of (half-)empirical solutions to describe the critical point of erosion. The strength and weaknesses of those approaches are discussed in Section 7.2.2. Prior to this, the governing influences of the erosion process on a grain scale are introduced in Section 7.2.1.

7.2.1 Incipient motion on a micro scale

The erosion process can be described on a micro scale by a force equilibrium at an individual particle placed on the boundary of a particle bed (see Figure 7.9). Thereby, the fluid-particle interaction forces are divided into driving forces and stabilizing forces. The driving forces are e. g. the drag force F_D, which acts in direction of the flow field and the lift force F_L, which acts orthogonal to the flow in z direction. Opposed to that, the submerged weight $F_{G'}$ and the frictional contact forces in the contact point P or rather the pivot angle ψ, are stabilizing the particle in its position.

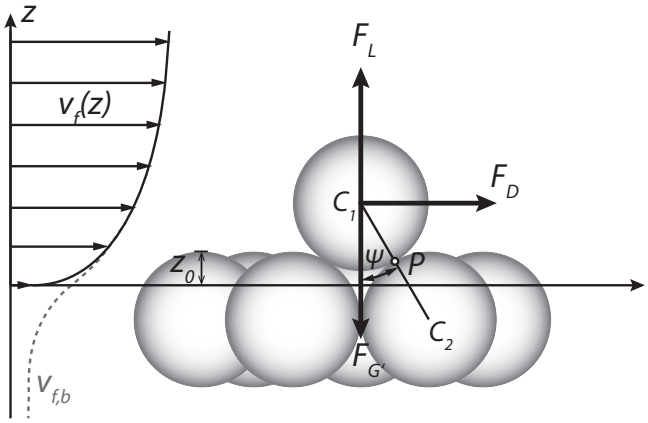

Figure 7.9: Forces acting on a single particle placed on a particle bed

With enhancing flow velocity, the driving forces increase till they reach a critical state and exceed the stabilizing forces. This state is described as the threshold of incipient motion. According to Dey et al. (2016), three different scenarios of incipient motion need to be distinguished:

- Rolling: the driving torque above the centre of gravity exceeds the stabilizing torques
- Sliding: the driving forces of the fluid exceed the resistance due to friction forces at the contact point
- Lifting/Saltation: the lifting forces exceed the submerged weight of the particle

All these scenarios represent forms of bedload transport, where the particle stays in contact with the bed during the transport process. Thereby, the first scenarios of rolling and sliding take place at lower transport stages and accordingly lower shear stresses, while a small increase in shear stress leads to saltation. According to García (2008), saltation is defined as a movement of consecutive jumps in the bed-near region and needs to be differentiated from suspended load in the free water column.

Section 2.2 gives an insight into detailed fluid-particle interaction forces. Thereby, the drag force represents the dominant interaction force (O'Sullivan, 2011). For the investigation of incipient motion the lift force represents an important influence as well, since it is directly opposed to the stabilizing particle weight. The previous presented approaches on fluid-particle interaction are based on the assumption of a fixed particle in an infinite flow

field. The influence of particle assemblies, walls or boundary layers is not considered in these common approaches. To consider the presence of neighbouring particles, the void fraction or porosity of the particle system is implemented in force calculation. However, the force models for particle assemblies are developed for uniform fluid-particle mixtures. The force estimation of a particle, which is embedded at the edge of a particle bed, is not a common approach for these empirical models. The complex flow characteristics in a boundary layer flow field complicate the force estimation. Due to the presence of a solid boundary, in form of the bed surface, the resulting flow field is highly asymmetric in normal direction to the boundary. As a result, the distribution of velocity, shear stresses and pressure defers significantly from the assumption of a infinite flow field in classical force models. This influence needs to be considered for the local particle force equilibrium, since the net forces will no longer necessarily act in the particle centre (Lee et al., 2012). So far, no common solution to estimate the drag and lift forces on a particle in a boundary layer or near-wall region in a direct way. Further details about the complex formulation of the force equilibrium at a particle placed on a particle bed are explained in Dey (2014), Kirchner et al. (1990), Lee et al. (2012), Schmeeckle et al. (2003), and Wiberg et al. (1987).

Force models for particles in contact of a rigid wall are rare. Even less models exist for the specific application of particles positioned on a porous particle bed. The reason for the absence of approaches in the past is a lack of adequate contactless measurement techniques. Early experiments as performed by Brenner (1961) or Goldman et al. (1967) are limited to particles in a distance to a rigid wall at small Reynolds numbers. Further, many investigations on the influence of a wall focus on the scenario of a moving particle and the significance of the particle distance to the wall (see e. g. Takemura et al., 2003; L. Zeng et al., 2005 and Krishnan et al., 1995). The case of a particle in contact with the wall is not considered. However, all those investigations proof the high sensitivity of the interaction forces to the position relative to a rigid wall. This is particularly true for the lift force. Depending on the wall distance and the Reynolds number, the amount and even the direction of the lift force vary (see Coleman, 1967; Kurose et al., 1999; Schmeeckle et al., 2007; Takemura et al., 2003).

Following, the few existing investigations and corresponding solutions for fluid-particle interaction forces on a particle, positioned near or at a solid boundary, are presented. All approaches have in common, that the forces are no longer distinguished by their detailed classification presented in Section 2.2. Rather, the drag force represents all driving forces acting along the direction of the flow, while lift forces represent the driving forces orthogonal to the flow direction. According to Schmeeckle et al. (2007), a measured lift force consists of a complex superposition of shear lift, vertical hydrodynamic drag, near-bed vertical fluid acceleration and other unidentified pressure effects.

Most of the presented force models are based on the advanced formulations of the drag (see Equation 7.22) and the lift force (see Equation 7.23). The formulations go back to the approach of Newton, who introduced a dimensionless coefficient to represent the flow behaviour for a wide range of Reynolds numbers. The dimensionless coefficients need to

be defined by experiments.

$$F_D = \frac{1}{2} A_c c_D \rho_f v_f^2 \tag{7.22}$$

$$F_L = \frac{1}{2} A_c c_L \rho_f v_f^2 \tag{7.23}$$

Thereby, A_c represents the cross sectional area of the particle exposed to the flow and c_D and c_L are the drag and lift coefficients. The flow velocity v_f is typically taken to be the velocity approaching in the particle centre. The formulations imply, that the particle exposure is an important factor for the force estimation. However, Lee et al. (2012) and Crowe et al. (2012) recommend the assumption of an ideal fully exposed particle ($A_c = {}^1\!/_4 \pi d_p^2$), since there is no clear solution on the force estimation of a mere partly exposed particle and the direct influence of A_c. Further, the assumption of a fully exposed particle constitutes an ideal scenario, which limits the formulation dependency to the Reynolds number.

Besides the above presented approach with a dimensionless coefficient, other authors define a relation between a non-dimensional force formulation $F^+ = {}^F\!/_{\rho_f \nu_f^2}$ and a non-dimensional particle radius $d_p^+ = {}^{d_p v_f^*}\!/_{\nu_f}$. This approach is applied in investigations of Hall (1988), Mollinger et al. (1996, 1995), and L. Zeng et al. (2009). However, those formulations can be transferred to the form of Equation 7.22 and Equation 7.23 (see Lee et al. (2012)).

With the assumption of a fully exposed particle, the influence of a solid boundary is limited to the determination of the force coefficients. Following, relevant approaches on the influence of a wall are presented. Thereby, it is distinguished between investigations concerning a particle position near and in contact with a smooth wall. Furthermore, the influences of turbulence and exposure are discussed.

Influence of a smooth wall near a particle

Goldman et al. (1967) investigated the effect of the drag force on a particle near a smooth wall in the Stoke's regime. The conducted experiments showed, that the drag coefficient can increase up to 70% of its value for uniform free flow, due to the influence of the wall. This observation is proven by numerical simulations of L. Zeng et al. (2009), who conducted DNS simulations on a particle with varying distance to a smooth wall in linear shear flow at Reynolds numbers up to 250. With decreasing distance from the wall, the drag coefficient increases independently from the Reynolds number. Interestingly, the drag coefficient showed also a minimal decrease for intermediate distances $L = 3.5\ d_p$ from the wall.

One of the first to consider the effect of a smooth wall was McLaughlin (1991, 1993), who developed a theoretically approach for the estimation of the lift coefficient. Thereby, the total lift force is represented by the sum of the Saffman lift and the lift due to wall effects. This approach was extended for translating particles in Cherukat et al. (1994). However, both approaches are limited to small Reynolds numbers $\mathrm{Re} << 1$. Takemura et al. (2003) conducted experiments considering the lift forces on rising bubbles in oil near a smooth wall at $\mathrm{Re} \leq 100$. At low Reynolds numbers $\mathrm{Re} < 35$, the obtained results showed good accordance with the low Reynolds number theory. The lift forces act in normal direction

opposed to the wall. In contrast, at higher Re the lift force acted towards the wall. This fact is also dependent on the distance of the bubble from the smooth wall. A similar application, was conducted in the DNS simulations of L. Zeng et al. (2005), where a rigid sphere is moving parallel to a wall with varying distance. At Re < 100 the lift coefficient tends to decrease with increasing Reynolds numbers as well as with decreasing distance to the wall. At Re > 100 the lift coefficient increases dramatically with increasing Reynolds numbers. A change in the lift force direction was not observed.

Influence of a smooth wall on a particle in contact

Mollinger et al. (1996) investigated the lift force on a particle in contact with a smooth wall in a wind flume. Thereby, the applied particle diameter was chosen sufficiently small to locate the particle fully in the viscous sublayer. Nevertheless, effects of turbulent fluctuations on the lift force have been observed during the tests. The ratio between the instantaneous to the mean lift force was calculated to 2.8. The resulting approach for the lift force near a wall is given by

$$F_L^+ = (5.69 \pm 1.1) \left(d_p^+\right)^{(1.87 \pm 0.04)} \quad . \tag{7.24}$$

This solution is analogical to the results of similar experiments with a less sensitive measurement device, conducted by Hall (1988).

Besides the effect of a near wall, L. Zeng et al. (2009) examined additionally the limit case of a particle in contact with a smooth wall at linear shear flow. The results show a clear increase in the drag coefficient for the position at the wall compared to the standard drag correlation. The results for the lift coefficient showed a good agreement with the classical approach of Saffman (1965). Compared to the results of Mollinger et al. (1996) or Hall (1988), the experiments of Saffman (1965) show smaller values. Even if the experiments of Mollinger et al. (1996) take place at slightly higher Reynolds numbers, this fact is reject by the author as a justification for the higher values. The final formulations for the approach of Zeng are defined as

$$c_D = \frac{40.81}{\mathrm{Re}_G} \left(1 + 0.104\ \mathrm{Re}_G^{0.753}\right) \quad , \tag{7.25}$$

$$c_L = \frac{3.663}{\left(\mathrm{Re}_G^2 + 0.1173\right)^{0.22}} \quad . \tag{7.26}$$

It need to be considered, that L. Zeng et al. (2009) applied a constant shear rate G in the flow field, which defers from the theory of boundary layer flow. However, for small particles the assumption of a linear velocity distribution over the particle diameter should be appropriate.

The investigations of Lee et al. (2012) concern the point of incipient motion for a particle on a particle bed. Lee et al. (2012) define an equilibrium state in which the observed particles start to roll over the underlying particles on its lee side. Therefore, the main driving forces are identified as drag force, lift force and driving torque. To obtain an advanced approach for the estimation of those forces, Lee et al. (2012) conducted numerical simulations. However, the numerical simulations do not contain the scenario of a particle laying on a

particle bed but rather a particle placed on a smooth wall. The effects taking place near a particle bed, are not part of the simulation. However, the influence of a rough wall on the velocity profile are considered. Contrary to the investigations of Z. Zeng et al. (2006), Lee et al. (2012) subjects the fully resolved particle to a logarithmic mean velocity profile which is defined by the approach of Swamee (1993) (see Equation 7.16). Thus, the mean velocity profile is adopted to the smooth or rough flow regime depending on the particle diameter. These are varied relative to a range of $2 < d_p^+ < 500$ represented in dimensionless wall units (see Equation 7.3). Contrary to previous presented numerical simulations, the turbulence around the particle is no longer resolved by DNS but by a time-averaged solution. The results of Lee et al. (2012) are based on the assumption of L. Zeng et al. (2009) and are given as

$$c_D = \frac{40.81}{\mathrm{Re}_p}\left(1 + 0.104\ \mathrm{Re}_p^{0.753}\right)\left[1 - \mathrm{erf}(0.002\ \mathrm{Re}_p)\right] + 0.54\ \mathrm{erf}(0.002\ \mathrm{Re}_p) \quad (7.27)$$

$$c_L = \frac{3.663}{\left(\mathrm{Re}_p^2 + 0.1173\right)^{0.22}}\left[1 - \mathrm{erf}(0.001\ \mathrm{Re}_p)\right] + 0.223\ \mathrm{erf}(0.001\ \mathrm{Re}_p) \quad . \quad (7.28)$$

Thereby, erf() denotes the error function.

Equation 7.27 is plotted and compared to other approaches in Figure 7.10a. At small particle Reynolds numbers, the results of Lee et al. (2012) are in accordance with those of L. Zeng et al. (2009). With increasing particle Reynolds numbers the results of Lee et al. (2012) deviate and are now smaller than the results of L. Zeng et al. (2009). The discrepancy between the linear shear flow and the logarithmic velocity profile seems to have an impact at $\mathrm{Re}_p \approx 20$. After $\mathrm{Re}_p \approx 1000$ the drag coefficient seems to convert to a constant value of 0.54. To compare the scenario of a particle in contact with a wall and a particle in unbound uniform flow, the empirical results of Clift et al. (1971) are illustrated as well. The comparison indicates, that the drag coefficient for a particle in contact with a wall is higher than for a particle in an infinite flow field.

The results for the lift coefficient are given in Figure 7.10b. Consistently, the approach of Lee et al. (2012) is in accordance with the results of L. Zeng et al. (2009) at small Reynolds numbers. At higher Reynolds numbers, the lift coefficient converts to approximately 0.2. The results are in good agreement with the observation of L. Zeng et al. (2005), that the lift coefficient decreases with increasing Reynolds numbers till $\mathrm{Re} \approx 100$. However, the dramatical increase of the lift coefficient at $\mathrm{Re} \geq 100$ found by L. Zeng et al. (2005), can not be confirmed in the results of Lee et al. (2012).

For the sake of completeness, the results for the torque acting on the particle are presented. As already mentioned above, Lee et al. (2012) introduced a torque T (see Equation 7.29) besides the drag and the lift force. Simultaneous to the other force formulations, the torque is a function of a dimensional coefficient c_M, which is a function of the Reynolds number (see Equation 7.30).

$$\mathbf{T} = \frac{\pi}{16} c_M \rho_f v_f^2 d_p^3 \quad (7.29)$$

$$c_M = \frac{15.104}{\mathrm{Re}_p}\left[1 + 0.0005\ \mathrm{Re}_p\ \mathrm{erf}(0.002\ \mathrm{Re}_p)\right] \quad (7.30)$$

A theoretical and experimental study of the drag and lift forces acting on a particle placed on a particle bed has been conducted by Coleman (1967). In the experiments, a layer of plastic balls has been arranged in a dense configuration and a particle with equal size was placed on top of three supporting particles. Coleman (1967) measured the drag and lift forces acting on the particle and developed a curve for the drag and the lift coefficient as a function of the particle Reynolds number Re_p. The drag coefficient curve gives similar results as Lee et al. (2012). However, for the lift force negative values are measured for particle Reynolds numbers greater than 100. An explanation is not given by Coleman (1967).

Influence of turbulence and exposure of a particle

In the previous discussed approaches, the mean velocity is assumed for the force estimation. However, since most scenarios of incipient motion are based on turbulent conditions, the instantaneous velocities or forces are of great importance. The instantaneous forces acting on a particle can far exceed the time-averaged mean values. Thus, the particle entrainment is induced by the instantaneous values and not by any average quantity. According to Schmeeckle et al. (2007), the mean values represent a parametrisation on the underlying physical processes only. Furthermore, the exposure of a particle represents an important influence on the force equilibrium of a particle on a bed. Schmeeckle et al. (2003) proofed, that the mean velocity subjected to a particle is significantly reduced if this particle is positioned on the lee side of another particle.

A wide experimental series considering the influences of turbulence and exposure on a fixed particle at a particle bed has been conducted by Schmeeckle et al. (2007). Thereby, a 1.9 cm particle was placed in a flume either above a smooth wall or a gravel bed with similarly sized particles. During the experiments the horizontal and vertical force components acting on the particle were measured in turbulence resolving frequencies. In the tests, Reynolds numbers between $5 \cdot 10^5 < \mathrm{Re} < 2 \cdot 10^6$ were achieved. The main purpose of the experiments of Schmeeckle et al. (2007) were the investigations of the differences between mean and instantaneous values.

The experiments revealed a significant influence of the bed characteristics, as a smooth wall or a particle bed, on to instantaneous drag force. The drag forces acting on a particle 0.5 cm above the smooth wall, are compared to the forces subjected to a particle 0.7 cm above the top edge of the particle bed. While the instantaneous drag forces on the particle near a smooth wall were measured as one third of the mean values, the instantaneous drag forces at the particle bed are given as more than three times the mean values. Moreover, the instantaneous lift forces show an increase of up to six times the mean value at the gravel bed. Furthermore, the effect of exposure on the mean and instantaneous forces were investigated. With increasing exposure, the mean values for the drag force increase rapidly, while the standard deviation of fluctuations increases only slightly. For the lift force, this influence is of contrary effect. While the mean lift forces increase with increasing exposure similar to the drag forces, the instantaneous lift forces decrease. Actually, the mean lift even exceeds the lift force deviations when the particle is over half of its diameter above the particle bed.

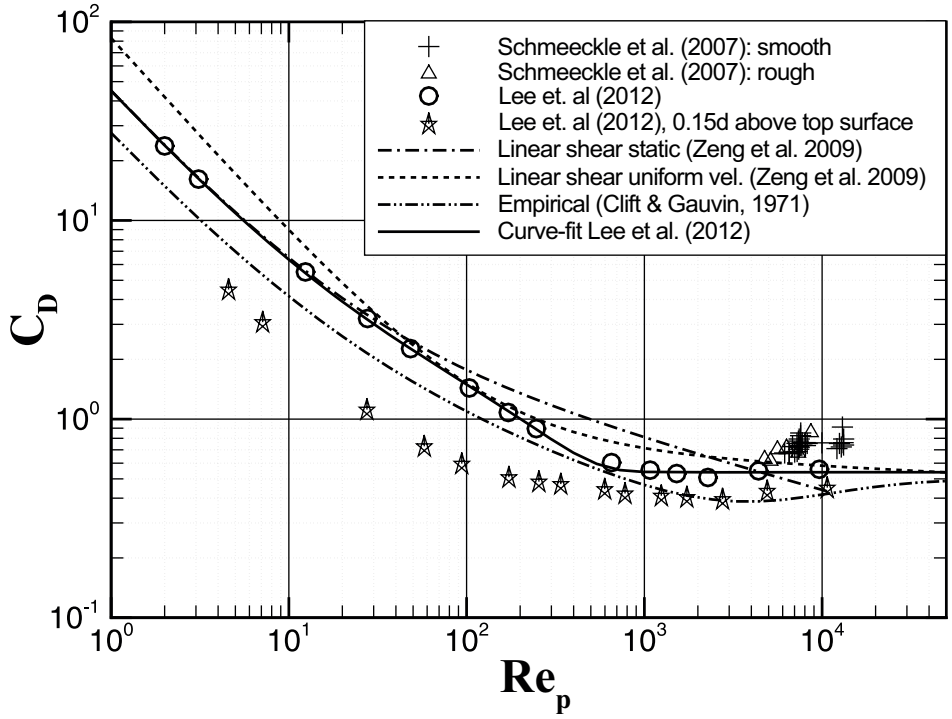

(a)

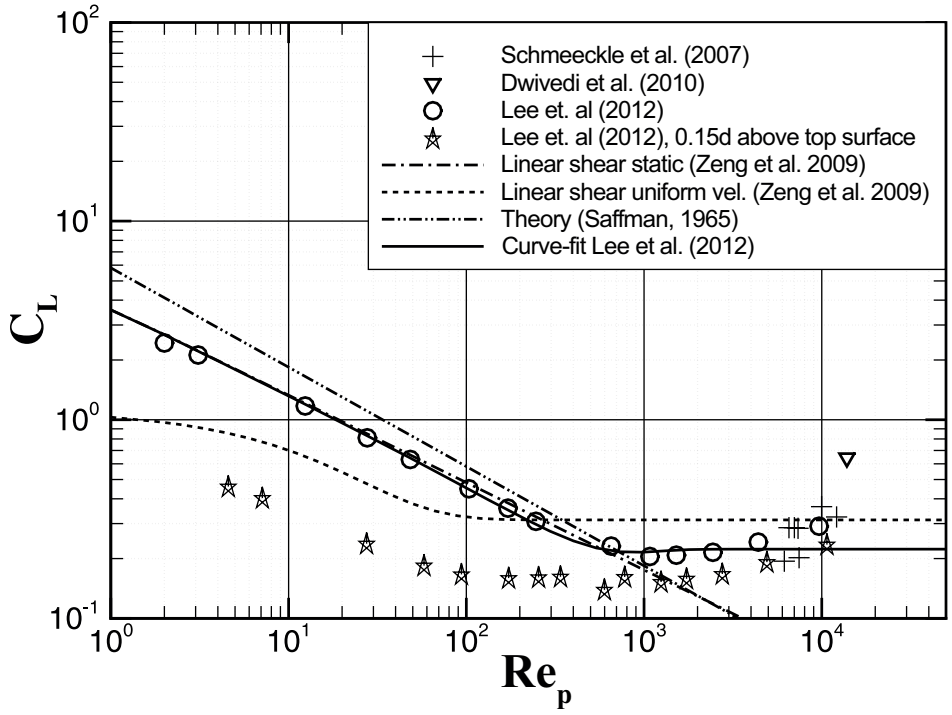

(b)

Figure 7.10: Comparison of drag coefficients (a) with curve fit of Equation 7.27 and lift coefficients (b) with curve fit of Equation 7.28 (adopted according to Lee et al., 2012)

The results of Schmeeckle et al. (2007) are also presented in the diagrams of Lee et al. (2012) (see 7.10a and 7.10b). While the results for the drag coefficient are slightly higher than in the approach of Lee et al. (2012), the results for the lift coefficient are in good accordance. Further details about the problematic nature of force estimation for the turbulent flow field at a wall can be found in Lee et al. (2012), Schmeeckle et al. (2003, 2007), and L. Zeng et al. (2009).

7.2.2 Incipient motion on empirical thresholds: Sediment transport models

In hydraulic engineering sediment transport is usually described by empirical or half-empirical models. Thereby, the models are distinguished by the quantity describing the critical state at the threshold:

- critical velocities
- critical bed shear stresses
- turbulence induced entrainment

The most common empirical approach of critical velocities has been developed by Hjulström (1935) in form of the Hjulström-Diagram. Thereby, the mean critical velocity is displayed directly against an average grain size. The original diagram was later expanded by Sundborg (1956) and Postma (1967). The simplicity of Hjulström's (1935) approach makes it attractive. However, since the approach of a critical velocity is strongly limited in its applicability, it is applied for a first rough estimation of the critical state only. Further details on Hjulström's experiments and more approaches for a critical velocity can be found in Dittrich (1998), Soulsby (1997), van Rijn (1984), and Zanke (1982).

In the past decades the most common approach to define incipient motion is represented by threshold critical shear stresses. Shields (1936) was the first to develop an half-empirical approach based on a force equilibrium at a particle on a bed. For the force equilibrium, the drag force was taken into account, while the lift force was neglected. Shields (1936) derived a dimensionless shear stress or Shields' parameter Θ^*, which represents the ratio between driving shear stresses and the surface weight of the particles at the bed subjected to this shear (see Equation 7.31).

$$\Theta^* = \frac{\tau_0}{(\rho_p - \rho_f) \cdot g \cdot d_p} \tag{7.31}$$

Shields (1936) showed, that the critical value of Θ^*_{cr} as a threshold of motion varies with a boundary Reynolds number Re^* as defined in Equation 7.32 (Buffington et al., 1997).

$$\mathrm{Re}^* = \frac{v_f^* \cdot d_p}{\nu_f} \tag{7.32}$$

For the particle diameter d_p, Shields (1936) employed the average grain size d_{50} of the applied material. To define the relation of $\Theta^*_{\mathrm{cr}} = f(\mathrm{Re}^*)$, Shields (1936) conducted physical tests with different sediment materials. These results as well as additional data from

physical tests of other authors are the base of the so called Shields curve. This curve, or rather band, represents the threshold critical state of incipient motion. The area above this curve represents sediment movements, while the area underneath assumes motionless conditions. The original curve was later corrected for the fine sediments region by Mantz (1977) and further complemented by measured data of other authors. A very detailed compilation can be found in Buffington et al. (1997).

Although, Shields defined the boundary Reynolds number Re^* differently than Nikuradse (1933), the flow regimes of Nikuradse can be identified by the Shields curve (Dey, 2014):

1. Hydraulically smooth flow for $\mathrm{Re}^* \leq 2$: the diameter d_p is much smaller, than the viscous sublayer thickness and the Shields curve is linearly varying.
2. Hydraulically transitional flow for $2 < \mathrm{Re}^* < 500$: the sediment particle diameters are similar to the viscous sublayer height.
3. Hydraulically rough flow for $\mathrm{Re}^* \geq 500$: the viscous sublayer is not existing and the Shields parameter tends to a constant of $\Theta^*_{cr} = 0.056$.

A drawback of the Shields diagram is the presence of the shear velocity in both characteristic quantities. As a consequence, the critical bottom shear stress cannot be determined from the diagram directly, but requires an iterative procedure (Malcherek, 2007b). Alternatively, the boundary Reynolds number Re^* can be replaced by a dimensionless particle diameter D^*, which is defined as

$$D^* = \left(\frac{\rho_p - \rho_f}{\rho_f} \frac{g}{\nu_f^2} \right)^{1/3} d_p \quad . \tag{7.33}$$

Beheshti et al. (2008) and Dey (2014) give summaries of different formulas for the modified Shields curve with $\Theta^*_{\mathrm{cr}} = f(D^*)$. Some selected formulas are plotted in Figure 7.11.

However, the boundary conditions of the physical tests of Shields (1936) are not fully clear. A discussion on the true conditions of Shields's (1936) tests can be found in the critical papers of Buffington (1999) and García et al. (2000). A major issue is the definition of the threshold of motion. It is not clarified, which method has been applied in the tests of Shields (1936), to identify incipient motion. Bechteler (2006) reproduces the extrapolation of Shields between the Shields parameter and the bed load transport. According to the transport stages of Schöberl (1990), Bechteler identifies Shields' threshold of motion in the region, where already partial transport occurs. According to Dittrich (1998), several authors proofed, that even below the Shields curve sediment transport can be observed. The reason is the negligence of turbulent lift force. Especially for coarse material, the Shields curve overestimates the critical values for incipient motion (García, 2008). Neill et al. (1969) recommends to divide the original values of Shields by a factor of 2 in the case of coarse material.

Another threshold approach based on a critical bed shear stress has been developed by Iwagaki (1956). The resulting half-empirical model analyses the equilibrium state of an isolated particle on a rough bed. Thereby, two zones of either viscous sublayer or turbulent flow conditions are distinguished. The surface of the considered particle is assigned to the respective zone. Based on the fractional surface area located in the flow region, a separate

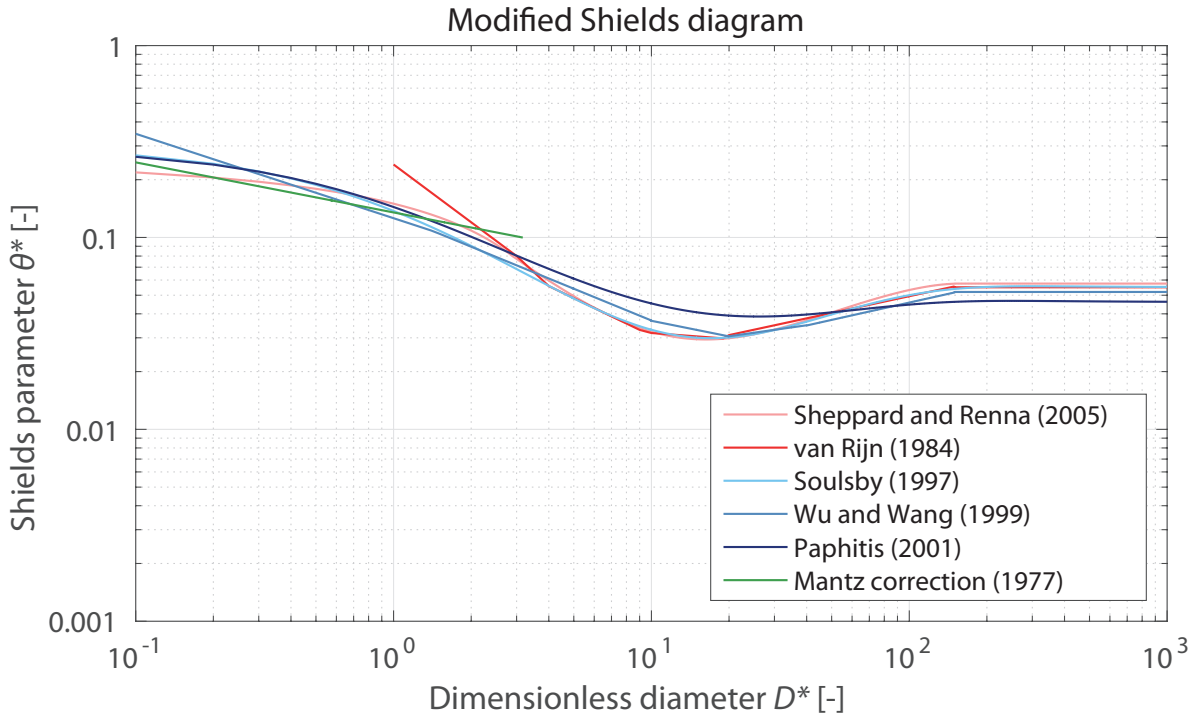

Figure 7.11: Modified Shields diagram with selected formulas given in Beheshti et al. (2008) and Dey (2014)

drag force for every flow region is calculated. Contrary to Shields (1936), Iwagaki (1956) takes the lift force due to pressure gradients into account. Opposed to the driving forces, the submerged weight and friction represented by the angle of repose ϕ are considered as resistance forces. Depending on the flow regime and the boundary Reynolds number Re^*, the approach consists of three formulations for the smooth, transitional and rough flow regime. Since the explicit formulations are very complicated, Iwagaki (1956) expressed these equations as an empirical curve fit in relation to the particle parameter D_{Iw}^* (see Equation 7.35):

$$\Theta_{cr}^* = \begin{cases} 0.14 & (D_{Iw}^* \leq 2.14) \\ 0.195 {D_{Iw}^*}^{-7/16} & (2.14 < D_{Iw}^* \leq 54.2) \\ 0.034 & (54.2 < D_{Iw}^* \leq 162.7) \\ 0.195 {D_{Iw}^*}^{3/11} & (162.7 < D_{Iw}^* \leq 671) \\ 0.05 & (S^* > 671) \end{cases} \tag{7.34}$$

$$D_{Iw}^* = {}^{d_p}/_{\nu_f} \left(\frac{\rho_p - \rho_f}{\rho_f} g d_p \right)^{0.5} \tag{7.35}$$

The research of Iwagaki (1956) in combination with the research of Coleman (1967) are the basis of the Ikeda-Coleman-Iwagaki model, which was presented by Ikeda (1982). The

model is based on the entrainment mechanism of sliding. At the equilibrium state, the model takes the drag force, the lift force, the submerged weight and frictional forces due to particle contact into account. As a simplification, all os these forces are assumed to act in the particle centre (García, 2008). Further, a logarithmic law is applied for the bed near velocity distribution. The equilibrium state is expressed by the critical bed shear stress as

$$\Theta^*_{cr} = \frac{4}{3}\frac{\mu_s}{(c_D + \mu_s c_L)}\frac{1}{F^2(Re^*)} \tag{7.36}$$

Thereby, the function $F^2(Re^*)$ denotes the relation between the flow velocity near the bed and the shear velocity v_f^*. The function can be replaced by the approach of Swamee (1993) (see Equation 7.16), which has the benefit of a continuous function for all of the different flow regimes.

The theoretical model was developed on the assumption of idealized spherical spheres, for which the angle of repose can be assumed as smaller than for natural materials. According to García (2008), the approach of Ikeda-Coleman-Iwagaki matches the Shields curve for an angle of repose of 60°. For a smaller angle of 40°, the results still follow the trend of the Shields curve, but reveal lower values by a factor of 1.6. This fact matches very well with the critisism of the Shields diagram, presented above.

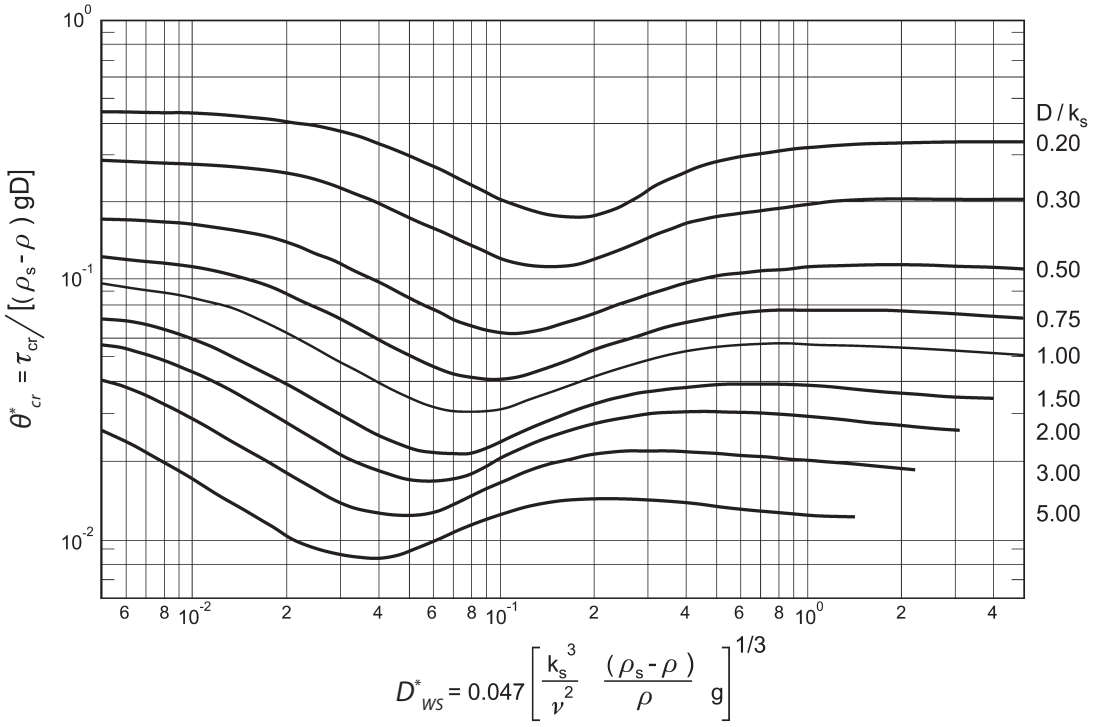

Figure 7.12: Modified diagram of Wiberg and Smith (1987) (adopted after García (2008))

The approach of Wiberg and Smith (1987) provides an almost identical solution considering the Ikeda-Coleman-Iwagaki model. The model assumes rolling as the incipient motion mechanism and considers, besides drag and lift forces, also turbulence to some extend

(Miedema, 2010). However, the difference between the Ikeda-Coleman-Iwagaki model and the Wiberg and Smith (1987) approach is the representation of friction due to particle contact. The Coulomb friction μ_s is defined by the angle of repose to $\mu_s = \tan(\phi)$. In most approaches such as in the Ikeda-Coleman-Iwagaki model, the angle of repose ϕ represents the effect of the geotechnical parameter of effective internal friction φ'. This is opposed to the approach of Wiberg and Smith (1987), where ϕ is replaced by the pivot angle ψ. Thereby, the pivot angle represents a geometrical angle, which characterises the configuration between the resting particle and the particle bed (Miedema, 2016). Thus, the Wiberg and Smith model is highly suitable to represent the critical state for heterogeneous material since the pivot angle can be described by the ratio between the size of the exposed particle and the particle bed. Hence, Wiberg and Smith (1987) provide the obtained results in a diagram with several curves at different D_p/k_s ratios. Figure 7.12 shows the plot of the modified model, which is no longer based on the boundary Reynolds number Re^* but on a non-dimensional particle diameter D^*_{WS}.

Such as Wiberg and Smith (1987) also Dey (1999) chose the rolling mechanism as the scenario on incipient motion. Dey (1999) applied drag and lift forces as driving forces and neglected turbulence. However, the lift force is distinguished into a shear induced part, based on Saffman (1965), and a part, based on the Magnus force (see Section 2.2.1). The Magnus effect is taken into account for higher Reynolds numbers. According to Miedema (2016), the resulting formulation for the critical Shields parameter of Dey (1999) is similar to the approach of Ikeda (1982) and Wiberg et al. (1987) but much more detailed. In Figure 7.13 the resulting critical state of the Shields parameter θ^*, is given as a function of the particle diameter D^*_{Iw} (see Equation 7.35) for different angle of repose ϕ.

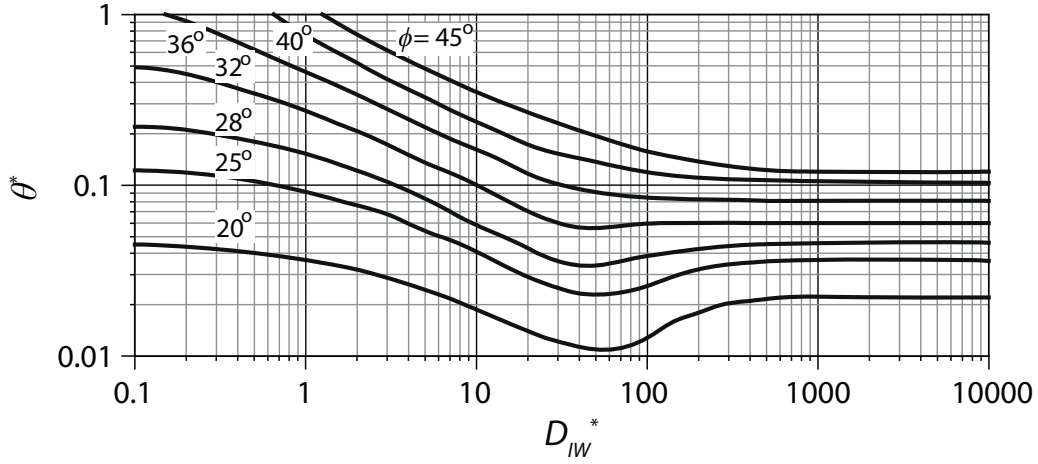

Figure 7.13: Modified critical bed shear stress diagram by Dey (2014)

In the previous half-empirical approaches for critical bed shear stress the mean fluid velocity is used to characterise incipient motion. In newer approaches the turbulence is identified as an important influence and taken into account. According to Zanke (2001, 2003), the mean value of critical shear stress is reduced by turbulence due to increased instantaneous shear stresses as well as an increased lift force implied by turbulent pressure

fluctuations. Both factors are taken into account in Zanke's (2001; 2003) formulation on critical shear stress, given as

$$\tau^*_{\text{krit}} = \frac{0.7 \tan \phi}{\left(1 + n \cdot \frac{v'_{rms,b}}{v_{f,b}}\right)^2 \left(1 + \frac{1}{2.5}\left(n' \cdot \frac{v'_{rms,b}}{v^*_f}\right)^2 \tan \phi\right)} \tag{7.37}$$

Thereby, $v_{f,b}$ represents the mean flow velocity acting on the particle and n' gives the probability of occurrence of an increased instantaneous value of velocity at the particle (with $1 \geq n \geq 3$). Further, $v'_{rms,b}$ describes the maximum turbulent fluctuation on the particle. The factor 0.7 in the enumerator represents the particle volume fraction for a bed material of a porosity $n = 0.3$. The first term in the denominator of Equation 7.37 represents the influence of the instantaneous shear stresses, while the second takes turbulence induced lift forces into account. The trend of the Shields curve can be achieved for $n' = 1.8$ and $\phi = 20°$. By an extension of Equation 7.37, the approach of Zanke (2001, 2003) provides the opportunity to consider the effect of cohesion for fine sediment particles.

7.3 Physical Tests on Incipient Motion on a Particle Bed

The previous Section 7.1 and Section 7.2 gave an insight into the complexity of the boundary layer flow at natural beds and the detection of incipient motion. The majority of the half-empirical approaches on incipient motion focus on the erosion or transport of particle groups or fractions rather than the processes on an individual grain. Further, it is little known about the forces acting on a particle near a smooth, rough or even permeable surface. To gain more informations on the point of incipient motion for individual single particles and the local flow situation, new physical tests are conducted.

The physical test shall give an better understanding on incipient motion on a particle scale. Therefore, it is crucial to have well defined and reproducible boundaries on particle level. As a consequence, the highly complex scenario of transport at a permeable layer of disperse particles is modified to a more controlled implementation. Thus, a rough impermeable boundary is applied, whereby the roughness elements are assembled by particles of equal particle diameter. The fixated particles of the rough boundary are arranged in a well structured hexagonal pattern. Thereby, intersecting rows of particles are arranged orthogonal to the flow direction. In the tests, a single particle is embedded on a well defined position on the rough particle boundary. Thereby, two different positions are distinguished (see Figure 7.14). The first position describes the lowest resistance due to the interaction between the free particle and the fixed particle layer against erosion. Thereby, the particle rolls exactly over the gap in between two particles on its lee side. The second position is characterised by a maximum resistance against erosion. In this case, the particle is embedded directly in front of an aligned particle. Thus, the free particle needs to roll over the crest of the particle on its lee side. Although in both cases, the exposure of the free particle as well as its height corresponding to the fictive origin of the velocity profile are equal, the resistance differs significantly due to different pivot angles ψ (see Figure 7.9). The pivot angle is an indicator for the torque, which is required to move the particle out

of its initial position. A greater pivot angle is equivalent to a higher required torque. The differentiation of the initial position should provide a wider range of informations on the point of incipient motion.

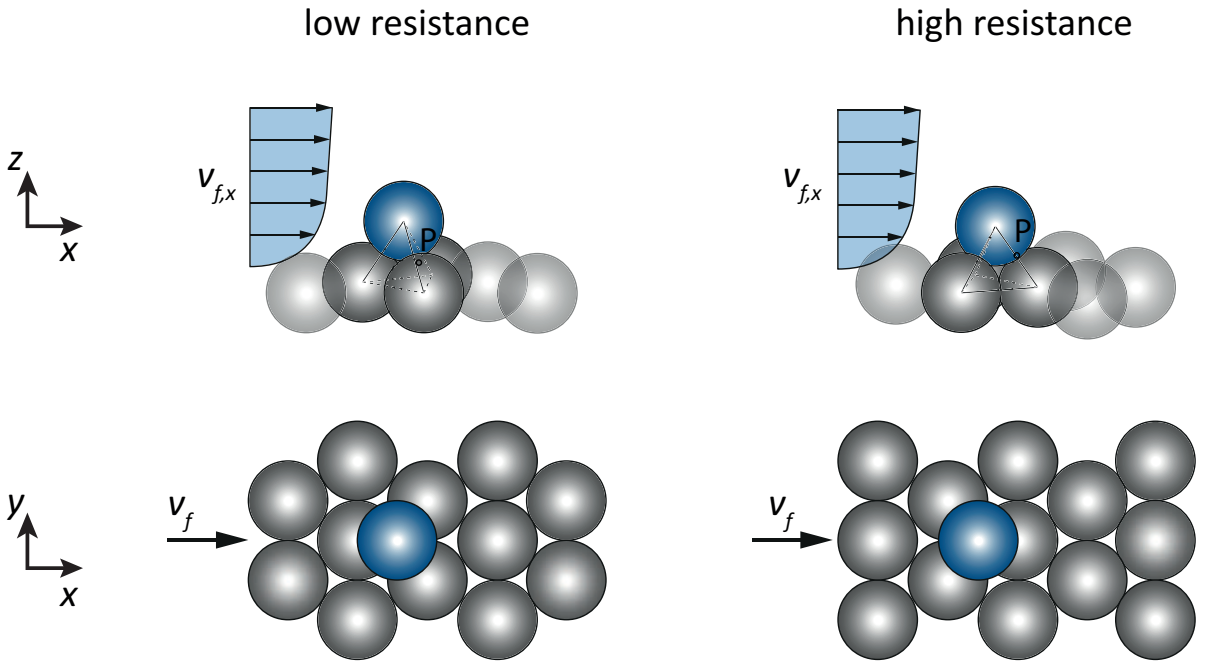

Figure 7.14: Investigated embedding positions of the single particle on the monodispersed particle layer: Position of lowest resistance against erosion (left) and position of highest resistance against erosion (right). The first row of figures represents the cross section in flow direction, while the second row represents the top view on the particle layer.

7.3.1 Setup of physical tests

The physical tests are conducted in a flume of the company G.U.N.T. (product identification HM-162) at the laboratory of the hydraulic department at TUHH. The flume has a testing area with a length of 5 m, a width of 30.9 cm and a height of 45.0 cm. A specially designed inlet element is positioned upstream of the testing area in the flume, to ensure little turbulences when the water enters the testing area. A flow straightener with a honeycomb structure is placed preceding to the transition between the inlet element and the testing area. The sides of the flume are fully made of glass to ensure an easy observation of the flow (see Figure 7.15). The flume has an enclosed water circuit. The flow can be induced by an adjustable inclination of the flume or by the adoption of the pump performance. Therefore, the pump speed can be adjusted by two different control options. The first option is an automatic adoption of the pump speed to reach a certain flow rate. Thereby, a flow meter, positioned downstream of the outlet element of the pump circuit, measures continuously the flow rate. This information is implied in the control

module, which adopts the pump speed based on the measurements. The second control option is the manual adjustment of the pump speed. Thereby, the pump speed is directly implemented in the control module. The pump speed can be specified percentaged of the maximum pump capacity of $Q_{P,max} = 132$ m^3/h (G.U.N.T. Gerätebau GmbH, 2018). For the investigation of the incipient motion, the flow needs to be increased slowly to identify the critical moment of incipient motion. The automatic adoption of the flow rate has the disadvantage of a minimal alternation of the flow rate by the continuous adoption of the pump speed. Thus, the manual control option was applied in the physical tests. The inclination of the flume has been adjusted to zero in all tests.

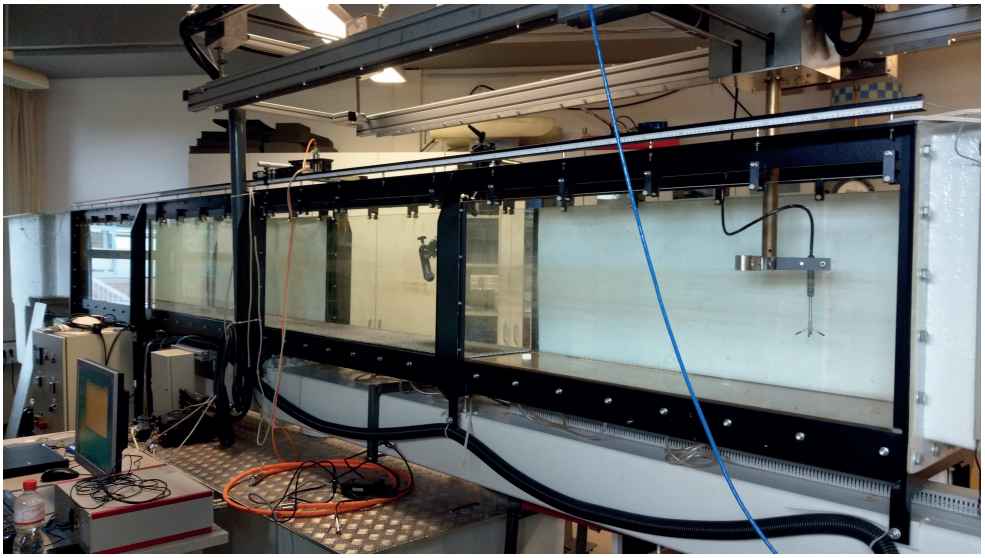

Figure 7.15: Experimental flume applied for the physical tests in incipient motion. On the left side the inlet element and on the right side the end of the testing area.

The water level inside the flume can be adjusted by built-in components. Therefore, bolt holes are positioned every 25 cm in the middle of the cross section orthogonal to the flow direction. The first bolt hole is positioned 12.25 cm downstream of the inlet element. In the physical tests a groundsill is positioned at the very end of the testing area, to guarantee a water height of approximately 8 cm in the channel at the required range of flow rate (see 7.16a).

Since the investigations focus on the incipient motion of a single particle, it is crucial to apply well defined and reproducible boundaries for the flow situation around the investigated particle. An essential factor is the position of the single particle on the particle layer and the arrangement of the particles of the rough particle layer around it. The initial position configurations of a minimal and maximal resistance due to the pivot angle (see Figure 7.14) has been detailed discussed in Section 7.3. However, to provide the exact arrangement of the initial positions, the underlying particles of need to be aligned in a well structured manner. To met this required conditions, a system of panels with fixated particles as material of a rough bottom layer is manufactured carefully. Thereby, the particles are applied as a monodisperse arrangement of one particle height. The panels

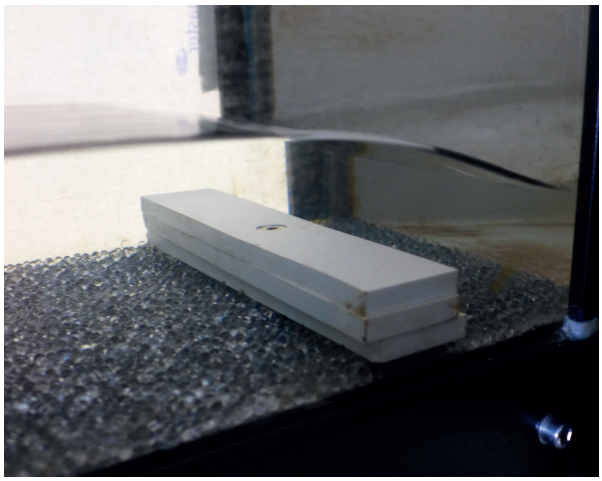

(a) Blockage at the end of the testing area to adjust the water height in the flume

(b) Fixation by screws of PVC-plate with glued particle layer

Figure 7.16: Built-in elements in the experimental setup of the flume

consist of black, rigid PVC-foam with a thickness of 3 mm. The black colour of the PVC foam is chosen to reduce the amount of reflections during the measurements. Four panels with a length of 1.25 m and a width of 0.308 m are provided, to fill the entire testing area of 5 m length. To fixate the particle as a thin layer on the panels, a clear silicone glue is applied with a fine toothed spatula. The thickness of the silicon coat is chosen thick enough, to provide adequate contact surface to fixate the particles, and simultaneously as thin as possible, to achieve as much void in between the particles as possible. The final optimal silicone glue coat height is a mere fraction of a millimetre (see 7.17a).

In total, 5 sets of panels with different particle diameters for the monodisperse fixated particle layer are manufactured. Particle diameters of 1-1.3 mm, 2 mm, 3 mm, 4 mm and 5 mm are applied. The used particles are of the same kind as in the investigations of the previous chapters. For further information on the material properties see Section 5.2.3. The gross of the particles are arranged in a dense but unstructured manner on the panels. However, to provide the required basis for the clear defined initial positions, a more structured arrangement is required. Therefore, a specific investigation area is manufactured. In this 10 by 10 cm wide area, the particles are aligned to a dense hexagonal pattern (see 7.17b). The fixed particles in the investigation area are coated with a matt black lacquer to reduce the amount of reflection from the glass particles. The investigation area is positioned in the middle of the third panel in flow direction approximately 1.35 m before the outlet element of the flume. The panels are kept in place by a screw near the front and the downstream end of the panel respectively (see 7.16b). In a few cases, the panels are fixated with an extra screw in the middle of the panel.

In the physical test, the incipient motion of the single particle and the corresponding flow situation are investigated. Therefore, high speed recordings are conducted. The applied camera and the associated LED technique is the same described previously in Chapter 6 (for details see Section 6.2.4). The camera is positioned near the testing area, orthogonal to the glass sides of the flume (see 7.18a). The distance of the camera to the recording

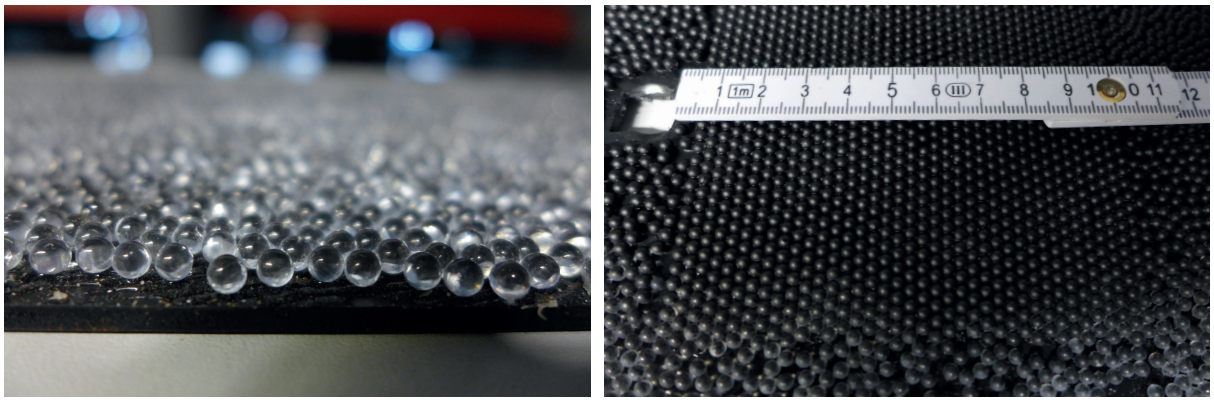

(a) (b)

Figure 7.17: Arrangement of particles on PVC panels: Side view on unsorted area at $d_p = 4$ mm (a) and top view on investigation area at $d_p = 3$ mm (b)

plane is arranged in such a manner, that the recorded picture comprises the gross of the investigation area. Inside the flume, the LED head of a LED-pulsing system is installed via a pivot mounted arm. The LED head is attached to a fibre optic and a prism, which is able to create a light-sheet. The light-sheet gives the opportunity, to visualise the flow situation in a certain plane. Therefore, polyamid seeding particles are added in the water cycle. These seeding particles have a size of $d_p = 57 \cdot 10^{-6}$ m and a density similar to water with $\rho_p = 1016$ kg/m^3. Due to the similar density to water, the seeding particles are spread over the whole height of the water volume and are carried with the flow. The seeding particles are highly reflective and due to the intense light of the LED light-sheet, the particles inside the plane become clearly visible (see 7.18b). Thus, the flow inside the light-sheet can be visualized. The seeding particle velocities can be analysed by the PIV-technique (see Section 6.2.1). The thickness of the light-sheet as well as the opening angle can be adjusted by shifting the light-sheet prism towards or away from the LED fibre optic. A thicker light-sheet gives the opportunity to contain a higher number of reflective particles and, thus, a higher number on informations for the PIV analysis. However, the increase of the light sheet thickness increases also the light scatter. Thus, the light intensity decreases with increasing thickness. Further, the distance between the prism and the water surface has an high impact on the light intensity. With increasing distance between prism and water surface, the intensity of the light-sheet decreases. To achieve a maximum light intensity, the light sheet is adjusted to a thickness of approximately 4 mm and the prism is positioned as near as possible to the water surface without dipping into the water. 7.18b presents the light-sheet position in flow direction over the investigation area in the tests with the illuminated seeding particles in the water column.

To monitor the water height in the flume during the testing, ultrasonic probes are installed in the flume near the investigation area. The measurements of supersonic probes depend on the density of the surrounding medium and, thus, from the room temperature. Since the temperature in the laboratory changed over the day, the ultrasonic probes need to be calibrated before every new test series.

Following, the testing procedure to investigate the threshold of incipient motion in the

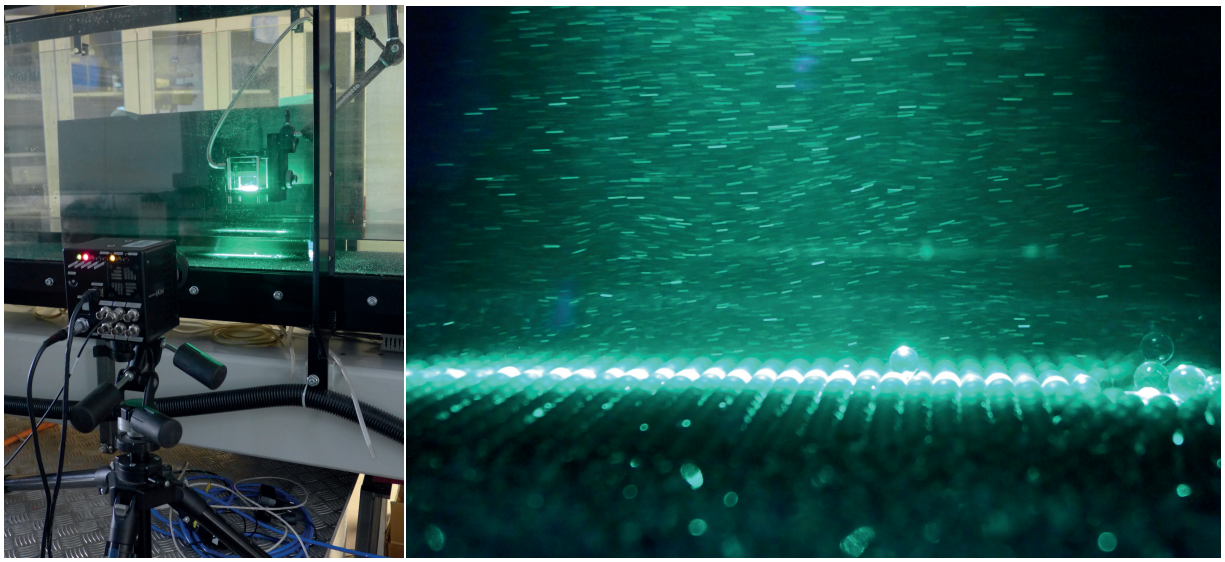

(a) (b)

Figure 7.18: Installation of the measurement equipment with high-speed camera and LED-light

previously describes test setup. In each test, the incipient motion of a single particle is investigated. Therefore, a single particle is positioned within the light sheet. Thus, the flow situation in the plane of the free single particle as well as the movement of the particle itself can be observed by the high-speed camera. The particle position in flow direction is arranged in such, that 2/3 of the light-sheet length is located on the particle luv side. The single particle is inserted at a slow flow velocity. By this means, the influence of a pressure blow due to the start of the pump should be avoided. The exceedance of a pressure blow through the flume system might already induce the first particle motion. After the installation at the initial position, the flow rate is increased slowly by increasing the pump capacity. The pump capacity can be adjusted in stages, which are equivalent to 1% of the maximum pump capacity. Each stage and the corresponding flow rate is kept constant for 60 s before the next stage is adjusted.

The framerate of the high-speed camera needs to be adopted to the maximum flow velocity in a certain test scenario, to achieve a high PIV analysis quality (see Section 6.2.1). Thus, a prior test is conducted for each test series of a certain particle diameter, to investigate the quality of the high-speed recordings at the implemented framrate. A higher framerate resolves the flow velocities better but is also equivalent to a high amount of data. Thus, an adequate compromise needs to be adopted. In the physical tests a framerate of 800 fps are adopted. To keep the amount of data small, the recorded time window in which the incipient motion occurs was chosen to 1 s. Thereby, approximately 75% of the frames take place before the incipient motion occurs and 25% subsequent. This equals approximately 600 frames before and 200 pictures after the first motion of the particle.

7.3.2 Analysis of the external flow field in the physical tests

To investigate the flow rate in the experimental flume, the average flow velocity in the flume are measured corresponding to each testing series. Therefore, the panels are installed in the flume and the pump flow rate is slowly increased from 3% to 15% of the maximum pump capacity. Thereby, the pump flow rate is kept constant till the flow is fully developed before the flow velocity is measured. The mean flow velocity in the flume is measured by a 3-dimensional acoustic Doppler velocimetre at a sample rate of 100 Hz. Thereby, the measured accuracy for the flow velocity is $\pm 1 \cdot 10^{-3}$ m/s (see Nortek, 2017). From the measured profile, the mean velocity above the boundary layer can be determined. Figure 7.19 presents the mean flow velocity over the flow rate at different roughness heights of the applied particle layers. The fluid velocity increases proportionally to the flow rate of the pump. Thereby, the results are independent from the roughness heights of the applied particle layer. The relation between the mean fluid velocity and the flow rate can be determined to $v_f = 0.0274 \cdot Q_p + 0.063$.

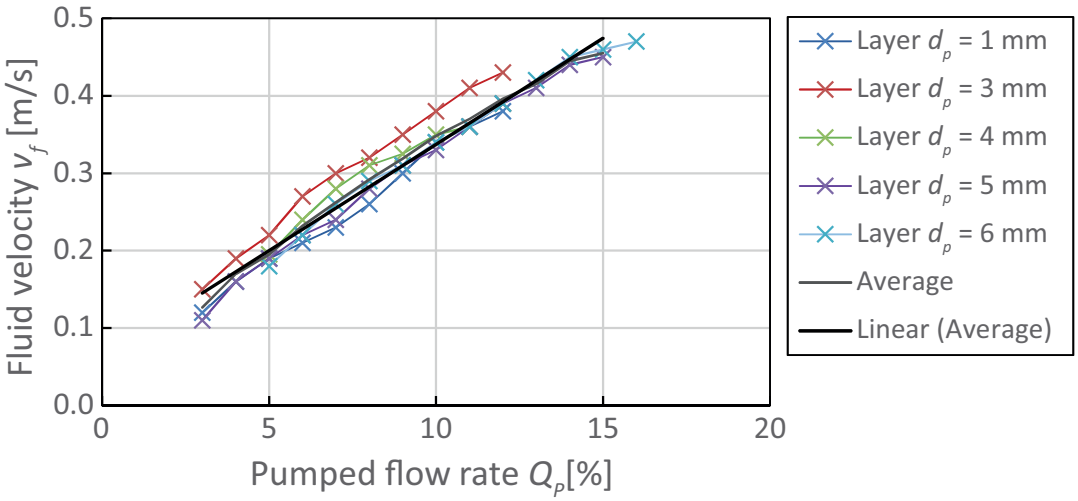

Figure 7.19: Increase of flow velocity with the pump rate for different panel roughness heights

The incipient motion threshold in the physical tests is clearly defined as the first rolling movement in which the particle leaves its initial position. To determine the driving forces at this moment, the external flow field above the rough particle boundary needs to be analysed. Therefore, the high-speed recordings of the reflecting tracer particles in the plane of the light sheet are analysed via the PIV analysis. 7.20a presents an image of a high-speed series for an particle diameter of $d_p = 4$ mm with an initial position of high resistance. The black and white image shows a high concentration of reflecting tracer particles as well as the reflections of the fixed particle layer and the free single particle on top. Here it becomes evident, why a coating of the fixed particles is required. Although, the particles are coated in mat black colour, the reflections are intense on the images. In a few cases, the coating of the particles detached at the end of a investigation series. As

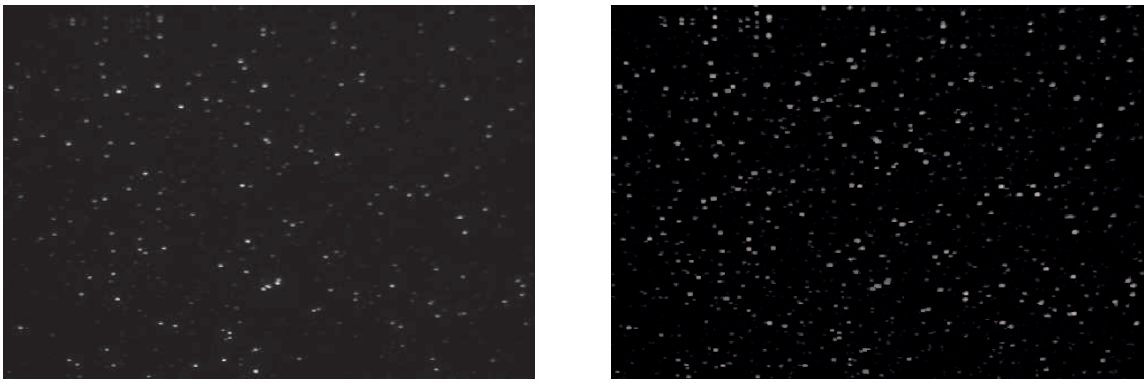

(a) Original high speed camera image (b) After image pre-processing

Figure 7.20: Cut-out of original image and result after pre-processing

a result, the uncoated particles lead to higher reflection of the light, which caused a spot of reflection above the particle layer within the image series. In the area of the reflection, the PIV algorithm lead to erroneous results. Thus, this blind spot needed to be excluded from the analysis.

Before the PIV algorithm was executed over a time series, the images were edited by a pre-processing via a CLAHE, highpass and Wiener2 denoise filter including intensity capping (see Section 6.2.1). As a result, the amount of visible seeding particles was increased significantly (see Figure 7.20). The higher number of seeding particles per interrogation area of the PIV algorithm increases the quality and reliability of the PIV results significantly. The PIV analysis was based on the FFT window deformation algorithm described in Section 6.2.1. Therefore, three passes with an interrogation area of 64 px, 32 px and 22 px size where analysed. Thereby the analysed plane area has a size of approximately 660 px hight and 800 px length.

The PIV analysis of the high-speed series gives a vector plot of the investigated plane orthogonal to the flow direction. This vectors need to be calibrated via a calibration image, which defines a certain distance within the observed image, and the duration in between images. The resulting vector plot gives detailed informations about the flow velocities above the rough particle layer and around the observed particle in a 2D plane. Thereby, the mixing processes within the boundary layer can be clearly observed. However, the chosen recording interval does not resolve the finer turbulences within the flow.

Figure 7.21 presents the boundary layer near the observed particle for the same test series as in Figure 7.20. Thereby, the vectors represent the direction and the magnitude of the flow velocities. The coloured area represents the velocity component $v_{f,x}$ in flow direction. 7.21a presents the external flow field for an very short duration of 1.25 ms. This situation is further denoted as instantaneous velocity field, since the time scale is still considerable small, even though the turbulent velocities are not fully resolved. The turbulent boundary layer field is clearly evident, with a high velocity gradient in z-direction near the fixed particle layer. In the vicinity of the fixed particles, the velocities are very small. However, especially in the gap in between two particles very small velocity values can be observed. This observation is congruent with the theory of fully rough boundary layer flow described

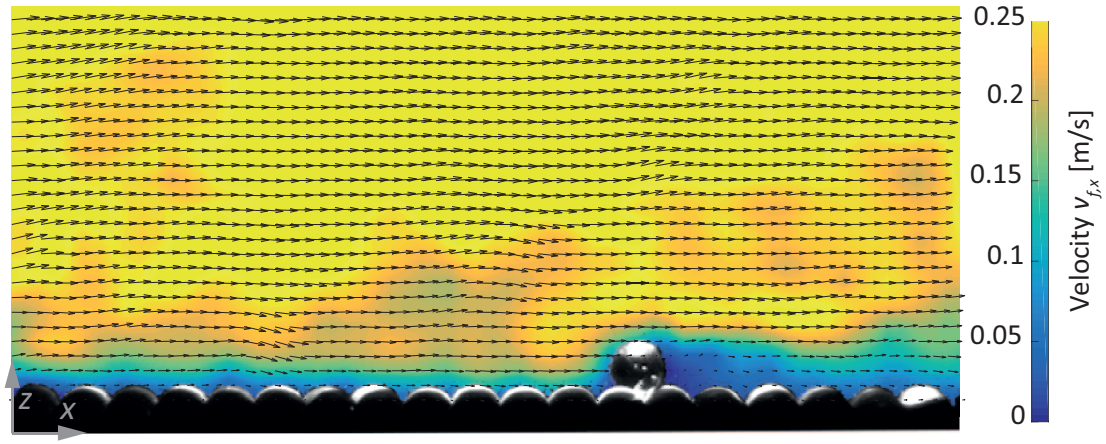

(a) Instantaneous external velocity field

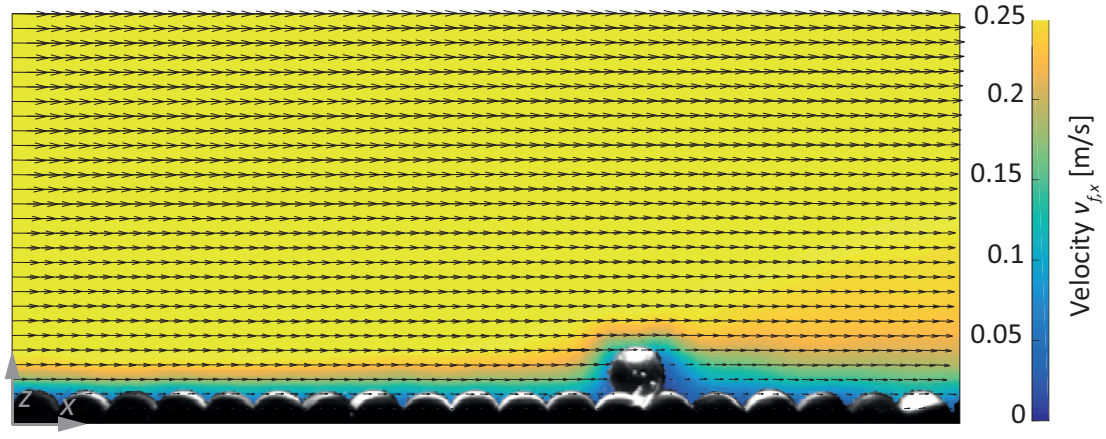

(b) Mean external velocity field determined over 300 images before incipient motion occured

Figure 7.21: External flow field around the particle at the boundary layer for $d_p = 4$ mm at high resistance

in Section 7.1.2, in which the roughness indicated vortices annihilate a viscous sublayer and the turbulence acts also in between the roughness elements. Thus, the roughness elements are fully exposed to the turbulent boundary flow region (see Figure 7.4). This observation is valid for the higher particle diameters from 3 mm to 5 mm. For the smaller diameters, the vector plot refinement is too coarse to refine this fine flow velocities. In the outer region of the turbulent boundary layer, turbulences of greater scale can be observed, which are moving with the flow. Further, the instantaneous flow situation around the free particle is illustrated in 7.21a. In the vicinity of the free particle, the flow velocities are reduced. This is minor due to the adhesion and friction at the particle surface as well as due to the blockage and the deviation of the flow around the particle. This observations illustrate the wall-induced symmetry breaking features of the flow, due to the presence of the rough particle layer. Although the refinement of the vector plot is not high enough to see the streamlines around the particle, this phenomena implement a certain flow behaviour and streamline pattern around the particle. 7.21a gives two areas of clearly reduced flow velocities around the particle. First, a very small area of reduced velocities forms at the lowest point of the particle on the luv-side. Second, a bigger area of reduced velocities is positioned on the lee side of the particles and along the downstream flow. Both areas imply a flow separation and recirculation of the flow around the particle. On the luv-side, the flow separates approximately at the half distance between the fixed particle layer and the crest of the free particle. The streamlines positioned over this point stay attached to the particle and proceed to the back side of the particle. Beneath this point, a recirculation area is formed which is equivalent to the area of reduced velocities described above. On the lee-side of the particle, the flow separates again near the particle crest. This separation develops a greater area of recirculation near the particle layer and into a wake. The asymmetry due to the presence of the fixed particle layer leads to a asymmetric wake structure. However, the refinement of the PIV vector plot does not allow a clearer impression on the wake structure or local vortex shedding. The occurrence of recirculation areas and a wake are more clear for the greater particle diameters of 3 mm to 5 mm. For lower particle diameters, the presence is less clear since the areas of reduced flow velocities are also of smaller size. The form of the areas of reduced flow velocities are similar for all the higher particle velocities. However, the comparison of the different initial embedding positions of the free particle imply, that the flow separation is of greater extent for the position with higher resistance. This observation is congruent to the general analysis of the motion threshold. To initiate movement of a particle positioned in the initial position of high resistance, the driving forces need to be greater than for a particle at the low resistance position. Thus, a flow field of greater flow velocities is required to exert sufficient driving forces to balance the holding forces resistance. As a result, independent from the particle diameter the tests with an initial embedding position of high resistance show greater velocities than those with low resistance.

7.21b illustrates the flow field of the mean flow velocities. Therefore, the mean of 300 images ($\approx$ 0.375 s) before the initiation of motion is determined. In comparison to 7.21a, the flow field is clearly more uniform, since the turbulent influences are cancelled out. Upstream of the free particle, the boundary layer is characterised by an evenly distributed high gradient near the fixed particle layer. The outer boundary layer as well es the free flow region are characterised by a very homogeneous velocity field. In the vicinity of

the free particle, the particle velocities are reduced. As in 7.21a, two smaller region of recirculation are noticeable near the fixed particle bed. Since the wake structure behind the particle is highly turbulent, the wake form in the mean flow field representation is of smaller size than in 7.21a. However, a wake behind the particle is also present for the mean representation.

The flow situation is further investigated by the mean flow profile of $v_{f,x}$ at the rough boundary. By this means, the observed flow situations at incipient motions shall be linked to the existing theory of incipient motion. Further, this gives the opportunity to compare the results with existing half-empirical motion threshold models. The velocity profiles are determined upstream of the free particle position to exclude possible influences due to its presence. Thereby, the distance between the particle and the x-position of the profile is at least four times the investigated particle diameter (for $d_p = 5$ mm) but significantly larger for the smaller particle diameters. The chosen x-position of the profile also depends on the quality of the PIV image analysis. Similar to the plot in 7.21b, the mean flow velocity of the horizontal flow component $v_{f,x}$ is determined from the 300 images ahead of the incipient movement. Therefore, the instantaneous flow profiles of a test are extracted and averaged to a mean flow velocity profile. The origin of the extracted profiles is for each case in the point of overlap of two neighbouring particles of the fixed particle layer. This provides a clear defines position as well as a constant ratio between the origin height z_0 and the particle diameter d_p. The resulting mean flow profiles for all tests are presented in Figure 7.22 and Figure 7.23. Besides the individual profiles, Figure 7.22 and Figure 7.23 include further an average profile of the whole test series (black line). Further, the position of the virtual origin displacement z_0 according to boundary layer flow theory is distinguished in the plots (dashed line). Therefore, fully rough flow field is assumed and z_0 is applied to $z_0 = k_s/30$ according to Equation 7.18. Additionally, the height of the free particle crest is illustrated in the individual figures (dashed dotted line).

By means of the determined velocity profiles, the free flow velocity is determined. Therefore, the upper 50% of the profile height are averaged. In the most tests, the flow velocity varies minor over this height. The mean free flow velocity for each test series as well as the corresponding standard deviation are presented in Table 7.2. More details to the individual test results are presented in Table C.1 and Table C.2.

Table 7.2: Mean free flow velocity $V_{f,x}$ for different particle diameters and initial embedding position

d_p	1 mm	2 mm		3 mm		4 mm		5 mm	
Init. pos.	-	low	high	low	high	low	high	low	high
$V_{f,x}$ Mean	0.2059	0.2024	0.2552	0.2331	0.3075	0.2970	0.3661	0.3391	0.3790
Std. dev.	0.0522	0.0179	0.0284	0.0222	0.0219	0.0111	0.0309	0.0195	0.0215

The profiles of the test show and increase of the flow velocity at incipient movement with increasing particle diameter. Further, it can be recognized that at constant particle

diameter the initial position with high resistance leads to higher velocities than for the position at low resistance. The diversity of the flow velocity for $d_p = 1$ mm is higher than for the other particle diameters. This is due to the missing of an distinction in a low and a high resistance initial position. In the physical tests, the 1 mm particles where so small, that the positioning at a certain initial position was not possible. Thus, the number of tests has been raised to 15, while a distinction was abandoned. However, the results imply, that the test results can be split in a fraction of greater velocities with a free flow velocity $V_{f,x} > 0.20$ m/s and a fraction of lower velocities below that threshold.

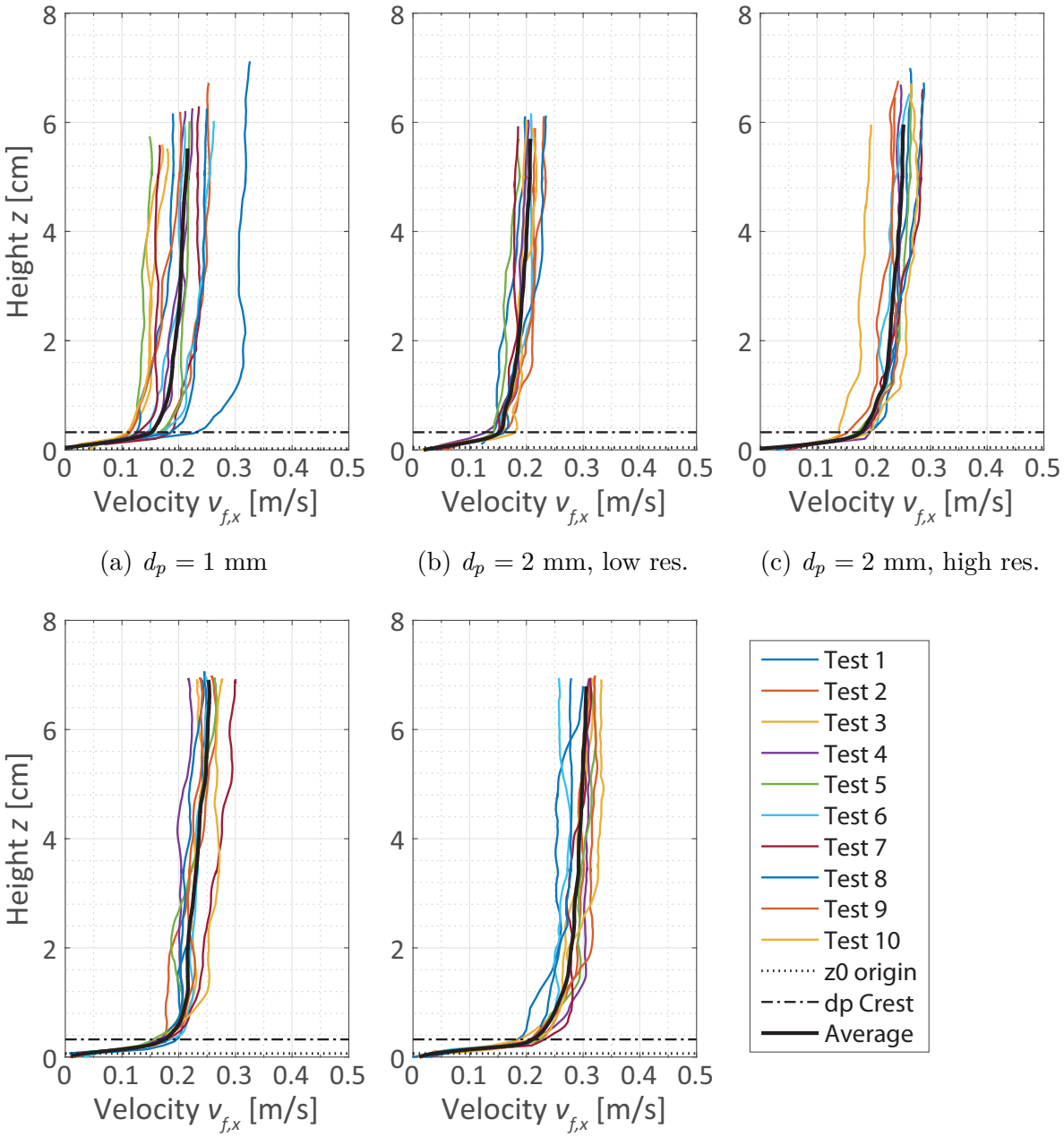

(a) $d_p = 1$ mm (b) $d_p = 2$ mm, low res. (c) $d_p = 2$ mm, high res.

(d) $d_p = 3$ mm, low res. (e) $d_p = 3$ mm, high res.

Figure 7.22: Resulting velocity profiles of the physical tests on incipient motion for the particle diameters $d_p = 1$ mm, $d_p = 2$ mm and $d_p = 3$ mm

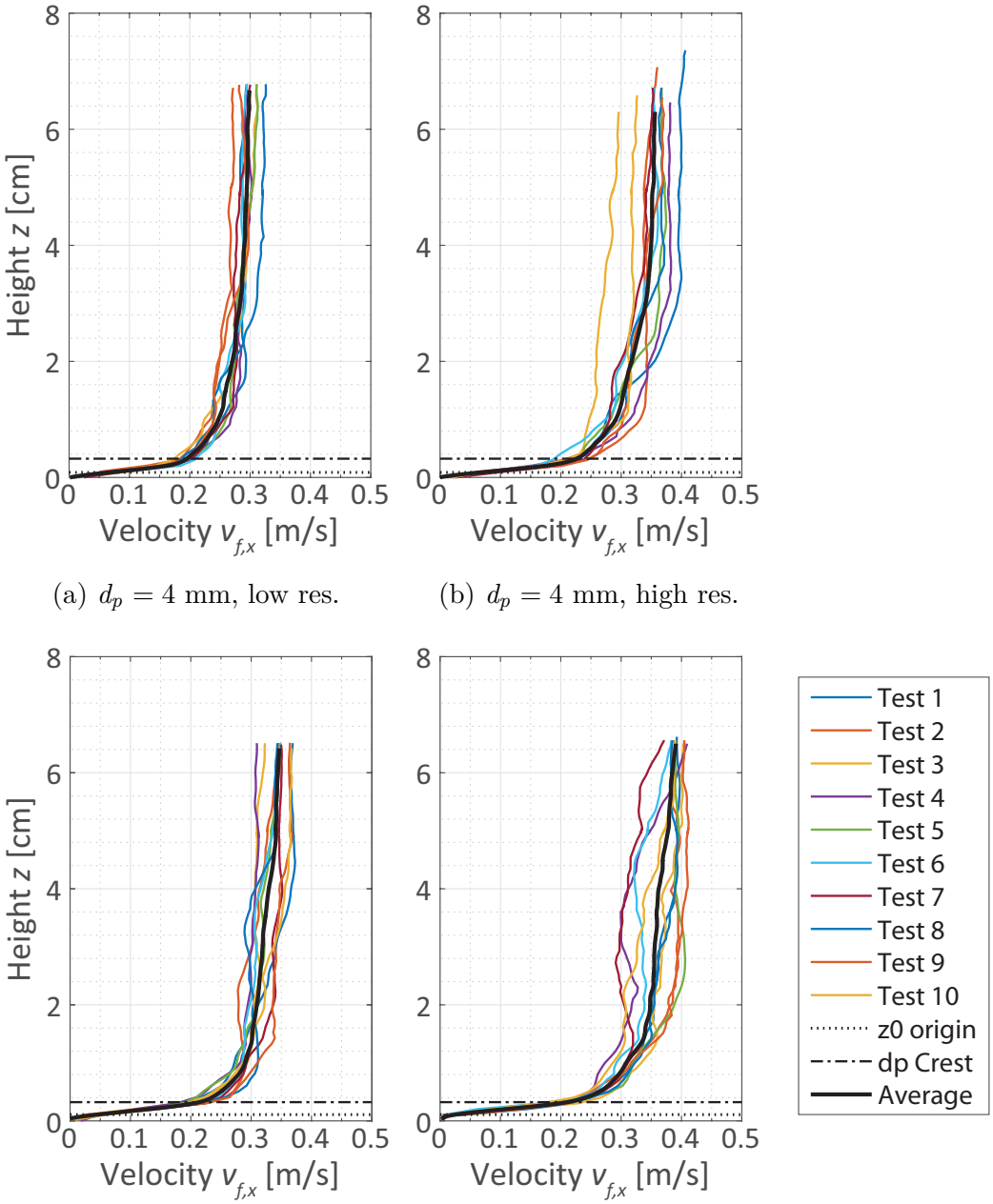

(a) $d_p = 4$ mm, low res. (b) $d_p = 4$ mm, high res.

(c) $d_p = 5$ mm, low res. (d) $d_p = 5$ mm, high res.

Figure 7.23: Resulting velocity profiles of the physical tests on incipient motion for the particle diameters $d_p = 4$ mm and $d_p = 5$ mm

7.3.3 Analysis of flow characteristics according to boundary layer flow theory

To analysis the flow situation at incipient motion further, it is required to know the characteristic numbers of the flow field. Those are amongst other the friction velocity v_f^*, the characteristic roughness number k_s^+ and the bed shear stress τ_0. However, the determination of bed shear stress τ_0 or the corresponding shear velocity v_f^* from experimental results is challenging, since the results are often not as explicit as necessary to obtain a conclusive interpretation of bed shear stress. However, in this thesis four different methods for bed shear stress estimation have been tested:

- Determination of τ_0 by velocity distribution
- Determination of τ_0 by averaged velocity
- Determination of τ_0 by Reynolds shear stress distribution

In the first method, a curve fit is applied on the mean velocity profile data to derive the friction velocity from the progression. In fully developed turbulent open channel flow, the whole velocity profile of the boundary layer flow including the inner and the outer wake layer can be described by Coles' (1956) log-wake law presented in Equation 7.10. This original equation can be adapted to the following form presented in Equation 7.38. By a numerical curve fit via the least-square-method the unknown constants K_1, K_2 and K_3 can be resolved (see Figure 7.24). By means of the constant K_2 the friction velocity v_f^* can be determined.

$$v_f = \frac{v_f^*}{\kappa} \ln\left(\tilde{z}\right) + \frac{v_f^*}{\kappa} \ln\left(\frac{H}{z_0}\right) + \frac{2\Pi}{\kappa} v_f^* \sin^2\left(\frac{\pi}{2}\tilde{z}\right) = K_1 \cdot \ln\left(\tilde{z}\right) + K_2 + K_3 \cdot \sin^2\left(\frac{\pi}{2}\tilde{z}\right) \quad (7.38)$$

The results of this method are very sensitive to measurement errors or inhomogeneities in the measured profile. Since, the mean is averaged over a small time difference, some measured profiles are not that steady than probably for a mean over o longer time duration. However, a greater time duration is not suitable for this purpose, since the flow velocity is slowly increased and the flow profile changes with time. Further, it turns out, that the results of the curve fit are very sensitive to the position of z_0. In the previous investigation, z_0 is assumed as $k_s/30$ for fully rough flow. This assumption is also applied for the curve fit. This means all measured values below this height are excluded from the curve fit. However, a small derivation from this assumption leads in parts to significant alterations of the results for v_f^*. As a result, the method was not considered as reliable.

In the second method, the bed shear stress is determined from the mean flow velocity by means of the dynamics pressure to

$$\tau_0 = \frac{\lambda_d}{8} \rho_f V_f^2 \quad . \quad (7.39)$$

Whereby, λ_d is the Darcy-Weissbach friction factor. To estimate λ_d the Colebrook and White (1937) equation is applied as given in Equation 7.40.

$$\frac{1}{\lambda_d^{0.5}} = -0.86 \ln\left(\frac{k_s P}{14.8A} + \frac{2.51}{\mathrm{Re}\lambda_d^{0.5}}\right) \quad (7.40)$$

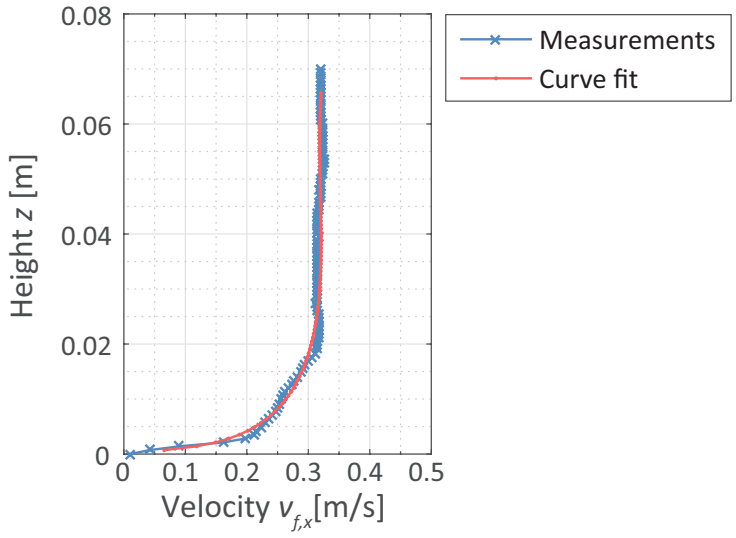

Figure 7.24: Mean velocity profile from measurements and curve fit for $d_p = 3$ mm at high resistance

Thereby, P represents the wetted perimeter and A represents the flow cross section. To take the composite roughness between the bottom and the sidewalls of the flume into account, Vanoni (1975) sidewall-correction can be applied further. More details on this approach can be found in Dey (2014). This method is recommended by Dey (2014) and leads to more consistent results than the previously described method.

The last method to determine the bed shear stress is based on the Reynolds shear stresses. Thus, τ_0 can be extracted from the measured profiles of the Reynolds shear stress distribution. Thereby, the shear stress can be determined to $\tau_{xz} = \rho_f \cdot \overline{v'_{f,x} v'_{f,z}}$. A measured shear stress plot determined from the Reynold shear stress distribution is presented in Figure 7.25. It can be observed, that the progression of the profile is not as distinct than in theory. In theory, the shear stress should increase constantly over the boundary layer. The bed shear stress can be obtained by this gradient. However, it might be problematic to determine the Reynold's stresses over such a short period of 300 images before particle motion is initiated. Further, the turbulences might be not fully resolved with the chosen frame resolution. Since there can be no clear gradient obtained from the plot, this method is excluded from further investigations.

The comparison of the previously presented results identified the second method of averaged velocities as the most reliable solution to determine the bed shear stress. The results of bed shear stress τ_0 are applied to compute the characteristic numbers of friction velocity v_f^*, the characteristic roughness number k_s^+ and the virtual origin z_0. The results of the bed shear stress analysis as well as the characteristic numbers of the rough flow are presented as mean values for each particle diameter and initial position in Table 7.3. The detailed results of the bed shear stress analysis for every individual test are presented in Table C.3 and Table C.4. To determine the test mean values, single outliers are excluded.

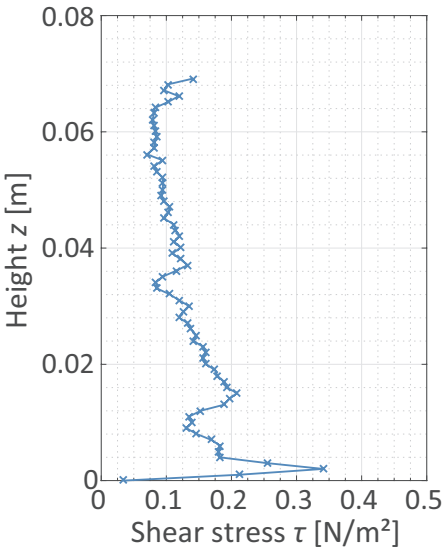

Figure 7.25: Shear stress profile approximated for $d_p = 3$ mm at high resistance

Table 7.3: Characteristic numbers of flow field at incipient motion

d_p	1 mm	2 mm		3 mm		4 mm		5 mm	
Init. pos.	-	low	high	low	high	low	high	low	high
v_f^* [-]	0.0103	0.0131	0.0157	0.0167	0.0203	0.0208	0.0222	0.0242	0.0265
τ_0 [Pa]	0.1054	0.1659	0.2350	0.2745	0.3444	0.4321	0.4844	0.5849	0.7079
k_s^+ [-]	10.3	26.2	31.4	50.1	60.9	83.1	88.7	120.9	132.6
z_0 [mm]	0.044	0.075	0.074	0.107	0.105	0.133	0.133	0.167	0.167

The virtual origin is estimated by the fit of Colebrook et al. (1937) in Equation 7.18. The presented values in Table 7.3 show, that the assumption of fully rough flow for all tests does not hold true for the particle diameters $d_p = 1 - 3$ mm. According to the theory of Nikuradse (1933), the fully rough regime requires dimensionless roughness numbers greater than $k_s^+ > 70$. These limit is not reached for the smaller particle diameters. Instead, the flow situation corresponds to the transitional flow regime with $5 < k_s^+ < 70$. In this transitional flow regime a viscous sublayer might be present, which is in the height of the particle diameter. As a result, the viscous effects need to be considered in the estimation of the virtual origin z_0. This leads to slightly higher values for the virtual origin in comparison to the estimate at rough conditions at $d_p = 1$ mm ($z_{0,\text{rough}} = 0.033$ mm) and $d_p = 2$ mm ($z_{0,\text{rough}} = 0.067$ mm). Since, the viscous effects are decreasing with increasing v_f^* and thus k_s^+, the differences in the resulting z_0 are marginal for the particle diameter $d_p = 3$ mm ($z_{0,\text{rough}} = 0.010$ mm).

7.3.4 Analysis of motion threshold in physical tests

In this section, the motion threshold in the physical tests is evaluated. Therefore, the incipient movement of the particles is analysed and common approaches of empirical sediment transport modelling are applied for comparison purpose (see Section 7.2.2). Contrary to the conducted tests of the common half-empirical models, in this physical test the boundaries for the incipient motion is clearly defined. Thus, the bed roughness is homogeneous in size and arrangement, the initial position of the observed loose particle as well as its geometrical resistance is known and the incipient movement is clearly defined to the first displacement from its initial position.

As defined in Section 7.2.1, the incipient motion scenario of rolling is characterised by lower shear stresses, than the other bed load transport processes sliding and saltation. Thus, rolling is also in the physical tests the incipient motion scenario. However, the characterisation of the incipient movement need to be distinguished for the initial positions. Thus, the displacement after the incipient motion is differently significant depending on the initial position. While for the initial positon at low resistance the first displacement takes place mostly over just a few particles, the displacement for the initial motion at high resistance is significantly larger. In many cases of the low resistance initial position, the particle rolls over the gap in between the two particles in its lee and becomes static again at a high resistance position. In contrast, the displacement at a high resistance initial position is so great, that the particle leaves the recorded section. This behaviour corresponds to the expectation of a low and a high resistance position in a bed. The lower resistance can be overcome at lower bed shear stresses and, thus, at lower velocity states. However, the particle moves just as far as it reaches a position of higher resistance, which cannot been overcome at this velocity stage. In contrast, if the high resistance is overcome, there is no position of higher resistance in the homogeneous arranged bed and the particle moves outside the investigation area before it gets to rest again in a greater gap of the more chaotic arranged area outside the investigation area. This means that for both initial positions erosion occurs for the loose particle, but just the velocity characteristics at the high resistance tests result also in particle transport.

The bed shear stresses determined in Section 7.3.3 are applied to define the critical threshold of motion. Therefore, the critical Shield's parameter θ^* (see Equation 7.31) and the dimensionless diameter D^* (see Equation 7.33) for each tests series are calculated. The resulting values are than included in the modified Shield's diagram (see Figure 7.11). For the Figure 7.26 presents the mean critical shield parameters and the corresponding standard deviation as a bound for the low and the high resistance flow situations. The modified Shield's diagram including the individual results of each tests is presented in Figure C.1. For the representation of the mean critical values in Figure 7.26, the results for the tests with $d_p = 1$ mm have been distinguished into lower and higher values. The analyses of the results identified the border between higher and lower values to approximately $\tau_0 = 0.1$ Pa, which is similar to the mean values. All higher values have been related to the initial position with higher resistance, while the lower ones are associated with the low resistance position.

The bound of the lower resistance threshold is having a similar trend than the original curve, while the bound of higher resistance is just slightly increasing with greater particle

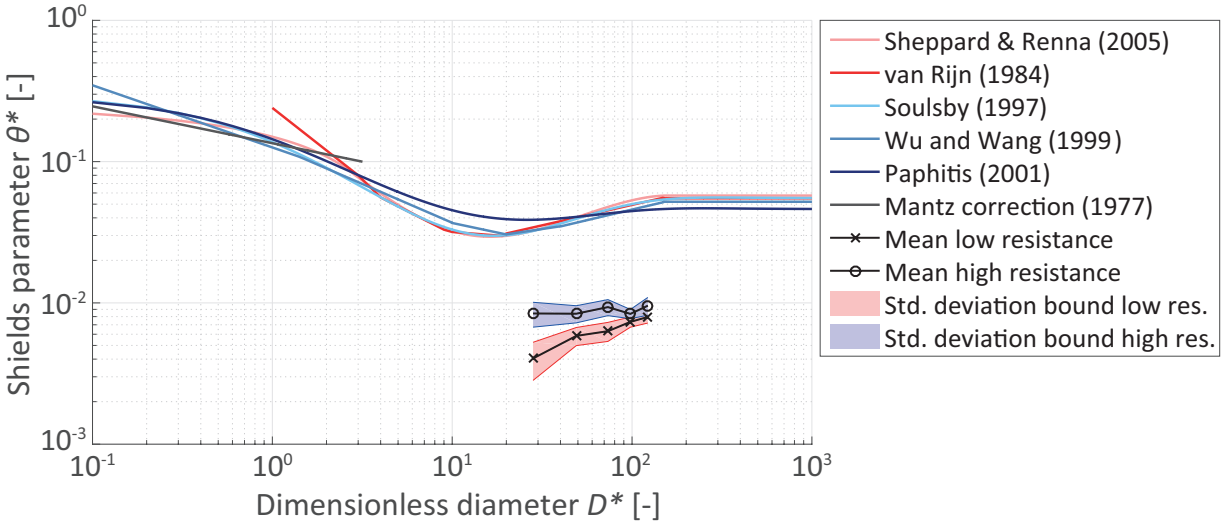

Figure 7.26: Modified Shield's diagram with the mean values and the standard deviation bound of the test results

diameters. However, this impression might also be affected by the chosen border for the critical values of $d_p = 1$ mm. As previously described, the critical values are higher for the initial position at high resistance than for low resistance. However, both bands are positioned significantly lower than the original curves. In comparison to the solution of Soulsby (1997), the tests results for the initial position at high resistance are ≈ 5 times smaller and for the initial position at low resistance even ≈ 7 times smaller than the original curve (see Table 7.4). The clearly lower threshold of incipient motion in the physical tests is based on several factors. First, a smaller torque is required to initiate the particle movement for the particle shape of perfect spheres than for irregular shaped natural grains. Second, the identification of incipient motion in the physical tests of Shields (1936) is not sure known as described in Section 7.2.2. According to García (2008) and other authors, the Shield's diagram overestimated the critical threshold especially for coarser material. Thus, motion occurs already at lower critical values as observed in the physical tests. Further, the conducted test of incipient motion are just on the edge of transport as described previously for the initial position at high resistance. Thus, the defined threshold in the physical tests is probably for lower critical values than those defined in the Shield's diagram.

7.4 Numerical Simulations on Incipient Motion

Originally, the numerical simulations should contain the process of incipient motion at a rough surface as well as the erosion processes at a rough permeable particle layer. The first case corresponds to the conducted physical tests and provides the possibility for calibration and validation. The validated model should than be assigned on the phenomenon of erosion at a thicker particle layer to investigate the processes and interaction in between

Table 7.4: Comparison of critical Shield's number according to Soulsby (1997) and the results fo the physical tests

d_p	D^*	θ^* Soulsby	θ^* low res.	θ^* high res.	ratio low res.	ratio high res.
[mm]	[-]	[-]	[-]	[-]	[-]	[-]
1	24.5	0.0312	0.0040	0.0083	7.8	3.7
2	49.0	0.0394	0.0058	0.0084	6.8	4.7
3	73.5	0.0457	0.0063	0.0093	7.3	4.9
4	98.0	0.0498	0.0073	0.0084	6.8	5.9
5	122.5	0.0523	0.0080	0.0096	6.5	5.5
				Mean	7.0	4.9
				Std. Dev.	0.5	0.8

the external flow field, the internal flow field and the granular particles. However, the numerical simulation of the incipient motion along a rough particle bed already evolved rather complex. Several restrictions, regarding the unresolved coupling procedure and the limitation of the available solvers and models lead to problems in the correct representation of a steady boundary layer flow. This restrictions and the resolving problems, where so significant, that a validation of the numerical model with the physical tests could not be conducted. Following, the varying setup of the numerical model are presented and the resulting limitations regarding the aspired objective is discussed. To differentiate between the problems evolving from the coupling restriction, the numerical simulation with the CFD-DEM method is confronted with a pure CFD simulation. Further, an invalidated model of the erosion along a particle bed is presented. In a last discussion, opportunities are presented to enable a validation and improved simulation of incipient motion processes.

7.4.1 Flow over a rough surface with a CFD approach

For the simulation of a steady flow over a fixated surface, a simulation domain of a narrow channel is applied. Thereby, the channel has a length of 0.40 m, a height of 0.06 m and a depth of 0.012 m (see Figure 7.27). The small depth of the channel is chosen to reduce computational costs. The flow is going to take place into the x directions. Thus, the flow characteristics are dominated by this direction and a symmetry can be assumed for the y-normal walls. The symmetric boundary condition defines the values of the different parameter fields for the cell face at the wall depending on the values in the cell centre. In the case of a scalar field, the value from the cell centre is adopted directly on the wall face. For vector fields, the all parallel components are mirrored, while the normal component is set to zero. The upper lid of the channel is defined as a slip wall. Thus, there is no in- or outflow via this boundary, while the flow velocity can develop without a no-slip condition at the wall. The lower bottom of the channel is treated as a no-slip wall. Thus, the velocity vector is set to zero directly at the wall surface. Further, boundary conditions

for the other simulation fields at the lower wall depend on the chosen turbulence model and are going to be discussed later. Beforehand, the initiation of the flow in the channel is presented.

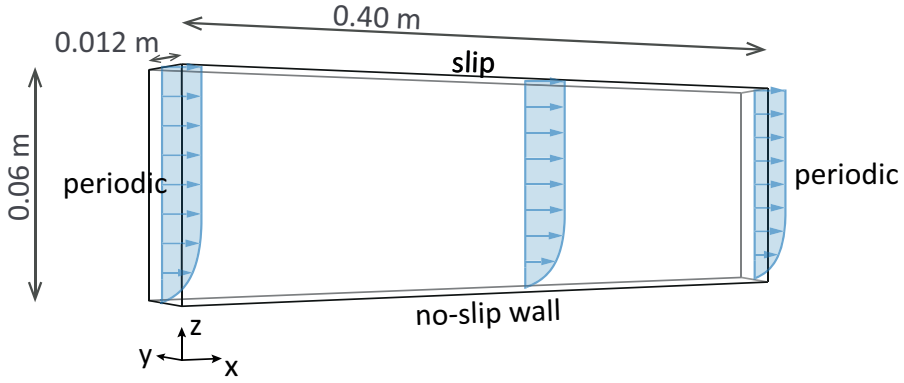

Figure 7.27: Scheme of the CFD simulation domain with the boundary criteria

The free toolbox OpenFOAM offers several solvers and utilities for CFD problems. For the recreation of boundary layer flow a transient flow solver is chosen, which is based on the PIMPLE algorithm, a combination of the SIMPLE (Semi-Implicit Method for Pressure-Linked Equations) and PISO (Pressure Implicit with Splitting of Operator) algorithm, to solve the partial differential equation system. This algorithm has improved convergence and is more robust to the other methods due to the introduction of under-relaxation factors (Venier et al., 2013). More details on this approach is given in Passalacqua et al. (2011). To induce flow inside a simulation domain, two major options are provided: the velocity-driven flow and the pressure-driven flow. In the case of the velocity-driven flow, the velocity field is defined at the inlet or outlet, while the dynamic pressure field is defined to a fixed value at the opposed boundary patch. For the pressure-driven flow, a pressure gradient is defined in between the inlet and the outlet, while the velocity is able to develop at those patches. However, in the case of turbulent flow, the turbulent mixing dissipates energy and the momentum decreases over the flow distance without a momentum source. To generate a turbulent but steady flow at a boundary, it is necessary to implement a momentum source to balance these dissipation. OpenFOAM provides a utility to overcome this problem. Thereby, the flow is not initiated via external boundary conditions, but via a momentum source. The momentum source is initiated by the definition of a mean velocity $\bar{V}_f$, which can be defined over a certain region or along a boundary patch. Based on this mean velocity, the momentum source is adjusted at every timestep such as the values is reached for the volume average velocity v_f at the defined region-patch. For more details see source code or Nozaki (2016). In this simulations, the mean velocity is defined at the top z-normal boundary patch. The given values are based on the measured average velocity in this height of the physical tests for the incipient motion at different initial positions (see Table 7.5). Since, the flow is induced by a momentum source, the boundary conditions at the x-normal inlet and outlet are defined for all fields as periodic conditions (see Figure 7.27).

The simulation of flow along a fixed surface with a pure CFD approach needs to recreate

Table 7.5: Mean velocities $\bar{V}_f$ for the momentum source, defined at the top z-normal boundary patch

	$d_p = 2$ mm		$d_p = 4$ mm	
	low res.	high res.	low res.	high res.
$\bar{V}_f$ [m/s]	0.2071	0.2523	0.2984	0.3562

the transition between the no-slip condition at the surface, the boundary layer and the fully developed flow in the free flow region. For turbulent boundary-layer-flow at $\mathrm{Re} > 1$, the viscous effects and the additional Reynolds shear stresses due to turbulent mixing need to be taken into account. Thereby, the dominance of the one or another depends amongst others on the Reynolds number, the roughness of the boundary surface and the distance from the surface (see Section 7.1). However, the turbulent effects dominate in the most areas of turbulent boundary layer flow. In Section 4.2.6 some possibilities to model turbulent effects are presented. All this possibilities can also be applied on the simulation of boundary layer flow. However, as discussed inSection 4.2.6 the turbulence modelling with DNS and LES require an extreme fine meshing and are computational very expensive. Thus, the turbulence modelling with RANS is chosen for the simulation of rough boundary layer flow. Three different turbulence models are applied in this simulations. Two high-Re models based on the k-ϵ model and the k-ω-SST model as well as a low-Re approach with the k-ω-SST model. For the low-Re turbulence models, the wall near velocities are induced by wall functions. For each turbulence parameter, a wall function is provided at the bottom boundary patch. The roughness k_s of the no-slip wall is implemented in the wall function of the turbulence viscosity ν_t and defined to $k_s = d_p$ (see Table 7.6). The implementation of wall functions is bound to a certain discretisation resolution orthogonal to the wall. Wall functions are not resolving the viscous boundary layer, but approximate the wall near flow by means of the logarithmic overlap layer (see Figure 7.1). Thus, the first node (here the cell centre) needs to be positioned in this logarithmic wall layer at $30 < z^+ < 100$. Depending on the free stream velocity and a characteristic boundary layer length, the corresponding z height to the z^+ value can be approximated.

Besides the high-Re approach of the k-ω-SST model, also the low-Re approach is applied in the simulations. Thus, the effect of the wall-near turbulences is not modelled by wall-functions but by the damping functions implemented in the turbulence model. In the k-ω-SST model, the wall-near damping is based on the k-ω approach, while the wall-far turbulence effects are estimated with the k-ϵ model. Such as in the high-Re approach, the correct modelling of turbulence parameters is based on an appropriate discretisation in the wall near area. However, it is necessary to resolve the viscous boundary layer. Thus, the first cell centre needs to be positioned at approximately $z^+ \approx 1$. The cell z height can increase with distance to the wall, but a growth factor of 1.2 should not be exceeded. The boundary conditions for the turbulence parameters are now based on turbulence theory. The turbulence parameters k and ν_t approach zero at the wall surface, while ω tends against infinity. Since, a parameter definition to zero might cause numerical problems, a value of 10^{-8} is applied. For the ω value, a low-Re wall function need to be defined in

Table 7.6: Boundary conditions (BC) at the bottom patch and initial conditions (IC) in the simulation domain for the k-ϵ model and the k-ω-SST model

		$d_p = 2$ mm		$d_p = 4$ mm	
		low res.	high res.	low res.	high res.
k [$m^2\,s^{-2}$]	BC	wall-function/10^{-8}		wall-function/10^{-8}	
	IC	1.65×10^{-4}	2.34×10^{-4}	3.38×10^{-4}	4.86×10^{-4}
ϵ [$m^2\,s^{-3}$]	BC	wall-function/-		wall-function/-	
	IC	1.59×10^{-5}	2.69×10^{-5}	4.65×10^{-5}	8.04×10^{-5}
ω [s^{-2}]	BC	wall-function		wall-function	
	IC	1.07	1.28	1.53	1.84
ν_t [$m^2\,s^{-1}$]	BC	wall-function/10^{-8}		wall-function/10^{-8}	
	IC	1.54×10^{-4}	1.84×10^{-4}	2.2×10^{-4}	2.65×10^{-4}

OpenFOAM.

Besides the boundary conditions at the no-slip wall, the turbulence parameters need also be defined for the simulation initial conditions. The implementation of realistic values is essential to create a stable simulation. The initial turbulence values can be approximated by the following equations in Equation 7.41.

$$k = \frac{3}{2}(I_t\, V_f)^2 \quad ; \quad \epsilon = 0.09\frac{k^{3/2}}{l_t} \quad ; \quad \omega = \frac{k^{0.5}}{l_t} \quad ; \quad \nu_t = \frac{k}{\omega} \tag{7.41}$$

Thereby, I_t represents a turbulence intensity and l_t a characteristic turbulent length scale. The turbulence intensity can be approximated to 5% for a medium turbulent situation. The turbulent length scale is defined to the channel depth of 0.012 m. The resulting initial conditions are presented in Table 7.6.

The resulting average velocity field in the simulations is presented by a y-normal cross section of the channel in Figure 7.28 for different turbulence models. The flow situation corresponds to the average velocity profile for $d_p = 2$ mm with the initial position at high resistance. To get an idea for the required meshing, the mesh with the required $y^+ > 30$ is presented for the high-Re approaches. The meshing of the low-Re approach is too fine to present in the cross section. For the simulation with high resistance flow situation, the cell height is 4 mm in the high-Re approaches and 0.45 mm for the low-Re approach for the situation at $d_p = 2$ mm, while the flow situation for $d_p = 4$ mm requires a cell height of 2.5 mm at the high-Re approach and 0.27 mm at the low-Re approach to reach the obliged resolution criteria. In all simulations a steady flow over the rough boundary is reached. The velocity distribution over the channel height is characterised by the mean-velocity boundary condition at the topmost patch and the boundary conditions at the bottom patch. The resulting velocity field is very similar for the high-Re turbulence models. The velocity is significantly reduced in the lowermost cell-row. At this row the velocity gradient is the greatest. In the overlying cell-rows, the velocity increases slightly before it reaches the applied mean velocity of 0.2523 at the topmost boundary patch. However, the gradient in z direction is smaller for the velocity field compared to the lowermost cell-row.

The low-Re approach shows a clearly reduced area of the low velocity values. Further, the transition from a high to a lower gradient in z-direction is smoother compared to the high-Re model simulations.

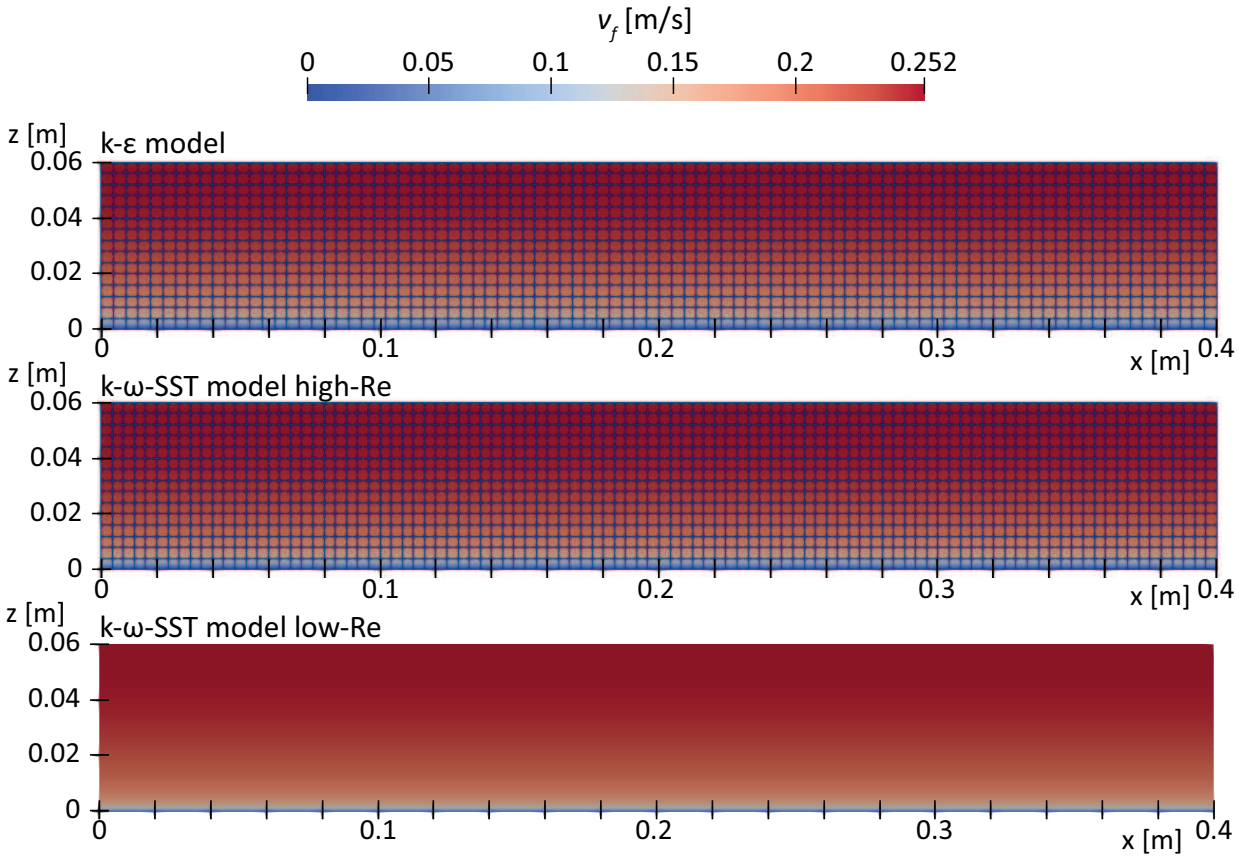

Figure 7.28: Cross section in y-normal direction of the simulation channel for the average velocity field v_f for the flow situation $d_p = 2$ mm at high resistance

The result of the CFD simulations is presented in Figure 7.29 by means of the x-component distribution of the velocity field over the channel height z. Therefore, the flow situations at a particle diameter $d_p = 2$ mm and $d_p = 4$ mm for the high and the low resistance initial position are applied. For each flow situation, the velocity profiles for all variations with different turbulence models are presented. Besides the simulation data, the data in form of the averaged flow profile from the physical tests are included further for validation purposes. To compare the simulation profiles with the results of the physical tests, the origin of the simulation profiles are placed on the height of the in Section 7.3.2 previously discussed z_0 position.

In all simulations the upper part of the velocity profile is in very good accordance with the results of the physical tests. For the flow situation based on the incipient motion of $d_p = 2$ mm, the lower section below $z \approx 2$ cm shows clear deviations from the test profile. In case of $d_p = 4$ mm, the deviation occur till a hight of approximately $z \approx 3.5$ cm, with is based on the overall higher velocities. The results of the high-Re approaches of

the k-ϵ and the k-ω-SST model are very similar for all flow situations. Thereby, the k-ω-SST model results in slightly higher velocities near the no-slip surface. In comparison to the averaged velocities of the physical tests, the high gradient next to the surface is not as good reproduced as in the low-Re simulation. In this area, the simulations give a almost linear increase of the velocity, whereby the increase is less in comparison to the physical tests. As a result, also the rest of the boundary layer velocities are slightly lower in comparison to the physical tests. The lowermost data-point in the simulations is based on the lowermost cell-height, which is based on the requirements for the wall function formulation. Since, the velocities for the flow situation at $d_p = 2$ mm are slower than for the $d_p = 4$ mm situation, the lowermost data-point is significant higher. Thus, the high-Re simulations of $d_p = 2$ mm seems to result in a velocity profile, which seems to have an kink at the position of the lowermost data point. This kink is not apparent in the simulation for $d_p = 4$ mm. However, also here is the surface near velocity gradient is underestimated. In contrast to the high-Re simulations, the low-Re model gives clearly better results. In all simulations, the model reproduces the high velocity gradient near to the surface and shows minor deviations, even for the flow situations at higher velocities with $d_p = 4$ mm. In the most simulations, the low-Re velocity profile results in slightly lower velocities than in the physical tests. An exception is the simulations for the low resistance flow situation at $d_p = 4$ mm, where the surface-near velocities are over predicted.

All results of the pure CFD-simulations are in good accordance to the physical tests. Especially, the low-Re model reproduces the surface near profile highly accurate. The results of the high-Re models underestimate the surface-near velocities and, thus, the velocity gradient. This is critical with respect to the simulations of incipient motion, since the greatest deviations are in the height of the free particle, if the position of the profile origin is approximated to the z_0 position (see position of particle crest in Figure 7.29). However, the functionality of the high-Re models near the no-slip surface is based on the performance of the defined wall function. In the simulations, the roughness parameter k_s for the ν_t wall function is chosen as $k_s = d_p$. It might be possible, to reach higher accuracies with variation of this roughness height. Further, the velocity profile in all simulations is based on the topmost value of the physical test at $z = 6$ cm for comparison purpose. Since the the wall-near velocities are of greater importance than the accuracy in the free flow, the momentum source for the flow initiation can be adopted to achieve a higher accordance near the wall. Nevertheless, the required great cell heights for the low-Re turbulence models might be a problem in the accuracy of the reproduction of the incipient motion. However, for the reproduction of the wall-near velocities, the low-Re k-ω-SST gives directly better results.

7.4.2 Flow over a rough surface with the coupled CFD-DEM approach

To model to flow over a fixed particle layer, the gained knowledge of the previous Section 7.4.1 shall be applied and adapted on the CFD-DEM approach. However, the number of utilities and solvers is clearly limited in the coupled CFD-DEM software CFDEMcoupling. Thus, there is no PIMPLE based solver available for the simulation of transient

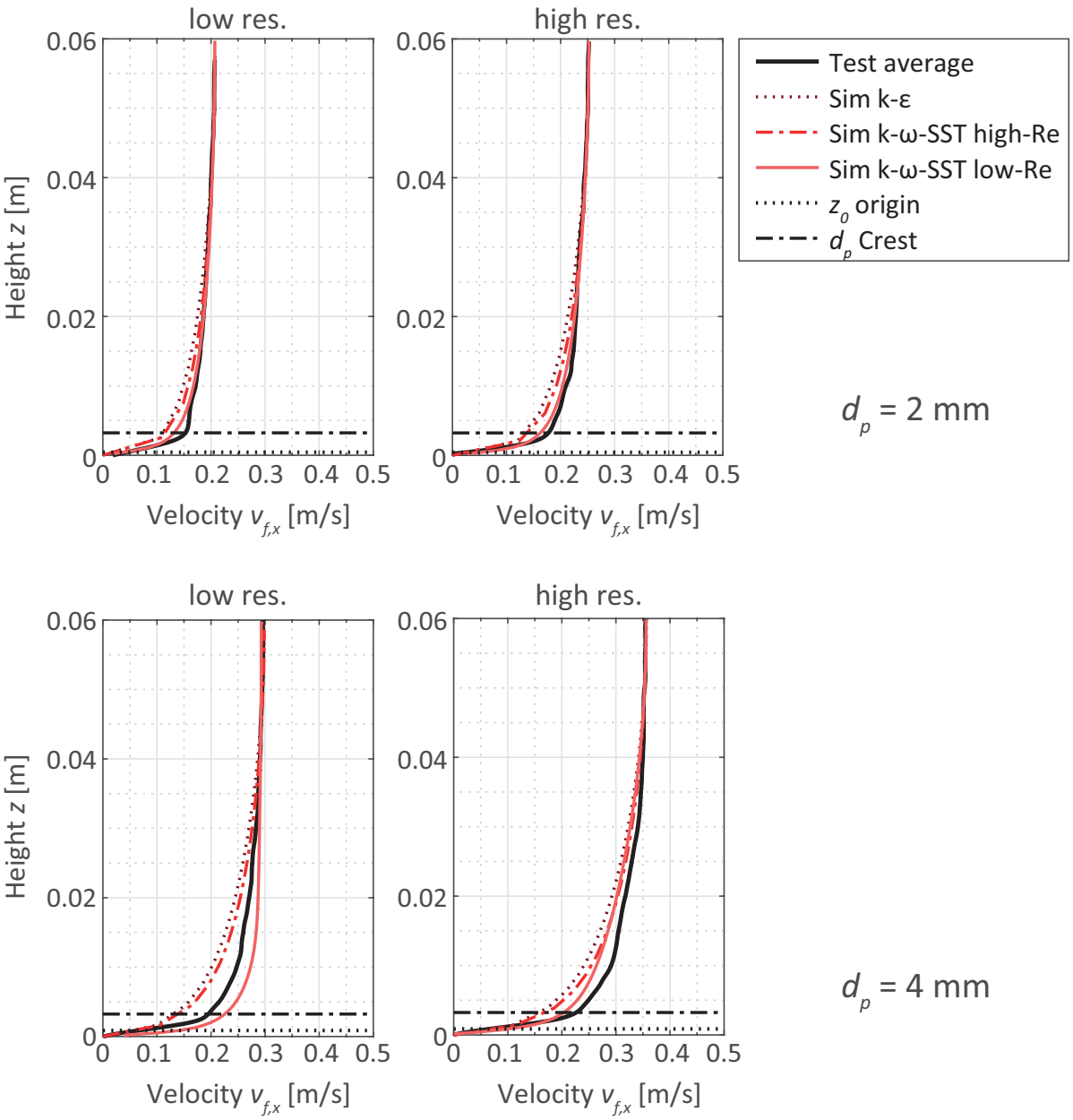

Figure 7.29: Velocity profiles of the CFD simulations with different turbulence models in comparison with the physical tests on incipient motion for the particle diameters $d_p = 2$ mm and $d_p = 4$ mm

flow, but rather a PISO based solver. Those is less stable than a PIMPLE algorithm and requires smaller timestep widths and lower Courant values to achieve a numerically stable simulation. This is caused by the limitation to one outer iterations of the PISO algorithm. While the PIMPLE algorithm provides the opportunity to increase the number of iterations till time step convergence is reached, this is not provided by the PISO algorithm. However, since simulation time is extremely costly in CFD-DEM simulations,

a solver which is optimised for long-time simulations as the PIMPLE based solver, makes less sense in that case than for other applications. Further, the utility to induce flow by a momentum source is not available for the standard CFDEM PISO based solver. Thus, the flow need to be induced velocity-driven or pressure-driven as described in the previous Section 7.4.1. This methods have some drawbacks compared to the method applied in the pure CFD simulations. First, the required definitions at the inlet and outlet prevent the application of periodic conditions. Thus, the boundary layer flow needs to develop from the inlet onwards. Second, the application of turbulence models results in dissipation and a loss of momentum due to turbulent mixing. Since there is no external momentum source, the turbulent dissipation is no longer compensated. As a result, the flow situation of the rough boundary can not converge to a steady state over the whole simulation domain, but rather changes over the flow distance. The problem and its influence on the simulation setup is discussed further after the presentation of the general simulation setup and the chosen boundary conditions.

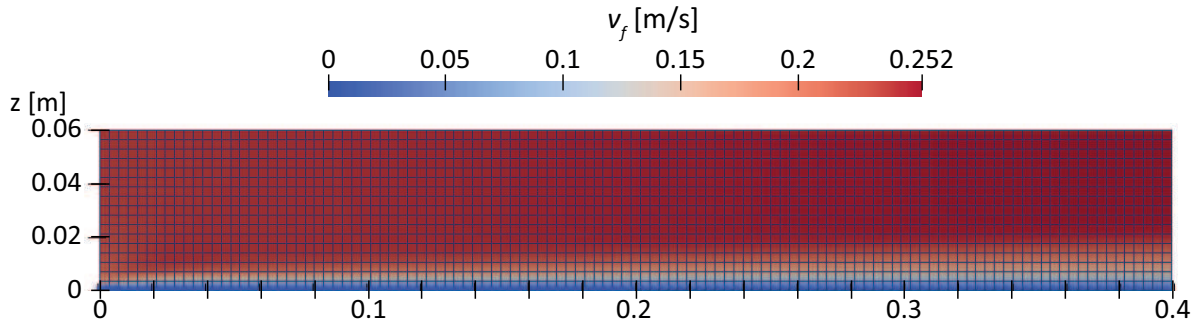

Figure 7.30: Cross section in y-normal direction of the simulation channel for the average velocity field v_f for the simulation with turbulence modelling by the k-ω-SST model for the flow situation with $d_p = 2$ mm at high resistance

The simulation domain of a narrow channel is adopted from the previous CFD simulations. However, as described in Section 6.5.1 two simulation domains for the CFD and the DEM simulation part need to be distinguished. On side of the CFD domain, the symmetry condition of the y-normal boundary patches as well as the slip-wall condition at the topmost z-normal boundary patch from the previous simulations is also assumed for the coupled simulations. To initiate the flow, a pressure-driven initiation is applied. Therefore, the boundaries for the pressure are applied at the inlet and the outlet patches of the channel (see Figure 7.31). In the OpenFOAM simulations, the absolute pressure value does not necessarily need to have a specific meaning, since only the pressure gradient is of importance to the governing equation system (see Equation 4.10). Therefore, it is necessary to define a static reference value for the pressure, whereby the chosen value itself is not of importance. In this simulations the reference pressure is defined at the outlet to an value of 0. The initiation of a flow due to a pressure difference is managed via a specific boundary condition at the inlet. Therefore, a total pressure value p_0 is defined. During the simulation the boundary condition reduces the initial p_0 value defined as total pressure with every timestep depending on the flux which is coming in via the patch. Thus, the

pressure at the inlet is equivalent to the total pressure value minus the dynamic pressure $p = p_0 - 0.5 \cdot |\mathbf{v}_f^2|$. Be aware, that the pressure in OpenFOAM is defined density independent for incompressible flows. With increasing velocity in the channel, the pressure value at the inlet decreases and, thus, the pressure gradient between inlet at outlet. At fully established flow, the velocity field reaches equilibrium. A pressure gradient, implemented by two static values at the inlet and the outlet, would lead to a infinite acceleration of the flow. The velocity field at the inlet patch is defined by a boundary condition, which provides the velocity field based on the pressure field. The bottom of the channel is assumed as a no-slip wall, where the velocity field becomes zero.

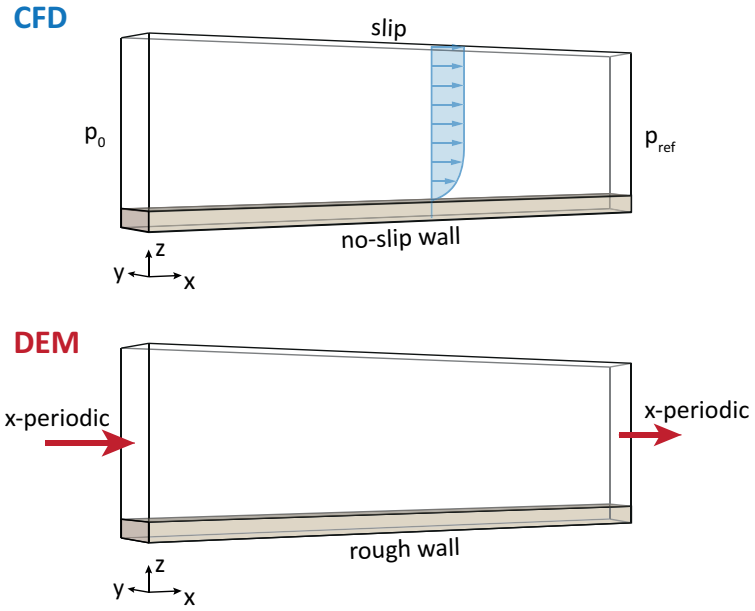

Figure 7.31: Scheme of setup with boundary conditions

The boundary conditions of the DEM domain are rather simple (see Figure 7.31). In x as well as in y-direction, the boundaries are assumed as periodic. The bottom of the simulation domain is defined to a rigid wall, which has the same properties as the DEM particles. Further, a layer of particles is initiated into the DEM domain. The particle layer consists of particles arranged in a hexagonal packing with one layer. During the simulations, the particles are fixed due to an exclusion from the DEM algorithm. However, their presence is considered in the coupled simulation.

As described earlier, the application of turbulence modelling is critical in the coupled CFD-DEM case, since the turbulent dissipation cannot be compensated by an external momentum source as presented in Section 7.4.1. However, also with the possibility to apply an external momentum source, the turbulence modelling would become critical regarding the boundary layer representation. Turbulence models with a high-Re approach require wall functions to model the near-wall velocity field, while the low-Re approach requires a very fine meshing to resolve the viscous boundary layer section. Both approaches deal with problems in the coupled simulations.

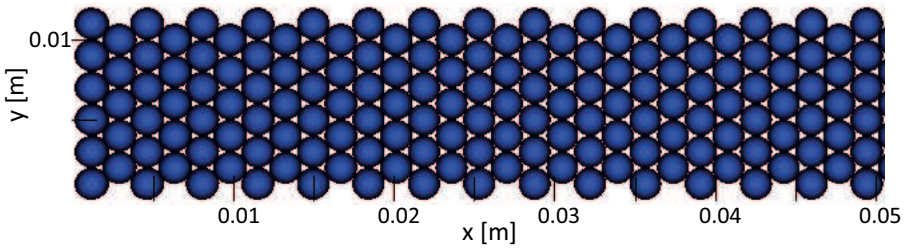

Figure 7.32: Top view on the front section of the particle layer in the DEM domain for a particle diameter $d_p = 2$ mm

The application of wall functions of the high-Re approach have a strict restriction regarding the cell-size or rather the position of the first calculation node. This restriction is related to the functionality of the wall function to reproduce the high gradient near the wall. However, due to the presence of the fixed particle layer, the cross section of the flow is shifted and, thus, the position of the boundary layer. As a result, the origin of the boundary layer is now defined at approximately one particle diameter minus the position of the assumed profile origin ($d_p - z_0$) instead directly next to the wall, as its is assumed in wall function modelling. Thus, the wall-function calculates a velocity gradient based on wrong assumptions of the flow situation. The first cell row is massively affected by the presence of the fixed particles and the flow velocities are significantly reduced directly at the wall. In case of the low-Re approach the discretisation criteria of the turbulence model and unresolved CFD-DEM are mutually exclusive. While the turbulence model requires a very fine meshing depending on the flow Reynolds number, the CFD-DEM code requires a cell size which is equally or bigger as a particle, since in the CFD simulation in each cell a fluid velocity need to be defined. As previously presented, the flow situations at incipient motion requires clearly a fraction of the particle diameter as cell height. Thus, the restrictions make the low-Re approach not applicable for the simulation of a coupled CFD-DEM simulation in the case of boundary layer flow.

Regarding the presented problematic of turbulence modelling, the numerical simulation of flow over a particle layer need to be performed without turbulence modelling. Thereby, the turbulent dissipation is neglected and a steady flow can be established. Further, the wall near velocities cannot be sufficiently reproduced by turbulence models due to the previously presented restrictions. Without turbulence modelling, the development of the boundary layer profile is uncontrolled. The only possibility to take influence on the particle layer-near velocity field is due to the ratio between the particle size and the cell size in z-direction. To evaluate the influence of the ratio of the meshing on the velocity profile, different ratios are investigated by means of a volume ratio between cell volume and particle volume. This volume ratio (VR) is varied to the cell volume equivalent to 2, 5 and 10 times the particle volume. The discretisation in the CFD-domain is based on cubic cells. Based on the volume ratios, the cells have a regular side lengths, which are presented in Table 7.7. Since, the detailed control of the flow velocity due to the regulation of the momentum source is not possible in this simulations, the initial total pressure value p_0 is adopted over and over. Thereby, the resulting flow velocities outside the wall influence are

adopted to agree with the values of the physical tests in $z = 6$ cm such as in the previous CFD simulations. The simulations are conducted for the flow situations with $d_p = 2$ mm and $d_p = 4$ mm for both initial resistance positions.

Table 7.7: Cell heights in CFD domain based on different volume ratios between cell and particle

Volume ratio [-]	Cell height [mm]	
	$d_p = 2$ mm	$d_p = 4$ mm
2	2.03	4.06
5	2.76	5.51
10	3.47	6.94

The results of the simulations are presented in Figure 7.33. For each flow situation, the velocity profiles based on varying volume ratio are included. Further, the averaged velocity profile of the physical tests is included for comparison purpose. The origin of the velocity profile in the simulations is adopted to correspond to the origin of the physical tests. The velocity profiles of the simulations clearly deviate from the physical tests and the theory of boundary layer flow. The majority of the profile is equal to a constant velocity. This constant value is present from a height of $z \approx 0.8$ cm (low resistance) and $z \approx 1.0$ cm (high resistance) upwards. Thereby, the individual height of the wall bound flow in the simulations is considerable depending on the height of the lower cell rows and thus, the volume ratio between the particles and the CFD cells. In the lowest cell row, the particle layer is present. Thus, the void ratio within the cells is very low. The void ratio increases with in creasing volume ratio, since the volume of the particles proportion inside the cells is getting less. The interaction between the particles and the fluid is mainly influenced by the void ratio. Thus, lower void ratios lead to greater interaction effects. In this simulation, the particles have no velocity. Thus, the interaction between particles and fluid is predominantly decelerating the fluid. The lower the void ration, the greater the deceleration effect. Thus effect can be clearly observed in the simulation results for $d_p = 2$ mm. The simulation with the lowest VR = 2 results in the greatest velocity gradient near to the particle layer, followed by VR = 5 and the greatest VR with the lowest velocity gradient. The transition between the velocity in the lowermost cell and the constant velocity in the upper regions is mainly depending on the lower velocity gradient. Besides the lowermost cell row, the two higher cells rows are further effected and show reduced velocities, although no particles are present. Since, the simulations with higher VR have also a greater cell height, the wall influenced flow height is greater for higher VR (see results $d_p = 2$ mm Figure 7.33). For $d_p = 4$ mm this influence is less clear, since the results are more similar than for $d_p = 2$ mm.

With respect to the goal to model the incipient motion of a particle on a particle layer, these results are critical. Although, the lowermost gradient near the particle bed can be reproduced by adopting the volume ratio between the particles and the CFD-cell, the

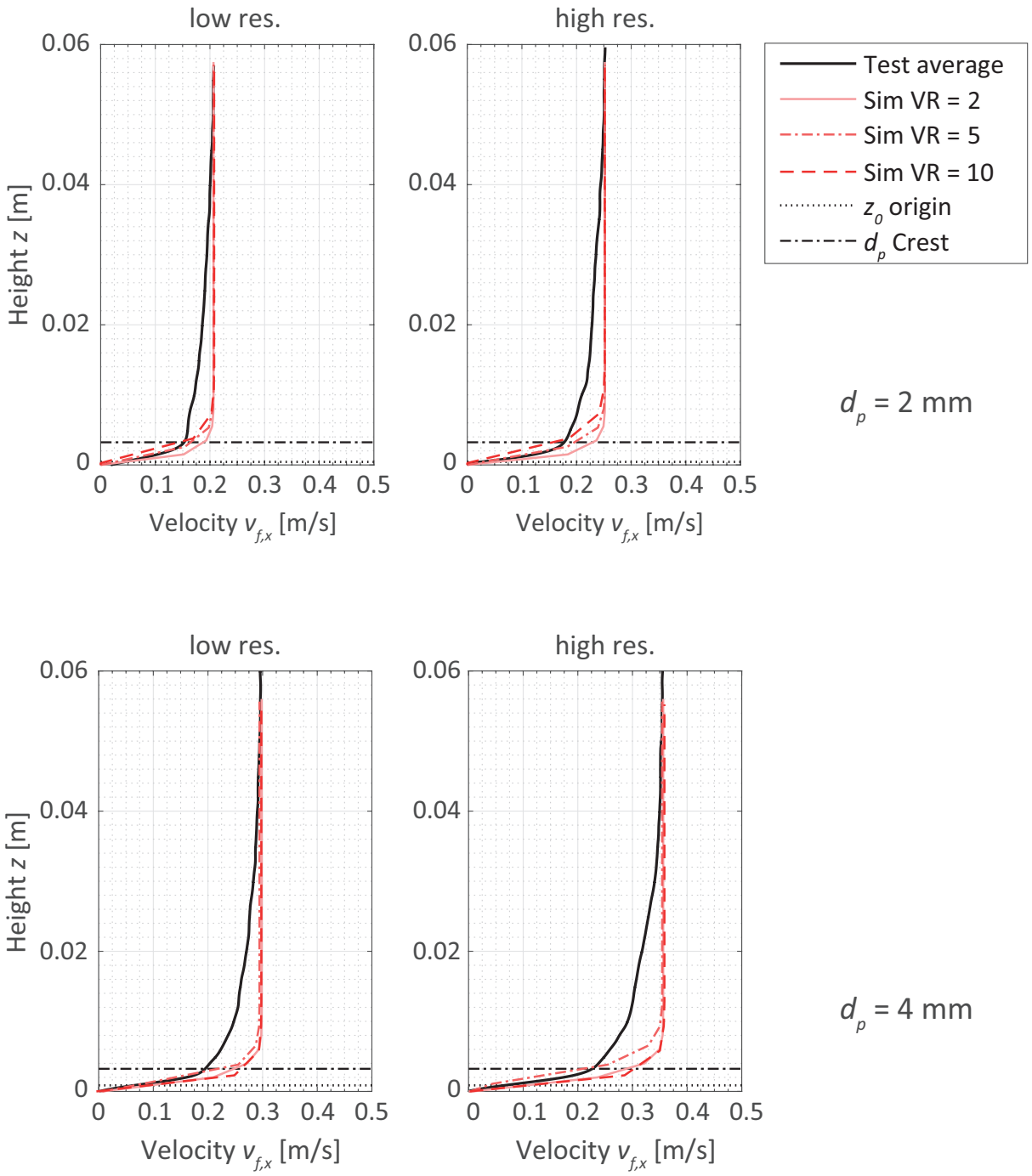

Figure 7.33: Velocity profiles of the CFDEM simulations without turbulence modelling over a fixed particle layer in comparison with the physical tests on incipient motion for the particle diameters $d_p = 2$ mm and $d_p = 4$ mm

velocity near the crest of the particle is overestimated. Thus, it is not possible to recreate the same velocity profile directly near to the particle layer in the height of the free particle.

7.4.3 Erosion processes on a particle bed with the coupled CFD-DEM

As discussed in the previous Section 7.4.2, the accurate simulation of the incipient motion on a particle layer such as performed in the physical tests is not possible, under the actual conditions of the unresolved CFD-DEM. However, although the exact relation between the velocity field and the incipient motion cannot be reproduced, erosion processes might be modelled by the approach already. Therefore, the erosion at a thicker particle layer due to overflow shall be investigated.

Therefore, a new simulation setup is created, which is based on the turbulence-neglected approach and the boundary conditions of the simulations in Section 7.4.2. Again, the simulation domain is based on a narrow channel with symmetric boundary conditions at its y-normal patches. The channel has a length of 15 cm, a depth of 2 cm and a height of 10 cm. The overflow is induced by a pressure difference. Inside this channel a layer with monodisperse particles of $d_p = 0.6$ mm is inserted to a height of 1 cm (see Figure 7.34). The simulation domain of the DEM case has again periodic boundary conditions in x-normal as well as in y-normal direction. Thus, particles leaving the domain, re-enter from the opposed patch. In the simulations, the pressure difference is chosen to achieve a slowly increase of the internal velocity till erosion occurs. The properties of the DEM particles is based on the property set in Section 6.3. Further, the Koch & Hill (2001) drag model is applied in the simulations.

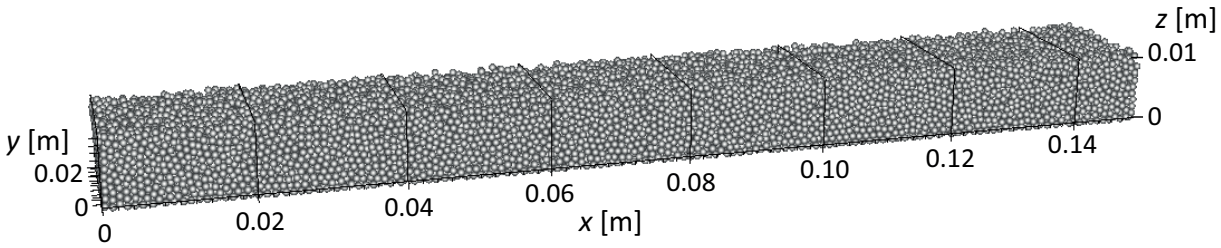

Figure 7.34: Particle layer in coupled simulation at its initial condition

Figure 7.35 presents the top-view on a specific cutout of the particle layer surface approximately in the middle of the channel length over time. Thereby, the initiation of the erosion process shall be observed. The colour of the particles correspond to the particle velocities. Figure 7.35-1 presents the initial position of the particles before movement occurs. With slowly increasing flow velocities, single particles in isolated spots start to move. Thereby, the particles are not moving over a big distance, but just to the next spot which gives more resistance against the flow (see Figure 7.35-2). This situation is comparable, with the majority of the incipient motion test at low resistance initial position, where the particle rolled just over the gap in between the two lee particle, to get static again at the high resistance position. With further increase of the flow velocity, the isolated movements increase in number as present in Figure 7.35-3. This isolated spots segue into greater groups of particles in motion. Now, a few particles are not just eroded but transported over greater distances (see Figure 7.35-4). A full transport of the topmost particles occurs

in Figure 7.35-5. More particles than countable are in motion and are transported over the particle layer surface. However, the transport at this stage is not yet affecting the particle bed configuration. The transport is still superficial. In contrast Figure 7.35-6, where the transport affects the bed configuration. The transport is no longer superficial, but also deeper laying particles are affected. Further, also lower particles which are not transported reconfigure and the whole bed layer rearranges slightly.

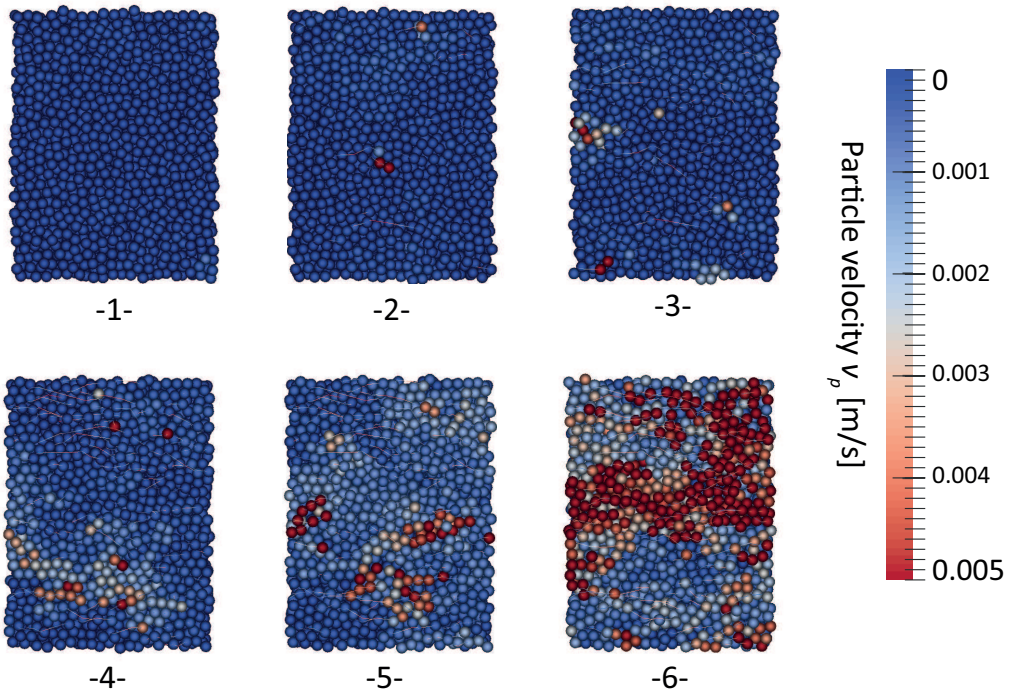

Figure 7.35: Cutout from the top-view on the particle bed surface at different stages of erosion

This stages of transport are equivalent to the transport stages identified by Kramer (1935). Although Kramer (1935) performed his tests with sand distributions, the characteristic different transport stages are visible in this monodisperse setting also. Kramer (1935) distinguished transport into

1. None
2. Weak - Several of the smallest particles are in motion at isolated spots and in countable numbers.
3. Medium - Movement is no longer local in character. It is not strong enough to affect bed configuration and does not result in transportation of an appreciable quantity of material.

4. General - It is sufficiently vigorous to change the bed configuration. There is an appreciable quantity of material transported

All this stages are recognisable in the numerical simulations of transport. Thus, the coupled CFD-DEM seems to be able to model realistic erosion along a disperse particle bed (see also Plenker, 2015).

7.5 Conclusion and Discussion

The physical tests in Section 7.3 give an insight into the flow processes at incipient motion of individual particles. Thereby, different particle diameters as well as the resistance due to positioning is varied. The position resistance is defined by a maximal and a minimal value due to a monodispersed particle layer, arranged in a dense hexagonal pattern. This innovative setup, gives the opportunity to investigate the incipient motion of an individual particle under well defined boundaries regarding the boundary layer. The PIV measurements give a detailed insight into the boundary layer flow and the flow around a highly exposed particle. The analysed velocity profiles for a certain particle diameter show mainly good accordance. Those velocity profiles have been further analysed to determine the related shear stress situation at the boundary. Thereby, a critical shear stress for a certain particle diameter can be determined. A direct comparison of the test results with the Shield's curve based on the theory of Soulsby (1997) shows, that the chosen test setup gives a significant difference to the Shield's band. Although the course of the test bands for low as well as high resistance position is considerable equivalent to those of the Shield's band, the critical values are of significant lower value. Thus, the results with an initial positioning with low resistance are smaller with factor 7, while the high resistance position is by a factor 4.9 smaller than the Shield's curve values. This fact is related to the monodisperse character of the boundary layer flow as well as the perfectly spherical shape of the particles, which impede a lower resistance against the first incipient movement. In contrast to the Shield's results, the test allow a clear relation between the local conditions such as exposure as well as the definition of incipient motion. Thus, the incipient motion of the Shield's data is defined as the first stage of transport, while in the tests the high exposure of the particles lead to an early incipient motion, at which other less exposed particles would not yet move. All these facts imply, that the investigation of the detailed incipient motion of individual particles require detailed physical tests since the common theory of empirical approaches do not cover such richness of detail.

The modelling of the boundary layer flow over a rough particle layer with the CFD approach has been successfully proven in Section 7.4.1. The velocity profiles had a good accordance with the results of the physical tests for the most part. However, the high-Re modelling based on wall functions was less accurate than the low-Re approach, which requires a higher resolution of the wall-near discretisation. The transfer of the physical test setup in numerical simulations to investigate further the interaction forces between particle and fluid was unsuccessful. The modelling of the same boundary layer flow over a particle layer failed by the mutually excluding restriction of the unresolved CFD-DEM approach as well as the turbulent boundary layer flow modelling (see also Plenker et al.,

2016a)). Thus, the restriction of a certain amount of fluid inside a CFD cell during a coupled simulation is excluding the low-Re approach to model the wall near boundary flow, since it requires a high resolution of discretisation. The high-Re approach in turbulent boundary layer flow modelling fails by the position of the wall-functions. Thus, the boundary of the simulation domain, where the wall-function is defined, represents the origin of the velocity profile of boundary layer flow. Due to the presence of the particle layer, this assumption is no longer correct, since the boundary layer origin is shifted into the simulation domain. As a result, the high damping effects of the wall functions concern the cell row, in which the particles are positioned.

A solution to overcome this mutually exclusiveness, might be the introduction of new wall-functions, in which the affected cell face can be defined. The meshing in the height of the particle layer or the particle bed must be arranged as such, that the cell face lies in z_0 distance from the topmost particle crests. However, this solution would be just sufficient for incipient motions, since with transport the position of the layer/bed surface varies. This problem could be just overcome with an dynamic CFD mesh, which moves with the particles. However, this approach is extremely complex and would be extremely computational costly. Another solution is the simulation of the incipient flow process with the resolved CFD-DEM approach. Thereby, the DEM particles as well as the void area is highly resolved by a high resolution of CFD cells. Thus, the RANS low-Re approach or event LES might be applicable here. The LES would further solve a major problem of the RANS modelling, which might constitute a significant factor on the investigation on incipient motion on a particle scale: turbulent anisotropy. All RANS turbulence models are based on the assumption, that the turbulent fluctuations are isotropic. But especially in boundary layer flow, this assumption is no longer valid. In the wall-near flow regions, significant differences between the flow-directional and non-directional turbulent fluctuations occur. Thus, the damping effects in orthogonal direction to the boundary are considerable higher than in flow direction. Thus, the assumption of isotropic turbulence is not applicable for the detailed investigation of the fluid-particle interaction at a boundary. However, the required fine meshing of the CFD domain of those methods cause very high computation costs and, thus, limit the amount of CFD-particles massively. Thus, this method might be sufficient to reproduce the incipient motion scenario of an individual particle, but could not be applied on the modelling of realistic transport of material. However, the resolved CFD-DEM might be a good solution to investigate the incipient motion and the forces acting on the individual particles, to gain more knowledge on the fluid-particle interaction, before the knowledge is transferred to simulations with greater numbers of particles. This might be possible with an adapted boundary layer flow modelling with the unresolved CFD-DEM or also the resolved CFD-DEM, if the computational power increases in the next years as rapid as in the previous.

Although the physical tests could not be modelled successfully with the unresolved CFD-DEM, the erosion process along a particle bed could be reproduced. Since, the correct boundary layer flow could not be modelled, the turbulence modelling is enable for this simulations. With increasing velocities in the free flow, the first incipient movement on the surface of the particle bed could be modelled. Thereby, the different grades of initiated transport according to Kramer (1935) are clearly observable in the simulations. At

lower velocities, just highly exposed particles move shortly into less exposed positions. With increasing velocities, the number of moving particles increases such as the transport distance. In the end, the whole particle bed undergoes a rearrangement. Further, under ongoing transport the development of transport bodies in the form of a small ripple could be recognised.

All in all, the coupled CFD-DEM has still several limits in the modelling of boundary layer flow situations, since the unresolved CFD-DEM is not able to reproduce a boundary layer flow correctly. This makes a direct comparison with physical tests difficult. As long as the boundary layer flow simulation could not be improved, further research is required to investigate possibilities to transfer the flow situation in the numerical simulations to realistic scenarios in the physical tests. A possibility might be the application of wall-near velocity gradients for comparison purpose. The modelling of particle transport with the coupled CFD-DEM is possible. However, also here a transfer of the flow situation in the simulations into realistic conditions is required, since the boundary layer flow cannot be reproduced.

8 Summary and Outlook

In this thesis, geotechnical phenomena of fluid-soil interaction arising from the multi-component characteristic of granular soil have been investigated by means of the detailed interaction processes between granular particles, the internal and external fluid. Therefore, a hybrid modelling approach is applied, including physical tests as well as numerical simulations with the unresolved CFD-DEM method. Since the CFD-DEM method is common in process-engineering but relatively new in geotechnical applications, a benchmark has been conducted to test the simulation of particle-fluid interaction by means of a free settling particle in fluid. Subsequent, two geotechnical applications have been investigated: the collapse procedure of a submerged particle packing and the erosion at a particle bed. Following, the results attained from the conducted investigations are presented. Based on this findings, an outlook is discussed afterwards.

In the benchmark, the sinking procedure of a fully exposed particle is simulated with the unresolved CFD-DEM method. This example represents a scenario, which has been extensively analytically analysed in previous research. As the unresolved CFD-DEM approach is optimised for the simulation of dense mixtures, the detailed investigation of a single particle represents an extremely limiting case for this method. The focus on an individual particle can unveil the numerical limits of this method. Following insights are obtained from the benchmark tests:

- The sedimentation process has been successfully modelled by the developed numerical model. The final settling velocity as well as the settling process match the results of common analytical approaches. The fluid-particle interaction for a single particle can be successfully reproduced although the method is optimized for dense mixtures.
- The interaction between fluid and particle has been reduced to the drag force. According to the conducted variations, the best results can be achieved with the models based on the approaches of Di Felice and Koch & Hill.
- The sensitivity study showed a high significance of the applied initial conditions and model setup of the numerical simulations. Thus, the position of the particle within a cell or its deviation over neighbouring cells is highly relevant for the accuracy of the numerical results. The division of the particle volume over several cells and, thus the division of the voidfraction over several cells, gives the most steady results. However, the voidfraction model, which equally distributes the particle volume over the adjacent cells, cannot operate over processor boundaries of parallelised runs, which has an high impact on the results as long as the focus lies on a single particle.

In the second application, extensive analysis of the collapse procedure of a particle packing under submerged conditions has been conducted. Therefore, physical tests as well as numerical simulations have been applied. Prior to the submerged case, scenarios under

dry conditions have been investigated to analyse the detailed dry collapse mechanism as well as the internal behaviour in between the particles. The analysis included different collapse procedures, to address different mechanisms within the particle packing. The macroscopic mechanism at the transition from a static to a dynamics state as well as internal mechanisms and their effects on the overall macroscopic behaviour have been investigated. Thereby, the dry scenarios focussed on the influence of the particle properties and the contact formulation on the collapse procedure. This extensive investigations gave a deep insight into the small scale particle interaction and the dominating mechanisms. In the submerged case, the focus lay on the interaction between the fluid and the particle phase. Interaction effects could be observed inside of the packing as well as at the deposit surface, which in turn affected the macroscopic behaviour of the particle mass. Following knowledge has been obtained from the hybrid investigations, based on physical tests and numerical simulations:

- Numerical models based on the DEM approach have been successfully developed for the investigation of the collapse procedure under dry conditions. The models were optimised for the distinguished collapse scenarios of a slow and a fast collapse and the corresponding dominating internal mechanisms. The accuracy of the numerical models has been successfully validated by the corresponding physical tests.
- The investigations on the dry collapse procedure gave a detailed insight into the internal slumping mechanisms and the relation to the processes which take place on a particle scale. The mechanism of the slow collapse procedure is dominated by alternating periods of stagnation and small slumping events. Thereby, the mechanism is comparable to the fracture mechanism of ground shear failure with a combined vertical and sideways displacement of the particle mass due to vertical loads. In between those slumping events, the grain skeleton of the particle mass recovers. In contrast, the fast collapse procedure is dominated by one highly dynamic slumping event. Thereby, the particle packing above the slip joint dissolves completely and the particle contacts are reduced to a fractional amount of approximately 30% compared to the initial packing. The internal mechanism of vertical and horizontal displacement is dominated by highly dynamic particle movements with short termed particle interaction events.
- Extensive sensitivity studies revealed the relation between the internal slumping mechanisms at a dry state, the particle-particle interaction and the sensitivity of the mechanism to the particle properties. The slow collapse collapse mechanism is unaffected by variations of the Young's modulus, the Poisson number and the coefficient of restitution. In contrast, the slumping mechanism as well as the development of the deposit is highly depending on the friction coefficients of particle-particle and particle-wall Coulomb friction as well as the inter-particle rolling friction. These assumptions differ significant from the conclusions of the fast collapse scenario. The numerical simulations of the sensitivity study reveal that in contrast to the slow collapse procedure the slumping mechanism of the fast collapse is dominated by the coefficient of restitution. Thereby, the internal mechanism is barely affected but rather the temporal evolution of the dissolved particles and the kinetic energy during the collapse process. Since the coefficient of restitution represents the energetic

damping effects in an impact event with other particles, an increased inter-particle damping results further in a damping of the collapse of the whole particle mass. Thus, the spreading velocity of the dissolved particles is clearly reduced for lower coefficients of restitution. In contrast, the process is minor affected by the friction of the particles. Thus, tests with the same aspect ratio with materials with equal coefficients of restitution are going to result in the same dissolved slumping mechanism and deposit spreading, although other properties might differ.

- The investigations have shown, that the developed and validated numerical models can be very well applied for further investigations regarding the collapse mechanism of dry granular material. The discrete representation of the particle phase enables to get detailed insights into the local particle interaction and their influence on the overall mechanism on a macroscopic level. The numerical simulation results are found to be highly reproducible. Nevertheless, there is a high dependency on the chosen initial packing of the particle phase.
- In the investigations of the collapse of a submerged particle column, the presence of fluid adds an additional resistance against the particle movement. The drag force acts opposed to the direction of the particle trajectory and increases the resistance with increasing relative velocities between fluid and particle. The whole collapse is significantly decelerated due to the presence of viscous fluid. Further, the particle packing dissolves completely. Thereby, dilatancy leads to an increased volume of the particle-fluid mixture and increases the dissolved separation of the particles in the mixture. Thus, the particle-particle interaction is significantly reduced in comparison to the dry scenarios.
- In contrast to the dry scenarios, the submerged scenarios show a significant impact of the particle diameter on the collapse development. This behaviour is directly related to the particle diameter or rather the permeability of the material. To investigate this relation further, more different particle diameters need to be investigated.
- The analysis of the individual phases in the simulations reveals new insights into the collapse process. The simulations reveal, that particles with higher drag force are positioned just at the surface of the collapsing particle mass and especially at the deposit tip. Thus, the free fluid is not significantly intruding into the voids and the particle mass and the accelerated averaged pore fluid acts with the particles like a continuous mass. Although, the particle mass is rather permeable, the collapse occurs to be too fast to allow a flow through the particles. However, the validation of the numerical simulations have shown, that the collapse development over time is less accurately reproduced in the simulations. Further, the significant dissolving on the physical tests is not captured in the simulations. Thus, the effect of dilatancy is not reproduced in the unresolved CFD-DEM. However, the dilatancy effect has a high impact on the collapse process over time and the collapse characteristics and, therefore, are required for an improved accuracy in the simulation. Since dilatancy cannot be captured without resolving the flow around the particles, a fluid-particle interaction model needs to be developed to cover the phenomenon of dilatancy in the unresolved CFD-DEM simulations. Also the inclusion of the lubrication force should lead to an improvement of accuracy.

Further, the fluid-soil interaction at a soil boundary has been investigated by means of the incipient movement at erosion. Therefore, physical tests have been conducted to define the incipient movement for a certain particle size under clearly defined boundaries and initial conditions at a mono-dispersed particle packing. Further, the coupled unresolved CFD-DEM has been applied for numerical simulation on erosion. In contrast to other approaches, the interface between external fluid and soil is reproduced by a permeable particle layer of dispersed particles. Thus, the interaction between the internal and the external flow field is enabled. To investigate the accuracy of the numerical model regarding the moment of incipient motion, the setup of the physical tests is investigated numerically by the resolved CFD-DEM. A validation base is given by the results of the physical tests. Although the erosion of individual and groups of particles at the surface of a particle packing could be modelled successfully, the reproduction of the correct boundary layer flow above the particle layer could not be modelled correctly. Thus, the simulation of incipient motion could not be modelled successfully, since the boundary layer flow regime could not be reproduced. The modelling of boundary layer flow in CFD simulations is based on the turbulence modelling approaches. Although several solutions exist for the RANS-turbulence modelling, the restrictions of the approaches are mutually exclusive with the restrictions of the coupled CFD-DEM. The boundary layer flow profiles resulting from the application of different turbulence models and from neglecting the turbulent viscosity have been investigated. In all cases, the gradients directly next to the boundary and, thus, directly next to the exposed particles could not be modelled correctly. The simulation of realistic boundary layer flow is so far a problem for the unresolved CFD-DEM approach. However, the following knowledge has been obtained from the conducted investigations:

- In the physical tests, the critical shear stress at incipient motion has been determined for glass particles on a mono-dispersed rough particle layer. Thereby, the resistance due to the embedding position of the particle has been varied to a maximum and a minimum resistance. The results have been compared to the widely applied theory of Shields. Thereby, the obtained results give significant lower critical values in comparison to the original Shields curve. This relates to the perfectly round shape of the glass particles and the high exposition of the particles on top of the particle layer. However, the critical moment in the theory of Shields is based on already higher transport stages rather than incipient motion of single highly-exposed grains. Thus, the empirical theory of Shields cannot be applied directly for highly detailed investigations on the incipient motion of single glass particles. For an approximation of the values under the chosen boundaries of the physical tests, the Shields values need to be reduced by a factor of ≈ 7 for an initial position of high resistance and by a factor of ≈ 5 for an initial position of low resistance.

- The simulation of incipient motion of single particles on a rough mono-dispersed particle layer with the unresolved CFD-DEM is not yet successful, since the sharp gradient of the boundary layer flow near the bed could not be reproduced by the unresolved CFD-DEM. The RANS modelling requires specific treatment of turbulence modelling to simulate the high gradients near a wall or bed. However, the normally applied tools of high-Re and low-Re modelling in CFD are not applicable for coupled CFD-DEM, since the gradient can be just calculated directly next

to a domain-boundary or has certain requirements regarding the spatial discretisation which are mutually exclusive to the specifications of the unresolved CFD-DEM. Thus, further development is required to allow a direct transmission of the flow situation in the numerical simulations of realistic boundary layer flow.

- A model has been developed to simulate the erosion at a disperse particle bed. Although the boundary layer flow at the bed and, thus, the exact motion threshold as obtained from the physical tests could not be reproduced, the erosion process could be modelled successfully. Thus, the different transport stages of single particle transport up to particle group transport and a change in bed configuration could be identified.

In summary, this thesis grants new insights in to the small-scale interaction between a granular particle packing and the internal as well as the external flow field for different applications. For several applications, such as settling process, granular slumping or sediment transport, the coupled CFD-DEM can be a valuable tool to investigate the detailed processes. Although the resolved CFD-DEM is not yet covering all the small-scale processes, that are required to reproduce the overall macroscopic behaviour, it gives detailed insights into the internal mechanisms of the granular phase and the interaction with the surrounding medium. On the other side, the fact that the macroscopic behaviour is not entirely reproduced, gives an idea on the significance of other influences on the investigated applications. Thus, each research contribution unveils new questions and motivation for further research. Some of those will be discussed hereinafter.

Outlook

The investigation of the submerged column collapse showed a high dependency of the internal mechanism from the temporal duration of the collapse process. Further, the fluid-particle interaction processes where affected by the velocity of the progression. Thus, the fast collapse of the submerged particle packing undergoes initially a dissolving process, in which the particle packing dissolves to a loose dynamic mixture. This, process cannot be reproduced correctly yet by the coupled CFD-DEM. The dissolving process is influenced by dilatancy effects, which cannot be modelled with the conventional force models. This problem is addressed within the connecting investigations of Kanitz (unpublished). Further, the lubrication force might be required to model the transition from a static to a dynamic state and vice versa. The development of corresponding force models should improve the modelling accuracy, especially for application in geotechnical engineering.

The boundary layer flow along a particle layer could not be modelled correctly, due to certain requirements regarding the turbulence modelling in RANS which are mutually exclusive to the specifications of the unresolved CFD-DEM. However, the correct modelling of the boundary layer flow field is of importance to investigate incipient motion and erosion problems and to compare those to the critical thresholds obtained in the physical tests. A possible solution for the simulation of incipient motion might be the resolved CFD-DEM in combination with LES turbulence modelling. However, this would limit the amount of particles in the simulation dramatically. Another possibility might be the adoption of the usually applied wall functions of the high-Re modelling for the application at a boundary which is positioned inside of the simulation domain. However, this solution would be just

valid for a bed without transport or just in the first moments of incipient motion, since particle transport at the surface would affect the boundary layer flow field.

In this thesis, the applied particles were perfectly shaped spherical glass particles. However, the grains of natural soil differ from this shape and are more edged or even sharp edged. Thus, the investigations neglect effects which evoke from the divergent grain shapes and the gained knowledge can be just transferred to real soil behaviour under restrictions. The coupled CFD-DEM gives limited possibilities, like the coefficient of rolling friction to take non-spherical grain shapes into account without and enormous increase of computational costs. In the sensitivity studies of the dry slumping investigations, this coefficient has been varied to investigate the effect on the slumping mechanism. It should be investigated, whether this behaviour holds true for the application of realistic soils. In this context, the effect of multi-disperse mixtures and the effect of packing density in the CFD-DEM simulations should be investigated as well.

The coupled CFD-DEM represents a powerful tool, for the investigation of fluid-particle interaction and their effect on macroscopic behaviour. However, the high computational costs limit its application for general problems of geotechnical engineering, since even small soil volumes of a few centimetres consists of millions of particles of different sizes, even if the fine sediments are neglected. Nevertheless, it is worth to develop this method further, since the computational power in the last decades developed exponentially. With this ongoing trend, the coupled CFD-DEM is probably getting more powerful and efficient in the coming years. Thus, the development of this method at this point of times, enables the possibility for further highly detailed investigations of natural small scale processes in the future.

Bibliography

Ai, J., J.-F. Chen, J. M. Rotter, and J. Y. Ooi (2011). "Assessment of rolling resistance models in discrete element simulations". In: *Powder Technology* 206.3, pp. 269–282.

Anderson, T. B. and R. Jackson (1967). "Fluid Mechanical Description of Fluidized Beds. Equations of Motion". In: *Industrial & Engineering Chemistry Fundamentals* 6.4, pp. 527–539.

Antonyuk, S. (2006). "Deformations- und Bruchverhalten von kugelförmigen Granulaten bei Druck- und Stoßbeanspruchung". Dissertation. Magdeburg: Otto-von-Guericke-Universität.

Auton, T. R. (1987). "The lift force on a spherical body in a rotational flow". In: *Journal of Fluid Mechanics* 183, pp. 199–218.

Auton, T. R., J. C. R. Hunt, and M. Prud'Homme (1988). "The force exerted on a body in inviscid unsteady non-uniform rotational flow". In: *Journal of Fluid Mechanics* 197, pp. 241–257.

Bagchi, P. and S. Balachandar (2002). "Effect of free rotation on the motion of a solid sphere in linear shear flow at moderate Re". In: *Physics of Fluids* 14.8, pp. 2719–2737.

Balevičius, R., A. Džiugys, and R. Kačianauskas (2004). "Discrete element method and its application to the analysis of penetration into granular media". In: *Journal of Civil Engineering and Management* 10.1, pp. 3–14.

Balmforth, N. J. and R. R. Kerswell (2005). "Granular collapse in two dimensions". In: *Journal of Fluid Mechanics* 538, pp. 399–428.

Bartzke, G. (2012). "Micro Scale Sediment-Fluid Interactions". PhD-Thesis. Bremen: Universität Bremen.

Basset, A. B. (1888). "On the Motion of a Sphere in a Viscous Liquid". In: *Philosophical Transactions of the Royal Society A: Mathematical, Physical and Engineering Sciences* 179.0, pp. 43–63.

Beavers, G. S., E. M. Sparrow, and R. A. Magnuson (1970). "Experiments on Coupled Parallel Flows in a Channel and a Bounding Porous Medium". In: *Journal of Basic Engineering* 92.4, p. 843.

Beavers, G. S. and D. D. Joseph (1967). "Boundary conditions at a naturally permeable wall". In: *Journal of Fluid Mechanics* 30.01, p. 197.

Bechteler, W. (2006). *Sustainable Sediment Management in Alpine Reservoirs considering ecological and economical aspects: Sedimentquellen und Transportprozesse*. Vol. 2. ALPRESERV. Neubiberg: Universität der Bundeswehr München.

Beheshti, A. A. and B. Ataie-Ashtiani (2008). "Analysis of threshold and incipient conditions for sediment movement". In: *Coastal Engineering* 55.5, pp. 423–430.

Biot, M. A. (1941). "General Theory of three-dimensional consolidation". In: *Journal of Applied Physics* 12.2, pp. 155–164.

Biot, M. A. (1956a). "Theory of Propagation of Elastic Waves in a Fluid-Saturated Porous Solid: I. Low-Frequency Range". In: *The Journal of the Acoustical Society of America* 28.2, pp. 168–178.

Biot, M. A. (1956b). "Theory of Propagation of Elastic Waves in a Fluid-Saturated Porous Solid. II. High-Frequency Range". In: *The Journal of the Acoustical Society of America* 28.2, pp. 179–191.

Blocken, B., T. Stathopoulos, and J. Carmeliet (2007). "CFD simulation of the atmospheric boundary layer: Wall function problems". In: *Atmospheric Environment* 41.2, pp. 238–252.

Bokkers, G. A., M. van Sint Annaland, and J. Kuipers (2004). "Mixing and segregation in a bidisperse gas–solid fluidised bed: A numerical and experimental study". In: *Powder Technology* 140.3, pp. 176–186.

Boltzmann, L. (1872). "Weitere Studien über das Wärmegleichgewicht unter Gasmolekülen". In: *Wiener Berichte* 66, pp. 275–370.

Bouillard, J. X., R. W. Lyczkowski, and D. Gidaspow (1989). "Porosity distributions in a fluidized bed with an immersed obstacle". In: *AIChE Journal* 35.6, pp. 908–922.

Boussinesq, J. V. (1885). *Applications des Potentiels a l'Etude de l'Equilibre et du Mouvement des Solides Elastiques*. Paris: Gauthiers-Villars.

Brenner, H. (1961). "The slow motion of a sphere through a viscous fluid towards a plane surface". In: *Chemical Engineering Science* 16.3-4, pp. 242–251.

Breugem, W. P. and B. J. Boersma (2005). "Direct numerical simulations of turbulent flow over a permeable wall using a direct and a continuum approach". In: *Physics of Fluids* 17.2, p. 025103.

Breugem, W. P., B. J. Boersma, and R. E. Uittenbogaard (2006). "The influence of wall permeability on turbulent channel flow". In: *Journal of Fluid Mechanics* 562, pp. 35–72.

Brinkman, H. C. (1949). "A calculation of the viscous force exerted by a flowing fluid on a dense swarm of particles". In: *Applied Scientific Research* 1.1, p. 1045.

Buffington, J. M. (1999). "The Legend of A. F. Shields". In: *Journal of Hydraulic Engineering* 125.4, pp. 376–387.

Buffington, J. M. and D. R. Montgomery (1997). "A systematic analysis of eight decades of incipient motion studies, with special reference to gravel-bedded rivers". In: *Water Resources Research* 33.8, pp. 1993–2029.

Ceccato, F. and P. Simonini (2017). "Numerical study of partially drained penetration and pore pressure dissipation in piezocone test". In: *Acta Geotechnica* 12.1, pp. 195–209.

Chen, S. and G. D. Doolen (1998). "Lattice Boltzmann Method for Fluid Flow". In: *Annual Review of Fluid Mechanics* 30.1, pp. 329–364.

Chen, X. and Y.-M. Chiew (2004). "Velocity Distribution of Turbulent Open-Channel Flow with Bed SuctionRead More: http://ascelibrary.org/doi/10.1061/%Velocity Distribution of Turbulent Open-Channel Flow with Bed SuctionVelocity Distribution of Turbulent Open-Channel Flowwith Bed Suction". In: *Journal of Hydraulic Engineering* 130.2, pp. 140–148.

Cheng, N.-S. and Y.-M. Chiew (1998a). "Modified Logarithmic Law for Velocity Distribution Subjected to Upward Seepage". In: *Journal of Hydraulic Engineering* 124.12, pp. 1235–1241.

Cheng, N.-S. and Y.-M. Chiew (1998b). "Turbulent open-channel flow with upward seepage". In: *Journal of Hydraulic Research* 36.3, pp. 415–431.

Cherukat, P. and J. B. McLaughlin (1994). "The inertial lift on a rigid sphere in a linear shear flow field near a flat wall". In: *Journal of Fluid Mechanics* 263, pp. 1–18.

Chmelnizkij, A., S. Nagula, and J. Grabe (2017). "Numerical Simulation of Deep Vibration Compaction in Abaqus/CEL and MPM". In: *Procedia Engineering* 175, pp. 302–309.

Choi, H. G. and D. D. Joseph (2001). "Fluidization by lift of 300 circular particles in plane Poiseuille flow by direct numerical simulation". In: *Journal of Fluid Mechanics* 438.

Christoffersen, J. B. and I. G. Jonsson (1985). "Bed friction and dissipation in a combined current and wave motion". In: *Ocean Engineering* 12.5, pp. 387–423.

Clift, R. and W. H. Gauvin (1971). "Motion of entrained particles in gas streams". In: *The Canadian Journal of Chemical Engineering* 49.4, pp. 439–448.

Colebrook, C. F. and C. M. White (1937). "Experiments with Fluid Friction in Roughened Pipes". In: *Proceedings of the Royal Society A: Mathematical, Physical and Engineering Sciences* 161.906, pp. 367–381.

Coleman, N. L. (1967). "A theoretical and experimental study of drag and lift forces acting on a sphere resting on a hypothetical streambed". In: *Proceedings of the 12th Congress of the International Association for Hydraulic Research*. Ed. by International Association for Hydraulic Research. Vol. 3, pp. 185–192.

Coles, D. (1956). "The law of the wake in the turbulent boundary layer". In: *Journal of Fluid Mechanics* 1.02, p. 191.

Committee on Hydromechanics of the Hydraulics Division (1963). "Friction Factors in Open Channels: Progress Report of the Task Force on Friction Factors in Open Channels of the Committee on Hydromechanics of the Hydraulics Division". In: *Journal of the Hydraulics Division* 89.2, pp. 97–143.

Coulomb, C. A. (1776). "Essai sur une application des regles des maximis et minimis a quelquels problemesde statique, relatifs a l' architecture". In: *Mémoires de mathématique et de physique, presentés à l'Académie royale des sciences* 7, pp. 343–382.

Crosta, G. B., S. Imposimato, and D. Roddeman (2009). "Numerical modeling of 2-D granular step collapse on erodible and nonerodible surface". In: *Journal of Geophysical Research: Earth Surface* 114.F3, pp. 1–19.

Crowe, C. T., J. D. Schwarzkopf, M. Sommerfeld, and Y. Tsuji (2012). *Multiphase flow with droplets and particles*. 2nd ed. Boca Raton, FL: Taylor & Francis / CRC Press.

Cundall, P. A. (1971). "A Computer Model for Simulating Progressive Large Scale Movements in Blocky Rock Systems". In: *Proceedings of Symposium of International Society of Rock Mechanics*. Ed. by H. R. Hardy Jr. Vol. 1, pp. 2–8.

Cundall, P. A. and O. D. L. Strack (1979). "A discrete numerical model for granular assemblies". In: *Géotechnique* 29, pp. 47–65.

Cundall, P. A. and R. D. Hart (1992). "Numerical Modelling of Discontinua". In: *Engineering Computations* 9.2, pp. 101–113.

DallaValle, J. M. (1948). *Micromeritics: The Technology of Fine Particles*. New York: Pitman Publishing Corporation.

Dandy, D. S. and H. A. Dwyer (1990). "A sphere in shear flow at finite Reynolds number: Effect of shear on particle lift, drag, and heat transfer". In: *Journal of Fluid Mechanics* 216.1, p. 381.

Davidsson, L. (2006). "Evaluation of the SST-SAS Model: Channel Flow,A symmetric Diffuser and Axi-Symmetric Hill". In: *Proceedings of the European Conference on Computational Fluid Dynamics*. Delft University of Technology.

Decker, S. (2005). "Zur Berechnung von gerührten Suspensionen mit dem Euler-Lagrange-Verfahren". Dissertation. Halle: Martin-Luther-Universit¨at Halle-Wittenberg.

Deutsches Institut für Normung e.V., ed. (1998). *DIN 18130-1: Bestimmung des Wasserdurchlässigkeitsbeiwerts*.

Deutsches Institut für Normung e.V., ed. (2017). *DIN 4085: Baugrund – Berechnung des Erddrucks*.

Dey, S. (1999). "Sediment Threshold". In: *Applied Mathematical Modelling* 23, pp. 399–417.

Dey, S. (2014). *Fluvial Hydrodynamics*. Berlin, Heidelberg: Springer Berlin Heidelberg.

Dey, S. and S. Z. Ali (2016). "Hydrodynamics of sediment transport: Grain scale to continuum scale". In: *Scour and Erosion*. Ed. by J. Harris, R. Whitehouse, and S. Moxon. London, UK: CRC Press - Taylor & Francis Group, pp. 29–40.

Di Felice, R. (1994). "The voidage function for fluid-particle interaction systems". In: *International Journal of Multiphase Flow* 20.1, pp. 153–159.

Dietrich, W. E. (1982). "Settling velocity of natural particles". In: *Water Resources Research* 18.6, pp. 1615–1626.

Dittrich, A. (1998). "Wechselwirkung Morphologie/Strömung naturnaher Fließgewässer". Habilitation. Karlsruhe: Universität Fridericiana zu Karlsruhe.

Dratt, M. and A. Katterfeld (2017). "Coupling of FEM and DEM simulations to consider dynamic deformations under particle load". In: *Granular Matter* 19.3, p. 49.

Ehlers, W. (1996). "Grundlegende Konzepte poröser Medien". In: *Technische Mechanik* 16.1, pp. 63–76.

Ergun, S. (1952). "Fluid flow through packed columns". In: *Chemical Engineering Progress* 48.2, pp. 89–96.

Ferziger, J. H. and M. Perić (2008). *Numerische Strömungsmechanik*. Berlin and Heidelberg: Springer.

Forchheimer, P. (1901). "Wasserbewegung durch Boden". In: *Verein Deutscher Ingenieure* Zeitschrift des Vereins deutscher Ingenieure, pp. 1782–1788.

Forkel, C. (2004). *Numerische Modelle für die Wasserbaupraxis: Grundlagen, Anwendungen, Qualitätsaspekte*. Vol. 130. Mitteilungen des Instituts für Wasserbau und Wasserwirtschaft der Rheinisch-Westfälischen Technischen Hochschule Aachen. Aachen: Shaker.

G.U.N.T. Gerätebau GmbH, ed. (2018). *HM 162: Experimental flume 309x450mm*.

García, M. H. (2008). "Sediment Transport and Morphodynamics". In: *Sedimentation engineering*. Ed. by M. H. García. ASCE manuals and reports on engineering practice. Reston, Va: American Society of Civil Engineers, pp. 21–163.

García, M. H., M. Laursen, C. Michel, and J. M. Buffington (2000). "Discussion on 'The legend of A. F. Shields' by John M. Buffington". In: *Journal of Hydraulic Engineering* 126, pp. 718–720.

Gibbs, R. J. and M. D. Matthews (1971). "The Relationship Between Sphere Size And Settling Velocity". In: *SEPM Journal of Sedimentary Research* Vol. 41.

Gidaspow, D. (1994). *Multiphase Flow and Fluidization: Continuum and Kinetic Theory Descriptions*. San Diego: Elsevier Science.

Goharzadeh, A., A. Khalili, and B. B. Jørgensen (2005). "Transition layer thickness at a fluid-porous interface". In: *Physics of Fluids* 17.5, pp. 0571021–0571029.

Goldman, A. J., R. G. Cox, and H. Brenner (1967). "Slow viscous motion of a sphere parallel to a plane wall—II Couette flow". In: *Chemical Engineering Science* 22.4, pp. 653–660.

Goniva, C., K. Gruber, and C. Kloss (2012). "Sediment erosion a numerical and experimental study". In: *River flow 2012*. Ed. by R. Murillo Muñoz. Leiden, Netherlands: CRC Press/Balkema, pp. 415–422.

Guo, N. and J. Zhao (2014). "A coupled FEM/DEM approach for hierarchical multiscale modelling of granular media". In: *International Journal for Numerical Methods in Engineering* 99.11, pp. 789–818.

Guo, N. and J. Zhao (2016). "Parallel hierarchical multiscale modelling of hydro-mechanical problems for saturated granular soils". In: *Computer Methods in Applied Mechanics and Engineering* 305, pp. 37–61.

Gupta, A. D. and G. N. Paudyal (1985). "Characteristics of Free Surface Flow Over Gravel Bed". In: *Journal of Irrigation and Drainage Engineering* 111.4, pp. 299–318.

Hadjiconstantinou, N. G. (2006). "The limits of Navier-Stokes theory and kinetic extensions for describing small-scale gaseous hydrodynamics". In: *Physics of Fluids* 18.11.

Hager, A. (2014). "CFD-DEM on Multiple Scales: An Extensive Investigation of Particle-Fluid Interactions". Dissertation. Linz: Johannes Kepler Universität Linz.

Hager, A., D. Plenker, and M. Kanitz (2017). "Multiscale Modelling of Physical Processes at the Water–Soil Interface with a Coupled CFD–DEM Method". In: *Conference on Maritime Energy - Decommissioning of Offshore Geotechnical Structures*. Ed. by J. Grabe. Veröffentlichungen des Instituts für Geotechnik und Baubetrieb der TU Hamburg. Hamburg, Germany.

Hall, D. (1988). "Measurements of the mean force on a particle near a boundary in turbulent flow". In: *Journal of Fluid Mechanics* 187.-1, p. 451.

Hart, R. D. (1988). *An Overview of Methods for Discontinuum Analysis*.

He, X., S. Chen, and G. D. Doolen (1998). "A Novel Thermal Model for the Lattice Boltzmann Method in Incompressible Limit". In: *Journal of Computational Physics* 146.1, pp. 282–300.

Heins, E., D. Plenker, and J. Grabe (2015). "Untersuchungen zum Absinkverhalten und zur Beanspruchung von geotextilen Sandcontainern als Kolkschutz unter offshore Bedin-

gungen". In: *14. Informations- und Vortragstagung über Kunststoffe in der Geotechnik* geotechnik Sonderheft.

Hertz, H. (1881). "Ueber die Berührung fester elastischer Körper". In: *Journal für die reine und angewandte Mathematik* 92, pp. 159–171.

Hjelmfelt, A. T. and L. F. Mockros (1966). "Motion of discrete particles in a turbulent fluid". In: *Applied Scientific Research* 16.1, pp. 149–161.

Hjulström, F. (1935). "Studies of the morphological activity of rivers as illustrated by the River Fyris". Dissertation. Uppsala: Universitet Uppsala.

Hokenson, G. J. (1985). "Boundary Conditions for Flow Over Permeable Surfaces". In: *Journal of Fluids Engineering* 107.3, p. 430.

Hu, G., Z. Hu, B. Jian, L. Liu, and H. Wan (2011). "On the Determination of the Damping Coefficient of Non-linear Spring-dashpot System to Model Hertz Contact for Simulation by Discrete Element Method". In: *Journal of Computers* 6.5.

Ikeda, S. (1982). "Incipient Motion of Sand Particles on Side Slopes". In: *Journal of the Hydraulics Division* 108.1, pp. 95–114.

Iwagaki, Y. (1956). "Hydrodynamical study on critical tractive force". In: *Transactions of the Japan Society of Civil Engineers* 1956.41, pp. 1–21.

Iwashita, K. and M. Oda (2000). "Micro-deformation mechanism of shear banding process based on modified distinct element method". In: *Powder Technology* 109.1-3, pp. 192–205.

Jensen, A., K. Fraser, and G. Laird (2014). *Improving the Precision of Discrete Element SImulations through Calibration Models*. 13th International LS-DYNA Users Conference.

Johnson, K. L. (1987). *Contact mechanics*. 1st pbk. ed. (with corrections). Cambridge [Cambridgeshire] and New York: Cambridge University Press.

Kafui, K. D., C. Thornton, and M. J. Adams (2002). "Discrete particle-continuum fluid modelling of gas–solid fluidised beds". In: *Chemical Engineering Science* 57.13, pp. 2395–2410.

Kanitz, M. and J. Grabe (2018). "Numerical investigations on the liquid-solid transition of a soil bed with coupled CFD-DEM". In: *Numerical Methods in Geotechnical Engineering IX*. Ed. by M. de Matos Fernandes. Milton: Chapman and Hall/CRC.

Kanitz, M. (unpublished). "On the numerical modelling of particle-fluid systems in geotechnical applications with unresolved coupled CFD-DEM". PhD thesis. Hamburg: Technische Universität Hamburg-Harburg.

Kerswell, R. R. (2005). "Dam break with Coulomb friction: A model for granular slumping?" In: *Physics of Fluids* 17.5, pp. 1–15.

Kim, J., M. Parviz, and R. Moser (1987). "Turbulence statistics in fully developed channel flow at low Reynolds number". In: *Journal of Fluid Mechanics* 177, pp. 133–166.

Kirchner, J. W., W. E. Dietrich, F. Iseya, and H. Ikeda (1990). "The variability of critical shear stress, friction angle, and grain protrusion in water-worked sediments". In: *Sedimentology* 37.4, pp. 647–672.

Klausner, Y. (1991). *Fundamentals of continuum mechanics of soils*. London, UK: Springer.

Kloss, C. (2016). *LIGGGHTS(R)-PUBLIC Documentation: Version 3.X*.

Kloss, C. and C. Goniva (2011). "LIGGGHTS - Open Source Discrete Element Simulations of Granular Materials Based on Lammps". In: *Supplemental Proceedings*. Ed. by The Minerals, Metals & Materials Society. Hoboken, NJ, USA: John Wiley & Sons, Inc., pp. 781–788.

Kloss, C., C. Goniva, A. Hager, S. Amberger, and S. Pirker (2012). "Models, algorithms and validation for opensource DEM and CFD-DEM". In: *PCFD (Progress in Computational Fluid Dynamics)* 12.2/3, pp. 140–152.

Kocak, B. (2017). "Zur numerischen Modellierung von hydraulisch-mechanisch gekoppelten Prozessen in gesättigten granularen Böden mittels Smoothed Particle Hydrodynamics". Dissertation. Hamburg: Hamburg University of Technology.

Koch, D. L. and R. J. Hill (2001). "Inertial Effects in Suspension and Porous-Media Flows". In: *Annual Review of Fluid Mechanics* 33.1, pp. 619–647.

Kolymbas, D. (2011). *Geotechnik: Bodenmechanik, Grundbau und Tunnelbau*. Berlin, Heidelberg: Springer-Verlag Berlin Heidelberg.

Kramer, H. (1935). "Sand mixtures and sand movement in fluvial models". In: *Transactions of the American Society of Civil Engineers* 100, pp. 798–878.

Krishnan, G. P. and D. T. Leighton (1995). "Inertial lift on a moving sphere in contact with a plane wall in a shear flow". In: *Physics of Fluids* 7.11, pp. 2538–2545.

Kurose, R. and S. Komori (1999). "Drag and lift forces on a rotating sphere in a linear shear flow". In: *Journal of Fluid Mechanics* 384, pp. 183–206.

Lajeunesse, E., J. B. Monnier, and G. M. Homsy (2005). "Granular slumping on a horizontal surface". In: *Physics of Fluids* 17.10, pp. 103301–103317.

Laurien, E. and H. Oertel jr. (2013). *Numerische Strömungsmechanik: Grundgleichungen und Modelle - Lösungsmethoden - Qualität und Genauigkeit*. 5., überarb. u. erw. Aufl. 2013. SpringerLink : Bücher. Wiesbaden: Imprint: Springer Vieweg.

Lee, H. and S. Balachandar (2012). "Critical shear stress for incipient motion of a particle on a rough bed". In: *Journal of Geophysical Research* 117.

Li, J. and J. A. M. Kuipers (2003). "Gas-particle interactions in dense gas-fluidized beds". In: *Chemical Engineering Science* 58.3-6, pp. 711–718.

Li, X. and J. Zhao (2016). "Numerical simulation of dam break by a coupled CFD-DEM approach". In: *Japanese Geotechnical Society Special Publication* 2.18, pp. 691–696.

Liang, S.-C., T. Hong, and L.-S. Fan (1996). "Effects of particle arrangements on the drag force of a particle in the intermediate flow regime". In: *International Journal of Multiphase Flow* 22.2, pp. 285–306.

Liu, S. (2016). "Implementation of a Complete Wall Function for the Standard k - epsilonTurbulence Model in OpenFOAM 4.0". In: *Proceedings of CFD with OpenSource Software*. Ed. by H. Nilsson.

Lu, X., C. M. Boyce, S. A. Scott, J. S. Dennis, and D. J. Holland (2015). "Investigation of Two-fluid Models of Fluidisation Using Magnetic Resonance and Discrete Element Simulations". In: *Procedia Engineering* 102, pp. 1436–1445.

Lube, G., H. E. Huppert, R. S. J. Sparks, and A. Freundt (2005). "Collapses of two-dimensional granular columns". In: *Physical review. E, Statistical, nonlinear, and soft matter physics* 72.4, pp. 1–10.

Lube, G., H. Huppert, R. S. J. Sparks, and M. A. Hallworth (2004). "Axisymmetric collapses of granular columns". In: *Journal of Fluid Mechanics* 508, pp. 175–199.

Luding, S. (2008). "Introduction to Discrete Element Methods: Basics of Contact Force Models and how to perform the Micro-Macro Transition to Continuum Theory". In: *European Journal of Environmental and Civil Engineering* 12, pp. 785–826.

Malcherek, A. (2007a). *Hydromechanik für Bauingenieure*. Ed. by Universität der Bundeswehr München.

Malcherek, A. (2007b). *Sedimenttransport und Morphodynamik*. Ed. by Universität der Bundeswehr München.

Manes, C., D. Pokrajac, I. McEwan, and V. Nikora (2009). "Turbulence structure of open channel flows over permeable and impermeable beds: A comparative study". In: *Physics of Fluids* 21.12, p. 125109.

Mantz, P. A. (1977). "Incipient Transport of Fine Grains and Flakes by Fluids: Extended Shields Diagram". In: *Journal of the Hydraulics Division* 103.6, pp. 601–615.

Maquignon, N. (2017). *Everything you need to know about the Lattice Boltzmann Method*. Ed. by C. Rusu.

McLaughlin, J. B. (1991). "Inertial migration of a small sphere in linear shear flows". In: *Journal of Fluid Mechanics* 224, pp. 261–274.

McLaughlin, J. B. (1993). "The lift on a small sphere in wall-bounded linear shear flows". In: *Journal of Fluid Mechanics* 246.1, pp. 249–265.

Mei, R. (1992). "An approximate expression for the shear lift force on a spherical particle at finite reynolds number". In: *International Journal of Multiphase Flow* 18.1, pp. 145–147.

Mendoza, C. and D. Zhou (1992). "Effects of Porous Bed on Turbulent Stream Flow above Bed". In: *Journal of Hydraulic Engineering* 118.9, pp. 1222–1240.

Meng, J.-h. (2004). "Schwarmverhalten von Steinschüttungen in Wasser". Dissertation. Berlin: Technische Universität Berlin.

Menter, F. R. (1992). *Improved Two-Equation k-omega Turbulence Models for Aerodynamic Flows*. Ed. by NASA. Moffett Field, California.

Menter, F. R. (1994). "Two-equation eddy-viscosity turbulence models for engineering applications". In: *AIAA Journal* 32.8, pp. 1598–1605.

Menter, F. R., M. Kuntz, and R. B. Langtry (2003). "Ten years of industrial experience with the SST turbulence model". In: *Turbulence, Heat and Mass Transfer 4*. Ed. by K. Hanjalić, Y. Nagano, and M. J. Tummers. Vol. 4. Turbulence, Heat and Mass Transfer. New York: Begell House.

Michael, M., F. Vogel, and B. Peters (2015). "DEM–FEM coupling simulations of the interactions between a tire tread and granular terrain". In: *Computer Methods in Applied Mechanics and Engineering* 289, pp. 227–248.

Michaelides, E., C. T. Crowe, and J. D. Schwarzkopf (2016). *Multiphase flow handbook*. Mechanical and Aerospace Engineering Series. Boca Raton: CRC Press.

Michaelides, E. and A. Roig (2011). "A reinterpretation of the Odar and Hamilton data on the unsteady equation of motion of particles". In: *AIChE Journal* 57.11, pp. 2997–3002.

Miedema, S. A. (2010). "Constructing the Shields Curve - A new Theoretical Approach and its Applications". In: *19th World Dredging Congress (WODCON XIX)*. Ed. by J. Dobson. Red Hook, NY: Curran, pp. 732–750.

Miedema, S. A. (2016). *Slurry Transport: Fundamentals, A Historical Overview & The Delft Head Loss & Limit Deposit Velocity Framework*.

Mindlin, R. D. and H. Deresiewicz (1953). "Elastic Spheres in Contact Under Varying Oblique Forces". In: *Journal of Applied Mechanics* 20.1, pp. 327–344.

Mollinger, A. M. and F. T. M. Nieuwstadt (1996). "Measurement of the lift force on a particle fixed to the wall in the viscous sublayer of a fully developed turbulent boundary layer". In: *Journal of Fluid Mechanics* 316.-1, p. 285.

Mollinger, A. M., F. T. M. Nieuwstadt, and J. M. Bessem (1995). "A new device to measure the lift force on a particle in the viscous sublayer". In: *Measurement Science and Technology* 6.2, pp. 206–213.

Morad, M. R. and A. Khalili (2009). "Transition layer thickness in a fluid-porous medium of multi-sized spherical beads". In: *Experiments in Fluids* 46.2, pp. 323–330.

Musall, M. (2011). "Mehrdimensionale hydrodynamisch-numerische Modelle im praxisorientierten und operationellen Einsatz". Dissertation. Karlsruhe: Karlsruher Institut für Technologie.

Nair, A. K. and A. Sameen (2015). "Experimental Study of Slip Flow at the Fluid-porous Interface in a Boundary Layer Flow". In: *Procedia IUTAM* 15, pp. 293–299.

Nakagawa, H., T. Tsujimoto, and Y. Shimizu (1988). "Velocity profile of flow over rough permeable bed". In: *Proceedings of the 6th APD-IAHR Congress*. Vol. 2, pp. 449–456.

Nakagawa, H. and I. Nezu (1993). *Turbulence in Open Channel Flows*. 1st ed. IAHR Monographs. Rotterdam: CRC Press.

Neale, G. and W. Nader (1974). "Practical significance of brinkman's extension of darcy's law: Coupled parallel flows within a channel and a bounding porous medium". In: *The Canadian Journal of Chemical Engineering* 52.4, pp. 475–478.

Neill, C. A. and M. S. Yalin (1969). "Quantitative Definition of Beginning of Bed Movement". In: *Journal of the Hydraulics Division* 95.1, pp. 585–588.

Nezu, I. (1977). "Turbulent structure in open-channel flow". PhD Thesis. Kyoto, Japan: Department of Civil Engineering.

Nguyen, V. P. (2014). *Material point method: basics and applications*. Cardiff.

Nield, D. A. (2009). "The Beavers–Joseph Boundary Condition and Related Matters: A Historical and Critical Note". In: *Transport in Porous Media* 78.3, pp. 537–540.

Nield, D. A. and A. Bejan (2017). *Convection in porous media*. Fifth edition. Cham: Springer International Publishing.

Nikuradse, J. (1933). *Strömungsgesetze in rauhen Rohren*. Vol. 361. Verein deutscher Ingenieure - Forschungsheft. Berlin: VDI-Verlag.

Nortek (2017). *Vectrino Profiler*.

Nosewicz, S., J. Rojek, M. Chmielewski, K. Pietrzak, and D. Lumelskyj (2017). "Application of the Hertz formulation in the discrete element model of pressure-assisted sintering". In: *Granular Matter* 19.1, p. 235.

Nozaki, F. (2016). *CFD with a mission: fvOptions meanVelocityForce*. caefn.com.

O'Sullivan, C. (2011). *Particulate discrete element modelling: A geomechanics perspective*. 1st ed. Applied geotechnics. London: Taylor & Francis.

Ochoa-Tapia, J. and S. Whitaker (1995). "Momentum transfer at the boundary between a porous medium and a homogeneous fluid—I. Theoretical development". In: *International Journal of Heat and Mass Transfer* 38.14, pp. 2635–2646.

Odar, F. and W. S. Hamilton (1964). "Forces on a sphere accelerating in a viscous fluid". In: *Journal of Fluid Mechanics* 18.2, p. 302.

Oesterlé, B. and T. B. Dinh (1998). "Experiments on the lift of a spinning sphere in a range of intermediate Reynolds numbers". In: *Experiments in Fluids* 25.1, pp. 16–22.

Oseen, C. W. (1927). *Neuere Methoden und Ergebnisse in der Hydrodynamik*. Vol. 1. Mathematik und ihre Anwendungen. Leipzig: Akademische Verlagsgesellschaft m. b. H.

Paladino, E. E. and C. R. Maliska (2004). "Virtual mass in accelerated bubbly flows". In: *Proceedings of 4th European Thermal Sciences*. Ed. by K. Cornwell and P. Kew.

Park, K. M., H. S. Yoon, and M. I. Kim (2018). "CFD-DEM based numerical simulation of liquid-gas-particle mixture flow in dam break". In: *Communications in Nonlinear Science and Numerical Simulation* 59, pp. 105–121.

Passalacqua, A. and R. O. Fox (2011). "Implementation of an iterative solution procedure for multi-fluid gas–particle flow models on unstructured grids". In: *Powder Technology* 213.1-3, pp. 174–187.

Pirker, S., D. Kahrimanovic, and C. Goniva (2011). "Improving the applicability of discrete phase simulations by smoothening their exchange fields". In: *Applied Mathematical Modelling* 35.5, pp. 2479–2488.

Plenker, D. (2015). "Expansion of CFD-modelling by the CFD-DEM Method for simulating erosion processes". In: *Morphodynamics 2015*. Ed. by J. Grabe. Vol. 33. Veröffentlichungsreihe des Instituts für Geotechnik und Baubetrieb der TU Hamburg-Harburg. Hamburg, pp. 125–141.

Plenker, D. and J. Grabe (2016a). "Simulation of sand particle transport by coupled CFD-DEM: First investigations". In: *Scour and Erosion*. Ed. by J. Harris, R. Whitehouse, and S. Moxon. London, UK: CRC Press - Taylor & Francis Group, pp. 109–118.

Plenker, D., E. Heins, and J. Grabe (2016b). "Shape Optimisation of Model Scale Geotextile Sand Containers (GSC) Regarding Sinking Behaviour: First Results of Physical Model Tests". In: *Proceedings of the ASME 35th International Conference on Ocean, Offshore and Arctic Engineering 2016*. New York, N.Y.: The American Society of Mechanical Engineers.

Pope, N. D., J. Widdows, and M. D. Brinsley (2006). "Estimation of bed shear stress using the turbulent kinetic energy approach—A comparison of annular flume and field data". In: *Continental Shelf Research* 26.8, pp. 959–970.

Pope, S. B. (2000). *Turbulent flows*. Cambridge and New York: Cambridge University Press.

Postma, H. (1967). “Sediment transport and sedimentation in the estuarine environment”. In: *Estuaries*. Ed. by G. H. Lauff. Vol. 83. American Association for the Advancement of Science Publication. Washington D.C., pp. 158–179.

Powers, M. C. (1953). “A New Roundness Scale for Sedimentary Particles”. In: *SEPM Journal of Sedimentary Research* Vol. 23.

Prandtl, L. (1905). “Über Flüssigkeitsbewegung bei sehr kleiner Reibung”. In: *Verhandlungen des Dritten Internationalen Mathematiker-Kongresses, Heidelberg 1904*. Ed. by A. Krazer. Leipzig: B. G. Teubner, pp. 484–491.

Radl, S., B. C. Gonzales, C. Goniva, and S. Pirker (2014). “State of the art in mapping schemes for dilute and dense Euler-Lagrange-Simulations”. In: *Progress in applied CFD*. Ed. by J. E. Olsen and S. T. Johansen. SINTEF proceedings. Oslo: SINTEF Academic Press, pp. 103–112.

Raffel, M., C. E. Willert, F. Scarano, C. J. Kähler, S. T. Wereley, and J. Kompenhans (2017). *Particle image velocimetry: A Practical Guide*. 3rd. New York NY: Springer International Publishing AG.

Reeks, M. W. and S. McKee (1984). “The dispersive effects of Basset history forces on particle motion in a turbulent flow”. In: *Physics of Fluids* 27.7, p. 1573.

Richardson, J. F. and W. N. Zaki (1954). “Sedimentation and Fluidisation: Part 1”. In: *Transactions of the Institution of Chemical Engineers* 32, pp. 35–53.

Rondon, L., O. Pouliquen, and P. Aussillous (2011). “Granular collapse in a fluid: Role of the initial volume fraction”. In: *Physics of Fluids* 23.7, p. 073301.

Rubinow, S. I. and J. B. Keller (1961). “The transverse force on a spinning sphere moving in a viscous fluid”. In: *Journal of Fluid Mechanics* 11.3, pp. 447–459.

Rumsey, C. (2015). *Turbulence Modeling Resource: The Menter Shear Stress Transport Turbulence Model*. Ed. by NASA.

Saffman, P. G. (1965). “The lift on a small sphere in a slow shear flow”. In: *Journal of Fluid Mechanics* 22.2, pp. 385–400.

Saffman, P. G. (1968). “The lift on a small sphere in a slow shear flow - Corrigendum”. In: *Journal of Fluid Mechanics* 31.03, p. 624.

Salinger, A. G., R. Aris, and J. J. Derby (1994). “Finite element formulations for large-scale, coupled flows in adjacent porous and open fluid domains”. In: *International Journal for Numerical Methods in Fluids* 18.12, pp. 1185–1209.

Schiller, L. and A. Z. Naumann (1933). “Über die grundlegenden Berechnungen bei der Schwerkraftaufbereitung”. In: *Verein Deutscher Ingenieure* 77, pp. 318–320.

Schlichting, H. and K. Gersten (2006). *Grenzschicht-Theorie*. 10., überarb. Aufl. Berlin [u.a.]: Springer.

Schlichting, H. and K. Gersten (2017). *Boundary-Layer theory*. Ninth edition. Berlin, Heidelberg: Springer Berlin Heidelberg.

Schmeeckle, M. W. and J. M. Nelson (2003). “Direct numerical simulation of bedload transport using a local, dynamic boundary condition”. In: *Sedimentology* 50.2, pp. 279–301.

Schmeeckle, M. W., J. M. Nelson, and R. L. Shreve (2007). “Forces on stationary particles in near-bed turbulent flows”. In: *Journal of Geophysical Research* 112.F2.

Schmoll, R. (2015). *Co-Simulation und Solverkopplung: Analyse komplexer multiphysikalischer Systeme*. Vol. 3/2015. Berichte des Instituts für Mechanik. Kassel, Hess: Kassel University Press.

Schöberl, F. (1990). "Erosionsprozesse in Gerinnen: Teil 1". PhD thesis. Insbruck, Austria: Universität Insbruck.

Shields, A. F. (1936). *Anwendung der Ähnlichkeitsmechanik und der Turbulenzforschung auf Geschiebebewegung*. Vol. 26. Mitteilungen der Preußischen Versuchsanstalt für Wasserbau und Schiffbau. Berlin: Eigenverlage der Preußischen Versuchsanstalt für Wasserbau und Schiffbau.

Silbert, L. E., D. Ertaş, G. S. Grest, T. C. Halsey, D. Levine, and S. J. Plimpton (2001). "Granular flow down an inclined plane: Bagnold scaling and rheology". In: *Physical Review E* 64.5.

Sommerfeld, M. (2000). *Theoretical and Experimental Modelling of Particulate Flows: Overview and Fundamentals*. Ed. by Martin-Luther-Universität Halle-Wittenberg. Halle (Saale), Germany.

Sommerfeld, M. (1996). *Modellierung und numerische Berechnung von partikelbeladenen turbulenten Strömungen mit Hilfe des Euler-Lagrange-Verfahrens*. Berichte aus der Strömungstechnik. Aachen: Shaker.

Soulsby, R. (1997). *Dynamics of marine sands: A manual for practical applications*. Thomas Telford.

Stanford, H. (2018). "Numerische Methoden in der Geotechnik: Einführung in die numerische Simulation des Bodens: Vorlesungsskript". Vorlesungsskript.

Stein, E., R. d. Borst, and T. J. R. Hughes (2004). *Encyclopedia of computational mechanics*. Chichester, West Sussex: John Wiley.

Stoesser, T., J. Fröhlich, and W. Rodi (2007). "Turbulent Open-Channel low over a permeable bed". In: *Harmonizing the demands of art and nature in hydraulics*. Venezia: CORILA.

Stokes, G. G. (1851). "On the effect of the internal friction of fluids on the motion of pendulums". In: *Transactions of the Cambridge Philosophical Society* 9, pp. 8–86.

Sun, X. and M. Sakai (2015). "Three-dimensional simulation of gas–solid–liquid flows using the DEM–VOF method". In: *Chemical Engineering Science* 134, pp. 531–548.

Sundborg, A. (1956). "The River Klaralven: A Study of Fluvial Processes". In: *Geografiska Annaler* 38.3, p. 238.

Swamee, P. K. (1993). "Generalized Inner Region Velocity Distribution Equation". In: *Journal of Hydraulic Engineering* 119.5, pp. 651–656.

Takemura, F. and J. Magnaudet (2003). "The transverse force on clean and contaminated bubbles rising near a vertical wall at moderate Reynolds number". In: *Journal of Fluid Mechanics* 495, pp. 235–253.

Tanaka, T., K. Yamagata, and Y. Tsuji (1990). "Experiment of fluid forces on a rotating sphere and spheroid". In: *2nd KSME-JSME Fluids Engineering Conference*, p. 366.

Thielicke, W. (2014). "The flapping flight of birds: Analysis and application". PhD Thesis. Groningen: University of Groningen.

Thielicke, W. and E. J. Stamhuis (2014). "PIVlab – Towards User-friendly, Affordable and Accurate Digital Particle Image Velocimetry in MATLAB". In: *Journal of Open Research Software* 2, pp. 1–10.

Tsuji, Y., T. Tanaka, and T. Ishida (1992). "Lagrangian numerical simulation of plug flow of cohesionless particles in a horizontal pipe". In: *Powder Technology* 71.3, pp. 239–250.

Vafai, K. and S. J. Kim (1990). "Fluid mechanics of the interface region between a porous medium and a fluid layer—an exact solution". In: *International Journal of Heat and Fluid Flow* 11.3, pp. 254–256.

Van der Hoef, M. A., M. Ye, M. van Sint Annaland, A. T. Andrews IV, S. Sundaresan, and J. A. M. Kuipers (2006). "Multiscale modeling of gas-fluidized beds". In: *Advances in chemical engineering*. Ed. by G. B. Marin. Advances in chemical engineering. Amsterdam and Boston: Elsevier, pp. 65–149.

Van Gent, M. R. A. (1993). "Stationary and oscillatory flow through coarse porous media". In: *Communications on hydraulic and geotechnical engineering*. Ed. by Division for Hydraulic and Geotechnical Engineering. Delft.

Van Rijn, L. C. (1984). "Sediment Transport, Part I: Bed Load Transport". In: *Journal of Hydraulic Engineering* 110.10, pp. 1431–1456.

Van Wachem, B. G. (2000). "Derivation, Implementation, and Validation of Computer Simulation Models for Gas-Solid Fluidized Beds". Dissertation. Delft: Technische Universität Delft.

Vangoe, M., S. Pirker, and T. Lichtenegger (2017). "CFD-DEM modelling of blast furnance tapping". In: *Progress in applied CFD - CFD2017*. Ed. by J. E. Olsen and S. T. Johansen. SINTEF proceedings. Oslo: SINTEF Academic Press, pp. 515–520.

Vanoni, V. A. (1975). "Sedimentation engineering". In: *ASCE Manuals and Reports on Engineering Practice* 54.

Venier, C., S. M. Damian, D. Ramajo, and N. Nigro (2013). "Numerical Analysis of Multiphase Solid-Gas Flow with Eulerian Models and Kinetic Theory Closure". In: *Macánica Computacional* 32, pp. 1849–1862.

Viggen, E. M. (2014). "The lattice Boltzmann method: Fundamentals and acoustics". PhD Thesis. Trondheim: Norwegian University of Sience and Technology.

Wen, C. Y. and Y. H. Yu (1966). "Mechanics of fluidization". In: *Chemical Engineering Progress Symposium Series*, pp. 100–111.

White, D. J., W. A. Take, and M. D. Bolton (2001). "Measuring soil deformation in geotechnical models using digital images and PIV analysis". In: *Computer methods and advances in geomechanics*. Ed. by C. S. Desai, T. Kundu, and S. Harpalani. Vol. 1. Rotterdam and Brookfield: A.A. Balkema, pp. 997–1002.

White, F. M. (1974). *Viscous fluid flow*. 2nd ed. New York: McGraw-Hill.

Wiberg, P. L. and J. D. Smith (1987). "Calculations of the critical shear stress for motion of uniform and heterogeneous sediments". In: *Water Resources Research* 23.8, pp. 1471–1480.

Wilcox, D. C. (1988). "Re-assessment of the scale-determining equation for advanced turbulence models". In: *American Institute of Aeronautics and Astronautics Journal* 26.11, pp. 1299–1310.

Wilcox, D. C. (1991). "A half century historical review of the k-omega model". In: *29th Aerospace Sciences Meeting*. Ed. by American Institute of Aeronautics and Astronautics. Reston, Virigina: American Institute of Aeronautics and Astronautics.

Wilcox, D. C. (1994). *Turbulence modeling for CFD*. La Canada: DCW Industries.

Winkler, P., M. R. Saheli Sadaghiani, H. Jentsch, and K. J. Witt (2014). "Granular packing generation using DEM – Modified Force-Biased-Algorithm". In: *Proceedings 7th International Conference on Scour and Erosion*. Ed. by L. Cheng, S. Draper, and H. An. Leiden, Netherlands: CRC Press/Balkema, pp. 345–349.

Winkler, P., M. R. Salehi Sadaghiani, and K. J. Witt (2015). "Packing Generation using DEM – Comparison of Methods". In: *Morphodynamics 2015*. Ed. by J. Grabe. Vol. 33. Veröffentlichungsreihe des Instituts für Geotechnik und Baubetrieb der TU Hamburg-Harburg. Hamburg, pp. 71–78.

Wittmann, L. (1980). "Filtrations- und Transportphänomene in porösen Medien". Dissertation. Karlsruhe: Universität Fridericiana zu Karlsruhe.

Zagni, A. F. E. and K. V. H. Smith (1976). "Channel Flow Over Permeable Beds of Graded Spheres". In: *Journal of the Hydraulics Division* 102.2, pp. 207–222.

Zanke, U. C. E. (1977). *Berechnung der Sinkgeschwindigkeiten von Sedimenten*. Vol. 46. Mitteilungen des Franzius-Instituts für Wasserbau und Küsteningenieurwesen der Technischen Universität Hannover. Hannover: Franzius-Institut für Wasserbau und Küsteningenieurwesen.

Zanke, U. C. E. (1982). *Grundlagen der Sedimentbewegung*. Hochschultext. Berlin and Heidelberg [u.a.]: Springer.

Zanke, U. C. E. (2001). *Zur Einfluss der Turbulenz auf den Beginn der Sedimentbewegung*. Vol. Heft 120. Mitteilungen. Darmstadt: Technische Universität Darmstadt.

Zanke, U. C. E. (2003). "On the influence of turbulence on the initiation of sediment motion". In: *International Journal of Sediment Research* 18.1, pp. 17–31.

Zeng, L., S. Blachandar, and P. Fischer (2005). "Wall-induced forces on a rigid sphere at finite Reynolds number". In: *Journal of Fluid Mechanics* 536, pp. 1–25.

Zeng, L., F. Najjar, S. Balachandar, and P. Fischer (2009). "Forces on a finite-sized particle located close to a wall in a linear shear flow". In: *Physics of Fluids* 21.3, p. 033302.

Zeng, Z. and R. Grigg (2006). "A Criterion for Non-Darcy Flow in Porous Media". In: *Transport in Porous Media* 63.1, pp. 57–69.

Zhang, J., L.-S. Fan, C. Zhu, R. Pfeffer, and D. Qi (1999). "Dynamic behavior of collision of elastic spheres in viscous fluids". In: *Powder Technology* 106.1-2, pp. 98–109.

Zhang, Q. and A. Prosperetti (2009). "Pressure-driven flow in a two-dimensional channel with porous walls". In: *Journal of Fluid Mechanics* 631, p. 1.

Zhang, W., R. Noda, and M. Horio (2005). "Evaluation of lubrication force on colliding particles for DEM simulation of fluidized beds". In: *Powder Technology* 158.1-3, pp. 92–101.

Zhang, X., Z. Chen, and Y. Liu (2016). *The material point method: A continuum-based particle method for extreme loading cases / Xiong Zhang, Zhen Chen, Yan Liu*. Amsterdam: Academic Press.

Zhao, J. and T. Shan (2013). "Coupled CFD–DEM simulation of fluid–particle interaction in geomechanics". In: *Powder Technology* 239, pp. 248–258.

Zhou, H., Z. Luo, T. Zhang, Y. You, H. Li, and Z. Zou (2016). "Influence of Rolling Friction Coefficient on Inter-Particle Percolation in a Packed Bed by Discrete Element Method". In: *Archives of Metallurgy and Materials* 61.4.

Zhou, Y. C., B. D. Wright, R. Y. Yang, B. H. Xu, and A. B. Yu (1999). "Rolling friction in the dynamic simulation of sandpile formation". In: *Physica A: Statistical Mechanics and its Applications* 269.2-4, pp. 536–553.

Zhou, Z. Y., S. B. Kuang, K. W. Chu, and A. B. Yu (2010). "Discrete particle simulation of particle–fluid flow: Model formulations and their applicability". In: *Journal of Fluid Mechanics* 661, pp. 482–510.

Zhou, Z. Y., A. B. Yu, and S. K. Choi (2011). "Numerical simulation of the liquid-induced erosion in a weakly bonded sand assembly". In: *Powder Technology* 211.2-3, pp. 237–249.

Zhu, H. P., Z. Y. Zhou, R. Y. Yang, and A. B. Yu (2007). "Discrete particle simulation of particulate systems: Theoretical developments". In: *Chemical Engineering Science* 62.13, pp. 3378–3396.

Zippe, H. J. and W. H. Graf (1983). "Turbulent boundary-layer flow over permeable and non-permeable rough surfaces". In: *Journal of Hydraulic Research* 21.1, pp. 51–65.

Appendix

A Nomenclature

Acronyms

CEL	Coupled Eulerian-Lagrangian
CFD	Computational Fluid Dynamics
CSF	Corey shape factor
DCC	Direct Cross Correlation
DEM	Discrete Element Method
DFT	Discrete Fourier Transform
FDM	Finite Difference Methode
FEM	Finite Element Method
FVM	Finite Volume Method
LBM	Lattice-Boltzmann Method
MPM	Material Point Method
PIV	Particle Image Velocimetry
RANS	Reynolds-averaged Navier-Stokes
SPH	Smoothed Particle Hydrodynamics
VANS	Volume-averaged Navier-Stokes

Dimensionless Characteristic Numbers

Re	Reynolds number
Re^*	boundary Reynolds number of Shields' diagram
Re_G	particle Reynolds number of shear
Re_ω	particle Reynolds number of rotation
Re_{p,α_f}	particle Reynolds number in a particle packing
Re_p	particle Reynolds number of translation
Ma	Mach number

Sl	Strouhal number	

Greek Variables or Constants

α	angle of wall inclination	$^\circ$
α_f	void fraction or fluid phase volume fraction	–
α_p	particle fraction	–
β	slope angle for earth pressure evaluation	$^\circ$
δ	thickness of the boundary layer	m
δ_a	active wall friction angle	$^\circ$
δ_v	thickness of the viscous sublayer	m
$\delta_{b,tr}$	thickness of the transition layer inside porous media	m
ϵ	dissipation rate	$\mathrm{m^2\,s^{-3}}$
η	dynamic viscosity	Pa s
κ	von Kármán constant	–
μ_r	coefficient of rolling friction	–
μ_s	coefficient of Coulomb friction	–
ν_p	Poisson number	–
ν_t	turbulent viscosity	$\mathrm{m^2\,s^{-1}}$
ν_f	kinematic viscosity	$\mathrm{m^2\,s^{-1}}$
ω	specific dissipation rate	$\mathrm{s^{-1}}$
ω_f	fluid rotational velocity	$\mathrm{m\,s^{-1}}$
ω_p	particle rotational velocity	$\mathrm{m\,s^{-1}}$
ω_r	relative rotational velocity between fluid and particle	$\mathrm{m\,s^{-1}}$
ϕ	angle of repose	$^\circ$
ψ	pivot angle	$^\circ$
ρ_f	fluid density	$\mathrm{kg\,m^{-3}}$
ρ_p	particle density	$\mathrm{kg\,m^{-3}}$

ρ_p	particle density	$\mathrm{kg\,m^{-3}}$
Θ^*	Shields' parameter	–
σ_s	standard deviation of a sample	–
τ	shear stress tensor	$\mathrm{N\,m^{-2}}$
τ_0	wall or bed shear stress tensor	$\mathrm{N\,m^{-2}}$
τ_t	turbulent shear stress tensor	$\mathrm{N\,m^{-2}}$
τ_v	viscous shear stress tensor	$\mathrm{N\,m^{-2}}$
Δt	timestep width of a simulation	s
ε_G	ratio between the shear rate and the slip velocity	–
φ'	effective friction angle	°
φ_r	angle of rolling resistance	°
ϑ	slip surface angle	°
ϑ_{ag}	active slip surface angle of earth pressure theory	°
ξ	drag interphase momentum exchange coefficient	$\mathrm{kg\,m^{-3}}$

Roman Variables or Constants

A_c	cross sectional area of a particle exposed to flow	$\mathrm{m^2}$
C	concentration of sediment suspension	–
c_D	dimensionless coefficient of drag force	–
c_M	dimensionless coefficient of torque	–
c_{Ba}	dimensionless coefficient of Basset force	–
$c_{L,Ma}$	dimensionless coefficient of Magnus force	–
$c_{L,Sa}$	dimensionless coefficient of Saffman force	–
c_{VM}	dimensionless coefficient of virtual mass force	–
D^*	dimensionless particle diameter $D^* = \left(\frac{\rho_p - \rho_f}{\rho_f}\frac{g}{\nu_f^2}\right)^{1/3} d_p$	–
D^*_{Iw}	dimensionless particle diameter of Iwagaki	–
D^*_{WS}	dimensionless particle diameter of Wiberg and Smith	–

D_p	particle diameter of an exposed particle	m
d_p	particle diameter	m
d_{50}	particle diameter corresponding to 50% mass fractio	m
D_{smooth}	diffusion coefficient of smoothing	–
E	Youngs modulus	$\text{N}\,\text{mm}^{-2}$
e	coefficient of restitution	–
$E_{\text{kin,rot}}$	rotational kinetic energy	J
E_{kin}	kinetic energy	J
F_B	buoyancy force	N
F_D	drag force	N
F_G	particle weight	N
F_L	lift force	N
F_L^+	dimensionless lift force	–
F_{Ba}	Basset force	N
$F_{G'}$	submerged particle weight	N
$F_{L,Ma}$	Magnus force	N
$F_{L,Sa}$	Saffman force	N
$F_{p,n}$	normal particle contact force	N
$F_{p,t}$	tangential particle contact force	N
F_P	pressure gradient force	N
F_{VM}	virtual mass force	N
G	velocity gradient or shear rate	–
g	gravitational acceleration	$\text{m}\,\text{s}^{-2}$
H	flow depth	m
I_t	turbulence intensity	–
K	permeability	m
k	kinetic energy	$\text{m}^2\,\text{s}^{-2}$

k_f	intrinsic permeability	m^2
k_s	sand roughness by Nikuradse	m
k_s^+	characteristic roughness number	–
K_{pf}	momentum exchange coefficient	$\mathrm{kg\,m^{-3}\,s^{-1}}$
l_m	mixing length of turbulence	m
l_s	acceleration distance for settling velocity	m
l_t	characteristic turbulence length scale	m
l_{smooth}	smoothing length	m
m	mass	kg
n	porosity (in geotechnical terms)	–
p	pressure	Pa
Q_P	Pump rate capacity	$\mathrm{m^3\,h^{-1}}$
r_p	particle radius	m
T	duration	s
t^*	normalised time $t^* = {}^{t}/_{T}$	–
t^+	scaled time in dam break problem	–
t_c	free fall time of particle column $t_c = \sqrt{{}^{H_0}/_{g}}$	s
t_s	acceleration time for settling velocity	s
V_f	freestream velocity	$\mathrm{m\,s^{-1}}$
v_f	fluid velocity	$\mathrm{m\,s^{-1}}$
v_f^*	friction velocity	$\mathrm{m\,s^{-1}}$
v_f^+	dimensionless wall near velocity	–
V_p	particle volume	$\mathrm{m^3}$
v_p	particle translational velocity	$\mathrm{m\,s^{-1}}$
v_s	settling velocity	$\mathrm{m\,s^{-1}}$
V_{cell}	volume of CFD cell	–
v_{filter}	filter velocity	$\mathrm{m\,s^{-1}}$

$v_{f,b}$	mean flow velocity acting on the particle	$\mathrm{m\,s^{-1}}$
$v'_{rms,b}$	maximum turbulent velocity fluctuation on the particle	$\mathrm{m\,s^{-1}}$
v_r	velocity at particle centre relative to fluid velocity at that point	–
$v_{s,c}$	settling velocity in a dense sediment suspension	–
X_0	width of initial volume in dam break problem	m
z^+	dimensionless wall distance	–
Z_0	height of initial volume in dam break problem	m
z_0	roughness length or virtual origin	m

B Investigations on slumping of a particle column - Additional information

B.1 Slumping under dry conditions - Additional figures

Slow collapse - Physical Tests

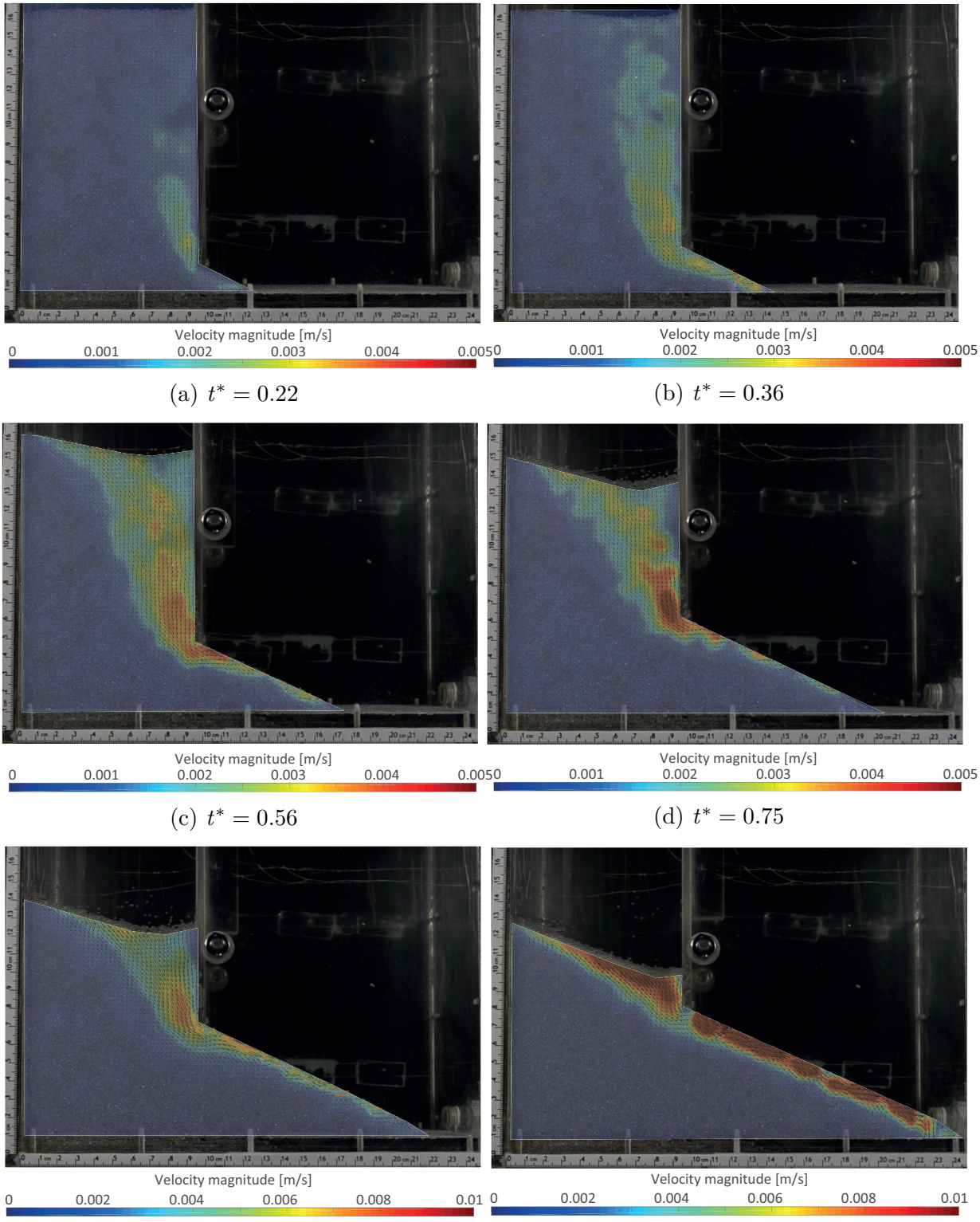

(a) $t^* = 0.22$ (b) $t^* = 0.36$

(c) $t^* = 0.56$ (d) $t^* = 0.75$

(e) $t^* = 0.86$ (f) $t^* = 0.98$

Figure B.1: Slow collapse of the particle column with 1.15 mm glass particles - Characteristic slumping mechanisms for different points in time presented by the velocity magnitude of the PIV analysis

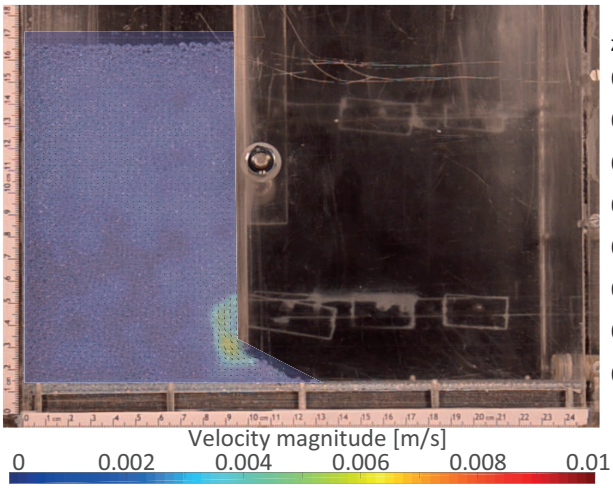

(a) $t^* = 0.22$

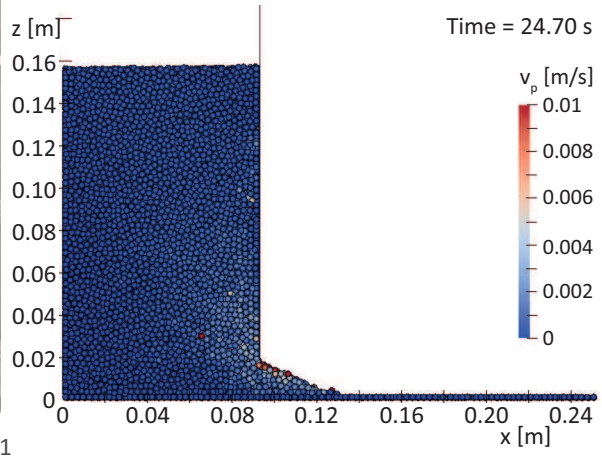

(b) $t^* = 0.22$

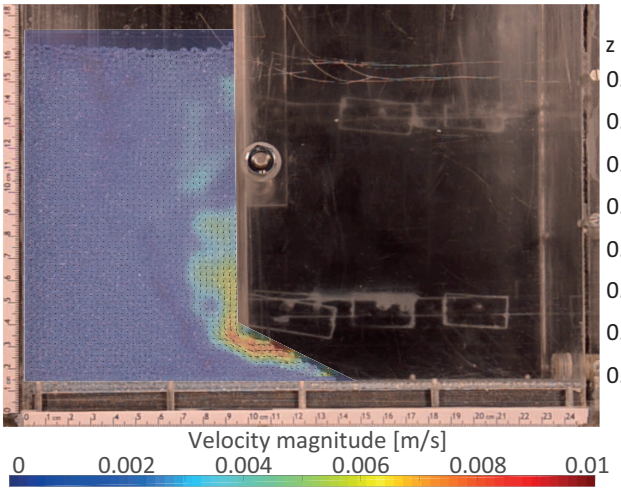

(c) $t^* = 0.32$

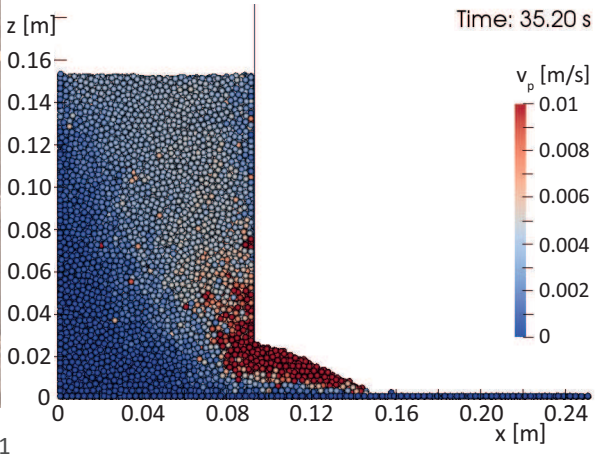

(d) $t^* = 0.32$

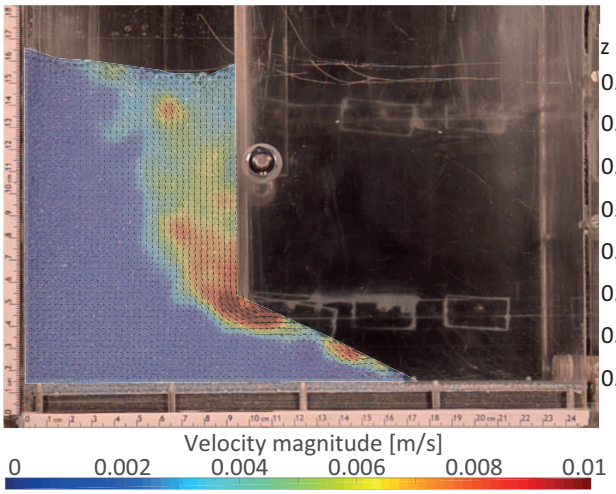

(e) $t^* = 0.51$

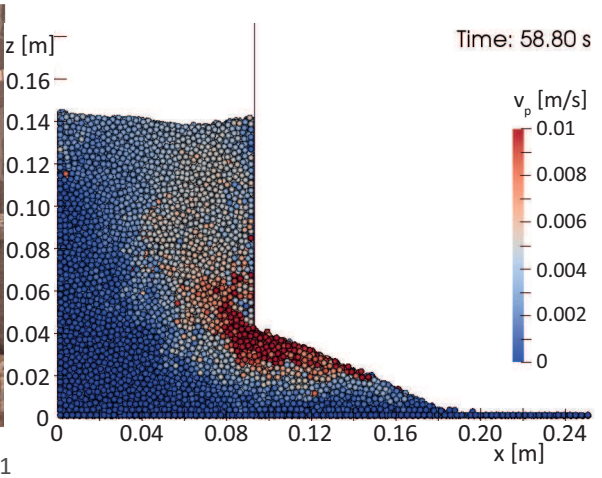

(f) $t^* = 0.53$

Figure B.2: Slow collapse of the particle column with 3 mm glass particles - Comparison between physical tests (left) and simulation for relative time t^* at 0.22, 0.32 and around 0.51

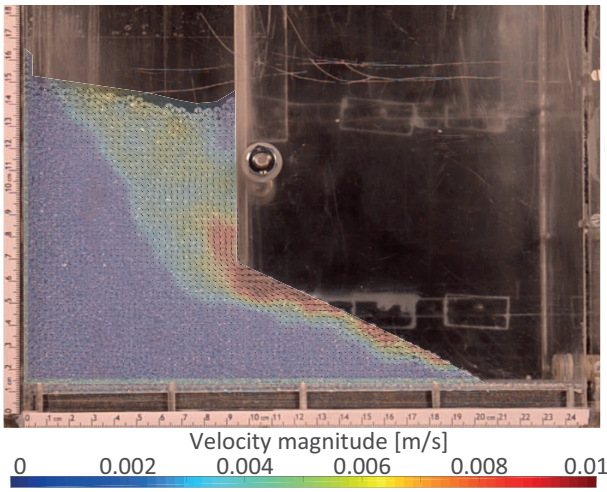

(a) $t^* = 0.70$

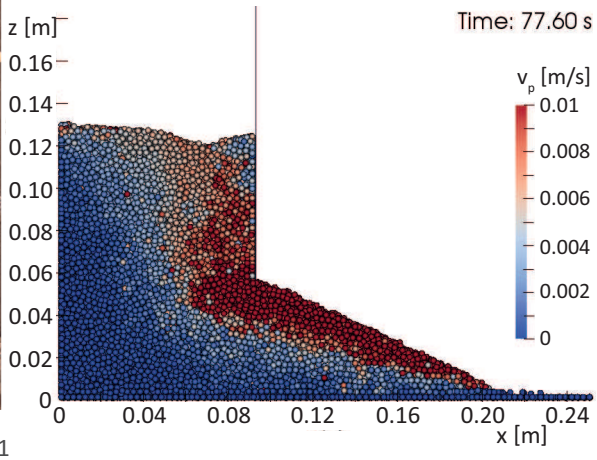

(b) $t^* = 0.70$

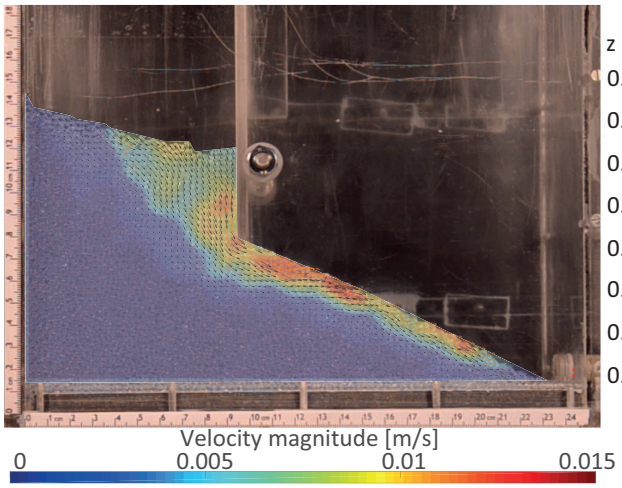

(c) $t^* = 0.83$

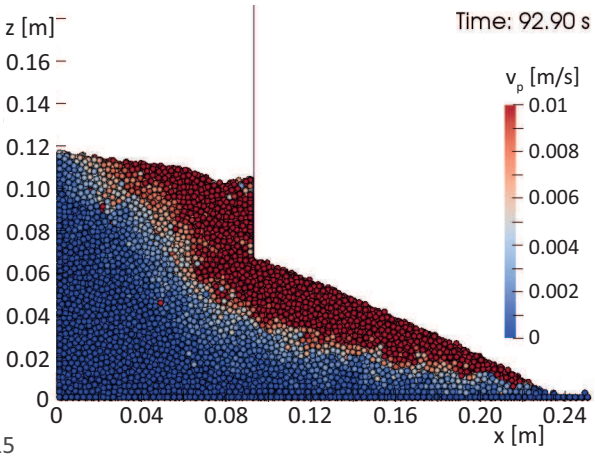

(d) $t^* = 0.84$

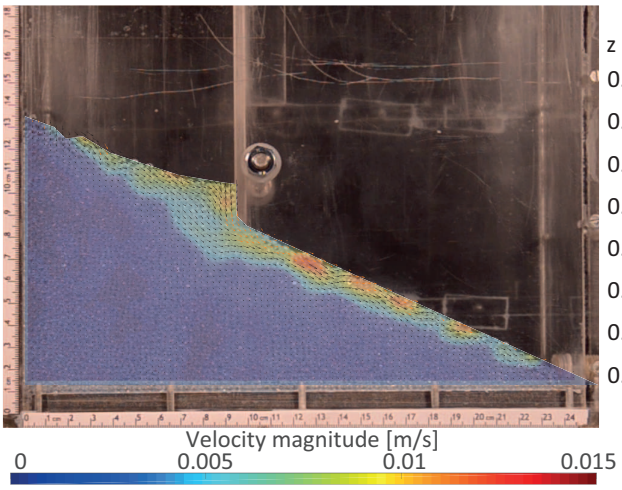

(e) $t^* = 0.90$

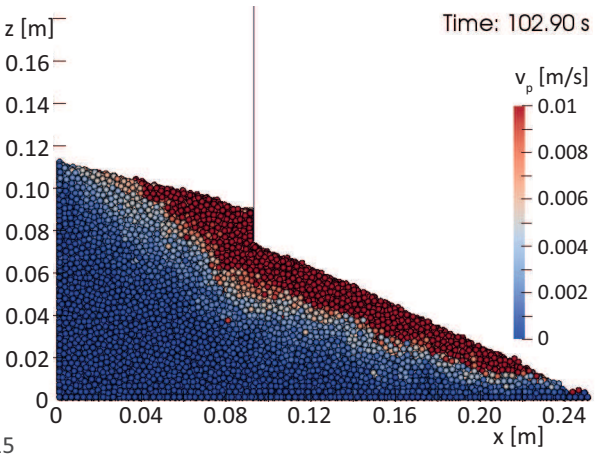

(f) $t^* = 0.93$

Figure B.3: Slow collapse of the particle column with 3 mm glass particles - Comparison between physical tests (left) and simulation for relative time t^* at 0.70, 0.83 and around 0.90

Slow collapse - Simulation

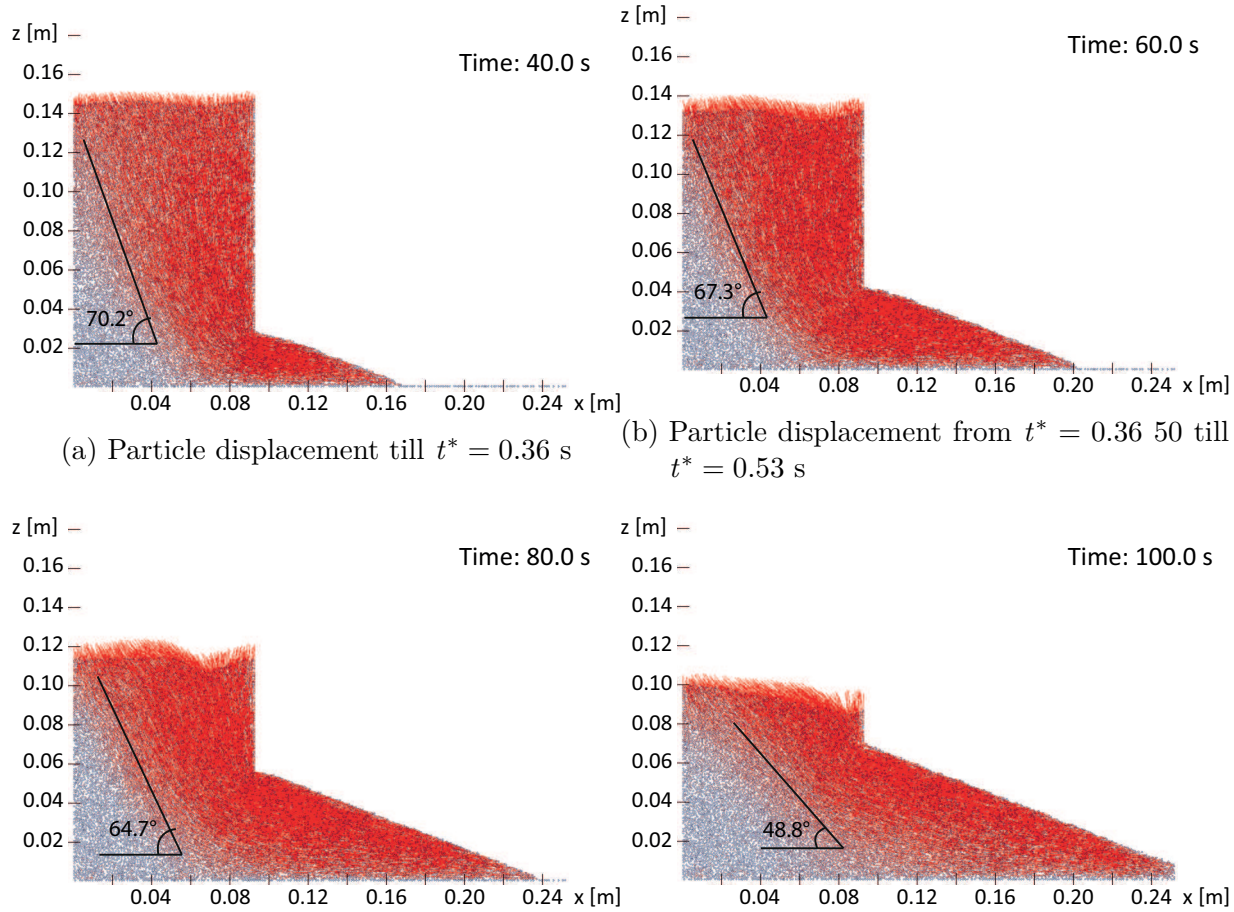

(a) Particle displacement till $t^* = 0.36$ s

(b) Particle displacement from $t^* = 0.36$ 50 till $t^* = 0.53$ s

(c) Particle displacement from $t^* = 0.53$ 70 till $t^* = 0.71$ s

(d) Particle displacement from $t^* = 0.71$ 90 till $t^* = 0.89$ s

Figure B.4: Slow collapse of the particle column with 3 mm glass particles - Particle displacements over the slumping process

Fast collapse - Physical tests

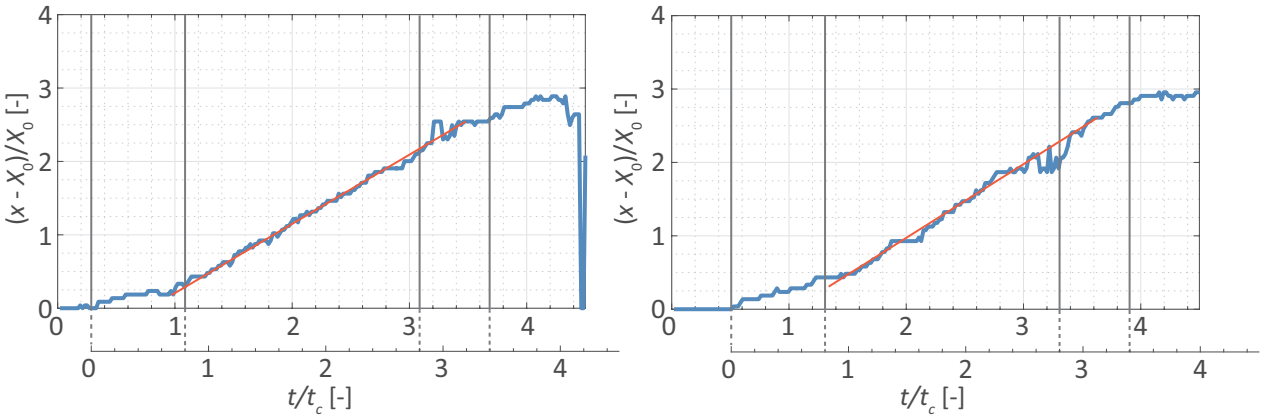

(a) Test 1 with $d_p = 3$ mm

(b) Test 2 with $d_p = 3$ mm

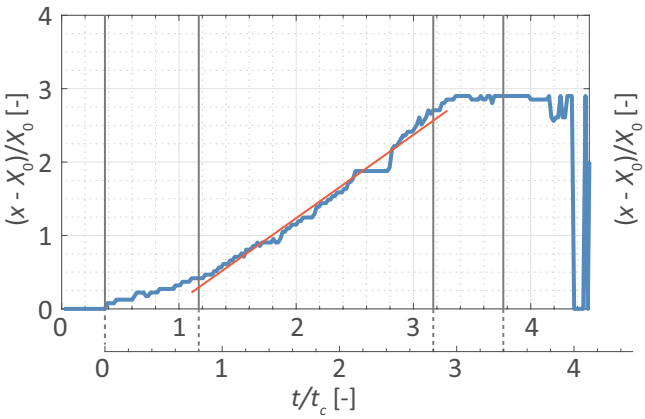

(c) Test 3 with $d_p = 3$ mm

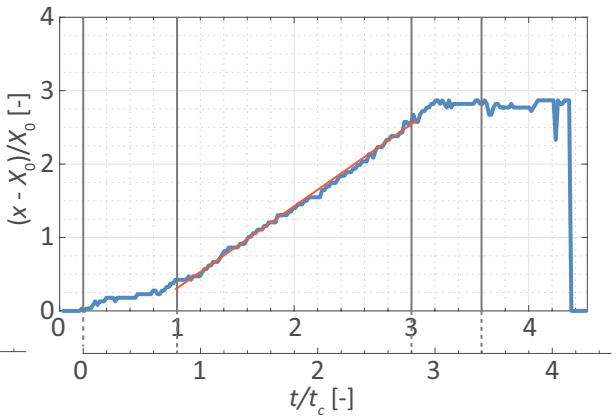

(d) Test 4 with $d_p = 3$ mm

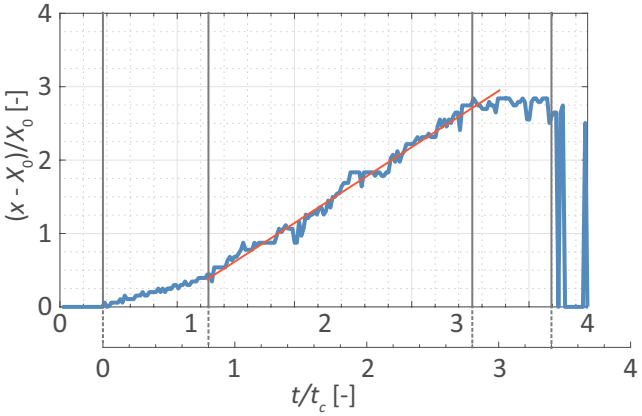

(e) Test 5 with $d_p = 3$ mm

Figure B.5: Fast collapse of the particle column with 3 mm glass particles - Evolution of deposit tip position during the slumping process in the physical tests

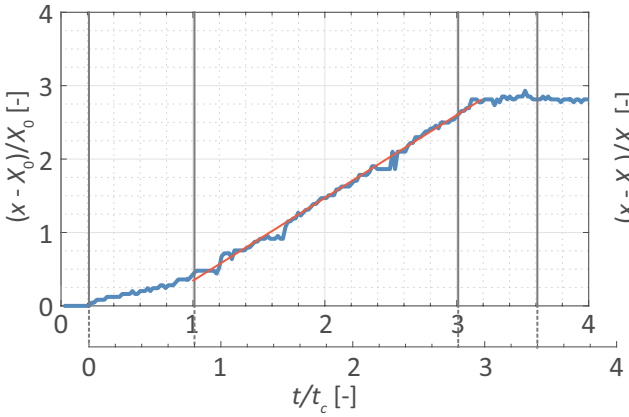

(a) Test 1 with $d_p = 1.15$ mm

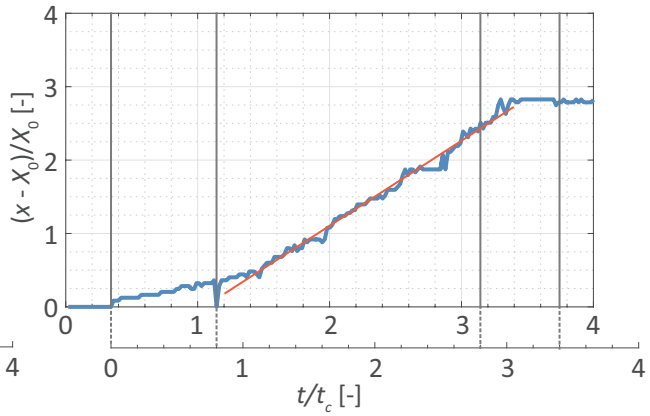

(b) Test 2 with $d_p = 1.15$ mm

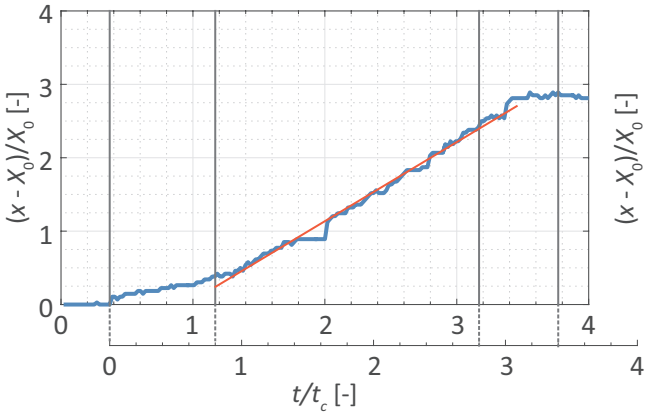

(c) Test 3 with $d_p = 1.15$ mm

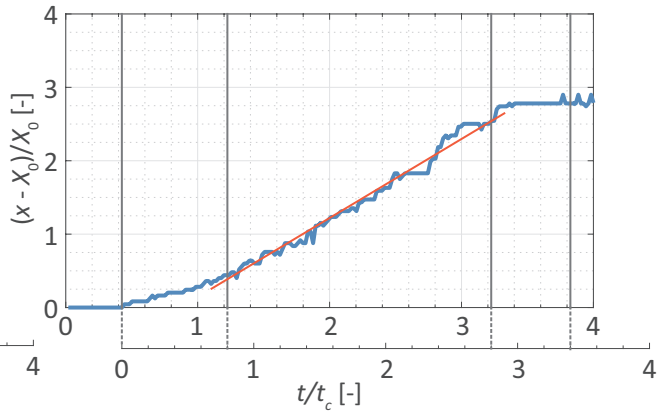

(d) Test 4 with $d_p = 1.15$ mm

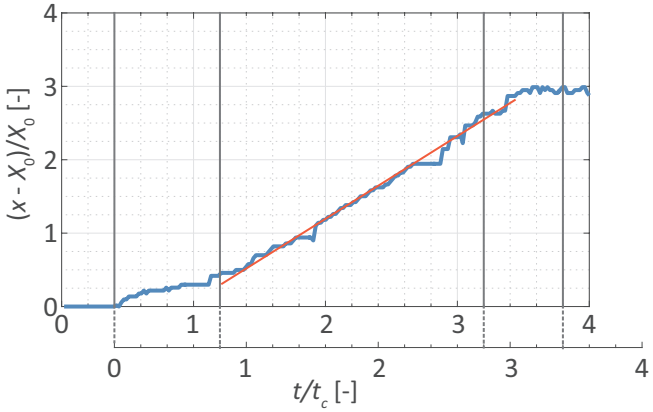

(e) Test 5 with $d_p = 1.15$ mm

Figure B.6: Fast collapse of the particle column with 1.15 mm glass particles - Evolution of the deposit tip over time during the slumping procedure in the physical tests

Fast collapse - Simulation

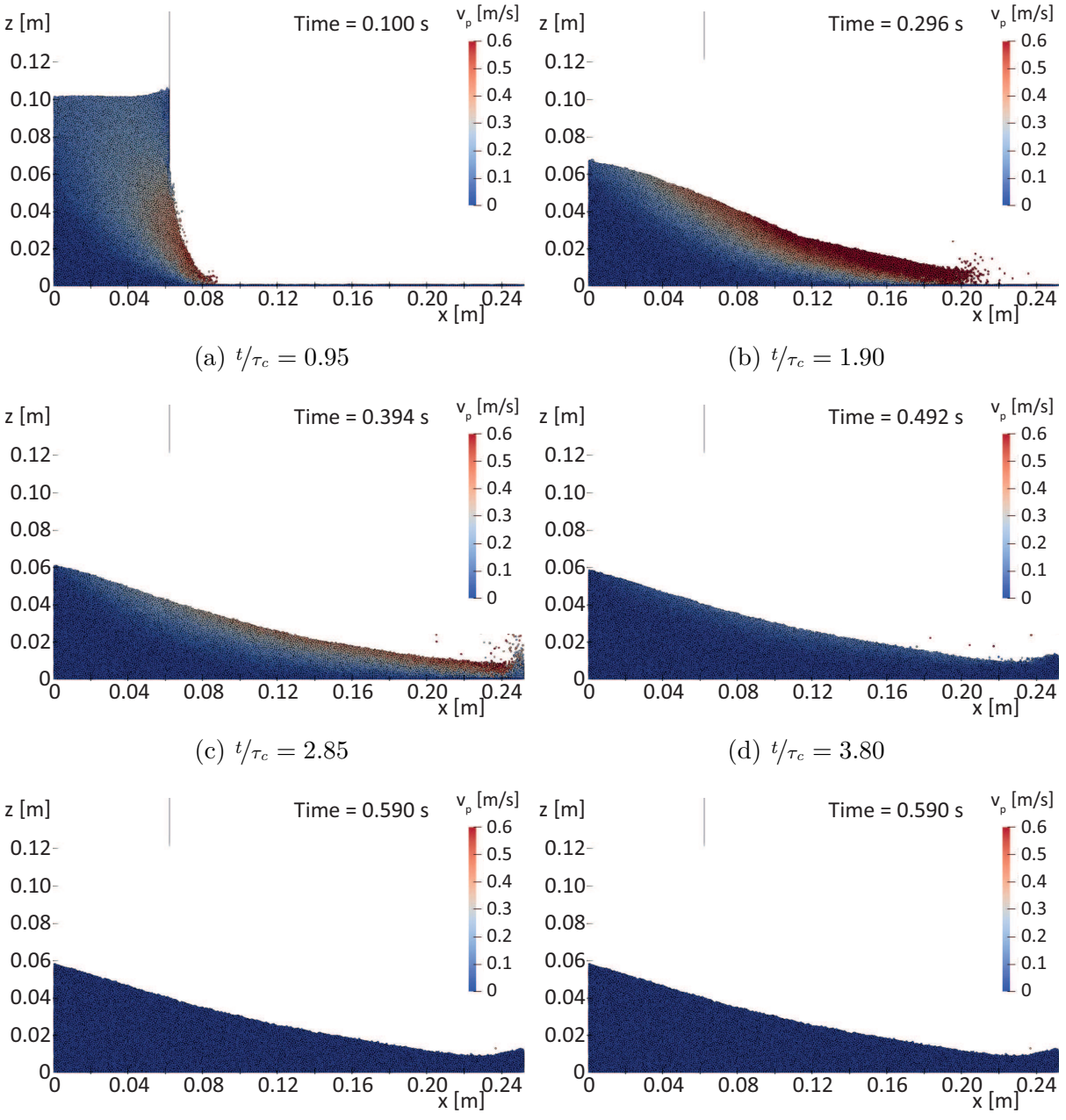

(a) $t/\tau_c = 0.95$

(b) $t/\tau_c = 1.90$

(c) $t/\tau_c = 2.85$

(d) $t/\tau_c = 3.80$

(e) $t/\tau_c = 4.71$

(f) $t/\tau_c = 5.96$

Figure B.7: Fast collapse simulation of the particle column with 1.15 mm glass particles - Characteristic slumping mechanisms over time represented by the particle velocity v_p

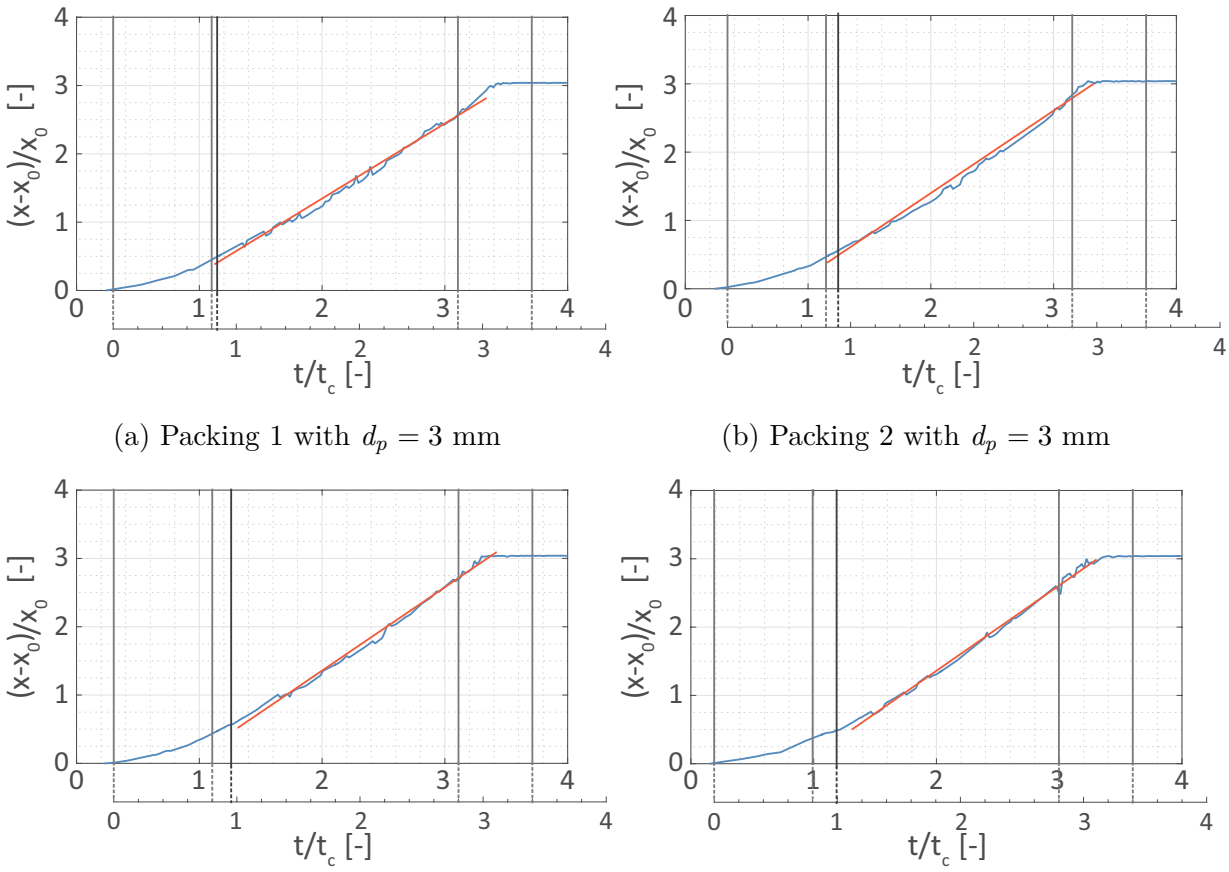

(a) Packing 1 with $d_p = 3$ mm

(b) Packing 2 with $d_p = 3$ mm

(c) Packing 3 with $d_p = 3$ mm

(d) Packing 5 with $d_p = 3$ mm

Figure B.8: Fast collapse simulation of the particle column with 3 mm glass particles - Evolution of deposit tip position over time

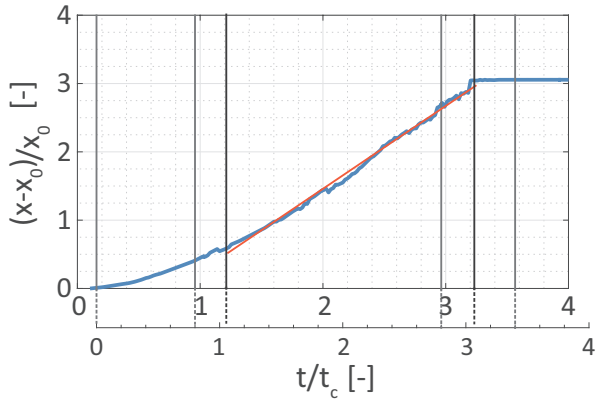

(a) Packing 1 with $d_p = 1.15$ mm

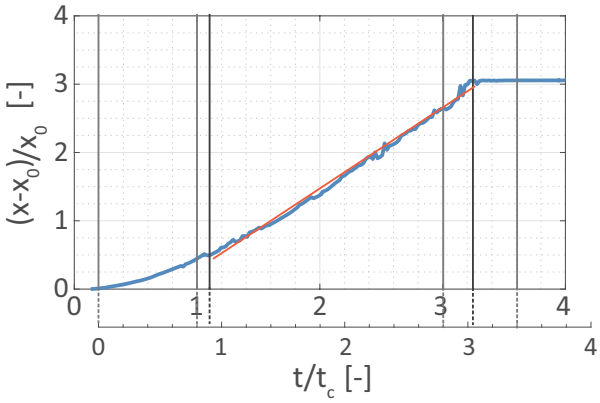

(b) Packing 2 with $d_p = 1.15$ mm

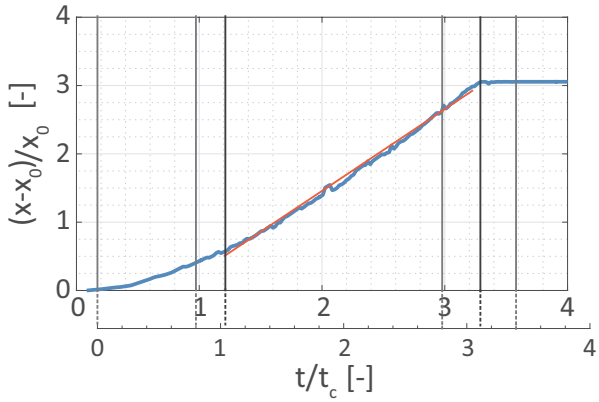

(c) Packing 3 with $d_p = 1.15$ mm

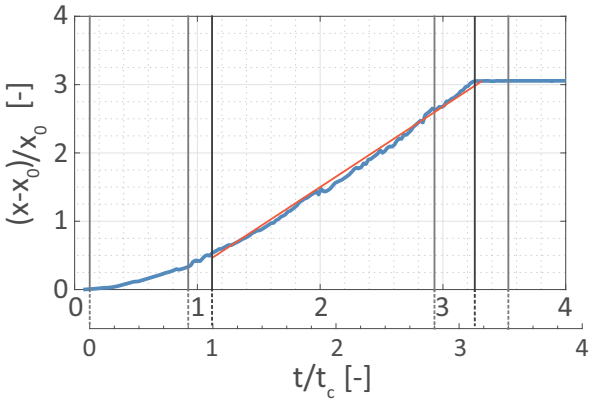

(d) Packing 4 with $d_p = 1.15$ mm

Figure B.9: Fast collapse simulation of the particle column with 1.15 mm glass particles - Evolution of deposit tip position over time

Fast collapse - Simulation sensitivity study: Variation of coefficient of restitution e

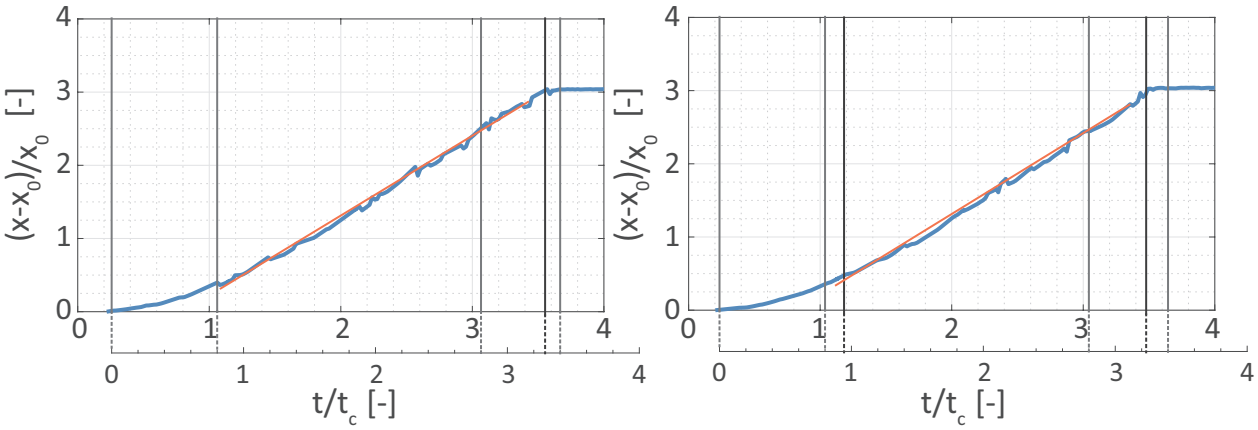

(a) Variation of packing 1

(b) Variation of packing 2

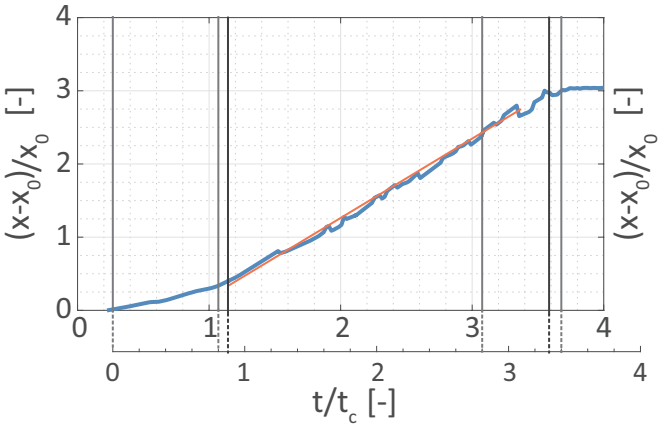

(c) Variation of packing 3

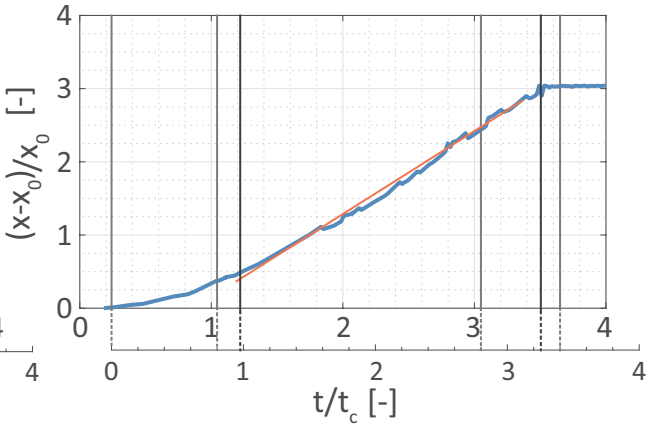

(d) Variation of packing 4

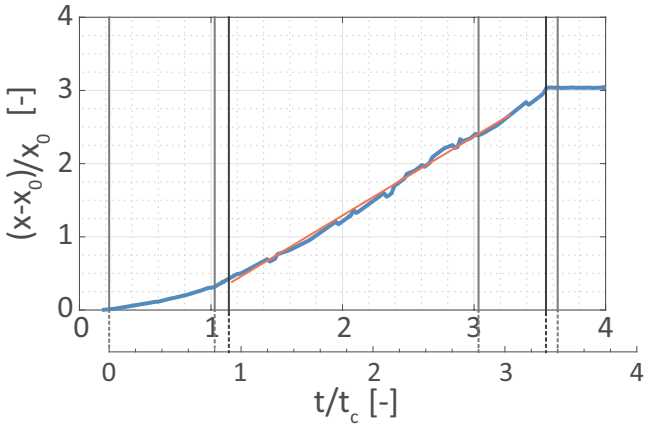

(e) Variation of packing 5

Figure B.10: Simulation of fast collapse for 3 mm glass particles and variation of the coefficient of restitution - Evolution of the deposit tip position over time for $e = 0.9$

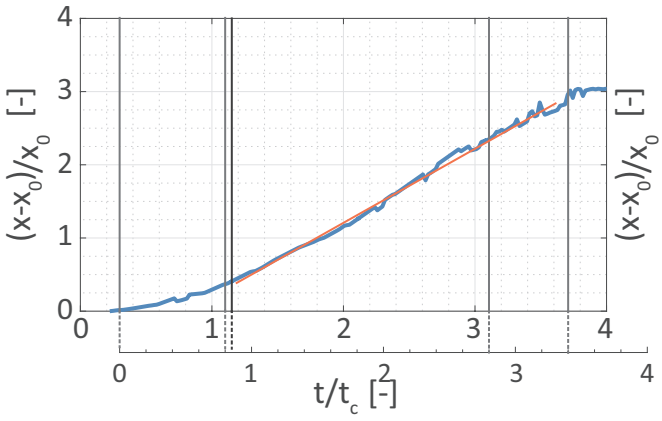

(a) Variation of packing 1

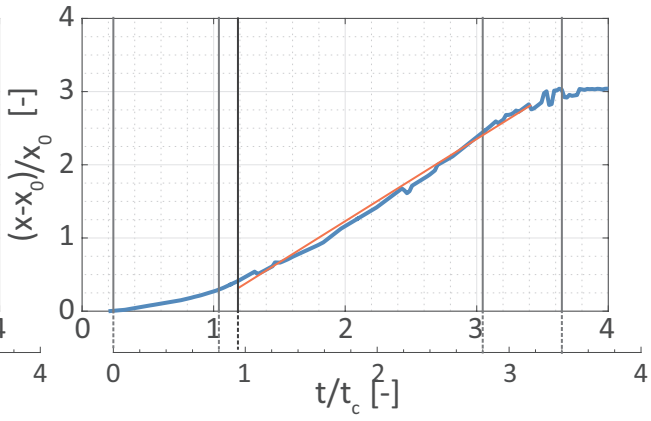

(b) Variation of packing 2

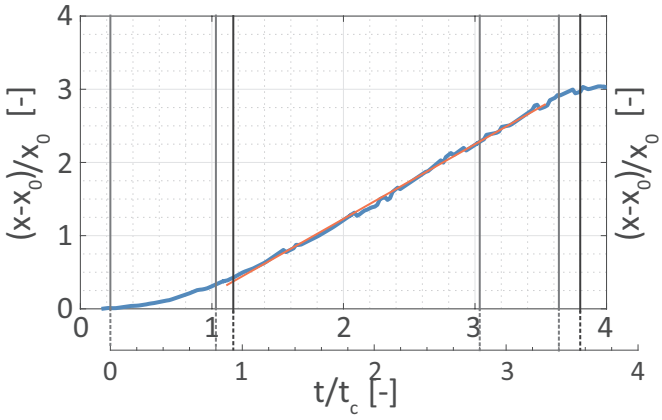

(c) Variation of packing 3

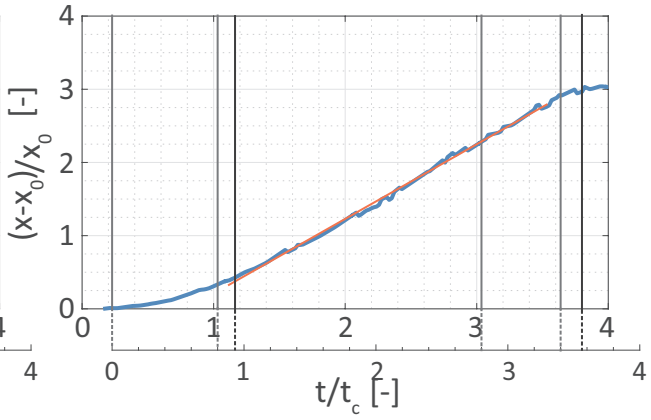

(d) Variation of packing 4

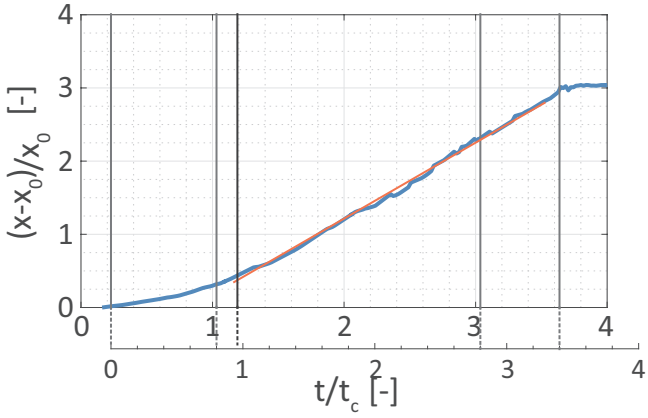

(e) Variation of packing 5

Figure B.11: Simulation of fast collapse for 3 mm glass particles and variation of the coefficient of restitution - Evolution of the deposit tip position over time for $e = 0.8$

Fast collapse - Simulation sensitivity study: Variation of particle-wall friction coefficient $\mu_{s,w}$

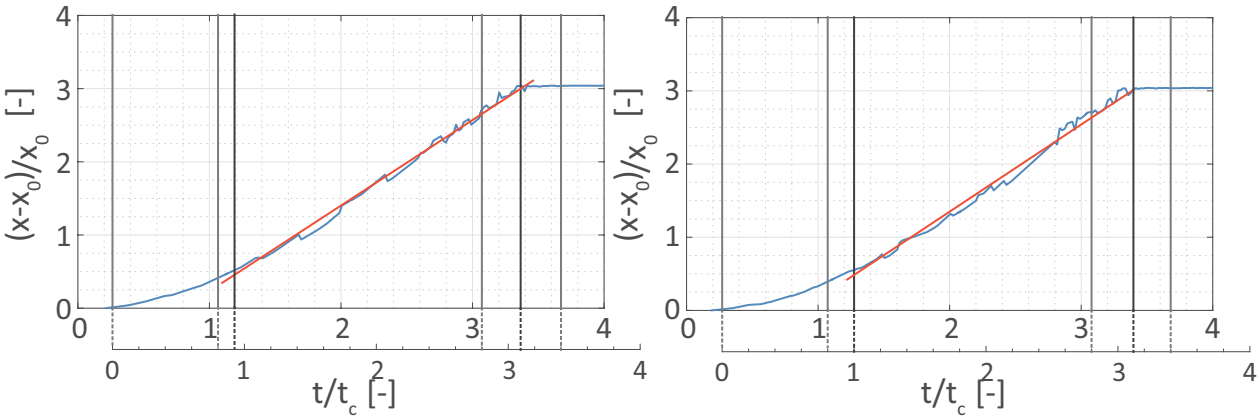

(a) Variation of packing 1

(b) Variation of packing 2

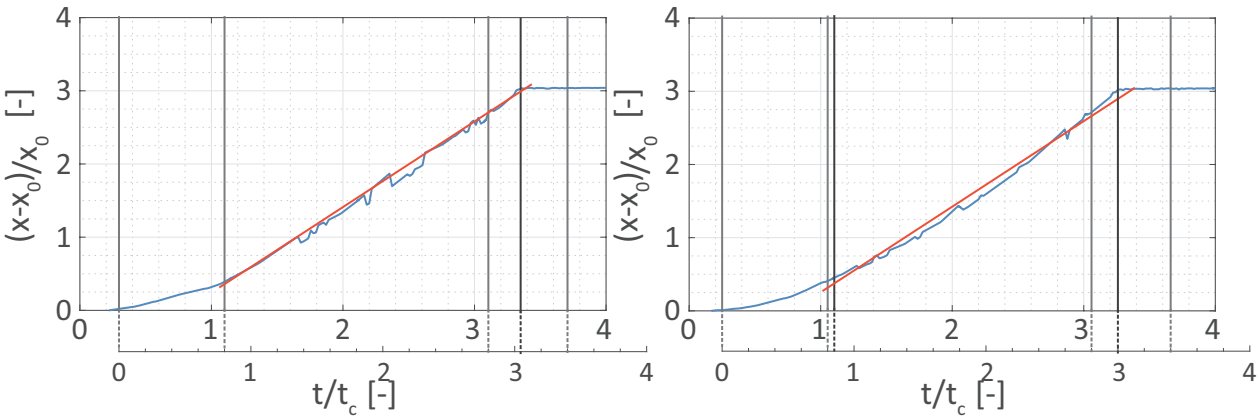

(c) Variation of packing 3

(d) Variation of packing 4

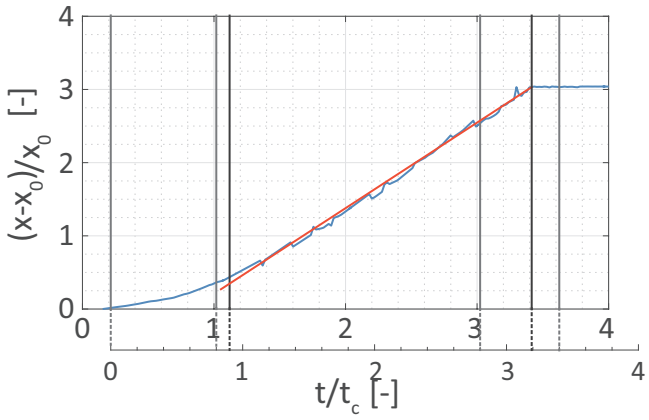

(e) Variation of packing 5

Figure B.12: Simulation of fast collapse for 3 mm glass particles and variation of the particle-wall friction coefficient - Evolution of the deposit tip position over time for $\mu_{s,w} = 0.5$

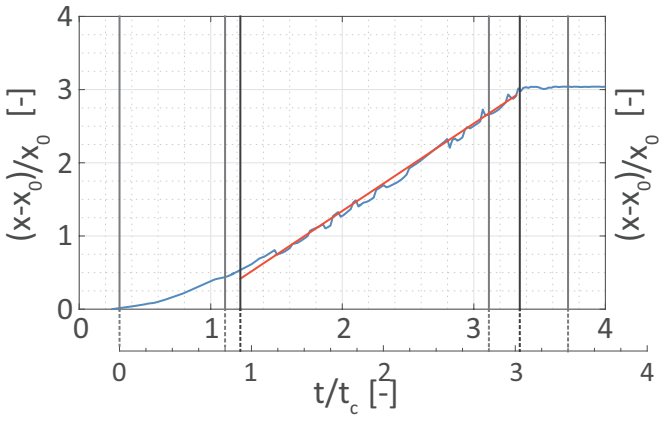

(a) Variation of packing 1

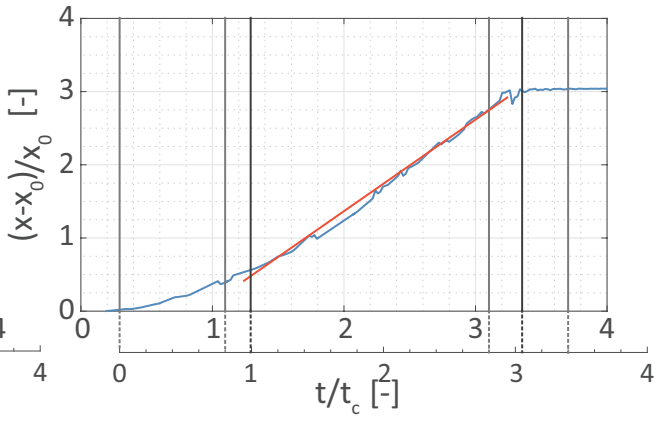

(b) Variation of packing 2

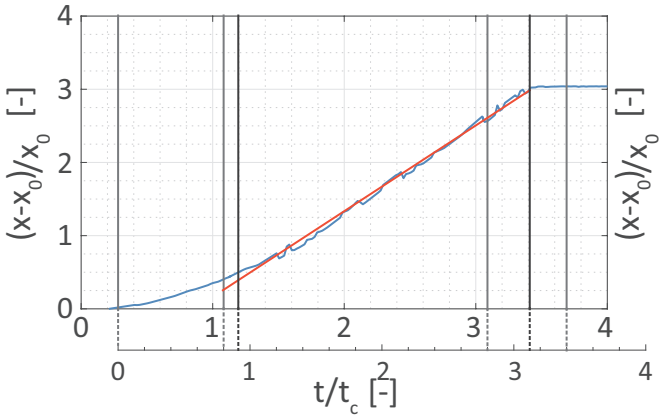

(c) Variation of packing 3

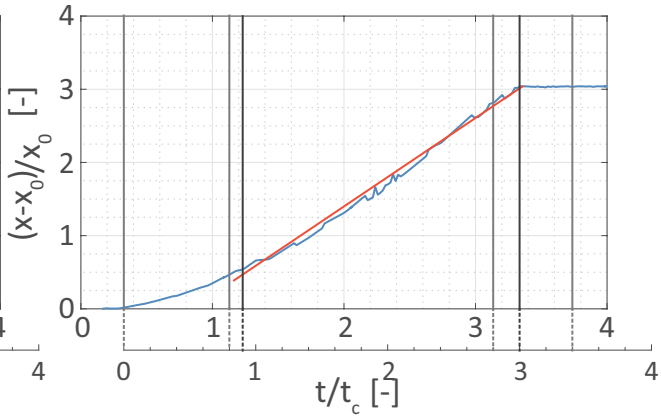

(d) Variation of packing 4

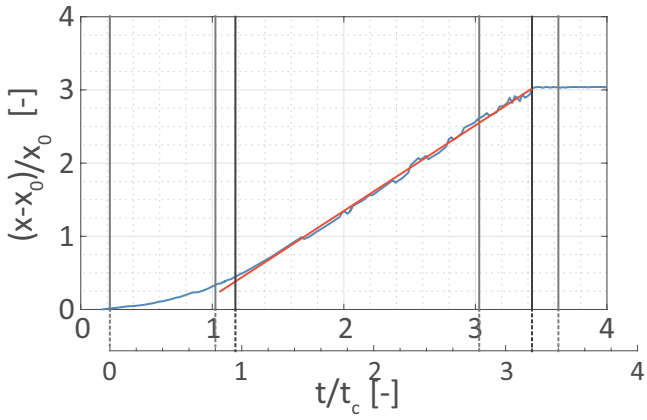

(e) Variation of packing 5

Figure B.13: Simulation of fast collapse for 3 mm glass particles and variation of the particle-wall friction coefficient - Evolution of the deposit tip position over time for $\mu_{s,w} = 0.6$

Fast collapse - Simulation sensitivity study: Variation of Coulomb friction coefficient μ_s

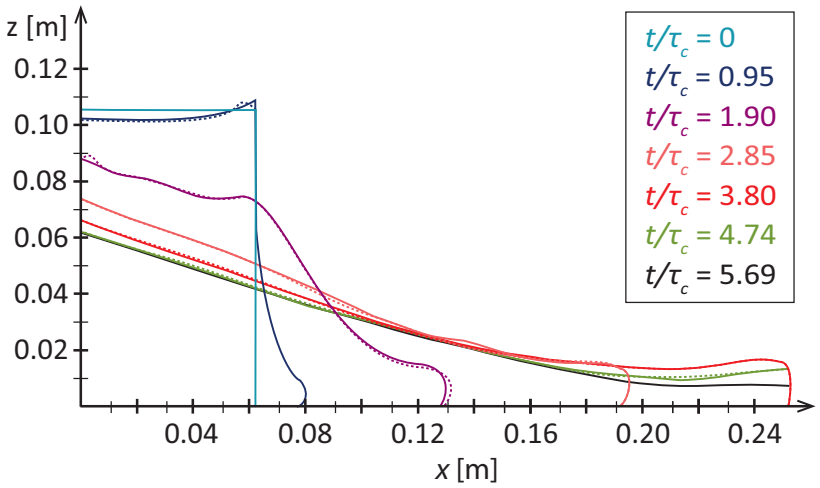

Figure B.14: Development of collapse process in the simulations with $\mu_s = 0.48$ (continuous line) and $\mu_s = 0.60$ (dashed line) represented by the outer silhouette of the 3 mm glass particles. The colour of the silhouette corresponds to equal time ratios t/τ_c

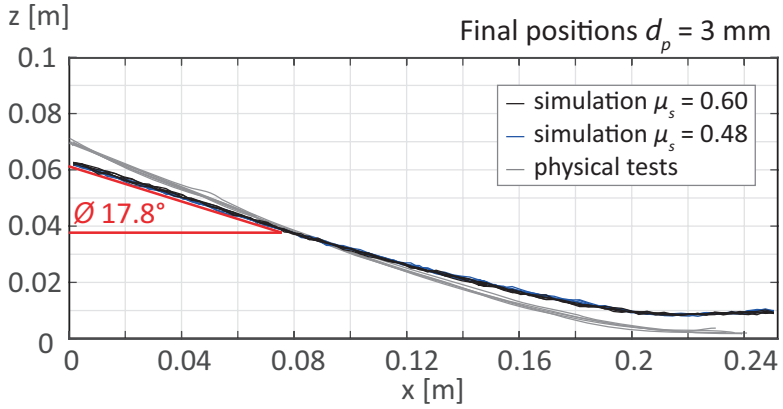

Figure B.15: Resulting final position for fast collapse simulation with 3 mm particles for $\mu_s = 0.48$ and $\mu_s = 0.6$ in comparison to the results of physical tests

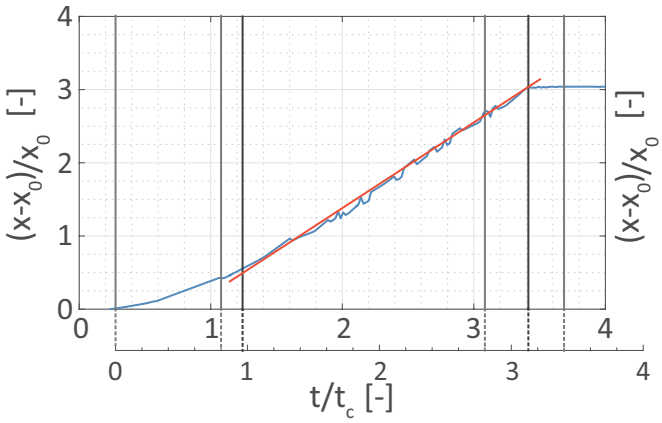

(a) Variation of packing 1

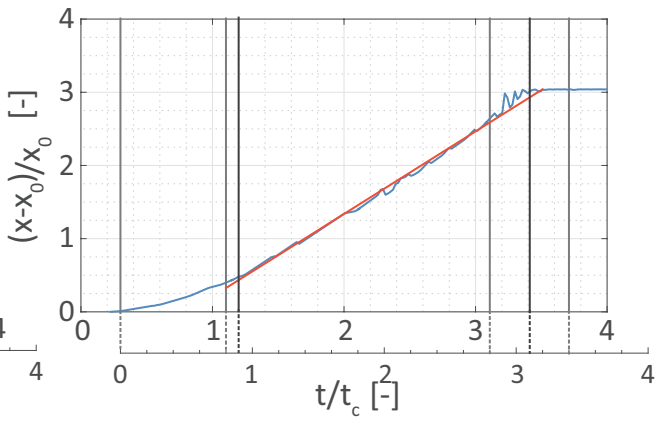

(b) Variation of packing 2

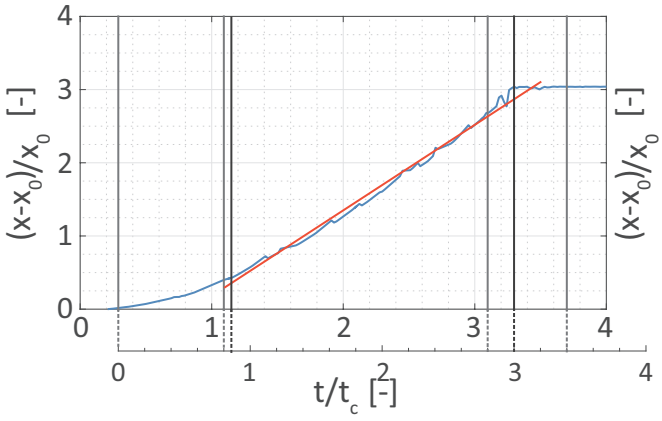

(c) Variation of packing 3

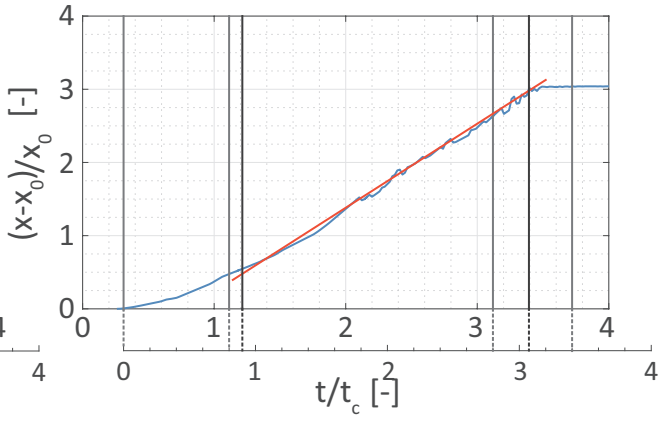

(d) Variation of packing 4

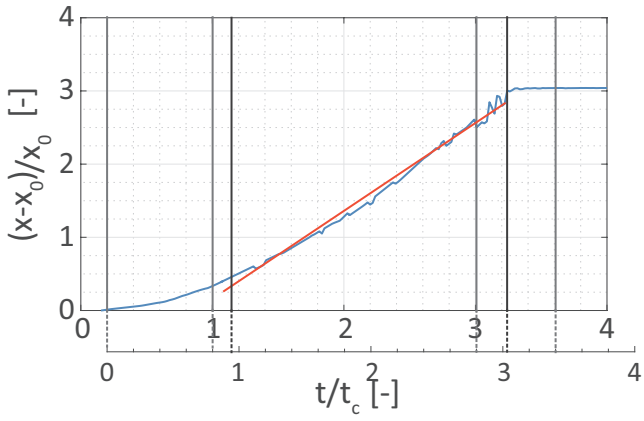

(e) Variation of packing 5

Figure B.16: Simulation of fast collapse for 3 mm glass particles and variation of the Coulomb friction coefficient - Evolution of the deposit tip position over time for $\mu_s = 0.55$

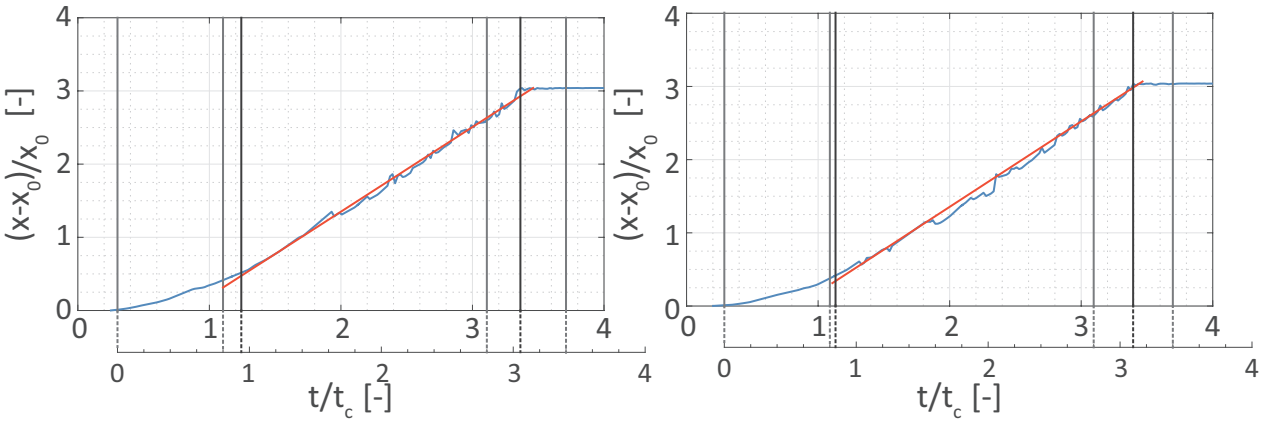

(a) Variation of packing 1

(b) Variation of packing 2

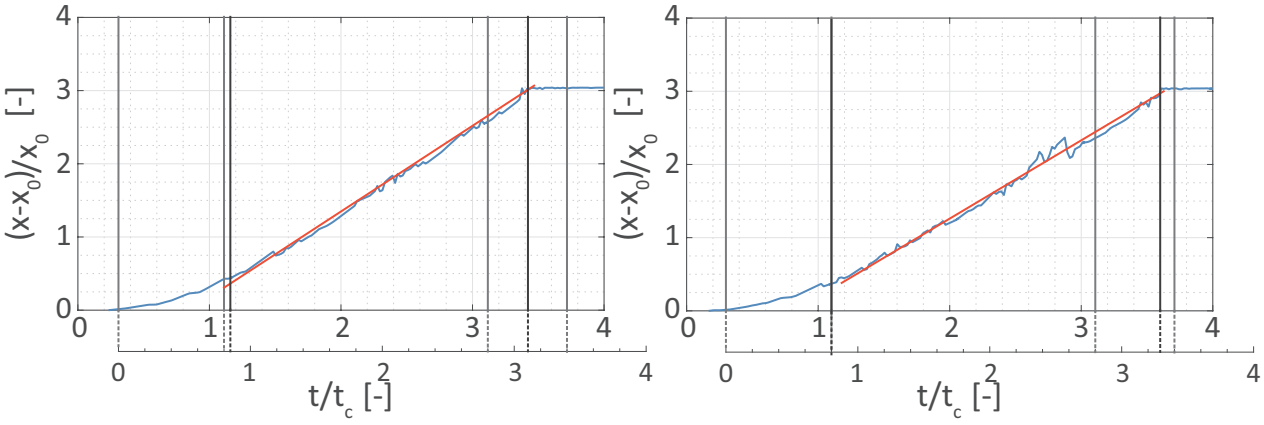

(c) Variation of packing 3

(d) Variation of packing 4

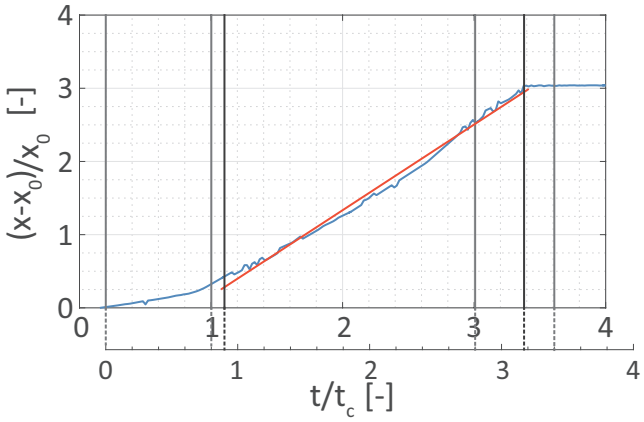

(e) Variation of packing 5

Figure B.17: Simulation of fast collapse for 3 mm glass particles and variation of the Coulomb friction coefficient - Evolution of the deposit tip position over time for $\mu_s = 0.6$

Fast collapse - Simulation sensitivity study: Variation of rolling friction coefficient μ_r

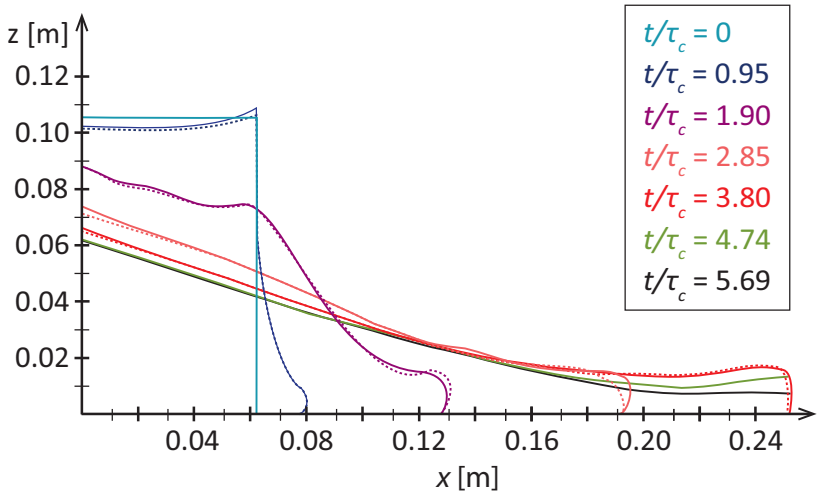

Figure B.18: Development of collapse process in the simulations with $\mu_r = 0.007$ (continuous line) and $\mu_r = 0.010$ (dashed line) represented by the outer silhouette of the 3 mm glass particles. The colour of the silhouette corresponds to equal time ratios t/τ_c

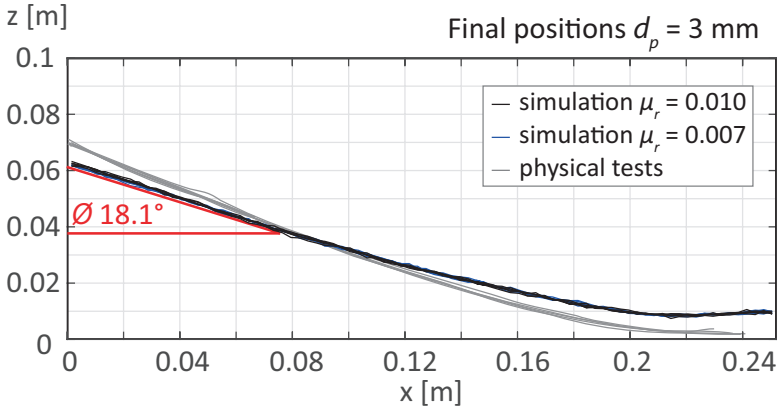

Figure B.19: Resulting final position for fast collapse simulation with 3 mm particles for $\mu_r = 0.007$ and $\mu_r = 0.010$ in comparison to the results of physical tests

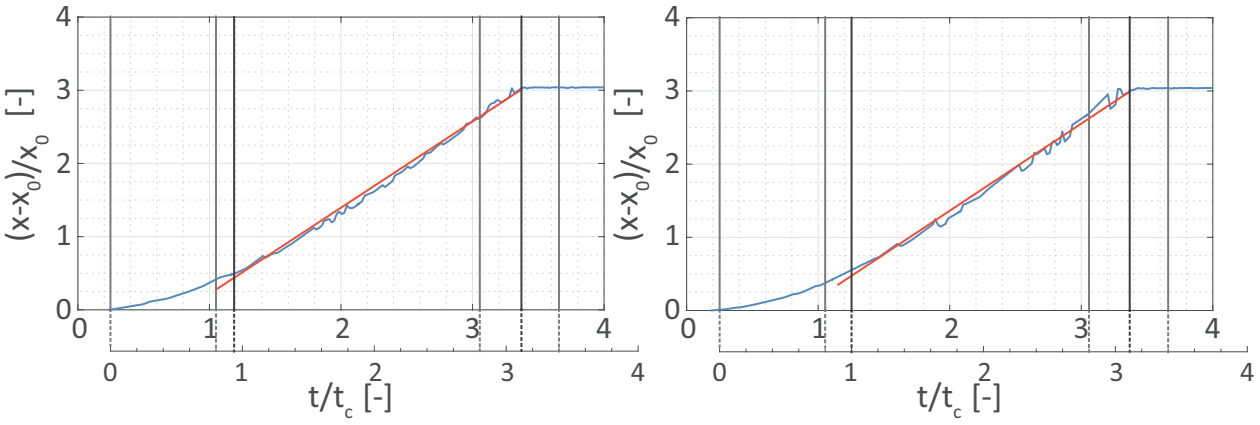

(a) Variation of packing 1

(b) Variation of packing 2

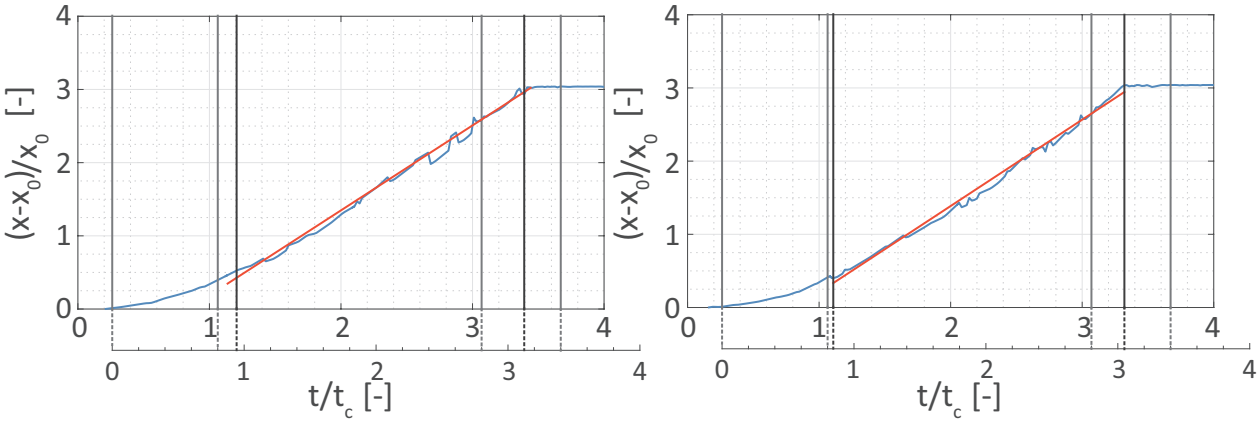

(c) Variation of packing 3

(d) Variation of packing 4

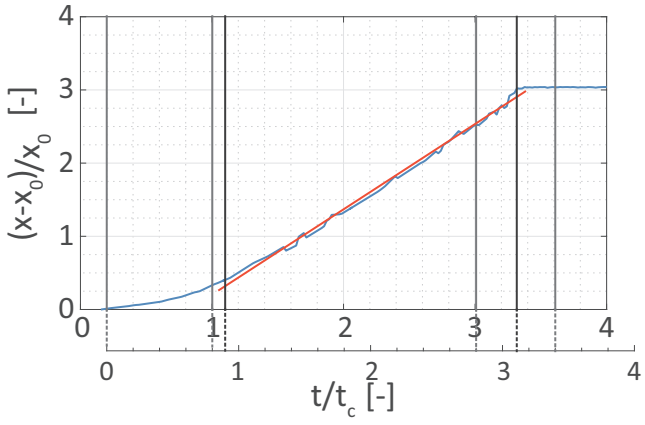

(e) Variation of packing 5

Figure B.20: Simulation of fast collapse for 3 mm glass particles and variation of the rolling friction coefficient - Evolution of the deposit tip position over time for $\mu_r = 0.008$

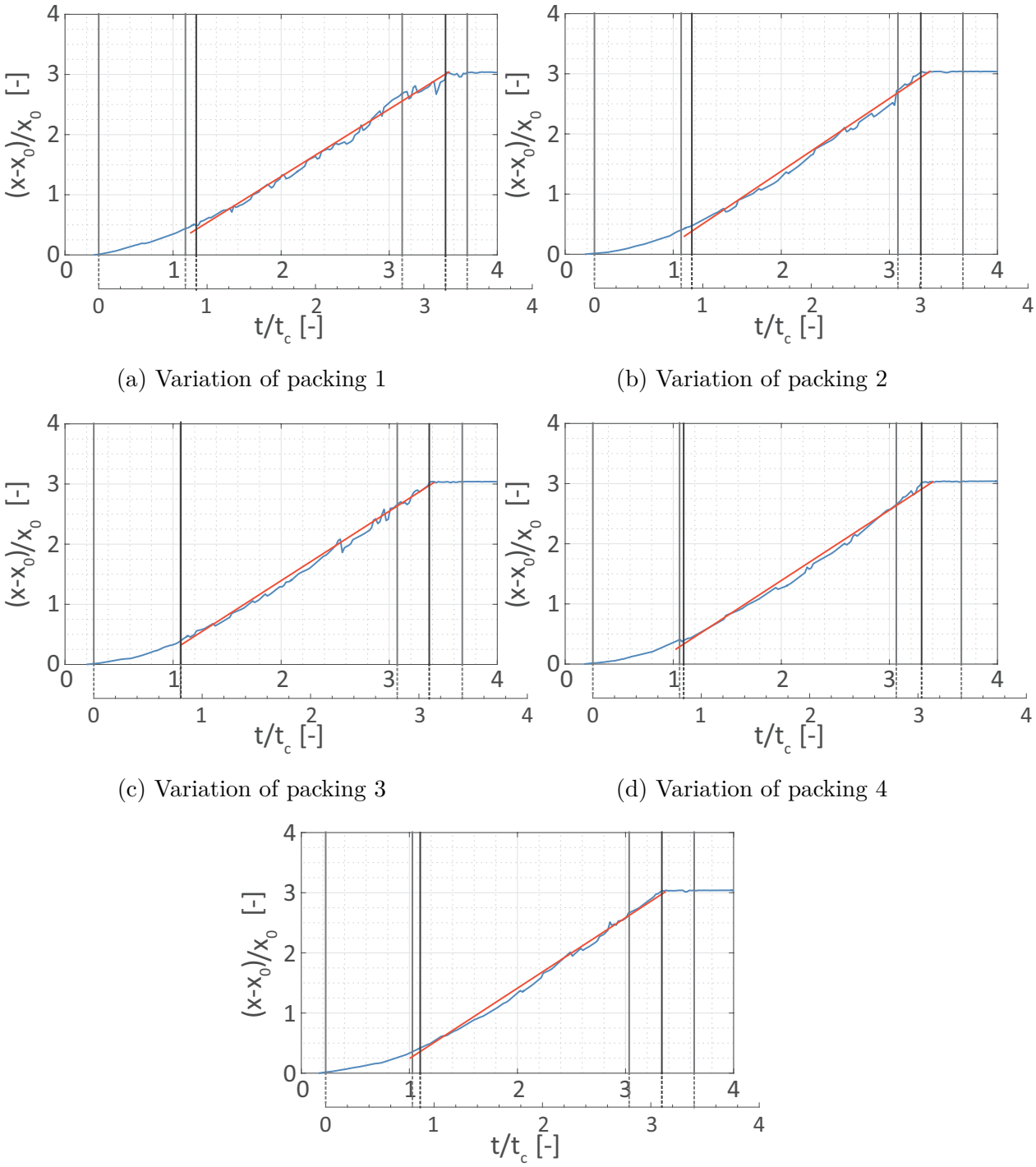

(a) Variation of packing 1

(b) Variation of packing 2

(c) Variation of packing 3

(d) Variation of packing 4

(e) Variation of packing 5

Figure B.21: Simulation of fast collapse for 3 mm glass particles and variation of the rolling friction coefficient - Evolution of the deposit tip position over time for $\mu_r = 0.009$

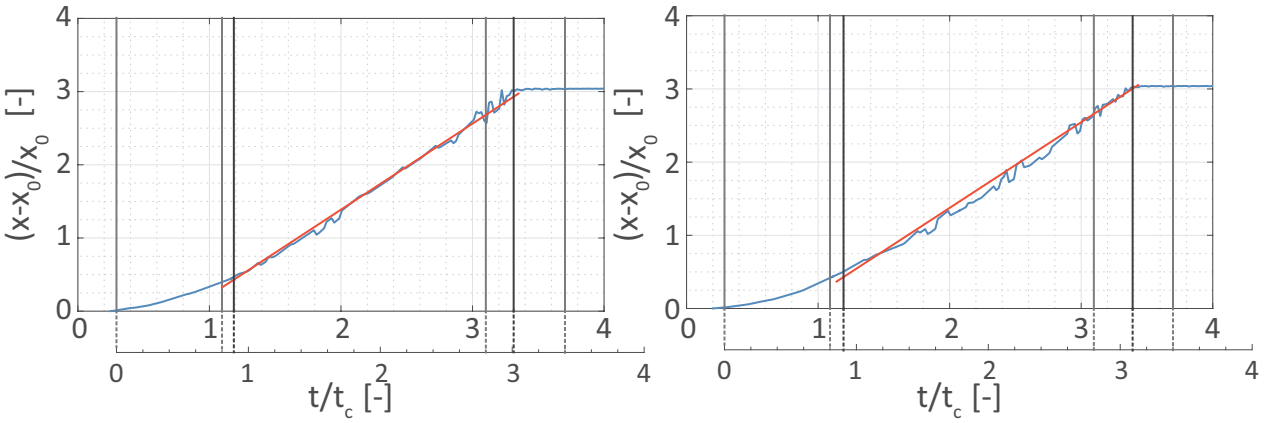

(a) Variation of packing 1

(b) Variation of packing 2

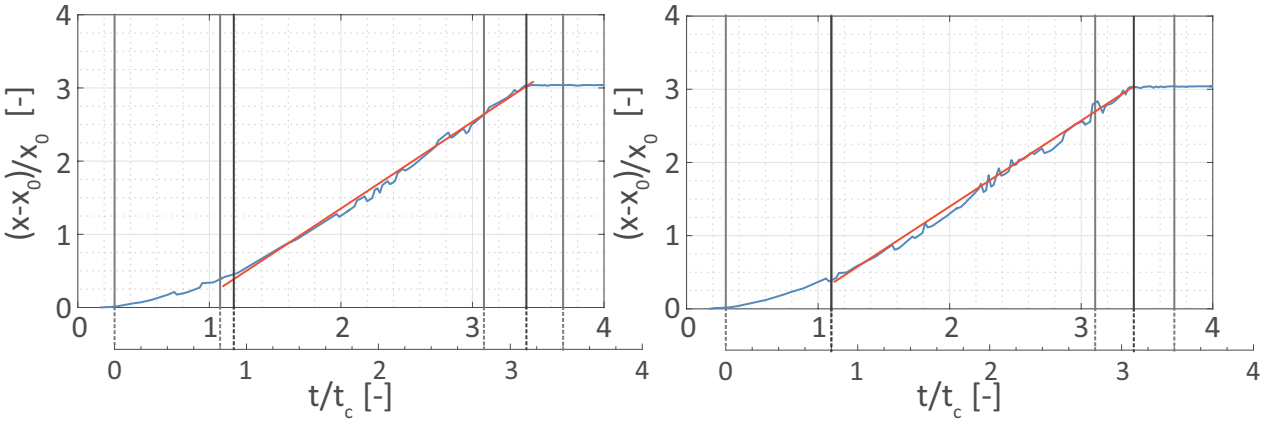

(c) Variation of packing 3

(d) Variation of packing 4

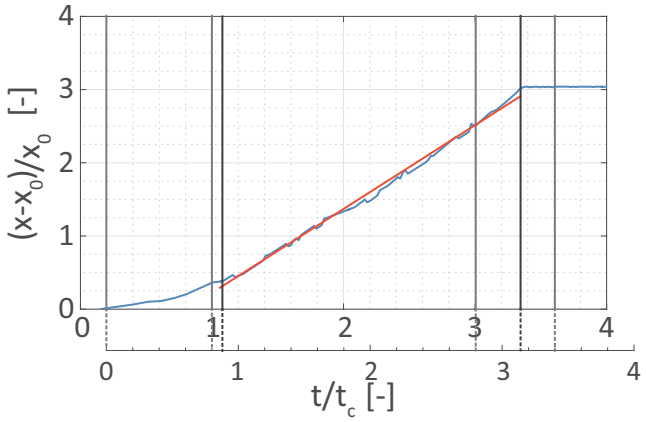

(e) Variation of packing 5

Figure B.22: Simulation of fast collapse for 3 mm glass particles and variation of the rolling friction coefficient - Evolution of the deposit tip position over time for $\mu_r = 0.01$

B.2 Slumping under dry conditions - Additional sensitivity studies on slow collapse

Influence of Young's modulus

The Young's modulus E has a high impact on the stability of a DEM simulation. As discussed in Section 4.1, the Young's modulus is the main property to define the timestep Δ_t in a simulation. Since the DEM algorithm is based on the partitioning of a contact event between two particles, the particle stiffness represents a major influence on the duration of such a contact event (see Section 4.1). With increasing material stiffness corresponding to an increasing Young's modulus, the duration of a particle-particle contact event decreases. As a result, the timestep of the simulation needs to be divided into smaller increments. The influence of the Young's modulus on the timestep is illustrated by the estimation of the characteristic Raleigh and Hertz time. As presented in Section 4.1, the Raleigh and Hertz time represent a criterion to ensure numerical stability in a DEM simulation. Therefore, the timestep of a simulation should be limited to 20% of the smallest value of the characteristic timestep. The equation for the calculation of the Raleigh and Hertz time are given in Equation 4.8 and Equation 4.7. For the Raleigh time, the Young's modulus is included in the denominator to the power of 0.5. Thus, the characteristic times decrease to the power of 0.5 with an increase of the Young's modulus. For the Hertz time, the Young's modulus is the only material property which is included in the denominator to the power of 2 and, thus, reduces the timestep with increasing values.

According to Section 5.2.3 the Young's modulus of the 3 mm glass particles has been defined to 2149.4 MPa for the Hertz contact model (Antonyuk, 2006). Besides the determined value, the Young's modulus is varied between 500 MPa, 3000 MPa and 5000 MPa. Due to the variation of the Young's modulus, the simulation timestep is adapted. While the timestep for the three higher Young's moduli remains at $1 \cdot 10^{-6}$ s, the timestep for the lowest Young's modulus of 500 MPa is increased to $2 \cdot 10^{-6}$ s. Thereby, the parallelisation of the simulations stay consistent on 24 processors. As a result, the calculation time of the higher timestep is almost divided in half. While the simulations with a timestep of $1 \cdot 10^{-6}$ s have a calculation time of approximately 75.6 h, the simulations with a timestep of $2 \cdot 10^{-6}$ s have a calculation time of 38.0 h only. Obviously, with increasing timestep the calculation time of the simulation decreases significantly.

No other parameters besides the Young's modulus are altered (compare Section 6.3.2 for these parameters). However, in this specific variation the coefficient of Coulomb's friction is with a value of 0.51 instead of 0.48 slightly changed compared to the other variations. This is due to a correction of this parameter after rectified results of triaxial tests.

In accordance with Section 6.2.3 and Section 6.3.2, the final state of the collapse is described by the angle at the foot of the deposit slope and the angle of the top of the slope. In Figure B.23 the resulting slope angles of the final state of the simulations are presented. Further, the average values for the individual Young's modulus variation are plotted. In addition, these average values, the average collapse duration and their standard deviation are given in Table B.1. Similar to the results used in Table 6.6, the results for the Young's

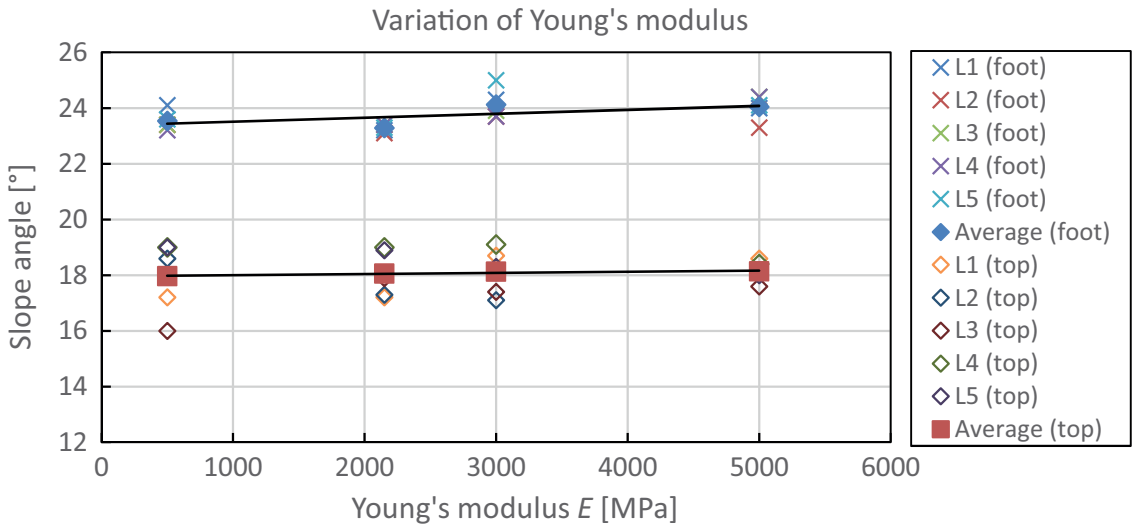

Figure B.23: Final top and foot angles at the final deposit shape for the Young's modulus variation with 3 mm glass particles

modulus variation show a dependency on the initial packing. The results of the five initial particle packings vary for the same value of the Young's modulus (see Figure B.23). Thereby, the standard deviation is higher for the final slope top angle than the foot angle. This corresponds to the original simulation results of the slow extraction and the physical tests. The maximum standard deviation in the Young's modulus variation is $\pm 0.55°$ for the foot angle and $\pm 1.32°$ for the top angle.

In Figure B.23, linear trendlines based on the average values are plotted. The trendline of the average top slope angles stays constant at approximately 18°. As a result, the final top slope angle seems to be independent of the applied Young's modulus. In contrast, the angle of the foot of the deposit slope seems to increase slightly with increasing values of the Young's modulus. While the simulations of $E = 500$ MPa and $E = 2149.4$ MPa lead to an average foot angle of 23.5° and 23.3°, the higher values of the Young's modulus of $E = 3000$ MPa and $E = 5000$ MPa result in an average foot angle of 24.1° and 24.0°. However, with a raise of 0.5° the increase in inclination is small and within the range of the standard deviation of the conducted simulations. Thus, the trend for the average foot angles is affected mainly by the effect of the initial setup variation. For geotechnical applications, the increase can be considered negligible.

The duration of the column collapse is in average slightly increased compared to the previous results of the initial simulations. The initial simulations result in an average duration of 77.6 s for the collapse. Hence, the average duration of the collapse in the simulations was slightly longer with approximately 78.4 s. However, the Young's modulus variation is conducted with an slightly increased coefficient of Coulomb's friction μ_s. Thus, the longer duration might result from a higher shear resistance of the particles at the final avalanche. This assumption is confirmed by the overall increase of the collapse duration for all variations of the Young's modulus. Further, also the simulation considered the initial Young's modulus of $E = 2149.4$ MPa shows an increase of the collapse duration.

Table B.1: Average results for the variation of the Young's modulus at the slow collapse with glass particles of 3 mm diameter

Young's modulus [MPa]	Slope angle top	Slope angle foot	Ratio foot/top	Duration [s]
500	18.0° ±1.32°	23.5° ±0.34°	1.28	78.3 ±1.5
2149.4	18.1° ±0.86°	23.3° ±0.13°	1.29	78.5 ±1.1
3000	18.1° ±0.85°	24.1° ±0.55°	1.33	78.4 ±1.5
5000	18.1° ±0.38°	24.0° ±0.45°	1.33	78.3 ±1.4
∅ Sim	18.5° ±0.54°	23.6° ±0.67°	1.28	77.6 ±0.27
∅ Tests	22.9° ±0.54°	23.9° ±0.30°	1.04	99.4 ±1.54

Thus, the longer duration can be explained by the higher friction coefficient. The standard deviation of the collapse duration is in the range of those of the physical tests.

The slumping mechanism in the variation shows no differences for the varied values of the Young's modulus. Neither, the position of the slip joints, the particle velocities, the particle displacements nor the progress of the discharge and avalanching seems to vary. However, the comparison of the kinetic energy development during the collapse proves that there is at least a slight differences within the development of the kinetic energy. Figure B.24 shows the development of the kinetic energy during the column collapse for the simulation series with a Young's modulus of $E = 500$ MPa (see Figure B.24a) and $E = 5000$ MPa (see Figure B.24b). All results of the individual simulations with different initial packings are included within graphic. The peaks of the global kinetic energy curves are clearly higher for the low Young's modulus of $E = 500$ MPa. The presented global kinetic energy is defined by the sum of kinetic energy (see Equation 6.6) of all particles in the system. Thus, the raised amount of E_{kin} might be caused by higher particle velocities and a higher number of moved particles. Since the slumping and discharge events are specific for every simulation, a direct comparison of particle velocities or numbers of moving particles at a certain time is not possible. A clear difference between the collapse progress is not visible. However, since an increase of the Young's modulus is equivalent to an increase of the material stiffness, the increased kinetic Energy for the lower Young's modulus variation is caused by the changed particle contact. The normal and tangential spring force should be unaffected by a higher stiffness. However, to achieve an unchanged contact spring force, the overlap distance needs to decrease for a higher stiffness. Thus, the particles in the column have an infinitesimal higher range to move in. As a result, the maximum contact force is reached after a slightly longer time of movement. For a single contact event, this effect is negligible. However, for a larger amount of particles in contact this effect causes an increase in global kinetic energy due to the high number of particle contacts. Besides the spring force, the damping constant for the normal and tangential contact are affected as well. For a smaller stiffness, the damping constant is reduced. Thus, the particle

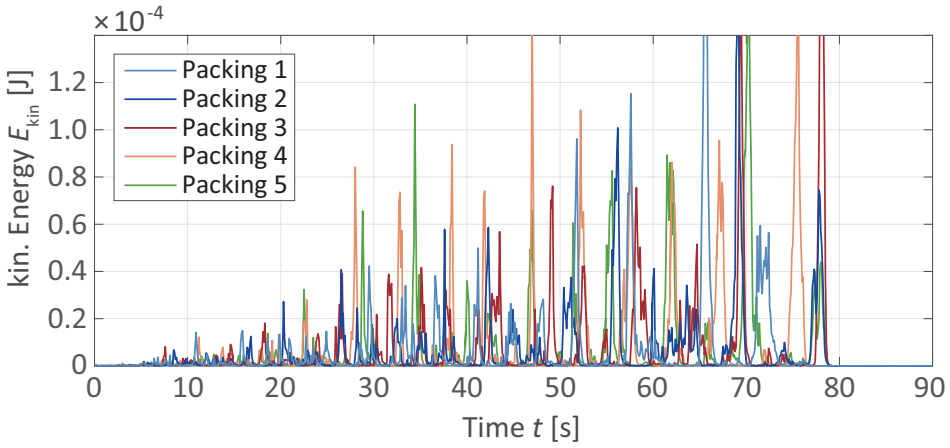

(a) $E = 500$ MPa

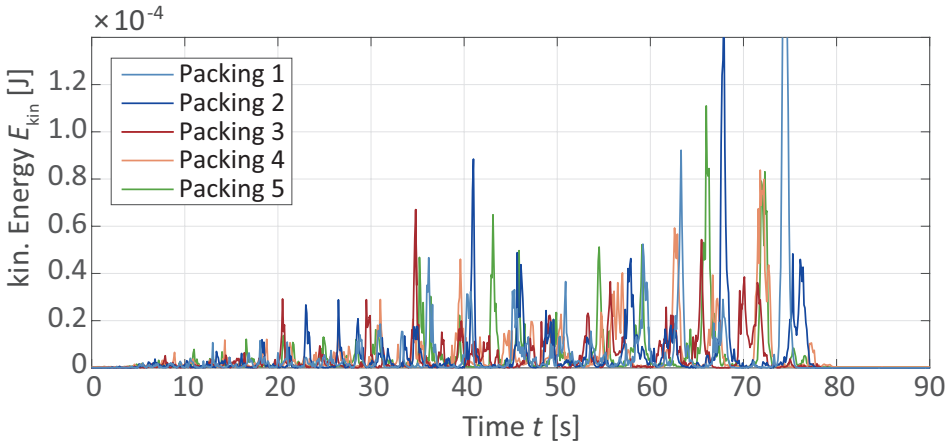

(b) $E = 5000$ MPa

Figure B.24: Compilation of kinetic energy evolution over time including all initial packings at the Young's modulus variation with $E = 500$ MPa and $E = 5000$ MPa

velocities are damped less than for stiffer materials. As a result, the particle velocities decrease slower than for stiffer material. Similar to the effect of the spring force, the high number of contact events with a slghtly higher particle velocity until the maximum contact force is reached, results in to an increase in the global kinetic energy.

Influence of Poisson's ratio ν

The Poisson's ratio represents the ratio of transverse strain to axial strain of materials. Within the contact formulation the Poisson's ratio is included in the spring force component as well as in the damping component by the specific Young's modulus and the specific shear modulus (see Section 4.1.1). In the tests of the slow collapse, this property is expected to have no significant impact on the collapse characteristics like the slumping mechanism or the development of the deposit slope since the particles experience no further loading besides the column dead weight. In the sensitivity analysis, the initial value $\nu = 0.3$ is varied to 0.2, 0.25 and 0.4. These values are within the limits, which are recommended in literature for glass (0.18 - 0.3) or sand particles (0.20 - 0.45).

The slope angles for the final state are presented in Figure B.25. The Figure illustrates the individual simulation results as well as the average values for every variation. The average values are used for linear trendlines. According to Figure B.25, the final state of the simulations is absolutely unaffected by the variation of ν. Neither the foot nor the top angles show a significant change for the varied ν. Although the individual simulation results for different particle packings deviate slightly, the average values are unaltered. Thus, the variations are effected by the variations of the initial packing rather than by the variation of ν.

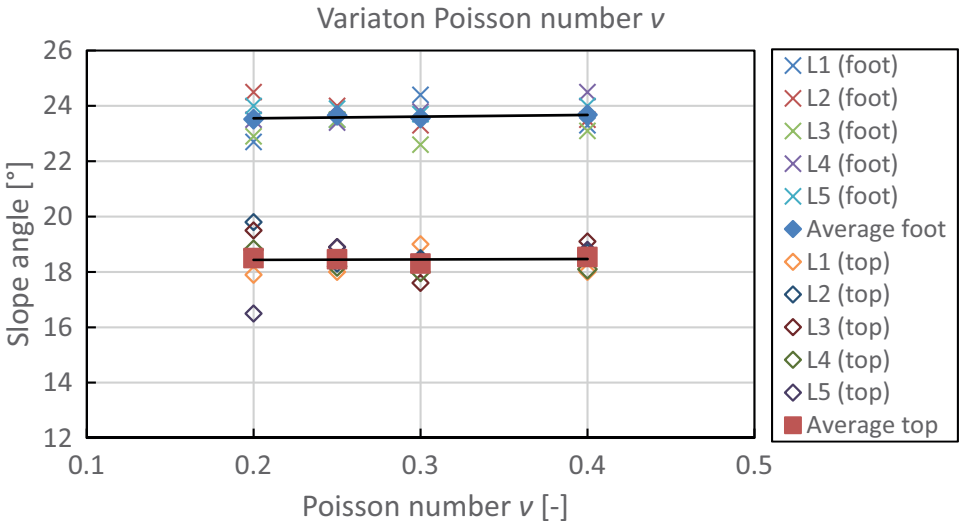

Figure B.25: Final top and foot angles for the final deposit shape for the Poisson's ratio variation with 3 mm glass particles

Table B.2: Average results of the variation of the Poisson's ratio for the slow collapse with glass particles of 3 mm diameter

Poisson's ratio	Slope angle top	Slope angle foot	Ratio foot/top	Duration [s]
0.20	18.5° ±1.34°	23.5° ±0.75°	1.28	77.4 ±0.71
0.25	18.5° ±0.42°	23.7° ±0.27°	1.28	78.0 ±1.66
0.30	18.5° ±0.54°	23.6° ±0.67°	1.28	77.6 ±0.27
0.40	18.5° ±0.47°	23.7° ±0.57°	1.28	78.3 ±1.41
∅ Sim	18.5° ±0.54°	23.6° ±0.67°	1.28	77.6 ±0.27
∅ Tests	22.9° ±0.54°	23.9° ±0.30°	1.04	99.4 ±1.54

Further, the average results of the variations are summarised in Table B.2. The consistency of the average values for the variation of ν is distinct. The difference between the average

results is 0.2° for the top and the foot angle. This underlines that with the chosen 5 different packings a sufficient number of variations is achieved to balance individual simulations results. Further, Table B.2 includes the average duration of the column collapse. Similar to the results of the final state, the total simulation duration varies slightly with a maximum deviation of the values of 0.9 s only. The development of the deposit slope and the slumping mechanism is unaffected by the variation of ν. The particle displacements and the slumping mass, represented by particle velocities, correspond well. Since this result was expected from a geomechanical perspective, the numerical contact formulation in this simulations describes the particle interaction and the whole collapse mechanism sufficiently.

Influence of coefficient of restitution e

The coefficient of restitution e represents the ratio between the initial and final relative velocities after a collision of two particles. It is an important material property to describe the elasticity of the colliding materials and to characterise the damping effects at contact of granular materials. Thus, the coefficient of restitution is included in the normal and tangential damping component of the Hertz contact force model. Since it is limited to the damping component, the variation of e is not expected to have a high impact on the simulation of the slow collapse case. Due to the alternating slumping mechanism and, thus, slow particle velocities during the collapse, the damping contact components are expected to be small compared to the spring component. The value of e was determined by laboratory tests, which resulted in an almost perfect elastic collision value of 0.98 (see Section 5.2.3). Since the deviation to a truly perfect elastic collision is too small to expect a real impact on the simulation, the variation of e has been conducted by significantly smaller values. Thus, the initial value of $e = 0.98$ is varied to $e = 0.8$ and $e = 0.6$ for the simulation of the slow collapse.

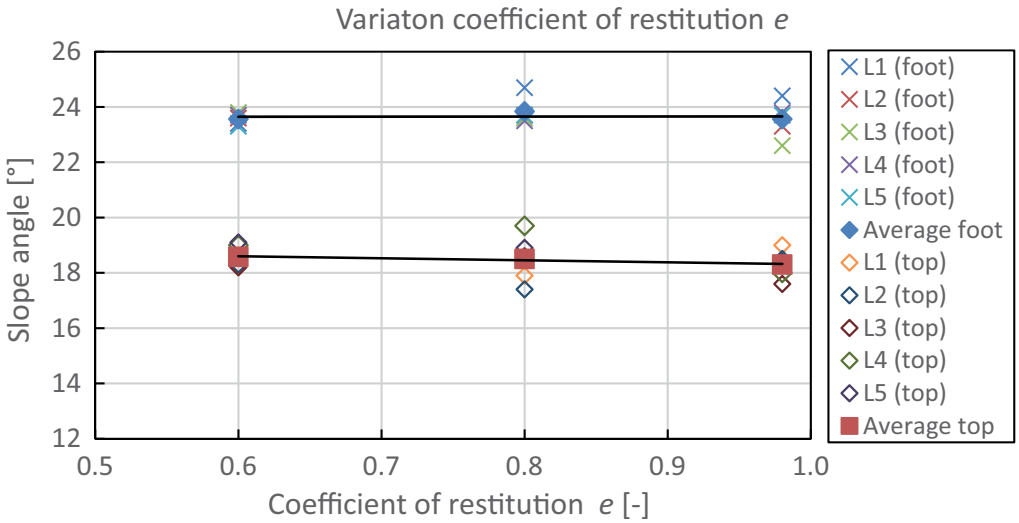

Figure B.26: Final top and foot angles for the final deposit shape of the variation of the coefficient of restitution with 3 mm glass particles

The top and foot angles of the slope for the final state are presented in Figure B.26. Further, the average values for each variation and a linear trendline based on this average

result are included in the figure. According to Figure B.26, the foot angle is unaffected by the variation of e. The angle remains consistent for the variations. The average values and their standard deviation are summarised in Table B.3. The maximum differences between the final average results are 0.2° only. The final slope top angle as well as the foot angle show the same consistent values for all variations. Although, the trendline is decreasing slightly with an increasing e, the differences between the average results are adequately small to assume that the differences are most likely based on the influences of the initial packing and the resulting standard deviation than on the influence of the variation of e. The standard deviations are at a maximum of ±0.89° for the final slope top angle and ±0.67° for the final slope foot angle. These results agree with the previously discussed expectation of the negligible influences of e on the collapse characteristics. However, the standard deviation seems to be significantly smaller especially in the case of the deposit foot angle for the variation considering $e = 0.6$ than for the variations with higher values. In the contact model, a smaller value of e results in a higher damping behaviour. It can be assumed that increased damping results in a smaller variation of the collapse mechanism. This holds especially true for the development of the deposit slope, while the mechanisms themselves seem to be unaffected. Thus, no extreme states such as the development of a plateau at the slope top is observed for $e = 0.6$. However, this phenomenon needs to be investigated considering a larger number of initial packings, to proof the trend of the standard deviation.

Table B.3: Average results for the variation of the coefficient of restitution for the slow collapse with glass particles of 3 mm diameter

Coefficient of restitution [-]	Slope angle top	Slope angle foot	Ratio foot/top	Duration [s]
0.6	18.6° ±0.43°	23.6° ±0.21°	1.27	77.4 ±1.39
0.8	18.5° ±0.89°	23.8° ±0.49°	1.29	77.3 ±0.94
0.98	18.5° ±0.54°	23.6° ±0.67°	1.28	77.6 ±0.27
∅ Sim	18.5° ±0.54°	23.6° ±0.67°	1.28	77.6 ±0.27
∅ Tests	22.9° ±0.54°	23.9° ±0.30°	1.04	99.4 ±1.54

Similar to the variation of the Poisson's ratio, no significant differences in the collapse characteristics can be observed. Neither the slumping mechanism nor the development of the deposit slope show significant differences. Further, no clear trends for the kinetic energy during the collapse progress for the variation can be observed. Additionally, the total duration of the collapse is almost equal for all variations. Thus, damping has no impact on the development over time of the collapse. However, since the collapse is divided by several small discharge/slumping events, the damping effect cannot effect the development over time significantly. This should be different for the fast slumping collapse,

which is limited to one big slumping event with higher particle velocities.

B.3 Slumping under submerged conditions - Additional figures

Fast collapse - Physical tests

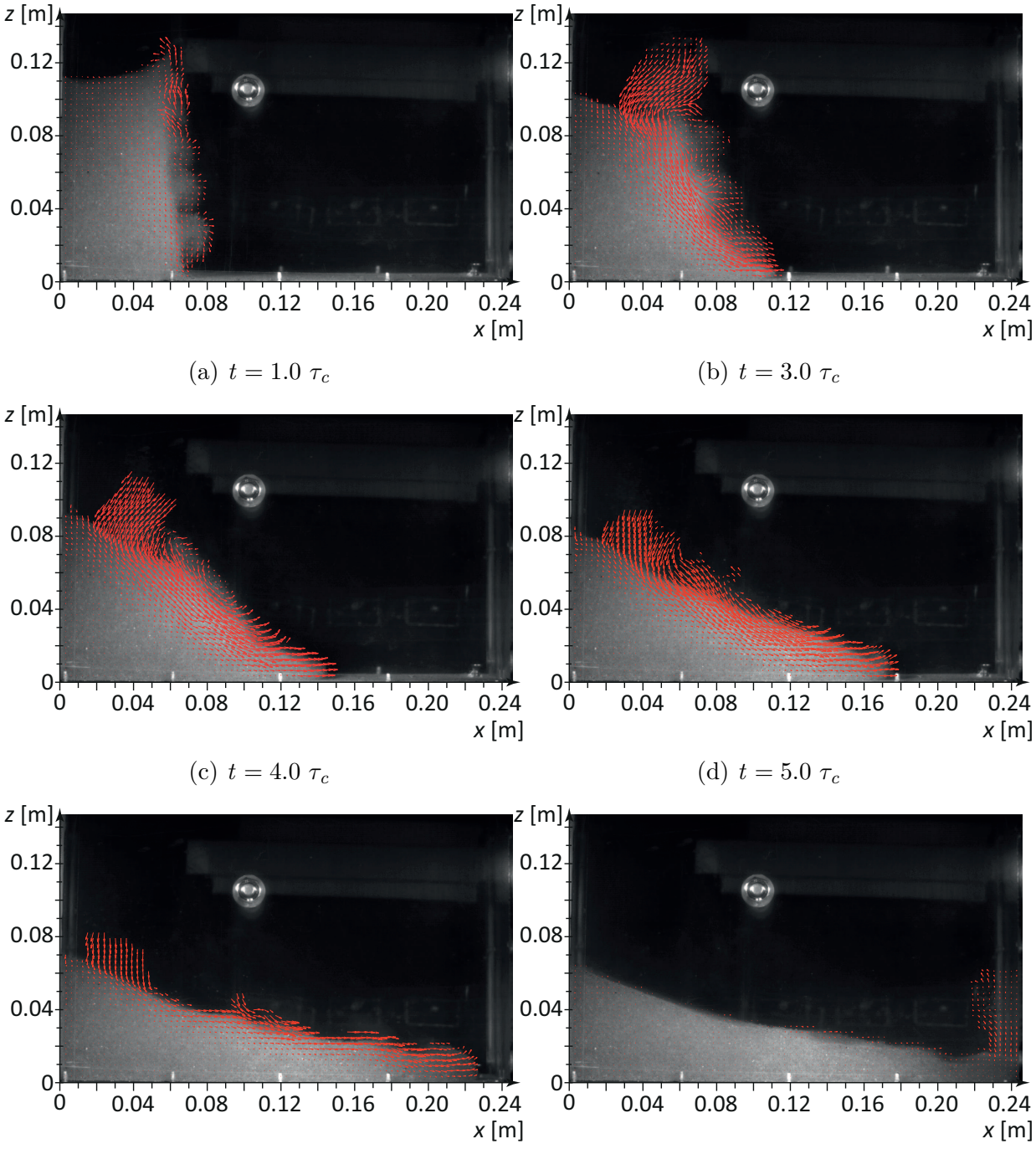

(a) $t = 1.0\ \tau_c$ (b) $t = 3.0\ \tau_c$

(c) $t = 4.0\ \tau_c$ (d) $t = 5.0\ \tau_c$

(e) $t = 7.0\ \tau_c$ (f) $t = 12.0\ \tau_c$

Figure B.27: Fast collapse of a submerged particle column with 1.15 mm glass particles - Collapse characteristics over time represented by the velocity magnitude of the PIV analysis

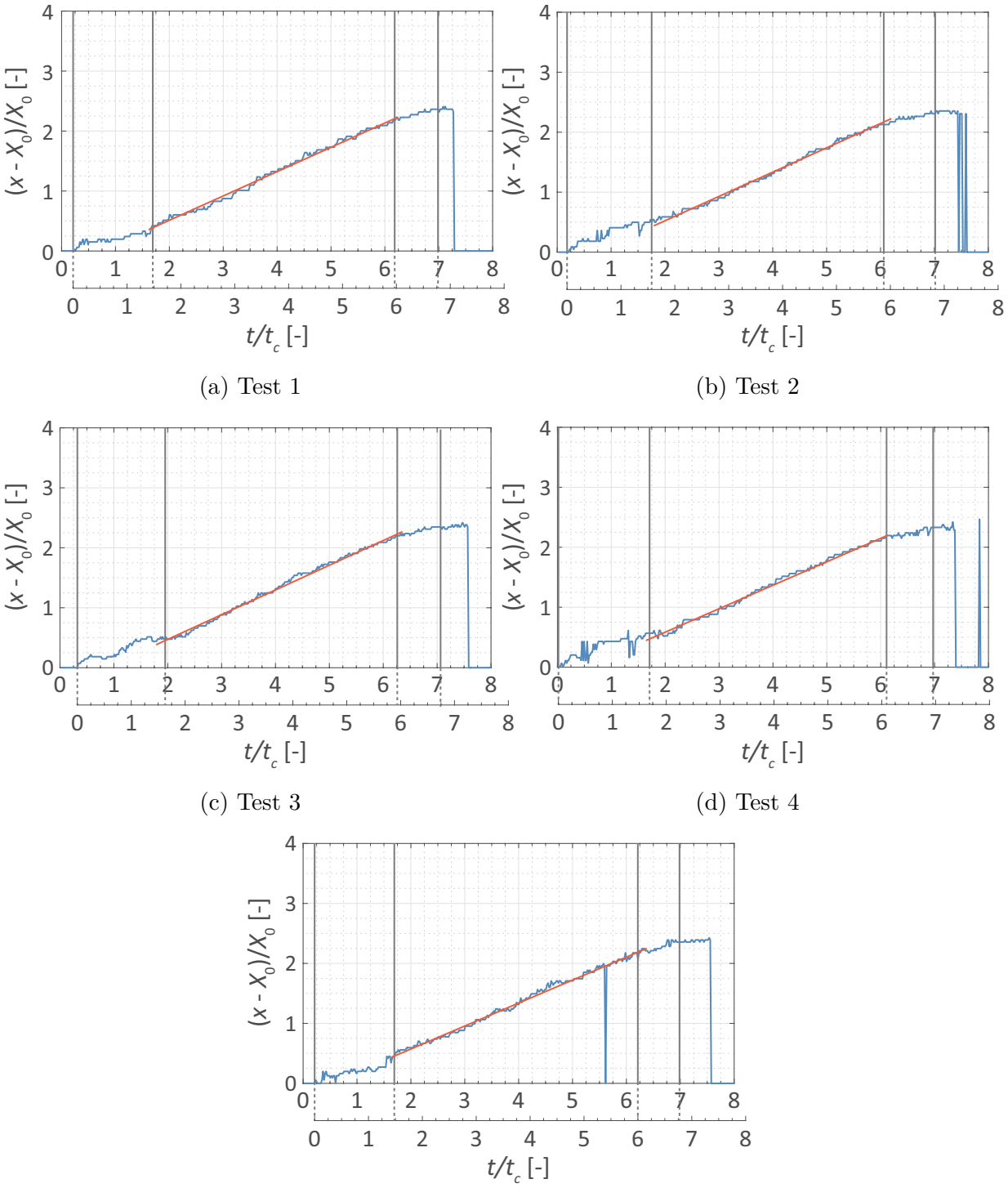

(a) Test 1

(b) Test 2

(c) Test 3

(d) Test 4

(e) Test 5

Figure B.28: Test of submerged fast collapse with 3 mm glass particles - Evolution of the deposit tip position over time

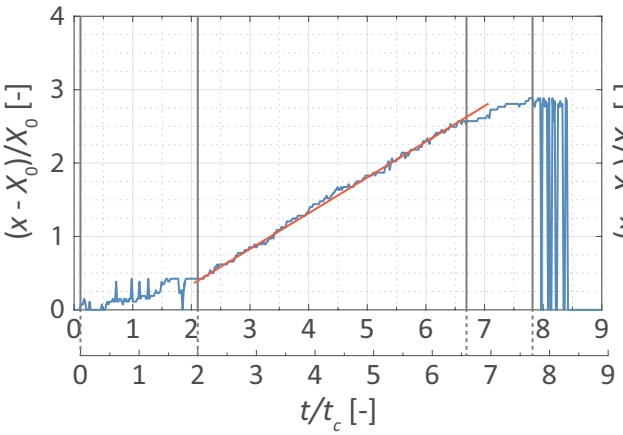

(a) Test 1

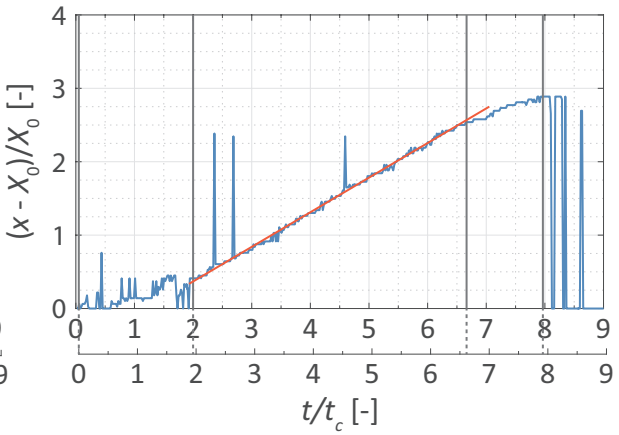

(b) Test 2

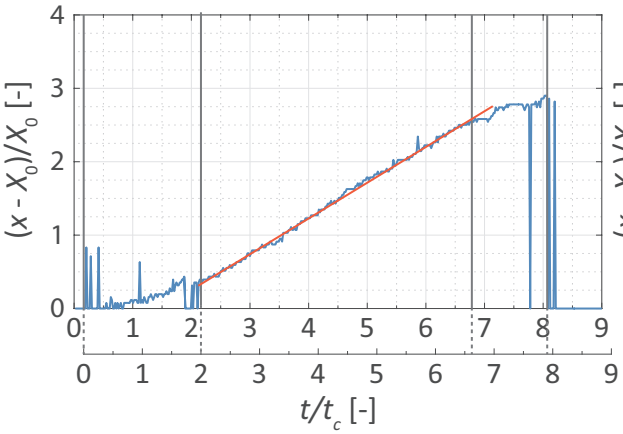

(c) Test 3

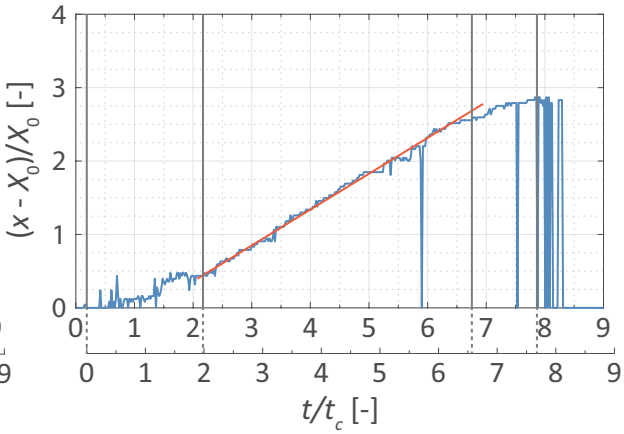

(d) Test 4

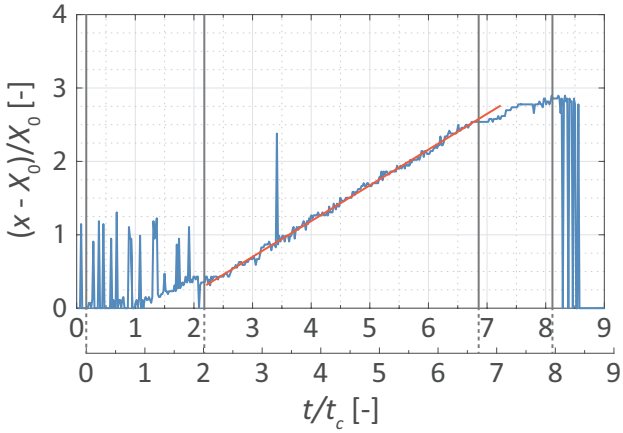

(e) Test 5

Figure B.29: Test of submerged fast collapse with 1.15 mm glass particles - Evolution of deposit tip position over time

Fast collapse - Simulation

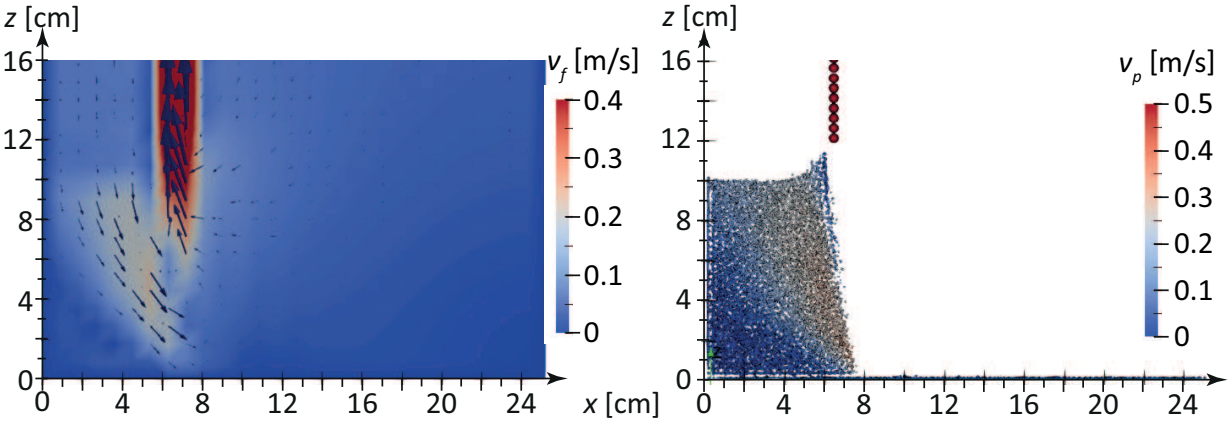

(a) $t \approx 1.0\ t_c$

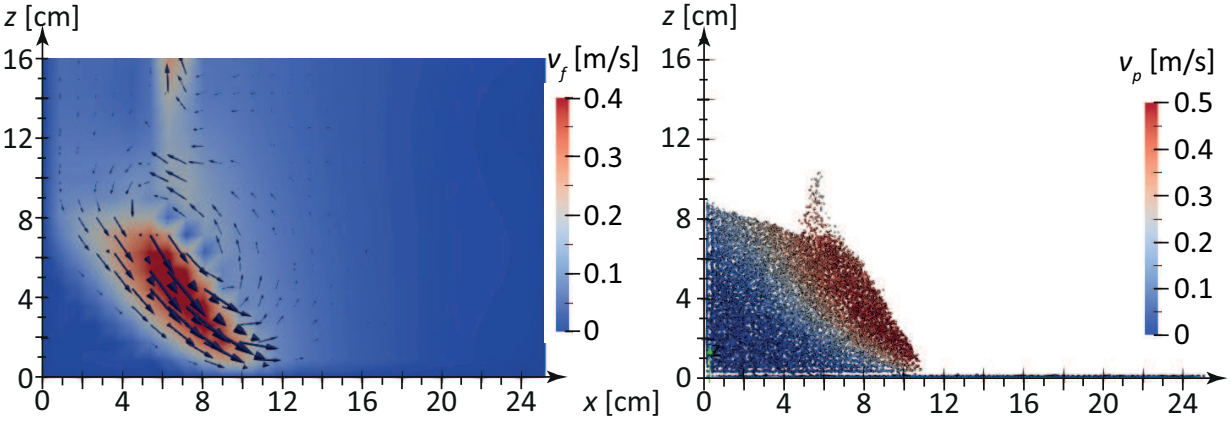

(b) $t \approx 2.0\ t_c$

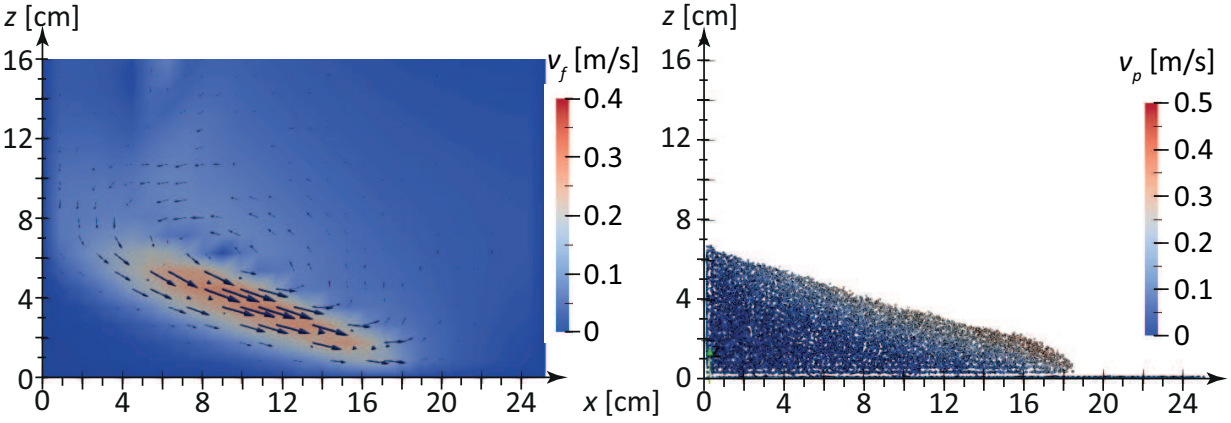

(c) $t \approx 4.0\ t_c$

Figure B.30: Fast collapse of a submerged particle column with 3 mm glass particles - Collapse characteristics over time for the fluid (left) and the particle phase (right)

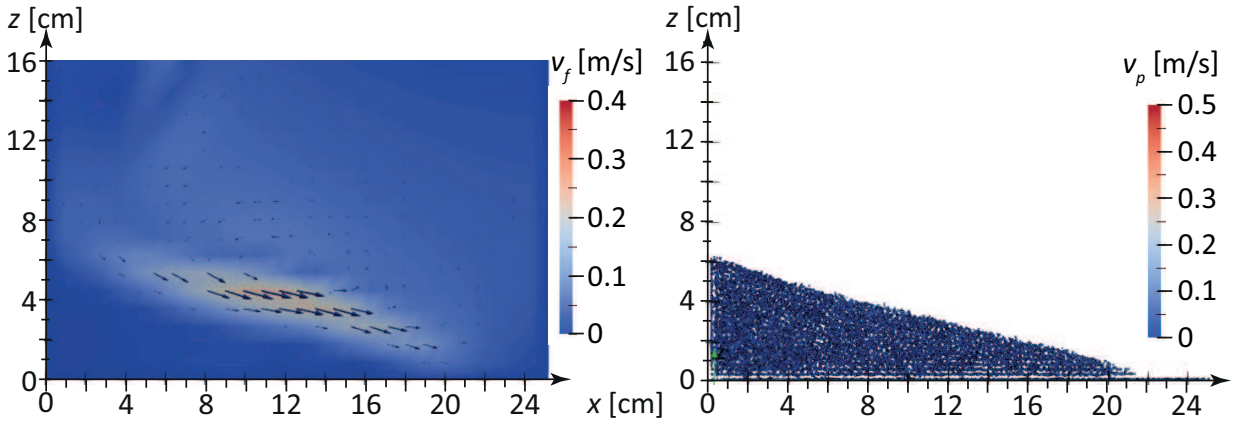

(a) $t \approx 6.0\ t_c$

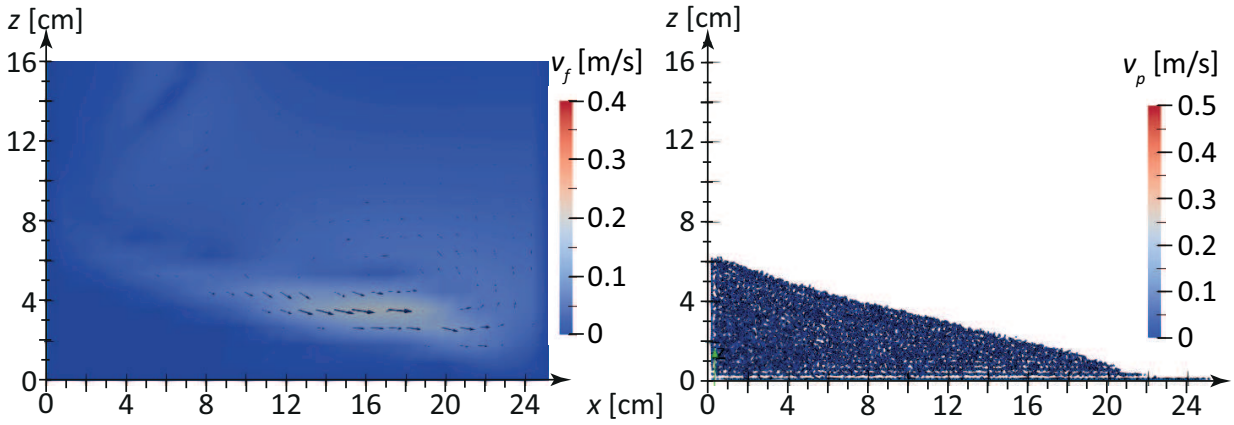

(b) $t \approx 10.0\ t_c$

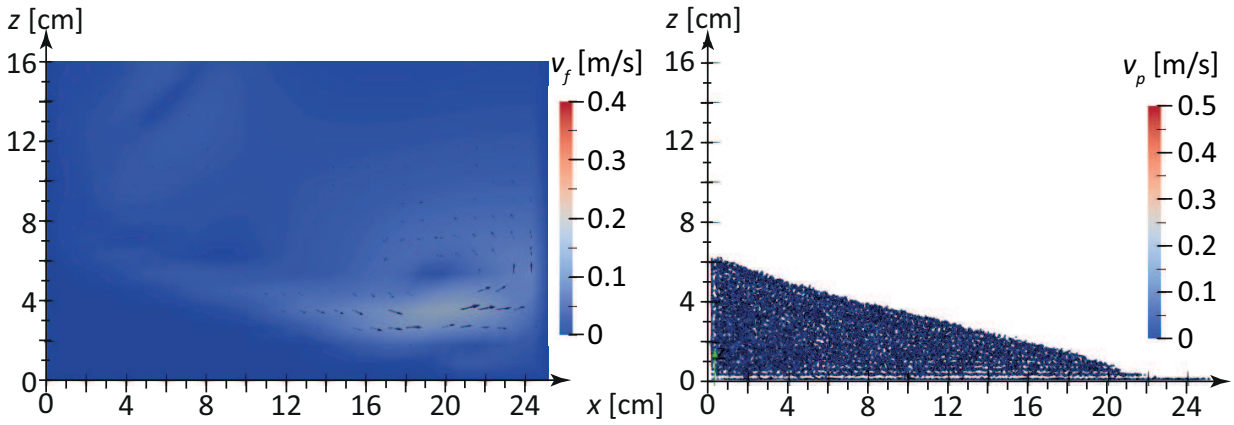

(c) $t \approx 14.0\ t_c$

Figure B.31: Fast collapse of a submerged particle column with 3 mm glass particles - Collapse characteristics over time for the fluid (left) and the particle phase (right)

C Investigations on the initiation of sediment transport - Additional figures

C.1 Physical Tests

Table C.1: Mean free flow velocity $V_{f,x}$ in [m/s] for test $d_p = 1$ mm

d_p	1 mm
Test 1	0.3163
Test 2	0.2516
Test 3	0.1631
Test 4	0.2047
Test 5	0.0986
Test 6	0.2037
Test 7	0.2336
Test 8	0.1864
Test 9	0.1905
Test 10	0.1497
Test 11	0.2146
Test 12	0.2167
Test 13	0.2517
Test 14	0.1612
Test 15	0.2461
Mean	0.2024
Std. dev.	0.0179

Table C.2: Mean free flow velocity $V_{f,x}$ in [m/s] for test $d_p = 2 - 5$ mm

d_p	2 mm		3 mm		4 mm		5 mm	
Init. pos.	low	high	low	high	low	high	low	high
Test 1	0.1915	0.2569	0.2380	0.2666	0.2899	0.3987	0.3679	0.3931
Test 2	0.2253	0.2316	0.2483	0.3015	0.2899	0.3459	0.3289	0.3885
Test 3	0.1942	0.1862	0.2361	0.3046	0.3041	0.2894	0.3122	0.3967
Test 4	0.1951	0.2443	0.2072	0.3076	0.2962	0.3802	0.3087	0.3615
Test 5	0.1767	0.2614	0.2414	0.3148	0.3034	0.3697	0.3347	0.3917
Test 6	0.2085	0.2393	0.2402	0.2673		0.3571	0.3334	0.3513
Test 7	0.1793	0.2809	0.2860	0.3023	0.2883	0.3468	0.3488	0.3349
Test 8	0.2286	0.2779	0.2220	0.2784	0.2880	0.3665	0.3329	0.3871
Test 9	0.2133	0.2323	0.2313	0.3198	0.3216	0.3636	0.3608	0.4072
Test 10	0.2109	0.2724	0.2679	0.3312	0.2918	0.3208	0.3632	0.3784
Mean	0.2024	0.2552	0.2331	0.3075	0.2970	0.3661	0.3391	0.3790
Std. dev.	0.0179	0.0284	0.0222	0.0219	0.0111	0.0309	0.0195	0.0215

Table C.3: Bed shear stress τ_0 in [Pa] for test $d_p = 1$ mm

d_p	1 mm	
Init. pos.	low	high
Test 1	0.0545	0.1892
Test 2	0.0466	0.1122
Test 3	0.0980	0.1538
Test 4	0.0841	0.1167
Test 5	0.0867	0.1173
Test 6	0.0499	0.1475
Test 7	0.0593	0.1604
Mean	0.0684	0.1424

Table C.4: Bed shear stress τ_0 in [Pa] for test $d_p = 2 - 5$ mm

d_p	2 mm		3 mm		4 mm		5 mm	
Init. pos.	low	high	low	high	low	high	low	high
Test 1	0.1412	0.2755	0.2680	0.1561	0.4309	0.7147	0.6446	0.7585
Test 2	0.2095	0.1869	0.2595	0.2065	0.3545	0.5540	0.5438	0.7587
Test 3	0.1564	0.1288	0.2676	0.1958	0.4401	0.2799	0.5344	0.7697
Test 4	0.1552	0.2372	0.2199	0.4399	0.4534	0.5147	0.5046	0.5932
Test 5	0.1120	0.2568	0.2581	0.4328	0.4554	0.5048	0.5641	0.8045
Test 6	0.1783	0.2087	0.2748	0.3283	-	0.4549	0.5608	0.6194
Test 7	0.1385	0.2670	0.3568	0.4094	0.4298	0.4479	0.6379	0.5601
Test 8	0.1986	0.2799	0.2238	0.3496	0.4294	0.4956	0.5692	0.7498
Test 9	0.1860	0.2253	0.2616	0.4614	0.4841	0.4731	0.6735	0.8316
Test 10	0.1834	0.2838	0.3402	0.4641	0.4110	0.4047	0.6165	0.6341
Mean	0.1659	0.2350	0.2745	0.3444	0.4321	0.4844	0.5849	0.7079

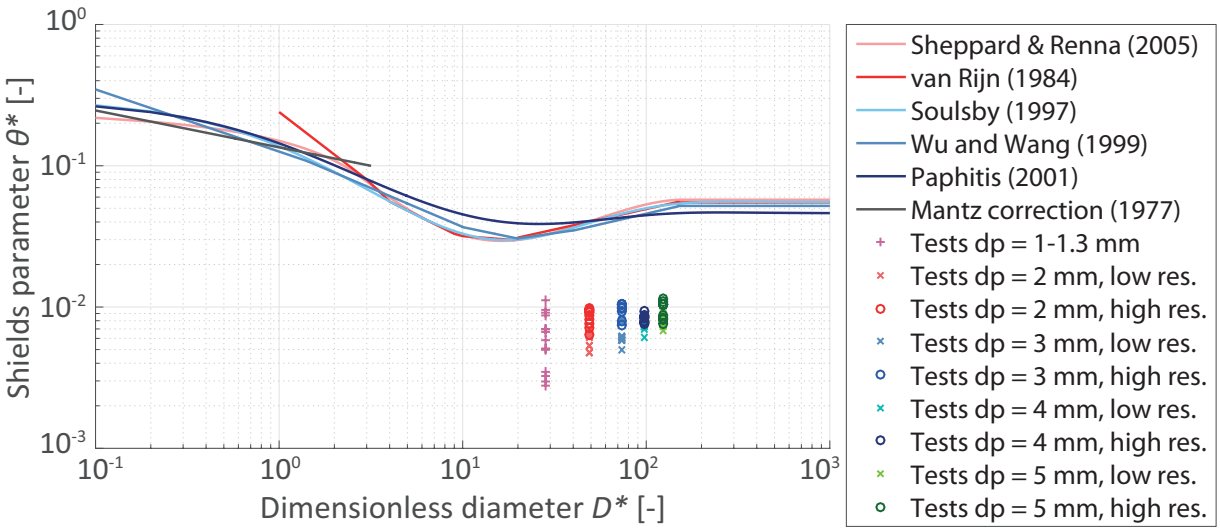

Figure C.1: Modified Shield's diagram including the critical Shields parameters resulting from the physical tests